University of Southampton

Faculty of Engineering and Physical Sciences

Computational Engineering and Design

Effects of morphing wings on aerodynamic performance and energy efficiency improvement for ground effect vehicles.

by

Dominic Robert Clements

Thesis for the degree of Doctorate of Philosophy

4th May 2023

University of Southampton

Abstract

Faculty of Engineering and Physical Sciences
Computational Engineering
Doctorate of Philosophy

Effects of morphing wings on aerodynamic performance and energy efficiency improvement for ground effect vehicles.

by Dominic Robert Clements

In this study, morphing wings in ground effect were investigated with the intent of applying to UAV craft in ground effect to improve the aerodynamic performance using CFD at a Reynolds number of 320,000. First, an aerofoil selection was carried out using RANS with K-Omega SST in two and three dimensions. The NACA6409 was a compromise between high aerodynamic efficiency, high lift, and substantial thickness for structural constraints and space to store morphing systems. Morphing was applied to a two-dimensional aerofoil in ground effect using the FishBAC morphing method and steady-state RANS CFD. Morphing the aerofoil increased the lift due to the reduced distance between the trailing edge and the ground, which enhanced the ground effect. Gains in aerodynamic efficiency were seen for low angles of attack up to 4 degrees with small trailing edge deflections. The same improvements were seen using unsteady dynamic morphing with URANS; this was due to considering UAV actuator speeds for the morphing period which resulted in a quasi-static flow. For the dynamic morphing, it was seen the lift was slightly higher and the drag somewhat lower from the increased detail captured by using URANS. The FishBAC morphing in ground effect was compared to traditional control surfaces in ground effect and morphing in freestream. For the same trailing edge deflection, morphing wings generated more lift and were more aerodynamically efficient due to a continuous surface and smooth changes in geometry. Periodic morphing was carried out in 10% ground clearance in two dimensions, which increased the aerodynamic efficiency by 80.5% and lift by 15.1% whilst reducing the drag by 36.7% for a Strouhal number of 3.58 and a trailing edge deflection of 1%. The increase in aerodynamic efficiency was due to the Von Karman shedding interaction between the shedding vortices and the motion of the ground plane, which caused thrust. Three-dimensional wings with morphing in ground effect were also investigated to see the impact of a finite aspect ratio. An optimisation study was carried out in three dimensions where a tip chord of 20% of the root with a forward wing tip position showed 12.42% higher lift and 35.95% higher aerodynamic efficiency at h/c = 0.1 compared to a rectangular wing. The low angle of attack at the root with forward wing tip position and small tip chord resulted in the pressure on the lower surface of the wing feeding the wingtip vortex less than the rectangular wing. The small tip chord also increased the aspect ratio of the wing. Camber morphing was applied to a three-dimensional wing where the start and end location of morphing along the span was investigated using steady RANS simulations. Applying the camber morphing along the full span length resulted in smaller trailing edge deflections to achieve the same change in lift compared to applying the morphing for a small proportion along the span. Morphing wingtips using FishBAC morphing in the span direction increased the lift and reduced drag. Starting the morphing earlier in the span direction resulted in a greater proportion of the lower surface being closer to the ground, further enhancing ground effect. For a fixed wing tip clearance of 2%, the root height was varied using FishBAC wing tip morphing to simulate an aircraft varying altitude. It was seen for a ground clearance of h/c = 0.1 that the drag reduced by 15% and for h/c = 0.3 the drag reduced by 23%. Finally, span morphing was also investigated to increase the wing aspect ratio, and it was seen the optimised wing efficiency increased from 22.7 for 100% span to 31.43 for 150% span length. Therefore, large spans show increased endurance and range whilst lower spans allow roll of the craft. The study focused on UAV craft where the optimised wing had an endurance of 0.95 hours and a range of 38.65km. The optimised wing endurance was 50.8% and the range was 73.7% higher than the baseline rectangular wing. Increasing the optimised wingspan to 150% increased the endurance to 2.12hours and range to 63.97km. Applying periodic morphing showed the optimised wing had a range of 48.4km and an endurance of 1.59hours which was a gain of 217.5% for the endurance and 252.3% for the range compared to the rectangular non-morphing wing. A span of 150% with periodic morphing showed an increase in range of 460.3% and endurance of 362%.

Table of Contents

Table of Tables

Table of Figures

Table of Figures

Table of Figures

Table of Figures

Table of Figures

Table of Figures

Table of Figures

Research Thesis: Declaration of Authorship

Print name: Dominic Clements

Title of thesis: Effects of morphing wings on aerodynamic performance and energy efficiency improvement for ground effect vehicles.

I declare that this thesis and the work presented in it are my own and has been generated by me as the result of my own original research.

I confirm that:

1. This work was done wholly or mainly while in candidature for a research degree at this University;
2. Where any part of this thesis has previously been submitted for a degree or any other qualification at this University or any other institution, this has been clearly stated;
3. Where I have consulted the published work of others, this is always clearly attributed;
4. Where I have quoted from the work of others, the source is always given. With the exception of such quotations, this thesis is entirely my own work;
5. I have acknowledged all main sources of help;
6. Where the thesis is based on work done by myself jointly with others, I have made clear exactly what was done by others and what I have contributed myself;
7. None of this work has been published before submission

Signature: ..... Date: .....

Acknowledgements

First and foremost, I would like to thank my funding body ESPRC for funding this project. Without their support this project would not have been possible. I would also like to thank my supervisor Dr Kamal Djidjeli for his help and advice throughout this project. Without his help and support, this project would have not been possible. I would also like to thank the people in my office where engineering discussions pushed the advancement of each other's projects. I would also like to thank everyone who helped me complete my undergraduate studies which without the immense help, support and one to one tutorials, I would have not reached PhD level and this research project would have not taken place.

Most importantly I would like to thank my parents Robert and Marina Clements, without their continuous and immense support, I would have not been able to carry out higher level education. I would like to thank my best friend Matthew Bennett for standing by me throughout my college and university studies and without him may have not found my passion for engineering. I would like to thank my cat Amber who has been by my side throughout my university studies, she has immensely helped to identify when I was stressed and then destress myself through wanting to be petted and played with and I dedicate this thesis to her. Finally, but by no means least, I would like to thank my girlfriend for her support and also her family.

Nomenclature

Definitions

A_{TE}.....Distance between trailing edge and ground.

A_x.....Distance between arbitrary point along chord on lower and ground.

Aw.....Wing planform area.

a_o.....Gradient of lift curve in two dimensions.

a.....Gradient of lift curve in three dimensions.

α.....Angle of attack.

α_r.....Angle of attack root.

α_t.....Angle of attack wingtip.

c.....Chord.

C_{batt}.....Battery Capacity.

Cd.....Coefficient of drag.

Cl.....Coefficient of lift.

Cd'.....Drag fluctuation.

Cl'.....Lift fluctuation.

Cp.....Pressure coefficient.

Ct.....Thrust coefficient.

d.....Distance from ground to wingtip.

Δx_g.....Mesh grid smallest cell size.

E.....Endurance.

e.....Oswald efficiency.

ε.....Relative error.

η.....Combined efficiency of power system of a UAV.

$f_{c,m,f}$.....Coefficient corresponding to mesh size.

f_o.....Oscillation frequency.

F_s.....Factor of Safety.

Nomenclature

F_T ..... Thrust.

Γ ..... Vortex strength.

h ..... Distance from trailing edge to ground.

h_s ..... Distance between arbitrary point along span on lower and ground.

K ..... Induced drag factor.

k ..... Reduced frequency.

L ..... Lift.

Λ ..... Sweep angle root and tip mid chord.

m_{flux} ..... Mass flux.

M ..... Maximum camber in percentage of chord.

m ..... Mass flow rate.

n_{batt} ..... Battery temperature and age parameter.

ω ..... Vorticity

p_{zero} ..... Zero grid spacing coefficient value.

x_{max} ..... Position along chord of maximum camber.

p ..... Pressure.

r ..... Grid refinement ratio.

R ..... Range.

ρ ..... Air density.

S ..... Wingspan.

Sw ..... Wing tip position.

t ..... Time.

T ..... Tip deflection.

τ ..... Shear stress.

t_{aero} ..... Aerofoil maximum thickness.

tc ..... Wingtip chord.

u ..... Velocity.

u_∞ ..... Velocity freestream.

u^+ .....Non-dimensional velocity.

V .....Battery voltage.

w_{te} .....Trailing edge deflection.

W .....Weight of aircraft.

x .....Arbitrary position along chord.

x_p .....Location from leading edge of maximum aerofoil thickness.

x_s .....Morphing start location from leading edge.

y^+ .....Non-dimensional wall distance.

y_c .....Aerofoil camber line y coordinate.

y_t .....Aerofoil upper and lower surface y coordinate.

y_{ts} .....Aerofoil trailing deflection in time.

z .....Arbitrary position along the span.

z/c .....Morphing start location along the span.

Abbreviations

AoA .....Angle of Attack.

AR.....Aspect Ratio.

CFD.....Computational Fluid Dynamics.

CFL .....Courant–Friedrichs–Lewy number.

GCI .....Grid Convergence Index.

GE.....Ground effect.

LSD .....Lower surface distance.

NC .....Neighbour Cell.

OC .....Owner cell.

TE .....Trailing edge.

URANS.....Unsteady Reynolds Average Navier Stokes.

RANS .....Reynolds Average Navier Stokes.

DES.....Detached Eddy Simulation.

Chapter 1 Introduction

1.1 Background

Wing in ground effect (WIG) crafts are marine transport in the category between ships and aircraft. Wings are used to generate lift to fly in proximity of a surface such as the sea reducing drag due to air being less dense than water, thus reducing fuel consumption. This allows marine vehicles to travel faster and more efficiently than conventional boats. WIG crafts make use of ground effect to produce a high aerodynamic efficiency. An advantage of WIG craft is that they can take-off and land on water and some cases on land such as beaches or slip ways.

Wings are typically designed to operate at a set flying condition and outside this condition, the wing is not at its maximum efficiency. By changing the shape of a wing, an aircraft can adapt to flying speed and mission to perform at the highest possible efficiency. Morphing can also be used to control the craft allowing control surfaces to be removed. This eliminated the gaps between control surfaces and the wing which are required for movement improving efficiency.

This study will extend the current research and combine ground effect and morphing wings for ground effect craft. This will be applied to a UAV model due to fewer restrictions than full-size craft.

1.2 Motivation

Birds fly by generating lift from their wings, by altering their wings they can manoeuvre seamlessly through the air. Contrary to this, man-made aircraft use fixed-wings with control surfaces that are hinged at the trailing edge to control the aircraft due to the challenges involved in creating a bio-like wing. As research is advanced in morphing wings the technology could provide many advantages.

Understanding the flow physics behind morphing wings will allow greater performance to be extracted from the wing to improve lift, drag and efficiency. Wings are typically designed for an aircraft to carry out a specific purpose or mission, this could include endurance, high-speed aircraft or a high payload mission. Understanding these physics will allow wings to change shape to provide optimum performance for that mission which would provide benefits. This would make the wing more efficient from the number of reduced compromises and in extreme cases reduce the number of wings that would need to be built for specific missions reducing aircraft costs.

Fixed and rotary wing aircraft experience a phenomenon known as ground effect during take-off and landing where pilots notice the characteristics of the craft change close to the ground. Many studies have investigated this phenomenon and have shown there are many benefits to flying close to the ground including increased lift and efficiency. Wings in ground effect are typically applied to marine vehicles. Flying above the water surface significantly reduces the drag due to the craft travelling through a less dense medium. This allows the craft to travel much faster with reduced fuel consumption compared to traditional boats and ships. Wings in ground effect have many challenges with one of the most significant issues being their stability and the complexity of the systems. Understanding the aerodynamics of wings in ground effect will allow greater levels of performance to be extracted from the wings further improving the performance.

Combining the areas of morphing wings and wings in ground effect is of great motivation due to being a newly entered area of research to the author's knowledge. Combining these two areas and understanding the flow physics will advance the understanding of wings in ground effect to improve the performance of the wings.

1.3 Aims and Objectives

The project aims to investigate morphing wings in ground effect to improve the aerodynamic efficiency and apply the morphing wings to a UAV ground effect vehicle to increase the range and endurance of the craft.

The aims will be achieved using the outlined objectives below,

- Carry out a literature review to gain an understanding of the approaches of both morphing wing and ground effect and identify approaches and gaps in knowledge.
- Use CFD to carry out a fixed-wing analysis to investigate the aerofoil performance in two and three dimensions, and key flow physics of wings in and out of ground effect.
- Carry out steady and unsteady simulations of a 2D morphing wing in and out of ground effect.
- Investigate the effect of dynamic periodic morphing on the aerodynamic efficiency of a 2D wing in ground effect.
- Extend the 2D morphing to 3D and investigate the effect of 3D span and wingtip morphing on the wing performance in ground effect.
- Apply the morphing wing to a UAV craft in ground effect and investigate its effect on the aerodynamics performance, range and endurance.

1.4 Research

The originality of the work in this study is combining two areas that have extensive literature (morphing wings and wings in ground effect) and combine them. This to the best of the author's knowledge has not been carried out in previous research. The list of publications and conferences attended confirms the originality of the work in this study.

Journal Papers

Aerodynamic Performance of Morphing and Periodic Trailing Edge Morphing Aerofoil in Ground Effect. (Published February 2023) (Journal of Aerospace Engineering).

Effect of Trailing Edge and Span Morphing on the performance of an Optimised NACA6409 Wing in Ground Effect. (Submitted to Journal of Aerospace).

Periodic Morphing of an Aerofoil in Ground Effect and its Wake mechanisms and Thrust Generation. (Waiting Submission).

Gains in Range and Endurance of a UAV Flying in Ground Effect Using Periodic Wing Morphing. (Waiting Submission).

Conferences

CDT SIS conference (UK) – University of Southampton – 20th November 2019.

Aero & Astro PGR Poster Conference- University of Southampton – 13th October 2020.

UK Fluids 2022 – Sheffield – 5th-8th September 2022.

1.5 Thesis Outline

Chapter 2-Literature Review

This study will be looking at combining morphing wings and wings in ground effect which this chapter gives a brief history and describes key findings from previous research in literature which this study aims to build on. From the literature review identifying the current state of work, the research gaps are identified and the areas of research to be carried out in this study are outlined.

Chapter 3- Theoretical Background and Methodology

In this chapter, a brief overview of higher and lower order methods of aerofoil analysis was discussed. The higher-order method used in this study was discussed in more depth along with some of the key fundamentals and equations being higher methods. An overview of how the

software uses these fundamentals was discussed in terms of how meshing, discretisation etc takes place within the software. The methodology was also presented for the work carried out in this study.

Chapter 4- Fixed-wing in and out of Ground Effect Analysis

This chapter first carried out a mesh independence study in two and three dimensions and validated the simulations to literature. Different aerofoil shapes were then investigated to gain an understanding of how different aerofoil profiles affect the aerodynamic performance of wings in ground effect in both two and three dimensions and to gain an understanding of the key concepts of ground effect. From this, an aerofoil was selected to carry forwards for the rest of the study. An optimisation study was also carried out to investigate the effect of wing twist, wing tip position, taper, and tip chord. An optimisation study was carried out in this chapter to find the optimum three-dimensional wing with the highest aerodynamic performance.

Chapter 5-2D Morphing Wings in and out of Ground Effect

This chapter used the selected aerofoil from chapter 4 and applied FishBAC camber morphing to the two-dimensional aerofoil. First, validation was carried out due to the increased camber which was significantly different to the validated aerofoil in chapter 4. Further validation was carried out for the unsteady simulations by comparing a pitching aerofoil to experimental data for validation of the dynamic mesh and set-up. Static morphing using steady-state simulations was first carried out to gain an understanding of morphing wings in both ground effect and freestream then compared to traditional control surface flaps. The static morphing using RANS was then compared to dynamic morphing with URANS. Periodic morphing was also introduced to improve the aerodynamic efficiency of a wing in ground effect.

Chapter 6-3D Morphing in and out of Ground Effect

This chapter applied morphing in three dimensions where first the effect of how much of the span that was morphed was investigated. Camber morphing was applied to the three-dimensional optimised wing with different start locations at the tip and root in the chord direction. So far, the FishBAC morphing was only applied in the chord direction therefore this was investigated in the span direction to morph the wingtips to further improve the aerodynamic performance of sealing the wingtip vortex. Finally increasing the span using morphing was investigated to improve the endurance and range of the craft whilst allowing a lower span to manoeuvre the craft in roll.

Chapter 7- Morphing Effect on Aircraft Performance

In the previous chapters, it was stated how the various morphing techniques in two and three dimensions improved the performance of the wing. This chapter quantified how much the

improved performance of the different morphed wings increased the range and endurance of a UAV by applying the technology to a wing in ground effect UAV.

Chapter 8- Conclusion

In this chapter the research carried out was summarised and the key findings and contributions to the research were stated. Recommendations are made for future work based on the research carried out in this study.

Chapter 2 Literature Review

2.1 Morphing Wings

2.1.1 Morphing Wings in General

Morphos is a Greek word meaning shape which has been adapted to morph in everyday language, in today's meaning, morph means the ability to transform shape (Li et al., 2018). Applying the word morph to wings describes how wings can change shape during flight known as morphing wings. Morphing wings are bio-inspired seen on birds and flying insects where their wings change shape to allow manoeuvrability, during flight (Groves-Raines et al., 2022; Kilian et al., 2022). Their wings can also rapidly change shape to suit different conditions such as cruising, aggressive manoeuvring, and fold back to allow walking (Bowman et al., 2002).

The first powered aircraft by the Wright brothers observed birds flying which inspired the use of twisting morphing wings to control the aircraft (Chaturvedi et al., 2022) however aircraft since have adopted control surfaces such as ailerons, flaps, rudders, and elevators due to lower complexity and maintenance compared to morphing wings. Research has however continued into morphing wings since the Wright flyer but very few aircraft have flown with morphing wings and the ones that have flown have been unmanned aircraft. With the advances in material technology and smart materials, new morphing technology is a hot topic for research to drive forward more efficient aircraft.

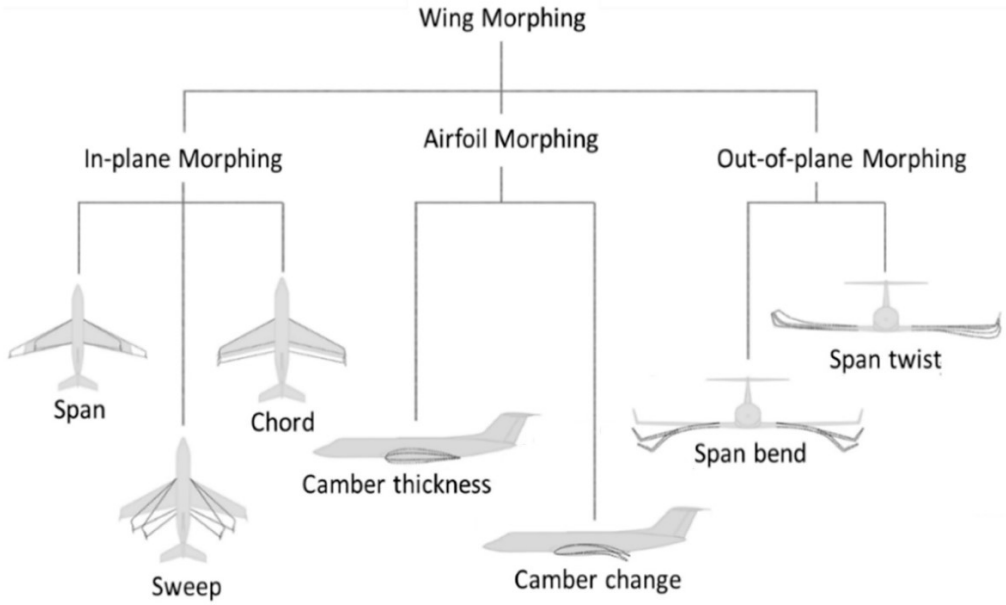

Figure 2.1: Morphing wing categorisation (La et al., 2018).

Morphing wings are classified into three different categories shown in Figure 2.1. In-plane morphing refers to the top view plane of the aircraft wing which includes span, chord or sweep angle geometry changes (Abdessemed, 2020; Bae et al., 2005; Blondeau et al., 2003; Li et al., 2018; Zaini & Ismail, 2016). Out-of-plane morphing refers to changes in geometry where the wing deforms out of the original top view plane such as bending wingtips and wing twisting (Healy et al., 2022; Meyer et al., 2022; Pecora et al., 2012) and the third category of morphing is varying the aerofoil profile, thickness or camber (Abdessemed, 2020; Gern et al., 2002; Li et al., 2018; Zaini & Ismail, 2016).

2.1.2 Advantages and disadvantages of morphing

Advantages

Morphing wings have both advantages and disadvantages which if the technology is to be used on an aircraft, then the advantages must out weight the disadvantages to provide an overall gain in performance. Aircraft wings usually have fixed-wing geometry with aerodynamic devices such as flaps, ailerons, and high lift devices to change the performance of the wing. A drawback to these devices is an increase in the drag from sharp changes in geometry especially with large displacements and also the discontinuous profile (Abdessemed, 2020). Morphing wings allow smaller displacements and provide a smooth continuous profile which increases the aerodynamic efficiency of the wing.

Also, the fixed geometry wing has typically been designed for a flight condition, therefore flying outside this condition will cause sub-optimal flight performance. Therefore, the morphing wing can be designed to switch geometry to the flight condition increasing the performance of the aircraft. Morphing wings can be put into three different levels (low, medium, and high) depending on the type of morphing required to suit the different flight conditions (Bashir et al., 2017). An advantage of a high morphing level is that greater geometry changes can be made, therefore the wing can adapt to a greater amount of flight conditions. The level for different morphing methods is shown in Table 2.1 along with the advantages each morphing method offers.

Table 2.1: Summary of each morphing strategy and morphing level (Bashir et al., 2017).

Morphing level	**Morphing method**	**Advantages**
High	Folding	Increase the critical Mach number. Decrease drags.
	Sweep	Increase the critical Mach number. Decrease high speed drag.
	Variable Span	Increase L/D, loiter time and cruise distance. Decrease engine requirements.
	Deployable	Increase L/D, loiter time and cruise distance. Decrease engine requirements.
Medium	Twist	Increase manoeuvrability. Prevent tip stall.
	Winglet bending	Increase L/D and manoeuvrability. Decrease induced wingtip vortex drag.
	Span bending	Increase L/D and manoeuvrability. Decrease induced drag.
	Variable Chord	Increase low speed aerofoil performance.
	Variable Camber	Increase aerofoil efficiency. Delay separation.
Low	Variable aerofoil	Increase high speed aerofoil performance.
	Camber thickness	Reduction in drag.
	Bulging	Increase wing efficiency. Decrease compressibility (wave) drag.

Figure 2.2 shows the aerodynamic efficiency for a variable camber aerofoil across a range of lift coefficients obtained from wind tunnel tests (Renken, 1985; SZODRUCH, 1985; Szodruch & Hilbig, 1988). The lift coefficient was increased by increasing the angle of attack, the camber was varied at each angle of attack to maximise the lift to drag ratio. Compared to the baseline aerofoil with no morphing, it was seen an increase in aerodynamic efficiency of between 3% and 9% as well as an increased stall angle. It was also observed that the non-morphing showed an abrupt stall signifying leading edge stall whereas the optimised camber was less abrupt signifying trailing edge stall which is safer. Increased aerodynamic efficiency translates into reduced fuel consumption, operational costs and emissions (Martins, 2016).

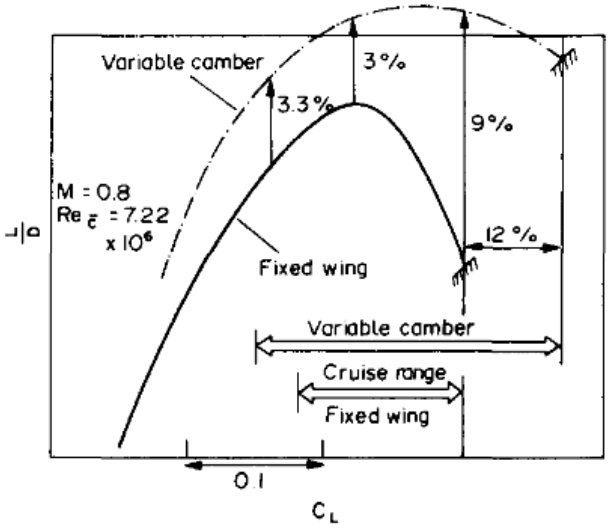

Figure 2.2: Efficiency comparison of fixed and variable camber wing (Szodruch & Hilbig, 1988).

Disadvantages

Although there are many advantages to each morphing method there are many disadvantages. Safety of morphing wings is a large priority and applying morphing wings to aircraft often adds extra points of failure and complexity to systems. Therefore, extra testing and increased inspection and sign-off procedures are required causing extra time and expense to get morphing wings into production. Increased maintenance from the morphing systems means the aircraft is not earning money from its missions. Morphing wings also add an increase in weight which the increase in weight consumes more fuel. If the purpose of the morphing wings is to reduce the fuel consumption, the overall gains in aerodynamic performance need to out weight the gains in mass of the system. For smaller aircraft such as UAVs, maintenance of systems is less of a factor due to smaller less complex systems compared to full-size craft and lower risk levels (Weibel & Hansman, 2005)

It's seen in Table 2.1 that the higher the morphing level the greater the change in aerodynamic performance but a major disadvantage to a high morphing level is the greater level of complexity and increase in weight compared to a lower level (Bashir et al., 2017; Frommer & Crossley, 2005).

Morphing wings such as telescopic span or folding require space to be stored when retracted, when fully deployed this becomes wasted space (Jacob & Smith, 2009). Also, additional space is required for actuators, wiring (Moosavian et al., 2013; Sofla et al., 2009) and mechanisms or linkages. For non-morphing wings, this space would have been used for fuel tanks or cargo.

Another important factor is energy consumption, morphing wings may reduce fuel consumption by improving the aerodynamics but this may be outweighed by the energy consumption required for actuation (Alulema et al., 2020; De Breuker et al., 2007; Vale et al., 2013). There is also the factor of additional weight which increases fuel consumption (Vale et al., 2013) which needs to be

offset by improvements in aerodynamic performance. Aircraft typically have a maximum take-off weight (Chati & Balakrishnan, 2018), therefore the extra weight gain from adding a morphing system would reduce the payload weight. Therefore, an aircraft with morphing will have a lower weight payload capacity than an identical non-morphing aircraft. Lastly, initial costs will be higher for a morphing aircraft, but these may be recovered over time with fuel savings. Initial costs are higher for a morphing aircraft due to the increased complexity, part count, additional sensors and the amount of research, development and testing required to ensure the systems work and function properly.

2.1.3 Camber Morphing

The camber of an aerofoil effectively describes the upper and lower surface of the aerofoil being asymmetric (Fincham & Friswell, 2015) with zero camber referring to a symmetrical aerofoil. Adding camber to an aerofoil typically increases the aerofoil curvature and lift below stall (Fincham & Friswell, 2015), slight increases in camber can have a significant effect on the aerodynamic forces of an aerofoil (Ai et al., 2016; Dhileep et al., 2020; Fincham & Friswell, 2015; Woods et al., 2014) and improve the aerodynamic efficiency (Abdessemed et al., 2022; Ai et al., 2016; Dhileep et al., 2020; Pecora, 2021).

Camber morphing allows the camber of the aerofoil to be increased with a continuous aerofoil surface compared to aerofoils using flaps as control surfaces to increase or decrease the lift to control the aircraft. The gap between the flap and main wing section and sharp changes in geometry cause sudden pressure spikes in the hinged region. Traditional control surfaces also cause instabilities in the flow and recirculation (Macaraeg, 1998). Morphing the camber allows for a continuous smooth aerofoil profile reducing drag and eliminating the pressure spike caused by the control surface gap. A key benefit to camber morphing is the morphed flap can provide the same amount of lift as a traditional flap (Jeong & Bae, 2022) at 30% less tip deflection (Daynes & Weaver, 2012). This reduces the induced drag and improves the aerodynamic efficiency. Figure 2.3 shows a comparison of the streamlines for a traditional flap and morphed flap showing morphing the aerofoil eliminates the discontinuity in the profile resulting in smoother streamlines. Not all flaps induce separation seen as seen in Figure 2.3 depending on the amount of displacement and flow conditions especially when optimised, however, morphing wings still show higher efficiency in these cases mainly due to morphing wings being a continuous surface.

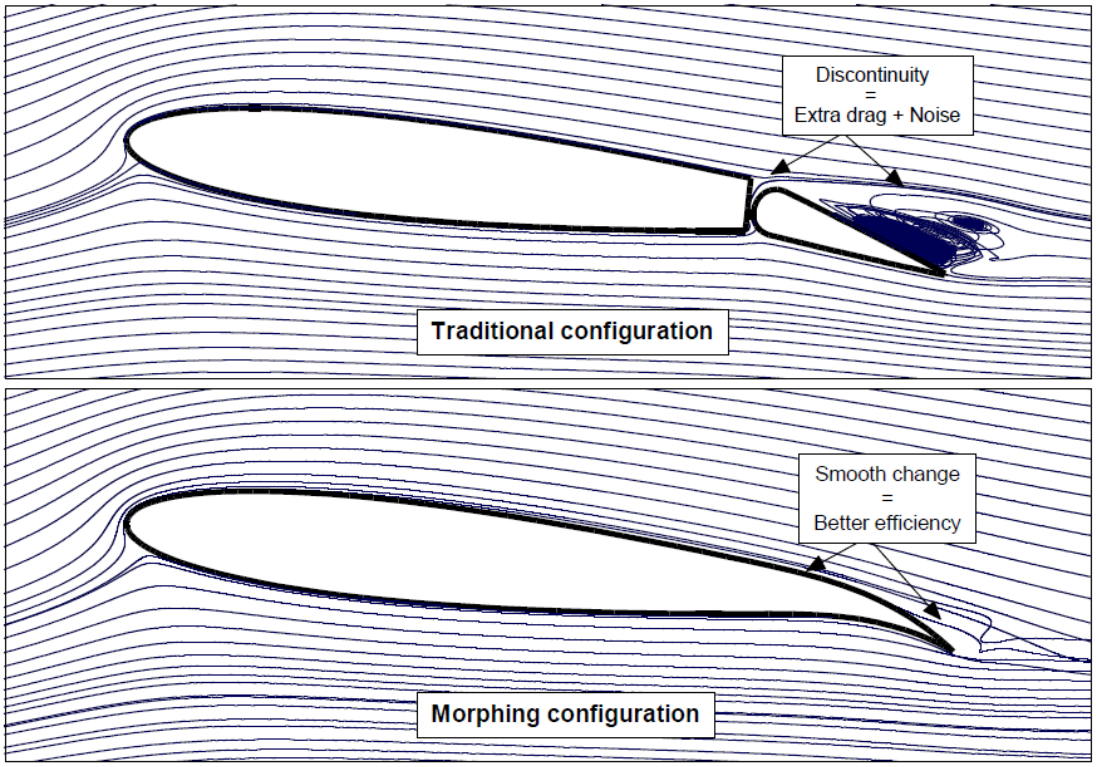

Figure 2.3: Streamlines around flap (upper) and morphed wing (lower) *(Abdessemed, 2020)*.

A morphing camber concept was proposed by Woods et al., (2008) where the camber line was displaced at a user-defined start location and displacement while maintaining the aerofoil thickness (Figure 2.4). This method of morphing has become popular in research (Abishek et al., 2016; Fincham & Friswell, 2015; Soni et al., 2020) due to the curvature being defined by an equation allowing the morphing to be defined in CFD and compared to other studies.

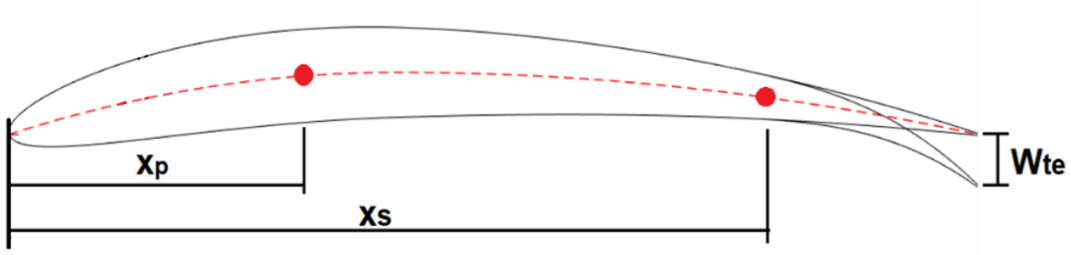

Figure 2.4: FishBAC morphed aerofoil schematic and equation definitions.

The camber line of the NACA aerofoil shown in Figure 2.4 was defined by three separate equations (Eq. 2.1) depending on the value of x along the chord. A non-morphing aerofoil is defined by two equations, first from the leading edge to point p (maximum aerofoil thickness) and from point p to the trailing edge. The FishBAC morphing uses an extra term added to the equation defining the camber from point p to the trailing edge to increase the curvature of the camber line with the start location of the morphing defined by the term x_s and total displacement by w_{te}. After defining the equation of the camber line in Eq 2.1 of the aerofoil, the thickness defined by Eq. 2.2 is then added to the camber line to define the profile of the aerofoil.

$$y_c = \begin{cases} \frac{M}{{x_p}^2}(2x_p x - x^2), 0 \le x < x_p \\ \frac{M}{(1-{x_p}^2)}(1 - 2x_p + 2x_p x - x^2), x_p \le x < x_s \\ \frac{M}{(1-{x_p}^2)}(1 - 2x_p + 2x_p x - x^2) + \frac{-w_{te}(x - x_s)^3}{(1-x_s)^3}, x_s \le x < 1 \end{cases} \quad 2.1$$

$$y_t = 5t_{aero}\left[0.2969\sqrt{x} - 0.126x - 0.3516x^2 + 0.2843^3 - 0.1015x^4\right] \quad 2.2$$

2.1.4 Boundary Layer Control and Periodic Morphing

Periodic excitation transfers a high momentum region to a low momentum region, this can be used to delay boundary layer separation to improve the performance of an aerofoil (Svorcan et al., 2022). Periodic excitation was originally tested using a small flap hinged on a flat surface (Figure 2.5), the hinge would be placed upstream of the flap and the flap would periodically oscillate (Katz et al., 1989; Reisenthel et al., 1985; Wygnanski, 1993). Closing the flap expels a jet-like flow and as the flap goes up a counter-rotating vortex is formed. Both these mechanisms add momentum to the flow (Greenblatt & Wygnanski, 2000).

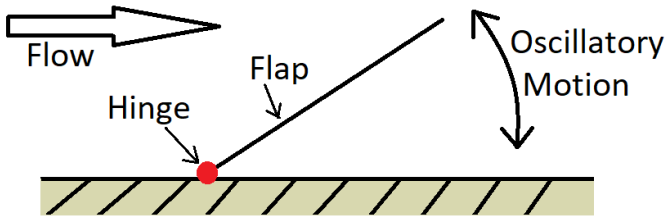

Figure 2.5: Periodic morphing flap schematic.

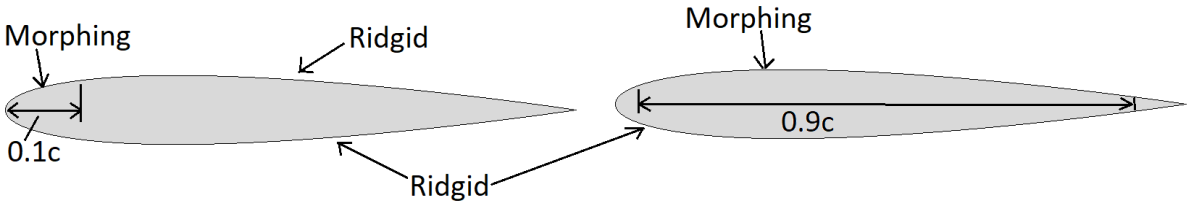

Figure 2.6: Leading edge (left) and upper surface (right) morphing aerofoil schematic.

Periodic morphing has been applied to aerofoils by morphing the upper surface of the leading edge (Kang et al., 2014, 2020) and morphing the majority of the upper surface (Jones, Santer, & Papadakis, 2018) and (Jones, Santer, Debiasi, et al., 2018) shown by the schematics in Figure 2.6. Morphing the aerofoil at low frequencies, showed minimal effect compared to a ridged aerofoil (Kang et al., 2020). Increasing the frequency to the lock-in frequency where the vortex shedding frequency coincides with the surface actuation frequency showed to increase the lift and efficiency as well as reduce the drag by the greatest amount. Increasing the actuation frequency

past the lock-in frequency reduced the gains in performance and at high actuation frequencies the aerofoil was like the ridged aerofoil. It was found that both morphing aerofoil types in Figure 2.6 increased the lift and efficiency and reduced the drag by the same underlying mechanism of adding momentum to the flow.

The underlying mechanism of the periodically morphing upper surface is the rolling up of the separated shear layer creating a clockwise rotating vortex Figure 2.7. This counter-rotating vortex rolls downstream along the upper surface and sheds into the wake. As this vortex sheds into the wake another vortex rolls up and the cycling continues as the surface is periodically actuated. The vortex transfers the momentum from the outer flow into the stagnated flow region (Kang et al., 2020). The mixing of momentum almost eliminates the dead air region shown by the green zone in Figure 2.7. It was also seen the higher actuation frequencies caused the vortex to start to form further upstream on the aerofoil upper surface comparing the two frequencies Figure 2.7b and Figure 2.7b. An interesting observation was made that only the morphing was applied to the suction surface, but the pressure field was affected on both the pressure and suction surfaces (Jones, Santer, & Papadakis, 2018; Kang et al., 2020) which further investigation in the reasons are required (Jones, Santer, & Papadakis, 2018).

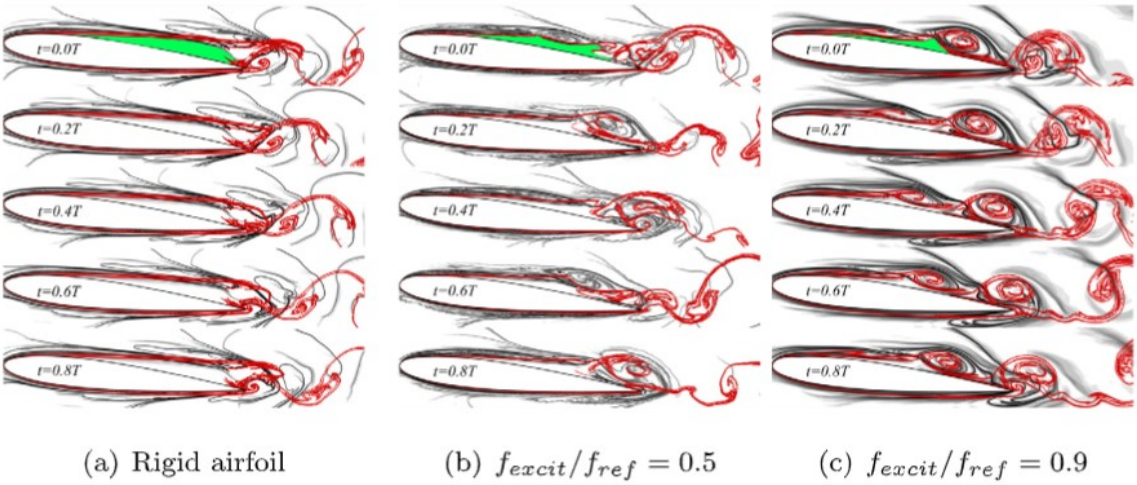

Figure 2.7: Static (a), low (b) and optimum frequency (c) periodic morphing (Kang et al., 2020).

So far, periodic morphing has been applied to the upper surface to reduce the stagnant flow region however a control surface is still required to control the aircraft which separately these two systems each add weight to the aircraft. Applying the camber morphing to the aerofoil trailing edge allows the aircraft to be controlled and periodic morphing of the trailing edge causes momentum transfer.

Applying periodic trailing edge morphing increases the lift and reduces the drag (Abdessemed et al., 2021; Jodin et al., 2017). Two different Strouhal numbers of 0.57 and 4.57 were tested on a NACA0012 for small trailing edge deflections of 0.01% and 0.1% chord (Abdessemed et al., 2021).

For the morphing of the trailing edge, it was identified that the lower frequency and trailing edge deflection had little effect. The higher frequency and 0.1% trailing edge deflection increased the lift by 0.7% and reduced the drag by 1.5% which improve the aerodynamic efficiency by 3%. A vortex formed and rolled down the upper surface before shedding into the wake, after the vortex had shed into the wake, another vortex forms due to the actuation frequency similar to (Jones, Santer, & Papadakis, 2018) and (Kang et al., 2020). Higher trailing edge deflections of 1.5% were tested on an A320 aerofoil (Jodin et al., 2017) where the wake thickness was reduced by 22% due to the actuation which caused a 5% reduction in drag and 2% enhancement in lift.

The stall angle of attack was increased by applying periodic trailing edge morphing (Kan et al., 2020) from 12 degrees to 16 degrees. Two different Strouhal numbers of 0.028 and 0.056 and trailing edge deflections of 0.7% and 1.4% chord were tested. Results clearly show from this study that the higher frequency and lower deflection showed the highest gains in lift. Hysteresis loops during periodic morphing show that the lift on the downstroke is larger than the upstroke which is linked to the flow reattachment being more difficult at higher deflection rates.

2.1.5 Span Morphing

Span morphing wings increase the wing lift by extending the span or reduce the lift by reducing the span (Ajaj et al., 2012; Jeong & Bae, 2022; Muhammad Umer et al., 2020; Y. Yu et al., 2009). Figure 2.8 shows a wing that consists of a base wing that does not morph which generates lift L. Morphing the wing in the span direction causes an increase in lift denoted by ΔL. This was shown in Eq (2.3), where it was seen the increase in lift was due to an increase in the surface area of the wing. On an aircraft, the span morphing can be carried out either symmetric or asymmetric morphing. Symmetric morphing is used to enhance the endurance of a craft whilst asymmetric is used to roll the craft. To achieve the same amount of roll an increase in span of 36% is required as demonstrated by (Ajaj et al., 2012) in freestream.

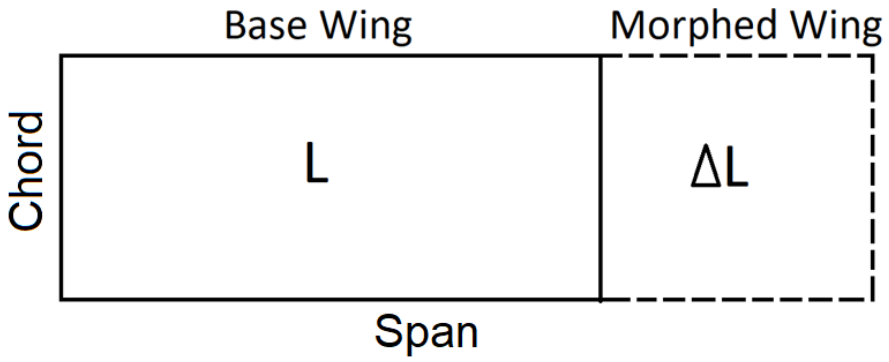

Figure 2.8: Plan view wingspan with no morphing (L) and with span morphing (L+ΔL).

$$L_{Total} = L_{base\_wing} + \Delta L = \frac{C_l u^2 \rho (Area_{base\_wing} + \Delta Area)}{2} \quad 2.3$$

An advantage of increasing the lift on a wing using span morphing compared to traditional control surfaces is having a lower drag value for the same amount of roll authority (Beaverstock et al., 2015). Increasing the area of the wing increases the skin friction drag (profile drag) due to extra shear stress from the increased area the fluid is flowing over the surface as shown in Figure 2.9. Increasing the span of the wing reduces the impact of the wingtip vortex on the wing and there is no increase in downwash compared to a control surface. Therefore, as the span increases the induced drag shown in Figure 2.9 is reduced. Summing both the skin friction and induced drag shows the total drag in Figure 2.9. In certain conditions, extending the span yields a minimum drag value at a certain span before the total drag increases with a further span increase (Ajaj et al., 2012).

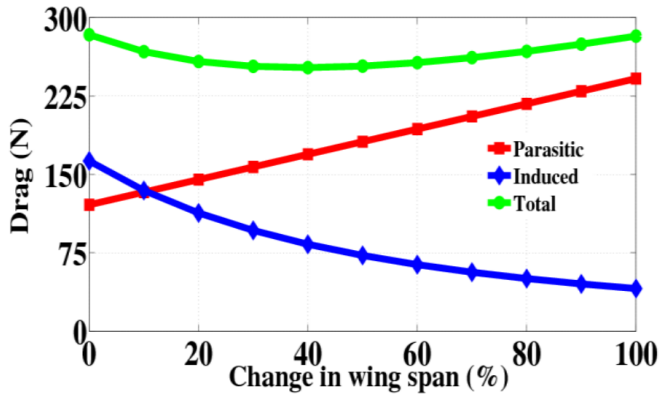

Figure 2.9: Drag of span morphing wing (Ajaj et al., 2012).

The main gains in aerodynamic performance translate into increased range and flight time (Bae et al., 2005) with the span increased for cruise and reduced for manoeuvrability. There are large aerodynamic gains to be achieved using span morphing compared to camber morphing or traditional control surfaces. However, the extra structural requirements and gains in weight make the technology difficult to implement to make an overall gain in performance. Therefore, the gains in aerodynamic performance need to out weight the reductions in performance from the gain in weight of the system need to ensure a sufficient overall gain in performance.

2.1.6 Mechanisms of Morphing

In a computational environment the morphing of a wing can be defined by an equation in which software can numerically deform the model. For real-world wings, the wing must be physically deformed by controlled displacements. There are two main ways to physically deform a wing which include actuators or smart materials. Using either actuators or smart materials is a key

design parameter; therefore, the method of actuation is chosen first when designing a morphing wing for an aircraft. Actuators provide either linear or rotational motion to move and control a mechanism. For UAV applications, the rotational and linear type actuators commonly used are electric in the form of motors, stepper motors and especially servos due to the vast amount of availability on the market.

One example of using a rotational actuator was suggested by Woods et al., (2008) who used a hobby-grade servo to operate a belt which was connected to the trailing edge shown in Figure 2.10 (left). This type of actuation is converting the rotational motion into a linear motion of the belt to morph the camber of the aerofoil. Directly applying the rotational actuator to the aerofoil shown in Figure 2.10 (right) on a segmented aerofoil was demonstrated by Pecora et al., (2016) and Jeong & Bae (2022). The aerofoil is split into multiple segments, an actuator is assigned to each segment and connected rotational point of each segment allowing each segment to be controlled individually. Applying multiple aerofoil profiles along the span allows the wing to be morphed shown in Figure 2.11.

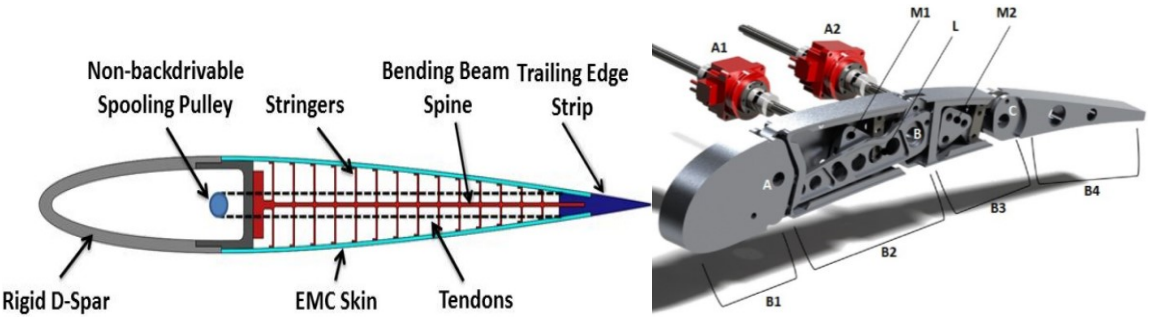

Figure 2.10: FishBAC camber concept (left) (Woods et al., 2008) and segmented camber morphing (right) (Pecora et al., 2016) using rotational actuators.

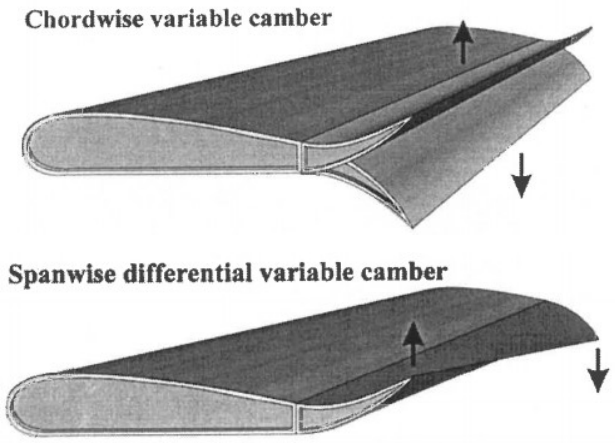

Figure 2.11: Variable camber wing (Monner et al., 2000).

Linear actuators can be used to vary the aerofoil thickness or change the aerofoil profile (Figure 2.12) to maintain the optimum shape and thickness for the flight conditions to significantly reduce drag (Jameson et al., 1994). It was identified that the amount of actuators on a single rib shown in Figure 2.12 adds significant weight and complexity and further research is required to make the concept more feasible for use on aircraft (Jameson et al., 1994). Further studies have been carried out using linear actuators with fewer actuators (Grigorie et al., 2009, 2015; Popov et al., 2010) shown in Figure 2.13 however these studies focus on the control of the system rather than the aerodynamics.

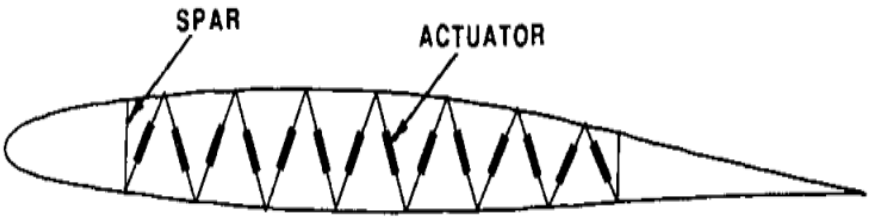

Figure 2.12: Linear actuators used for aerofoil profile adjustment (Jameson et al., 1994)

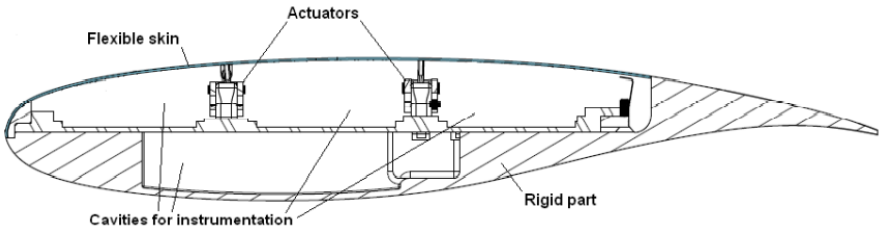

Figure 2.13 Linear actuators applied to aerofoil upper surface (Grigorie et al., 2009)

Linear actuators have also been used for telescopic span morphing (Bishay et al., 2019; Jeong & Bae, 2022; C. Wang et al., 2018) shown in Figure 2.14 where a single linear actuator is aligned with the spars to change the wingspan. A major disadvantage is the substantial increase in weight and complexity and increased aerodynamic loading in the spanwise direction.

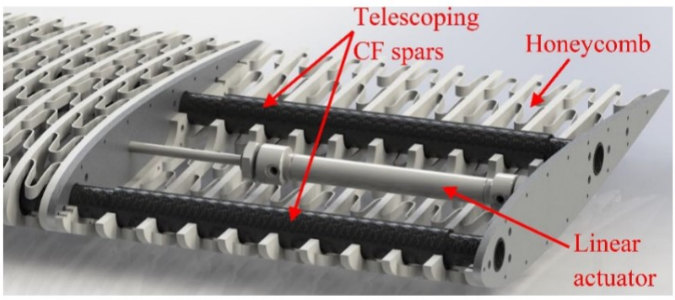

Figure 2.14: Morphing span using a linear a actuator (Bishay et al., 2019).

Smart alloy materials are a class of material that remember their original shape before deformation and returns to their original shape when heat is applied (Leary et al., 2010; Madan et al., 2022). This allows smart alloys to be used as an actuator by cooling and heating the alloy

(Shimoga et al., 2021). Cooling a smart alloy causes the crystal structure to change from an Austenite to a Twinned Martensite, over time the atoms realign themselves relative to their neighbours known as twinning (Bhadeshia, 2017). The Twinned Martensite then becomes Deformed Martensite. Cooling the Martensite from either the Twinned or Deformed crystal structures results in the material returning to its Austenite structure. A schematic of this process is shown in Figure 2.15 however the whole process is relatively slow (Russell & Gorbet, 1995; Tadesse et al., 2010) shown by the time taken to morph the carbon composite wing in Figure 2.18. A key advantage to SMA actuators is the high-power density, lightweight and compact design compared to traditional actuators. An SMA wire can increase its length up to 6-8% however using an SMA wire to create a coil the actuator can increase its length up to 100% of its original length (Koh, 2018). (Russell & Gorbet, 1995; Tadesse et al., 2010).

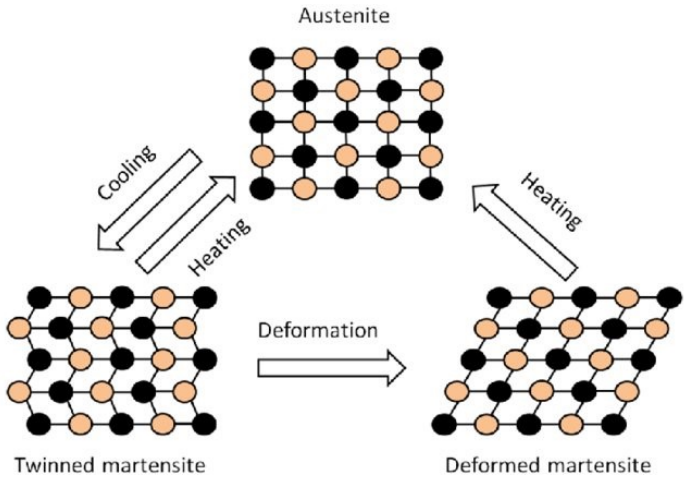

Figure 2.15: Phase transformation of smart alloy materials (Zainal Abidin et al., 2020).

An example of SMA alloys is shown in Figure 2.16 on a segmented aerofoil where a SMA coil is used to deform the aerofoil (Ko et al., 2014). Using SMA as the aerofoil skin eliminates the need for mechanisms within the wing to deform the aerofoil. This can be seen in Figure 2.17 (left), where applying heat to either the upper or lower surface causes deformation of the structure (Elzey et al., 2005) which can be applied to aerofoils (Sofla et al., 2010) shown in Figure 2.17 (right).

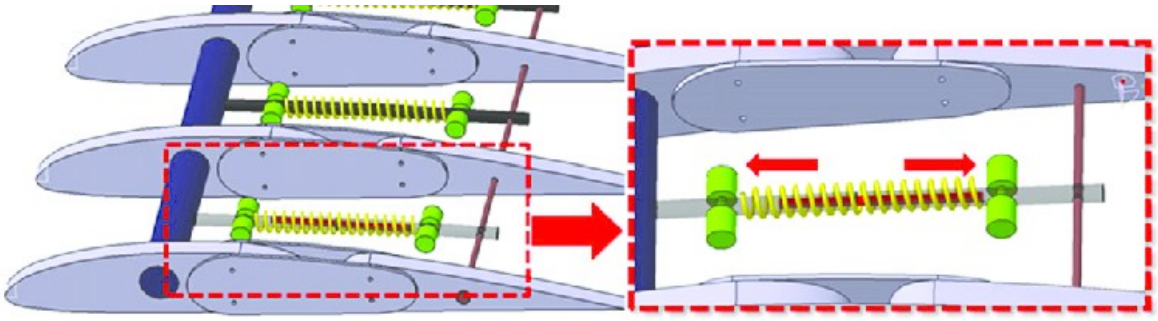

Figure 2.16: Variable camber using SMA actuators (Ko et al., 2014).

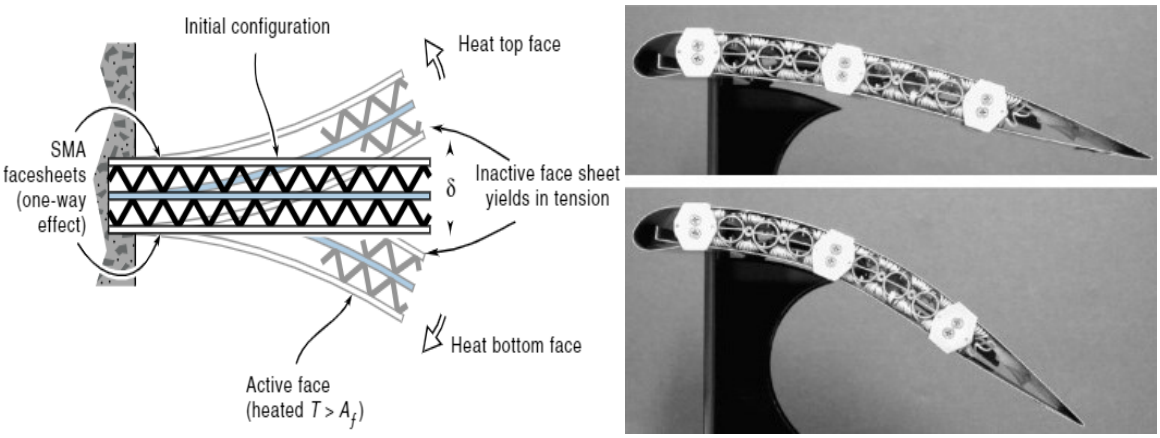

Figure 2.17: Schematic of SMA bending structure (left) (Elzey et al., 2005) and SMA strip applied to a wing in unmorphed and morphed states (right) (Sofla et al., 2010).

Smart polymers are polymers that change their shape by an external stimulus (heat, light, electricity, magnetism, moisture or change in pH level) (Bashir et al., 2017). SMP can be used as a morphing membrane over a structure allowing large deformations of up to 100% strain. These materials are not commonly used in industry due to their low strength and are easily deformed. However, combining composites and SMP has been experimented with to create a structural polymer structure that can change shape (K. Yu et al., 2009; Y. Yu et al., 2007) shown in Figure 2.18.

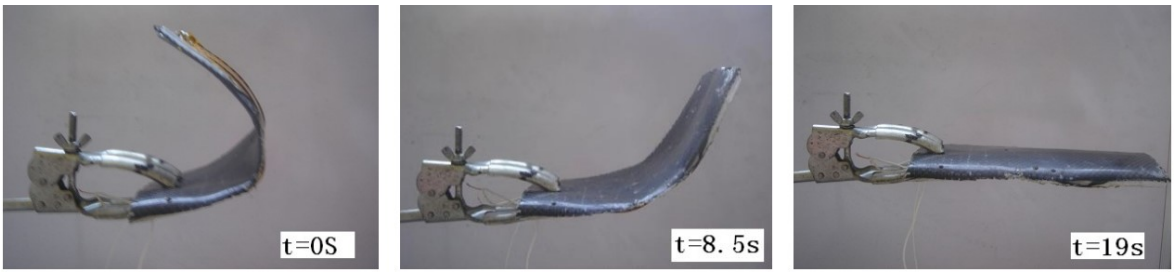

Figure 2.18: SMP carbon composite morphing over time (K. Yu et al., 2009; Y. Yu et al., 2007).

2.2 WIG craft and Wings in Ground Effect

2.2.1 WIG Craft History

Ships and boats have used hydrofoils since the 1950s to lift the craft out of the water reducing drag and increasing the speed. A major problem of hydrofoils is cavitation where the upper lifting surface pressure drops below the water vapour pressure reducing lift and increasing drag (Sinitsin, 1993). Therefore, the wings were placed out of the water to allow the craft to fly in ground effect above the water surface.

In the late 1960s (Rozhdestvensky, 2006) and a team created the first WIG craft the SM-1 (Figure 2.19) which at flew 200km/h over calm water. The design had a low-mounted horizontal tail which caused major pitch stability issues as the horizontal stabilising surface also experiences large variations in lift from ground effect. The SM project evolved through iterations from the SM-1 through to the SM-10 to improve stability issues, increase speed and increase cargo take-off weight.

Figure 2.19: SM-1 Ekranoplan (Yun et al., 2010).

From the SM-5 the project was run alongside the KM project also known as the Caspian Sea Monster (Figure 2.20). The KM could carry 900 marines travelling at 470km/h weighing 544 tonnes, 92.3m long, 37.6m wide and 22m high flying between 4 and 14m above the surface and used 8 jet engines each producing 13 tonnes of thrust (Je, 1995). Over time there were multiple tail variations which confused military observers as it was believed there were multiple KM crafts (Yun et al., 2010). The KM was a top-secret craft developed during the Cold War and spotted on satellite images before being disclosed after the war (Hiemcke, 1994).

Figure 2.20: KM (Caspian Sea Monster) Ekranoplan (Yun et al., 2010).

Smaller versions were created known as the Orlyonok (Figure 2.21) which used a propeller propulsion system with two jet engines to save costs (Yun et al., 2010). This was then adapted to carry guided missiles (Figure 2.22), but the extra weight of the missiles meant the design required a jet engine propulsion system. Also, the craft did not require a bespoke runway and could land on shores. Due to budget cuts and the large expense of the crafts and research, the project was scrapped in 1993 (Yun et al., 2010).

Figure 2.21: Orlyonok WIG craft in flight (Nebylov, 2010).

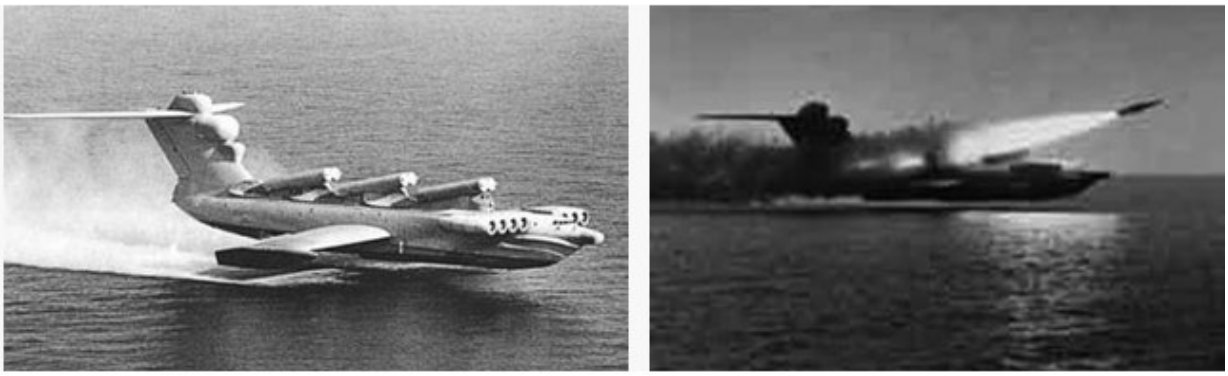

Figure 2.22: Lun WIG craft in flight (left) and missile launch (right) (Yun et al., 2010).

Since the KM project was scrapped there have been several passenger WIG craft developed but most projects never made it past the prototype stages. One craft that is still in development and is available for purchase is the Wigetworks Airfish 8 (Figure 2.23). The craft began development in Germany with the flight trials of the prototype in the 1990s and extensive flight tests carried out in 2001 and 2004. The project was then transferred to a company in Singapore in 2004 (Yun et al., 2010). The craft is made from carbon fibre and is powered by a v8 producing 500hp consuming 70 litres of petrol per hour and a range of 300 miles. The craft is 17m long, 15m wide and 3.5m high and can carry up to 8 people. The top speed is 196km/h with a cruising speed of 148km/h which is much faster than a typical ferry (typical ferry max speed of 50km/h), the craft can fly at a maximum height of 7m (Flaig, 2019).

Figure 2.23: Wigetworks Airfish 8 (Flaig, 2019)

2.2.2 Two-Dimensional Ground Effect

To understand how wings in ground effect work, the research is split into first the aerodynamic effect from the aerofoil profile known as chord-dominated and second the three-dimensional effects known as span-dominated. First looking at chord-dominated effects, it was seen bringing a wing into ground effect increases the lift of the wing (Ahmed & Sharma, 2005; Halloran & O'Meara, 1999; Jamei et al., 2012; K. H. Jung et al., 2008; Wu et al., 2012; Zerihan, 2001). The limiting factor for improved lift is when the aerofoil touches the ground and no flow can pass beneath the aerofoil (Halloran & O'Meara, 1999; Nirooei, 2018). For inverted wings or low angle of attack symmetrical wings, the limiting factor is when stall occurs on the lower surface from extreme ground effect clearances after reaching peak lift in ground effect (Zhang et al., 2006). In literature there are three regimes of ground clearances stated by Rozhdestvensky (2006) which define the ground clearance of an aerofoil by the distance between the trailing edge and ground divided by the chord shown in Figure 2.24. For values of h/c < 0.1 or 10% chord, this is known as extreme ground effect and values of h/c = 0.1 to 0.4 or 10% to 40% known as ground effect and h/c > 0.5 or 50% is known as freestream (Rozhdestvensky, 2006; Yun et al., 2010).

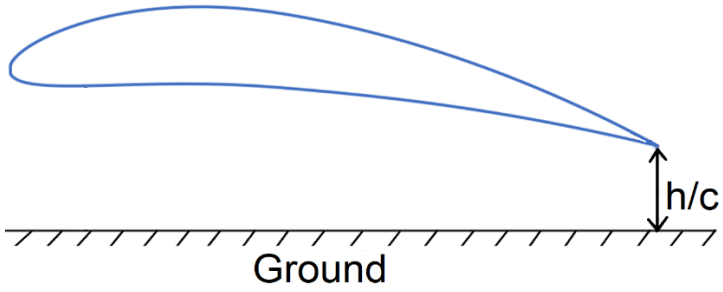

Figure 2.24: Schematic of showing definition of ground clearance.

The increase in lift of an aerofoil is explained by an increase in pressure on the lower surface of the aerofoil. The Kutta condition defines the pressure at the trailing edge which is a fixed value. Therefore reducing the ground clearance caused the pressure to increase upstream of the trailing edge (Qu et al., 2014). This is observed by looking at the pressure distribution shown in Figure 2.25 where the pressure at the trailing edge was the same for all conditions. It was seen that the pressure increased on the lower surface and upper surface when brought into ground effect, this increased the lift generation on the lower surface and reduced the lift generation on the upper surface. Although the lift is reduced on the upper surface, the large gains in pressure on the lower surface results in an overall gain in lift (Qu et al., 2014, 2015; Tremblay Dionne & Lee, 2018). Increasing the angle of attack in ground effect caused the pressure to increase on the lower surface and reduce on the upper as seen in freestream.

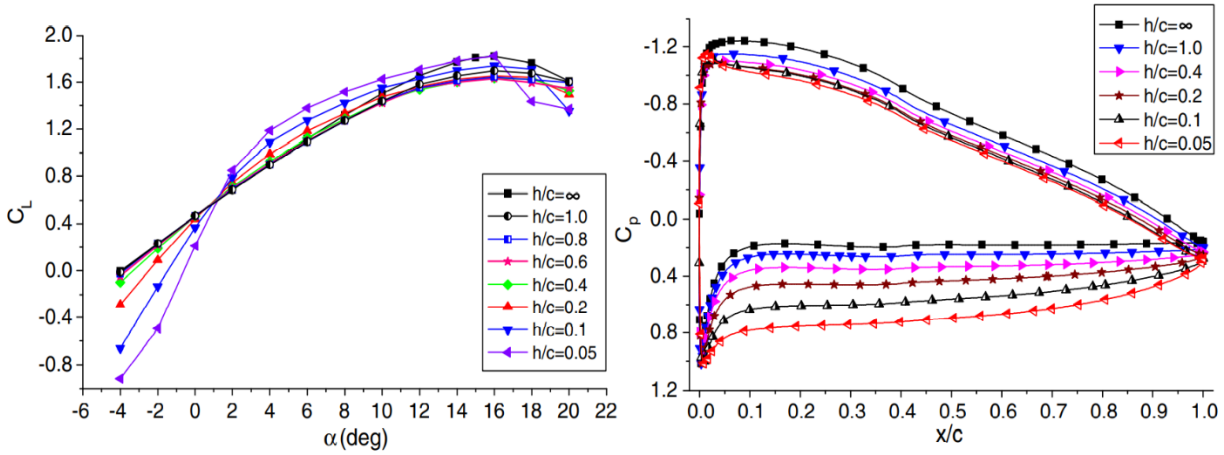

Figure 2.25: NACA4412 lift (left) and 4deg AoA pressure distribution (right) at various ground clearance two dimensions (Qu et al., 2015).

An explanation for the rise in pressure on the lower surface is stated by Halloran & O'Meara (1999) stating that the streamlines are compressed in ground effect and not allowed to expand as seen in freestream (Figure 2.26). The total pressure of the flow must remain constant and can be divided into static and dynamic pressure. The static pressure is associated with the surface pressure and the dynamic pressure is associated with the velocity. As the flow is forced between the aerofoil and ground the dynamic pressure is transferred into a static pressure rise which increases the lift (Halloran and O'Meara, 1999). It was also seen that bringing an aerofoil into ground effect increases the recirculating flow on the upper surface shown in Figure 2.27 (Qu et al., 2015).

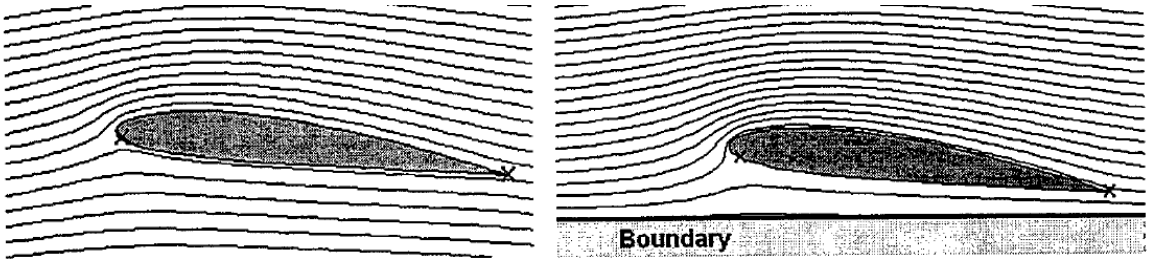

Figure 2.26: Aerofoil streamlines freestream (left) and ground effect (right) (Halloran and O'Meara, 1999).

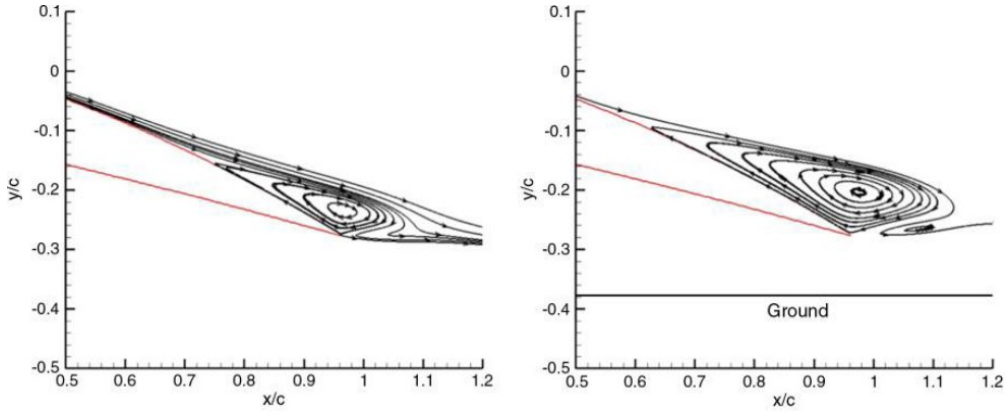

Figure 2.27: Aerofoil in freestream (left) and ground effect (right) showing recirculating flow.

A consequence of the increased pressure on the lower surface is the blockage beneath the aerofoil which reduced the mass flow rate beneath the aerofoil (Nirooei, 2018). The reduced mass flow under the aerofoil means there is a higher amount of accelerated flow over the upper surface causing a stronger suction spike at the leading edge.

The shape of the lower surface of the aerofoil profile and the angle relative to the ground have a large influence on the aerofoil performance. The geometry of the lower surface with respect to the ground is classed as either parallel, convergent, divergent geometry or a combination (Nirooei, 2018) shown in Figure 2.28. The pressure at the trailing edge remains fixed which causes the pressure upstream to vary. Therefore, a convergent passage will increase the pressure upstream of the trailing edge increasing lift. Divergent lower surface geometry will cause the pressure to reduce upstream of the trailing edge causing suction and, in some cases, causing an overall negative lift (Nirooei, 2018; Qu et al., 2015).

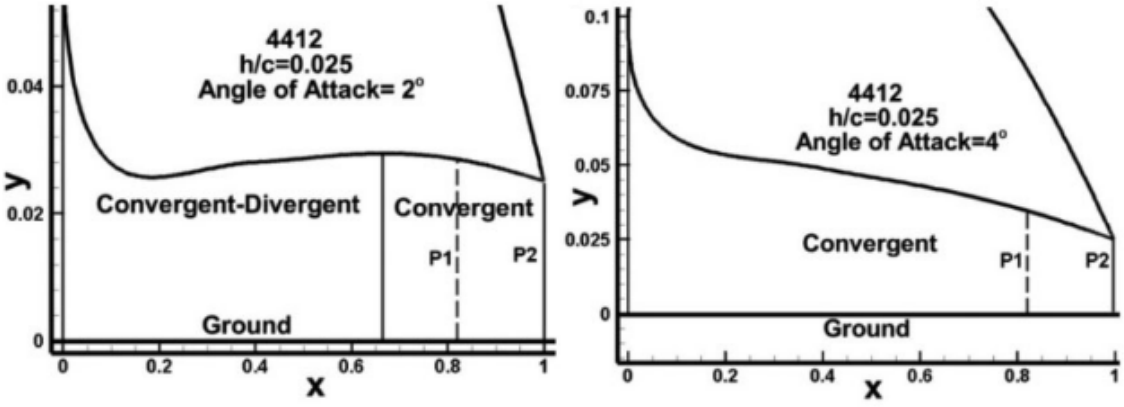

Figure 2.28: Lower surface shape of NACA4412 at 2 and 4 degrees AoA (Nirooei, 2018).

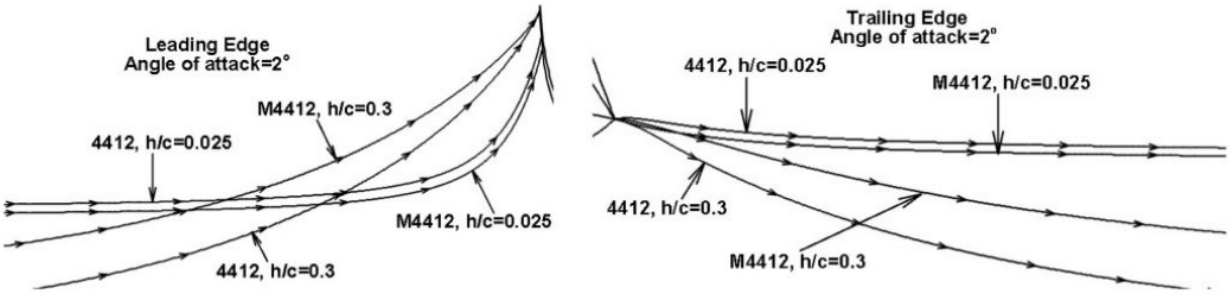

Figure 2.29: Stagnation streamlines of aerofoil at the leading and trailing edge (Nirooei, 2018).

There are two stagnation points on an aerofoil where the velocity becomes zero, one at the leading edge and one at the trailing edge (Nirooei, 2018). The sharp trailing edge defines the location of the trailing edge stagnation point for both freestream and ground effect governed by the Kutta Condition. Reducing the ground clearance reduces the downwash of the streamlines leaving the trailing edge (Nirooei, 2018; Qu et al., 2015; Vogt & Barber, 2012; Xin et al., 2010) due to the proximity of the ground and for small clearances, the streamlines become parallel to the ground (Figure 2.29). The leading-edge stagnation point can vary in location depending on aerofoil geometry and angle of attack. Figure 2.29 shows bringing an aerofoil into ground effect causes the stagnation point to move downstream along the lower surface (Qu et al., 2015; Vogt & Barber, 2012). This is due to a reduction in mass flow rate beneath the aerofoil resulting in a greater amount of flow being accelerated around the leading edge (Nirooei, 2018).

2.2.3 Flaps in Ground Effect

Flaps have been applied to a NACA0015 symmetrical wing (Tremblay Dionne & Lee, 2018) and a NACA4412 non-symmetrical wing (Ockfen & Matveev, 2009) in ground effect. Applying flaps to wings in ground effect causes the trailing edge to become closer to the ground as the flap is deployed shown in Figure 2.30. Deploying the flaps reduces the mass flow beneath the aerofoil forcing a large amount of flow around the upper surface. This caused the lower surface pressure and suction peak to increase observed by the pressure distribution (Figure 2.31) until the limiting case where the flap touches the ground (Ockfen & Matveev, 2009; Tremblay Dionne & Lee, 2018). In the limiting case, nearly all the flow is stagnated beneath the lower surface and the freestream is diverted over the upper surface.

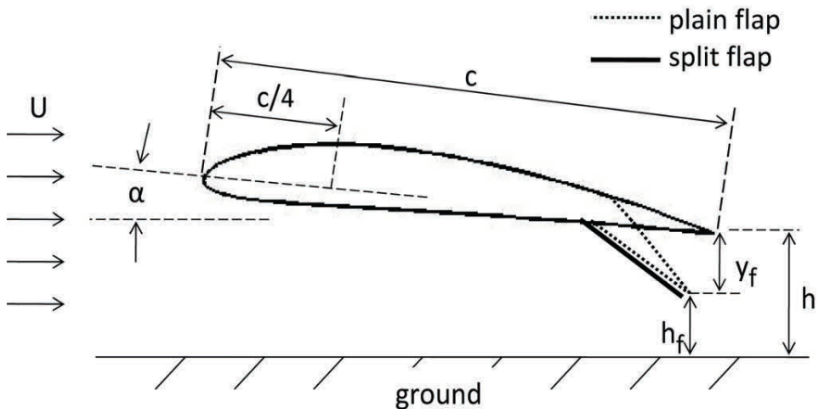

Figure 2.30: Wing in ground effect with flap schematic (Ockfen & Matveev, 2009).

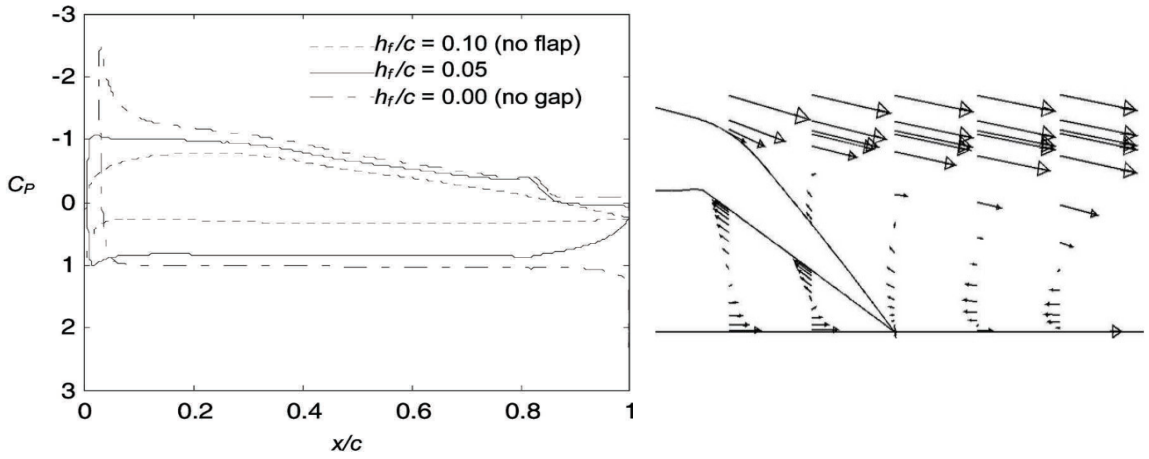

Figure 2.31: NAAC4412 with flap in GE pressure distribution (left) and velocity vectors behind the trailing edge flap (right) (Ockfen & Matveev, 2009).

The key findings mentioned by both Ockfen & Matveev (2009) and Tremblay Dionne & Lee (2018) was for small flap deflections, up to 5% of the chord, that the aerodynamic efficiency increased. Increasing the flap deflection caused the separation point to move further upstream on the flap upper surface (Tremblay Dionne & Lee, 2018). The reason for the separation on the flap is due to the sharp discontinuous geometry shown in Figure 2.31 and the gap between the trailing edge and ground causing a jet-like flow (Ockfen & Matveev, 2009).

2.2.4 Three-Dimensional Ground Effect

Aircraft wings have high pressure beneath the wing and low pressure on the upper surface which causes the high pressure to drive a flow around the wingtip and form a wingtip vortex (Chow et al., 1997) seen by the aircraft in freestream (Figure 2.32). This wingtip vortex reduces the lift and increases the drag of the aircraft wing. The wingtip vortex forms rapidly but can take between 10 to 100 chord lengths to fully develop (Ramaprian & Zheng, 1997). These vortices are highly three-dimensional with strong vorticity components, especially in the span and normal directions to the wing (Ramaprian & Zheng, 1997). The reduction in lift and increase in drag are due to the wingtip

vortices deflecting the flow downwards increasing the lift-induced drag (Chow et al., 1997). Increasing the angle of attack increased the lift linearly as well as increasing the vortex strength and peak value of vorticity. However, the size of the wingtip vortex has no correlation to the angle of attack.

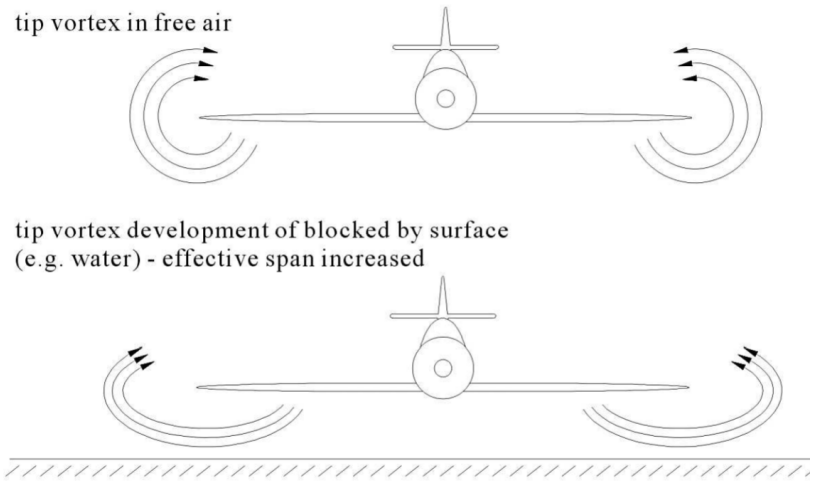

Figure 2.32: Wingtip vortex in freestream (top) and ground effect (lower) (Abramowski, 2007).

Bringing a three-dimensional wing into ground effect pushes these vortices outboard which effectively increases the wingspan (Abramowski, 2007) increasing the lift of the wing and aerodynamic efficiency (Ahmed & Sharma, 2005; K. H. Jung et al., 2008; J. Lee et al., 2010; Lu et al., 2019; Wei & Zhigang, 2012). This was shown by bringing the aircraft into ground effect in Figure 2.32. The proximity of the ground also reduces the downwash reducing the induced drag of the wing (Ahmed & Sharma, 2005; K. H. Jung et al., 2008; J. Lee et al., 2010; Lu et al., 2019; Wei & Zhigang, 2012).

The reduction in drag for a wing in ground effect was seen for a NACA6409 K. H. Jung et al., (2008) in Figure 2.33 and shown for a NACA4406 forward swept wing in a study by Wei & Zhigang, (2012) from carrying out experiments. For a symmetrical NACA0012, the drag was seen to reduce as the wing was brought into ground effect at low angles of attack (J. Lee et al., 2010; Lu et al., 2019). Experiments carried out by Lu et al., (2019) showed above 2 degrees that the drag increased when brought into ground effect which is thought to be due to using a stationary ground. With a moving ground, it was seen by Ahmed & Sharma (2005) who used a NACA0015, that the drag decreased when brought into ground effect for angles of attack from 0 to 10 degrees. It was therefore seen that the type of ground modelling, (stationary or moving) had a large impact on the results of the experiment (Lu et al., 2019) and has a strong influence on the wingtip vortex. The moving ground represents the interaction of the flow with the ground when the reference frame is changed from the aerofoil moving in the real world to being held stationary in CFD or

experiments. The moving ground can be difficult in experiments and often has a higher initial cost therefore many experiments use a stationary ground with boundary layer eliminating techniques.

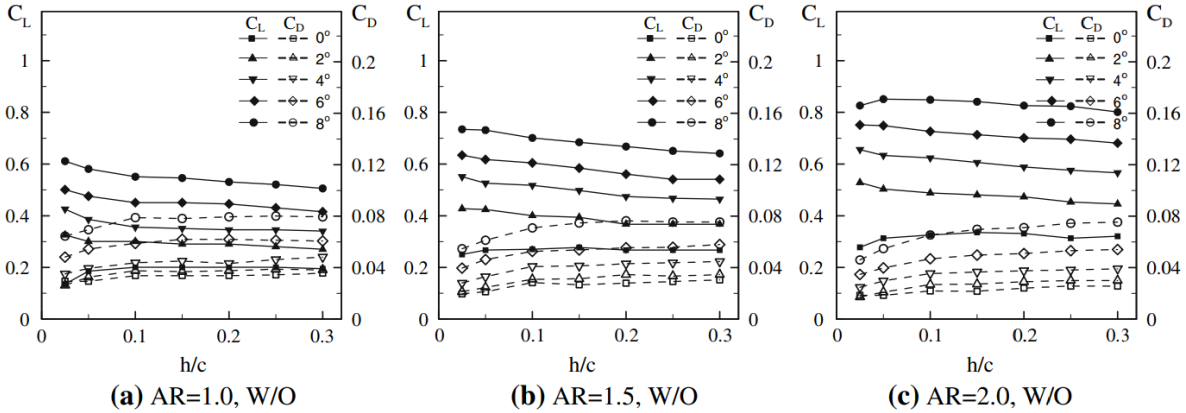

Figure 2.33: Experimental lift and drag of three-dimensional NACA6409 in GE varying AoA and ground clearance without endplates aspect ratios of 1, 1.5 and 2 (K. H. Jung et al., 2008).

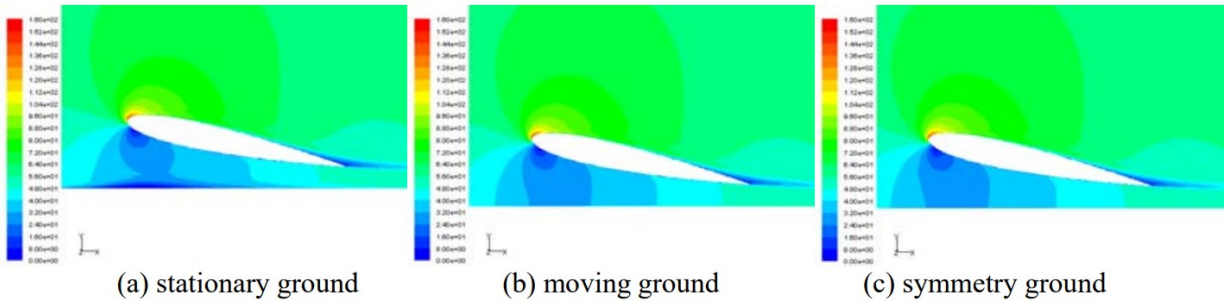

Figure 2.34: Velocity distribution of NACA0012 in GE for different ground conditions.

At the root of the wing, there is high pressure which decreases towards the wingtip, this drives a flow along the span. The induced flow along the ground causes a boundary layer to form on the ground. Since the static pressure within the boundary layer is determined by the freestream, there is an adverse pressure gradient as the flow passes under the wingtip vortex. As the ground clearance is reduced the main wingtip vortex becomes closer to the ground increasing the boundary layer pressure gradient increases causing a separation bubble to form on the ground (Figure 2.35 left). This separation bubble contains vorticity in the opposite direction to the main vortex, the bubble increases in size and then detaches forming a secondary counter-rotating vortex shown in the right image of Figure 2.32. As the secondary vortex rotates in the opposite direction to the main vortex, the secondary vortex induces an upwash which causes the main vortex to elevate compared to the vortex in freestream (Ciffone & Pedley, 1979). The position of the secondary wing tip vortex in the streamwise direction will vary depending on angle of attack and how close the wing is to the ground. For example, a wing in extreme ground effect will show the secondary wing tip vortex upstream of the trailing edge but for a wing just approaching

ground effect this maybe seen several chord lengths downstream as the wing tip vortex increases in diameter.

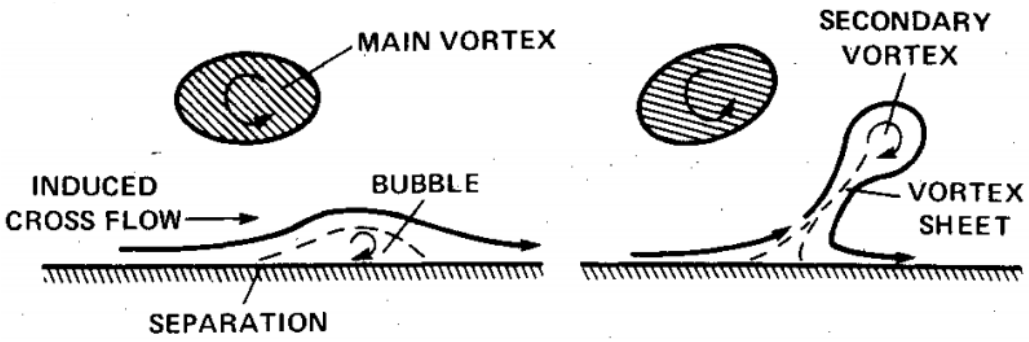

Figure 2.35: Induced span cross-flow of initial boundary layer and separation bubble (left) and later developed secondary vortex (Harvey & Perry, 1971).

2.2.5 Ground Effect End Plates and Wingtips

From the literature review of three-dimensional wings, it has been identified that the wingtip vortex has a strong negative influence on the wing performance increasing induced drag. There is also a reduction in lift due to a spanwise flow element reducing the pressure on the lower surface. The effect of the wingtip performance is considerably stronger for low aspect ratio wings (Fink & Lastinger, 1986; K. H. Jung et al., 2008). Various studies have looked at improving the performance of three-dimensional wings using endplates (J. H. Jung et al., 2012; K. H. Jung et al., 2008; Kumar et al., 2022; Park et al., 2008; Park & Lee, 2008; Wei & Zhigang, 2012).

Endplates are flat plates normal to the span of the wing to try and prevent the high pressure from causing a flow around the wingtip. Attaching the endplate increases the lift with minimal gain in drag when in ground effect and can increase the wing aerodynamic efficiency by 46% (J. H. Jung et al., 2012). The overall effect of the endplate on the tip vortex has increased the vortex strength and the centre of the vortex is pushed outboard (J. H. Jung et al., 2012; Park et al., 2008). This is shown in Figure 2.36 where the main wingtip vortex was pushed outboard. It is also observed that the secondary vortex (discussed in section 2.2.4) is present for the endplate due to the wingtip vortex sitting lower than a wing without the endplate.

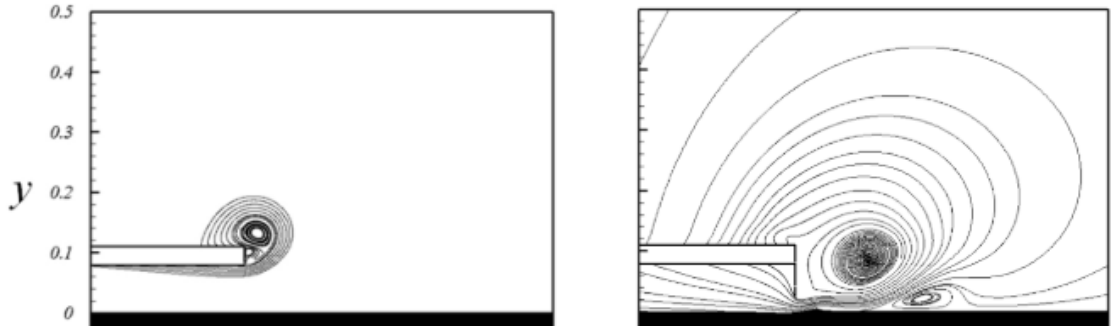

Figure 2.36: Effect of endplate on wingtip vortex for no endplate (left) and endplate (right) in ground effect (J. H. Jung et al., 2012).

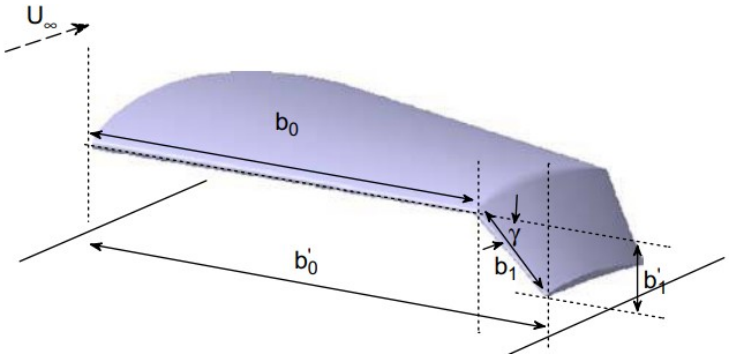

Figure 2.37: Tiltable endplate schematic (Wei & Zhigang, 2012).

The height of the bottom edge of the wingtip to the ground is crucial to sealing the lower surface and this clearance should be as small as possible for maximum performance gains. A study (Wei & Zhigang, 2012) has investigated tiltable wingtips shown by the schematic (Figure 2.37) to seal the lower surface. Figure 2.38 shows the static pressure contours and streamlines for both freestream and ground effect at multiple deflection angles (Wei & Zhigang, 2012). As the wingtip is deflected, the physical span decreases which in freestream shows no aerodynamic improvement (Figure 2.38 right). There are several key observations made, first in both ground effect and freestream the wingtip vortex was pulled downwards as the wingtip was deflected which increased the intensity of the vortex. In ground effect, it was shown (Figure 2.38 left) that the pressure increased beneath the wing as the endplate was deflected due to the deflected wingtip reducing the amount of leakage of high pressure around the wingtip. At high deflection angles in ground effect and low deflection angles in extreme ground effect, a secondary vortex is formed. This is due to the larger adverse pressure gradient on the ground in the spanwise direction from the streamlines being squeezed through a small gap compared to lower deflections.

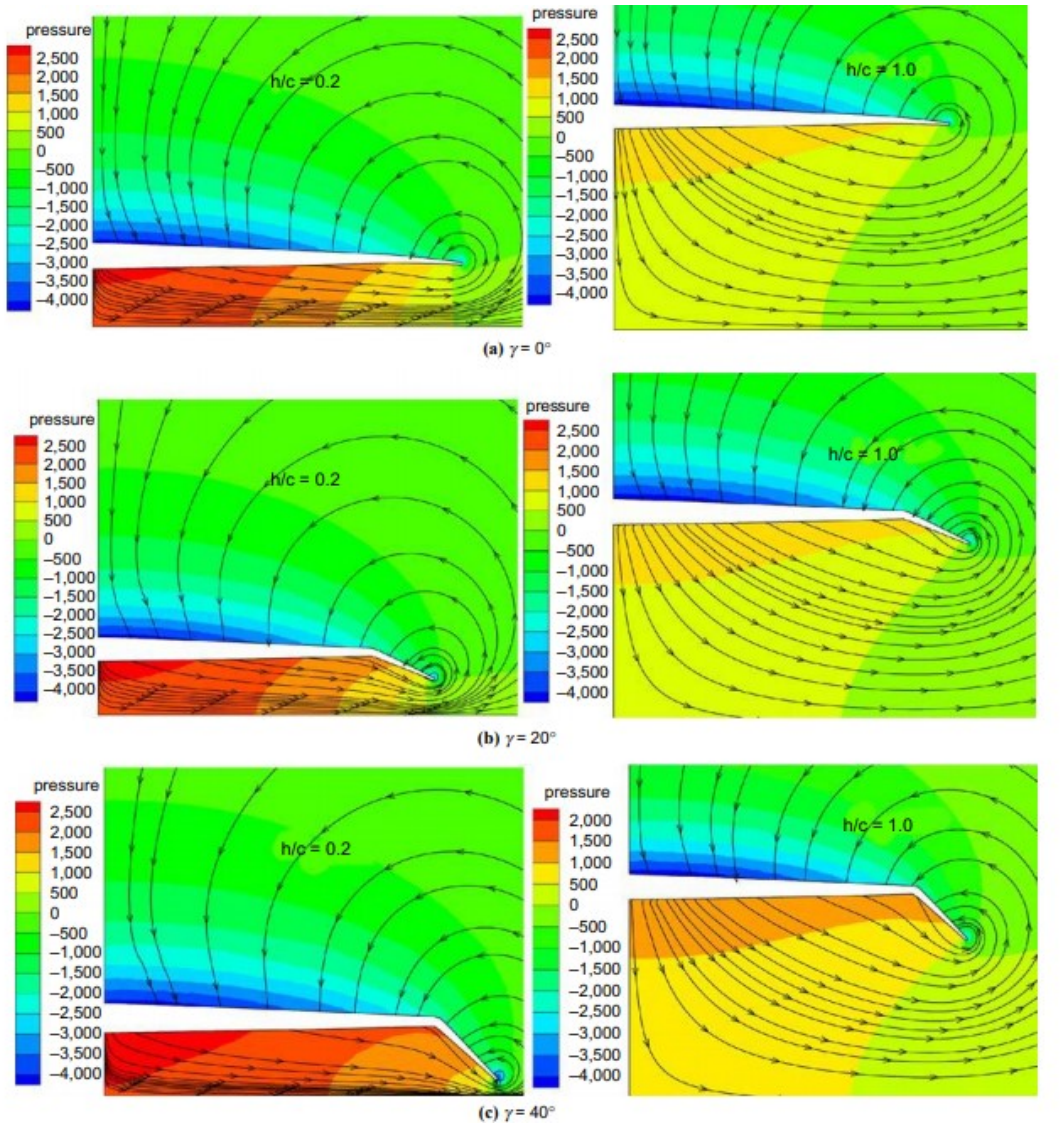

Figure 2.38: Static pressure contours of a tiltable endplate in ground effect (left) and freestream (right) (Wei & Zhigang, 2012).

2.2.6 Pitching Wings in Ground Effect

Ground effect has largely been researched using steady-state and fixed geometry. Studies have investigated pitching aerofoils close to the ground. This was first investigated by Tanida (2001) who investigated pitching aerofoils close to the ground for propulsion inspired by the biology of fish and birds flying close to the ground. It was found that flying close to the ground increased the aerodynamic efficiency and propulsive efficiency of the pitching soft plate. This gain in aerodynamic performance and thrust efficiency was also seen by Quinn et al., (2014).

Thrust generating wakes have heavily been researched for pitching aerofoils in freestream (Andersen et al., 2017; Dong et al., 2022; Koochesfahani, 1989; Triantafyllou et al., 1991) and some studies add a plunging element (Baik et al., 2010; Z. Wang et al., 2020). A study by Quinn et al., (2014) investigated the wake of a pitching aerofoil near a solid boundary and showed the

mechanisms of thrust generation. It was seen in ground effect that the thrust generation was due to the interaction between two counter-rotating vortices shown by the schematic in Figure 2.39. The vortex pairs were counter-rotating and the interaction between the two vortices caused a jet flow which produced thrust. As the vortex pairs travelled downstream, they became more upright, and the resultant velocity vector became parallel to the ground. The study by Quinn et al., (2014) was carried out using particle image velocimetry experiments in which the non-dimensional time average velocity is shown in Figure 2.40. Apparent in the velocity field is the jet flow at the trailing edge caused by the interaction of the two vortices.

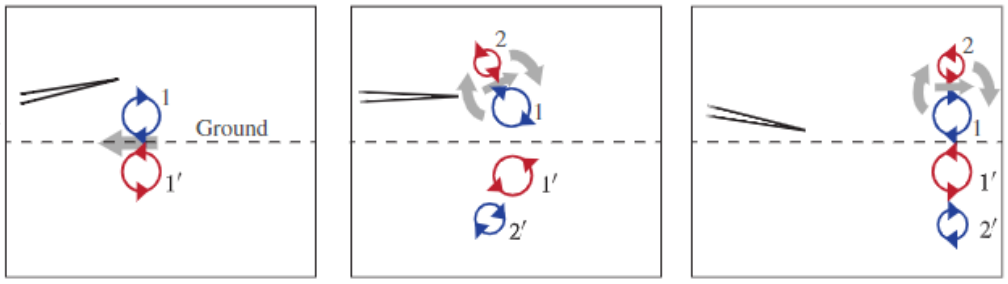

Figure 2.39: Pitching aerofoil vortex pairs in ground effect (Quinn et al., 2014).

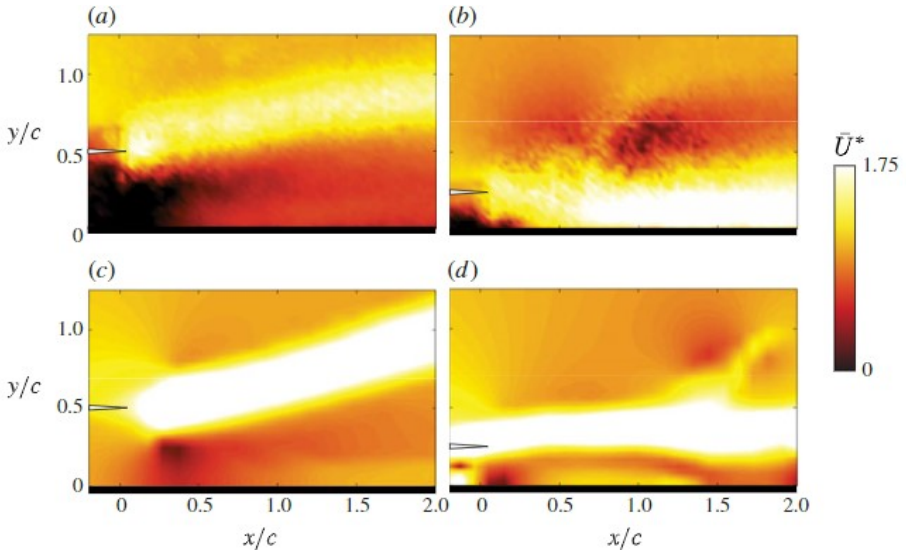

Figure 2.40: Time-averaged velocity of pitching aerofoil using PIV (a, b) and potential flow (c, d) with 50% (a, c) and 25% (b, d) ground clearance (Quinn et al., 2014).

2.2.7 Morphing Wings in Ground Effect

It was seen in literature that there is very minimal research into wings in ground effect. Bio-inspired span morphing was investigated by Hui et al., (2019) applied bird-like folding wings to a wing in ground effect UAV craft seen in Figure 2.41. Although there was no direct comparison to a fixed-wing configuration, it was stated that the morphing wing can reduce induced drag by reducing the wingtip vortex strength. Asymmetrically morphing the wing was investigated and it

was seen the craft can achieve high levels of roll control of the UAV. The Reynolds number was also varied from 93,000 to 187,000 and the span morphing allowed optimum aerodynamic efficiency at each Reynolds number.

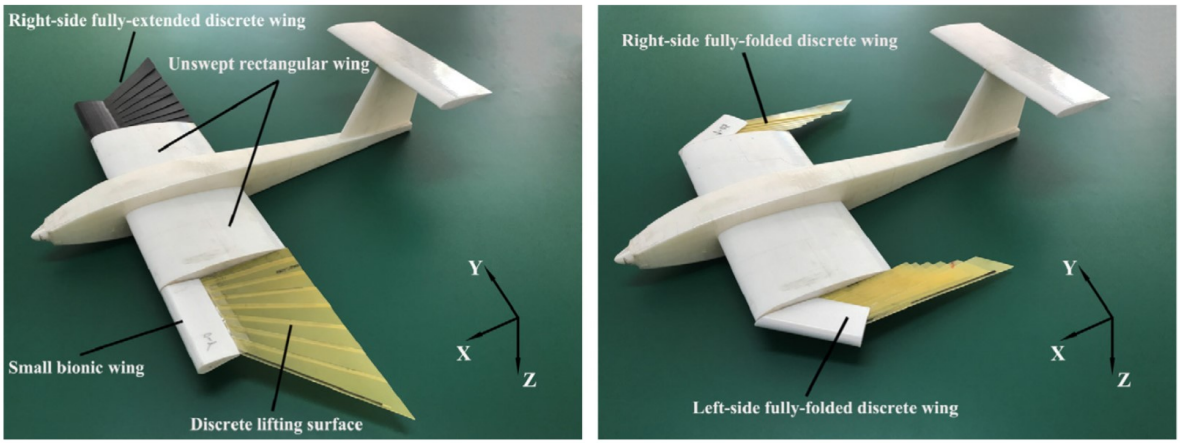

Figure 2.41: Bio-inspired wing in ground effect span morphing UAV (Hui et al., 2019)

2.2.8 Computational Fluid Dynamics for Morphing Wings

Computational fluid dynamics is commonly used for morphing wing application as physical models do not need to be built which to morph a wing structure is a rather complex engineering task. CFD in aerospace has been around since approximately 1960 (Versteeg & Malalasekera, 1995). Since first CFD codes emerged, aerofoil studies were carried out primarily on fixed wing geometry and as CFD codes advanced, Adjoint solvers were used to optimised designs (Albring et al., 2015). Panel codes were first used to investigate shape changing devices seen in a study by Scott et al., (1998) due to limitations in CFD code. One of the limiting factors in the application of CFD highlighted by Levy (2001) was that mesh needed to be regenerated and the simulation would then have to be started from scratch. Chimera grids first emerged in the mid-1980s (Benek et al., 1985; Dougherty et al., 1985; Steger & Benek, 1987), the idea was to produce independent meshes for each component (e.g. a separate mesh for both fuselage and wing) which the meshes can be moved independently to simulate a ridged body motion (Houzeaux et al., 2014). A study by Levy (2001) used FA3DMB finite volume code with overset meshes to simulate half an aircraft with an example given for an elastic fuselage, wing and tail. An example of a overset mesh is shown in Figure 2.42 which shows the geometry cuts a hole in the main background so the region where the geometry is on the main mesh is not computed. It is seen there is an overlap between the main mesh and the mesh of a part which interpolation of the solution is carried out however this interpolation can cause issue from flow properties not being conserved (*User Manual Star CCM+ 14.04.013*, 2019). Overset meshes can be used for morphing multiple segment wings seen in the CFD study by Katam et al., (2005) and experimental study by Pecora et al., (2016).

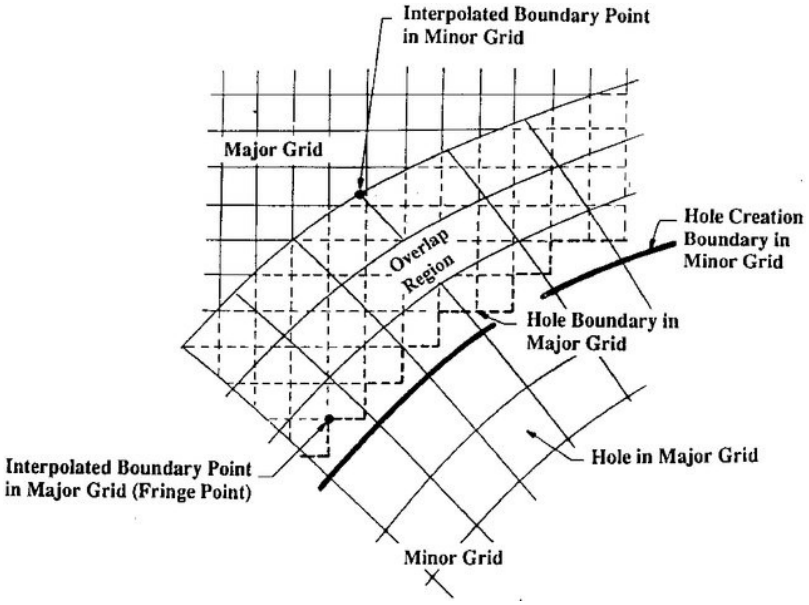

Figure 2.42: Schematic of two meshes for Chimera overset grid (Kao & Liou, 1997).

As both CFD software and hardware has evolved according to Moore's law, higher power simulations. Morphing wings began to gain large interest the early 2000's and the study of morphing wings emerged in the mid 00's using CFD in a study by Chinnassamy & Chen (2005) using Fluent with two-dimensional aerofoils. This paved the way for future studies where morphed aerofoil geometry was imported into CFD software and steady or unsteady simulations ran in early research (Detrick et al., 2006; Secanell et al., 2006; Wilson et al., 2009; K. Yu et al., 2009).

CFD codes as they are developed incorporate new features and new versions are released which in the past few decades have incorporated a morpher to deform meshes. There are two popular methods for deforming meshes which are the Radial Basis Function and the BSpline which translates the vertices of the mesh (*User Manual Star CCM+ 14.04.013*, 2019). The BSpline uses a fitting curve defined by Eq. (2.4) which the control points in the mesh (usually mesh vertices) are superimposed onto where $f(x)$ is the fitting curve, B a weighting function, $\emptyset$ a coefficient and s the normalised distance between the control point intervals. The method of using BSpline was first used for optimisation of morphing aerofoil profiles seen in studies (Jasa et al., 2018; Lyu & Martins, 2015). In recent studies applied to camber morphing aerofoils (Abdessemed, 2020) however BSpline is a challenge for more complex shapes as the number of polynomials increase.

$$f(x) = \sum_{k=0}^{3} B_k(s)\emptyset_k \qquad 2.4$$

The RBF morpher provides constraints for vertices that are on the morphing boundary by using a boundary plane are allowed to move within a plane when morphing motion is specified. The user specifies the morphing displacement $\boldsymbol{d}_i$ the user specified displacement and transformed to $\boldsymbol{d'}_i$

by solving Eq. (2.5) where $\boldsymbol{n}_p$ is the normal to the plane, N_p the number of planes, and functions s_p and t_p depending on the function.

$$\boldsymbol{d}_i = \prod_{p=1}^{N_p} \left[s_p \boldsymbol{n}_p n_p^t + t_p \left(1 - \boldsymbol{n}_p \boldsymbol{n}_p^t\right) \right] \boldsymbol{d'}_i \tag{2.5}$$

These techniques for morphing have only been applied to morphing wing using CFD for the past decade as morphing wings were pretty much only tested using experimental methods. One of the first studies to use the RBF morpher for wings was looking at icing of aerofoil leading edge and how it affected the performance of the aerofoil (Biancolini & Groth, 2014; Marco et al., 2013). Alongside ice studies, it was seen in literature that the RBF morpher was originally used for aeroelastic studies (Cella, 2012; Lamorte & Friedmann, 2012, 2013; Sommerwerk et al., 2016).

2.3 Gaps in Literature

It has been seen from the literature review that there is a large gap in literature combining both morphing and wings in ground effect. It was seen both areas separately have been heavily investigated however minimal research combines the two.

Current research has investigated flaps in ground effect which has shown small improvements in performance however flaps show sharp geometry changes and a gap between the flap and aerofoil. This study replaces the flap with camber morphing and investigates the aerodynamics to identify any further performance improvements. This study applies this knowledge of improved aerodynamic performance and applies the technology to wings in ground effect. A gap in the literature for span morphing in ground effect has been identified which shows a large potential for an increase in aerodynamic performance when looking at the performance gains in freestream. Gains in aerodynamic performance translate into reduced fuel consumption or for electric craft reduced current draw which increases flight time and range of the wing in ground effect craft. It was clear from looking at literature that there were three paths for morphing wing which include the aerodynamics, morphing wing structure including mechanisms of morphing and also stability. The stability looks at how the aerodynamic moment changes therefore the aerodynamic moment was not included in this study therefore stability and mechanisms of morphing are suggested for future work.

2.4 Summary

Morphing wings show enhanced improvement with camber morphing being heavily researched to replace traditional control surfaces. Although this shows improvements the limiting factor is the complexity, structural and materials technology to apply to aircraft. Other morphing technology

such as span morphing can dramatically increase the cruising performance however there are large gains in weight compared to other morphing techniques.

In summary, the aerodynamics of a wing in ground effect is split into chord and span-dominated analysis. The chord-dominated shows the effect of the aerofoil profile in two dimensions and it was seen that the trailing edge pressure is fixed by the Kutta condition which causes the pressure to increase upstream of the trailing edge which increases the lift as the ground clearance is reduced. The stagnation point at the leading edge moves downstream along the lower surface whilst the downwash reduces as the aerofoil is brought into ground effect. In three dimensions it was seen bringing a wing into ground effect pushed the wingtip vortices outboard of the wing effectively increasing the aspect ratio. The proximity of the ground also reduced induced drag from the wingtip vortex. It has been stated in the literature review that chordwise ground effect is associated with the increase in lift and the spanwise the decrease in drag.

It was seen that there has been little research into morphing wings in ground effect, this study aims to fill this gap by applying camber tailing edge morphing, periodic morphing, and span morphing to wings in ground effect to improve the aerodynamic performance.

Chapter 3 Theoretical Background and Methodology

3.1 Governing Equations

Fluid dynamics are governed by three fundamental equations, the conservation of mass, momentum equations and energy equations. These equations define all fluid flow from external vehicle aerodynamics to blood flow in the human body. In this study no work was done on the fluid therefore the energy equation was not discussed. This means that this study limits the study of WIG craft to incompressible flow below a Mach number of 0.3.

The conservation of mass states that mass cannot be created or destroyed from a system of interest (Eq. 3.1) (Tu & Liu, 2008). In cases where the flow is incompressible, the density remains constant, and Eq. (3.1) is simplified to Eq. (3.2), where the net flow in and out of a surface is equal to zero. Eq. 3.1, Eq. 3.2 and Eq. 3.3 are expressed in tensor notation where the subscripts denote the direction ranging from 1 to 3 for each term i and j.

$$\frac{\partial \rho}{\partial t} + \frac{\partial (\rho u_i)}{\partial x_i} = 0 \tag{3.1}$$

$$\frac{\partial u_i}{\partial x_i} = 0 \tag{3.2}$$

The momentum equations also known as the Navier Stokes equations are essentially Newton's second law of motion written for fluid flow based on the conservation of momentum. The Navier Stokes equation is shown in Eq. (3.3) (Tu & Liu, 2008) in incompressible form and is usually solved computationally due to the non-linear second-order partial differential equations.

$$\frac{\partial u_i}{\partial t} + \frac{\partial (u_i u_j)}{\partial x_j} = -\frac{1}{\rho}\frac{\partial p}{\partial x_i} + \frac{\partial}{\partial x_j}\left(\frac{\mu}{\rho}\frac{\partial u_i}{\partial x_j}\right) + Source\_term_i \tag{3.3}$$

3.2 Boundary layer Theory

Boundary layers are important especially for aerofoil analysis as they define the separation of the flow from the pressure gradient within them. A boundary layer is a thin layer of flow next to a fixed surface and this flow is slower than the freestream velocity. The boundary layer is formed by fluid flowing over a surface, the friction between the surface and fluid causes the no-slip condition where the fluid is stationary on the surface. At a point away from the surface the fluid moves at

freestream velocity. The difference between the freestream velocity and the zero velocity at the wall causes shear stress and therefore a velocity gradient near the wall. A schematic of a boundary layer over a flat plate is shown in Figure 3.1.

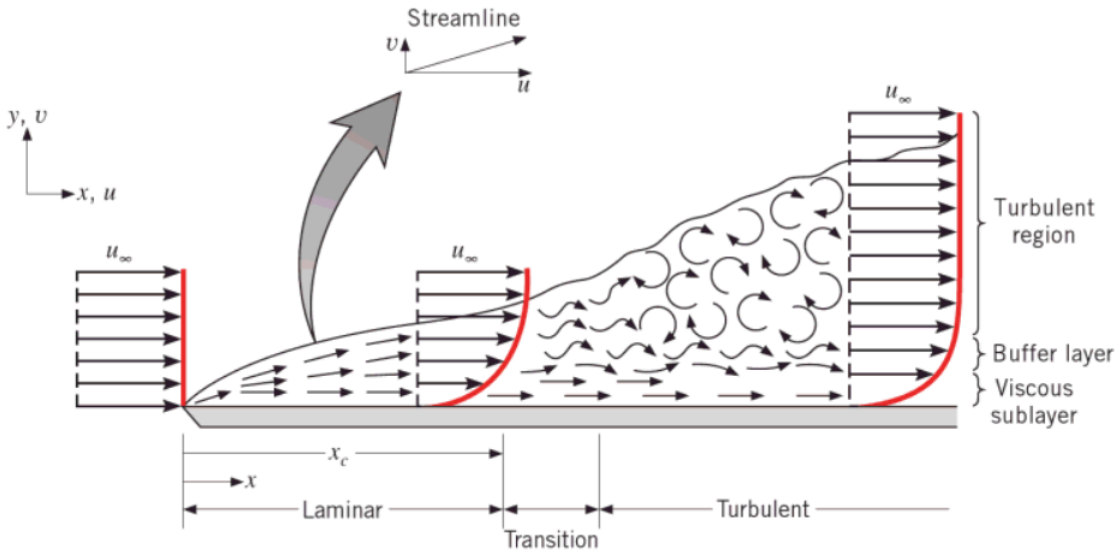

Figure 3.1: Flat plate boundary layer schematic and velocity profile (Theodore et al., 2011).

Boundary layers start at zero thickness when the flow first meets the surface at the leading edge, the boundary layer then grows in thickness downstream shown in Figure 3.1. Initially the boundary layer is laminar and can be thought of as layers of fluid flowing over each other. As the boundary layer grows in thickness downstream, there is a point at which the boundary layer starts to transition to turbulent and then becomes fully turbulent as shown in Figure 3.1.

The velocity profile of the fluid going from zero velocity to freestream varies depending on the boundary layer being laminar or turbulent. In the laminar region, the velocity is zero at the plate and gradually increases parabolically until the freestream is reached. In the turbulent region, the velocity profile is much flatter near the wall then sharply increases until the freestream is reached. Figure 3.2 shows the velocity is much higher near the wall for the turbulent boundary layer. This means there is more momentum in the turbulent boundary layer which therefore will remain attached a longer distance along the surface compared to the laminar layer.

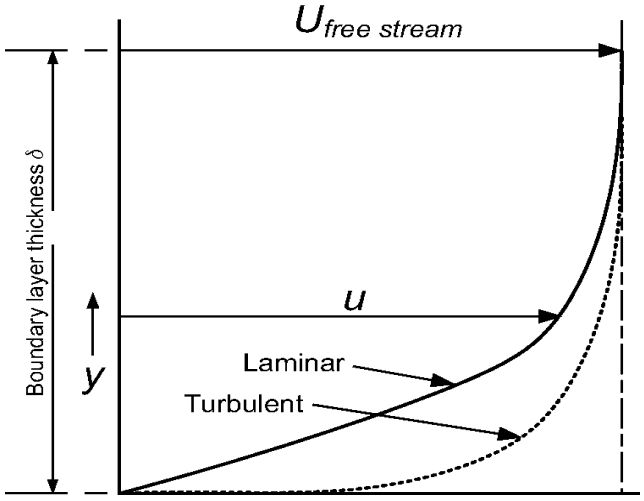

Figure 3.2: Turbulent and laminar boundary layer velocity profiles (Molland et al., 2017).

Near the wall, the boundary layer is accelerated due to favourable pressure gradients and decelerated due to adverse pressure gradients. When there is an adverse pressure gradient the fluid loses momentum overcoming the pressure gradient and causing the flow to decelerate. Initially, the fluid has enough momentum to overcome the adverse pressure which results in a positive velocity profile (Figure 3.3 (a)). As the fluid decelerates, the velocity profile becomes zero and then gradually increases at a distance above the wall (Figure 3.3 (b)). At this point, the shear stress at the wall is zero and the boundary layer separates. Further downstream after separation the adverse pressure gradient will cause negative velocity (Figure 3.3 (c)) where the flow is reversed. Boundary layers remain attached when there is a favourable pressure gradient and separate when there is an adverse pressure gradient. Once the flow separates there is a recirculation zone and the boundary layer no longer exists in this zone.

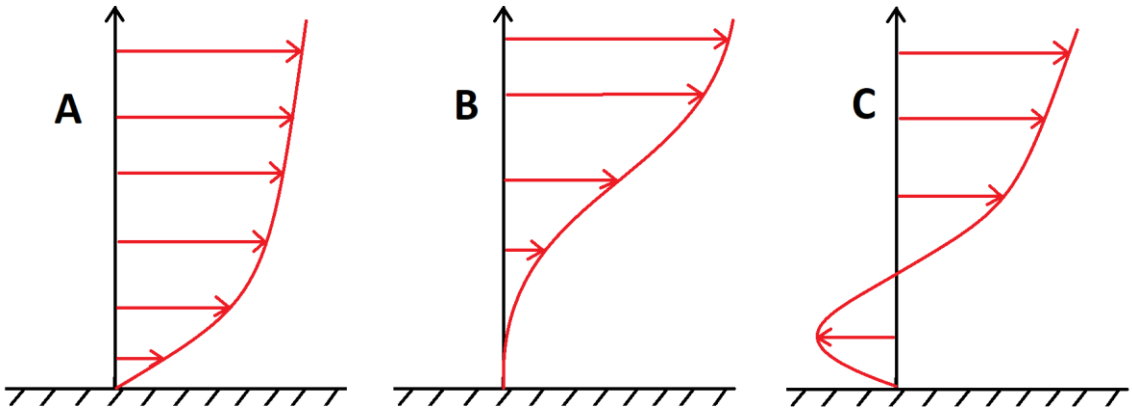

Figure 3.3: Boundary layer velocity profile attached (a) separation point (b) and reversed flow (c).

In a laminar boundary layer, layers of fluid slide past each other with little exchange of mass and momentum. Turbulent boundary layers have more momentum closer to the wall compared to laminar boundary layers therefore the velocity of the flow in a laminar boundary layer is more susceptible to faster deceleration leading to separation. When a laminar boundary layer

separates, the separated region becomes highly turbulent with large momentum transfer normal to the wall. This causes a small bubble to form and later reattach downstream as a turbulent boundary layer. If the laminar separation bubble breaks down, the flow separates and remains separated known as leading edge stall (Chang, 1970). Turbulent boundary layers have high levels of mixing between the layers causing turbulent layers to have a greater tendency to remain attached.

A separated laminar boundary layer will have a bigger wake than a separated turbulent boundary layer. Therefore, a separated laminar boundary layer will have a larger amount of pressure or form drag than a separated turbulent boundary layer. A fully attached laminar boundary layer will have less skin friction drag than a turbulent boundary layer of the same thickness due to the turbulent boundary layer containing swirls and eddies.

3.3 Inviscid Flow Methods

Inviscid flows have no viscous effects which reduced the complexity of modelling as well as the computational resources required. Inviscid flows are solved using lower-order methods such as the panel, vortex lattice and doublet lattice methods model the flow using singularities such as sinks, sources, doublets, and vortices. These singularities can easily be computed using linear equations, this allows quick computation with minimal computational recourses. Although the methods are practical and work well, they have limitations. These limitations include the flow only being solved for inviscid, irrotational and incompressible flows. Therefore, these methods cannot predict separated flow, predicting transition from laminar to turbulent location and the inability to provide a detailed flow behaviour for the user. Due to these reasons, lower-order methods are favourable in the initial design stages of an aerofoil design process for low angles of attack and incompressible flow speeds.

Panel Method

Analysis of aerofoils using the panel method requires the aerofoil surface to be split into segments, a vortex is then applied halfway along each segment line shown in Figure 3.4. To obtain the correct solution of the aerofoil, the Kutta-Joukowski is implemented to enforce the correct circulation. A series of linear equations are then used to determine the vortex strength of each segment to calculate the lift and pitching moment. As the panel method assumes inviscid flow a simple one-dimensional boundary layer theory model is used to calculate the drag.

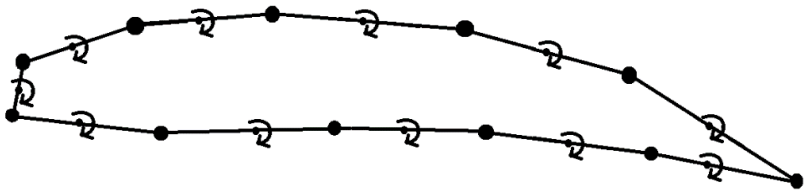

Figure 3.4: Panel method schematic.

Vortex Lattice Method

The vortex lattice method models three-dimensional wings ignoring the aerofoil thickness. Vortices are placed in a horseshoe configuration shown in Figure 3.5 (left). A wing planform to be analysed is split up into sections shown in Figure 3.5 (right) and the horseshoe vortex is applied to each segment at ¼ the distance along the segment. A normal vector is placed at ¾ the distance along the segment to impose a Neumann boundary condition that prescribes the velocity normal to the camber surface is zero.

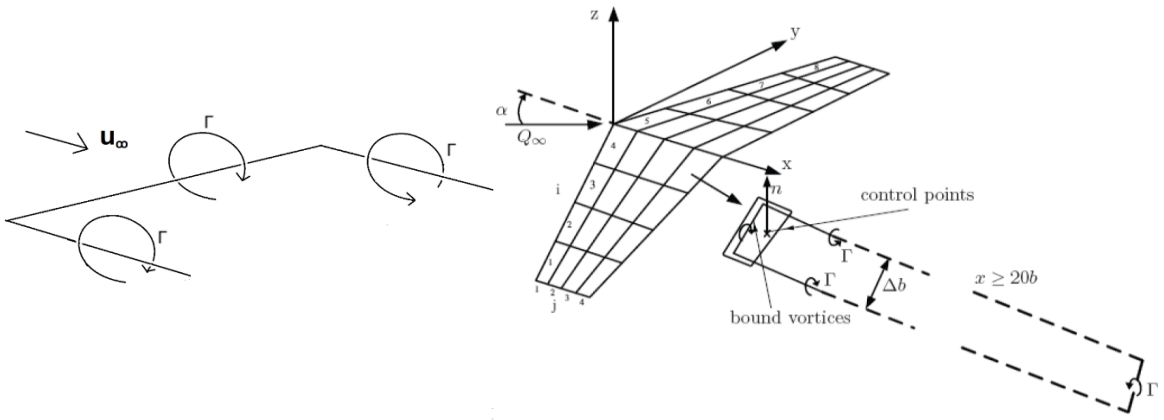

Figure 3.5: Horseshoe vortex (left) and horseshoe vortex applied to a wing (Bulletin, 2010) (right).

The vector placed on each panel is normal to the aerofoil camber line whilst the horseshoe vortex is placed on a flat plane demonstrated in Figure 3.6. The strengths of the vortices are then determined to satisfy the boundary conditions and from this the lift and pitching moment of the wing is calculated. The method can be used on rectangular, twisted, taper, and swept wings. The aerofoil lifting surfaces are also assumed to be thin with a low angle of attack.

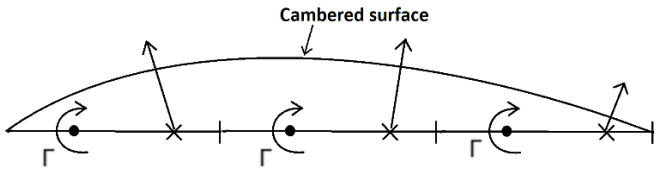

Figure 3.6: Vortex and normal vector section view.

Doublet Lattice Method

The doublet lattice method uses doublets rather than vortices on panels which make up the wing planform. A doublet consists of a source and sink which are placed close together and interact seen in Figure 3.7. Placing the source and sink infinitely close to each other known as a doublet causes a dominant force in the x direction shown in Figure 3.7. A doublet line is placed ¼ along the panel and a control point is located at ¾ the chord of each panel mid-span which is used to evaluate the upwash.

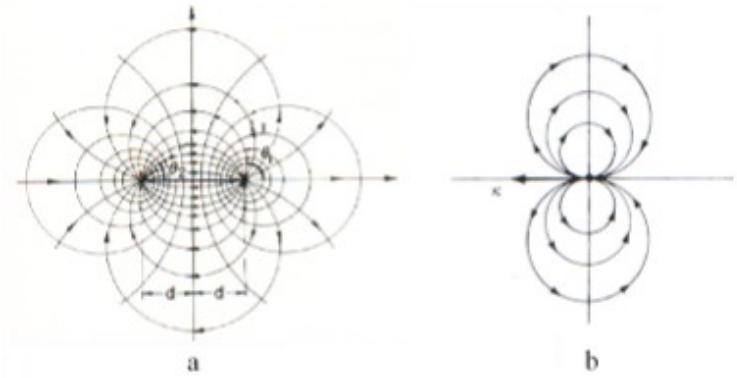

Figure 3.7: Source and sink (left) with distance d reduce to zero (Bear, 1972), (right) to create a doublet with lifting force in x direction (J. Anderson, 2007).

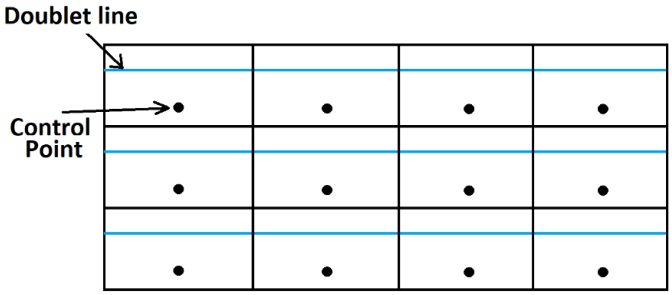

Figure 3.8: Planform view of doublet Lattice Method applied to a rectangular wing.

3.4 Computational Fluid Dynamics Overview

Computational Fluid Dynamics (CFD) is a higher-order method which can be highly accurate at predicting the solution of flows. Unlike the lower order methods mentioned, CFD does not make the same level of assumptions compared to lower order methods allowing separation of flows to be predicted. CFD packages split the problem into stages known as pre-processing, solver, and post-processing.

The first stage in a CFD problem is pre-processing which defines the geometry in the computational domain, fluid properties and boundary conditions from user inputs. The geometry

is subtracted from the domain using a Boolean operation and then split into small subdomains called a mesh.

The second stage known as the solver computes the problem, most commercial CFD packages use the finite volume method for this stage. This converts the difficult-to-solve second-order partial differential equations into a set of linear algebraic equations. The finite volume method is split into three steps. First, the governing equations are integrated over all the individual sub-domain control volumes in the mesh. Second, the integrated equations are discretised by substituting a differencing scheme for the convection, diffusion, and source terms to convert the integrals into algebraic equations. Lastly, the algebraic equations are then solved iteratively until a stable solution is achieved.

The third stage of CFD analysis is post-processing, this stage is extracting data from the simulations such as lift, drag, temperature, pressure etc. Flow visualisation can be carried out to view pressure, velocity fields, streamlines etc. Flow visualisation is a major advantage of higher-order methods while lower order methods cannot produce this level of information about the flow.

3.4.1 Discretisation Schemes

Linear/ Central Differencing

Linear or central differencing uses linear interpolation between the known cell centres and the distances between the cell centres and face (Figure 3.9) to determine the value on the cell face (Eq. 3.4). The equation is simply a linear interpolation across the cell using the known values at eth cell centres to obtain the value at the cell face. This scheme is easy to compute and carry out and is second-order accurate as there is a linear variation which results in a more accurate face value. Linear differencing is prone to oscillations which can result in the solver not converging and giving unrealistic flow characteristics. The subscript f denoted the cell face whilst the subscripts NC and OC denote the neighbour and owner cells.

$$\emptyset_f = \emptyset_{OC} + \left(X_f + X_{oc}\right)\frac{\emptyset_{NC} + \emptyset_{OC}}{X_{NC} - X_{OC}} \qquad 3.4$$

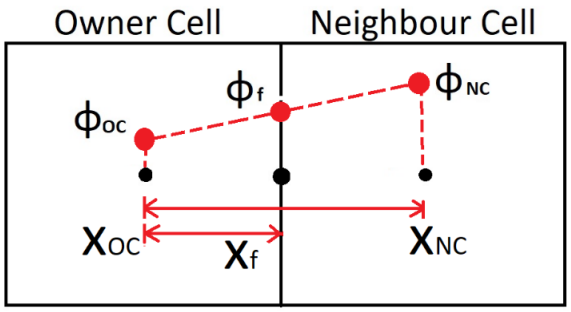

Figure 3.9: Linear/ Central Differencing.

Upwind Differencing

Upwind differencing uses the values at the cell centre and projects them directly onto the cell face seen in Figure 3.10. The software decides to project either the owner or neighbour cell centre value onto the face depending on the direction of the mass flux defined by (Eq. 3.5). In Figure 3.10 the owner cell value was projected onto the face due to the direction of the mass flux shown by the arrows on the cell faces. Upwind is only first-order accurate as the value does not vary across the cell giving inaccurate values on the cell faces but is stable for convection-dominated flows. The model can be used initially in CFD to generate an initial stable solution before switching to another model to improve the accuracy.

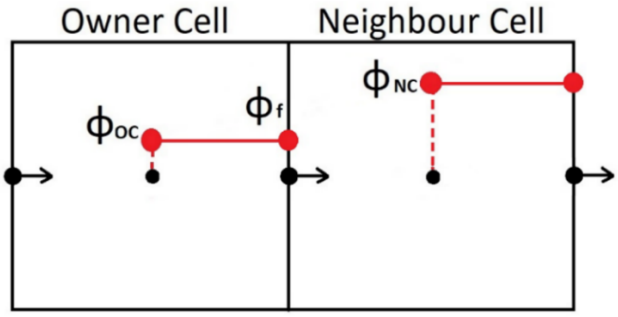

Figure 3.10: Upwind differencing.

$$\emptyset_f = \begin{cases} \emptyset_{OC}, & m_{flux} > 0 \quad (Mass\ Flow\ In) \\ \emptyset_{NC}, & m_{flux} < 0 \quad (Mass\ Flow\ Out) \end{cases} \qquad 3.5$$

Linear Upwind Differencing

Linear Upwind extends the upwind scheme by adding a gradient to the projection line seen in Figure 3.11 to vary the cell centre value linearly across the cell. The value on the cell face is then calculated using Eq. 3.6 depending on the direction of mass flux. The scheme is classed as second-order accurate but can be unstable. The gradient can be predicted to step and cause unrealistic values and therefore gradient limiters are used to apply a maximum possible gradient. The term $\boldsymbol{r}$ is the vector between the cell centre value and the value on the cell face.

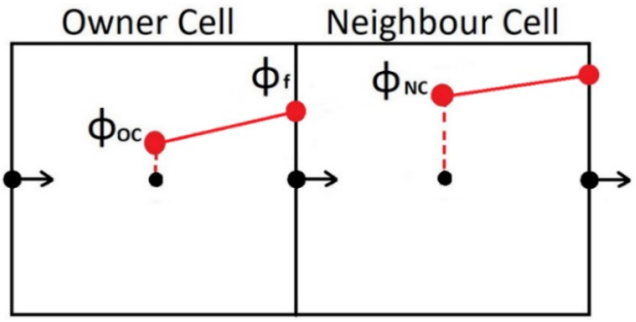

Figure 3.11: Linear Upwind Differencing.

$$\emptyset_f = \begin{cases} \emptyset_{OC} + (\nabla\emptyset)_{oc} \cdot \boldsymbol{r}, & F_f > 0 \quad (Mass\ Flow\ In) \\ \emptyset_{NC} + (\nabla\emptyset)_{NC} \cdot \boldsymbol{r}, & F_f < 0 \quad (Mass\ Flow\ Out) \end{cases} \tag{3.6}$$

Blending Schemes

Blending schemes aim to have the stability of upwind and the accuracy of linear differencing by using a combination of linear and upwind schemes. Eq. (3.7) shows the face value is a contribution of the upwind and central differencing with a bias factor Ψ (between 0 and 1) which determines how much each scheme contributes to the face value. This scheme is difficult to apply and achieve stability, so the other schemes are more favoured in CFD practice.

$$\emptyset_f = \Psi\phi_{upwind} + (1 - \Psi)\phi_{Linear/Central} \tag{3.7}$$

3.4.2 Wall Functions

Wall functions are used to model the flow near a surface when the no-slip condition is applied to a boundary. As seen in section 3.2, a boundary layer is present near a no-slip wall causing a velocity profile between the wall and freestream. To accurately capture this profile seen in Figure 3.2, a high grid resolution is required near the wall shown in Figure 3.12. This can cause problems with the mesh of high aspect ratio cells and high skewness for geometry with any curvature. The main problem is that the velocity varies linearly across the cells therefore a high resolution is required to accurately capture the velocity profile. Wall functions apply a non-linear profile across the cell using experimental profiles measured from a flat plate seen in (Figure 3.13). Due to the non-linear profile being applied across the cell, fewer cells are required to model the velocity profile near the wall. This reduces the high aspect ratios and skewness of the cells. Also, a major advantage to wall functions is a lower cell count near the wall reducing the computational cost.

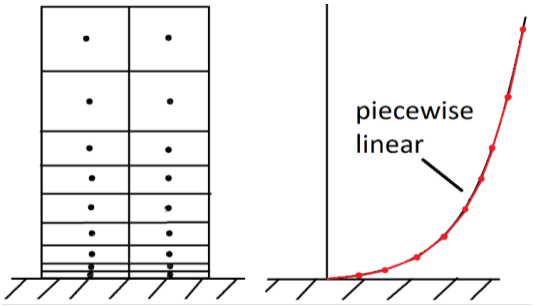

Figure 3.12: Piecewise linear profile.

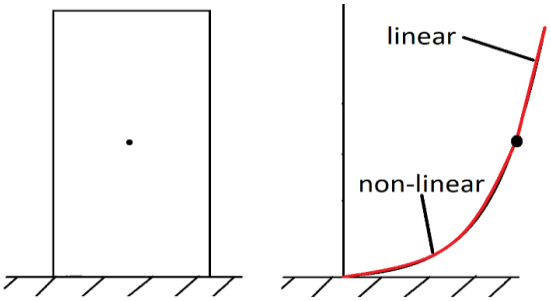

Figure 3.13: Wall function with a single cell.

The experimental velocity profile near the wall is plotted non-dimensionally in terms of the wall distance y^+ and velocity u^+ (Figure 3.14). There are three regions including the viscous sub-layer, buffer layer and the log law region (Versteeg & Malalasekera, 1995). The viscous sub-layer shows a linear fit below a y^+ of 5 and the log region shows a logarithmic fit above a y^+ of 30. Placing cells in the buffer region is avoided, this is due to the linear and log curves do not closely match that of the experimental data seen in Figure 3.14 in the buffer region. Figure 3.14 was carried out for a flat plate but is considered in the industry to produce an accurate enough result. The accurate enough result is deemed from considering the uncertainties of the experimental measurements and the errors of modelling the flow. A Spalding function fits the experimental data closely but there is a lack of validation and unknown accuracy in the buffer layer so is not generally used.

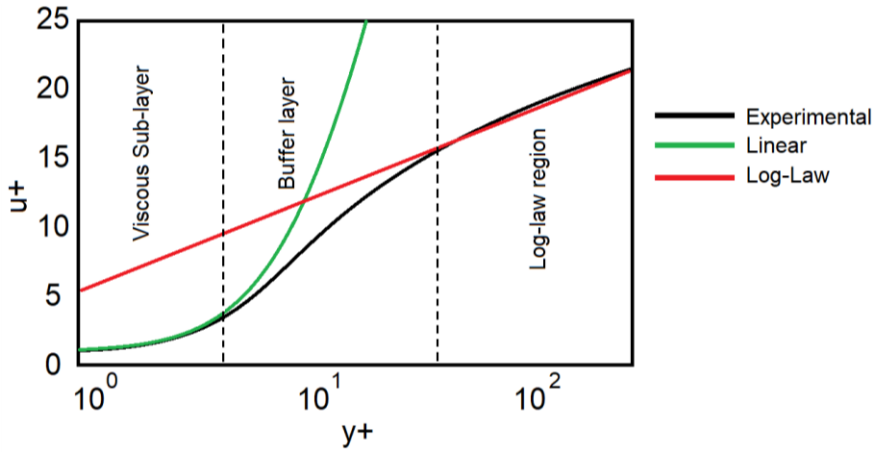

Figure 3.14: Law of the wall experimental velocity profile with linear and log curve fits.

The viscous sub-layer is modelled by (Eq. 3.8) and the log law region by Eq. (3.9) where k_v is the Von Karman coefficient 0.4187 and E is 9.793 (Nazif & Basirat Tabrizi, 2014) determined experimentally. The software switches between the linear and log regions at a y^+ of 11.25 where the linear and log curves intercept in Figure 3.14.

$$u^+ = y^+, \quad y^+ < 5 \tag{3.8}$$

$$u^+ = \frac{1}{k_v}\log(Ey^+), \quad y^+ > 30 \tag{3.9}$$

3.4.3 Explicit and Implicit

Explicit and implicit treatments describe how the solution is advanced in time to update the values at the cell centre using values at neighbouring cells. Where $\emptyset$ is a physical flow quantity such as velocity, temperature etc, an explicit solution to the value $\emptyset$ at time $n+1$ is dependent on the value for time n and its neighbouring cell values at time n. The implicit method to solve the value $\emptyset$ at $n+1$ requires the value of $\emptyset$ at time n and the values of neighbouring cells at $n+1$. For example, the value of the cell in Eq. (3.10) can be approximated over a time step Δt using the Euler explicit approach Eq. (3.11) using previous values of neighbouring cells or an Euler implicit approach in Eq. (3.12) using neighbouring cell values at the current time step $n+1$.

$$\frac{d\emptyset}{dt} = f(t, \emptyset) \tag{3.10}$$

$$\emptyset_{(n+1)} = \emptyset_{(n)} + \Delta t f(t_n, \emptyset_n) \quad \text{(Explicit)} \tag{3.11}$$

$$\emptyset_{(n+1)} = \emptyset_{(n)} + \Delta t f\left(t_{(n+1)}, \emptyset_{(n+1)}\right) \quad \text{(Implicit)} \tag{3.12}$$

The Explicit method is always a function of known values whereas the implicit is a function of known and unknown values. The neighbouring cells to ϕ at n+1 are unknowns and are computed simultaneously based on their neighbours therefore implicit schemes require an iterative approach. The grid points in the domain can be solved iteratively or all at once by using matrices for the implicit approach. This makes the implicit method more computationally expensive compared to the explicit method. Explicit schemes require a very small-time step to ensure stability compared to Implicit schemes that can handle larger time steps and have much higher stability. Implicit schemes are computationally more expensive for highly non-linear equations as the governing equations are all solved iteratively.

3.4.4 Temporal Discretisation

Temporal discretisation is required to discretise transient terms for unsteady time-dependent problems. The governing equation is parabolic in time therefore the solution in time depends upon previous values and not the future values making the process easier than spatial discretisation. Temporal discretisation involves integrating each PDE term over the time step (Eq. 3.13) where the function F(∅) contains the non-transient diffusion, convection, and source terms. Star CCM+ uses the backwards Euler implicit scheme to approximate the transient term in either first (Eq. 3.14) or second-order (Eq. 3.15) using the current time (n+1) and the previous time (n) (*User Manual Star CCM+ 14.04.013*, 2019).

$$\frac{\partial \emptyset}{\partial t}(x,t) = f(\emptyset) \tag{3.13}$$

$$\frac{d}{dt}(\rho \emptyset V)_0 = \frac{(\rho \emptyset V)_0{}^{n+1} - (\rho \emptyset V)_0{}^{n}}{\Delta t} \tag{3.14}$$

$$\frac{d}{dt}(\rho x \emptyset V) = \left(\frac{3}{2}(\rho x \emptyset V)_{n+1} - 2(\rho x \emptyset V)_n + \frac{1}{2}(\rho x \emptyset V)_{n-1}\right) \tag{3.15}$$

3.4.5 CFD Turbulence Modelling Techniques

Capturing the eddy structures in a simulation requires large computational resources as the size of the mesh needs to be an order of magnitude smaller than the smallest eddy. This results in extremely fine meshes to capture the flow characteristics and large computational costs due to the large number of equations to solve. Different methods can be used to either solve or model eddies to reduce computational costs. The different approaches are shown in Figure 3.15 (left) this diagram shows the cost compared to the level of the physics that is modelled or solved for each approach. The methods discussed in this section include Direct Numerical Simulation (DNS), Large Eddy Simulation (LES), Detached Eddy Simulation (DES) known as a hybrid and Reynolds Averaged Navier Stokes (RANS). Figure 3.15 (right) shows a comparison of a jet flow carried out using DNS, LES and RANS showing the detail captured in the simulation.

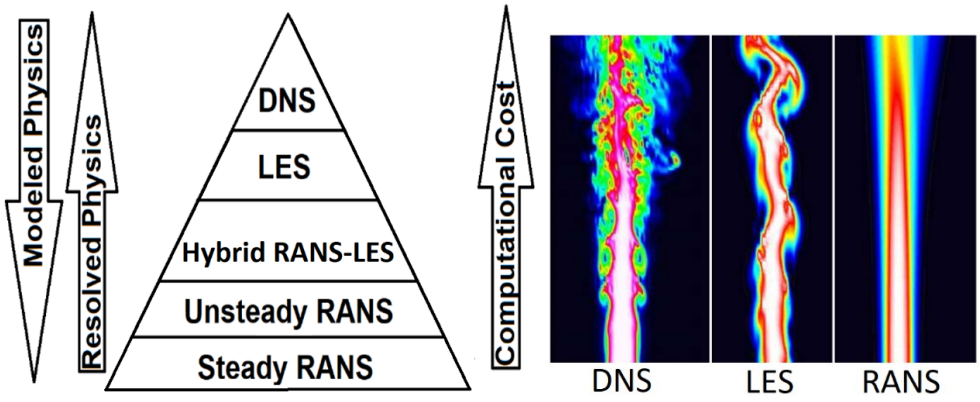

Figure 3.15: CFD turbulence modelling approaches against costs (left) and Comparison of DNS, LES and RANS (right) (Maries et al., 2012).

The large eddies in the flow transfer energy to slightly smaller eddies, these slightly smaller eddies then transferer energy into smaller eddies and so on until a viscous level where the energy is absorbed by the viscosity and transferred into heat. This transfer of energy is known as the energy cascade, Figure 3.16 shows the kinetic energy (E) for the size of the eddies (wave number k) where there are three regions seen in this graph. The first region is the production of eddies, the second is the transfer of energy from the large scales to the small scales and the third disruption

of energy. The rotation of smaller eddies is much faster than the larger eddies so there is a large variation in length and time scales. In CFD it's very difficult to model the turbulent flow as high spatial and temporal resolutions to be able to capture the length and time scales of the eddies.

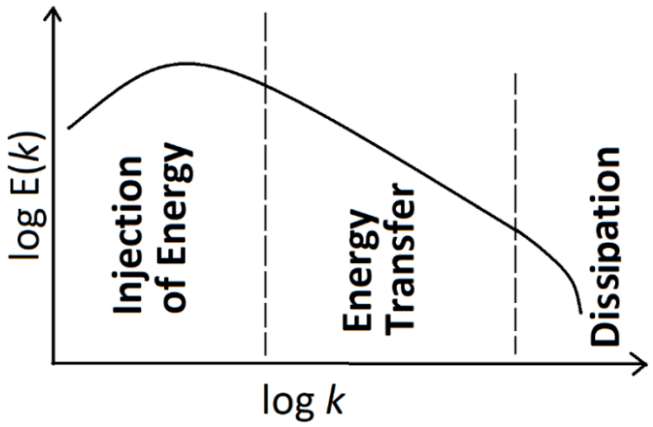

Figure 3.16: Energy cascade schematic using energy spectrum.

DNS

Direct Numerical Simulation (DNS) directly solves the Navier Stokes equations and can solve the smallest eddies in a flow (Molland & Turnock, 2007) , the increased mesh resolution required makes DNS the most computationally expensive approach. Due to its high computational expense requiring large supercomputers for simple problems, it's limited to research applications of low Reynolds numbers and simple geometries (Z. Y. Yang, 2015).

LES

Large Eddie Simulation (LES) categorises eddies in a simulation into large- and small-scale eddies. The large eddies in the flow have higher levels of energy and are more effective at carrying the conserved properties than the smaller eddies. Therefore, the large eddies are solved by directly solving the Navier Stokes equations as in the DNS, but the smaller eddies are approximated by models. LES is slightly less accurate than the DNS approach but is less computationally expensive (Lund, 2003). LES requires a small grid to be able to capture the eddies, each eddy requires a minimum of 4 cells to solve the eddy seen in Figure 3.17 (middle). Sub-grid models are used for eddies smaller than the size of a cell which does not resolve the flow. Typically for a good LES simulation, the LES will resolve at least 80% of the turbulent kinetic energy in the energy cascade (Z. Y. Yang, 2015).

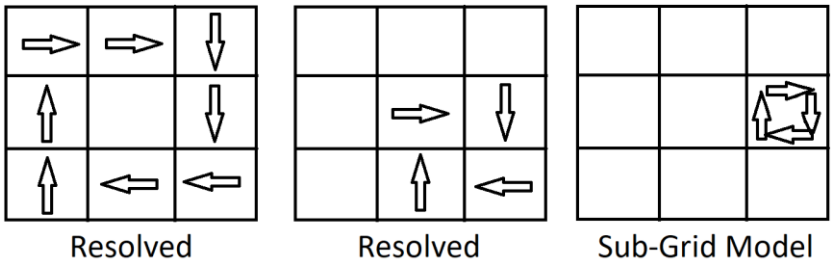

Figure 3.17: Resolution of spatial grid to capture eddies.

RANS

Reynolds Average Navier Stokes (RANS) fully models the turbulence by time averaging the Navier Stokes equations (Eq. 3.3); due to the time averaging this method is far less computationally expensive than DNS and LES. Due to the low cost and reasonable accuracy of results, it is the most widely used method. Averaging the Navier stokes equations yields the RANS equation (Eq. 3.16), the term seen in Eq. 3.17 is known as the Reynolds Stress term which requires a closure model to be able to model this term (Alfonsi, 2009). Various models exist and there is no one universal term so the correct model needs to be selected depending on the application. The RANS equation ignores the time derivative in Eq. (3.16) which results in the simulation having no knowledge of transient behaviour. In URANS the time derivative is included in the RANS equation (D.Narasimhamurthy, 2004).

$$\left[\frac{\partial \overline{u_\iota}}{\partial t} + \overline{u_J}\frac{\partial(\overline{u_\iota})}{\partial x_j}\right] = -\frac{1}{\rho}\frac{\partial \bar{p}}{\partial x_i} + \nu\frac{\partial^2 \overline{u_\iota}}{\partial x_j \partial x_j} - \frac{\partial}{\partial x_j}\left(\overline{u_\iota u_j}\right) \qquad 3.16$$

$$\tau_{ij} = -\frac{\partial}{\partial x_j}\left(\overline{u_\iota u_j}\right) \qquad 3.17$$

RANS Closure Models

To close the RANS equations, the Reynolds Stress needs to be modelled using turbulence models. There are many different turbulence models, but the 4 most common turbulence models are the K Omega, K Omega SST, Realizable K Epsilon and Spalart-Allmaras for aerofoil analysis.

Spalart-Allmaras is a linear one equation model that was developed purely for aerodynamic flows. It is a simple model that solves a modelled transport equation for turbulent eddy viscosity (ANSYS, 2009). The model uses the Boussinesq approximation and applies to applications with attached boundary layers and mild separation due to being applied without wall functions. (P. Spalart & Allmaras, 1992). The model is used in aerofoil analysis due to its low computational cost but is limited to non-separated flow.

The K Epsilon model is a two-equation model that solves turbulent kinetic energy and turbulent dissipation rate which is used to determine the turbulent eddy viscosity. The Realizable K-Epsilon model is a variation of the standard K-Epsilon model. The model replaces a constant with a function of mean flow and turbulence properties for the turbulent viscosity and dissipation rate. (Tsan-Hsing et al., 1995). A two-layer approach is also used which splits the computation into two layers to including the near-wall layer. Near the wall, the model uses the wall distance for the dissipation rate epsilon and turbulent viscosity. This model is suitable for low Reynolds number types with a y^+ ~1 or wall function type meshes with y^+> 30. (Rodi, 1990).

The K Omega model is a two-equation model that solves for the turbulent kinetic energy k and the specific dissipation rate omega for each unit of turbulent kinetic energy in the transport equation to determine the turbulent eddy viscosity. An advantage to the model is that it performs well in boundary layers with strong adverse pressure gradients. The model is very sensitive to the inlet and freestream conditions compared to the K Epsilon model. (Wilcox, 2006). The K-Omega SST model solves the sensitivity issue of the K-Omega model by effectively using the K Epsilon in the far field and K Omega in the flow close to the wall (Florian, 1993).

DES

LES is still a highly computationally expensive approach to real-world applications, a common approach for highly turbulent flows is the Detached Eddy Simulation which is a hybrid approach. The detached large eddies in the simulation are solved using LES but the smaller eddies which has a much lower impact on the flow and therefore less significant are modelled using the RANS method (Shur et al., 1999; P. R. Spalart, 2009). For a given grid of same size, DES can be less accurate than RANS, especially where there is high turbulence, therefore a finer mesh is required for DES to accurately capture the flow details to make full use of the DES approach.

3.5 Methodology

3.5.1 CFD Software

For this project Star CCM+ CFD software is used due to being industry-known and used software which pushes its development to produce high-quality software. The software manufacturer also provides extensive documentation on the software as well as examples and training to aid its users. Star CCM+ is a powerful multi-physics Computational Aided Engineering (CAE) package allowing solving of problems of solids or fluids, heat transfer, battery simulation and stress analysis. The software allows for all key stages in a simulation to be set-up in a single navigation tree including importing and creating geometries, mesh generation, physics set-up, solution of

governing equations, post-processing, design exploration and linking with other software such as CAD. Star CCM+ was built-in Java and allows all actions in the user interface to be recorded using Java macros. These can then be played back to perform actions within the software saving the user time. An example of this is recording a simulation set-up of an aerofoil. This can then be played for different aerofoil geometries and angles of attack to save the user from setting up multiple different simulations with the same set-up parameters. Star CD was originally developed by CD Adapco and in 2004 a completely new developed software Star CCM+ was released to make use of new and updated advances in the field. CD Adapco was then sold to Siemens in 2016. Siemens offer support to its users by creating an extensive user manual with worked examples of some of its key features such as simulating aerofoils, the motion of meshes, and heat transfer. There is also an online support centre which has documentation and articles and a technical forum to ask questions to other users and the company.

3.5.2 Meshing in Star CCM+

Star CCM+ has built-in meshing capabilities as well as allowing meshes to be imported. With the built-in mesher within Star CCM+, the user has less control over the mesh as the meshing is automated, however remeshing can be carried out quickly, easily, and reliably.

In Star CCM+ there are 5 types of mesh models (tetrahedral, polyhedral, trimmed, thin mesher and advanced layer mesh), the tetrahedral which consists of tetrahedral cell shapes for the core mesh. Polyhedral consist of arbitrary polyhedral-shaped cells and trimmed mesh consists of hexahedral or polyhedral cell shapes. The thin mesher consists of tetrahedral or polyhedral-based prismatic thin mesh allowing meshing to take place in small gaps. Advancing Layer mesh consists of a polyhedral core mesh with built-in prismatic layers advancing inward from a polygon surface mesh.

In this study, the trimmed mesher is used due to its robustness and efficiency. Also testing wings in ground effect will have the least variation on the trimmed mesher, due to reducing the ground clearance involves just cutting a slice off the bottom of the domain and adding it back on to increase the ground clearance. The other meshing methods after remeshing from changing the ground clearance would show the cells reordered.

The trimmed mesher works by applying a hexahedral cell template mesh and laying it over the geometry with all the volumetric controls applied. The mesher then trims the core mesh around the geometry, this workflow is shown in Figure 3.18. Volumetric controls can be applied to the template mesh to refine the size of the mesh in key areas. Some of the desirable meshing features of the trimmer mesher include predominantly hexahedral mesh with minimal cell skewness. The refinement is based upon surface mesh size and other user-defined refinement controls. The

mesh is independent of the surface quality and the template mesh can be aligned in and oriented in the specified coordinate system (*User Manual Star CCM+ 14.04.013*, 2019).

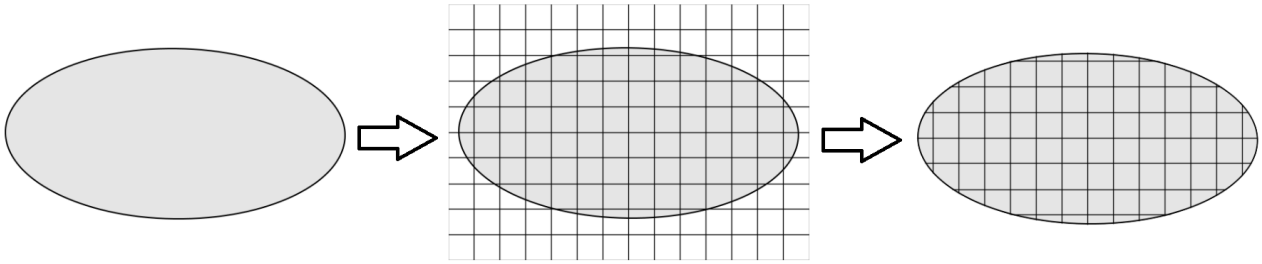

Figure 3.18: Trimmed mesher workflow (*User Manual Star CCM+ 14.04.013*, 2019).

3.5.3 Modelling Time in Star CCM+

In Star CCM+ time models are used to provide solvers with a time-dependent term. There are 5 models which include steady, explicit unsteady, implicit unsteady, PISO unsteady and harmonic balance.

Steady is used in steady-state calculations where physical time is not of importance and is meaningless. Explicit Unsteady is a model that uses the cell of interest values plus its neighbouring cell to advance the solution in time. In Star CCM+ this model is only available with the coupled solver, inviscid and laminar models. The Implicit model requires the cell value plus the values of the cell and neighbour cell at the next time step. The implicit can be used with a wider range of solvers and models. The PISO unsteady model uses the PISO algorithm when solving the discretised equation. An initial guess is made for the pressure field and velocity components using the discretised momentum equations. These guesses are then corrected using corrector steps. The harmonic balance is designed for flows that repeat periodically over time using a steady solver.

This study will focus on steady-state simulations for static analysis of aerofoil due to being less computationally demanding compared to modelling in time. Time dependent such as morphing an aerofoil over time, the implicit simple model is used due to being less sensitive to large timesteps reducing computational resources.

3.5.4 Modelling Motion in Star CCM+

In Star CCM+ there are four categories of motion which include mesh displacement in real time, stationary mesh in moving reference frame, harmonic balance flutter and morphing in steady-state. The stationary mesh method models motion by moving the reference frame and is generally used where the time accuracy is not of importance and is computationally cheap. Harmonic balance flutter is designed for periodic flows that repeat such as turbo machinery or

rotorcraft. The main benefits of this are as the flow is repeating steady-state simulations can be carried out reducing computational costs compared to unsteady simulations.

Dynamic morphing simulations in this study use the morpher motion method to move the boundaries of a defined displacement. Start CCM+ morpher uses a set of control points which are usually defined by the location of the vertices of the mesh. The location or more points can be read from a table created by the user, but the default locations and the number of points are usually more than adequate for most cases. Each control point has an associated vector defining the displacement for each time step. The displacement is defined by the user either using displacement per time step or by velocity which the displacement is then calculated in the software. The morpher uses the following steps to morph the mesh, first the morpher identifies the grid control points and the known displacements. Second the known displacements of the control points are used to generate an interpolation field. Third the mesh vertices are then applied to the interpolated grid control points and finally adjustments are made to the mesh near wall boundaries. A morphing mesh included in the Star CCM+ tutorial serries in the user manual is shown on Figure 3.19 demonstrating show the mesh deforms over time.

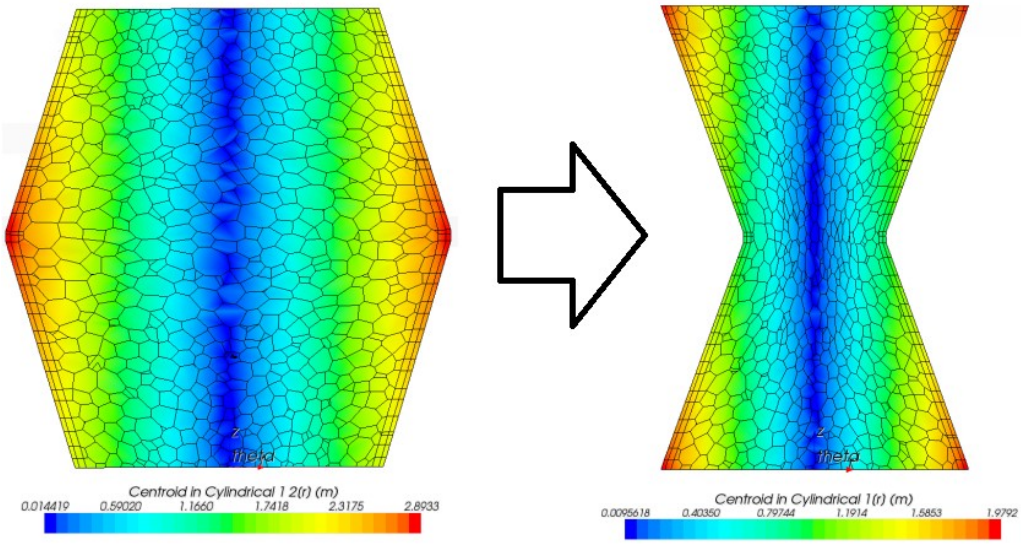

Figure 3.19. Demonstration of cylinder morphing mesh (Profir, 2012).

3.5.5 CFD Set-up

Geometry

Aerofoil profiles were imported into Star CCM+ as a comma-separated variable file and a spline was generated from these points in a sketch which was then extruded to three dimensions. Building the aerofoil in Star CCM+ allows the aerofoil to be rotated and the ground clearance changed within a sweep. For the NACA6409 aerofoil, the locations of each point were defined by a linear vertical and horizontal dimension shown in Figure 3.20 by the construction lines. This

allows the aerofoil to be parametric allowing it to be scaled by multiplying each construction line length by a percentage of the non-dimensional root chord length. This allows the twist, taper, wing tip position, tip chord and ground clearance to be adjusted, then these parameters are loaded into Design Manager built into Star CCM+ where sweep and optimisation studies can be carried out.

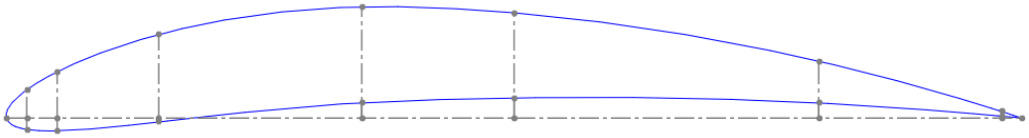

Figure 3.20: Parametric set-up of NACA6409 aerofoil.

Physics, Domain, and Boundary Conditions

The domain was 4 chord lengths above the aerofoil, 5 lengths upstream and 15 lengths downstream and the distance below the aerofoil was varied to change the ground clearance (Figure 3.21). In three dimensions the domain was 8 chord lengths wide. This domain size was deemed sufficient from observing the velocity scenes in the CFD software and from recommendations in the CFD user manual. Reducing the length downstream to 10 chord lengths caused reversed flow on the outlet therefore this was too small and was increased back to 15 lengths. boundary conditions of the domain were set to no-slip for the roof and side wall and symmetry plane, velocity inlet for the inlet plane, and pressure outlet for the domain outlet shown in Figure 3.21. The ground plane was set as a wall and used a tangential velocity vector to simulate a moving ground at freestream velocity. The moving wall was required as the reference frame was different to real world applications where the aerofoil moves however in the CFD the aerofoil is fixed and the airflow is moved over the aerofoil. Moving the flow over the ground will therefore cause a boundary layer in the streamwise direction which is not present when the aerofoil is moved which the moving ground eliminates this streamwise boundary layer. As the geometry is symmetrical, the wing can be split down the centreline and half the geometry tested to reduce computational costs.

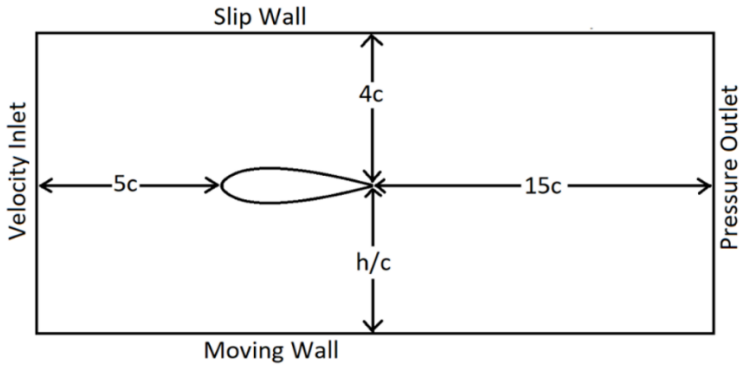

Figure 3.21: Domain size and boundary conditions.

Initially, simulations are carried out using steady-state simulations using Reynolds Average Navier Stokes (RANS) in Star CCM+ using the Finite Volume Method. RANS requires a closure model which the K-Omega SST turbulence model was selected. This model was selected due to the ability to predict separation and robustness of the model. From the literature review, it was seen this model is widely used for wings in ground effect due to higher levels of separation than freestream. Unsteady simulations are also carried out using Unsteady Reynolds Average Navier Stokes (URANS) where time dependency is required. The Detached Eddy Simulation (DES) was used for periodic morphing where there were more flow details to be captured but is computationally more expensive than URANS. The flow is assumed to be incompressible due to simulations being carried out at a Mach number of 0.14.

The study is carried out at a Reynolds number of 320,000 for all cases which is of a typical value for a UAV. This study aims to apply the morphing wing technology to UAV craft due to fewer restrictions allowing the technology to be implemented easier. Figure 3.22 shows the regimes of Reynolds numbers for various bio, aircraft, and wind turbine applications (Lissaman, 1983). UAV craft falls into the model aeroplane category and has a Reynolds number range of 10^3 and 10^6. It is seen that the Reynolds number of 320,000 falls into this range. It was stated by Winslow et al., (2018) that below 100,000 the lift and drag coefficients became very sensitive to the Reynolds number. Above a Reynolds number of 100,000, the lift and drag coefficients varied a minimal amount as the Reynolds number was increased. Therefore, the Reynolds number of 320,000 selected for this study can be used to directly compare against higher Reynolds numbers of other studies showing similar flow characteristics.

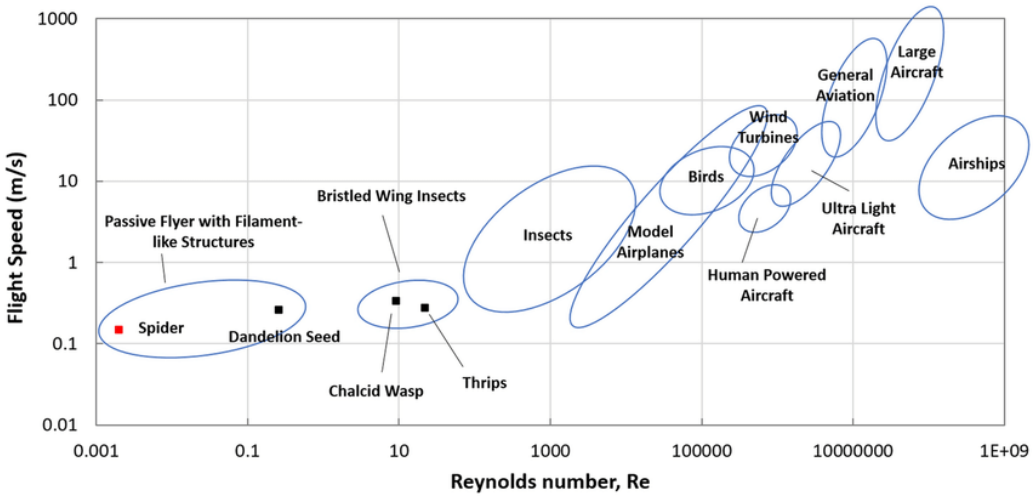

Figure 3.22: Reynolds number flight spectrum (Cho, 2021).

Mesh

The mesh used in this study uses the trimmer mesh as discussed in section 3.5.2 with a minimum cell size of 0.2% chord in two dimensions shown in Figure 3.23 and 0.4% in three dimensions

Figure 3.24. The size of the mesh was important to capture all the important flow details but also to try and minimise the computational cost. The cells were allowed to grow towards the domain walls as the flow at the domain walls was not of interest in this study reducing computational costs. As the flow around the aerofoil is of high importance the cell growth was restricted around the aerofoil using volumetric controls shown by the high-density mesh region in Figure 3.23. The trimmer wake refinement was also used which restricts the growth rate directly behind the aerofoil.

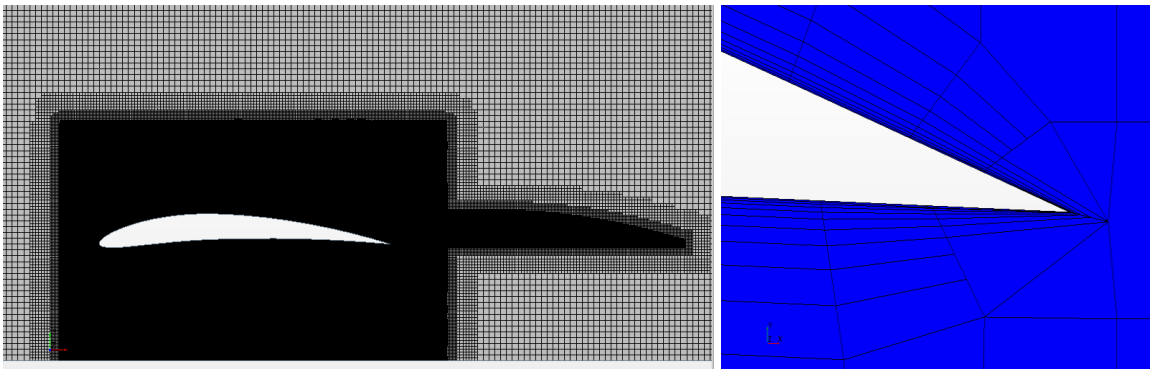

Figure 3.23: Mesh around aerofoil with volumetric and wake refinement zones in two-dimensions (left) and zoomed-in trailing edge (right).

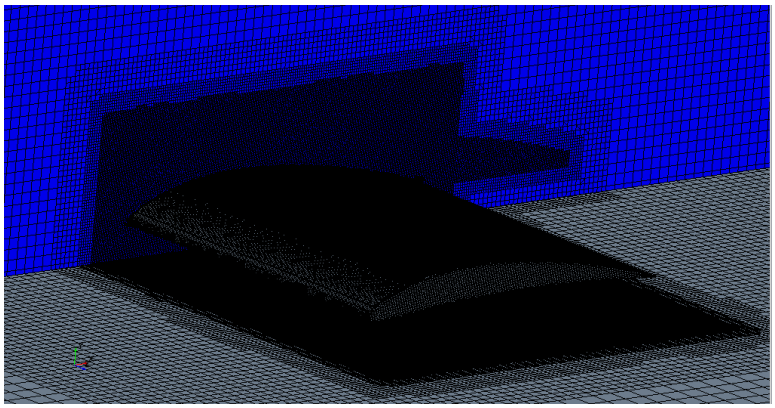

Figure 3.24: Mesh around the aerofoil in three dimensions.

Prism layers is a term used in Star CCM+ for cells around a boundary to capture the flow in the boundary layer, these are small cells that grow normal to the surface. In this study boundary layers were used around the aerofoil and are critical to be able to capture the separation which is of high importance as wings in ground effect tend to separate earlier than freestream. Due to the importance of capturing the boundary layer, 10 prism layers were used. The prism layer had a total thickness of 0.6% chord normal to the aerofoil and a growth rate of 1.2. The prism layer was turned off at the domain walls to reduce computational costs due to the slip condition being applied to these and a tangential velocity vector set to the floor therefore no boundary layers form on these boundaries. At the trailing edge of the aerofoil, the prism layers reduced to allow the trailing edge to go to a point (Figure 3.23 right).

3.5.6 Morphing and Remeshing

This study focused on camber morphing and uses the FishBAC camber morphing method identified in the literature review. This method defines an equation (Eq 3.18) for the morphing displacement along the chord (y_x) with w_{te} being the total displacement at the trailing edge. The equation is initially turned off up to the start location of morphing (x_s).

$$y_x = \frac{w_{te}(x - x_s)}{(c - x_s)} \qquad 3.18$$

The schematic for the morphing wing in two dimensions is shown in Figure 3.25 with the morphed aerofoil shown by the green profile. The schematic defines the variables used in (Eq 3.18) with x_s being the start location of morphing, w_{te} the max deflection at the trailing edge and h/c the ground clearance.

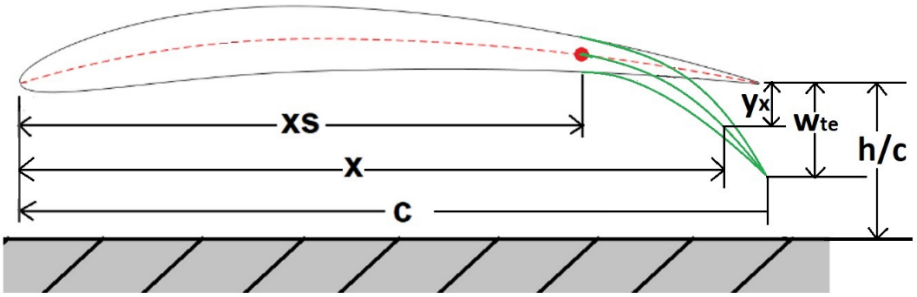

Figure 3.25: Two-dimensional aerofoil schematic of original and morphed profiles.

Two types of morphing were carried out using static and dynamic; static simulations used a fixed morphed geometry created in CAD whilst dynamic simulations morphed the aerofoil over time from an initial unmorphed state. For the static morphing, the aerofoil profile along with morphed profiles was generated in MATLAB for each morphed displacement and start location and ran separately in Star-CCM+

Dynamic morphing uses the built-in morpher inside Star CCM+ to move the vertices of the mesh with a defined displacement. The mesh displacement over time is specified by applying the FishBAC equation along the chord line. The FishBAC equation is written in java form in Eq. (3.19), the equation was written using an if statement which told the morpher that if the position is less than the user-defined morphing start location then there was no morphing. The equation also states if the position is greater than the morphing start location to switch on the morphing. Initially, the simulations were carried out with no morphing to allow the simulation to reach a steady out after 0.1 seconds. The morphing was then turned on using the term $Switch in Eq. (3.19) which is a time defined by the user to start the morphing. The morphing location is defined in Eq. (3.19) from the leading edge using the Cartesian 1 coordinate system.

$$y_x = [0, (\$\$\text{Position}(\text{“Cartesian 1”})[0] < \$\text{xs}) \ ? \ 0 : \$\text{wte} * (\text{pow}(\$\$\text{Position}(\text{“Cartesian 1”})[0] - \$\text{xs}, 3))/(\text{pow}(\$\text{c} - \$\text{xs}, 3))) * \$\text{Switch}\}, 0] \quad 3.19$$

The morpher does not account for the cell volume, faces or edges so the mesh quality needs to be monitored. Over time the mesh will show cells with high skewness, aspect ratios, etc and overall bad quality, then a re-mesh procedure is carried during aerofoil morphing.

The typical method of remeshing is to monitor the number of low-quality cells and re-mesh once this reaches a certain threshold. Due to a wide range of angles of attack and ground clearances tested the threshold will vary depending on the number of cells in the mesh. Therefore, a periodic meshing method was used remeshing at user-defined intervals in time. The time interval between remeshing period was based on the frequency and displacement of morphing. Larger displacements or higher morphing frequencies would result in smaller time intervals between remeshing. The quality of cells was monitored manually using plots to ensure the mesh quality was of an acceptable level throughout morphing. The entire morphing and remeshing process is shown in Figure 3.26.

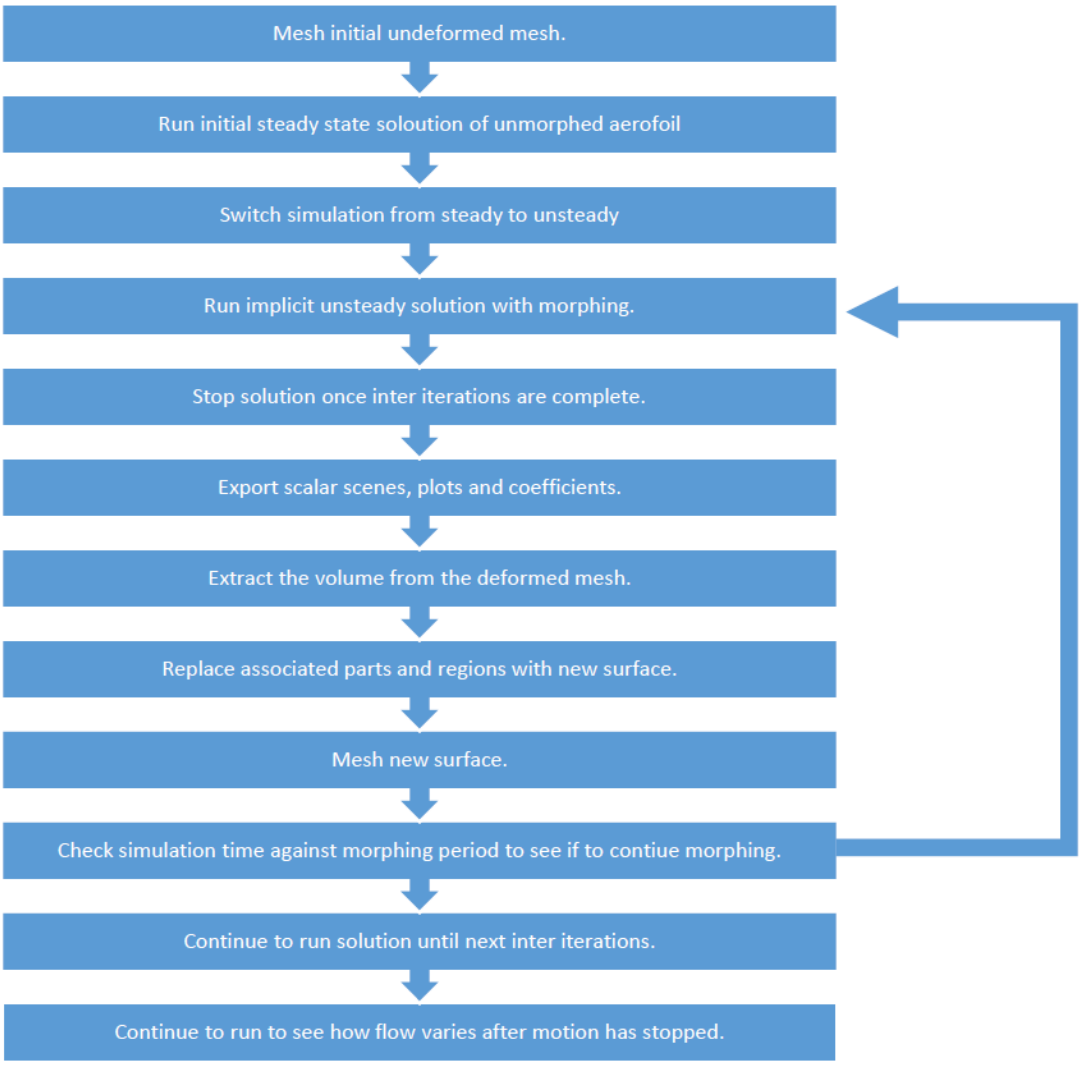

Figure 3.26: Automatic re-meshing morphing workflow.

Having shown the 2d morphing methodology using the FishBAC equations applied in the chord direction, the 2d can be expanded into three dimensions. Different proportions of the wing can be morphed in the span direction shown in Figure 3.27. To ensure the mesh did not sharply change from the non-morphed portion to the morphed portion, a transition region in the geometry was defined.

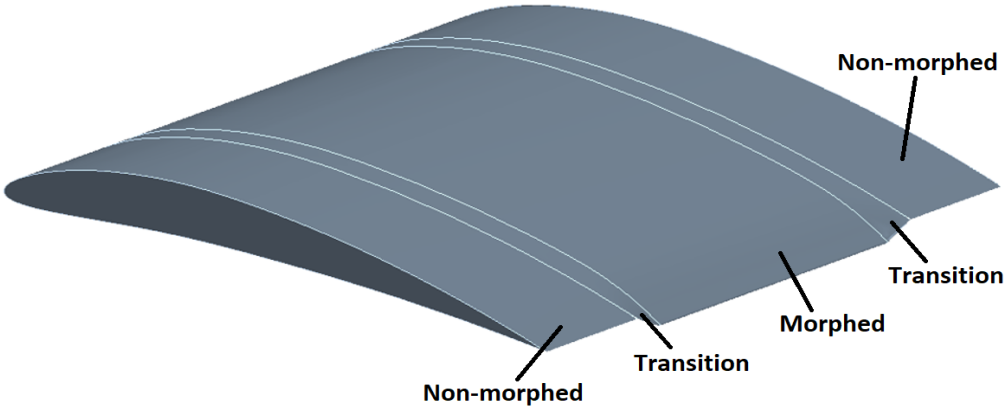

Figure 3.27: 3d morphed wing showing FishBAC morphing applied in chord direction.

The FishBAC morphing was applied in the chord direction in Figure 3.27 however this was also applied in the span direction in this study to morph the wingtips shown in Eq. (3.20). This required a modification to Eq. (3.19) to account for applying the morphing in a different direction on the coordinate axis shown in Eq. (3.20). The schematic of the defined variables was shown in Figure 3.28. The simulation was set up with the wing against a symmetry plane so Figure 3.27 is half the span therefore the edge against the symmetry plane is the midspan location. Various morphing lengths along the span were tested including partial and full span morphing.

$$y_z = [0, (\$\$\text{Position}(\text{“Cartesian 1”})[2] < \$zs)\ ?\ 0 : \$tc * (\text{pow}(\$\$\text{Position}(\text{“Cartesian 1”})[2] - \$zs, 3))/(\text{pow}(\$s - \$zs, 3))) * \$\text{Switch}\}, 0] \quad (3.20)$$

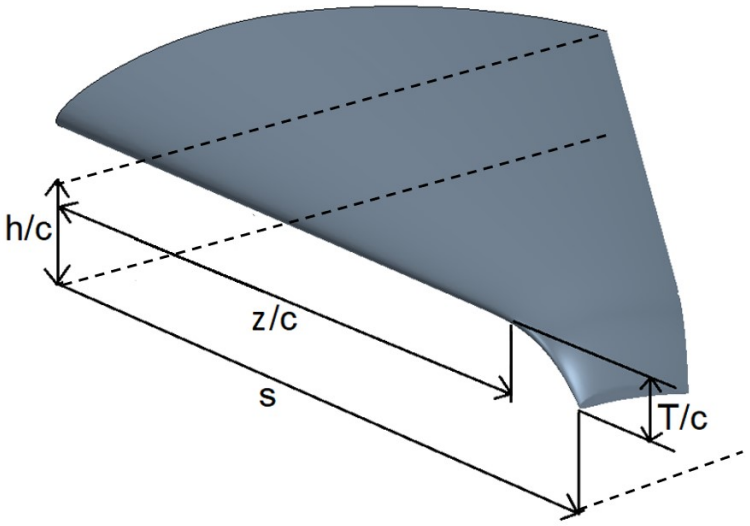

Figure 3.28: Schematic of FishBAC morphing in span direction.

3.5.7 Multidisciplinary design optimisation

Design optimisation is the process of finding the best possible design with a given set of design constraints. Start CCM+ has built-in methods for an automated approach to carry out design optimisation within Design Manager. There are two types of optimisation studies within Design Manager known as a weighted sum of objective and multiple objective trade-off study (Pareto front) which both uses the SHERPA algorithm. The weighted sum of objectives is based on a single objective, if multiple objectives are selected a linear weighting algorithm is used to combine all the objectives into one single performance function.

The Multi-objective trade-off study used in this study optimises the design based on two competing objectives therefore there is no single optimum design. This type of study outputs a curve known as the Pareto front which shows all the possible non-dominated designs which is a

trade-off between the competing objectives. Figure 3.29 shows an example Pareto front in the Star CCM+ user manual where the objectives are the lift set to maximum and drag to a minimum. Other designs not on this curve are non-optimum designs and should be discarded. The user then selects the design from the Pareto based on design criteria such as an aircraft wing requiring a certain amount of lift.

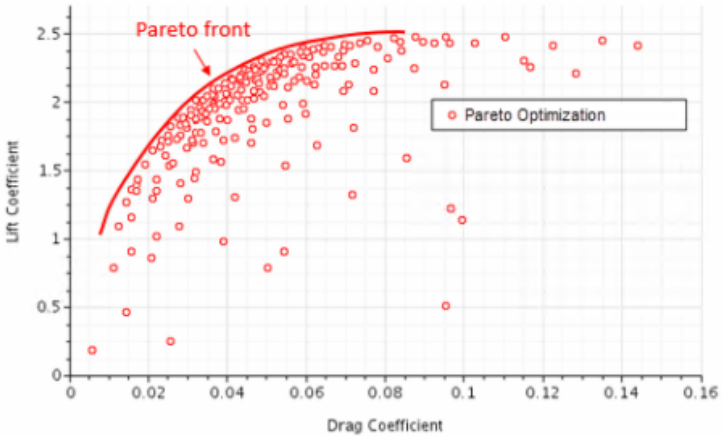

Figure 3.29: Example Pareto Front for aerodynamic efficiency (Chase et al., 2009).

The Multi-objective trade-off study uses a unique search algorithm during the optimisation study known as SHERPA (Simultaneous Hybrid Exploration that is Robust, Progressive, and Adaptive) (Chase et al., 2009). This method uses a combination of between two and ten global and local search methods at any given instance. As SHERPA learns about the design space it will decide which search methods to use and when to apply them. A unique feature is that the tuning parameters are automatically modified during the search within Design Manager. The multi-objective studies modify SHERPA known as the MO-SHERPA which allows the algorithm to handle multiple objectives independently of each other. Due to this study optimising the aerodynamic efficiency there are two competing objectives to maximise lift and minimise drag. Therefore, the Multi-objective trade-off study was used in this study with MO-SHERPA.

3.6 Summary

In this section an overview of different tools and methods were discussed which are used for the analysis of aerofoil. The methodology was also presented for the study stating that the trimmer mesh was selected and the domain size and boundary conditions. A moving ground plane was applied using a tangential velocity vector set to the freestream speed to replicate the real word interaction between the airflow and ground as in this study the reference frame was changed. Steady state RANS was used with the K-Omega SST turbulence model, for morphing over time the URANS model was used and for periodic morphing the DES model was used due to the high flow details which both used Implicit. The study was carried out using commercial CFD software which

also has built in multidisciplinary design optimisation tools. In the subsequent chapters the analysis of wings in ground effect and also morphing will be investigated and applied to a UAV.

Chapter 4 Fixed-wing in and out of Ground Effect Analysis

4.1 Introduction

In the previous chapter, an overview of governing equations and analysis methods were described as well as the methodology of tools and methods used in this study. In this chapter, validation is carried out by using a mesh independence study and comparison to experimental literature data. After completing the mesh independence and validation, an analysis of steady-state simulations of aerofoils in and out of ground effect was carried out in two dimensions. This allowed a vast amount of aerofoil geometries to be tested before a select few high performing geometries were tested in three dimensions before selecting the highest performing aerofoil to carry forward for the rest of the study.

4.2 Validation

4.2.1 2D Mesh Independence Study

The computational domain is split into a grid known as a mesh. To ensure the mesh is an adequate size to capture the low details, yet not too big that computational costs are increased, a mesh independence study was first carried out. This was done by varying the size of the mesh and recording the lift and drag coefficients and comparing this to zero grid spacing values. A constant boundary layer mesh height was kept throughout the mesh independence to ensure the y^+ remained equal to 1 as recommended in the software user manual (*User Manual Star CCM+ 14.04.013*, 2019) for the K-Omega SST turbulence model.

The mesh independence study was carried out using the ASME V & V 20 Committee (Coleman & Members, 2009) standard for verification and validation to determine the discretization error. The lift and drag coefficients are shown in Table 4.1 at three different grid spacings computed using steady RANS for the NACA6409 at 0-degrees AoA in freestream.

Table 4.1: RANS mesh cell count with corresponding lift and drag values in two dimensions.

Mesh Refinement	Cell Count	Cl	Cd
Fine	2746470	0.596	0.0131
Medium	724877	0.599	0.0131
Coarse	148704	0.618	0.0128

Using the Richardson extrapolation method with the fine and medium mesh, the zero-grid spacing value p_{zero} for both lift and drag values can be determined using Eq 4.1 where the lift and drag coefficients are denoted by f and the subscript denoting fine, medium, and coarse meshes. The order of convergence in Eq 4.1 was determined by $p_{zero} = \ln\left[(f_c - f_m)/(f - f_f)\right]/\ln(r)$ using the lift ad drag values and the grid refinement ratio was set to r = 2 (Coleman & Members, 2009). This resulted in a calculated value of lift of Cl = 0.596 and drag Cd = 0.0131 at zero grid spacing.

$$p_r = f_f + (f_f - f_c)/(r^{p_{zero}} - 1) \qquad 4.1$$

To ensure the values of lift and drag at the specified cell counts in Table 4.1 when used in Eq 4.1 yield a horizontal asymptotic behaviour at zero grid spacing, the grid convergence index (GCI) is used (Eq 4.2) as confirmation of the zero grid spacing value. For comparisons over three or more grids, a factor of safety of F_s = 1.25 was used (Coleman & Members, 2009). The relative error was denoted by $\varepsilon = (f_f - f_m)/f_f$ for the fine mesh and $\varepsilon = (f_m - f_c)/f_m$ for the coarse mesh. For the lift, the grid convergence index was GCI = 0.114% for the fine and GCI = 0.723% and for the drag, the grid convergence index was GCI = 0.0116% for the fine and a GCI of 0.572% for the course for the drag values.

$$GCI = \frac{F_s|\varepsilon|}{(r^{p_{zero}} - 1)} \qquad 4.2$$

The solution was then checked with Eq 4.3 which used the grid convergence index for both the fine and coarse mesh and the grid resolution $r^{p_{zero}}$ to ensure the value is within the asymptotic range of convergence. This yields a value of 0.9951 for the lift and 0.9987 for the drag, these values are approximately equal to 1 which satisfies Eq 4.3 showing that the zero-grid spacing calculated is a horizontal asymptote.

$$1 = \frac{GCI_{fm}}{(r^{p_{zero}} GCI_{mc})} \qquad 4.3$$

Using the zero grid spacing values for the lift and drag the errors were determined and shown in Table 4.2 for the lift and drag of each of the grid spacings. The fine and medium mesh show a

small error and the coarse mesh a much larger error. The medium mesh converged to within 0.58% for the lift and 0.16% for the drag. Whilst the fine mesh had a slightly smaller error, the gains in computational cost for the smaller mesh outweighed the reduction in error therefore the medium mesh was carried forward for the two-dimensional study using RANS.

Table 4.2: RANS mesh size error in two dimensions.

Mesh Refinement	Cl error%	Cd error %
Fine	0.09	0.01
Medium	0.58	0.16
Coarse	3.58	2.69

4.2.2 3D Mesh Independence Study

The mesh independence study was also carried out for the three-dimensional rectangular NACA6409 at 4 degrees angle of attack using the same method as the two-dimensional mesh independence using the ASME V & V 20 Committee (Coleman & Members, 2009) standard for verification and validation. The three mesh refinements using RANS was shown in Table 4.3.

Table 4.3: RANS mesh cell count with corresponding lift and drag values in three dimensions.

Mesh Refinement	Cell Count	Cl	Cd
Fine	74121642	0.708	0.0489
Medium	20017574	0.712	0.0492
Coarse	6178815	0.724	0.0500

Using the three grid resolutions the theoretical zero grid spacing for lift was Cl = 0.706 and drag Cd = 0.0487. As with the two-dimensional case, the zero grid spacing was checked and the solution showed an asymptote using the CGI check. Using Eq 4.2 and putting the values of CGI for lift and drag into Eq 4.3 resulted in the values being approximately equal to 1, therefore the check showed the valid zero grid spacing.

Table 4.4: RANS mesh size error in three dimensions.

Mesh Refinement	Cl error%	Cd error %
Fine	0.30	0.36
Medium	0.85	0.97
Coarse	2.42	2.56

The lift and drag values of the three-dimensional wing were compared with the zero-grid spacing and the errors are shown in Table 4.4. As the medium mesh almost had an error of 1% for the drag and 0.9% for the lift, the fine mesh was selected as this had an error of 0.3% for the lift and 0.36% for the drag. Although there are increased computational costs for the fine mesh, this mesh gave much lower errors compared to the medium mesh therefore the fine was carried forward for the study.

4.2.3 2D Validation

Validation was carried out and compared to the literature to ensure the simulation was set up correctly ensuring the values including lift and drag correspond to the literature. A comparison was made against experimental data to ensure errors and uncertainties have not been carried forward from other CFD studies in literature. The two-dimensional NACA6409 was compared against wind tunnel data, due to a lack of experimental high aspect and two-dimensional approximation studies in ground effect, only freestream was compared.

Two data sets from literature were used which include Lim et al., (2009) and Selig et al., (1989) at a Reynolds number of 200,000. The lift was shown in Figure 4.1 where the lift follows the experimental data very closely, especially at low angles of attack. It was seen in this study that stall occurred at 10 degrees AoA which showed stall at approximately 9 degrees and Selig et al., (1989) at approximately 10 degrees; however the CFD in this study predicted a slightly higher peak lift of 2.3% compared to literature. The CFD in this study remained approximately 2% higher than in the literature as the angle of attack was increased.

The drag was also used for validation in this study using the literature values from Lim et al., (2009) and Selig et al., (1989) shown in Figure 4.2. It was seen below 6 degrees that the experimental data and CFD matched very closely however as the drag values are an order of magnitude less than the lift, above 6 degrees there is a bit more of a variation in drag. Above 12 degrees it was seen the drag was similar between both the experiment and CFD in this study.

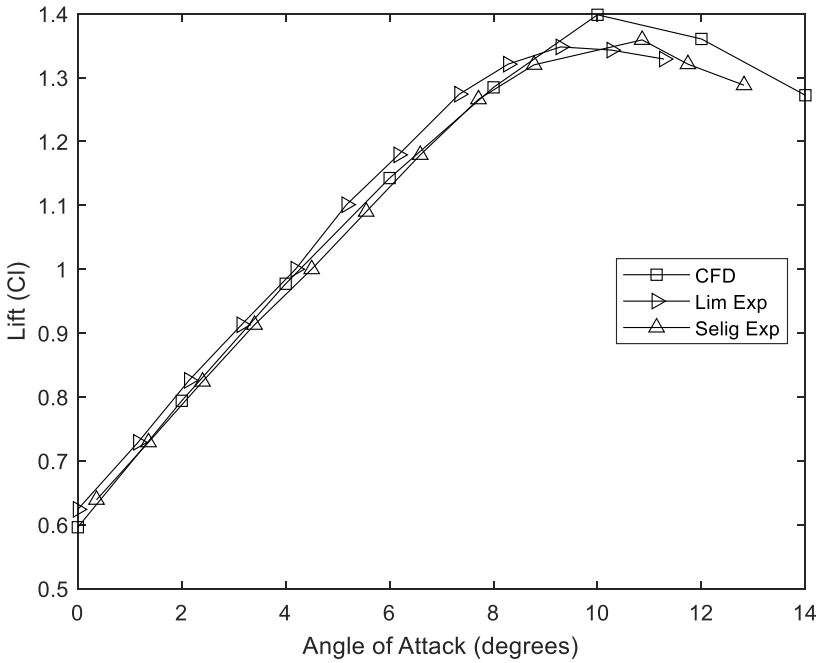

Figure 4.1: Lift experimental freestream comparison to CFD of NACA4412.

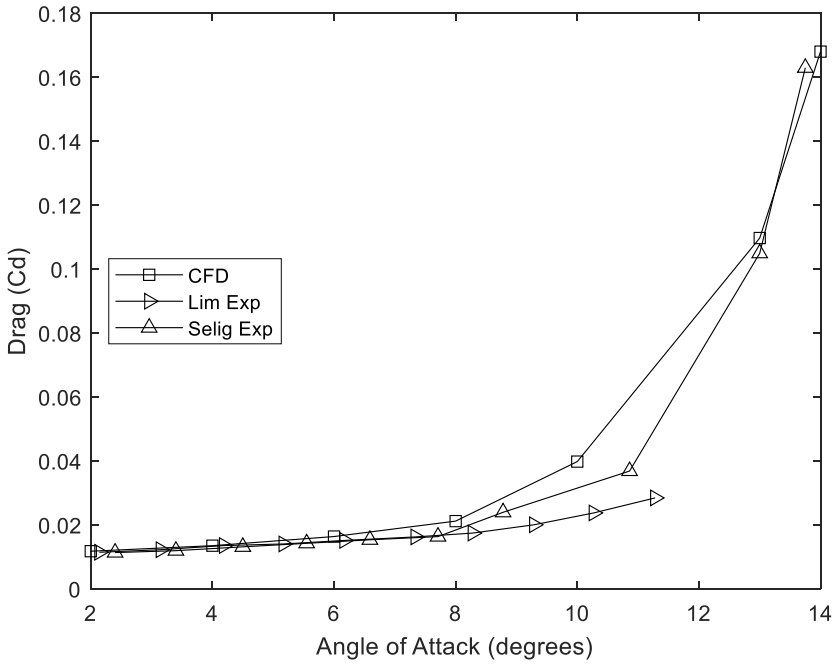

Figure 4.2: Drag experimental freestream comparison to CFD of NACA4412.

The differences between the experimental literature and CFD are considered small when considering the experimental uncertainties and errors induced in CFD. In the experiments, the aerofoils needed to be held in the flow, however, it was unclear how the aerofoils were mounted. There are other uncertainties such as angle of attack, and data acquisition resolution which all add up to a noticeable uncertainty value. The sources of error for CFD include rounding, iterative, convergence, and discretisation errors (Feszty & Jakubík, 1998).

Considering the errors of the CFD and uncertainties of the experimental data, it was seen that the CFD and literature show very similar lift and drag values along with very similar trends showing the validity of the CFD in this study.

4.2.4 3D Validation

Having carried out validation in two dimensions, validation was then extended to three dimensions using RANS with K-Omega SST. A comparison was made using the mesh-independent solution from section 4.2.2 with experimental data. A study carried out by K. H. Jung et al., (2008) researched endplates attached to the NACA6409 in ground effect for low aspect ratios (1, 1.5, 2) at various ground clearances. The data used from this study was for a NACA6409 with an aspect ratio of 2 without an endplate and Reynolds numbers of 3.4×10^5 as this closely represented the set-up in this study. Figure 4.3 shows the comparison of the experimental data for both lift and drag at a ground clearance of h/c = 0.1 from 0 to 8 degrees angle of attack. Both the experimental and CFD showed very similar drag and lift coefficients. The lift showed an offset of 4% with the experimental lift being slightly higher than the CFD. The drag showed slightly higher offset of 7% where the CFD was slightly higher than the experimental data.

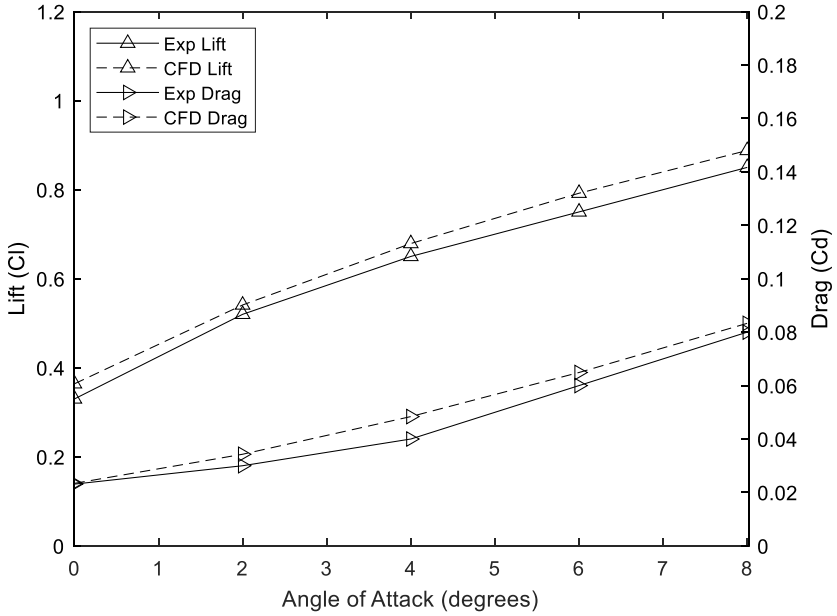

Figure 4.3: Lift and darg comparison ground effect experimental comparison.

As well as the errors of the CFD and the uncertainties of the experiments mentioned in the two-dimensional validation, additional errors were stationary in the experiment compared to the moving ground. Jamei et al., (2018) and Yang et al., (2010) showed similar offsets in lift and drag for a compound wing in ground when comparing a fixed and moving ground. Considering the uncertainties and errors mentioned in the two-dimensional validation, the three-dimensional data

closely matched the experimental. The key validation was the trends of both the experimental and CFD closely followed the same trends.

4.3 2D Aerofoil Discussion

To gain an understanding of different aerofoil geometries in ground effect, a study was carried out analysing a vast amount of aerofoil profiles as shown in Table 4.5. Although the upper surface of positive lift-producing aerofoils can have different curvatures or slight variations in shape, the lower surface significantly varies between different profiles compared to the upper surface. This allows the aerofoil geometries to be split into three categories defined as concave, flat or convex as shown by the schematics of each type in Table 4.5. For each aerofoil, a range of angles of attack from 0 to 18 degrees for each ground clearance ranging from 5% to 40% ground clearance with 100% being freestream. The lift, drag and efficiency were then plotted and shown in the results (Figure 4.4, Figure 4.5, and Figure 4.6) with the full aerofoil data tabulated in appendix A.1.

Table 4.5: Aerofoil lower surface categories.

Concave	Flat	Convex
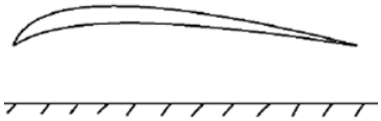	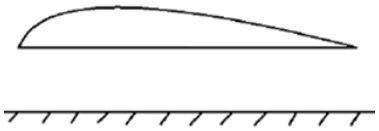	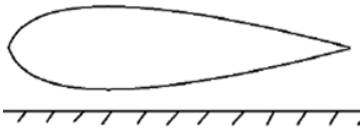
BE50	Clark Y	B707b
Clark W	Curtis C72	BOE106
E58	DHMTU 10-40.12-10.2-60-21.5	K3311
E376	DHMTU 12-35.3-10.2-80.12	KC135b
E396	Eiffel 385	NACA0012
GOE395	FX77 x121	PMC19
GOE802b	Sikorsky GS1	
GOE803h	ISA961	
HS1708	MUE139	
M25	NACA4412	
MH115	Prandtl D	
NACA6409	R3A	
NACA6412		
NACA M8		
Waco Cootie		

Analysing the different types of aerofoils has shown the lower surface geometry had a significant effect on the aerodynamic performance in ground effect. The lift increases on an aerofoil when brought into ground effect due to an increase in pressure on the lower surface. Analysing the different aerofoil profiles in Table 4.5 showed a significant difference between the concave, flat and convex lower surfaces.

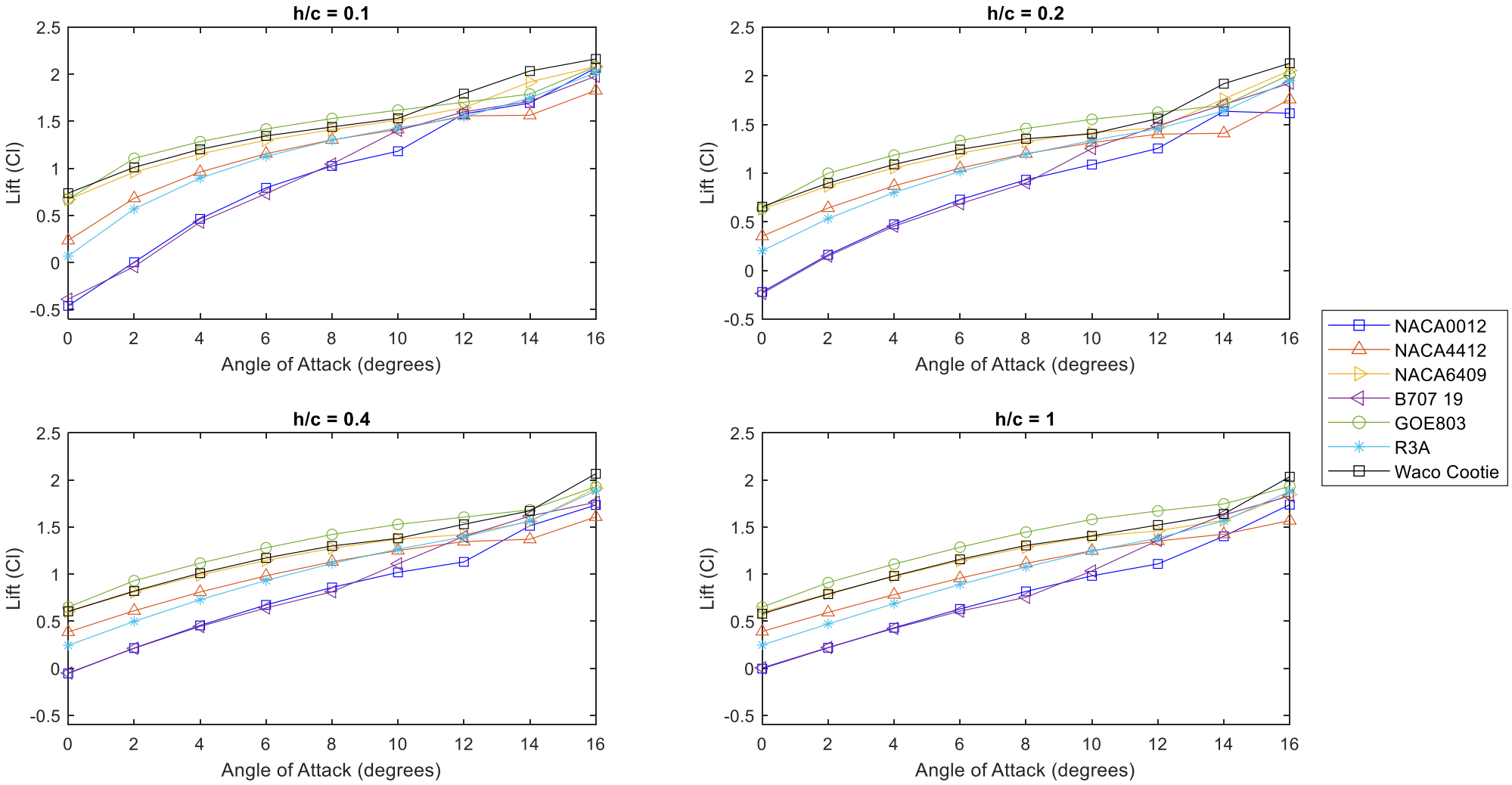

Figure 4.4: 2D lift results for different profiles.

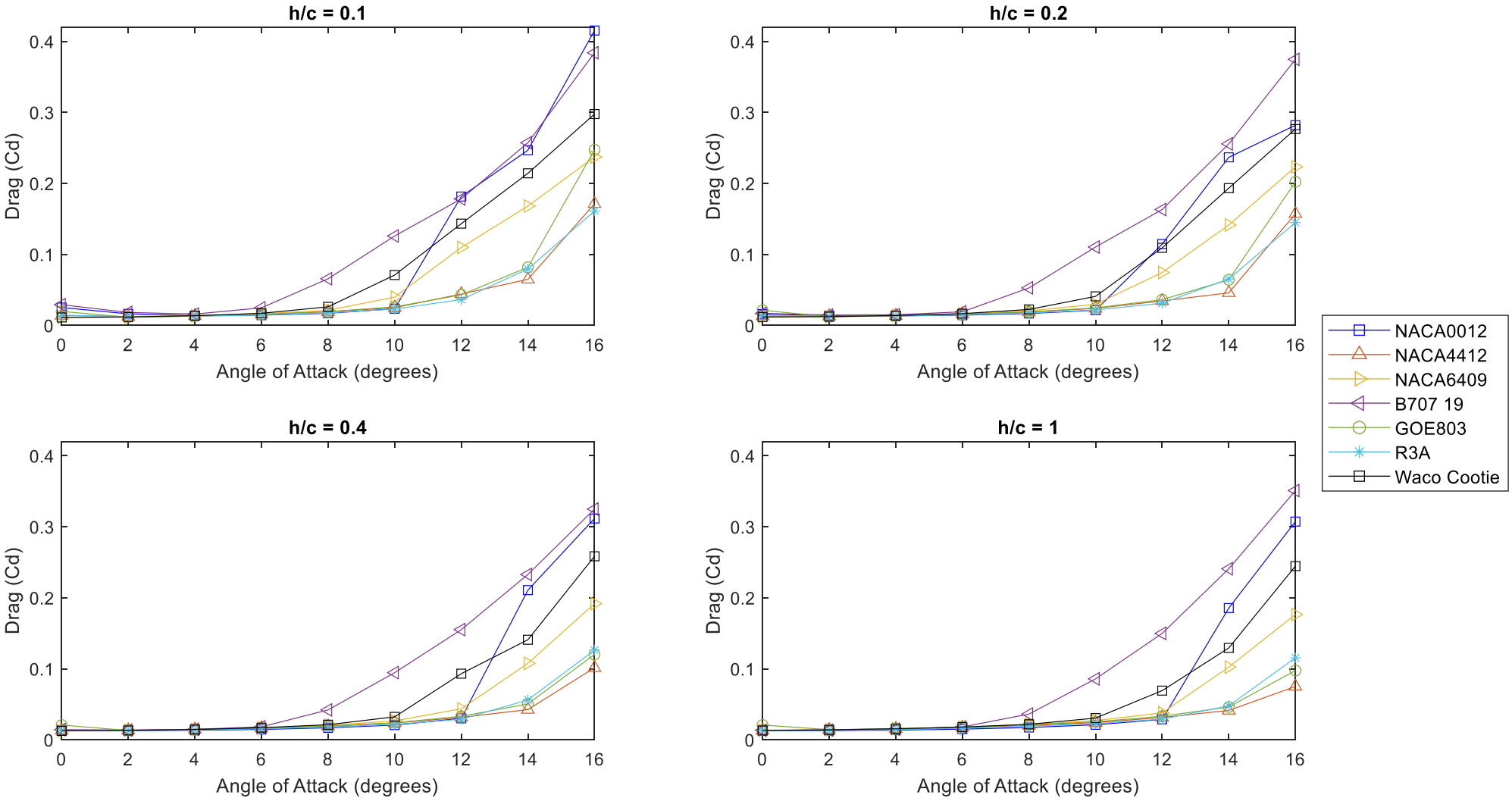

Figure 4.5: 2D drag results for different profiles.

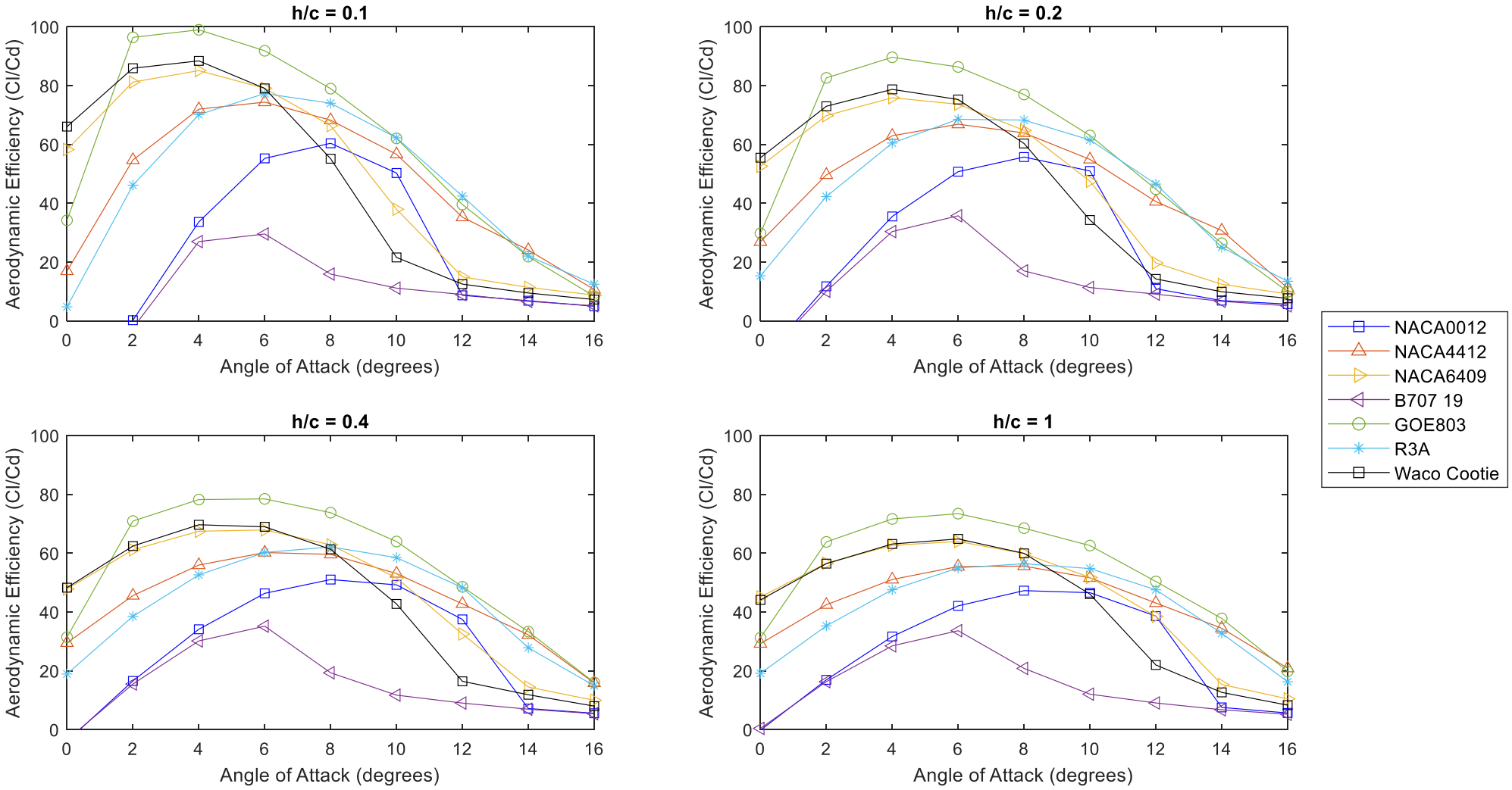

Figure 4.6: 2D efficiency results for different profiles.

This was due to the Kutta condition fixing the trailing edge pressure which caused the pressure to vary upstream of the trailing edge as the angle of attack and ground clearance varied. For a given ground clearance and angle of attack, the distance between the lower surface and ground will vary depending on the lower surface geometry of the aerofoil profile. The effect of the lower surface geometry on the pressure can be shown using Bernoulli and continuity equations. Substituting the continuity equation (Eq. 4.5) into Bernoulli's (Eq. 4.4) yields Eq. (4.6) shows increasing Ax increases the overall pressure beneath the aerofoil, this shows the area ratio between the trailing edge and distance upstream is of key importance. Also decreasing Ate is seen to increase the pressure beneath the wing.

$$P_x + \frac{1}{2}\rho u_x^2 = P_{TE} + \frac{1}{2}\rho u_{TE}^2 \quad 4.4$$

$$u_x = \frac{A_{TE}}{A_x} u_{TE} \quad 4.5$$

$$P_x = P_{TE} + \frac{1}{2}\rho u_{TE}^2 \left[1 - \left(\frac{A_{TE}}{A_x}\right)^2\right] \quad 4.6$$

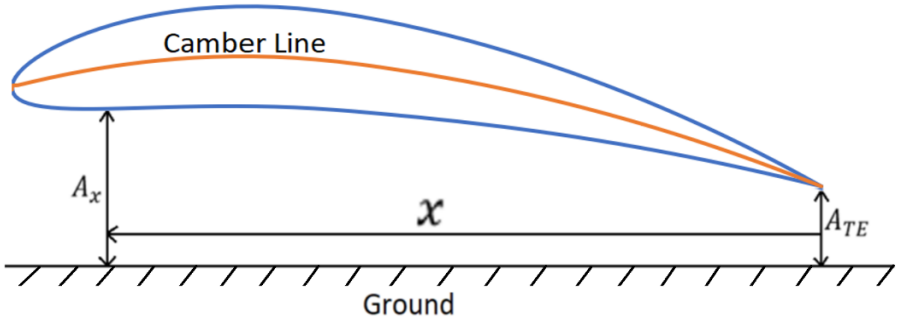

Figure 4.7: Aerofoil in ground effect schematic.

This can be seen by comparing the static pressure (Figure 4.8) around the GOE803 concave, NACA4412 flat and NACA0012 convex aerofoils showed in ground effect with 10% ground clearance. It was seen all the aerofoils have the same trailing edge pressure defined by the Kutta condition. Upstream of the trailing edge on the lower surface showed the pressure to increase for the high camber concave aerofoils (Figure 4.8a) due to the increased Ax value. With the convex aerofoils (Figure 4.8b) the pressure reduced upstream of the trailing edge due to Ax reducing which can cause suction on the lower surface at low angles of attack when in ground effect. This suction pulls the aerofoil towards the ground reducing the overall lift, if the suction on the lower surface is greater than the suction on the upper surface then the overall lift would become negative. Some of the aerofoils tested showed negative lift at zero or small angles of attack due to the suction on the lower surface being greater than the upper surface suction. This was seen in Figure 4.4 where the NACA0012 and B707-19 produced negative lift at 10% and 20% ground

clearance. Other aerofoils (appendix A.1) showed negative lift were the KC135, Prandtl D, NACA0012, B707-19, PM19, R3A, BOE106, KC135 and both DHMTU profiles. As the angle of attack increased, the lower surface became higher than the trailing edge resulting in the value of Ax increasing reducing the suction on the lower surface. Flat bottomed aerofoils (Figure 4 12c) have a constant value of Ax; therefore, the pressure did not vary along the lower surface. In all cases increasing the angle of attack increases the pressure on the lower surface causing the lift to increase due to the increased value of Ax.

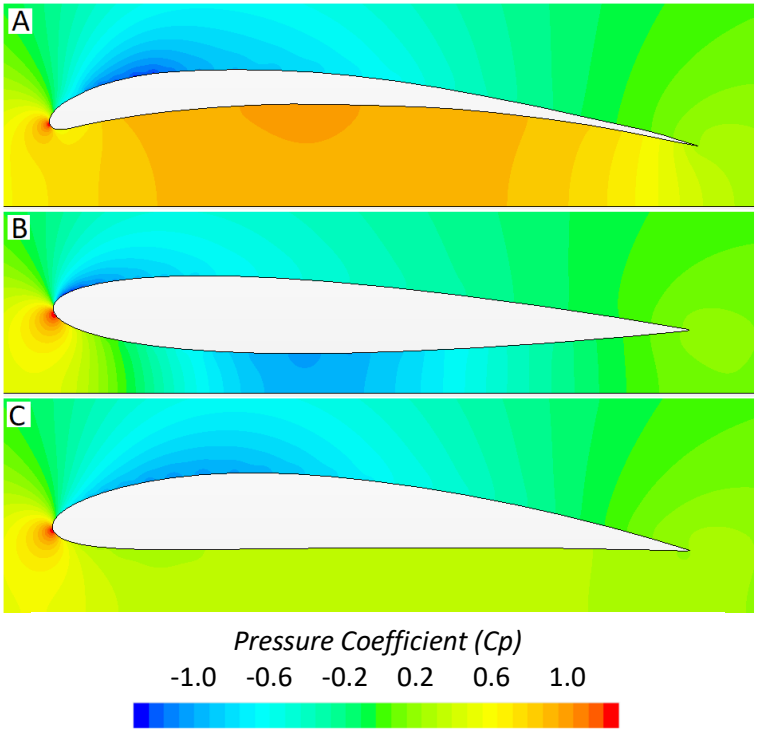

Figure 4.8: GEO803 (A), NACA0012 (B), NACA4412 (C) static pressure.

Analysing the pressure around the NACA4412 (Figure 4.9) varying the ground clearance at 4- and 12-degree angles of attack showed reducing the ground clearance increased the pressure on the on the lower surface. As the aerofoil became close to the ground the rate at which the pressure increased went up. This was shown by the spacing in pressure between 40% and 20% ground clearance being much smaller than the spacing between the 10% and 5% ground clearance in Figure 4.9. It was noted that the pressure on the upper surface had a very minimal change as the ground clearance varied except for the suction peak as the ground clearance varied.

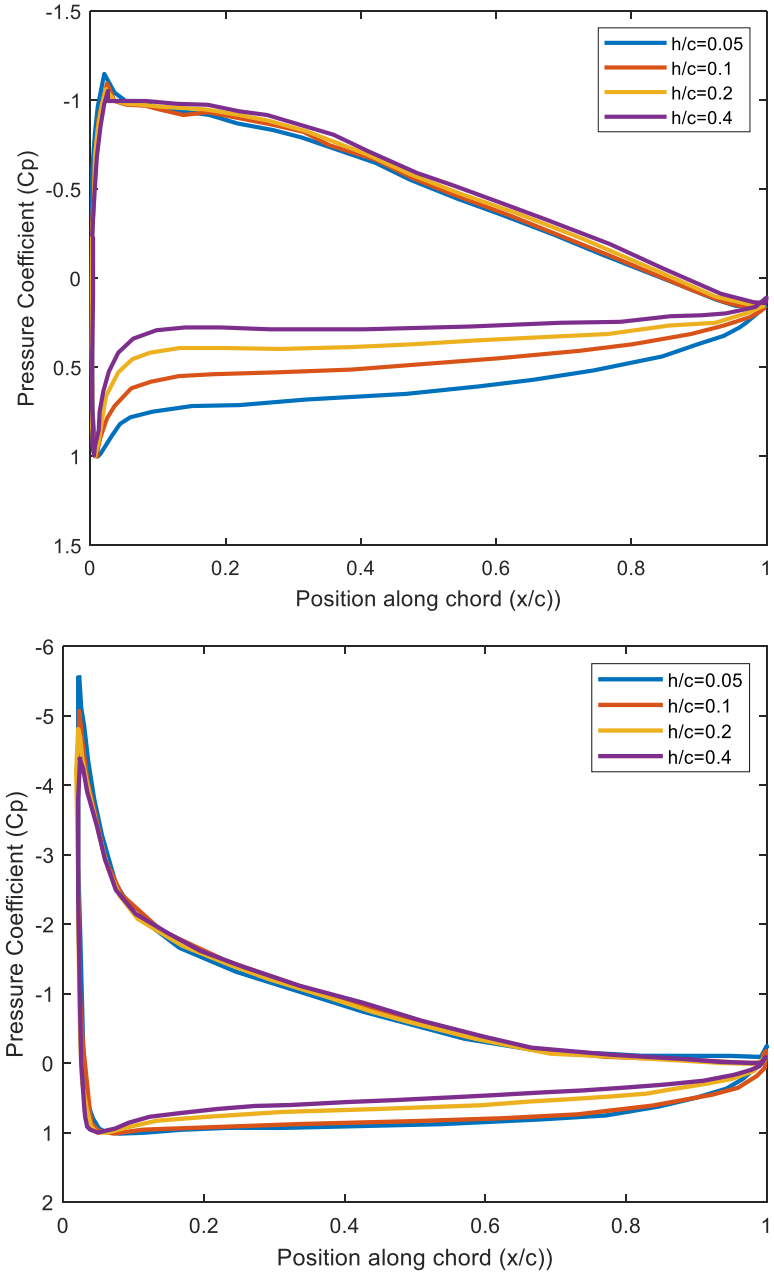

Figure 4.9: Pressure coefficient around NACA4412 at 5%, 10%, 20% and 40% ground clearance at 4deg (top) and 12 deg (bottom) AoA.

This was visualised on the aerofoil by looking at the static pressure coefficient for the NACA4412 in freestream and 10% ground effect at 8 degrees angle of attack (Figure 4.10). It is seen that both the freestream and the trailing edge have the same trailing edge pressure whilst in 10% ground effect that the pressure was much higher upstream of the trailing edge compared to freestream. Both ground effect and freestream showed similar upper surface pressures.

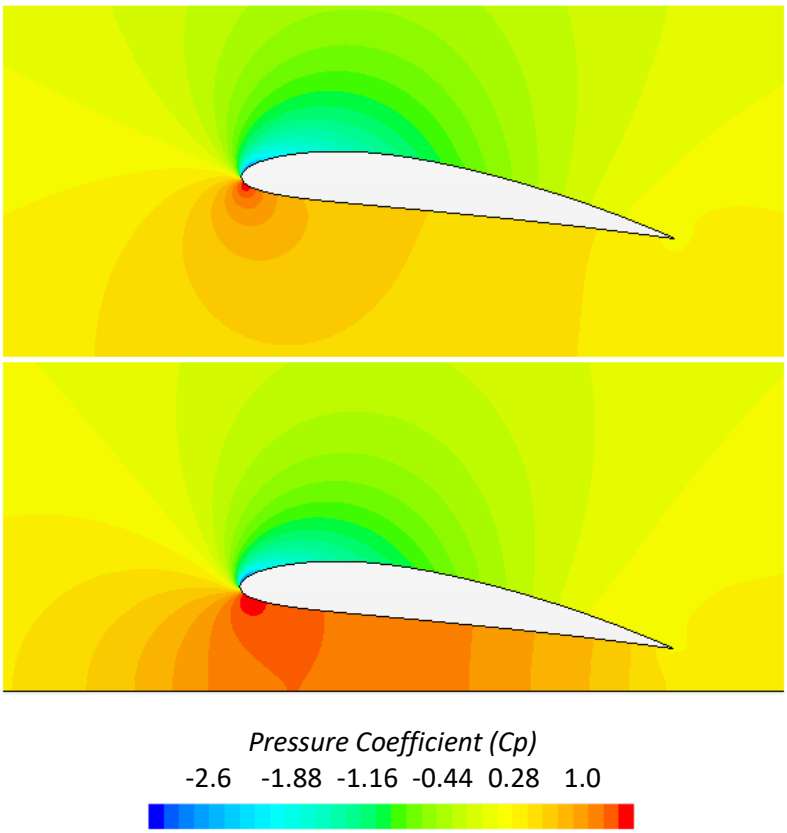

Figure 4.10: NACA4412 pressure at h/c = 10% (lower) and freestream (top) at 8 degrees AoA.

The pressure contours of the NACA4412 were also analysed at 10% and 40% ground clearance varying the angle of attack (Figure 4.11). Varying the angle of attack in ground effect shows the suction to increase on the upper surface and a pressure increase on the lower surface. A key observation was the suction peak was much higher at a higher angle of attack when in freestream compared to ground effect. At both clearances, suction was the same with only the lower surface pressure varying for the 0-to-12-degree AoA. Comparing the 16-degree angle of attack in ground effect showed a lower peak and that the pressure coefficient in 10% ground effect had a flat pressure region up to 0.2c which signifies the flow separated. This shows the flow separates earlier in ground effect compared to freestream. However, in Figure 4.4 it was seen that the lift continues to increase due to the lower surface still generating ground effect enhancement.

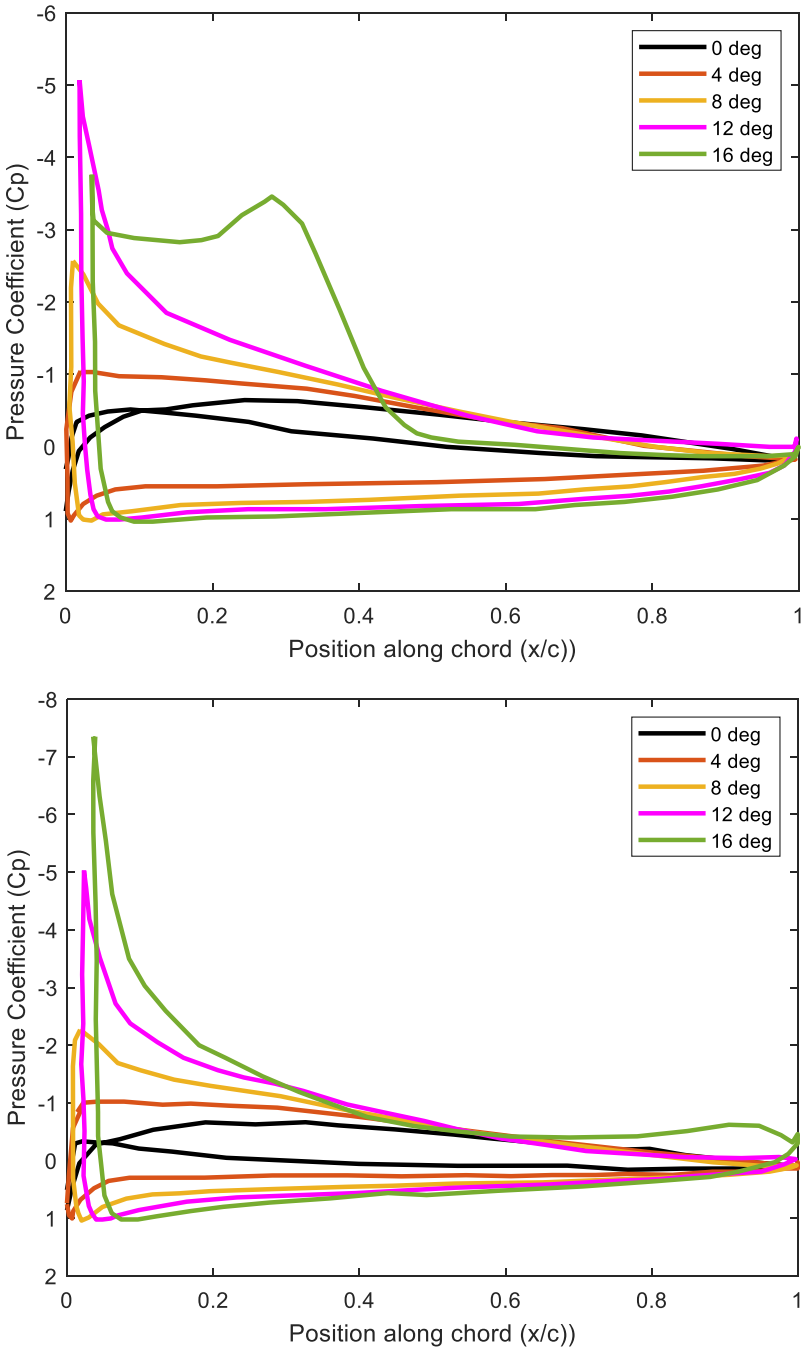

Figure 4.11: Pressure around NACA4412 varying AoA in 10% (top) and 40% (lower) ground clearance.

Other aerofoils the same behaviour was observed, and it was seen for the NACA0012 that a separation bubble also occurred at a lower angle of attack when in ground effect compared to freestream. The separation bubble occurred at 12 degrees in ground effect compared to 14 degrees in freestream (Figure 4.12).

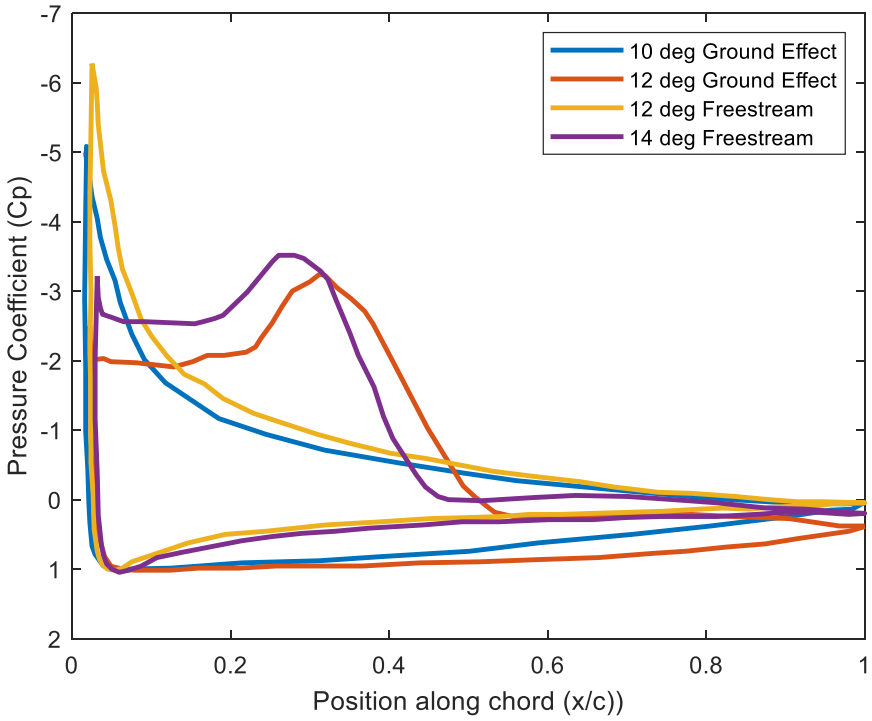

Figure 4.12: NACA0012 pressure plots showing separation bubble.

The greater amount of separation on the upper surface can be visualised by the non-dimensional velocity contour plots around the NACA6409 at 11 degrees angle of attack (Figure 4.13). In freestream (Figure 4.13 left) there was a small region of stagnate separated flow at the trailing edge on the upper surface. In ground effect, there was a separation bubble at the leading edge before the flow reattached then showed a larger region of separation on the upper surface (Figure 4.13 right). The high suction peak observed in freestream at the leading edge was not present in ground effect due to the separation bubble.

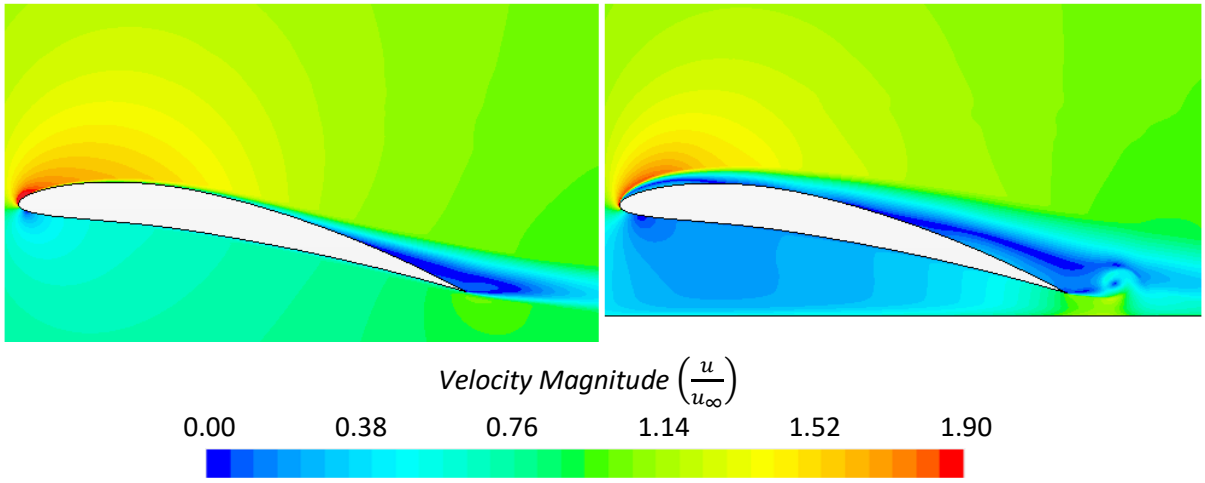

Figure 4.13: Velocity contour plot of NACA6409 in freestream (left) and 10% ground effect (right).

There are two reasons leading to greater separation in ground effect, the first is due to the proximity of the ground reducing the downwash at the trailing edge causing a reduction in

downwards momentum. The second is due to the stagnation point at the leading edge moving downstream on the lower surface when the wing was brought into ground effect shown in Figure 4.14 for the NACA0012. The stagnation point moving downstream causes a greater distance and curvature for the streamline to travel around the leading edge, therefore, is prone to earlier separation. This was also seen for increasing the angle of attack in ground effect (Figure 4.15) where the stagnation point moved downstream on the lower surface.

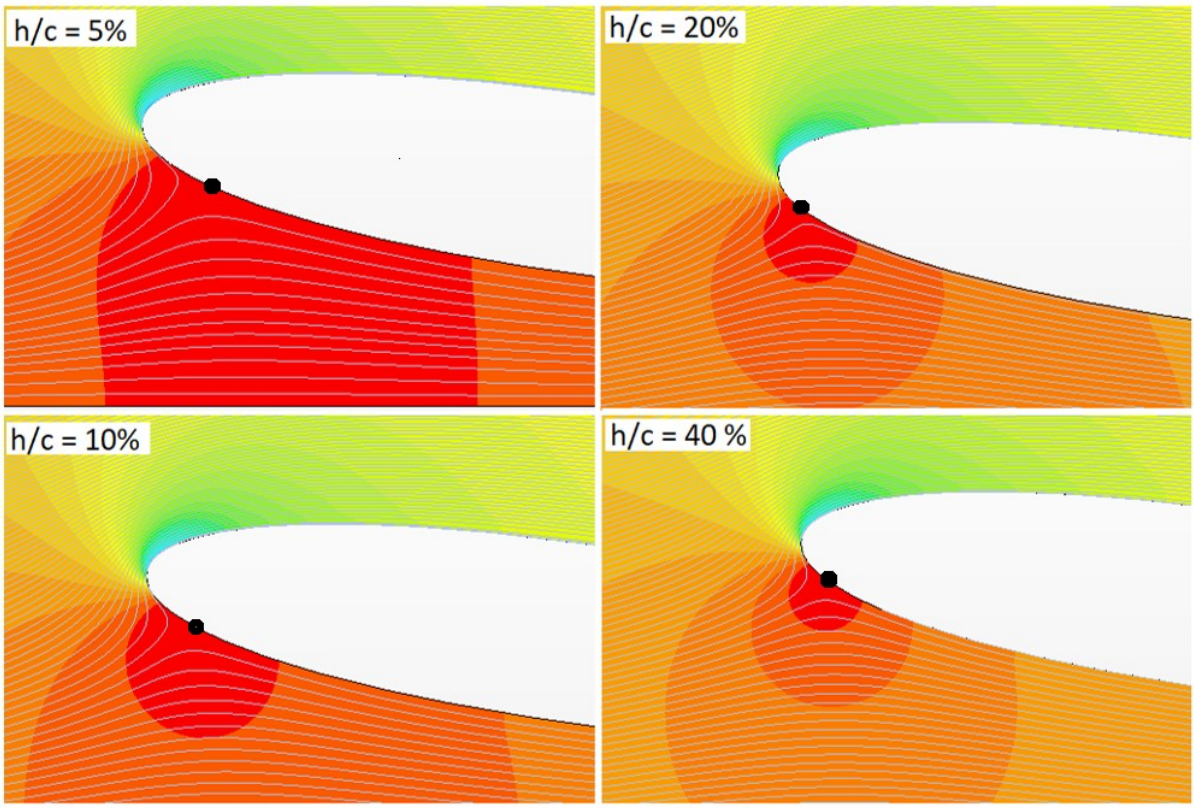

Figure 4.14: Stagnation point shown by streamlines varying ground clearance of 8 deg NACA0012.

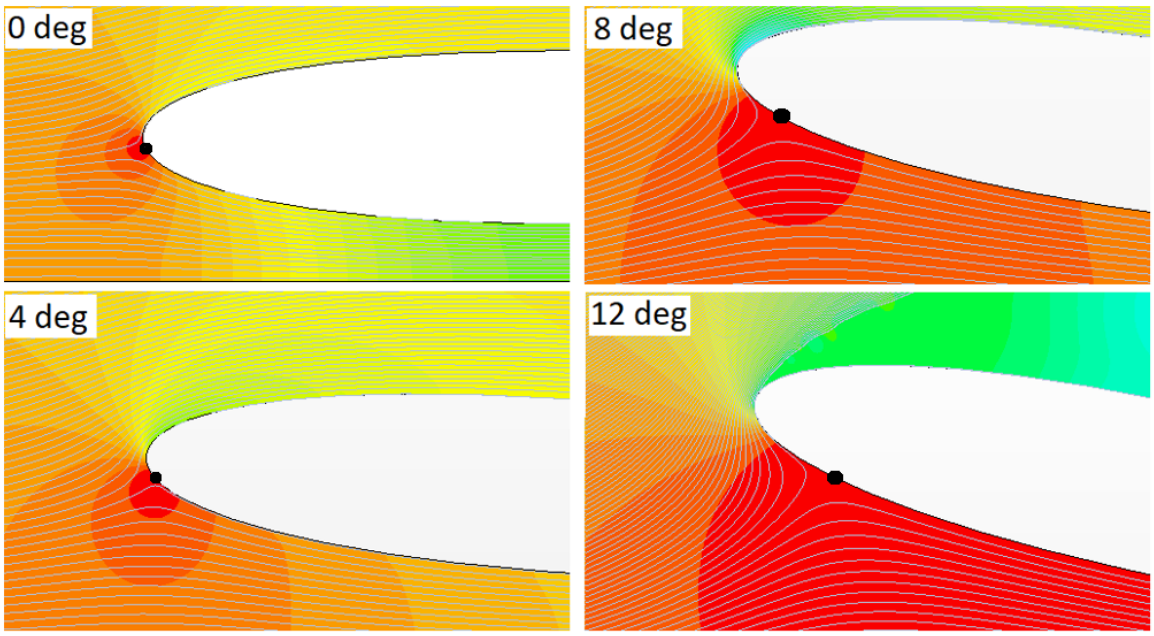

Figure 4.15: Stagnation point shown by streamlines varying AoA of NACA0012 and h/c = 0.1.

One reason the stagnation point moves downstream on the lower surface when brought into ground effect was due to a reduction in mass flow rate beneath the aerofoil when in ground effect. This was investigated with the NACA6409 at 3 degrees angle of attack at various ground clearances and the mass flow rate measured at the trailing edge. The mass flow rate was written non-dimensionally against the mass flow rate in freestream. It is seen (Figure 4.16) reducing the ground clearance caused the mass flow rate to reduce. The reduction in mass flow rate beneath the aerofoil in ground effect demonstrates the high blockage effect for a wing in ground effect.

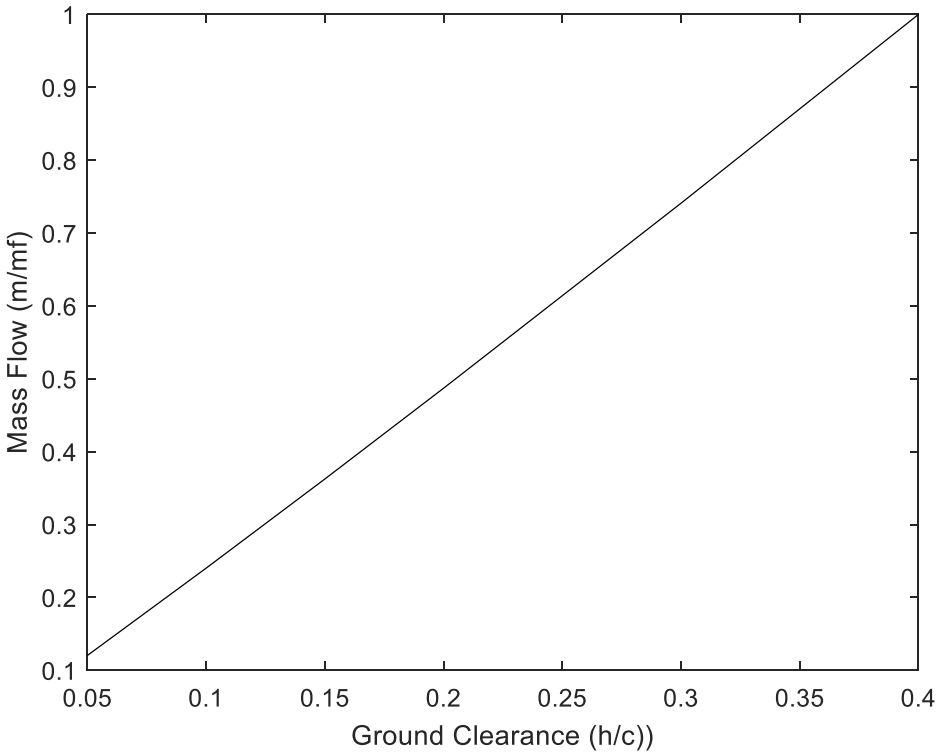

Figure 4.16: Mass flow rate beneath NACA6409 at 3 degrees AoA varying ground clearance.

Ground clearance in the literature review and this study was always referred to as the distance from the trailing edge to the ground. At low ground clearances and low angles of attack, convex aerofoils may touch the ground shown by the KC135 aerofoil (Figure 4.17 left). The blockage of flow beneath the aerofoil caused the flow to stagnate and the drag to dramatically increase, the stagnant flow caused the pressure to increase which dramatically increased the lift. The high increase in lift compared to drag resulted in high aerodynamic efficiency. This type of aerofoil however can be dangerous to use on a wing in ground effect craft due to sudden increase in lift making the craft very sensitive to ground clearance changes. Increasing the altitude slightly so the flow can pass freely beneath the wing would cause a sudden loss in lift and a sharp change in pitching moment which is more sensitive as the wing is closer to the ground.

Comparing the convex to a concave aerofoil shows the concave lower surface does not touch the ground at low ground clearances. Figure 4.17 right shows the lower surface curvature of the concave aerofoils caused separation to occur on the lower surface at low angles of attack. This stagnant region of low-velocity results in a high-pressure region increasing lift and is slightly less sensitive in ground effect compared to the concave aerofoil.

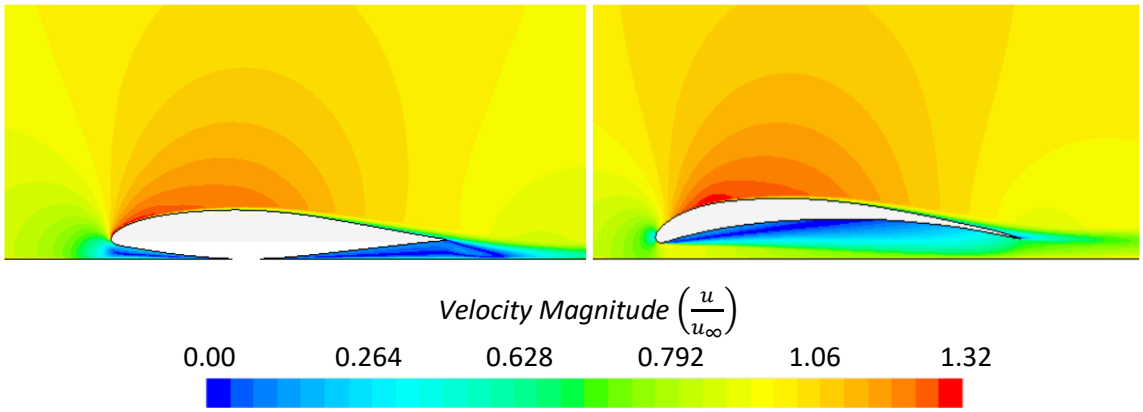

Figure 4.17: Velocity of KC135 (left) and GOE803 (right) at 0 degrees AoA and h/c = 0.05.

Comparing the efficiencies of all the aerofoils (appendix A.1) it was found the highest performing aerofoils were the concave aerofoils with low thickness. The e376 showed the highest peak efficiency for all ground clearances however at low angles of attack up to 4 degrees the efficiency was low compared to the other aerofoils due to the amount of lower surface separation. Although this had the highest efficiency, the low thickness makes this aerofoil difficult to apply to aircraft to be able to withstand structural loads. The GOE803 was a concave aerofoil that consistently performed well in terms of high lift and efficiency throughout all ground clearances and angles of attack. The reason the high camber aerofoils produce the highest efficiency is due to the larger area ratio on the lower surface demonstrated by Figure 4.7 causing the highest pressure on the lower surface.

By far the worst performing aerofoil was the B707b which had a sharp geometry change on the lower surface. This caused separation on the lower surface increasing drag at low angled of attack. Also due to the shape of the leading edge, the flow easily separated on the upper surface which increased drag.

Overall, the highest performing aerofoils in terms of lift and efficiency were the thin high camber aerofoils but for practical use, the aerofoil needs to be of a substantial thickness to be structurally feasible. Therefore, the GOE803, NACA6409, Waco cootie and BE50 were selected. To be able to compare to other studies, commonly used aerofoils were also selected including the NACA4412 and Clark Y.

4.4 3D Aerofoil Discussion

Extruding a two-dimensional aerofoil to a three-dimensional wing introduces a directional element in the spanwise direction. The key feature of a wing in three-dimensions which is not present in two dimensions is a wingtip vortex (Figure 4.18) caused by the high pressure beneath the wing driving a flow around the wingtip to the lower pressure on the wing upper surface. The

high pressure at the root shown in Figure 4.19 is seen to drive the spanwise flow towards the wingtip shown on the front view plane located at mid-chord.

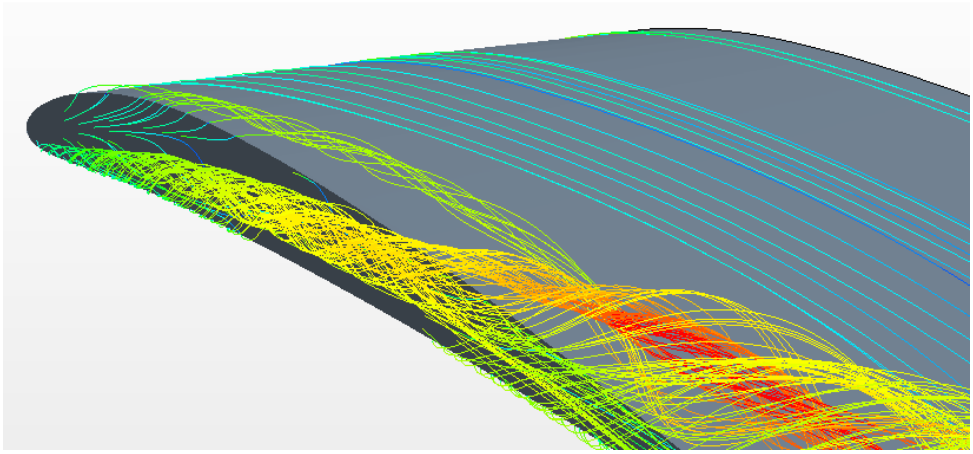

Figure 4.18: Wingtip vortex streamlines.

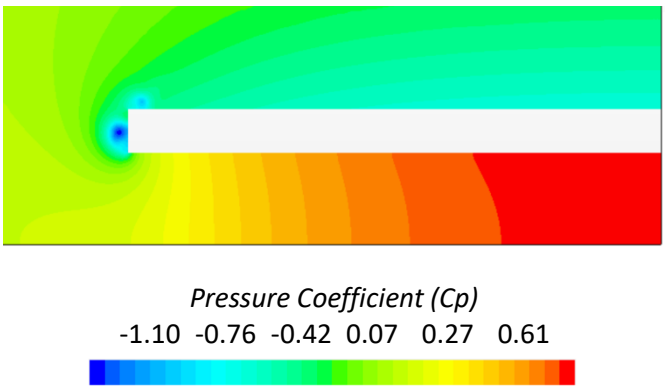

Figure 4.19: NACA6409 pressure distribution on a plane at mid-chord.

The pressure on the wing lower and upper surface was shown in Figure 4.21 (left) for the NACA6409 in both ground effect and freestream. It was seen the wingtip vortex affected the pressure on the lower surface near the wingtip, especially in ground effect which reduced the overall lift compared to two dimensions (Figure 4.20 left). On the lower surface, the pressure at the mid-span was like that of two dimensions, the pressure gradually decreases in the span direction towards the wingtip and more rapidly decreased at the wingtip. Ground effect increases the pressure on the lower surface therefore there is a greater pressure variation between the root and wingtip feeding the wingtip vortex when compared to freestream (Figure 4.21 top). The variation in pressure was seen to be far less on the upper surface Figure 4.21 as the wingtip vortex was pushed outboard in ground effect Figure 4.18.

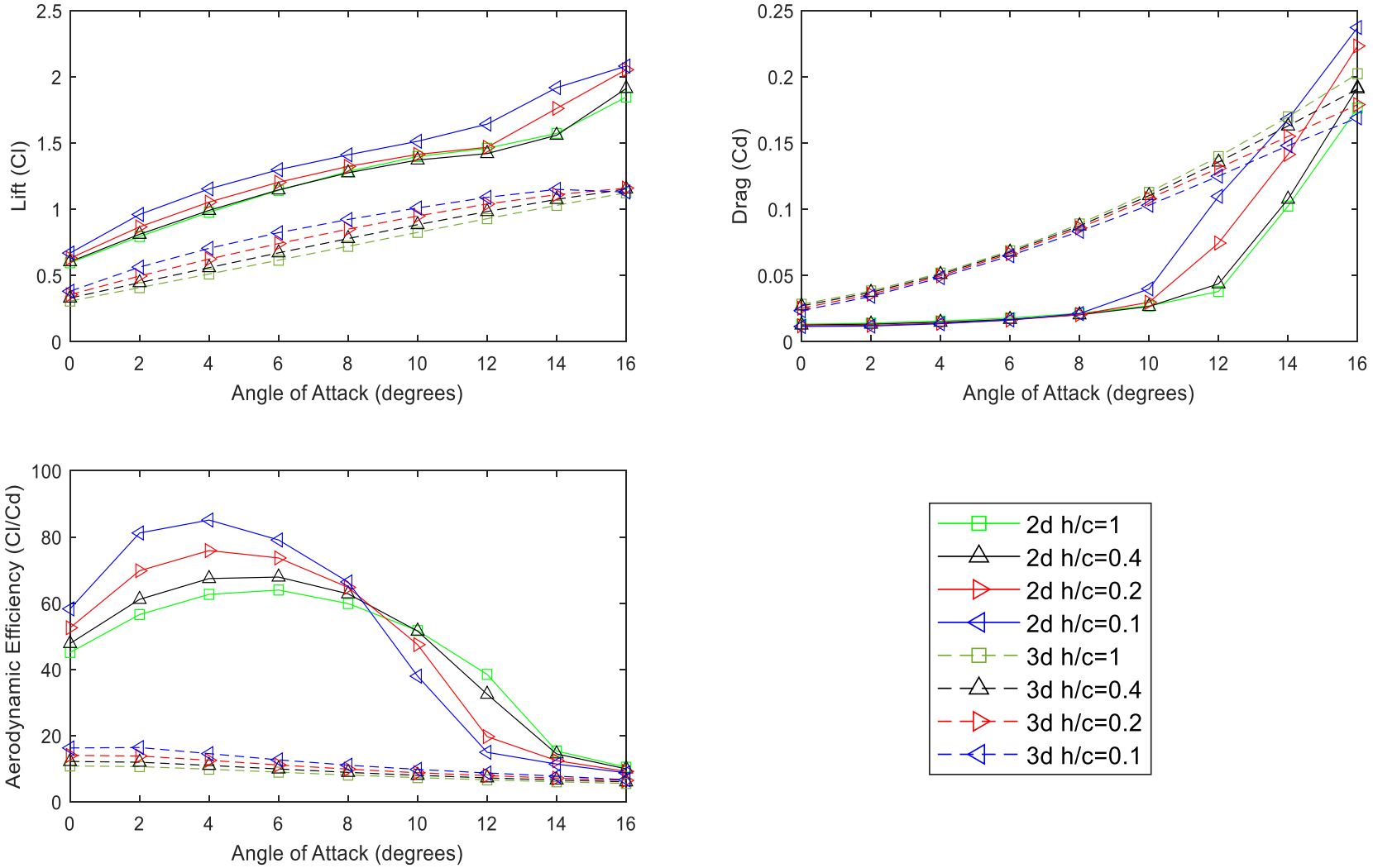

Figure 4.20: Lift comparison of 2d and 3d NACA6409 profile.

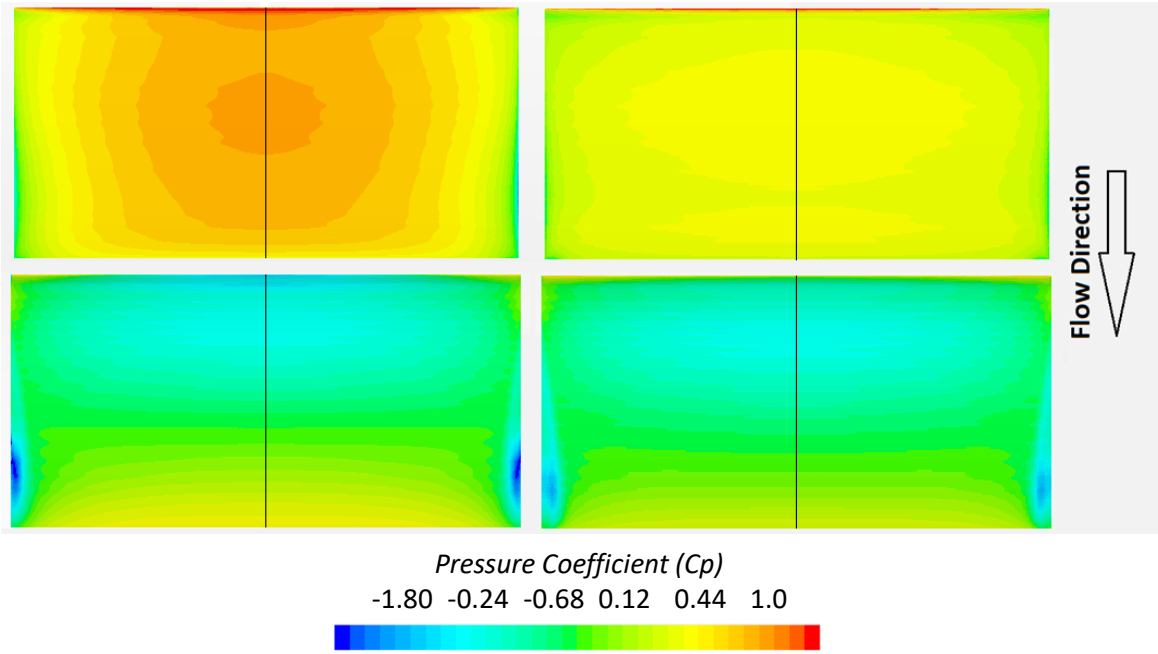

Figure 4.21: Surface pressure on upper surface (lower image) and lower surface (top image) of NACA6409 aerofoil 8-degrees AoA in 10% ground effect (left) and freestream (right).

Plane sections were analysed for the static pressure around three different aerofoils (Clark Y, NACA6409, and GOE803) at the mid-span (Figure 4.22 left) and wingtip (Figure 4.22 right). It was seen at mid-span that the pressure around the aerofoil was like the two-dimensional profiles seen in section 4.3. Also seen in the two-dimensional study was the high camber aerofoils have the highest pressure on the mid-span plane (Figure 4.22 left). At the wingtip plane, it was seen the wingtip vortex causes the pressure to be significantly different to the two-dimensional profiles showing minimal lift generation due to differences in pressure between the lower and upper surface. The low pressure of the wingtip vortex was seen on the wingtip plane (Figure 4.22 right). Increasing the camber increased this low-pressure region of the wingtip vortex as demonstrated in Figure 4.22. In Figure 4.22 right, the top aerofoil had minimal camber, the lower aerofoil profile had a much higher camber which showed a much larger vortex core. The large vortex core caused a large increase in drag however as seen in Figure 4.21 did cause a small increase in suction on the upper surface which increased the lift a small amount.

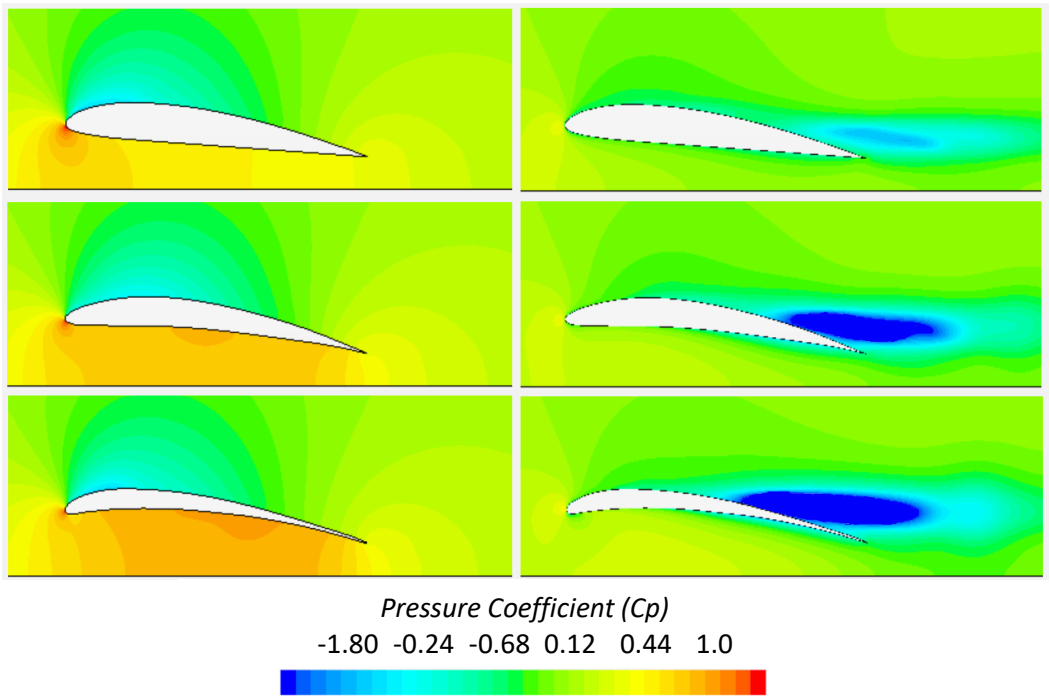

Figure 4.22: Pressure at mid-span (left) and wingtip (right) of Clark Y (upper), NACA6409 (middle) and GOE803 (lower) for 0.1 ground clearance and 4 deg angle of attack.

Comparing the pressure for ground effect (Figure 4.22) to the pressure in freestream (Figure 4.23) at mid-span shows similar upper surface pressures when brought from freestream to ground effect as seen in section 4.3. It is also seen between the different aerofoil profiles that the upper surface pressure was similar which was attributed to the similar upper surface geometry. Comparing the lower surface pressure shows a much lower pressure on the lower surface in freestream (Figure 4.23) compared to ground effect (Figure 4.22) for all the tested profiles.

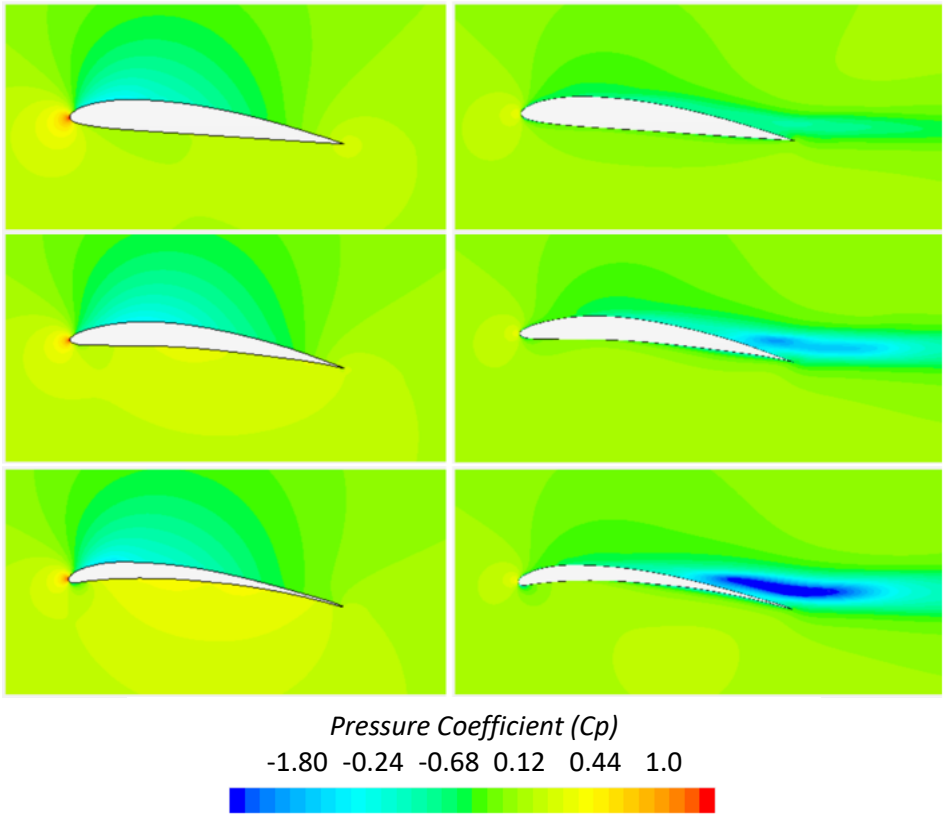

Figure 4.23: Pressure at mid-span (left) and wingtip (right) of Clark Y (upper), NACA6409 (middle) and GOE803 (lower) in freestream and 4-degree angle of attack.

In three dimensions there was a large difference in the lift (Figure 4.24) and drag (Figure 4.25) between freestream and 40% ground clearance, in two dimensions there was minimal difference between freestream and 40% ground clearance. This was due to the three-dimensional wing having a wingtip vortex with the core located near the wingtip. This means considering the diameter of the vortex, some of the outer edge of the vortex sits below the wing. Therefore, the wingtip vortex becomes affected by the ground at higher ground clearances than the aerofoil profile seen in the section 4.3 in two dimensions.

.

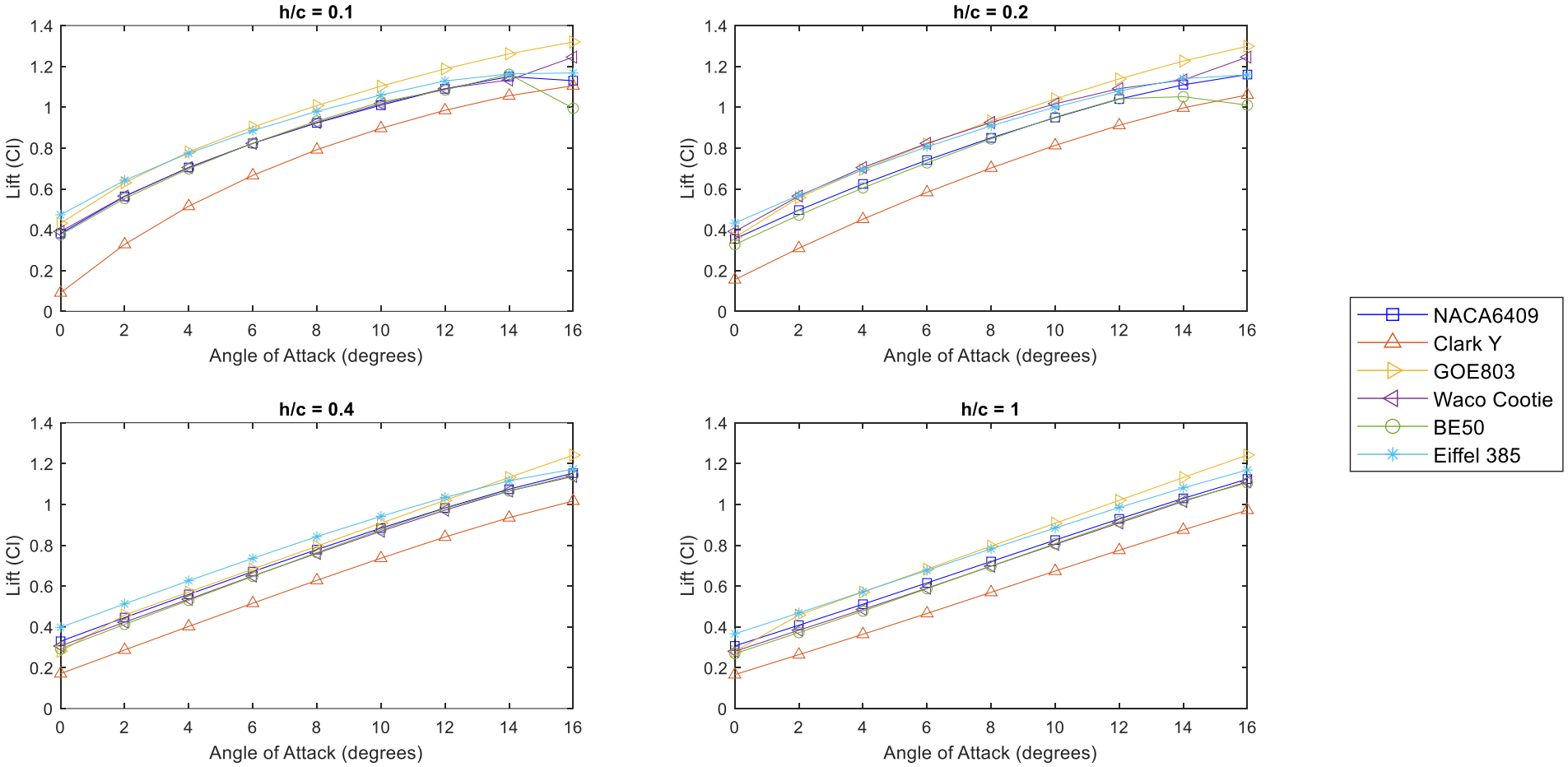

Figure 4.24: 3D lift results for different profiles.

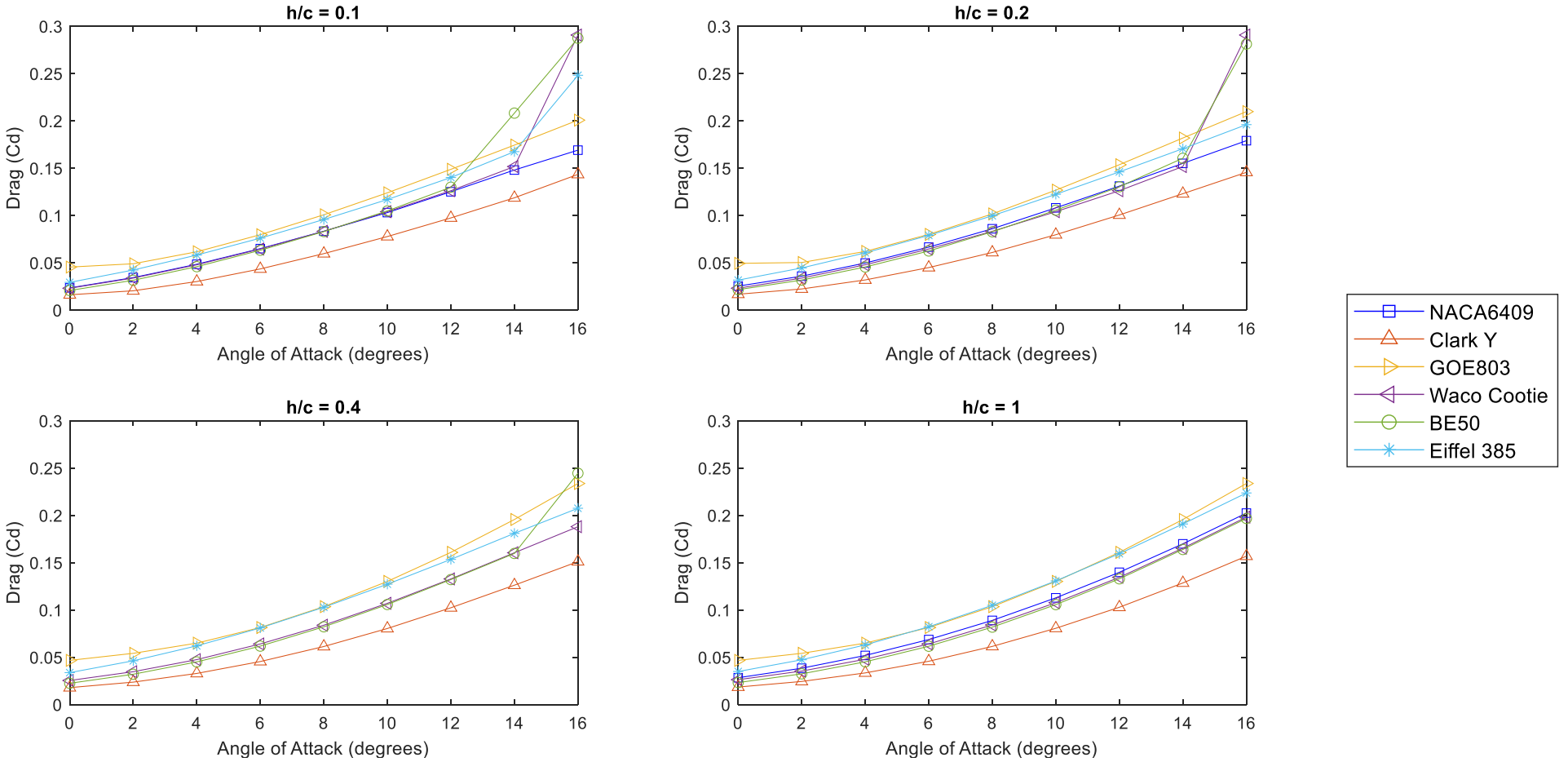

Figure 4.25: 3D drag results for different profiles.

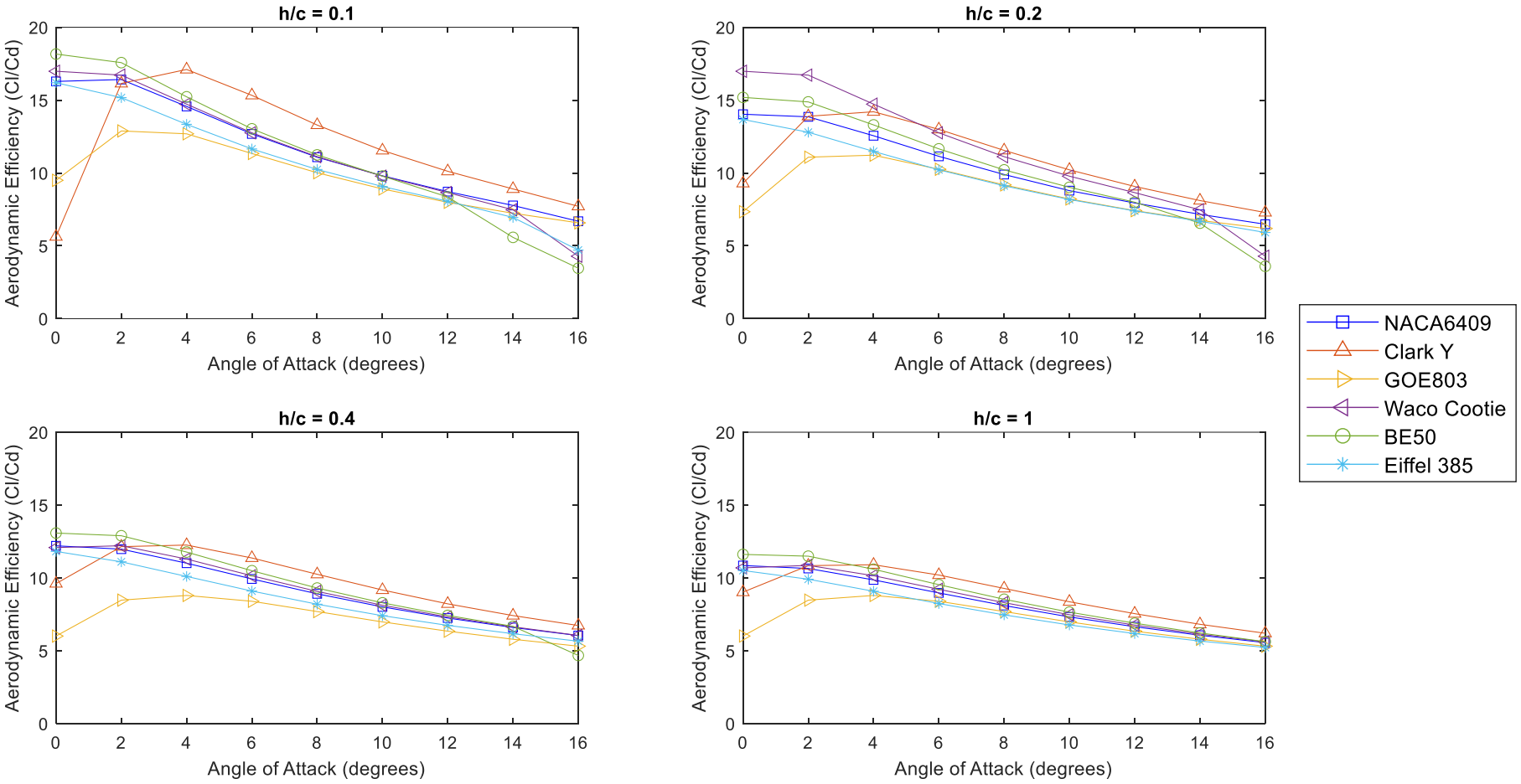

Figure 4.26: 3D efficiency results for different profiles.

There was also a greater amount of downwash in three-dimensions therefore the wingtip vortex was affected at high ground clearances. The high levels of downwash in three dimensions in freestream are shown in Figure 4.27 (upper left) and reducing the ground clearance to 10% shows the large reduction in downwash in Figure 4.27 (upper right). Another significant observation seen in Figure 4.27 (lower) was that the wingtip vortex got pushed outboard in ground clearance compared to freestream. The figure also shows a larger proportion of the streamlines leaving the trailing edge are being fed into the wingtip vortex for the wing in ground effect compared to freestream

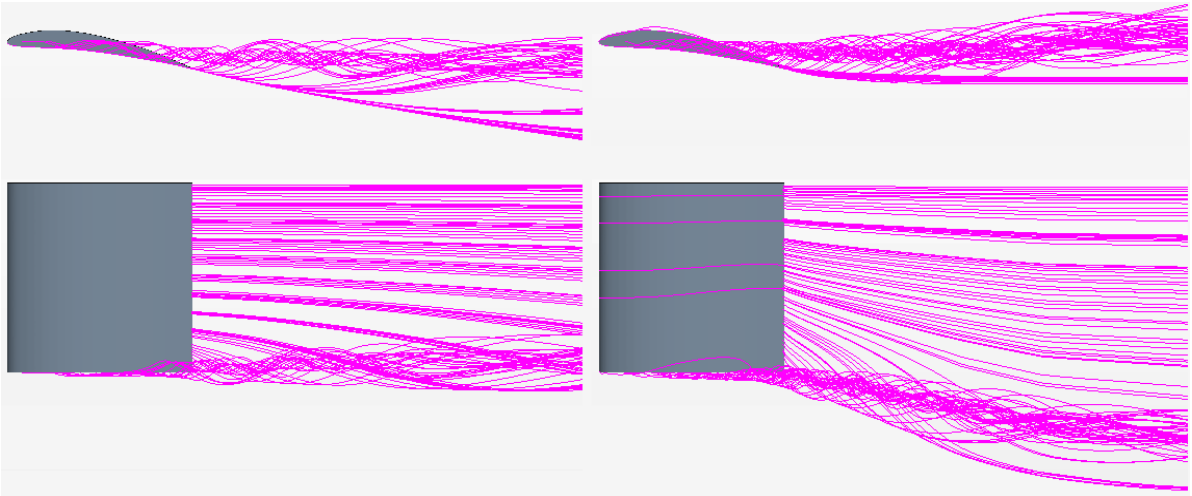

Figure 4.27: NACA6409 side view (upper) and planar view (lower) of streamlines in freestream (left) and 01 ground effect (right) at 8 degrees angle of attack.

In three dimensions the wing stalled earlier compared to two dimensions shown by the lift in Figure 4.20. One reason for this was the downwash was initially higher in three dimensions and in ground effect these streamlines become parallel to the ground due to the proximity. Therefore, the downwash is reduced the greatest amount in three dimensions causing a greater amount of separation on the upper surface. The sudden reduction in lift in ground effect indicated leading edge stall for 5% ground clearance indicating stall from a separation bubble.

As mentioned in the literature review a key aspect of extreme ground clearance is the formation of a boundary layer on the ground. This was due to strong spanwise flow caused by the high pressure beneath the wing driving the flow around the wingtip towards the low-pressure region on the aerofoil upper surface. This is significant in extreme ground effect as this boundary layer on the ground can separate and form a secondary counter-rotating vortex. For the NACA6409 at 10% ground clearance, it was clearly seen (Figure 4.28) that a boundary layer formed on the ground in the span direction. At 5% ground clearance the boundary layer was a greater thickness with higher levels of vorticity.

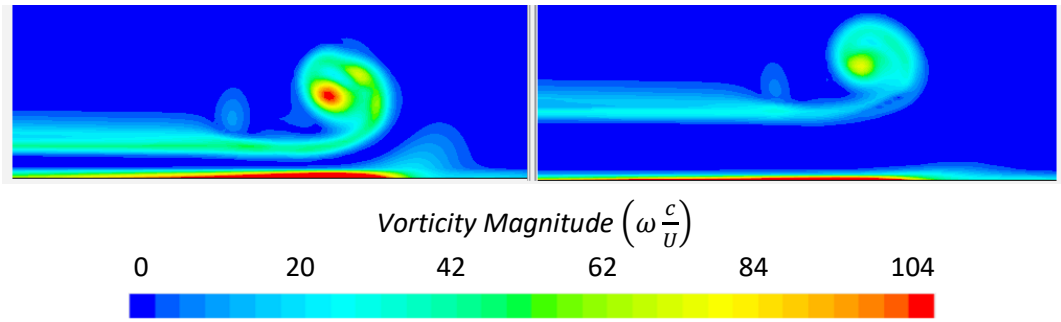

Figure 4.28: NACA6409 vorticity at 5% (left) and 10% (right) ground clearance at 4 degrees AoA on a plane 5% the chord length behind the trailing edge.

Further downstream this boundary layer on the ground separated causing a secondary counter-rotating vortex compared to the main wingtip vortex (Figure 4.29). This secondary vortex is of a smaller diameter and lower strength than the main wingtip vortex. Comparing the vorticity at 4- and 10-degrees angle of attack at 10% ground effect shows increasing the angle of attack increases the vortex core strength and diameter (Figure 4.30).

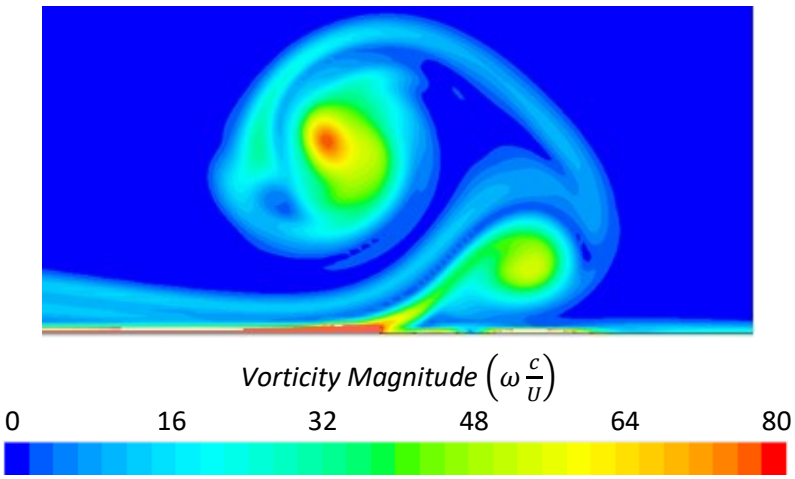

Figure 4.29: NACA6409 vorticity at h/c = 5% and x/c = 40% behind the trailing edge at 4 degrees AoA.

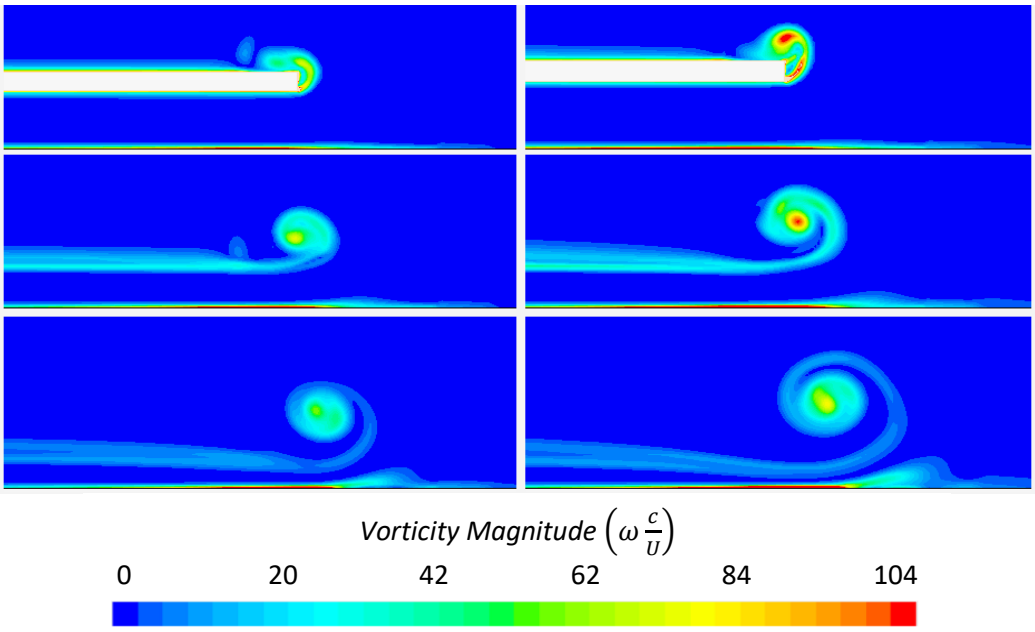

Figure 4.30: NACA6409 vorticity at h/c = 10%, 4 degrees (left) and 10 degrees (right) AoA at 0.02c upstream (top), 0.1c downstream (middle) and 0.4c (lower) downstream of TE.

For the three-dimensional analysis the NACA6409, Clark Y, GOE803, Waco Cootie and BE50 were compared. A key finding was the GOE803 produced the highest lift of the tested aerofoils but unlike the two-dimensional case had the lowest efficiency. This was due to the GOE803 having the highest camber therefore the highest pressure beneath the wing caused the highest lift, but the high pressure caused greater drag from the wingtip vortex. The Clark Y produced the highest efficiency for all ground clearances, between 4- and 14-degrees angle of attack but at low angles of attack caused negative lift from the convex lower surface.

The BE50, NACA6409 and Waco Cootie showed very similar levels of lift and drag. The BE50 low thickness resulted in low drag but had a slight camber increasing the lift. The NACA6409 was slightly thicker than the BE50 which allowed a greater curvature on the upper surface delaying the separation of the flow.

Aerofoils with a large camber that fall in the concave aerofoil category are beneficial to lift and convex aerofoils are beneficial to efficiency. A good compromise between the high lift of the GOE803 and the high efficiency of the Clark Y was the NACA6409 which was of medium camber and thickness as well as having substantial thickness from a structural perspective.

4.5 3d Wing Multidisciplinary Design Optimisation

In section 4.4, three-dimensional rectangular wings were analysed in ground effect. It was seen that the NACA6409 was a compromise between high lift and high efficiency of the tested aerofoils. In three dimensions, there are far more parameters that can be varied which include

twist, taper ratio, dihedral, wing tip position and tip chord along with the parameters tested in two dimensions of ground clearance and angle of attack. With so many parameters in three dimensions, an optimisation study was carried out on the NACA6409 to find the highest performing aerodynamic efficiency wing and a comparison was made against the rectangular wing.

For the optimisation study, both the design goal and parameters need to be defined. The design goal of this study was to maximise the aerodynamic efficiency which was done by setting the lift to maximum and drag to a minimum for the study goals. The parameters to be adjusted were defined in Table 4.6 for the wing tip position, dihedral, tip chord and angle of attack of the root and wingtip where differences in the root and tip angle of attack define the wing twist. The range and increment was selected based on the information learned in section 4.3 and 4.4 of the highest performing aerofoils and also considering easy of manufacturability and feasibility. A separate study was carried out using these parameters for each ground clearance. These parameters are visualised on the wing shown in Figure 4.31.

Table 4.6: Input Parameters for Parametrisation.

Parameter	Baseline Value	Range	Increment
Root Angle	4.0 deg	[2.0, 8.0] deg	1.0 deg
Tip Angle	0.0 deg	[0.0, 8.0] deg	1.0 deg
Tip Chord	100% root chord	[20, 100] % root chord	20% root chord
Tip Height	0% root chord	[0, 40] % root chord	20% root chord
Tip Position	80% root chord	[0, 80] % root chord	20% root chord

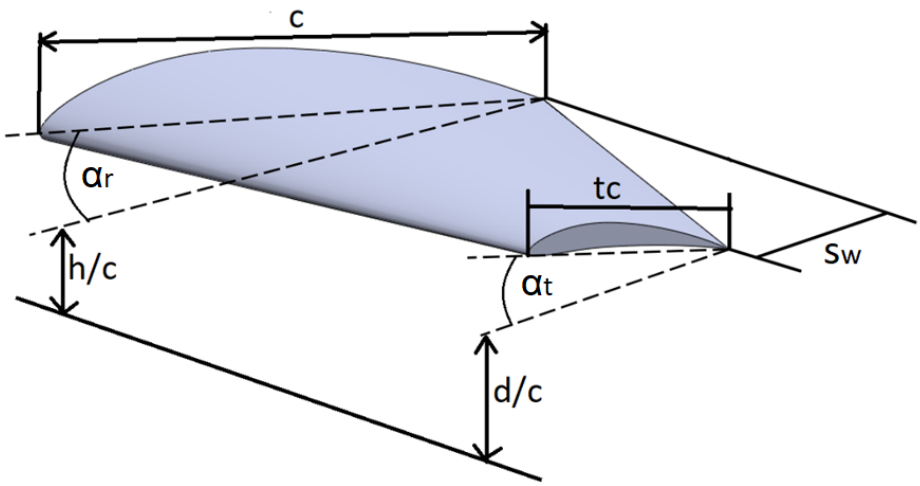

Figure 4.31: Schematic of 3D parametric wing adjustable parameters.

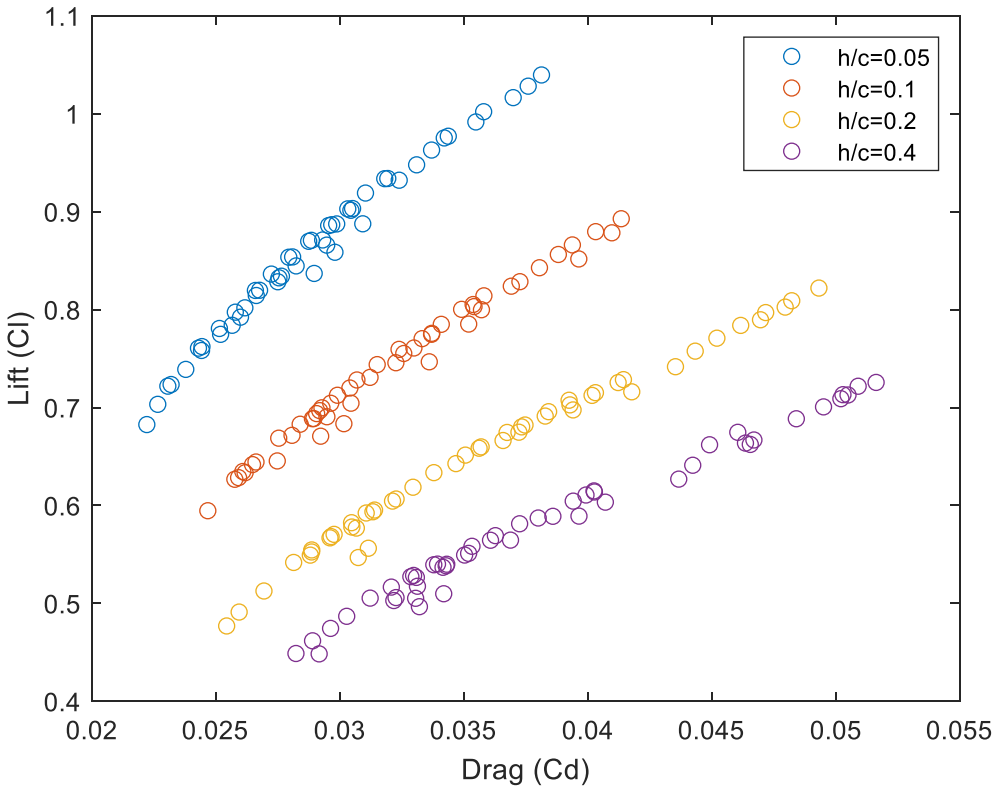

Figure 4.32: Pareto front for each ground clearance NACA6409 wing.

For each ground clearance, the optimisation was carried out and the outputted data shown in appendix A.2. For all ground clearances, the designs with the optimum performance occurred between the drag values of 0.028 and 0.035. Figure 4.32 shows the Pareto front for each ground clearance. It is seen that reducing the ground clearance increases the lift and reduces the drag of the front. Also, as the ground clearance was reduced, the Pareto front become further spaced apart. It was clear from the results that there was no one optimal design that performed the highest across all ground clearances. As this study focused on ground effect, the optimal design was chosen from below 20% ground clearance. For each ground clearance, 200 designs were tested and ranked in terms of performance. Comparing the designs from ground clearances of 5%, 10% and 20% it was seen the wing with a root angle of attack of 4 degrees and a tip 6 degrees with a tip chord of 20% and a forward wing tip position of 80% upstream of the trailing edge. For each ground clearance there was a separate optimum, so a compromise was selected that performed the highest consistently across the ground clearances.

Table 4.7 showed the optimised wing across a range of ground clearances compared to a rectangular wing. It was seen there was an increase in aerodynamic efficiency and that there was a greater increase when at lower ground clearances. There was also a reduction in drag and an increase in the lift for both optimised wings compared to the rectangular wings.

Table 4.7: Increase in performance of optimised wing compared to rectangular wing.

h/c	Root AoA (deg)	Lift Increase compared to rectangular wing (%)	Drag Decrease compared to rectangular wing (%).	Aerodynamic Efficiency Increase compared to rectangular wing (%)
0.05	4	18.16	28.24	41.27
0.1	4	12.42	26.86	35.95
0.2	4	8.50	24.55	30.96

Analysing the results showed the highest performing wings had a root angle of attack between 2 and 4 degrees. As seen in section 4.4 the higher the angle of attack the higher the pressure was at the root which increased the span low on the lower surface feeding the wingtip vortex, therefore, lower angles of attack produced higher efficiencies. Contrary to the high effect the root angle of attack had on the aerodynamic efficiency, the wingtip angle showed minimal impact on the wing performance.

Throughout all the simulations it was seen that adding dihedral dramatically reduced the performance of a wing in ground effect. This was due to the wingtip vortex not being pushed outboard as far as a wing with no dihedral reducing the effective span. Also, the downwash at the wingtip increases with increased dihedral increasing induced drag. Adding dihedral to the wing also increased the ground clearance along the span therefore there was less ground effect enhancement for dihedral wings in ground effect. Therefore, it can be concluded adding dihedral is analogous to increasing the ground clearance. In freestream, the dihedral had minimal impact on the aerodynamic performance and therefore is often seen on aircraft due to increased roll stability.

The aspect ratio of a wing is defined by Eq. (4.7) which shows the aspect ratio is proportional to the span squared and inversely proportional to the wing plan form area. The rectangular wing in this study had an aspect ratio of 2 as larger spans limit the roll of WIG craft close to the ground. Reducing the tip chord reduced the wing planform area which increased the aspect ratio shown in Eq. (4.7). This means a higher aspect ratio wing can be used to increase the aerodynamic efficiency without increasing the span. For the optimisation study, a tip chord of 20% had the highest performance for all ground clearances as this effectively increased the aspect ratio.

$$Aspect\ ratio = \frac{s^2}{Aw} \tag{4.7}$$

A sweep simulation was carried out varying the wingtip chord to show the effect on aerodynamic efficiency compared to the aspect ratio. Figure 4.33 showed the rectangular wing with an aspect ratio of 2 had the lowest aerodynamic efficiency. Reducing the tip chord increased the aspect ratio and aerodynamic efficiency.

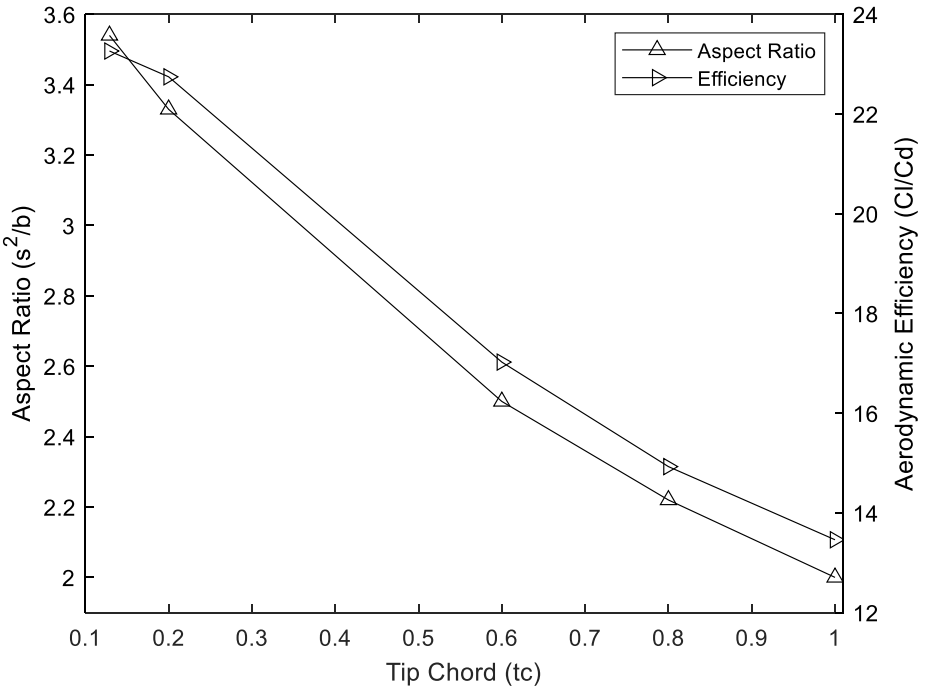

Figure 4.33: Plot of how the tip chord affects aspect ratio.

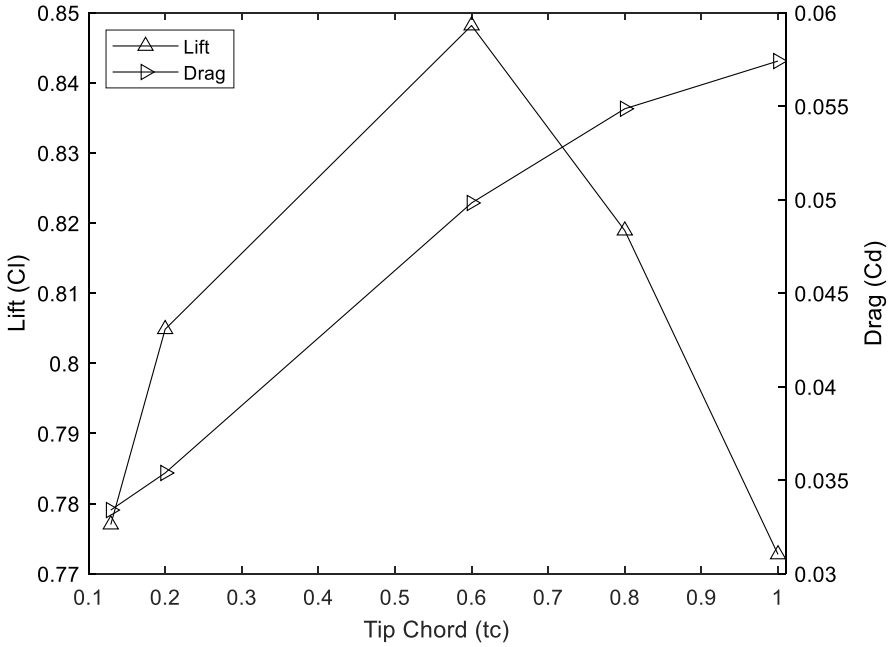

Figure 4.34: 3D NACA6409 wingtip chord sweep for root at 4 degrees angle of attack and tip at 6 degrees AoA at h/c = 10% ground clearance.

Analysing the lift and drag coefficients (Figure 4.34) it was seen the drag reduced as the wingtip chord reduced due to a smaller diameter wingtip vortex. The lift initially increased as the tip chord reduced from 100% to 60%. Analysing the pressure coefficients on the lower surface (Figure 4.35) showed for the 60% tip chord that the high-pressure region grew along the span and that the peak value of the pressure coefficient was higher than the 100% tip chord. Figure 4.34 showed reducing the wingtip from 60% to 20% chord reduced the lift, although the high-pressure region on the lower surface (Figure 4.35) was forced along the span further as the tip chord reduced, the

pressure coefficient magnitude reduced. The reason this reduced was due as the chord reduced along the span the effective ground clearance reduced along the span which reduced ground effect enhancement along the span for small tip chords. Reducing the tip chord further resulted in a steeper reduction in the lift (Figure 4.34) due to the reduction in lower surface pressure seen in Figure 4.35 for the 13% tip chord.

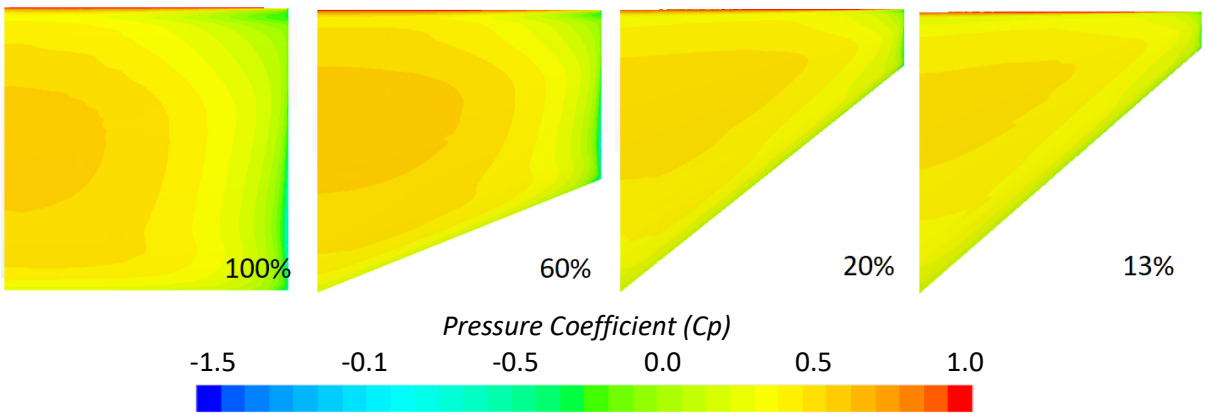

Figure 4.35: Lower surface pressure varying tip chord in 10% ground effect and 4-degree root AoA and 6-degree tip AoA.

Although it was seen (Figure 4.34) there was a reduction in the lift for smaller tip chords it was also seen there was a reduction in drag. The rate the drag increased was much higher compared to the lift which resulted in overall gains in aerodynamic efficiency for smaller tip chords and higher aspect ratios. However, there was a sharp reduction in lift below 20% tip chord which resulted in no gains in aerodynamic efficiency due to the same rate of decrease in both lift and drag.

A forward wing tip position with the tip chord located at 60 to 80% root chord upstream of the root trailing edge showed the highest efficiency. The reason a forward wing tip position performed higher was due to the high pressure at the root causing a spanwise flow, a forward wing tip position resulted in the wingtip vortex being fed less from the spanwise flow. An explanation for this is that the velocity vectors of the spanwise flow have the span direction component from the high pressure driving a flow from the root to the tip as well as a vector component from the flow in the freestream direction. The resultant vector for the rear wing tip position is aligned with the quarter chord line therefore the flow travels along the wing to feed the wingtip vortex. The forward-swept wing in this study had the quarter chord of the tip ahead of the quarter chord of the root. Therefore, the spanwise flow leaves the trailing edge rather than feeding the wingtip vortex. Figure 4.36 shows a greater proportion of the streamlines feeding the wingtip vortex for the rearward wing tip position compared to the forward.

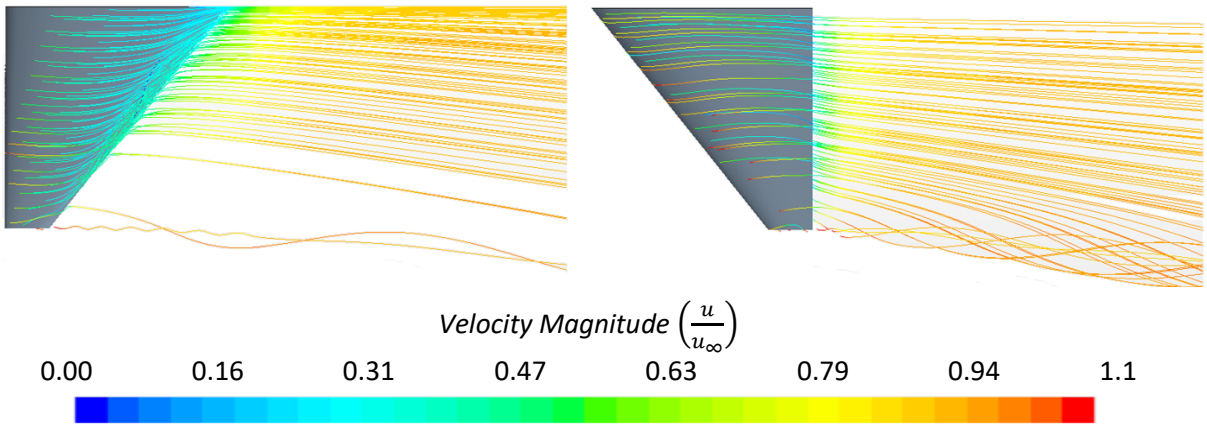

Figure 4.36: Top view of streamlines of forward wing tip position (left) and rear wing tip position (right).

The wingtip vortex has previously been seen to significantly affect the performance of the wing and a comparison of the wingtip vortex was made between the optimised and rectangular wings shown by the vorticity plots Figure 4.37. The magnitude of vorticity was higher for the optimised wing, but the diameter of the vortex was significantly smaller compared to the rectangular wing. Both the rectangular and optimised wings showed the vortex diameter to increase, and the vorticity reduced as the vortex travelled downstream. The optimised wing remained to have a higher strength and smaller diameter vortex as the vortex travelled downstream compared to the rectangular wing. This was seen in Figure 4.37 where the vorticity on planes at multiple locations downstream of the trailing edge was analysed.

As the wingtip vortex travelled downstream it was pushed outboard of the wing. At locations 0% and 10% of the root chord downstream, the wingtip vortex got pushed outboard the same distance for both the rectangular and optimised wing. At a location of 80%, the optimised wingtip vortex got pushed outboard a distance of 5% chord compared to the rectangular wing where the vortex got pushed outboard a distance of 17% of the root chord.

Due to the larger diameter of the rectangular wingtip vortex, the vortex naturally sat higher compared to the optimised wing. It was observed that the spanwise flow of the lower surface pressure feeding the wingtip caused a boundary layer to form on the ground (Figure 4.37) in the spanwise direction as discussed in section 4.4. The larger wingtip vortex caused a large separation bubble to form on the ground and at a location of 20%, this formed into a secondary counter-rotating vortex for the rectangular wing. The optimised wing showed a small separation bubble which grew downstream but did not separate into a secondary counter-rotating vortex unlike the rectangular. The optimised wing improved the efficiency of the wing by reducing the induced drag from the combination of these wing tip vortices. Also, for the rectangular wing, there was a much higher amount of vorticity in the spanwise ground boundary layer shown in Figure 4.37.

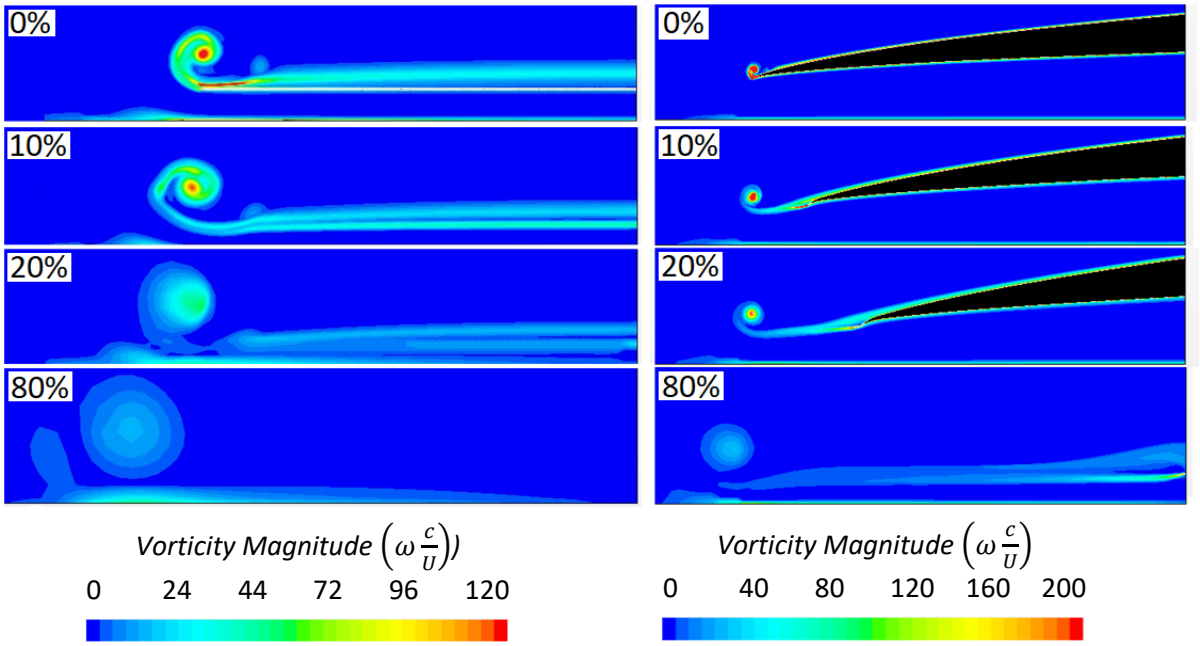

Figure 4.37: Comparison of wingtip vortex for rectangular wing (left) and optimised wing (right) I 10% ground effect at different plane locations behind the wing.

4.6 Summary

At the start of this chapter, a mesh independence study was carried out for both two- and three-dimensions using RANS and validated against experimental literature data. A two-dimensional study was carried out where it was seen the Kutta condition fixed the trailing edge pressure which caused the pressure to increase upstream of the trailing edge on the lower surface when brought into ground effect. The lower surface that was a greater distance from the ground caused the largest gains in lift. The stagnation point also moves downstream in ground effect with a reduction of downwash and mass flow rate beneath the aerofoil in proximity to the ground and increased upper surface separation. In three dimensions a wingtip vortex was present from the high root pressure driving a spanwise flow on the lower surface. In ground effect, this wingtip vortex was pushed outboard effectively increasing the span of the wing and reducing downwash. The NACA6409 showed a good compromise between high lift and efficiency of the aerofoils tested.

A wing optimisation was carried out and it was found there was no single wing that performed the highest across all ground clearances. The highest performing wing that occurred at 5%, 10% and 20% ground clearance was identified to have a root angle of attack of 4 degrees and a tip of 6 degrees with a tip chord of 20% and forward wing tip position of 80% upstream of the trailing edge and zero dihedral.

Chapter 5 2D Morphing Wings in and out of Ground Effect

5.1 Introduction

In the previous chapter, the mesh was validated for a steady RANS for both a two-dimensional aerofoil and a three-dimensional rectangular wing and compared against experimental data. An analysis was carried out of two- and three-dimensional wings in and out of ground effect with the key flow physics discussed and an optimisation study of the three-dimensional wing was carried out. This chapter applies the FishBAC morphing method to the NACA6409 aerofoil in two-dimensions using steady-state simulations in and out of ground effect. A comparison was also made against traditional flaps. Dynamically morphing over a period was also compared against the steady static simulations. Finally, in this chapter periodic morphing was investigated to improve the efficiency of wings in ground effect.

5.2 Validation of Steady and Time Dependant Morphing

5.2.1 Static Morphing Validation

Morphing was applied to the two-dimensional NACA6409 aerofoil in this chapter using the FishBAC morphing method in the chordwise direction. Further validation was initially required due to the high curvature of the aerofoil surface after morphing compared to the validation carried out in section 4.2.1.

Due to the lack of experimental data for FishBAC morphed aerofoils, a comparison was made against CFD literature (Woods et al., 2014). A zero displacement was used to compare the aerofoil data validated against experimental data in this study to the CFD data used for comparison of the FishBAC morphing by Woods et al., (2014). Trailing edge displacements of 0% and 5% were used at a start location of 75% chord from the leading edge for angles of attack from 0 to 14 degrees.

Figure 5.1 presented the NACA6609 lift and drag comparison for both the CFD in this study and the CFD carried out by Woods et al., (2014) at 0% and 5% trailing edge deflection. Comparing the 0% deflection it was seen that the lift and drag were almost identical between this study and the literature. The 5% trailing edge defection showed a slightly larger variation in lift compared to the 0% deflection. The drag showed a slightly higher difference than the lift due to measurements of drag being an order of magnitude less than the lift. Both the drag and lift showed identical trends

and with minimal difference in lift and drag it was deemed that the comparison of the CFD in this study that was validated against the literature in section 4.2.1 agreed with Woods et al., (2014).

Although both studies use the K-Omega SST and RANS models, different software packages were used, and the K-Omega SST was modified in Open FOAM resulting in different versions being used. Also, a Reynolds number of 675,000 was used by Woods et al., (2014) compared to 320,000 which there would be a slight variation in lift and drag although this is above 100,000 so the two numbers can be compared with only minimal variations in Cl and Cd (Winslow et al., 2018).

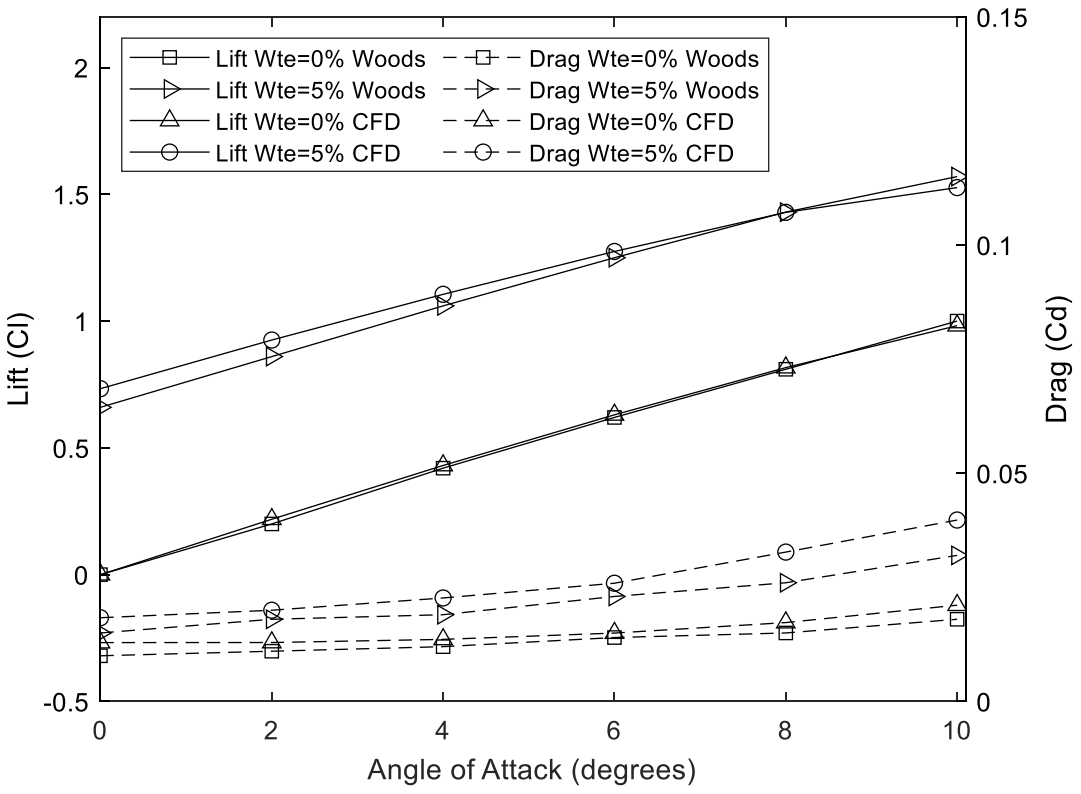

Figure 5.1: Lift of morphed NACA0012 compared to literature.

5.2.2 Unsteady Time Step and Mesh Independence

To ensure the mesh and time step were valid for unsteady time dependent simulations, a mesh and time independence study were carried out. Unsteady Reynolds Average Navier Stokes (URANS) and Detached Eddy Simulation (DES) capture more of the flow details including small eddies; therefore, separate mesh independence studies are required for both URANS and DES methods. Unlike RANS, both URANS and DES have a time component in which the simulation is advanced in time using a timestep. Therefore, it has to be ensured that both a spatial and temporal resolution captures the flow details as well as considering the computational cost. The two-dimensional NACA6409 aerofoil at 4 degrees angle of attack was used for the mesh and time independence.

The Courant–Friedrichs–Lewy number is a value that shows how far the flow has moved across the cell in one time step. A Courant–Friedrichs–Lewy number of approximately 1 was recommended in the CFD user manual (*User Manual Star CCM+ 14.04.013*, 2019). The Courant–Friedrichs–Lewy number in Eq 5.1 is dependent on the grid spacing Δx_g and the time step Δt_s and was varied accordingly to keep a constant Courant–Friedrichs–Lewy number approximately equal to 1. This was demonstrated in Figure 5.2 where the time step was shown for the corresponding cell count where the cell count was increased by increasing the grid spacing.

$$CFL = u\frac{\Delta t_s}{\Delta x_g} \qquad 5.1$$

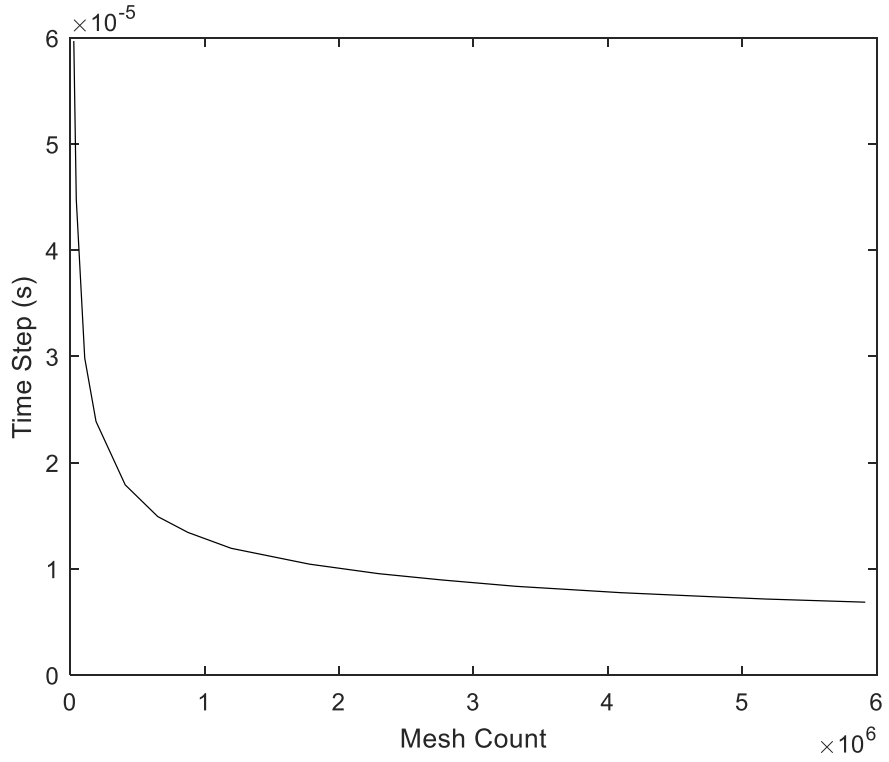

Figure 5.2: Time step according to mesh size based on a Courant–Friedrichs–Lewy number of 1.

The same process was carried out as shown in section 4.2.1 using the grid convergence index to compute the zero-grid spacing value using computed values of the lift and drag for three grid spacings and compare the computed values to the zero spacing lift and drag. The three-grid spacing for the fine, medium and coarse mesh values were shown in Table 5.1 for URANS and in Table 5.2 for DES.

Table 5.1: URANS lift and drag values.

Mesh Refinement	Cell Count	Cl	Cd
Fine	6714691	1.016	0.0147
Medium	1197355	1.027	0.0148
Coarse	295310	1.064	0.0161

Table 5.2: DES lift and drag values.

Mesh Refinement	Cell Count	Cl	Cd
Fine	19627910	1.060	0.0167
Medium	5168628	1.062	0.0166
Coarse	1197355	1.089	0.0135

Using the values in Table 5.1 the zero-grid spacing for the URANS was a lift of Cl = 1.011 and drag of Cd = 0.0147 and for DES the lift was Cl = 1.059 and drag Cd = 0.0167. With the grid spacings used for the fine, medium and coarse meshes, the values of the GCI yielded an asymptote value approximately equal to 1 which satisfied the asymptote being approximately horizontal. The errors for the lift and drag are shown in Table 5.3 for URANS and Table 5.4 for DES. The URANS showed that the lift had an error of 1.53% so the fine mesh was selected which had a much lower error of 0.46% for the lift and 0.01% for the drag. Although the computational cost is higher for the fine mesh for the URANS, the large error for the medium meant the fine mesh gives a more accurate result. For the DES however the medium mesh was selected as this only had an error of 0.21% for the lift and 0.72% for the drag compared to the coarse mesh which had an error of 2.66% for the lift and 27.07% for the drag, therefore the coarse mesh was rejected. The fine mesh had a much larger computational cost with little reduction in error compared to the medium mesh.

Table 5.3: URANS mesh size error.

Mesh Refinement	Cl error%	Cd error %
Fine	0.46	0.01
Medium	1.53	0.30
Coarse	4.95	9.70

Table 5.4: DES mesh size error.

Mesh Refinement	Cl error%	Cd error %
Fine	0.02	0.02
Medium	0.21	0.72
Coarse	2.66	27.07

5.2.3 Dynamic Morphing Validation

Validation of the dynamic mesh is required to show the set-up and mesh within the computational domain had been set up correctly. From the literature review it was identified that there was no experimental work investigating dynamic morphing wings in or out of ground effect. However, a heavily researched area is pitching wings in freestream. Pitching wings require large mesh deformations, therefore, showing the validity attached and large separated flow as well as reattachment.

A study carried out by T. Lee & Gerontakos, (2004) investigated pitching a NACA0012 aerofoil in a wind tunnel at a Reynolds number of 1.35×10^5 with a chord of 0.15m and 2.5 aspect ratio. Endplates were used to eliminate 3d effects. The pitching motion was described using a sinusoidal motion and an instantaneous angle of attack of Eq. (5.2) where α_m is the start angle the aerofoil is pitching about. The amplitude is described by $\Delta\alpha$, solution time by t and ω the circular frequency. The circular frequency is defined by $\omega = 2\pi f_o$ where f_o is the oscillation frequency. The aerofoil was pitched about the quarter chord position from the leading edge. The results were shown using the reduced frequency Eq. (5.3), by matching the reduced frequency a direct comparison can be made to this study which had a different chord and freestream velocity. For validation, a comparison was made using $k = 0.1$ corresponding to a pitching oscillation frequency of $f_o = 2.97Hz$. Values of $\alpha_m = 10°$ and $\Delta\alpha = 15°$. This approach of validation was also carried out by (Abdessemed, 2020) who simulated morphing aerofoils in time.

$$\alpha_t = \alpha_m + \Delta\alpha \sin(\omega t) \quad 5.2$$

$$k = \frac{\omega c}{2u_\infty} \quad 5.3$$

The validation was carried out for both URANS and DES and was compared against experimental data and a CFD literature case carried out by Abdessemed (2020) using the mesh size and time step independent solution shown in section Figure 5.22.

It was seen that the angle of attack that the peak lift Figure 5.3 and drag Figure 5.4 occurred at for URANS and DES was at 22 degrees. This was similar to a study by Abdessemed (2020) who observed the peak lift and drag occurred at 22.6 degrees and the experimental data at 24.5 degrees. The values of these peaks showed the lift was 2% higher for URANS and 6% lower for DES whilst the drag was seen to be 8% higher for URANS and identical for DES compared to the experimental data. This peak was closer to the experimental data than Abdessemed (2020) where the drag was 14% higher however the lift value was similar. A secondary peak also occurred for all the CFD data for both this study and Abdessemed (2020) but was not seen in the experimental data. This is thought to be due to the prediction methods in the software rather than the setup Abdessemed (2020).

In Figure 5.3 and Figure 5.4 it was observed there was a hysteresis loop also seen in the experimental (T. Lee & Gerontakos, 2004) and literature CFD (Abdessemed, 2020) data as the aerofoil was pitched. As the pitch increased the lift and drag were higher compared to when the aerofoil pitch decreased. The cause of this hysteresis was due to there was not sufficient time for the flow to attach from the stalled high angle of attack.

The drag showed strong a correlation between -5 and 10 degrees and although the experimental data showed a slightly higher lift at -5degrees, the lift also showed a correlation in this range. At 10 degrees the URANS and DES lift increased by 15% due to separation on the upper surface although the drag remained very similar to the experimental data.

The validation was accepted due to following the same trends as the experimental data from the literature and showing the same two peaks observed by Abdessemed (2020). Although the data was not an exact fit, considering experimental uncertainties and the errors within the CFD, the small differences for both URANS and DES were deemed acceptable. Therefore, the set-up and mesh were carried forward for the time-dependent simulations used in this study.

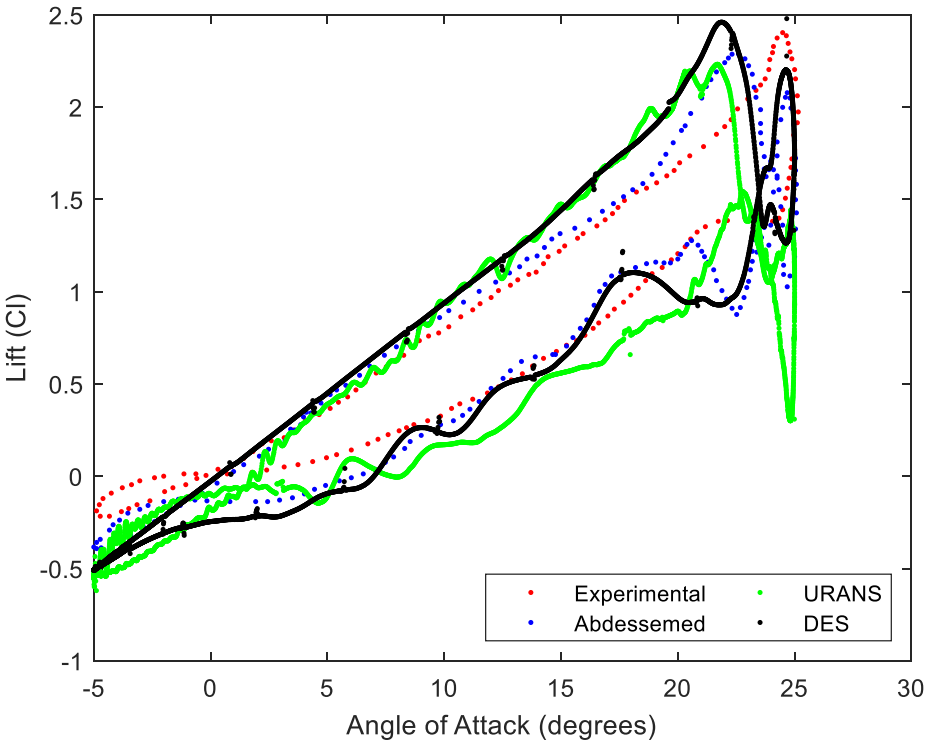

Figure 5.3: NACA0012 pitching aerofoil lift freestream.

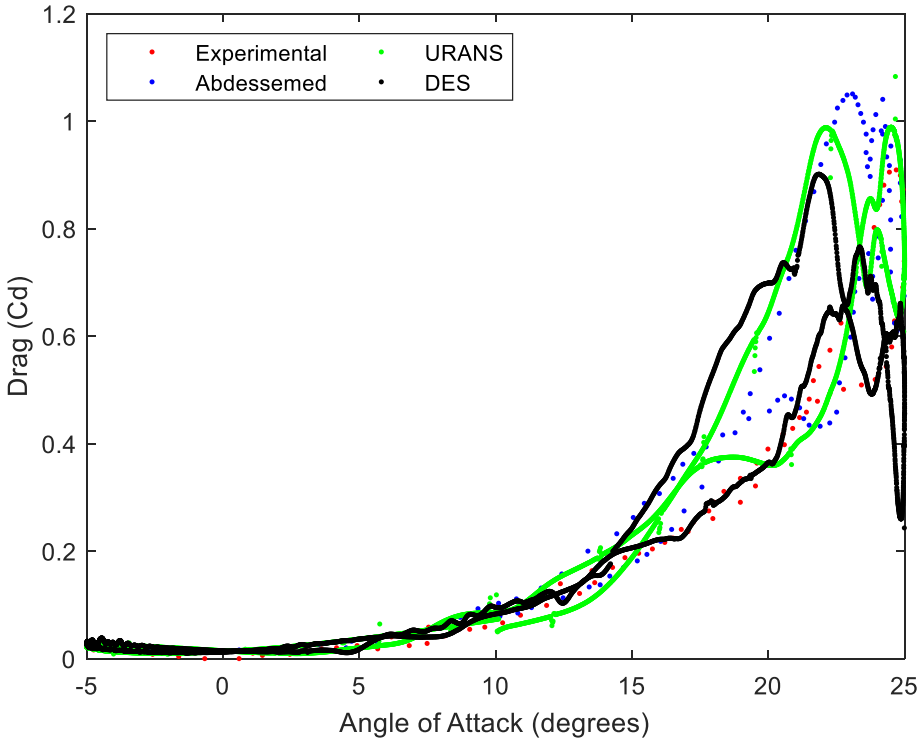

Figure 5.4: NACA0012 pitching aerofoil drag freestream.

5.3 Static morphing

5.3.1 Static morphing Discussion

Initially morphing was applied to a NACA6409 aerofoil using steady-state simulations by importing the morphed geometry created in MATLAB into Star CCM+ as previously mentioned in the methodology. The angle of attack and ground clearance was varied, and the lift, drag and aerodynamic efficiency shown in Figure 5.5, Figure 5.6 and Figure 5.7.

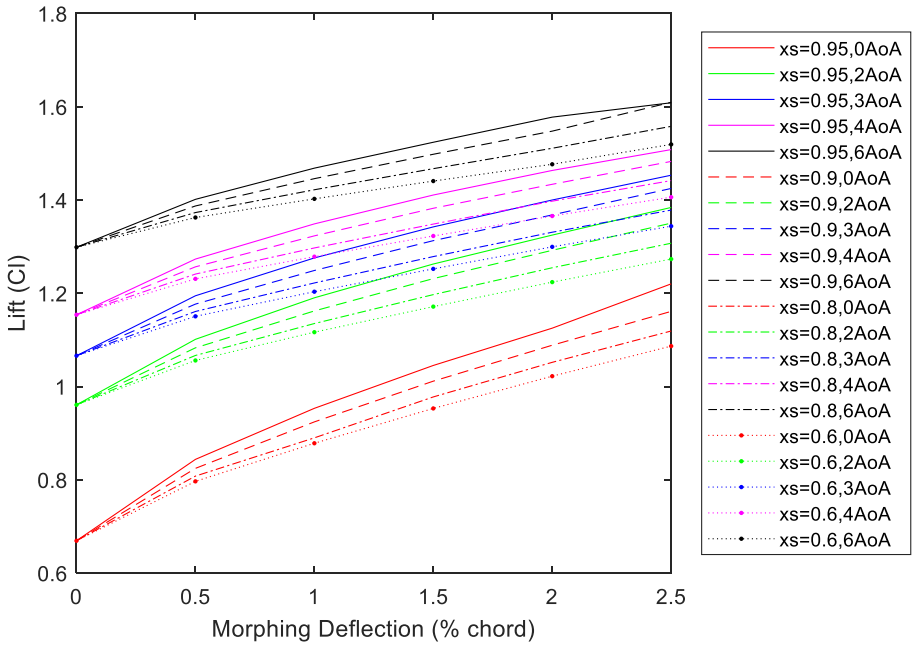

Figure 5.5: Static 2d morphing lift.

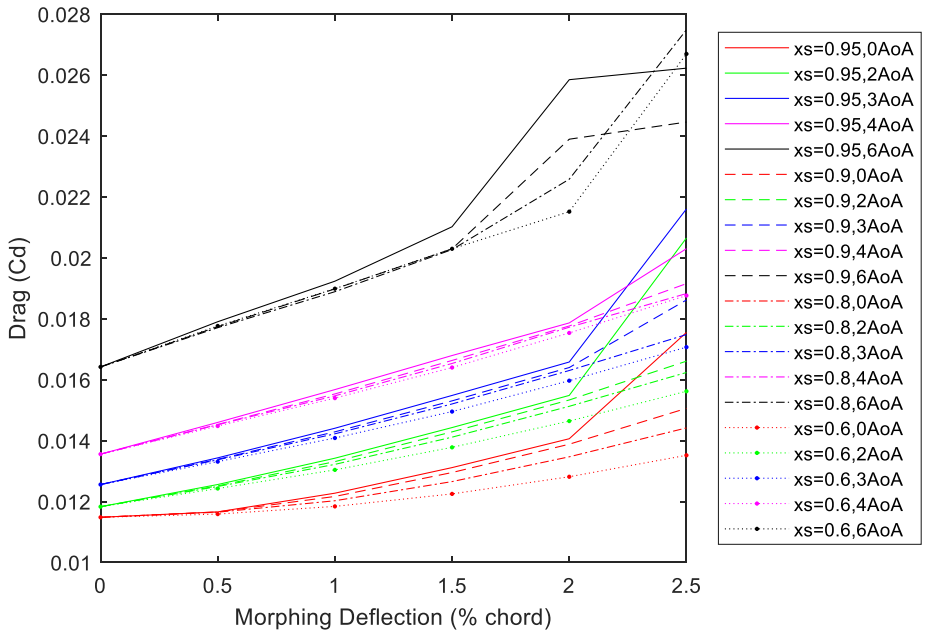

Figure 5.6: Static 2d morphing drag.

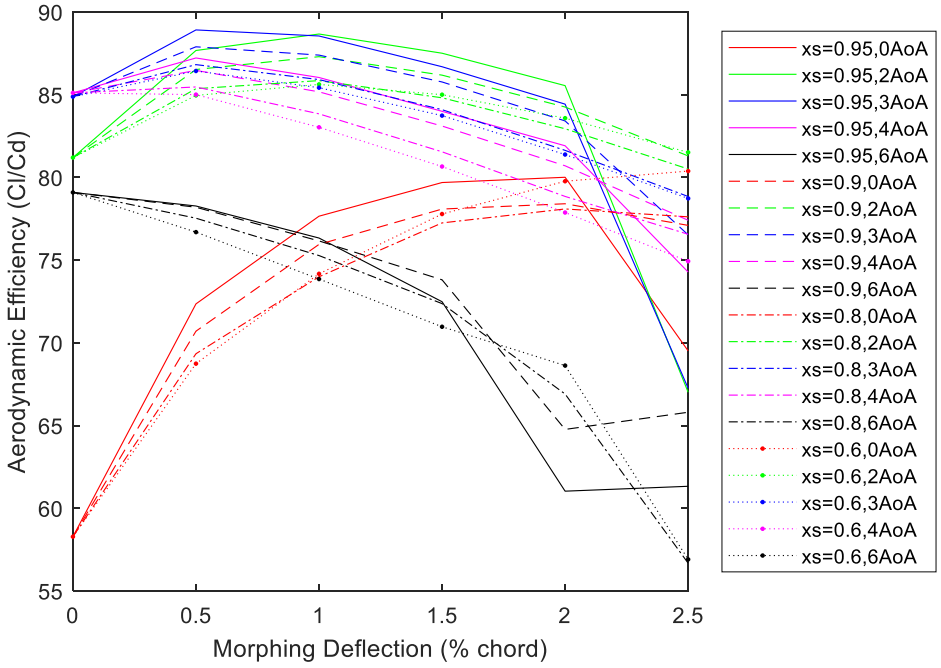

Figure 5.7: Static 2d morphing efficiency.

Statically morphing the aerofoil showed to increase the lift (Figure 5.5) when the deflection increased seen for all angles of attack tested. The lift increase was due to the reduction in height between the trailing edge and ground which increased the pressure upstream of the trailing edge seen in and discussed in Figure 4.7. Analysing the pressure plots (Figure 5.8) for different deflections (0%, 1% and 2.5%) showed for the NACA6409 at 4 degrees angle of attack that both the lower surface pressure and upper surface suction increased as the aerofoil was morphed. The suction peak almost doubled for 2.5% trailing edge deflection before dropping and remaining flat before decreasing. This signified a laminar separation bubble at the leading edge for the 1% and 2.5% morphed aerofoils.

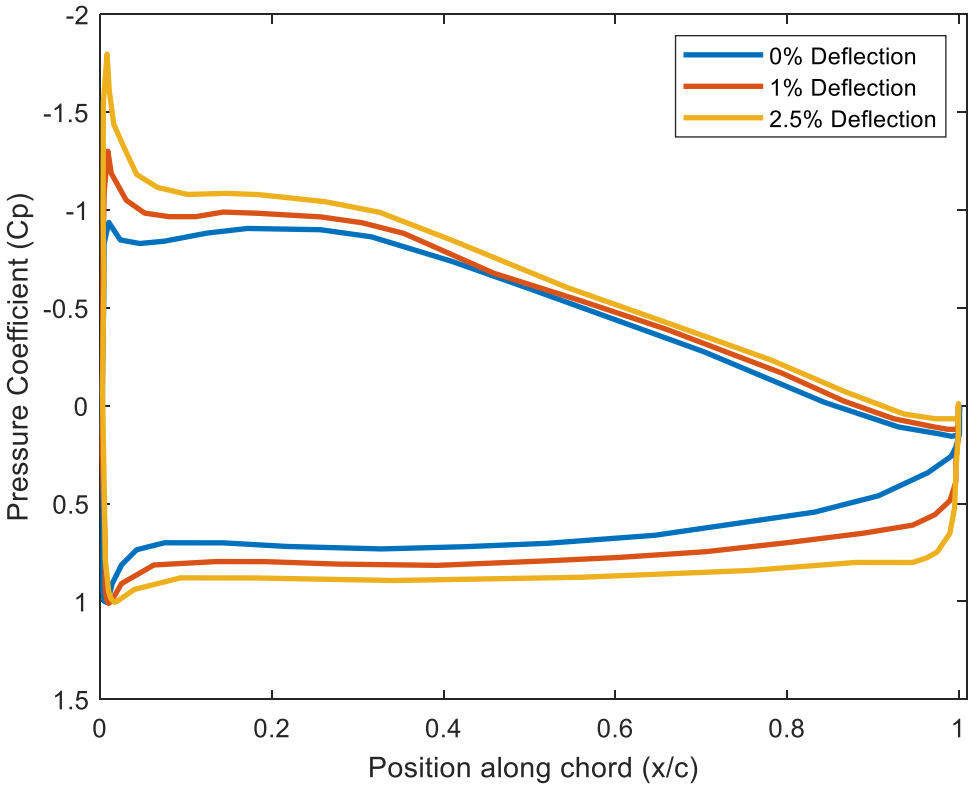

Figure 5.8: NACA6409 pressure coefficients in 10% ground effect at 4 degrees AoA at 95% start location and 0%, 1% and 2.5% morphed deflections.

The start location for Figure 5.8 was at 95% chord from the leading edge, in Figure 5.9 the start location was varied from 60%, 80%, 90%, and 95% with 2.5% trailing edge deflection. The trailing edge pressure was fixed by the Kutta condition which means all changes occur upstream of the trailing edge. Varying the start location showed to only change the pressure on the morphed proportion of the aerofoil lower surface. This was due to the distance between the trailing edge and ground and the distance between the lower surface and ground of the non-morphed proportion of the aerofoil did not change with different start locations. With the trailing edge pressure fixed and the lower surface pressure unchanged the pressure only varied on the morphed proportion of the aerofoil which was seen in Figure 5.9. For later start locations, a rapid jump in pressure from the trailing edge to the lower surface was seen compared to an earlier start location. This was caused by the later start location causing a greater volume beneath the aerofoil therefore there was a greater amount of high pressure beneath the wing demonstrated in Figure 5.10. A higher suction peak of 14% was seen for the 95% start location compared to the earlier start location due to the increased blockage beneath the aerofoil.

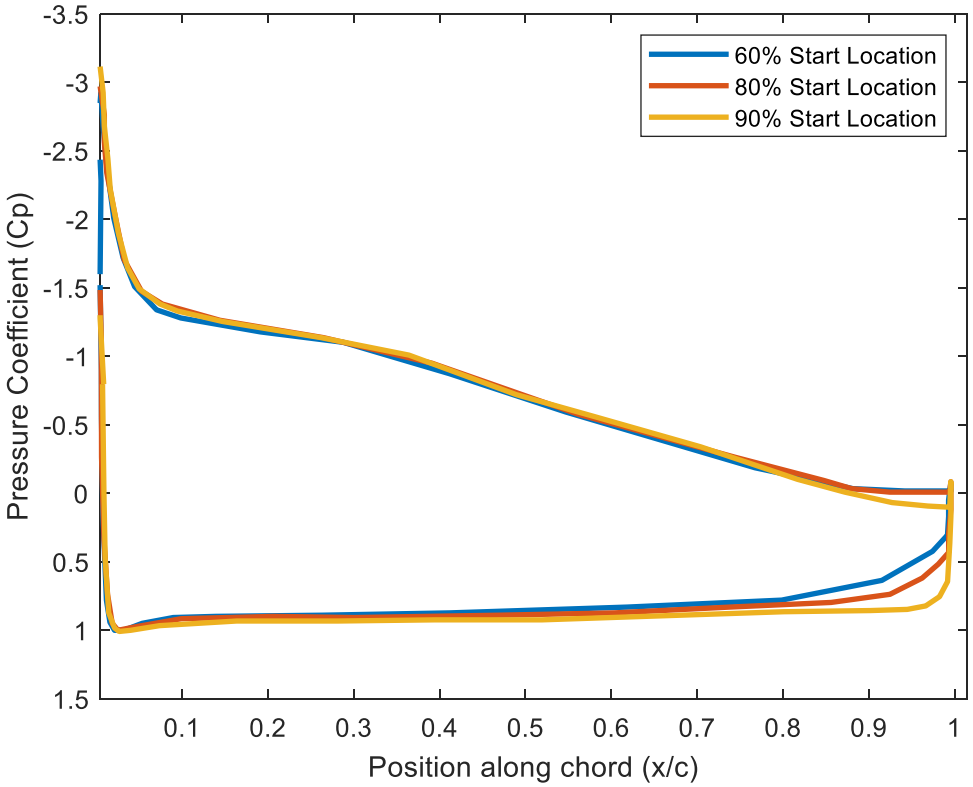

Figure 5.9: NACA6409 pressure at 6-degree AoA and 10% ground clearance varying morphing start location.

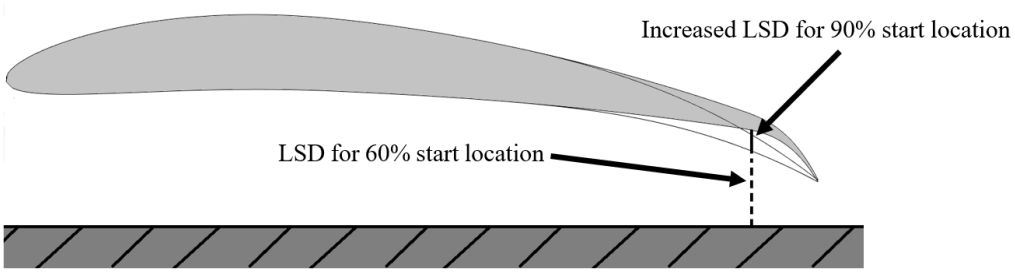

Figure 5.10: Schematic of lower surface distance (LSD) for 60% and 90% start location.

Morphing the aerofoil showed to increase the drag seen in Figure 5.6 due to increased blockage beneath the aerofoil as well as separation of the flow occurring on the morphed section on the upper surface of the aerofoil shown in Figure 5.11.

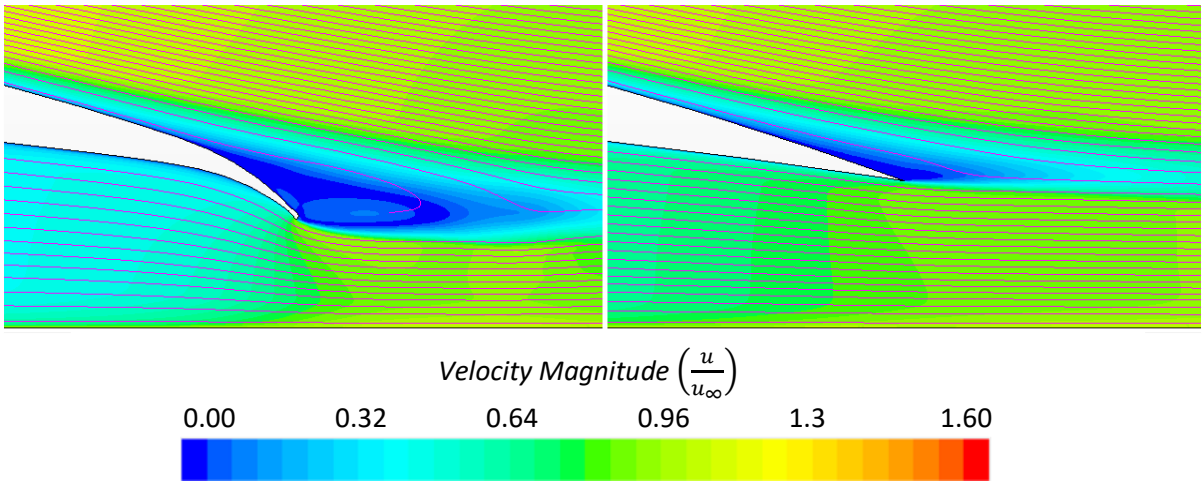

Figure 5.11: Velocity of NACA6409 with streamlines for morphed at 2.5% (left) and 0% (right) in 10% ground effect at 4 degrees AoA at trailing edge.

For 0 degrees angle of attack, the drag increased by 15% as the aerofoil was morphed from 0% to 2.5% deflection and a start location of 60%, for a start location of 95% this increased to 35% as the aerofoil was morphed. At 8 degrees angle of attack, the drag increased by 34% for a start location of 60% and the drag increased by 57% for a start location of 95%. This shows a later start location, and a higher angle of attack increased the drag the most.

Pressure plots around the morphed and un-morphed aerofoils were compared (Figure 5.12) at higher angles of attack. For 10% trailing edge deflection and morphing starting at 80%, a large separation appeared at 12 degrees angle of attack which this bubble was not present at 10 degrees angle of attack when in 10% ground effect. This bubble was shown by the region on the upper surface leading edge where the plot flattened and showed to reattach at 40% from the leading edge. This shows increasing the angle of attack in ground effect could lead to a sudden leading-edge stall. Increasing the trailing edge deflection to 20% showed that the separation bubble appeared at 10 degrees angle of attack showing the greater the deflection the lower the angle of attack the separation bubble occurs.

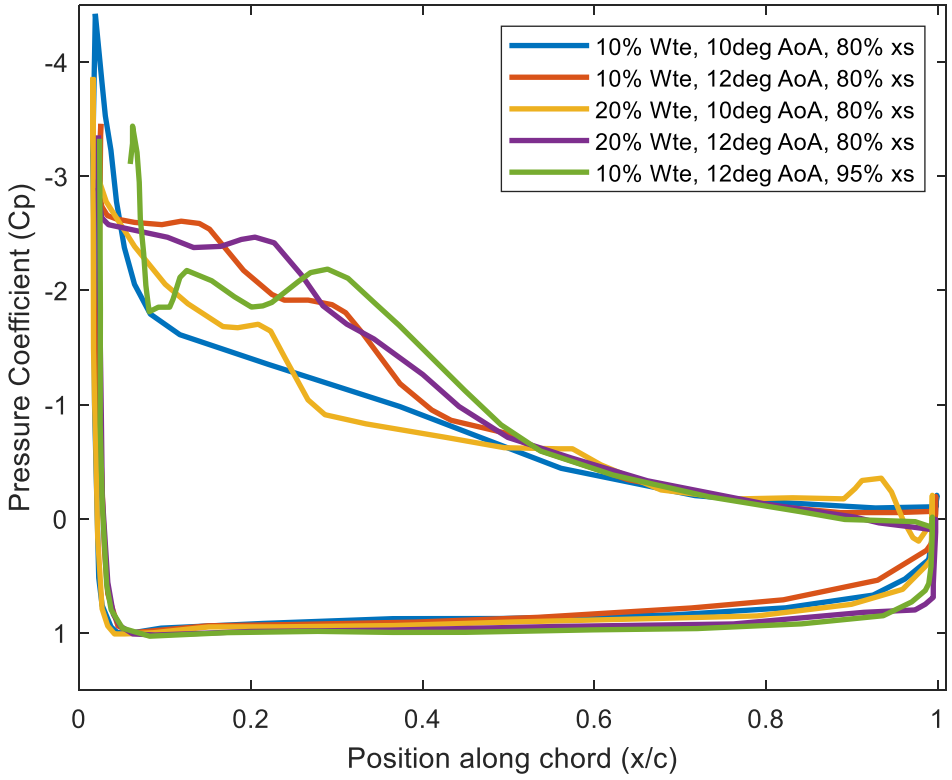

Figure 5.12: Pressure contours of NACA6409 morphed at higher angles of attack in 10% ground effect.

Two start locations of 80% and 95% were compared at 12 degrees angle of attack and 10% trailing edge deflection. Both showed identical suction peaks however the latter start location of 95% was reattached at a later distance of 50% from the leading edge compared to the 80% start location which reattached at 40% on the upper surface. This demonstrates that later morphing means separation bubble re-attaches later along the upper surface. For the 20% deflection at 10 degrees angle of attack at 80% start location on the upper surface at the trailing edge it was noted the pressure increased then decreased before returning to the trailing edge pressure. This was due to unsteadiness in the separated wake on the aerofoil surface shown in Figure 5.13. Also seen in Figure 5.13 is the corresponding separation bubble discussed and shown in Figure 5.12.

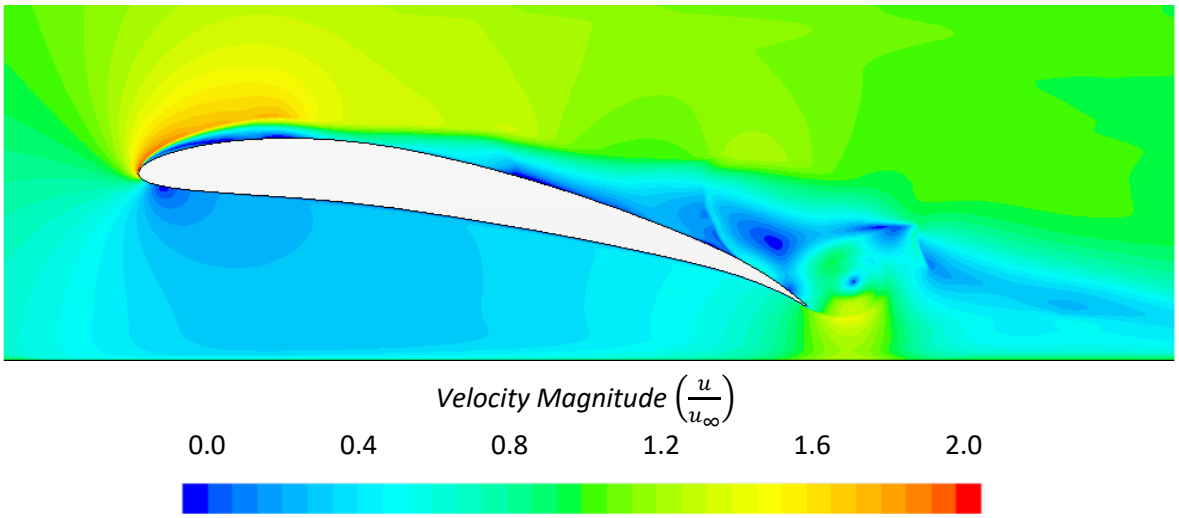

Figure 5.13: Velocity around NACA6409 morphed at 20% deflection starting at 80% from the leading edge in 10% ground effect and 10 AoA.

The efficiency was shown (Figure 5.7) to be optimal between 2- and 4-degrees angle of attack. At zero deflection and the 4 degrees, the efficiency was the highest followed by the 3 degrees then the 2-degree angle of attack. The aerodynamic efficiency was seen (Figure 5.7) to increase as the aerofoil was morphed from 0% to 0.5% trailing edge deflection and for 2 degrees angle of attack, there was an aerodynamic efficiency increase between 0% and 1% trailing edge deflection. This was due to small changes in drag between 0% and 0.5% for 3- and 4-degrees angle of attack and 0% to 1% trailing edge deflection for a 2-degree angle of attack. Therefore, morphing a wing in ground effect shows larger displacements are more efficient on wings at lower angles of attack. For 2 degrees angle of attack and 60% start location the peak efficiency occurred at 1% displacement with the 2.5% displacement showed an identical efficiency to the zero-displacement morphing. At 4 degrees for a 60% start location, the rate of increase of drag was higher than the lift throughout the morphing causing a decrease in aerodynamic efficiency. Increasing the 4-degree morphing from 60 to 95% start location shows an initial jump in aerodynamic efficiency at 0.5% trailing edge deflection from an initial greater increase in lift. This was also seen for 3 degrees angle of attack. This shows that later start locations cause a large increase in lift and for 0.5% trailing edge deflection this rate of increase of lift was greater than the rate of drag increase causing an overall increase in efficiency. After 0.5% deflection, the drag increased at a much greater rate, therefore, causing a reduction in aerodynamic efficiency.

5.3.2 Static Morphing Comparison to Flaps

Current technology of control surfaces consists of the main aerofoil section with the trailing edge hinged to alter the aerofoil lift, this caused a discontinuous profile as the aerofoil and flap are in two sections. The static morphing discussed in this section was compared to a traditional flap, in

literature this is modelled without a gap between the aerofoil (Ockfen & Matveev, 2009; Tremblay Dionne & Lee, 2018). In this study, the aerofoil with a flap was tested with and without a gap to compare the differences and compared to the static morphing. The NACA6409 was shown in Figure 5.20 with and without a gap between the flap and wing, also shown is the morphed aerofoil profile with the same length and trailing edge deflection.

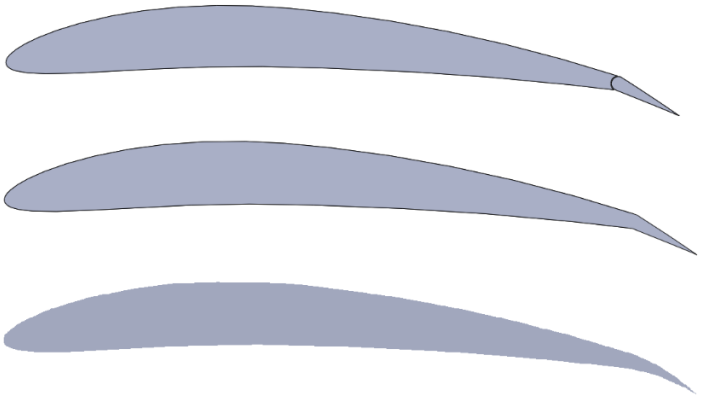

Figure 5.14: Flap with gap (top), flap (middle) and morphed (lower) NACA6409 aerofoil.

Initially, the flap without gap was compared to the FishBAC morphed aerofoil seen in section 5.3.1 for two start locations of 80% and 90% of the chord from the leading edge in 10% ground clearance and 3 degrees angle of attack. Both cases start at 0% deflection with the same lift and drag values and deflecting the trailing edge increased the lift for both the flap and morphed profile. As seen in Figure 5.15, morphing the aerofoil at both 80% and 90% start locations showed a higher lift than the traditional flap throughout the trailing edge displacement.

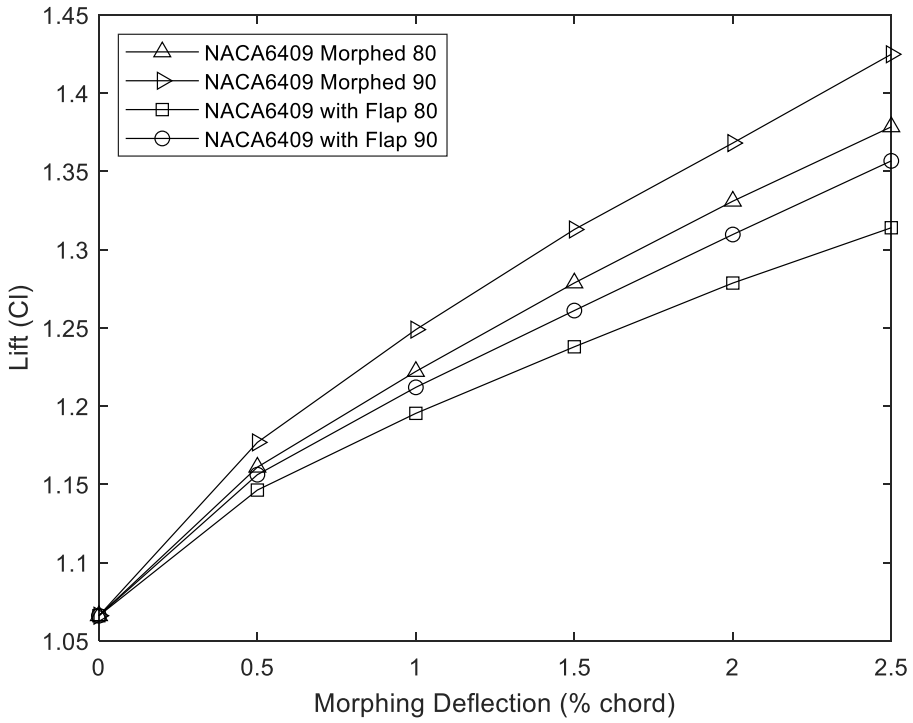

Figure 5.15: Lift comparison of NACA6409 of morphed and flap at 3 degrees and 10% ground clearance.

Analysing the pressure plots (Figure 5.16) around the aerofoil showed the main differences in pressure were on the morphed section of the aerofoil. This was to the morphed section in ground effect showed a higher ground clearance shown in Figure 5.17. In Figure 5.17 the morphed and flap profiles were overlayed with the distance shown by a black line from the ground to the flap. An additional red line is seen for the morphed section showing it was a greater distance from the ground to the lower surface of the morphed section. As mentioned in Figure 4.7, this increased the pressure and rate of pressure increase from the trailing edge to the non-deflected part of the aerofoil. This results in smaller trailing edge deflections for a morphed aerofoil profile to achieve the same lift as a flap resulting in less drag and improved aerodynamic efficiency compared to a flap. Investigating other angles of attack of 0 and 6 degrees (appendix A.2), the lift follows the same trends as the 3-degree angle of attack.

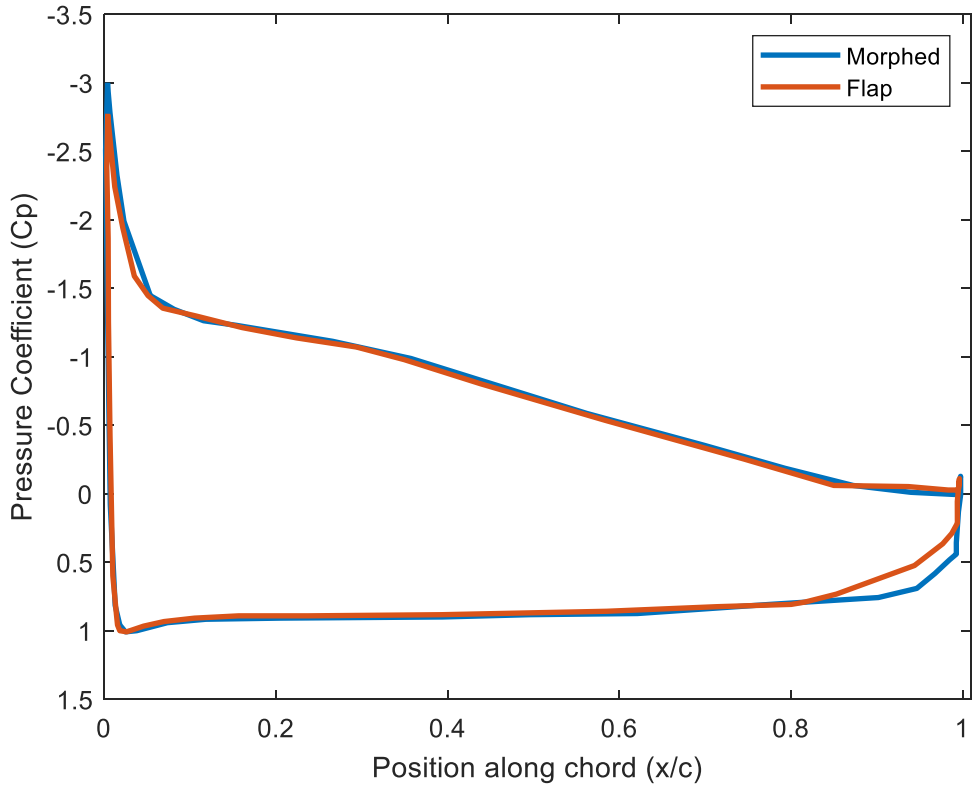

Figure 5.16: Pressure coefficient comparing a flap and morphed aerofoil at a start location of 80% chord, 6 degrees AoA and 10% ground clearance.

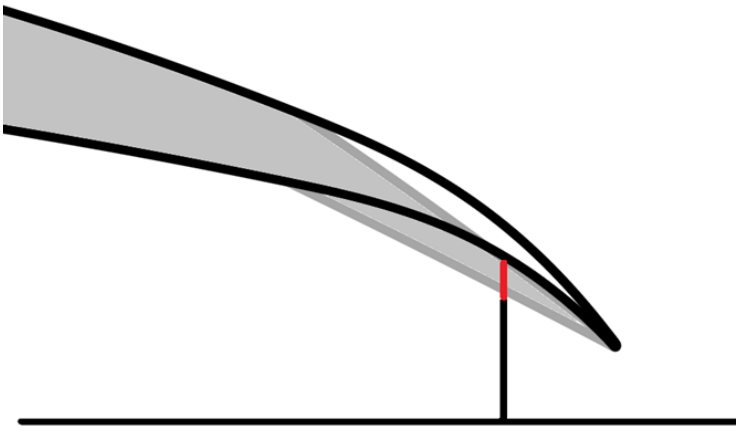

Figure 5.17: Morphed and flap geometry overlaid comparison showing a black line for flap ground clearance with red extension for morphed ground clearance.

It was seen for all cases in Figure 5.18 that increasing the trailing edge displacement increased the drag and that at small displacements there was minimal difference in drag between all cases tested. The start location of 80% showed the highest drag for the flap however the 80% morphed section showed the lowest drag. This was due to the abrupt sharp change in geometry caused separation on the upper surface from the flap. The smooth morphed geometry allowed the flow to remain attached after the point where morphing began causing lower drag. For the morphed aerofoil at a start location the was a sudden increase in drag at 2.5% deflection seen in Figure 5.18, this was due to the flow separating from the high curvature at the trailing.

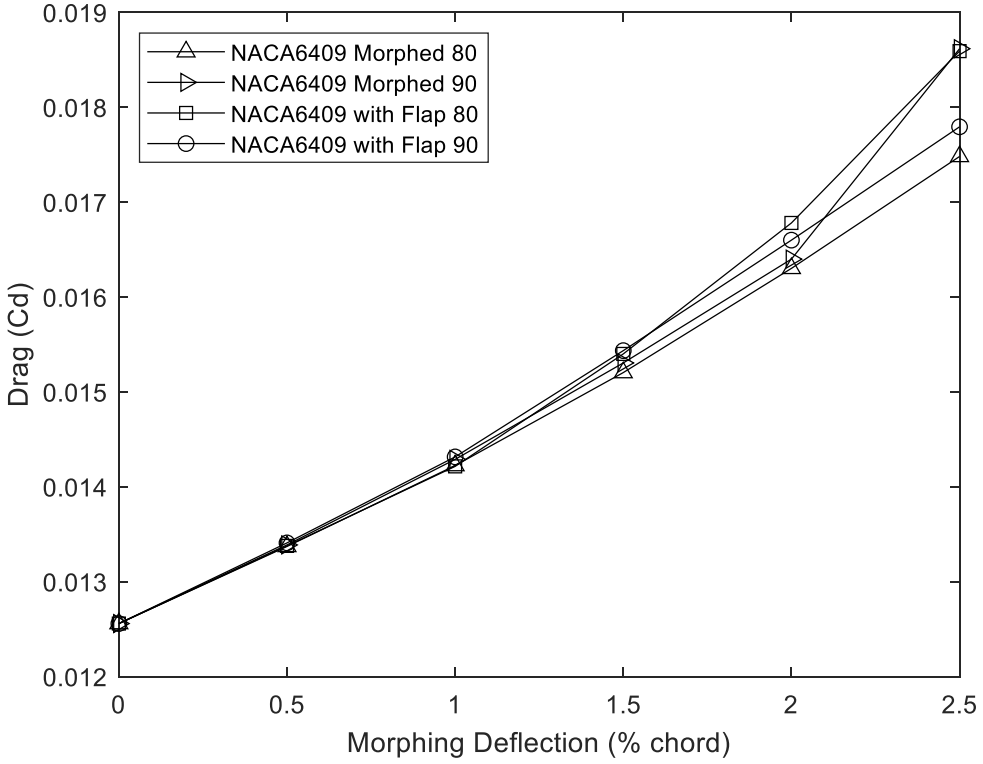

Figure 5.18: Drag comparison of NACA6409 of morphed and flap at 3 degrees and 10% ground clearance.

Analysing the aerodynamic efficiency (Figure 5.19), for all the cases of the flap and morphing that the efficiency initially increases due to a sharper rate of increase of lift compared to drag. All the configurations reached a peak efficiency at 0.5% trailing edge displacement. Due to the very similar drag values at 0.5% trailing edge deflection, the peak efficiency was mainly determined by the lift. Therefore, the configuration of morphing at a 90% start location had the highest lift and efficiency and the 80% start location had the lowest efficiency and drag. The efficiency at 0.5% trailing edge deflection increased by 3.5% compared to the flap which increased to 4.5% at a start location of 90% chord. For an 80% start location, it was seen there was an increase in efficiency of 2.4% for the morphing and 1.8% for the flap. For 0 degrees the peak efficiency was at 2% trailing edge deflection and for 6 degrees the efficiency decreased as soon as morphing started (appendix A.2). This showed as the angle of attack increased the location of peak efficiency decreased for both the flap and morphed section.

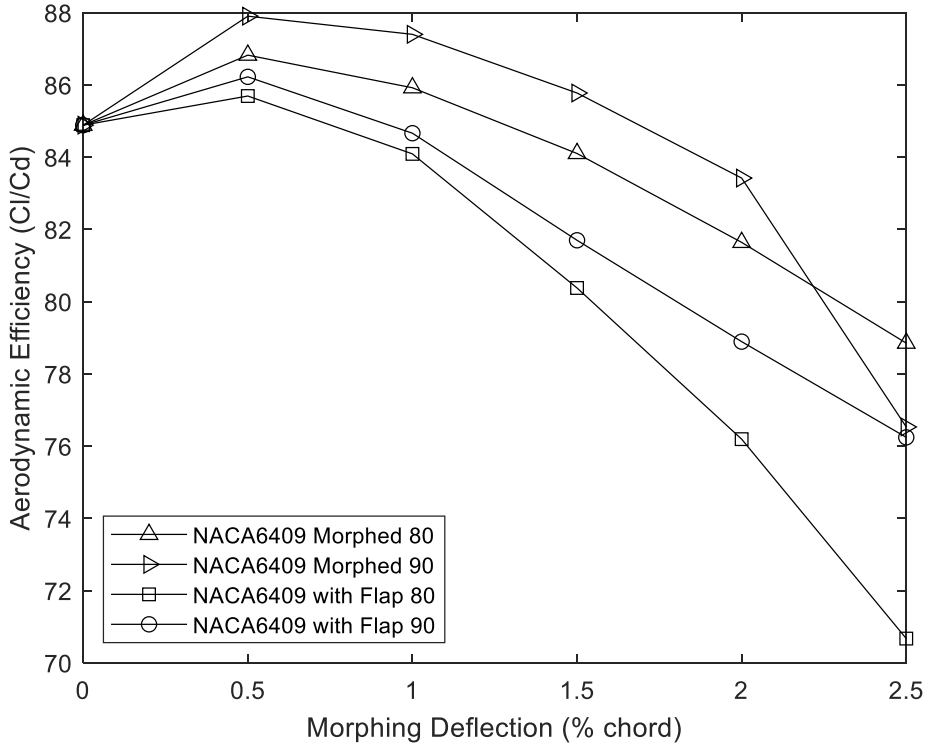

Figure 5.19: Efficiency comparison of NACA6409 of morphed and flap at 3 degrees and 10% ground clearance.

In studies such as Ockfen & Matveev (2009) and Tremblay Dionne & Lee (2018), the gap between the flap and aerofoil was not modelled to simplify the problem. Other studies have gone as far as to attempt to model the gap such as Bofeng et al., (2018) and Liu et al., (2008). A gap between the flap and wing is common in aircraft design due to hinging a flap or control surface from a wing is the easiest method of control and without a gap, the two surfaces would mechanically bind.

It's seen that at 0% deflection, there was minimal difference in the lift (Figure 5.20), drag (Figure 5.21) and aerodynamic efficiency (Figure 5.22). Deflecting the trailing edge shows with a gap present there is a small reduction in lift and a small increase in drag which overall caused a reduction in efficiency of 2.9% to 4.2% across the trailing edge displacements when compared to the morphed aerofoil.

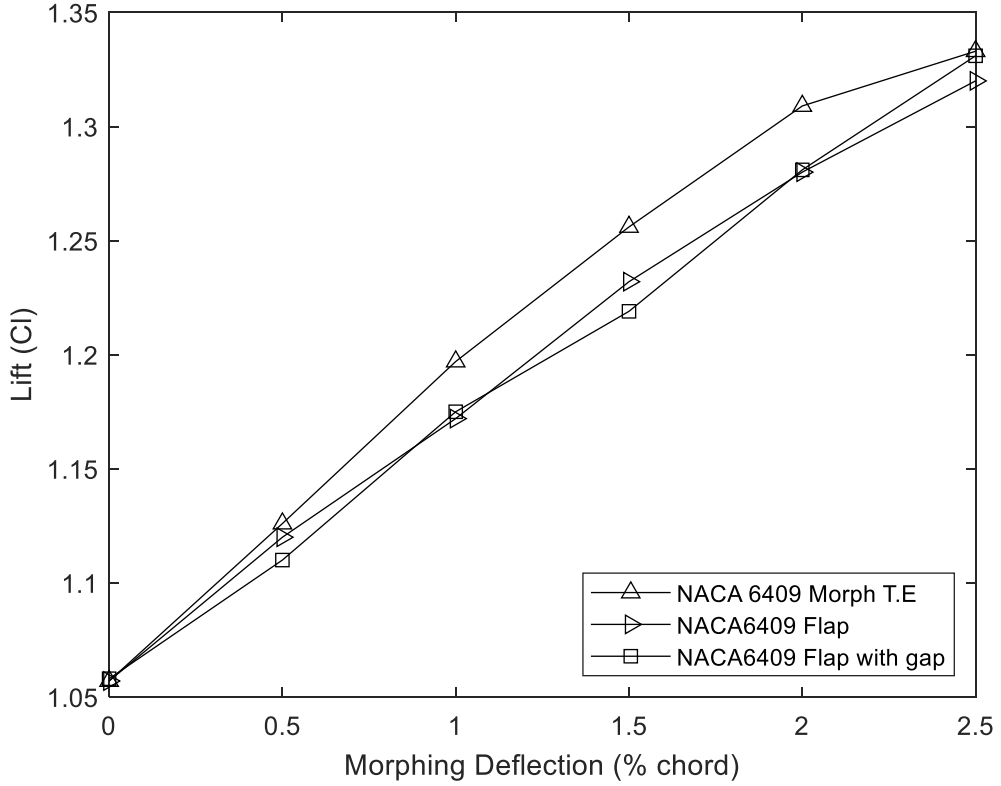

Figure 5.20: Lift comparison of NACA6409 of morphed, flap and flap with gap at 3 degrees and 10% ground clearance.

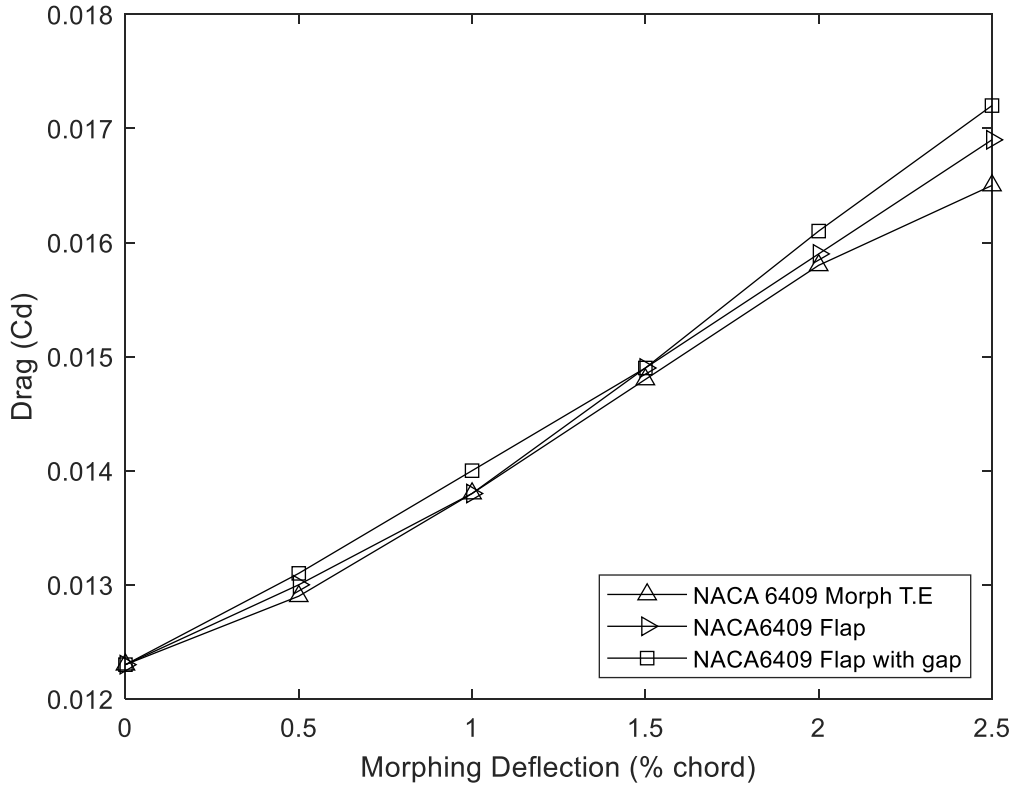

Figure 5.21: Drag comparison of NACA6409 of morphed, flap and flap with gap at 3 degrees and 10% ground clearance.

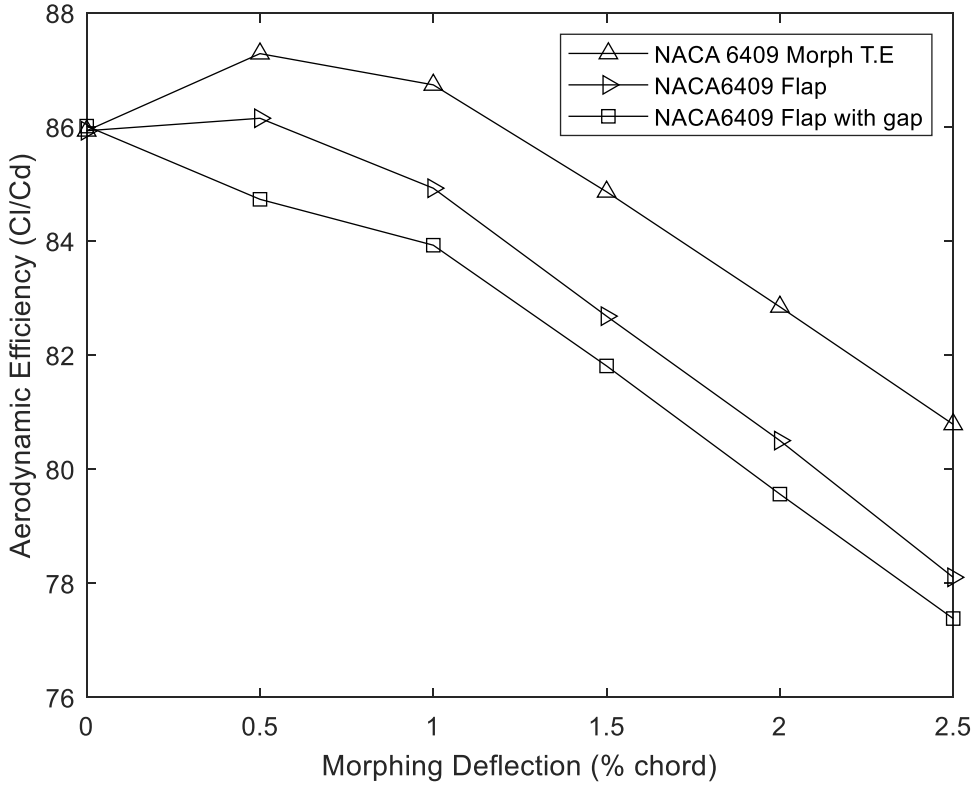

Figure 5.22: Efficiency comparison of NACA6409 of morphed, flap and flap with gap at 3 degrees and 10% ground clearance.

The pressure distribution of a flapped aerofoil was shown for 0% and 2.5% deflection in Figure 5.23 and compared against the morphed aerofoil at 2.5% trailing edge deflection. A flap with a gap increased the pressure on the lower surface and suction on the upper as the trailing edge deflection was increased which was also seen for the morphed aerofoil (Figure 5.8). For both the 0% and 2.5% deflections it was seen there was a jump in pressure in the gap between the flap and aerofoil due to the surface discontinuity, this was not present on the morphed profile due to not having a gap. With the presence of a gap between the aerofoil and flap, the profile is split into two sections, the main profile and the flap element (Cerra & Katz, 2008).

The spike in pressure can be linked to the dumping effect observed by Smith (1975), each element will have a circulation Figure 5.24 which causes a jump in pressure in the gap. The spike in pressure caused a reduction in lift and an increase in drag because of the dumping effect. A study carried out by Bofeng et al., (2018) also showed the gap between the flap and aerofoil had a negative effect.

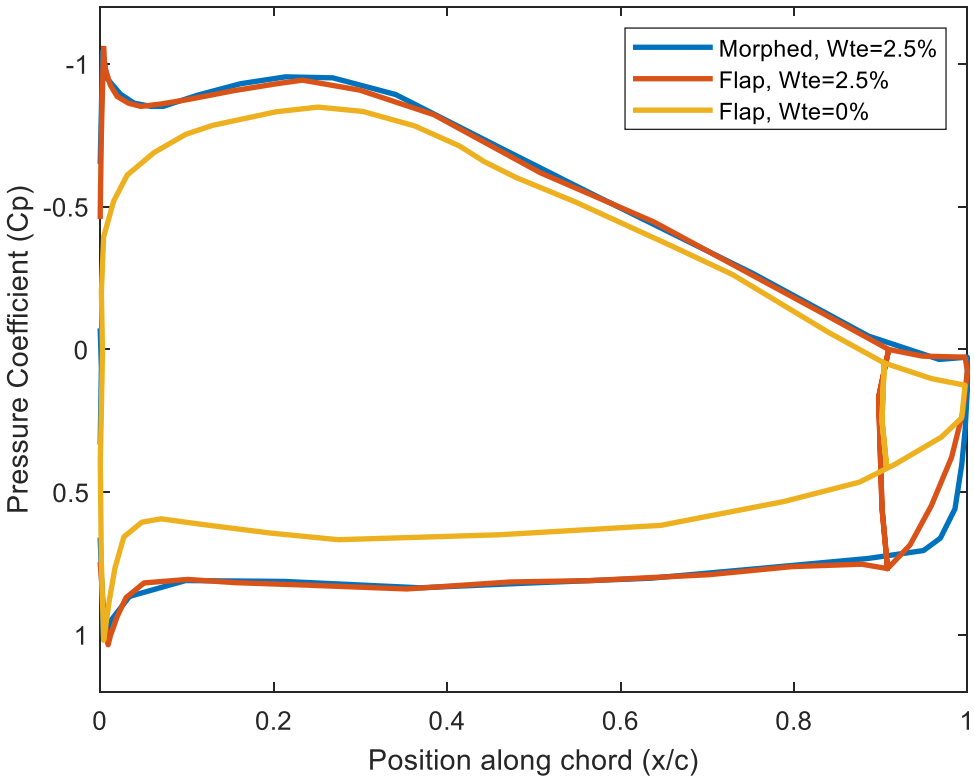

Figure 5.23: Pressure distribution around NACA6409 at 3 degrees angle of attack and 0.1 ground clearance for flap with gap and morphed trailing edge.

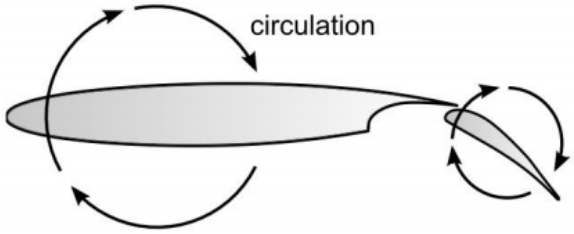

Figure 5.24: Schematic of circulation around main element and flap (Hahn et al., 2012)

5.4 Dynamic Morphing

Morphing the FishBAC aerofoil was extended from the static morphing shown in section 5.3 to morphing over time with URANS, and the static and dynamic morphing results were compared. The dynamic morphing was carried out from a converged unsteady simulation with zero morphing. Once the simulation had the force values and residuals converged, the morphing was turned on, and the aerofoil morphed over the specified time period. The morphing was started from zero trailing edge deflection at 0 seconds and morphed dynamically over time to reach a maximum deflection of 2.5% chord after 1 second. A start location of 80% was tested for a range of angles of attack with a ground clearance of 10% and freestream.

5.4.1 Dynamic and Static Morphing Comparison

The aerofoil was morphing dynamically over time starting with zero trailing edge deflection from a fully converged solution. After a 1 second morphing period the aerofoil had reached maximum trailing edge deflection. A morphing period of 1 second was selected based on the application of morphing wings applied to UAV craft which this period is of typical actuator speeds. Also, a UAV craft typically has low inertia control surfaces allowing fast actuation.

Different morphing periods (0.05, 0.1, 0.5, 1 and 1.5 seconds) were tested to see how the period affected the lift and drag for the NACA6409 in 10% ground effect and 4 degrees angle of attack. It was seen that for both the lift in Figure 5.25 and drag in Figure 5.26 that varying the morphing period did not vary the final converged value of lift or drag. A quicker morphing period increased the rate of lift and drag increase.

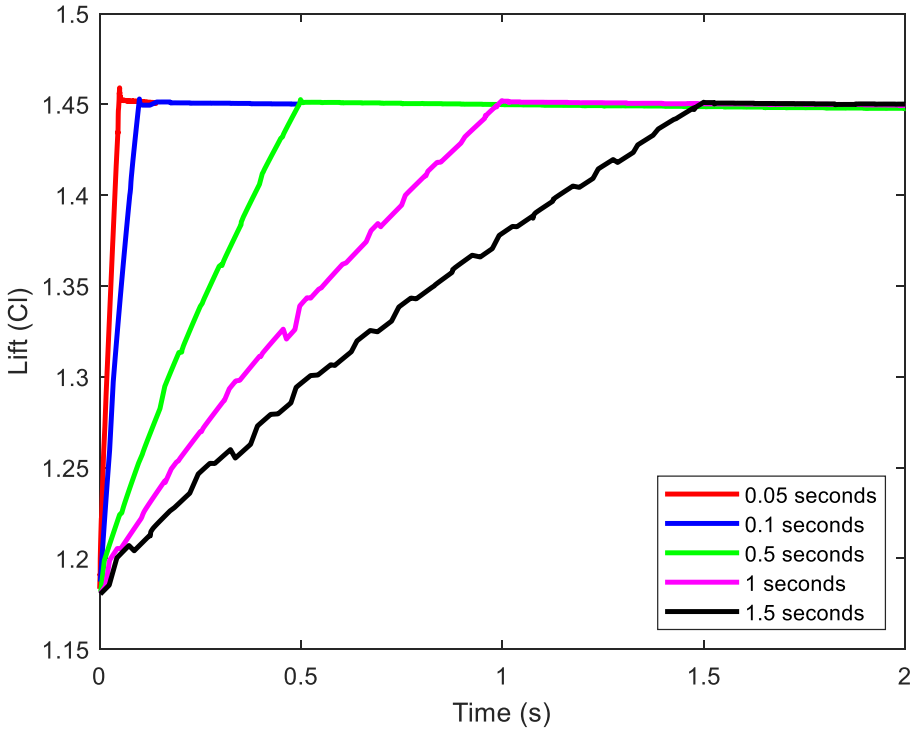

Figure 5.25: NACA6409 lift varying morphing period.

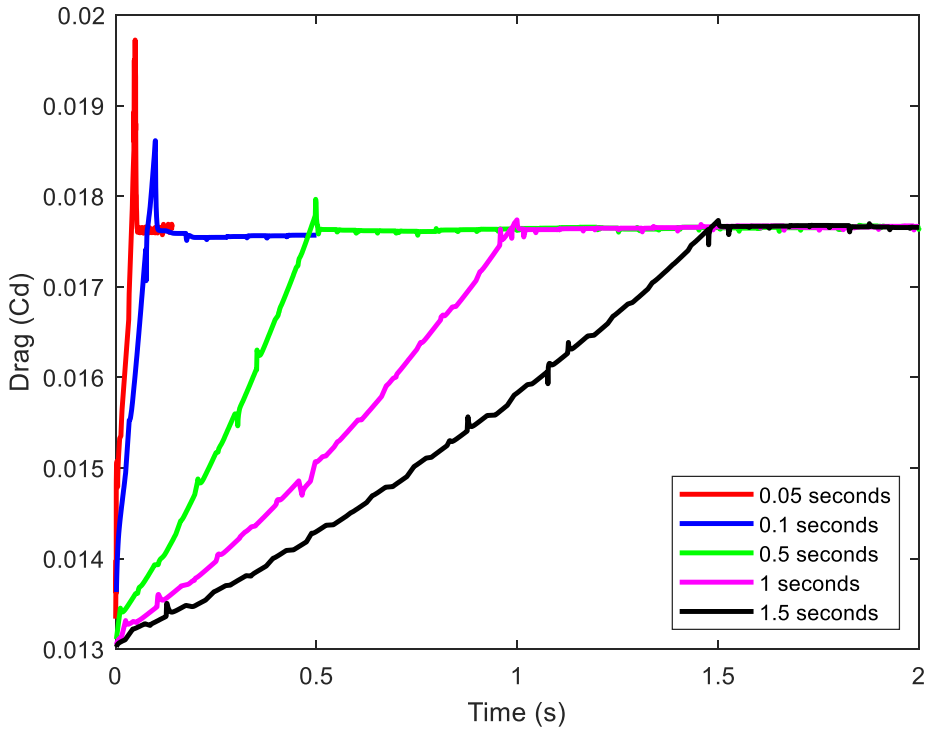

Figure 5.26: NACA6409 drag varying morphing period.

It was observed in this study and also by Abdessemed et al., (2019 and 2022) that there was an overshot in drag after morphing before the drag reduced to its final value. This overshoot was 10.8% for a morphing period of 0.05 seconds, 5.4% for a morphing period of 0.1 seconds and 1.2% for 0.5 seconds. There was no noticeable overshoot for morphing periods of 1 and 1.5 seconds. The overshot was due to unsteadiness and separation on the upper surface which rapid morphing caused separation before reattaching, the slower the morphing the better the flow could remain attached. A morphing period of 1 second was selected for the test for the rest of this study.

The dynamic morphing was first investigated at low angles of attack of between 0- and 4-degree angles of attack over a 1-second morphing period. The trailing edge displacement of the dynamic morphing was compared to the static case. Figure 5.27 showed the dynamic lift was slightly higher than the static lift and Figure 5.28 showed the dynamic drag was slightly lower than the static drag. The reason the lift was higher and the drag lower for the dynamic case was due to the use of URANS in the dynamic morphing which can capture more flow details compared to RANS used in the static morphing. This meant that more turbulent mixing was captured when using URANS which moved the location of separation downstream on the upper surface. The lower drag and higher lift throughout the morphing for the dynamic case caused a higher aerodynamic efficiency compared to the static morphing seen in Figure 5.29. The lift and drag showed to follow the same trends comparing the static and dynamic cases. This was due to the morphing period of 1 second being used which corresponded to a Strouhal number of 2×10^{-3} which showed the flow is quasi-static. Therefore, at lower angles of attack the dynamic was comparable to the static morphing.

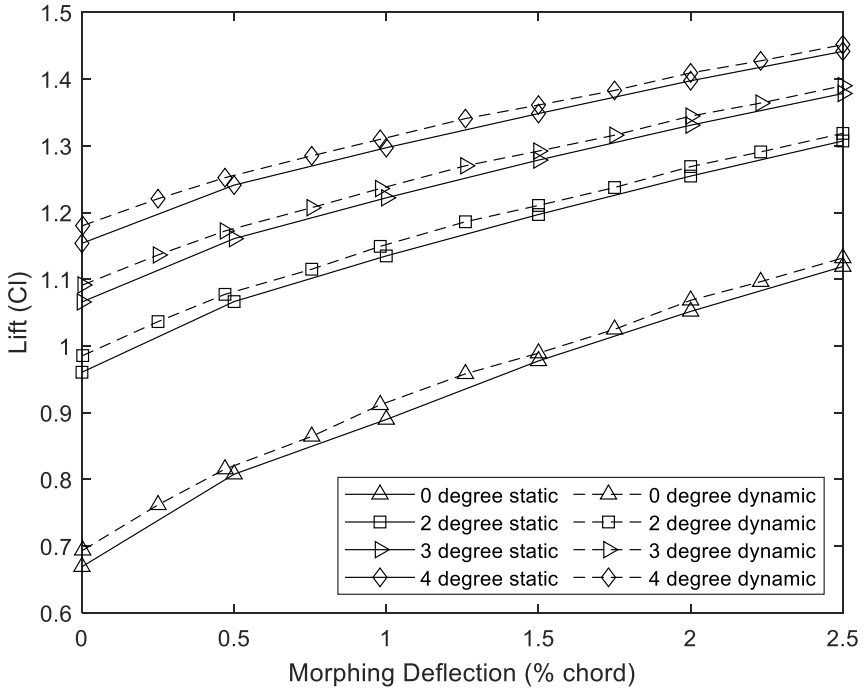

Figure 5.27: Static and dynamic morphing lift comparison up to 4-degree AoA.

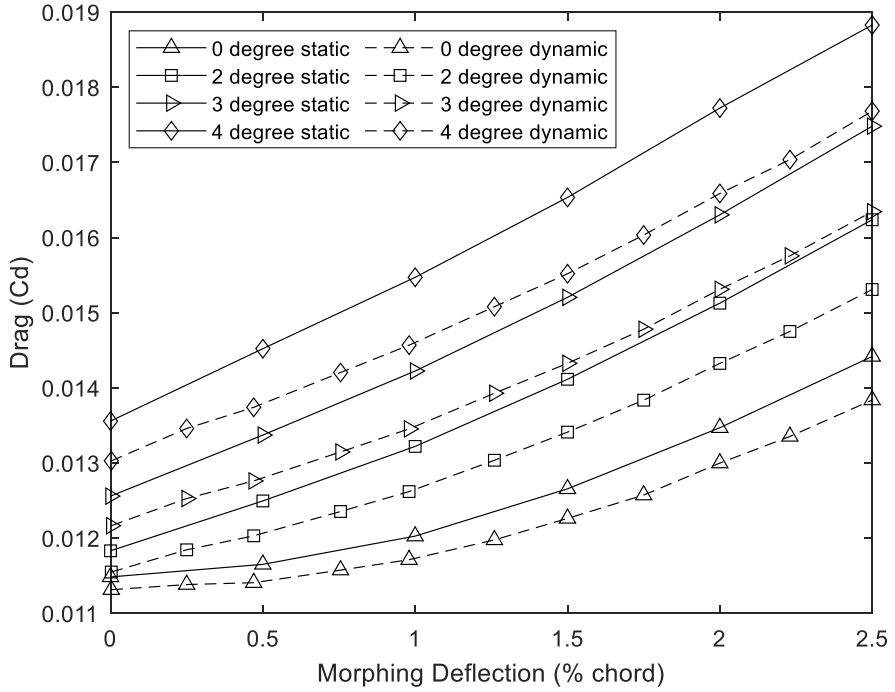

Figure 5.28: Static and dynamic morphing drag comparison up to 4-degree AoA.

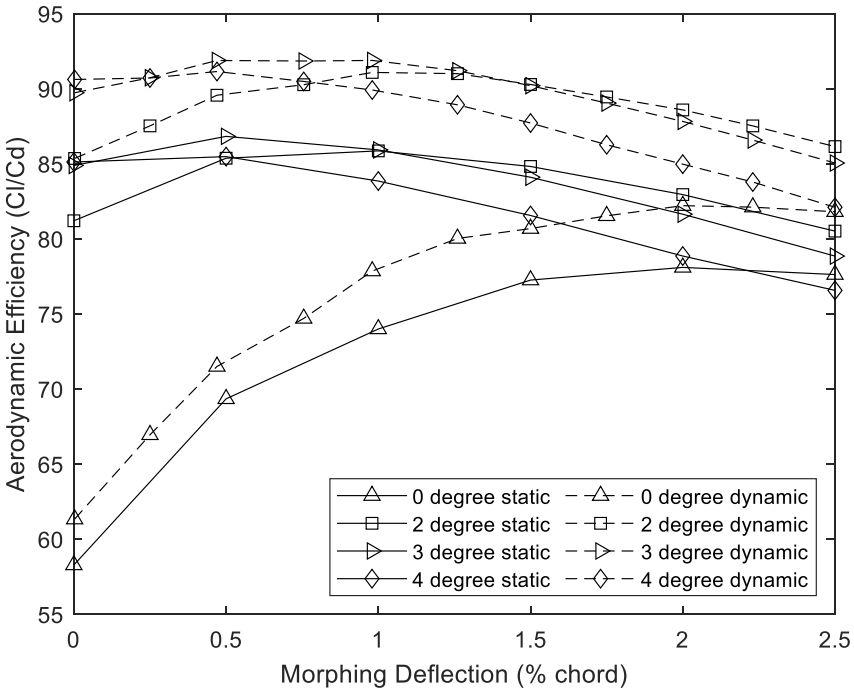

Figure 5.29: Static and dynamic morphing efficiency comparison.

5.4.2 Dynamic Behaviour at High Angles of Attack

Having compared the static and dynamic morphing against the trailing edge deflection in section 5.4.1 for low angles of attack, it was found the dynamic and static were comparable due to the quasi-static flow. The dynamic morphing was investigated further in this section for higher angles of attack and comparisons made between freestream and ground effect. Therefore, further investigation of dynamic was carried out for just for the 1 second morphing period.

First, the freestream was investigated at high angles of attack using unsteady morphing looking at the lift (Figure 5.30) and drag (Figure 5.31). In freestream at zero morphing deflection, the 12-degree angle of attack showed the maximum lift. As the 12-degree aerofoil was morphed, the lift increased, however, the rate of increase was less than that of the 10-degree angle of attack during morphing and at 0.5 seconds the 10-degree angle of attack showed higher lift than the 12 degrees. This was due to the aerofoil at 12 degrees angle of attack approaching stall and increasing the aerofoil camber further caused the aerofoil to stall.

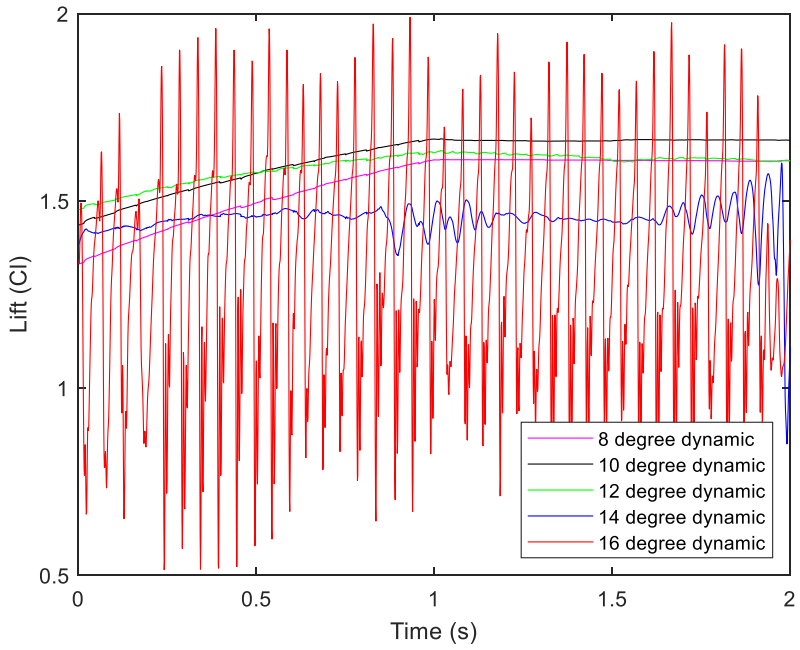

Figure 5.30: Dynamic NACA6409 morphing lift in freestream for 1 second morphing period.

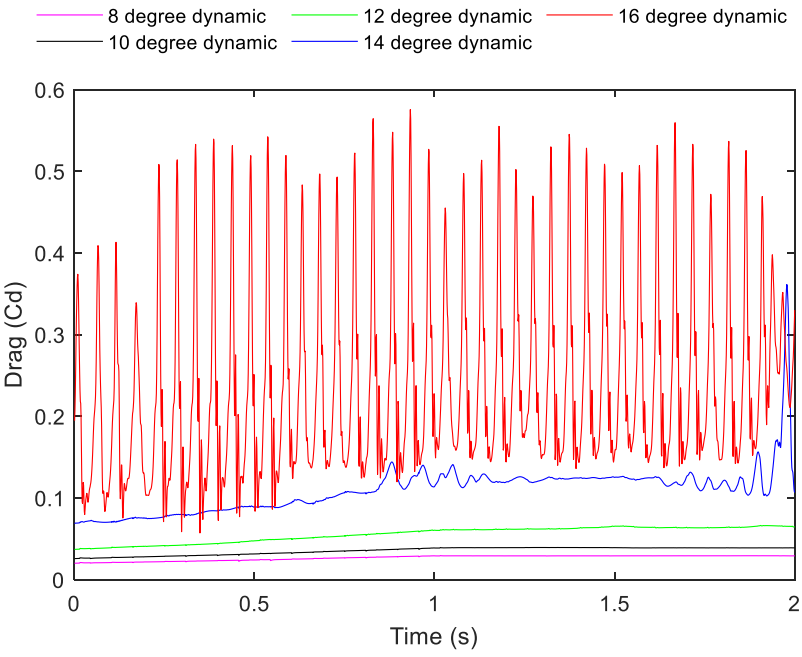

Figure 5.31: Dynamic NACA6409 morphing drag in freestream for 1 second morphing period.

Increasing the deflection from 0% to 2.5% trailing edge deflection for the 1 second morphing period showed a gain in lift (Figure 5.30). This gain in lift reduced as the angle of attack increased. The lift increased by a Cl of 0.264 for 8 degrees, a Cl of 0.233 for 10 degrees and a Cl of 0.155 for 12 degrees. At 14 degrees the lift was initially much lower than the 12-degree angle of attack showing the zero morphed 14-degree aerofoil had stalled, as the aerofoil was morphed there was no gain in lift and the flow became slightly unsteady at 0.8 seconds. At 16 degrees the lift was highly oscillatory seen in Figure 5.30 throughout the entire morphing period. The average lift for

the 16-degree angle of attack was less than that of the 14-degree angle of attack showing the 16 degrees had fully stalled.

At 150% chord location downstream of the trailing edge, the non-dimensional vertical velocity was shown in Figure 5.34 which showed the vortex downstream. With the non-dimensional vertical dimension zeroed at the trailing edge zero deflection height, the plot showed an increase in vertical velocity beneath the aerofoil and reversed velocity above the aerofoil. The flow at 16 degrees was highly unsteady, with turbulent mixing from freestream and the flow separating and reattaching continuously which caused the unsteadiness seen in freestream. Figure 5.33 compares the TKE for the 12 and 16 degrees angle of attack in freestream showing the much higher levels of separation for the 16 degrees compared to the 12 degree. The TKE over time shows how the flow continuously separated and reattached for the 16 degree and was shown in appendix A.4. The high levels of separation and reattachment also caused high fluctuations in the drag seen in Figure 5.31 where the mean drag for the 14- and 16-degree angle of attack was significantly higher than the other angles of attack tested. Due to the higher drag at 14 and 16 degrees angles of attack, and that the 12-degree was on the verge of stalling, the aerodynamic efficiency (Figure 5.32) was much lower than smaller angles of attack (Figure 5.29).

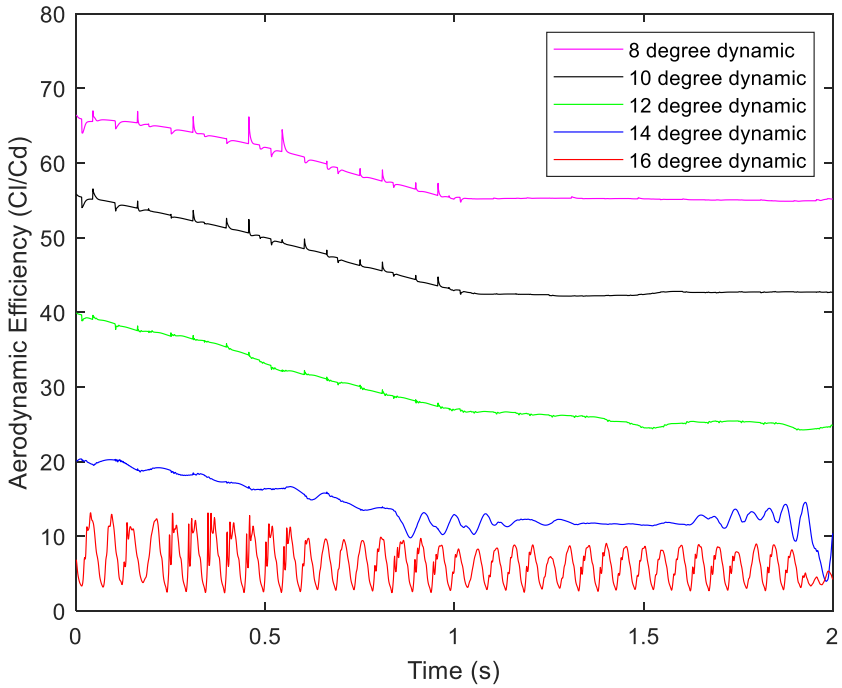

Figure 5.32: Dynamic NACA6409 morphing efficiency in freestream.

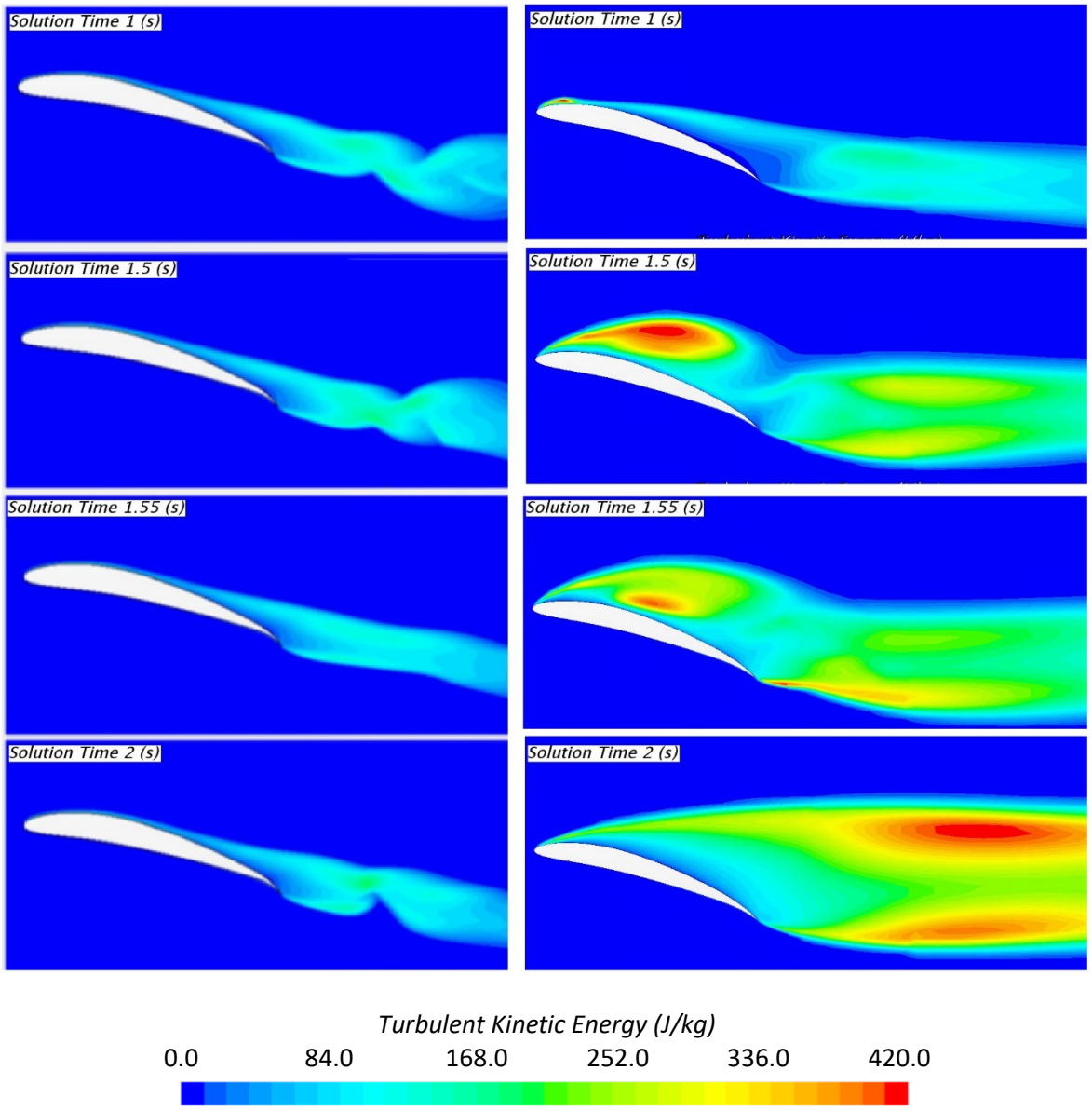

Figure 5.33: Dynamic freestream 12-degree AoA (left) and 16-degree (right) NACA6409 TKE.

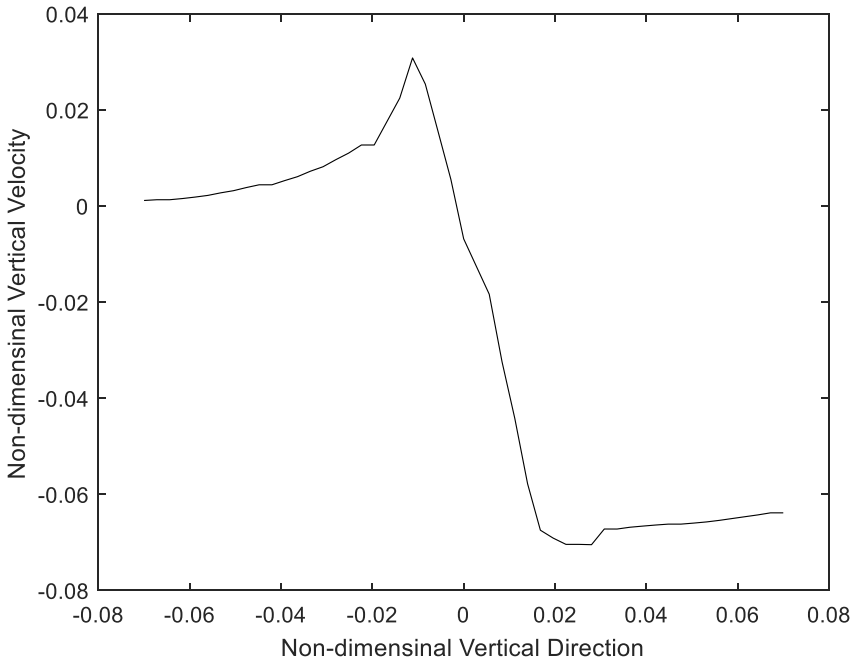

Figure 5.34: Non-dimensional vertical velocity in wake at 150% downstream of the trailing edge for 16-degree AoA in freestream.

After looking at the high angles of attack in freestream, the aerofoil was then brought into ground effect for high angles of attack. In ground effect, it was seen (Figure 5.35) the 10-degree angle of attack produced the highest lift at zero morphing deflection compared to freestream where the highest lift at zero morphing occurred at 12 degrees. As the 10-degree was morphed, the aerofoil did not produce any gains in lift after 0.5 seconds and after 0.8 seconds the flow became highly unsteady also seen by the drag in Figure 5.36. Figure 5.37 showed the aerofoil at 10 degrees in 10% ground effect and it was seen that the unsteadiness after 0.8 seconds was due to the wake becoming highly unsteady and at 1 second the laminar separation bubble had separated. The flow then reattached and then separated as time progressed causing the high fluctuation in the lift in Figure 5.35 and in drag Figure 5.36. This showed that the aerofoil was on the verge of stall at 10 degrees angle of attack when in ground effect and that wings in ground effect stall at earlier angles of attack compared to freestream.

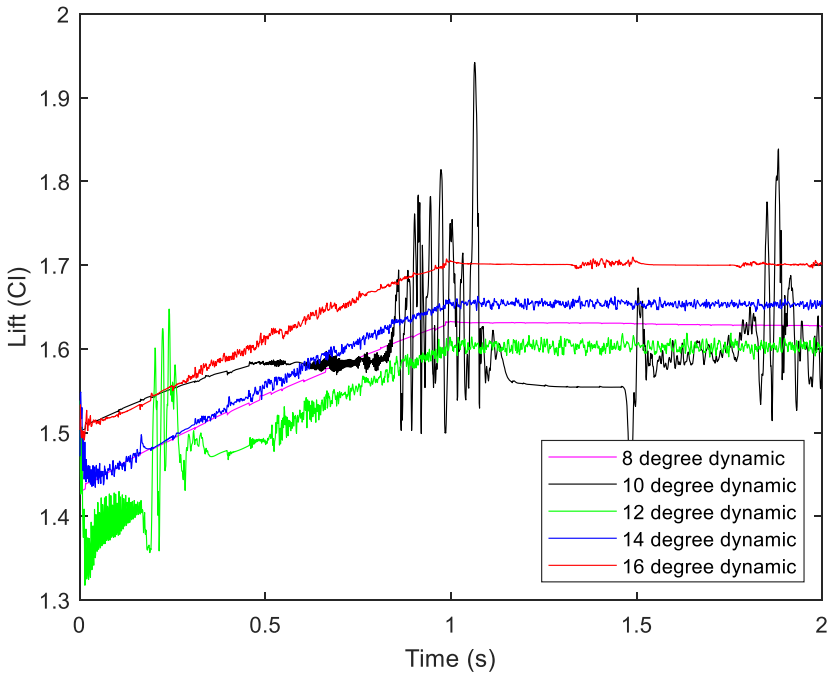

Figure 5.35: Dynamic NACA6409 morphing lift in ground effect.

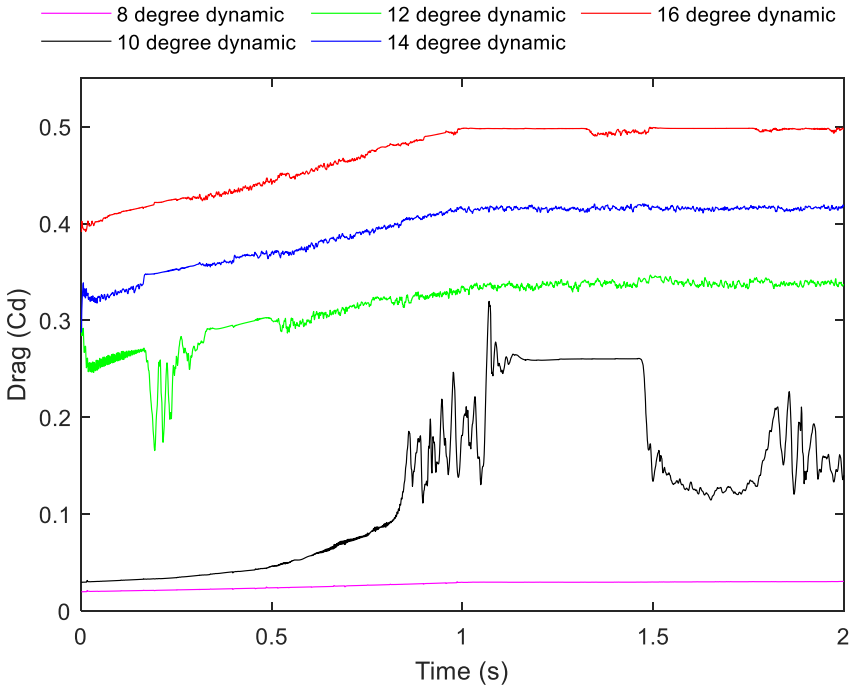

Figure 5.36: Dynamic NACA6409 morphing drag in ground effect.

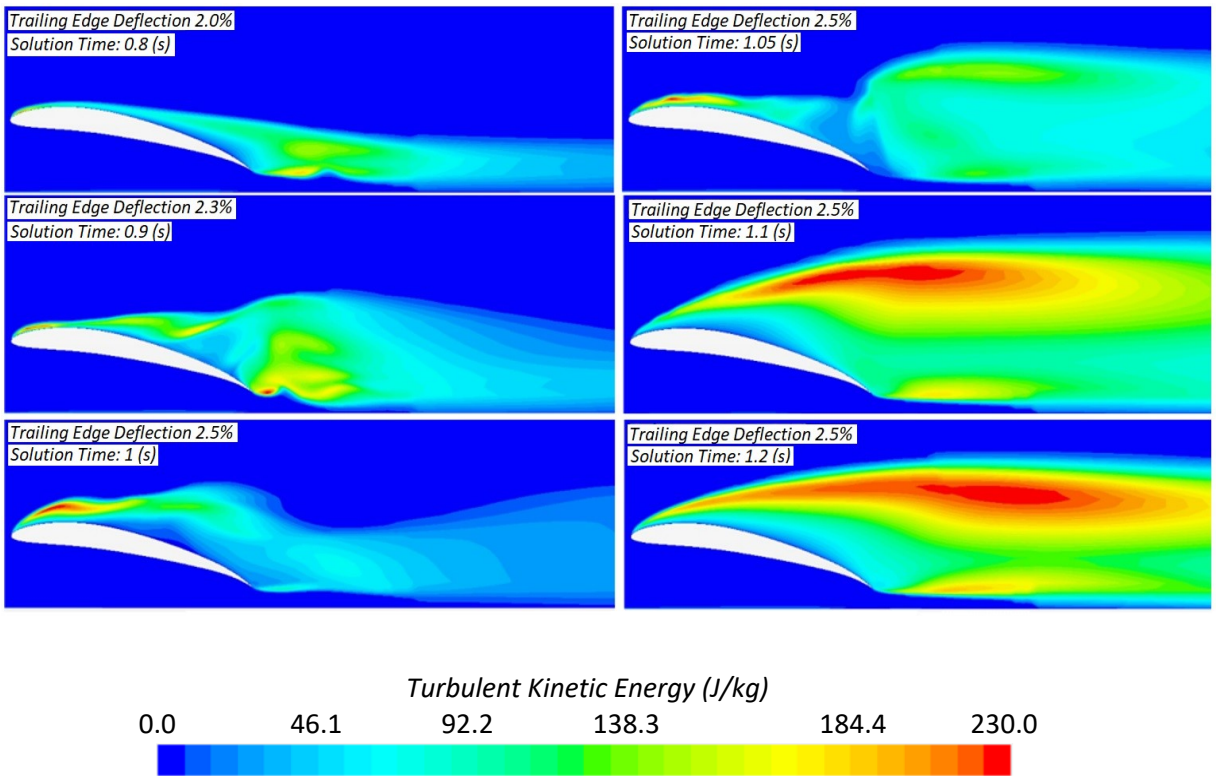

Figure 5.37: NACA6409 Dynamic morphing TKE at 10-degree AoA in 10% ground effect.

In ground effect, increasing the angle of attack from 10 to 12 degrees showed a significant reduction in lift, this showed the aerofoil had fully stalled on the upper surface in ground effect at 12 degrees angle of attack. Although the 12-degree upper surface had stalled, increasing the angle of attack to 14 and 16 degrees saw an increase in lift and reduced oscillatory behaviour of the coefficients. The increase in lift although the upper surface had stalled was due to further ground effect enhancement as the angle of attack increased. This was due to an increase in the distance between the aerofoil lower surface and the ground upstream of the trailing edge. As mentioned in section 4.3, increasing this distance caused gains in ground effect enhancement for a fixed ground clearance. The unsteadiness of the flow was reduced due to a reduction in downwash and downward momentum of the flow caused by the proximity of the ground. This meant the proximity of the ground forced the separated flow to remain fully separated without reattachment. The separated flow in ground effect was seen in Figure 5.38 compared to the high oscillatory flow of freestream by comparing the TKE.

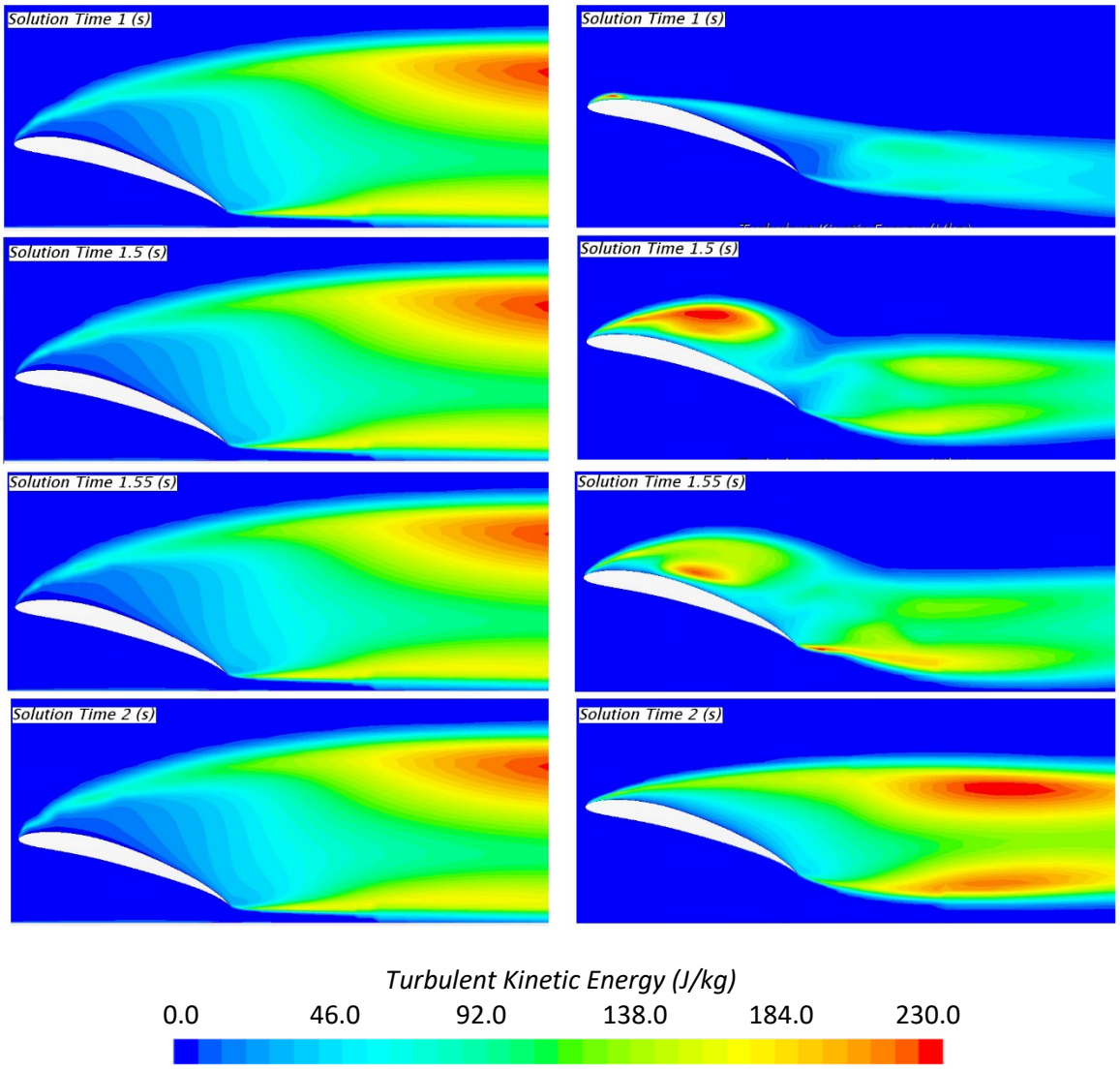

Figure 5.38: Dynamic morphing TKE in ground effect (left) and freestream (right) at 16-degree AoA and 95% chord morphing start location.

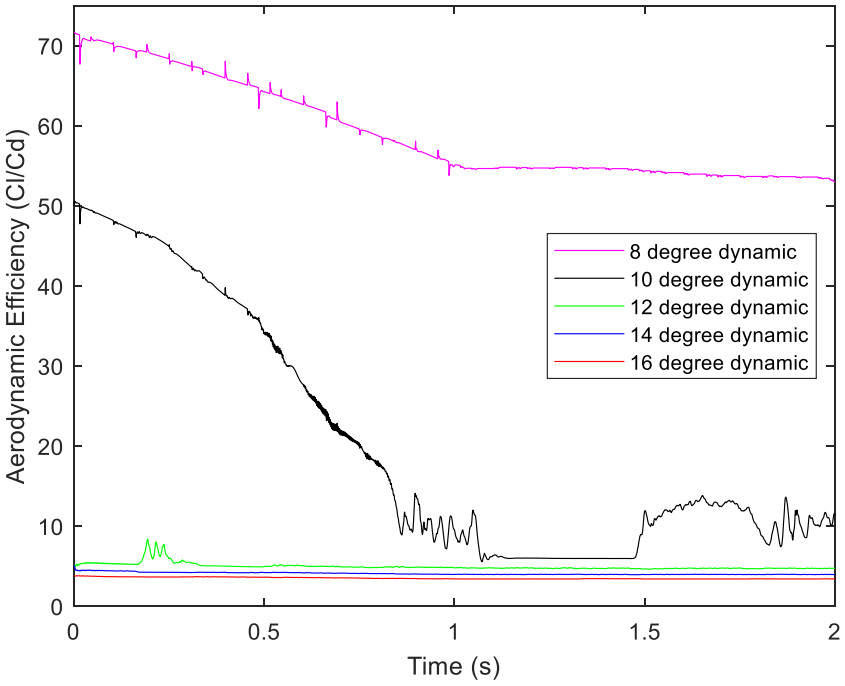

Figure 5.39: Dynamic NACA6409 morphing efficiency in ground effect.

Figure 5.39 shows the aerodynamic efficiency of the morphing wing in ground effect. The peak aerodynamic efficiency occurred with zero morphing at 8 degrees angle of attack. Increasing the angle of attack from 8 to 10 degrees caused the aerodynamic efficiency to drop by 20 at zero morphing. At full trailing edge deflection seen at 1 second in Figure 5.39, this difference increased to approximately 55. This shows as the aerofoil stalls; the aerodynamic efficiency drops dramatically. It was also seen that for the 8-degree ground effect that at zero morphing, the aerodynamic efficiency was higher than the freestream (Figure 5.32); however, at full morphed deflection, the freestream had higher aerodynamic efficiency. This was due to wings in ground effect being prone to earlier stall from the reduced downward momentum. For angles of attack of 10 degrees and higher, it was seen freestream had higher aerodynamic efficiency.

5.5 Periodic Morphing

5.5.1 Discussion

Periodic morphing was investigated using the FishBAC morphing method applied in a sinusoidal motion on a NACA6409 aerofoil in ground effect. Applying morphing to an aerofoil in two dimensions in ground effect results in many variables that include, angle of attack, ground clearance, morphing start location, morphing frequency, and trailing edge displacement. To reduce the number of variables and computational costs of running high-power simulations, a fixed value of start location, angle of attack and ground clearance was tested. The angle of attack was fixed at 4 degrees due to the high aerodynamic efficiency seen in section 5.3. The focus was

applying the morphing in ground effect therefore a ground clearance of 10% was selected. The periodic morphing was performed in a sinusoidal motion (Eq.5.4) with both upwards and downwards deflections shown by the schematic Figure 5.40.

$$y_{ts} = \frac{wte(x - xs)^3}{(c - xs)^3} sin(2\pi f) \quad 5.4$$

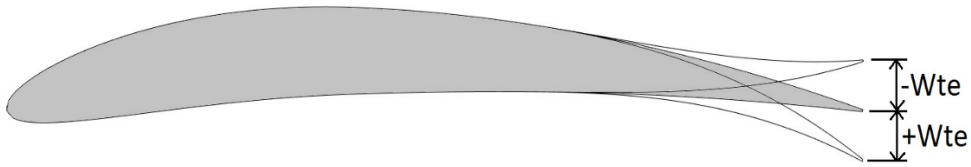

Figure 5.40: Schematic of periodic morphing trailing edge deflection.

The simulation for the periodic morphing was carried out using Detached Eddy Simulation (DES) due to the greater accuracy and prediction of separation required and better capturing of turbulent mixing. The simulation was left to run for 0.1 seconds with the morphing switch off to allow the flow to settle and gain a steady converged solution. The morphing was then turned on after 0.1 seconds and the simulation was carried out for up to 0.4 seconds. Both the lift and drag were time averaged between 0.15 and 0.4 seconds. This was due to observing the flow had settled and converged at approximately 0.15 seconds. This explanation was demonstrated in Figure 5.41 where the initial non-morphing and morphing periods are shown.

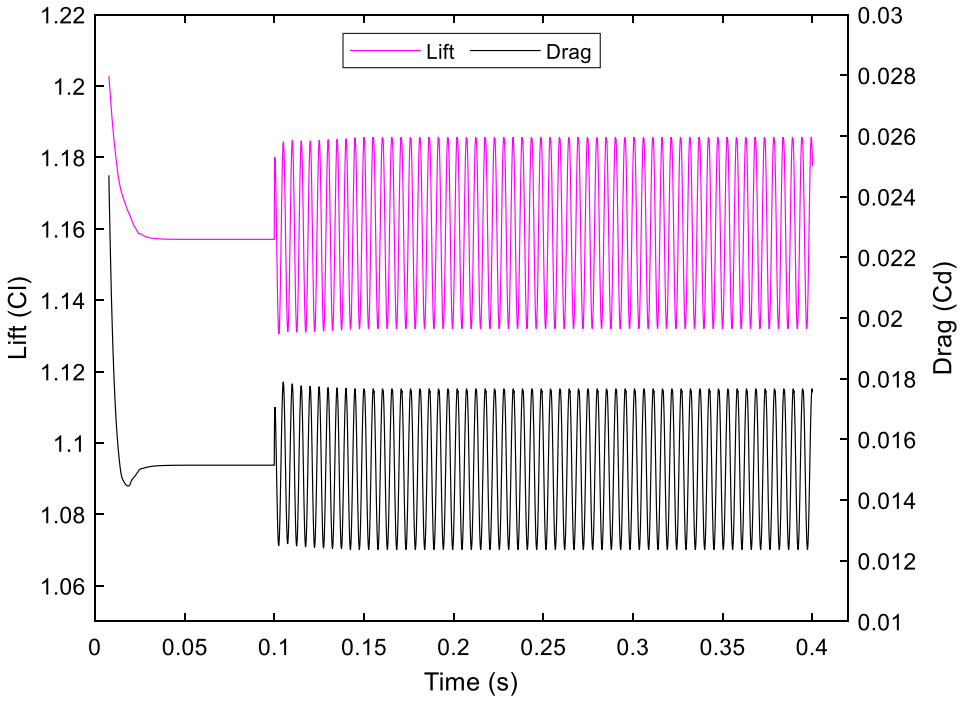

Figure 5.41: Lift and drag over time for Strouhal number = 0.9 and 0.125% trailing edge deflection.

5.5.2 Small trailing edge deflections.

First, periodic testing was carried out with small trailing edge deflections as this was commonly used in literature (Abdessemed et al., 2021; Kang et al., 2020; J. J. Wang et al., 2008). Therefore, periodic morphing was carried out for a range of trailing edge deflections between 0.05% and 0.15%. A range of morphing frequencies was tested between 100Hz and 800Hz which corresponded to a Strouhal number of 0.45 to 3.58. A start location of x_s = 0.25 was selected due to separation occurring.

Analysing the lift (Figure 5.42) and drag (Figure 5.43) showed the lowest drag coincided with the lowest lift at a Strouhal number of 0.9 and trailing edge deflection of 0.125%. Compared to the baseline lift of zero morphing, the lift reduced from 1.157 to 1.149 and the drag from 0.0152 to 0.0143. This corresponded to a 1% lift reduction and a 6% drag reduction. Due to the reduction in drag being 6% and the lift only 1%, it was seen (Figure 5.44) the aerodynamic efficiency increased by 5.4% for a Strouhal number of 0.9 and trailing edge deflection of 0.125%. Aerofoils produce maximum lift with some separation on the upper surface therefore the reduction in separated flow for the periodic morphing caused a reduction in lift. The reduction of separation on the upper surface also explained the reduction in drag.

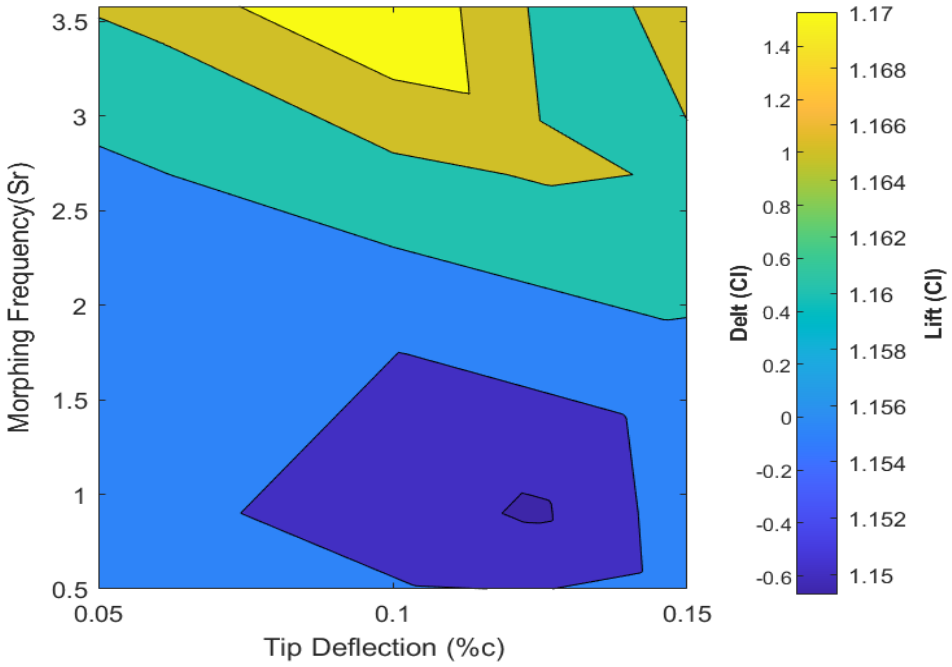

Figure 5.42: Periodic morphing lift 4degree AoA, x_s = 25%, 10% ground clearance low trailing edge deflection.

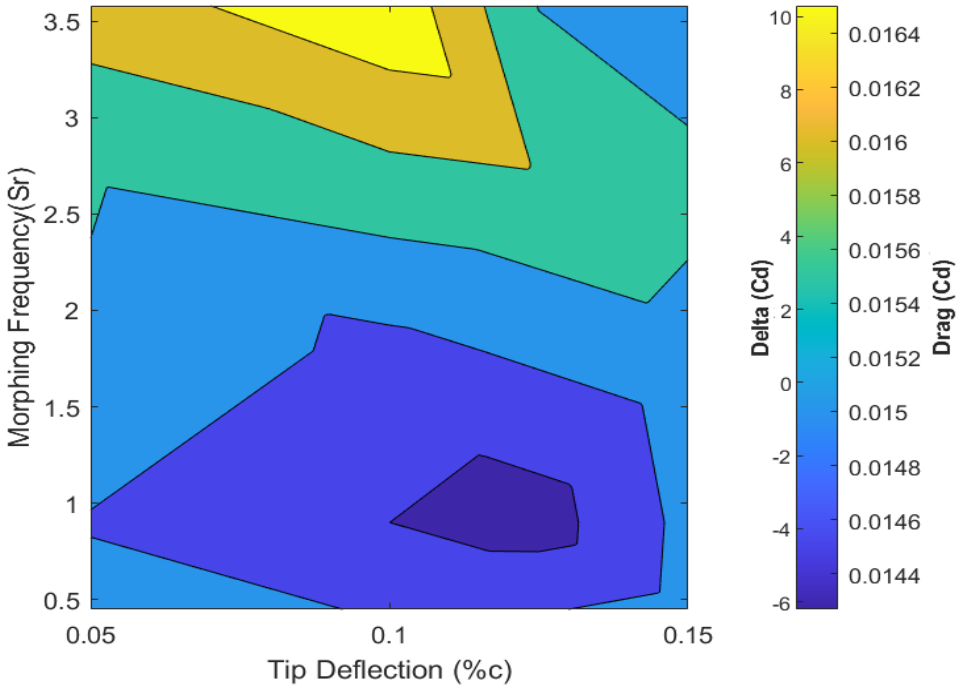

Figure 5.43: Periodic morphing drag 4degree AoA, x_s = 25%, 10% ground clearance low trailing edge deflection.

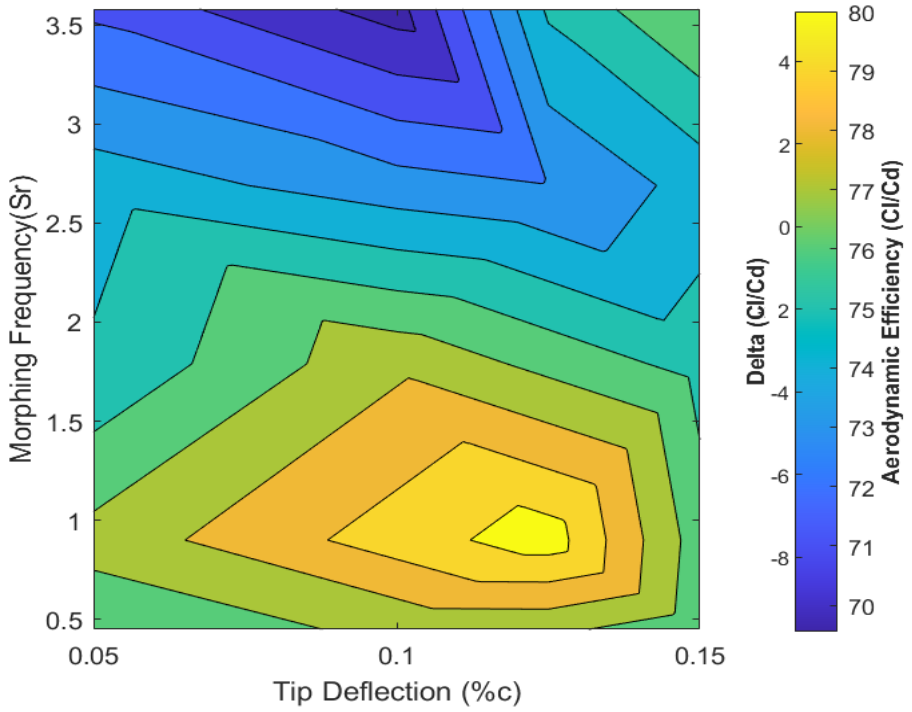

Figure 5.44: Periodic morphing aerodynamic efficiency 4degree AoA, x_s = 25%, 10% ground clearance low trailing edge deflection.

Analysing the wake of the aerofoil showed Kelvin Helmholtz instability. This was caused by the interaction of the two shear layers from both the upper and lower surface leaving the trailing edge. As the trailing edge was morphed periodically these two shear layers slide over each other causing instability. This was also observed by Jodin et al., (2017) when morphing an aerofoil

trailing edge and shown by the schematic in Figure 5.45a. Comparing the schematics of the two shear layers seen in Figure 5.45a shows close similarities to this study seen in (Figure 5.45b) for the Strouhal number of 0.9 and trailing edge deflection of 0.125%.

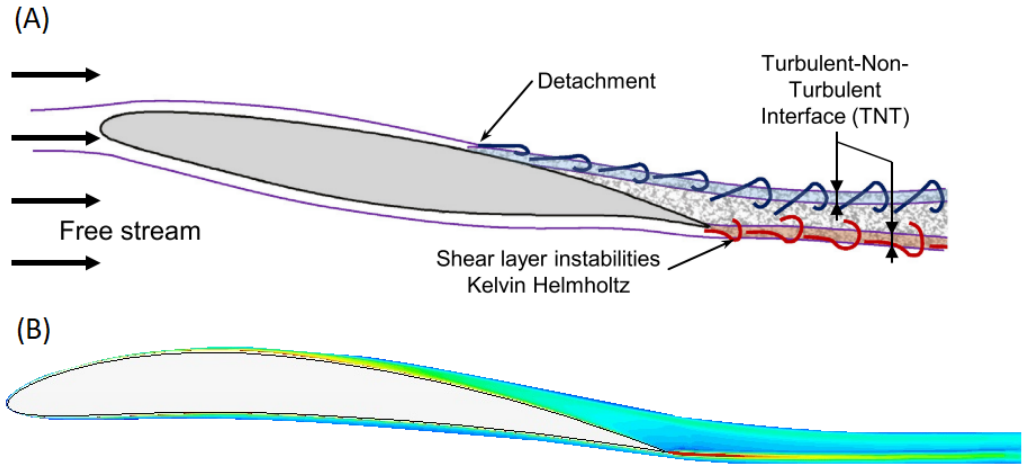

Figure 5.45:Wake dynamics sketch showing shear layers (a) (Jodin et al., 2017) and vorticity of NACA6409 periodically morphing in ground effect at Sr = 0.9 and 0.125% trailing edge deflection showing clear vorticity shear layers (b).

Although the aerodynamic efficiency (Figure 5.44) increased for a Strouhal number of 0.9 and trailing edge deflection of 0.125%, the gains in performance were very sensitive to the Strouhal number and trailing edge deflection variations. Increasing or decreasing both the Strouhal number and trailing edge deflection caused the efficiency to decrease and become lower than the non-morphing aerofoil. This means low trailing edge deflections for the flow conditions tested are not feasible as the aerodynamic efficiency can suddenly drop and decrease the aircraft's performance.

5.5.3 Large morphing frequencies and trailing edge deflections.

To overcome this sensitivity shown by small trailing edge deflections, larger trailing edge deflections were tested. Larger deflections were carried out in literature by Jodin et al., (2017) and Kan et al., (2020) to delay stall and improve aerodynamic performance. The trailing edge deflection range was increased to 0.5% to 1% of the chord with morphing frequencies of 100Hz to 900Hz corresponding to a Strouhal number range of 0.45 to 4.

Analysing the lift (Figure 5.46), it was seen for the lift there was a clear relation between the morphing frequency and trailing edge deflection. Increasing the trailing deflection from 0.5% to 1% increased the lift by 3% at a Strouhal number of 0.45 and increased the lift by 11.2% for a Strouhal number of 4. At a trailing edge deflection of 1% of the chord length, it was seen the lift increased by 30% when the Strouhal number was increased from 0.45 to 4. At 0.5% trailing edge

deflection the lift increased by 21%. At low Strouhal numbers below 1.79, it was seen the lift was lower than the baseline non-morphing wing and above a Strouhal number of 1.79 the lift was higher than the baseline wing. This showed high morphing frequencies caused the largest gains in lift and showed an improvement in lift compared to the non-morphed wing.

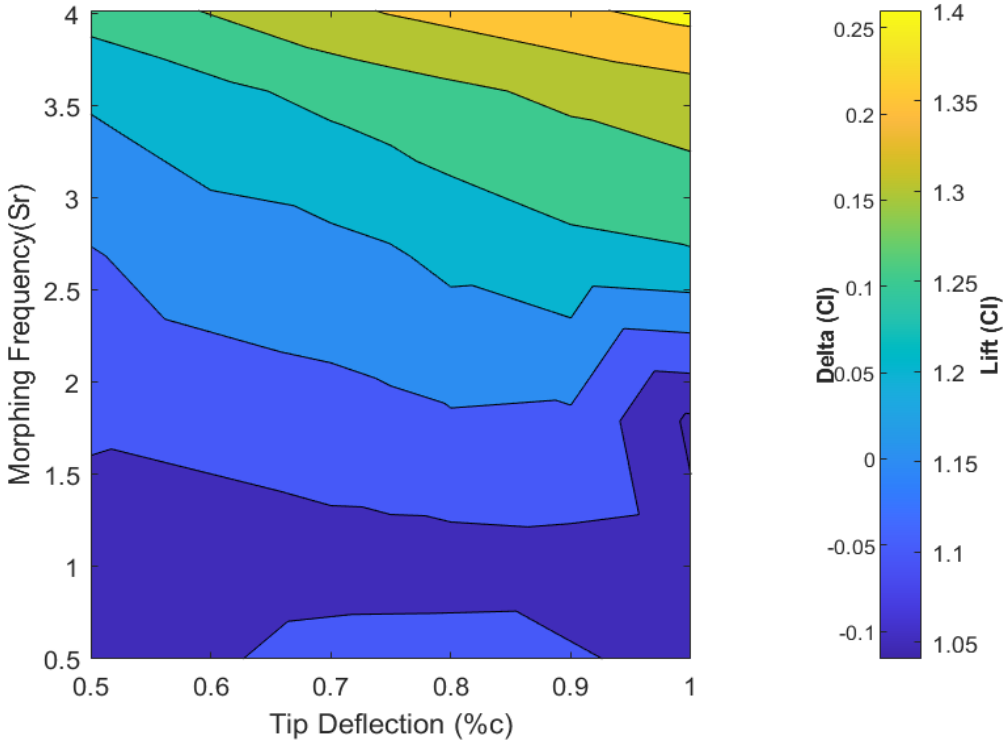

Figure 5.46: Periodic morphing lift 4degree AoA, x_s = 25%, 10% ground clearance high trailing edge deflection.

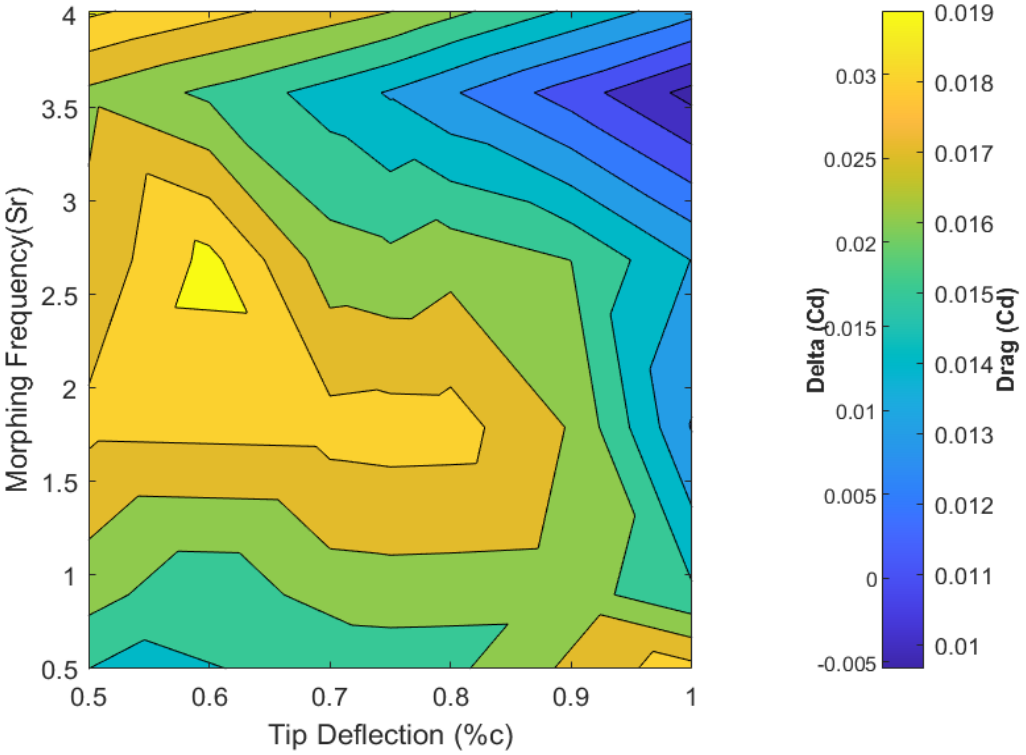

Figure 5.47: Periodic morphing drag 4degree AoA, x_s = 25%, 10% ground clearance high trailing edge deflection.

The drag (Figure 5.47) showed less of a clear relation when the morphing frequency and trailing edge deflection were varied. It was seen the drag was highest for a Strouhal number of 2.69 with a trailing edge deflection of 0.6% chord, increasing or decreasing the trailing edge deflection and morphing frequency. It was seen at low trailing edge deflections and morphing frequencies that the wake showed Kelvin Helmholtz instability (Figure 5.45) and high trailing edge deflections and morphing frequencies showed vortex shedding. For trailing edge deflections below 0.6% chord and Strouhal numbers of 2.69 the wake showed Kelvin Helmholtz instability, above this value Von-Karman shedding occurred. Morphing at a trailing edge deflection of 0.6% chord and Strouhal number of 2.69 was in between the Von-Karman and Kelvin Helmholtz wake which this cross-over region caused a chaotic wake shown in (Figure 5.48). This chaotic wake caused an overall higher drag than the other trailing edge deflections and morphing frequencies.

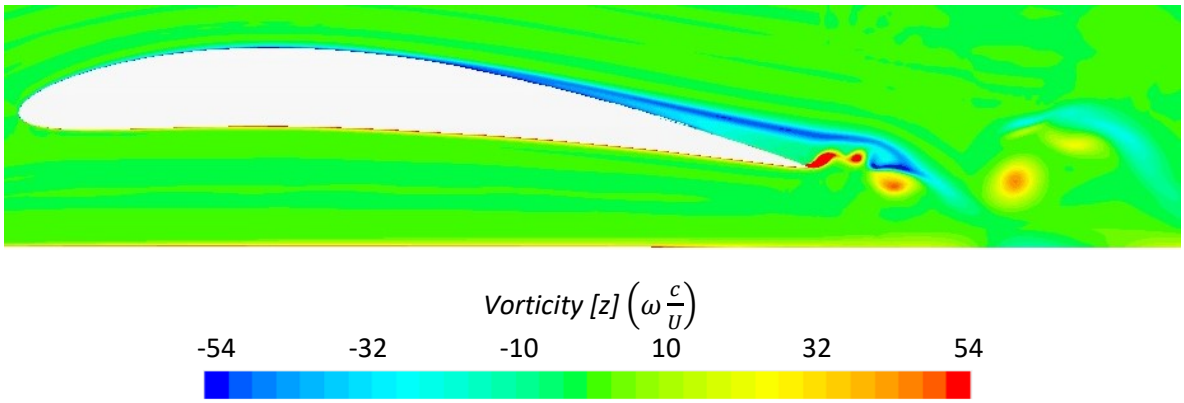

Figure 5.48: Periodic morphing at a Strouhal number of 2.69 and deflection of 0.6% chord.

Looking at the aerodynamic efficiency (Figure 5.49) it was seen at low trailing edge deflections and low morphing frequencies that the aerodynamic efficiency was the lowest and lower than the non-morphing aerofoil. It was seen at a trailing edge deflection of 1% and morphing frequency of 3.58 that the aerodynamic efficiency increased from 76.4 for the non-morphing aerofoil to 137.8 for the morphing aerofoil. This was an aerodynamic efficiency gain of 81% compared to the baseline morphing aerofoil. The gains in aerodynamic efficiency came from the 15.1% increase in lift and 36.7% reduction in drag.

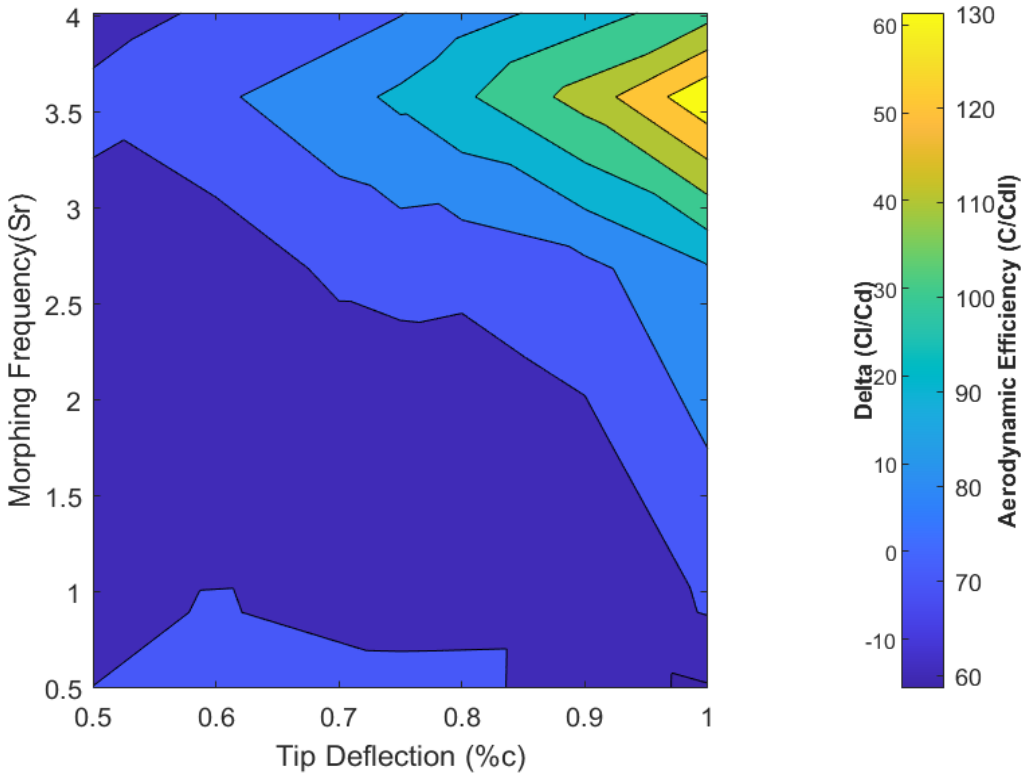

Figure 5.49: Periodic morphing aerodynamic efficiency 4degree AoA, x_s = 25%, 10% ground clearance high trailing edge deflection.

The aerofoil was morphed using a sinusoidal motion therefore the lift and drag would increase on the downwards deflection and decrease on the upwards defections. The lift and drag values shown in the periodic morphing results (Figure 5.42 to Figure 5.49) are the mean values taken over the morphing period between 0.15 and 0.4 seconds. However, the lift and drag will fluctuate about these values as shown in Figure 5.50. These fluctuations were shown in Figure 5.51 for the lift and Figure 5.52 for the drag. It was seen increasing both the trailing edge deflection and morphing frequency increased the lift and drag fluctuation.

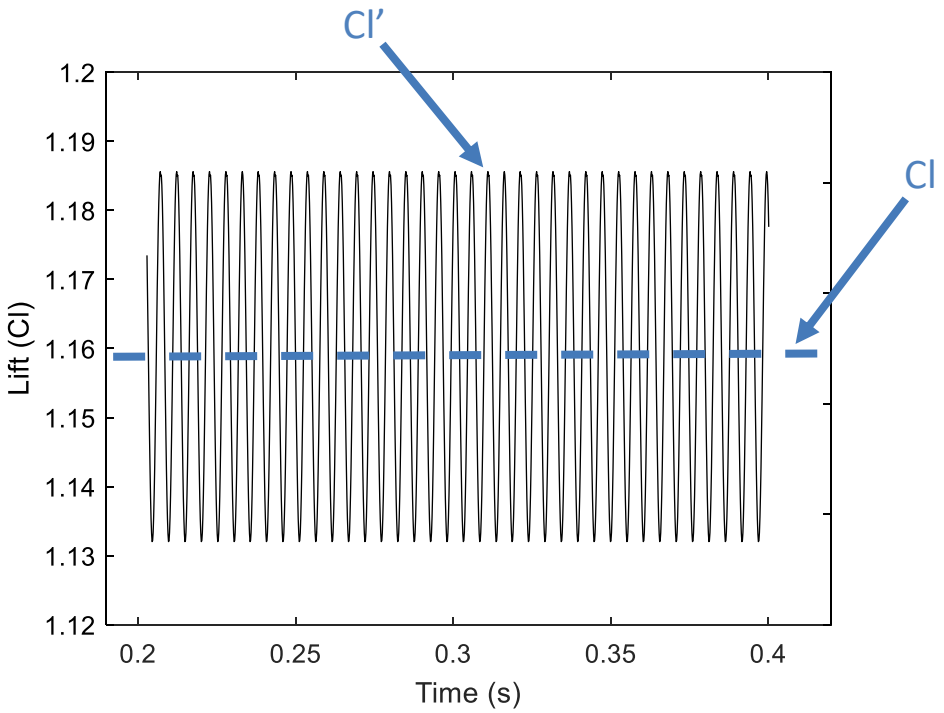

Figure 5.50: Mean lift and lift fluctuation for 200Hz and 0.125% deflection.

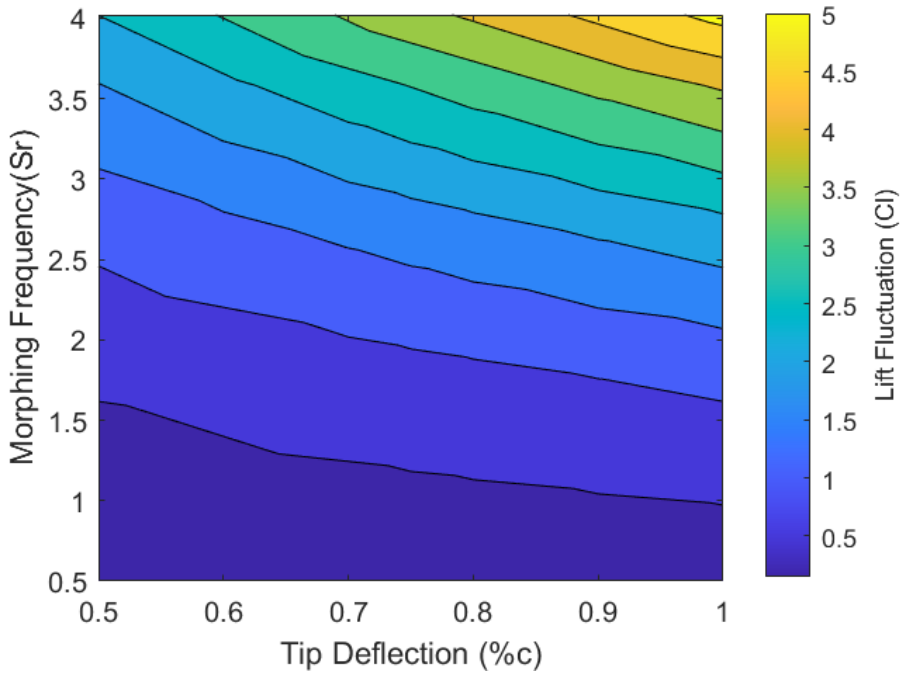

Figure 5.51: Fluctuation in lift about average lift for periodic morphing in ground effect.

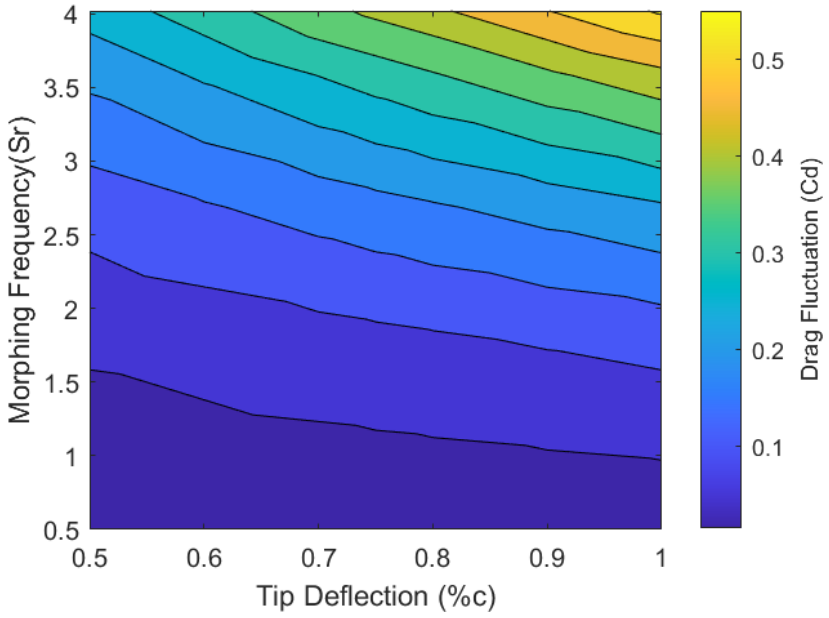

Figure 5.52: Fluctuation in drag about average drag for periodic morphing in ground effect.

For the highest aerodynamic efficiency aerofoil of 137.8 which occurred at a Strouhal number of 3.58 and trailing edge deflection of 1% chord, the morphing was analysed. The pressure was first analysed at 0.2 seconds in the morphing cycle between a maximum and minimum trailing edge deflection shown in Figure 5.53. For a maximum downward deflection, it was seen the lower surface pressure and the overall suction on the upper surface was the highest. As the aerofoil was morphed upwards the lower surface pressure and upper surface overall suction both reduced however it was seen the lower surface pressure reduced at a much larger rate than the upper surface.

As the aerofoil deflection was morphed upwards past zero deflection it was still seen the lower surface pressure and upper surface suction reduced. For the trailing edge deflection of -0.5% on the upward deflection, at approximately 30% location from the leading edge, the lower surface produced suction. This suction then increased as the trailing edge deflection increased to -1% and the location at which suction began reduced to 10% chord from the leading edge.

At a location, approximately 45% along the chord from the leading edge, the suction on the lower surface became greater than the upper surface for the 0.5% upward deflection. For the 1% upward deflection this distance where the lower surface suction became greater than the upper surface was closer to the leading edge at approximately 35%. The point where the lower surface suction became greater than the upper surface can be seen in Figure 5.53 by the -0.5% and -1%. This suction on the lower surface reduced the lift of the aerofoil. When the lower surface suction became greater than the upper surface caused a negative lift in the cycle shown in Figure 5.54.

As maximum upwards deflection was reached and the downwards cycle began, the pressure increased on the lower surface and suction increased on the upper surface until maximum downwards deflection and the cycle repeated.

The increased pressure on the lower surface for the downwards deflection explained the increase in the lift (Figure 5.46) and due to the increased blockage explained the increase in drag (Figure 5.47). The pressure increases on the upper surface and reduction on the lower also explained the reduction in the lift as well as allowing the air to flow more freely beneath the lower surface which reduced the drag. The reason the pressure varied around the aerofoil during the morphing cycle was due to the trailing edge becoming closer to the ground enhancing ground effect and the trailing edge becoming further from the ground reducing the ground effect enhancement. The second reason was due to the change in camber which increases lift and drag when the camber increased and reduced lift and drag when the camber decreased.

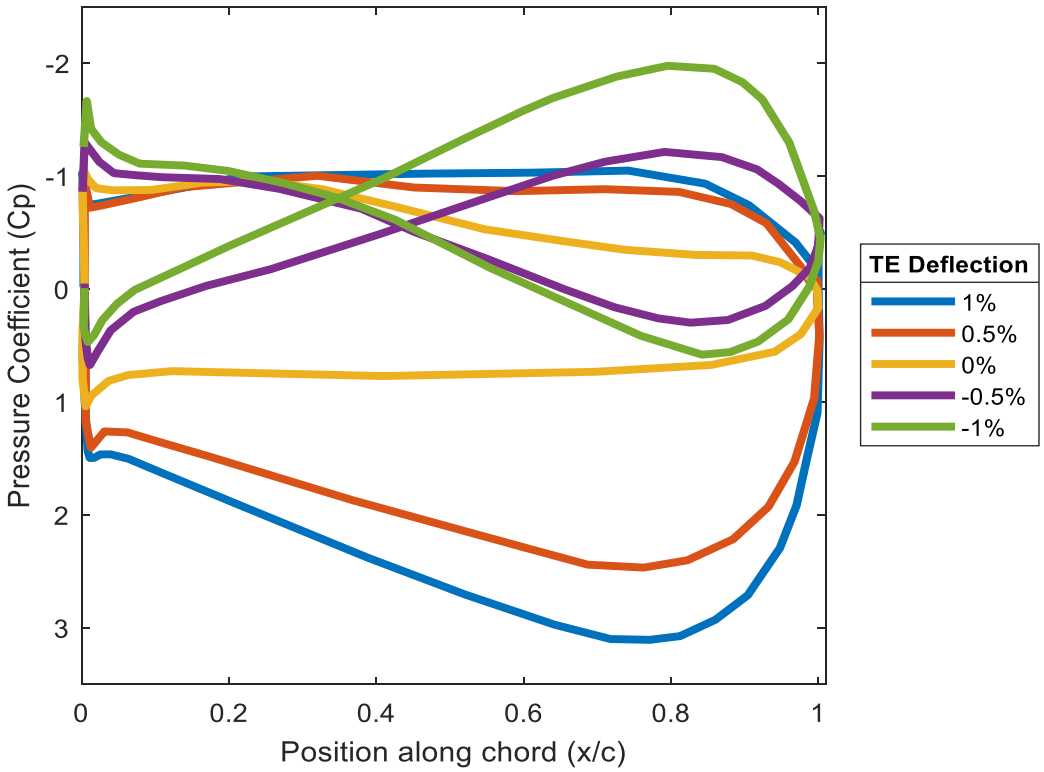

Figure 5.53: Pressure coefficient around aerofoil for maximum to minimum deflections for a Strouhal number of 3.58 and max deflection of 1% chord.

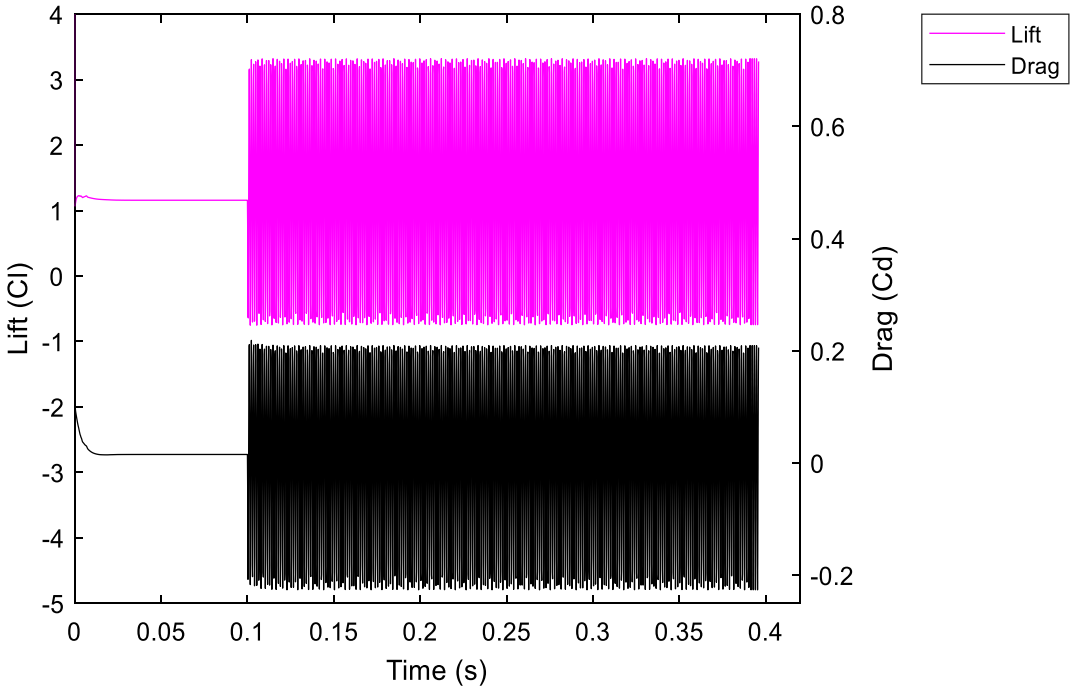

Figure 5.54: Lift for trailing edge deflection of 1% chord and Strouhal number of 3.58.

For the periodic morphing with a Strouhal number of 3.58 and trailing edge deflection of 1%, the spectra plot was shown in Figure 5.55 where it was seen two dominant peaks occurred. The first was a peak from the morphing frequency and the second from the shedding of the wake. The

second peak occurred at a Strouhal number of 0.3 which is a signature of Von-Karman shedding. Looking at the vorticity plots (Figure 5.56) confirmed Von-Karman vortex shedding. It was seen (Figure 5.56) for the vorticity in the k direction that a counter-clockwise vortex forms off the trailing edge on the downward stroke which travels downstream over time. As the trailing edge moves upwards (shown at 0.2006 seconds in Figure 5.56), another vortex forms from the upper shear layer rolling up at the trailing edge which rotates clockwise. As the aerofoil begins another downwards cycle the clockwise vortex shedding and a counter-clockwise vortex forms.

The shedding of counter-clockwise and clockwise vortices alternates depending on the trailing edge being deflected upward or downwards, as a new periodic cycle begins the shedding repeats. The vortices are spaced approximately 0.1 chord lengths from centre to centre between a counter-clockwise and clockwise rotating vortex. The close spacing means these vortices interact and where the counter-clockwise and clockwise interact it was seen there was zero vorticity (Figure 5.56).

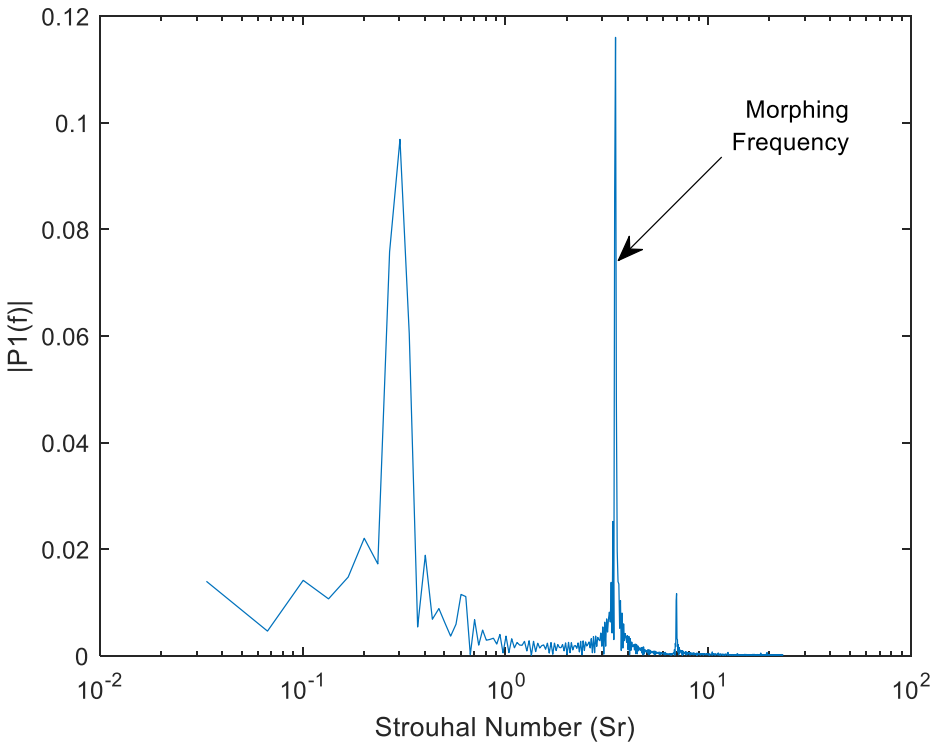

Figure 5.55: Spectra plot for Strouhal number 3.58 and deflection of 1% periodic morphing.

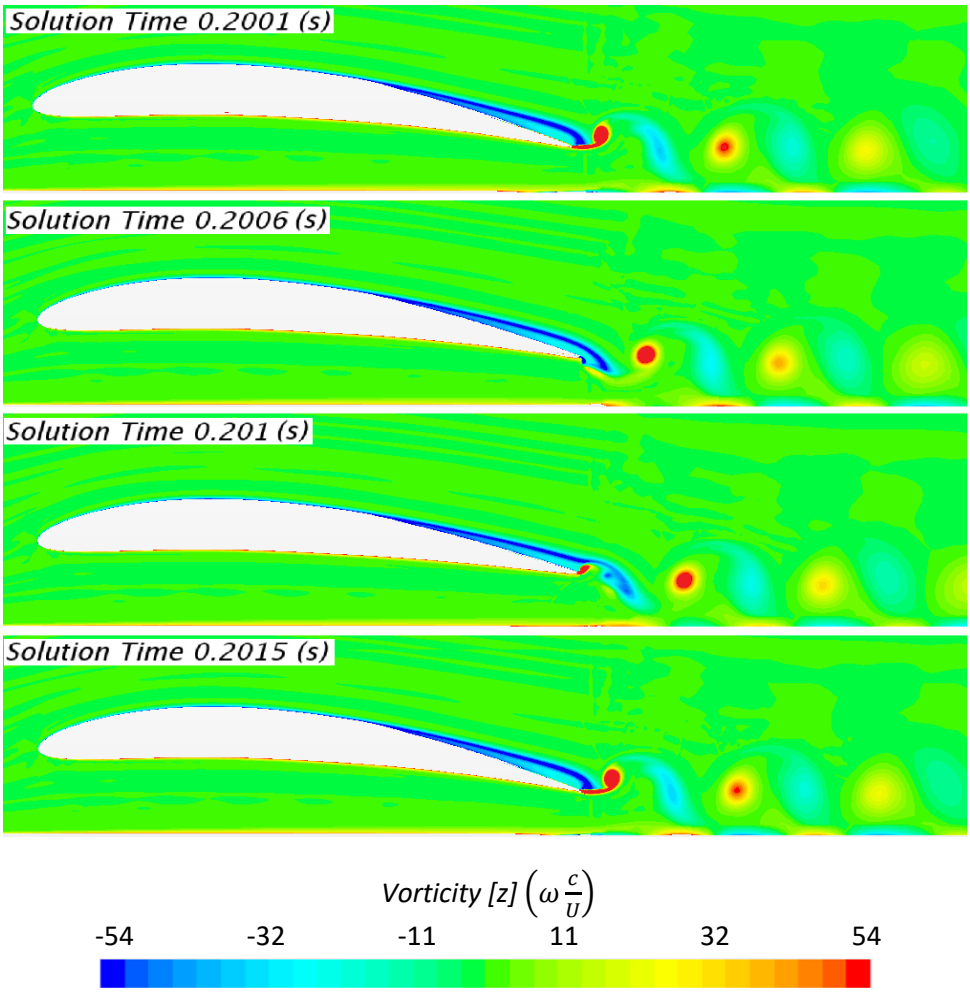

Figure 5.56: Vorticity plot of periodic morphing Strouhal number 3.58 and deflection of 1%.

Comparing the drag for the periodic morphing at a Strouhal number of 3.58 and trailing edge deflection of 1% to the non-morphing has shown the drag decreased by 36.7% even though there are high levels of wake shedding. The reduction in drag with wake shedding suggested that the periodic morphing produced thrust causing a reduction in drag. For the range of morphing frequencies and trailing edge deflections tested in this study, it was seen the net thrust was less than the total drag which resulted in positive drag values. The total thrust produced could be determined by subtracting the drag of the non-morphing aerofoil from the periodic morphing aerofoil. The coefficient of thrust (Eq 5.5) was determined and shown in Figure 5.57 for trailing edge deflections between 0.5% to 1% deflections at a Strouhal number of 3.58. It was seen (Figure 5.57) at low trailing edge deflections that the drag was higher than the baseline drag, therefore negative thrust was produced. Increasing the trailing edge deflection reduced the negative thrust and at approximately 0.65% trailing edge deflection, zero thrust was produced. Increasing the trailing edge deflection further increased the thrust with maximum thrust being produced at 1% trailing edge deflection.

$$C_t = \frac{F_T}{\rho f^2 c^4} \quad 5.5$$

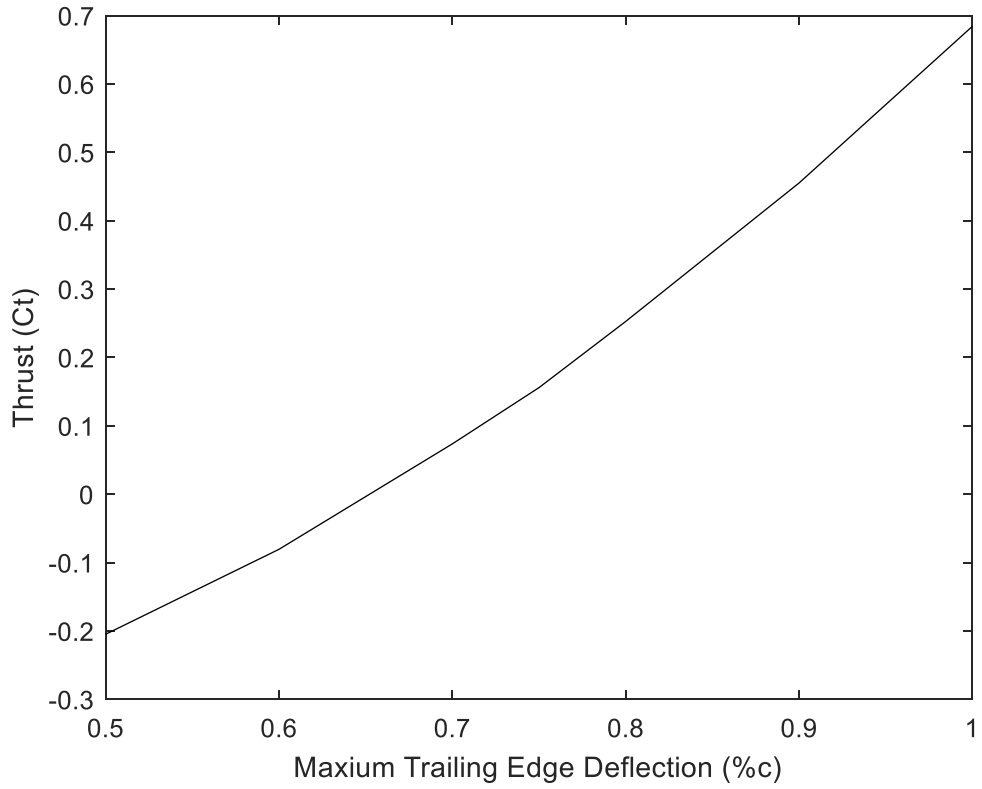

Figure 5.57: Coefficient of thrust for morphing frequency of 3.58 Strouhal number and trailing edge deflections from 0.5% to 1% chord in 10% ground effect and 4deg AoA.

Having identified the aerofoil-produced thrust, the mechanisms were analysed to identify the reasons behind the aerofoil-producing thrust. It was seen in literature that flapping aerofoils can produce thrust both in freestream and near the ground however this was due to reversed Von-Karman shedding (Boudis et al., 2019; Hu et al., 2011; Koochesfahani, 1987; Meskell & Pellegrino, 2019; Quinn et al., 2014; Young & Lai, 2004).

It was identified in this study however that reversed Von-Karman shedding did not occur and it was due to the identified Von-Karman shedding that produced the thrust. The reversed Von-Karman seen in literature in freestream (Quinn et al., 2014) produced thrust from the interaction of the shedding vortices. The interaction of these two counter-rotating vortices a jet-like flow which generated thrust (Quinn et al., 2014). The Von-Karman shedding seen in this study also shows the interaction between the two vortices in the wake with a jet-like flow where the vortices interacted however this jet-like flow was in the upstream direction which increased drag. This was demonstrated by the schematic shown in Figure 5.58.

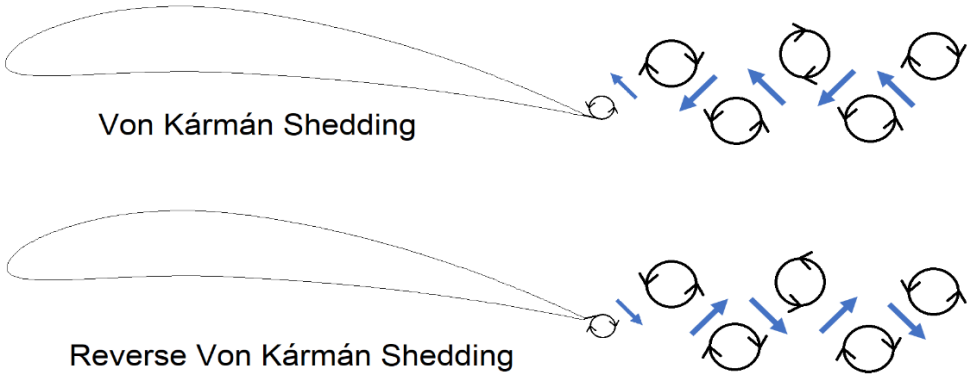

Figure 5.58: Von-Karman shedding (top) and reversed von-Karman shedding (lower).

Looking at the velocity in the x direction (Figure 5.59) shows that, unlike freestream, the Von-Karman vortex shedding interacted with the moving ground plane. The rotation direction of the vortex produced from the downstroke had a tangential velocity vector in the same direction as the moving ground plane. The interaction between the ground plane and vortex caused an increased velocity of the flow near the ground which was the reason the Von-Karman shedding produced thrust when the aerofoil was in ground effect. The schematic of the vortex and ground was shown in Figure 5.60. Therefore, there are two velocity vector components in the streamwise direction. The first was the vortices interacting with each other seen in Figure 5.58 and literature and the second is the vortex interaction with the ground shown in Figure 5.60. It was seen that the vortex core moved downstream at freestream velocity. Therefore, the tangential velocity vector is greater than the ground moving velocity which causes slip. The forward velocity vector component caused by the counter-rotating vortex interaction was greater than the backward downstream velocity vector component from the interaction of the vortex and ground. This resulted in overall positive drag values however the drag had been reduced from the thrust generation between the vortex and ground interaction.

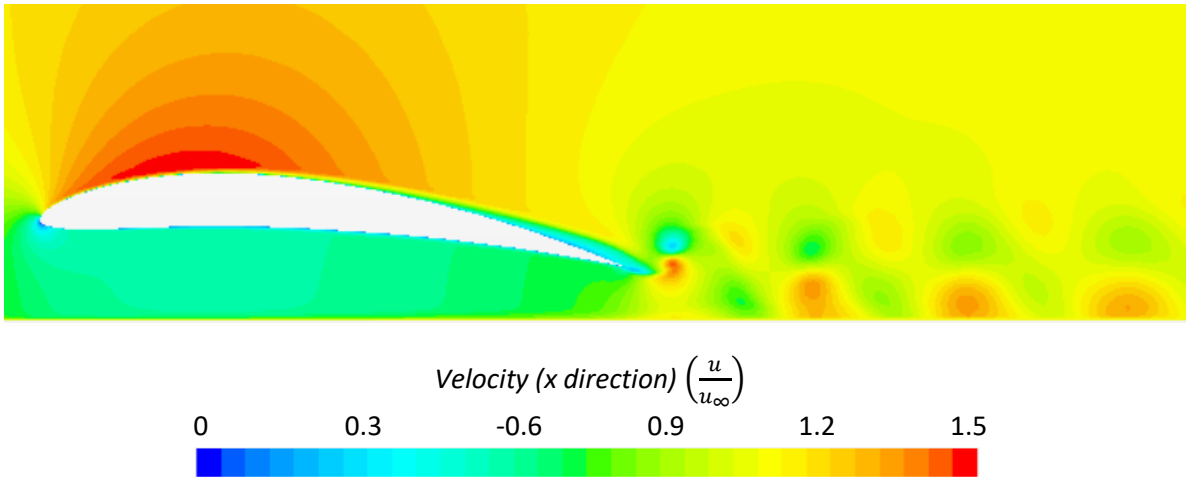

Figure 5.59: Velocity in x-direction non-dimensional with freestream for Strouhal number of 3.58 and 1% trailing edge deflection.

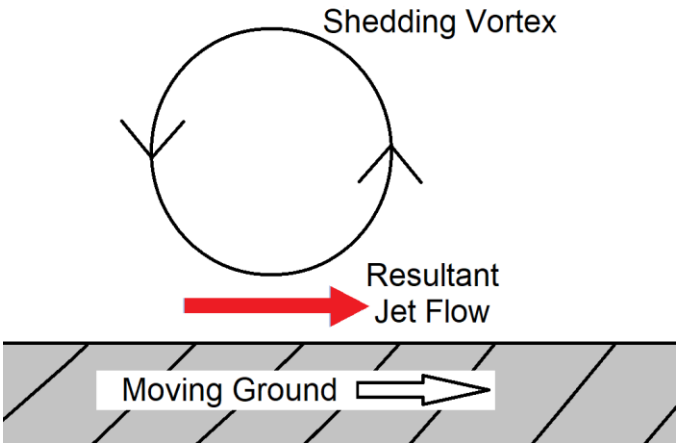

Figure 5.60: Schematic of interaction between Von-Karman vortex shedding and ground.

The lift and drag during one cycle were shown in Figure 5.61 for a morphing frequency of 3.58 Strouhal number and 1% trailing edge deflection. In Figure 5.61, downwards deflections were positive as seen throughout this study. It was seen that a hysteresis loop occurred where the lift and drag of the upward deflection were slightly different to the downward deflection. The reason the lift and drag values were different between the upstroke and downstroke was due to the downward deflection pulling the attached airflow downwards which caused some separation on the morphed trailing edge. On the upstroke, the aerofoil pushed the flow upwards which caused the flow to remain attached to the upper surface.

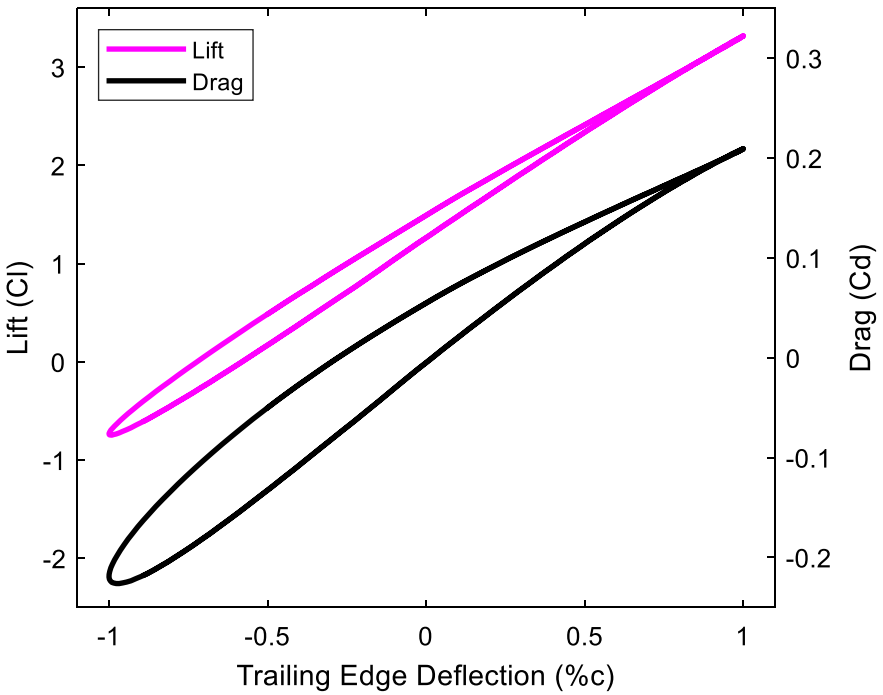

Figure 5.61: Lift and drag over one cycle for Strouhal number of 3.58 and 1% TE deflection.

Although a hysteresis loop is stated, this loop was seen only on the maximum upward displacement whilst on the downward deflection both the lift and drag showed similar values.

This was explained by considering the flow being braked on the downward deflection or free to continue moving upward on the upward deflection. On the upper surface when the trailing edge motion is upwards, the upper surface flow has upward momentum. When the motion of the trailing edge stops at its maximum, the flow still has upward momentum which causes the flow to continue in an upward direction until this momentum has diffused. On the downward deflection, the flow was pulled downwards with the downwards motion however the sinusoidal motion slowed the flow down as the maximum deflection was reached acting as a break. This is because nothing is stopping the flow in the upward motion however in the downward motion the flow cannot travel through the aerofoil surface, so the flow is effectively braked. Kan et al., (2020) who used periodic morphing to delay stall however this was due to much higher angles of attack.

Large trailing edge deflections varying ground clearance.

A comparison was made between freestream and ground effect for the periodic morphing aerofoil with the trailing edge deflection of 1% of the chord and morphing frequency Strouhal number of 3.58. This configuration showed the highest aerodynamic efficiency with gains in lift and reductions in drag for 10% ground clearance.

Initially comparing the baseline non-morphing aerofoil (Table 5.5) has shown to increase the lift and aerodynamic efficiency and reduce the drag as seen throughout this study. This was also seen (Table 5.5) when the periodic morphing in freestream was brought into ground effect. Morphing the aerofoil in freestream showed to have minimal impact on the lift, drag and aerodynamic efficiency compared to ground effect where the periodic morphing had a significant improvement in aerodynamic performance.

Table 5.5: Baseline non-morphing wing values.

	10% GE baseline	10% ground effect morphing	Freestream baseline	Freestream morphing.
Lift (Cl)	1.157	1.332	0.985	0.992
Drag (Cd)	0.0151	0.0097	0.0174	0.0169
Aerodynamic Efficiency (Cl/Cd)	76.4	137.8	56.8	58.8

To understand why there was minimal variation in performance between the morphing and non-morphing aerofoil in freestream, the vorticity plots were initially investigated in Figure 5.62. It was seen that both the freestream (Figure 5.62 lower) and ground effect (Figure 5.62 upper) showed Von Karman vortex shedding. Comparing the difference between the freestream and ground

effect showed that the vortices had a smaller diameter with lower magnitude and dissipated sooner for freestream.

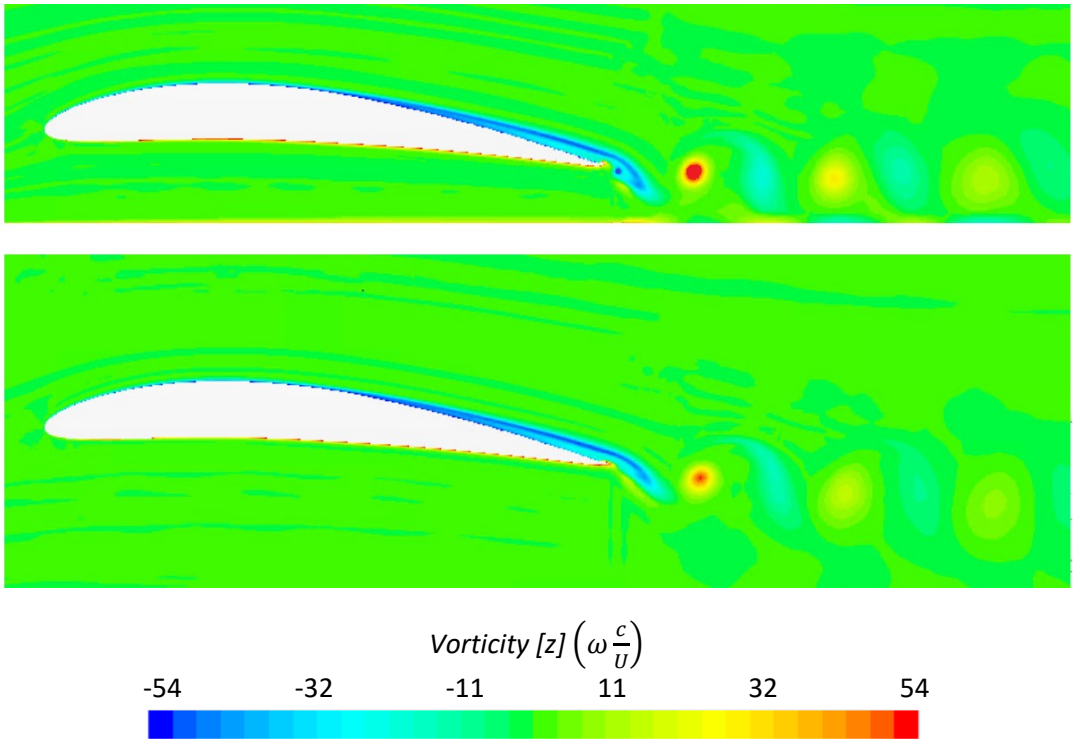

Figure 5.62: Aerofoil non-dimensional vorticity in 10% GE (upper) and freestream (lower) for periodic morphing aerofoil with 1% TE deflection and 3.58 Strouhal number.

The velocity in the freestream direction was also investigated, shown in Figure 5.63. The ground effect (Figure 5.63 upper) was discussed that the interaction between the ground and shedding vortex caused forward thrust as demonstrated in Figure 5.60. Comparing the vortex shedding in freestream to ground effect showed that as there was no ground plane in freestream, therefore the shedding in freestream could not produce thrust from the shedding vortices as there was no interaction between these vortices and the moving ground plane.

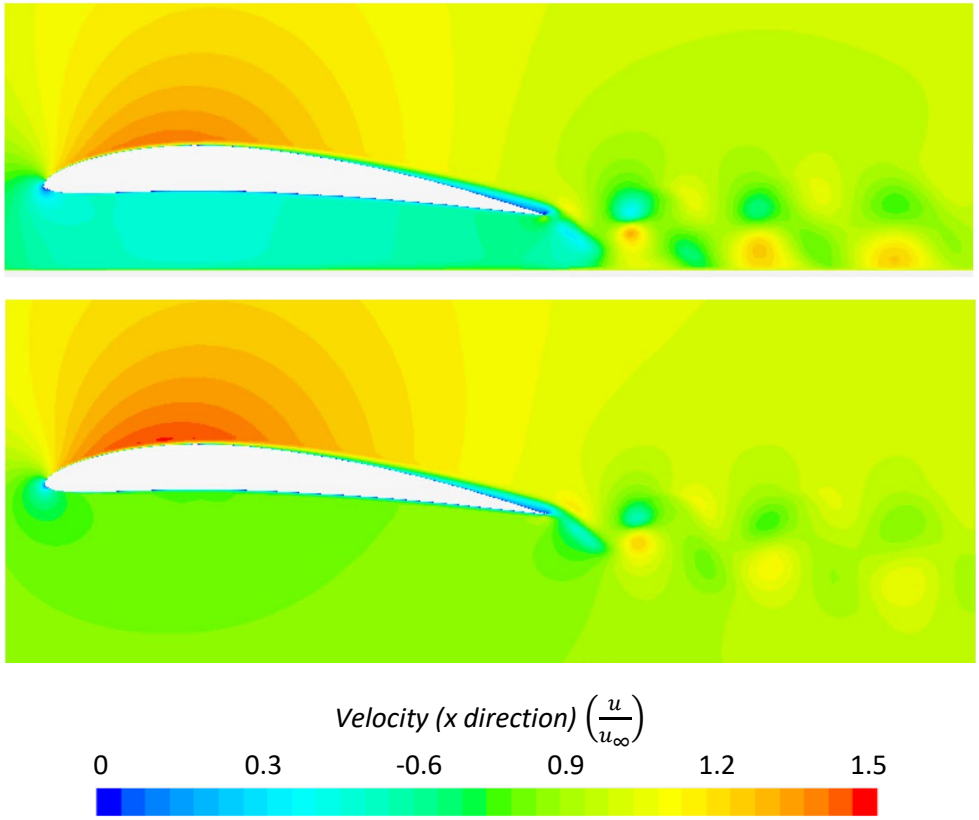

Figure 5.63: Aerofoil non- dimensional velocity in 10% GE (upper) and freestream (lower) for periodic morphing aerofoil with 1% TE deflection and 3.58 Strouhal number.

5.6 Summary

Static morphing was applied to a NACA6409 aerofoil using the FishBAC morphing method in the chord direction to gain an understanding of morphing a wing in ground effect by carrying out steady-state simulations. It was found that morphing the wing in freestream increased the lift of the aerofoil by increased circulation from the increased camber. In ground effect there was an extra gain in lift for higher trailing edge deflection, this was due to the shorter distance from the trailing edge distance to the ground which increased the ground effect enhancement. Increasing trailing edge deflection increased the pressure on the lower surface of the aerofoil with a small increase in suction on the upper surface. The lower surface pressure increased due to the Kutta condition fixing the trailing edge pressure which caused all effects to occur upstream of the trailing edge. To keep the trailing edge pressure constant at the trailing edge the pressure must increase upstream. A key finding was the pressure rise between the trailing edge and lower surface occurred over the length of the morphed section therefore starting the morphing later along the chord caused an overall greater amount of pressure on the lower surface. Comparing the static morphing to a traditional flap showed morphed wings can be deflected a smaller amount to achieve the same level of gains in lift therefore morphing wings are more aerodynamically efficient than flaps.

Morphing the aerofoil over time dynamically has shown very similar results to static morphing for low angles of attack for the reduced frequency of morphing tested in this study. The study focused on applying morphing wings in ground effect to UAVs therefore the morphing period was selected based on UAV actuator speeds. For a period of 1 second morphing the trailing edge a displacement of 2.5% chord showed a Strouhal number of 2×10^{-3} therefore dynamic morphing is quasi static. For the dynamic case the lift was slightly higher and the drag slightly lower due to a greater amount of turbulent mixing being captured by introducing the time element of URANS. This resulted in the dynamic simulations showing a higher efficiency compared to the static. At higher angles of attack, it was seen that the flow stalled earlier for the dynamic case. Periodic morphing was seen to increase the aerodynamic efficiency to 137.8 compared to the baseline non-morphing of 76.4 which was a gain of 80.5%. The lift also increased by 15.1% and the drag was reduced by 36.7% showing the benefits of periodic morphing in ground effect. The reason the drag was reduced was due to thrust generation caused by the Von Karman vortex shedding. The shedding vortices interacted with the ground plane which caused an almost jet-like flow along the ground. This jet-like flow was comparable to literature in freestream from the interaction of two counter-rotating vortices causing a jet-like flow. This caused a reduction in drag from thrust generation and gains in lift from the periodic morphing which resulted in an overall gain in aerodynamic efficiency.

Chapter 6 3D Morphing in and out of Ground Effect

6.1 Introduction

In the previous section, morphing was applied to the NACA6409 aerofoil in both ground effect and freestream in two dimensions. It was found that morphing wings increased the lift of the wing. For small deflections at low angles of attack, small gains in aerodynamic efficiency are made. In this section, morphing wings are extended to three dimensions where the proportion of span that the camber morphing was applied was investigated on a rectangular wing. The morphing was then applied to the optimised rectangular wing found in section 4.5. So far, the focus of this study was camber morphing, other types of morphing were investigated including morphing the wingtips to seal the lower surface and increasing the span by the use of morphing.

6.2 Effect of Morphing Span Location

In three dimensions there are extra parameters for the length and position of the morphing in the spanwise direction. This section investigated the start and end positions of the camber morphed proportion of the aerofoil in the span direction. A fixed start location of x_s = 80% was used in this section and applied to the rectangular NACA6409 wing.

As shown in Figure 6.1, morphing can be applied to a proportion of the span which Abdessemed et al., (2022) showed a smooth transition between the morphed and non-morphed section improved aerodynamic performance compared to a gap between these two sections. Therefore, in this study a linear transition was used with the length of this transition 5% chord. Due to a symmetry plane being used in the CFD set-up, mid-span was defined as the location where the inboard and outboard are referenced from in Figure 6.1. Therefore, an inboard distance of zero means the morphing started at the mid-span of the wing.

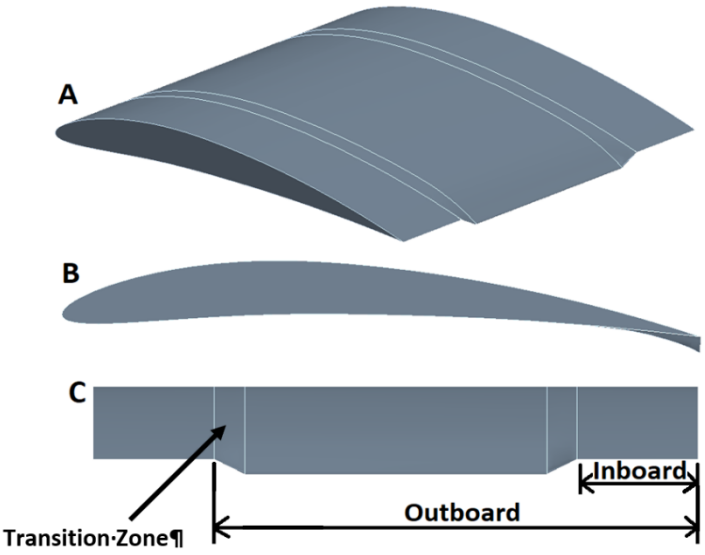

Figure 6.1: Transition between non-morphed to morphed aerofoil, isometric view (A), side view (B) and backwards view (C).

Table 6.1: Baseline non-morphed 3d rectangular NACA6409 data.

h/c	AoA	Lift (Cl)	Drag (Cd)	Aerodynamic Efficiency (Cl/Cd)
0.1	0	0.3810	0.0234	16.2821
0.1	4	0.7050	0.0484	14.5661
1	0	0.3067	0.0283	10.8495
1	4	0.5111	0.0518	9.8632

Figure 6.2 to Figure 6.7 shows the lift, drag and aerodynamic efficiency for 0.5% and 2.5% trailing edge deflection in and out of ground effect where the asterixis represent the data points used to generate the plots. The results for varying the length of the morphed section are shown in Figure 6.2 to Figure 6.7 for 0% and 2.5% trailing edge deflection at 0- and 4-degrees angle of attack in both freestream and ground effect of h/c = 10% ground clearance. Extra results of 8 degrees angle of attack, h/c = 20% and 1% trailing edge deflection (appendix A.5). Observing the differences between all the results showed there is little variation in the trends between the different angles of attack, ground clearances and trailing edge deflection for the lift and drag.

Also, it was seen by varying the outboard and inboard distances that both the outboard and inboard had an equal effect on the lift (Figure 6.2 to Figure 6.7) and drag (Figure 6.3 and Figure 6.6) of the wing. Varying these distances, the same amount results in equal variation in lift and drag for the 5%,

and 25% deflection. This means both the inboard and outboard locations have equal weighting on the aerodynamic performance.

From the contour plots (Figure 6.2 to Figure 6.7) it was observed deflecting the trailing edge, increasing the angle of attack and reducing ground clearance all increased the lift from the baseline rectangular wing shown in Table 6.1. This was also seen in section 5.3 for the two-dimensional morphing which shows the same principles apply to three dimensions when morphing a wing in ground effect. Full span morphing was achieved by setting the inboard location to zero and the outboard location to the wingspan length. Figure 6.2 and Figure 6.5, showed that the full span length caused the highest lift and drag.

Due to the differences in the rate of change of lift compared to drag, Figure 6.4 and Figure 6.7 showed that the aerodynamic efficiency did not always obey equal variation in aerodynamic efficiency when the inboard and outboard locations were increased or decreased the same amount. This was more predominant for the 0 degrees angle of attack.

For 0 degrees angle of attack for 5% deflection, it was seen the efficiency is highest when the inboard location was at 0 and the outboard was at 70% chord for both 10% ground clearance and freestream. For 5% deflection in 10% ground clearance, it was seen that the inboard location had a greater impact on the aerodynamic efficiency compared to varying the outboard however in freestream this became the outboard location that had the greatest impact on aerodynamic efficiency. The reason for this was in ground effect due to the proximity of the ground that moving the deflected section towards the wingtip did not increase the induced drag of the wingtip vortex compared to freestream. For the inboard in ground effect, moving the start location towards the mid-span (as the inboard distance tends to zero) increased the pressure at the mid-span, therefore, causing a greater spanwise flow feeding the wingtip vortex. Comparing the increased deflection for 10% and 25% shows the same finding.

Compared to the baseline non-morphed aerofoil, it was seen the aerodynamic efficiency in Figure 6.4 and Figure 6.7 was significantly less compared to the baseline aerodynamic efficiency seen in Table 6.1 for all the configurations tested. Although the sizing of control surfaces is selected to achieve a desired roll rate, it is seen from an aerodynamic perspective that full-length morphing along the span allows greater changes in lift for smaller trailing edge deflection. If the distance between the inboard and outboard is made small, then greater trailing edge deflections are required to achieve the same increase in lift which results in lower aerodynamic efficiency.

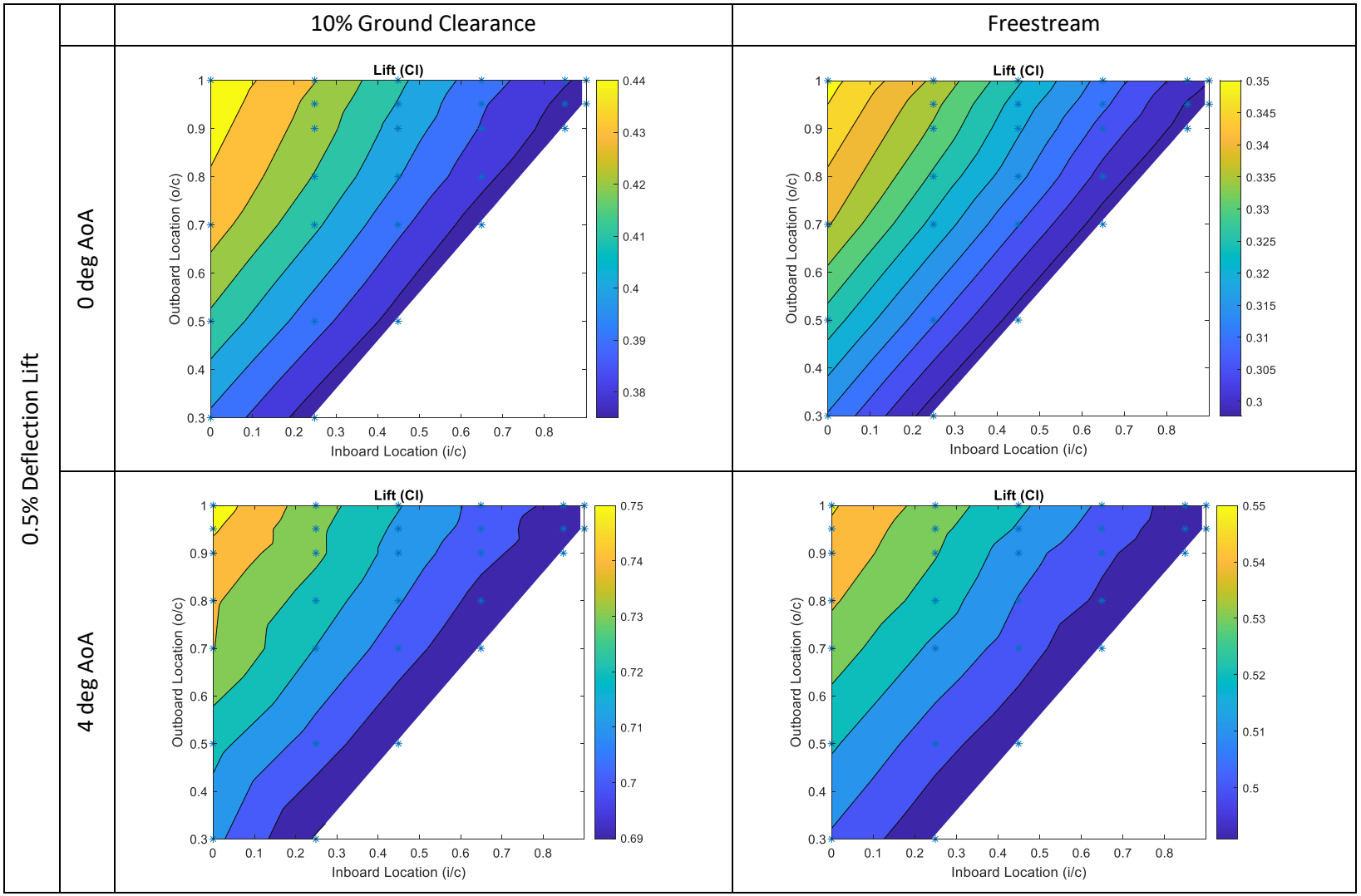

Figure 6.2: Lift of span morphing of rectangular wing with 5% trailing edge deflection.

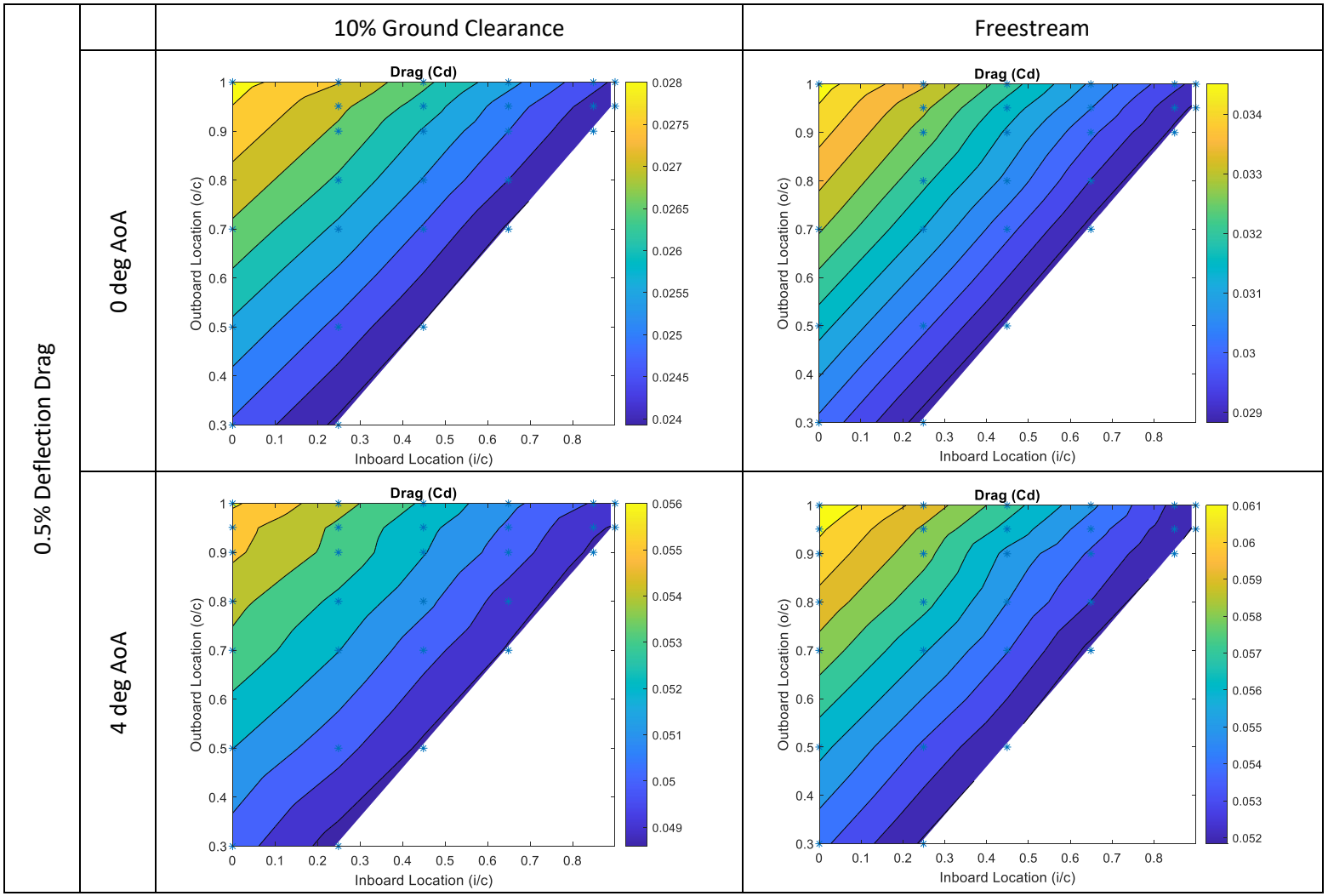

Figure 6.3: Drag of span morphing of rectangular wing with 5% trailing edge deflection.

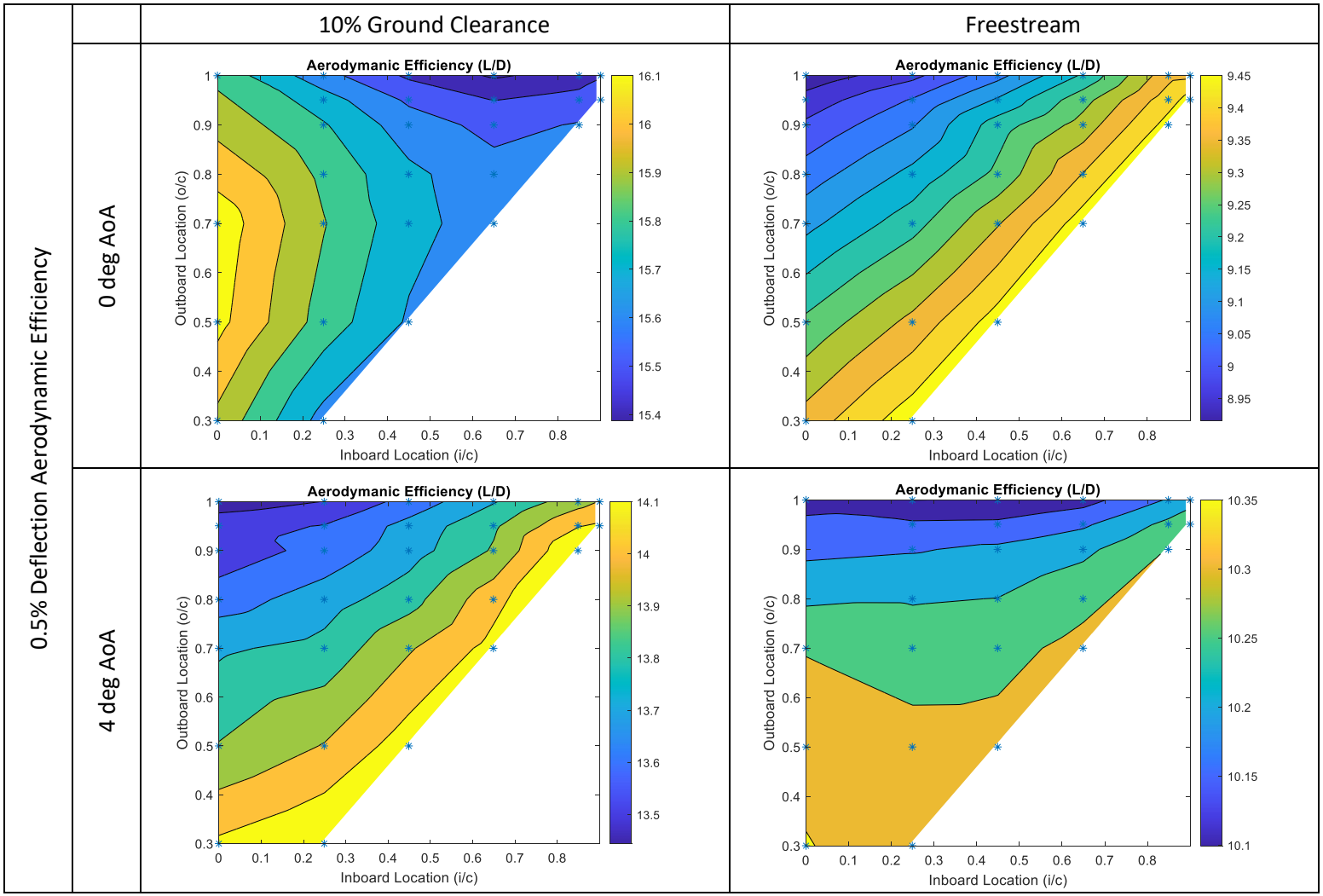

Figure 6.4: Aerodynamic efficiency of span morphing of rectangular wing with 5% trailing edge deflection.

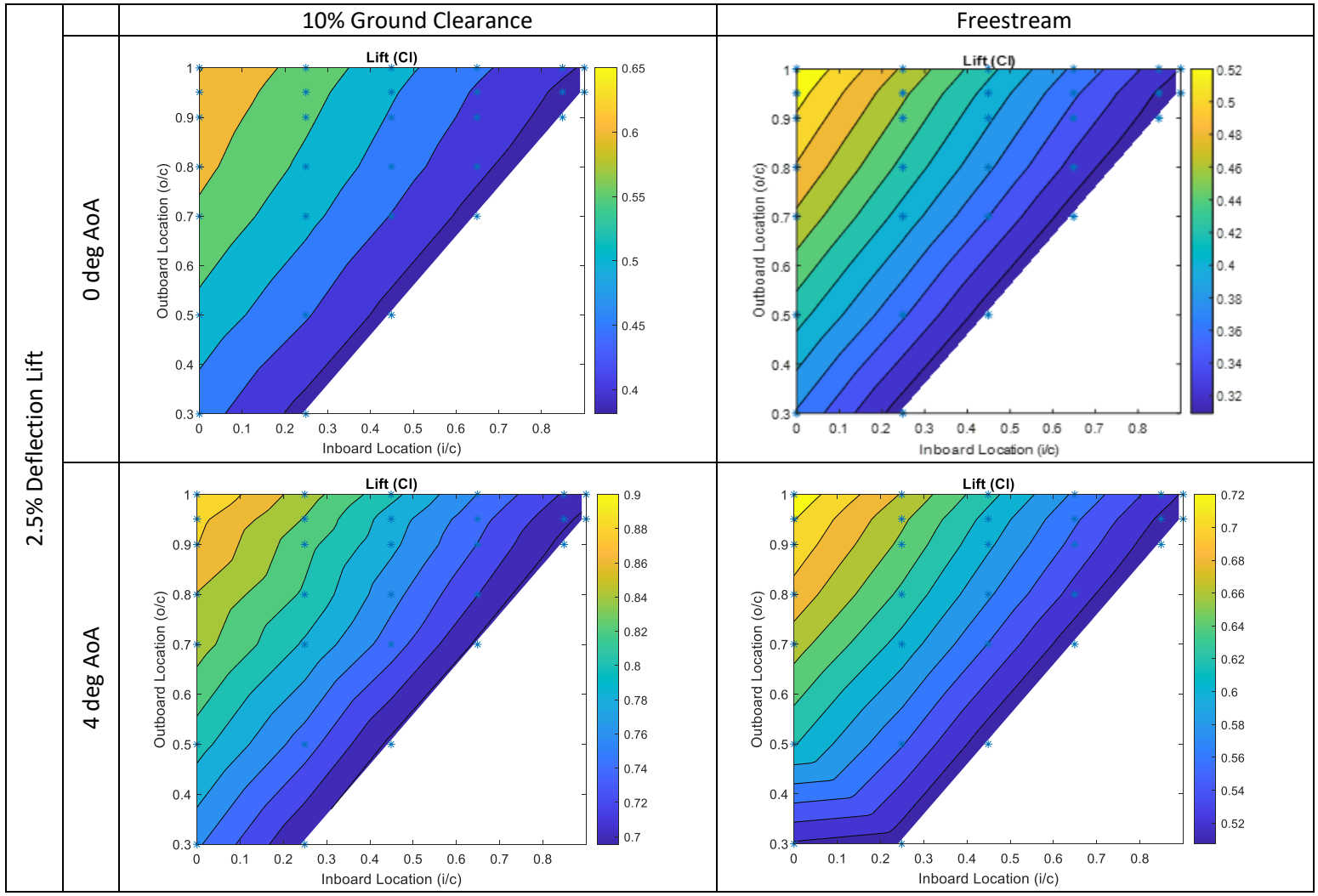

Figure 6.5: Lift of span morphing of rectangular wing with 25% trailing edge deflection.

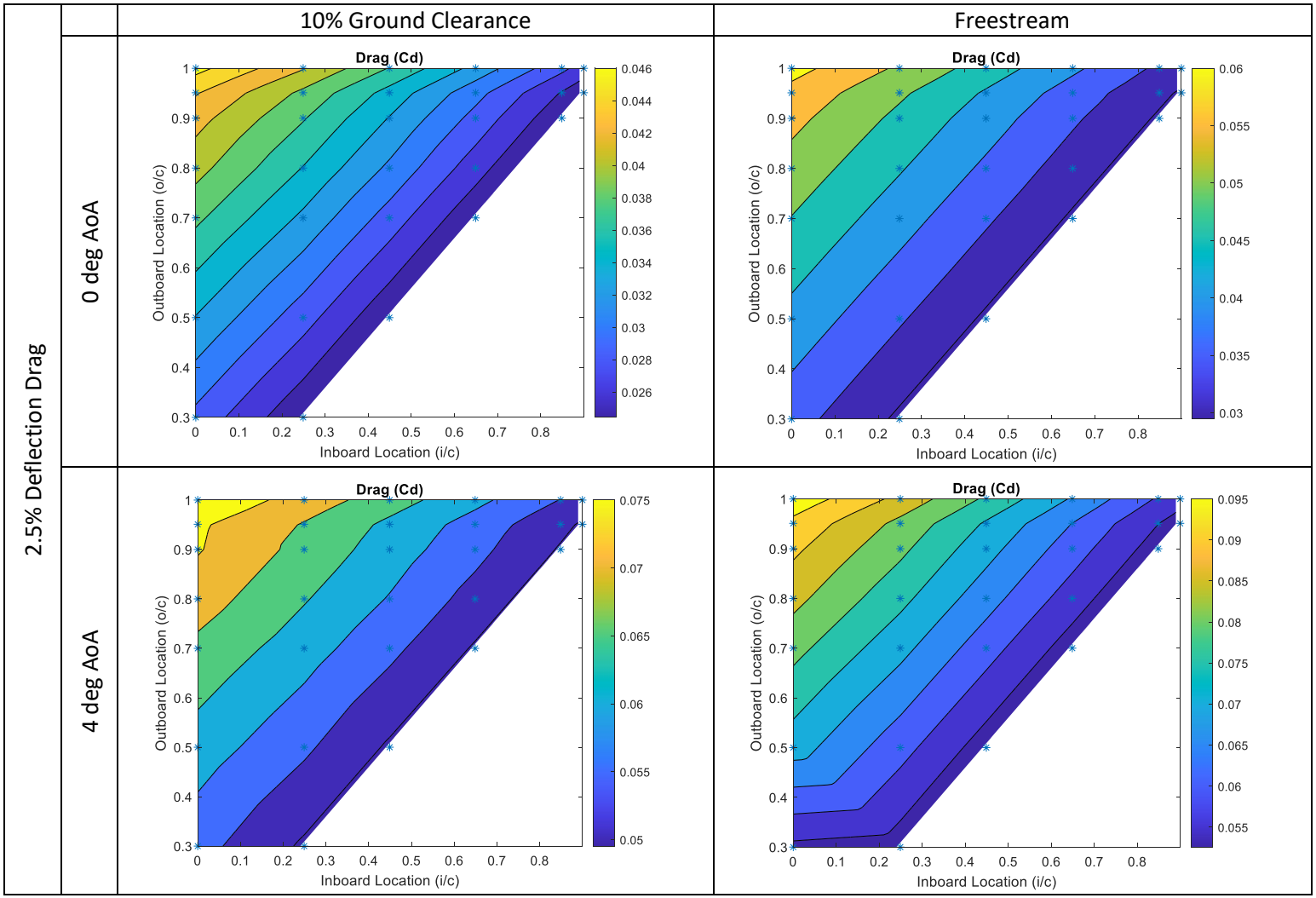

Figure 6.6: Drag of span morphing of rectangular wing with 25% trailing edge deflection.

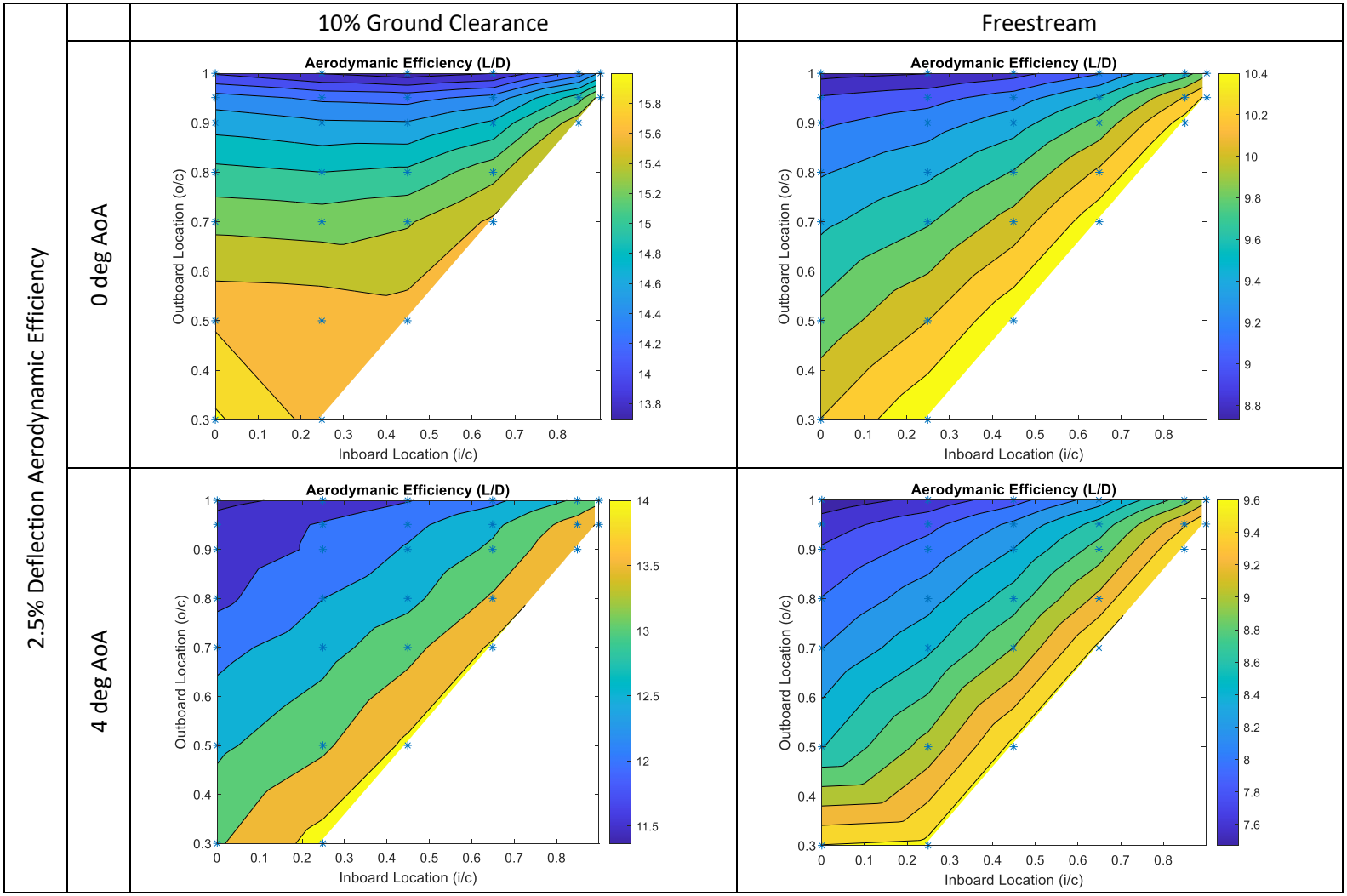

Figure 6.7: Aerodynamic efficiency of span morphing of rectangular wing with 25% trailing edge deflection.

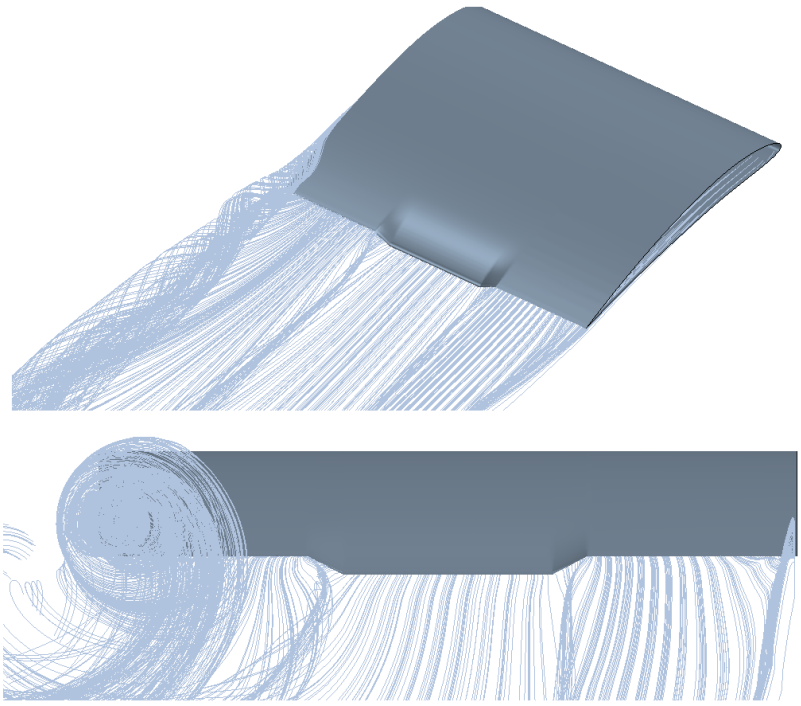

Figure 6.8: NACA6409 at 4 degrees angle of attack in freestream with inboard located at 25% and outboard at 70% chord and 2.5% deflection at x_s = 80%.

With the morphed span smaller than the span of the wing, a vortex appears on each of the transition sections between the non-morphed and morphed profiles shown in Figure 6.8 also seen in the study by Abdessemed (2020) in freestream. For the low aspect ratio wing in Figure 6.8, the inboard vortex on the transition section is visible but much less distinct compared to the outboard transition section. Also, the wingtip vortex was far more dominant than the vortices on the transition sections.

In ground effect it was observed (Figure 6.9) increasing the outboard location increased the wing tip vortex core strength, this was because of two reasons. The first was due to increasing the pressure on the lower surface across the span which increased the spanwise flow feeding the wingtip vortex. The second reason was the vortex of the outboard transition section was closer to the wingtip vortex which helped feed the wingtip vortex.

It can be seen (Figure 6.9) that only the vorticity magnitude was affected on the wingtip vortex and the size and location remained constant as the outboard location was increased. It was observed that varying the inboard location within the range tested had no impact on the wingtip vortex or the vortex on the morphed transition section. The location of the wingtip vortex and diameter remained constant for all displacements and the only difference observed when increasing the displacement was a stronger wingtip vortex core. Due to the size and lower vorticity of the vortex on the transition section compared to the wingtip vortex, the vortex on the

transition section has a lower impact on the lift, drag and efficiency of the wing as the outboard location was varied.

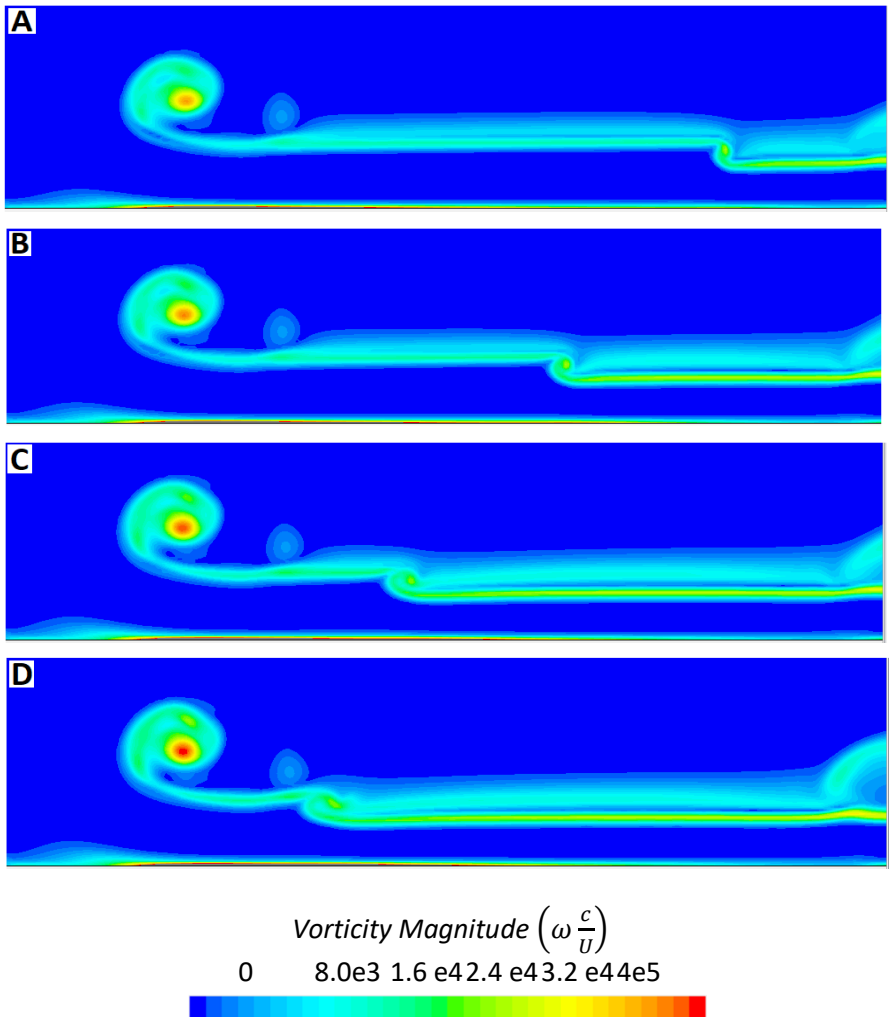

Figure 6.9: Vorticity magnitude at 5% chord downstream of the NACA6409 at 4 degrees AoA in 10% ground effect for 30% (A), 50% (B), 70% (C) and 80% (D) outboard locations and inboard = 0%.

In freestream, however, the wingtip vortex and the vortex on the transition section are independent of each other (Figure 6.10). In section 4.4 it was seen bringing the baseline wing from freestream into ground effect pushed the wingtip vortex outboard. This also occurred on the vortex on the transition section with the proximity of the ground pushing the vortex on the transition section outboard which further fed the wingtip vortex. Downstream these two vortices merged, and the diameter naturally grew.

Figure 6.10 demonstrates this by visualising the streamlines for the wing in both freestream and 10% ground effect which clearly showed the transition section vortex being pushed outboard by the ground proximity. Also, in Figure 6.10, it was noted that there was a large amount of recirculation only present in ground effect at the mid-span of the wing. This was due to the reduction in downwash in ground effect and as seen in section 4.4 wings stall at lower angles of

attack in ground effect with separation first occurring at the mid-span as the wingtip vortex is weakest at the mid-span.

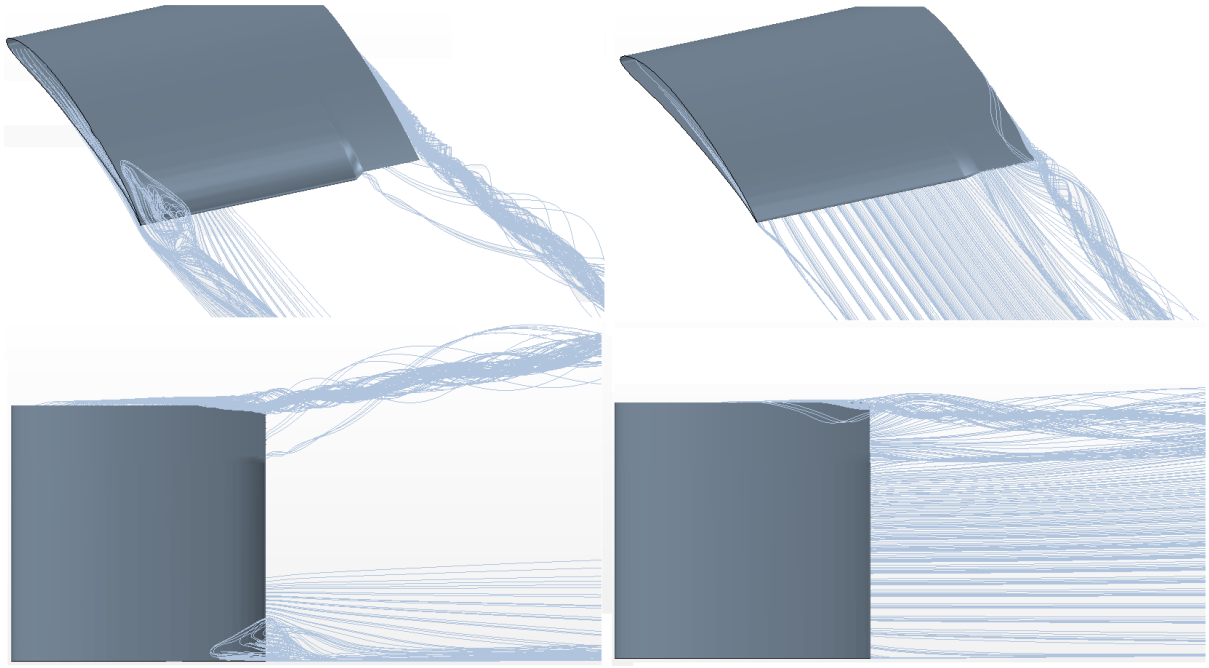

Figure 6.10: NACA6409 in 10% ground effect (left) and freestream (right) at 4 degrees angle of attack with 25% morphing displacement and 80% outboard location.

Comparing the streamlines (Figure 6.11) for the 0.5% and 1% displacement in ground effect showed the vortex on the outboard transition section beginning to form for the 0.5% displacement. Increasing the displacement to 1% showed a more distinctive vortex on the transition section. This shows the greater the morphed deflection the stronger and more distinctive the vortex on the outboard transition section became.

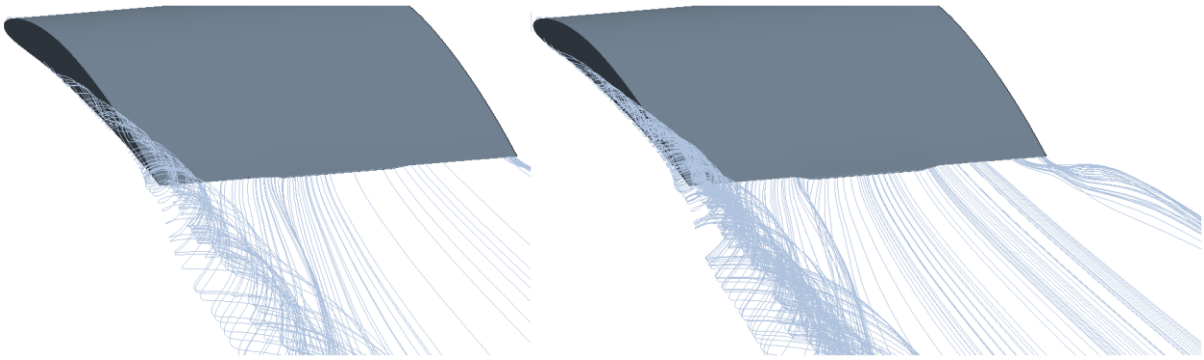

Figure 6.11: NACA6409 in 10% ground effect and 4 degrees angle of attack with 0.5% (left) and 1% (right) trailing edge deflection at 4 degrees angle AoA with 25% inboard and 80% outboard location.

Comparing Figure 6.10 (left) with an inboard location starting at zero and Figure 6.12 with an inboard location starting at 25% shows a high level of separation for the 0% inboard location

(Figure 6.10 right) at the mid-span on the morphed section compared to Figure 6.12. This shows for smaller inboard start locations with high displacements of trailing edge deflection, separation occurs at earlier angles of attack compared to larger inboard start locations.

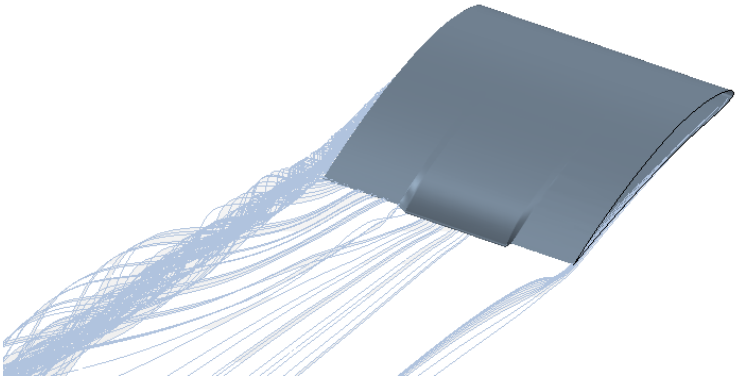

Figure 6.12: NACA6409 in 10% ground effect and 4 degrees angle of attack with 2.5% trailing edge deflection at 4 degrees angle of attack with 25% morphing displacement and 80% outboard location.

Figure 6.13 compares the wing configuration with inboard location at 25% chord and outboard at 70% chord from the mid-span plane, x_s = 80% and 4 degrees AoA in 10% ground effect for 0.5%, 1% and 2.5% trailing edge displacements. Figure 6.13 shows the pressure coefficient of the upper and lower surface for 0.5%, 1% and 2.5% deflections with the inboard location at 25% and outboard at 70%. It is observed morphing the wing has minimal impact on the upper surface however there was an increase in pressure on the lower surface as the aerofoil was morphed (Figure 6.13 top). The Kutta condition fixed the pressure at the trailing causing all changes to occur upstream of the trailing edge seen in section 4.4. This can be seen on the lower surface directly behind the morphed section (Figure 6.13 lower) where the pressure increased as the trailing edge displacement increased. There was also a slight increase in pressure on the section between the mid-span and 25% along the span even though this section was not morphed due to increased blockage on the lower surface from the span morphing. At the wingtip, the flow could easily feed the wingtip vortex or leave the trailing edge therefore the pressure did not increase on the lower surface between 70% and 100% span location.

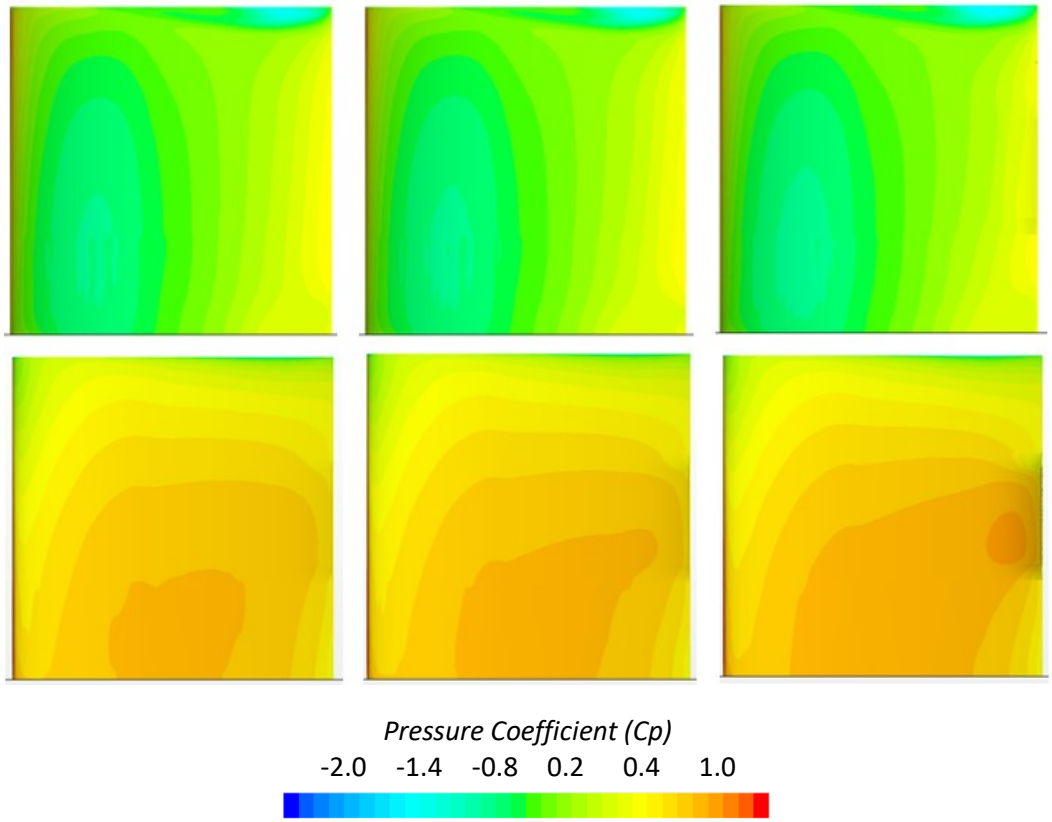

Figure 6.13: Pressure coefficient NACA6409 at 4-degree AoA in 10% ground effect upper surface (top), lower surface (lower) and 0.5% (left), 1% (middle) and 2.5% (right) morphed deflection.

Comparing the lower surface pressure in both freestream and ground effect for 2.5% deflection (Figure 6.14) shows the pressure to be higher for the wing in ground effect on the lower surface and showed a similar pressure pattern. Starting the inboard morphing location at zero has been shown to increase the pressure on the lower surface in Figure 6.15. This was due to a greater proportion of the trailing along the span being closer to the ground which caused an increase in pressure on the lower surface upstream of the trailing edge.

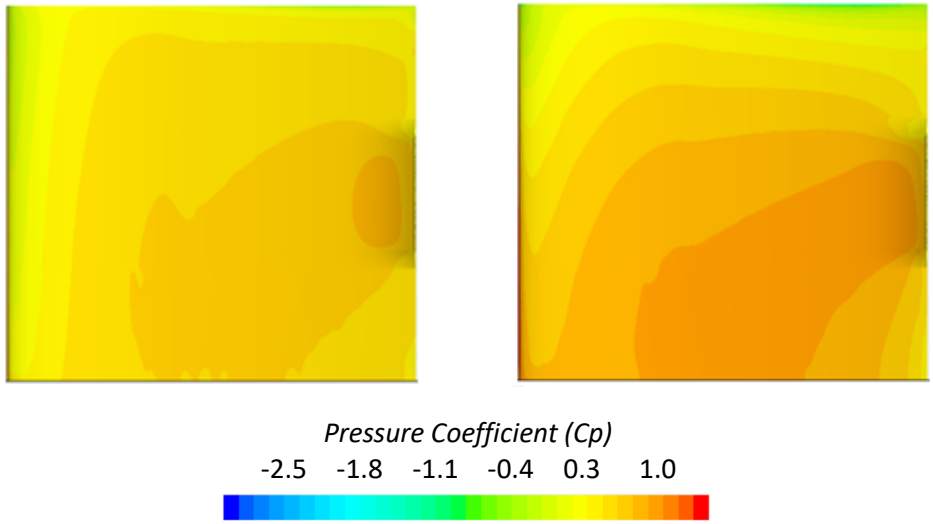

Figure 6.14: NACA6409 at 25% deflection in freestream (left) and 10% ground effect (right) lower surface pressure coefficient.

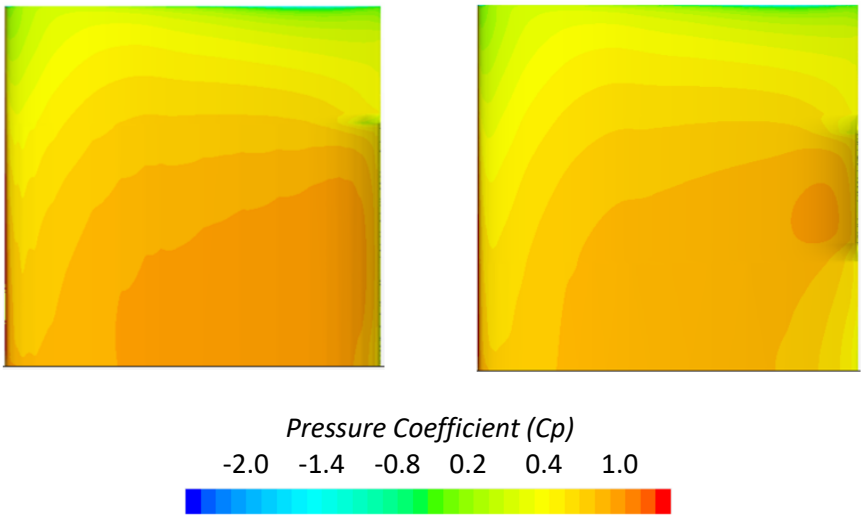

Figure 6.15: NACA6409 pressure coefficient on lower surface for 4-degree AoA in 10% ground effect for inboard location starting at 0% (left) and 30% (right) span and outboard at 70%.

6.3 Morphing applied to Optimised Wing

Full-span morphing was applied to the optimised wing from section 4.5 which had 4 degrees angle of attack at the root and 6 degrees at the wingtip. The tip chord length was 20% of the root chord with a forward wing tip position. Full span morphing was applied in this section as full span allows smaller trailing edge deflections for the same increase in lift for higher performance. Static morphing was applied to the optimised wing in this section rather than dynamic due to lower computational costs. With the intended application in this study of applying morphing wings to UAVs, the flow physics and speed of actuators for UAVs mean the flow is quasi-static and therefore little difference between static and dynamic morphing.

Throughout the rectangular morphing, the start location along the chord was defined as a percentage of the chord from the leading edge. The different start locations tested were shown in Table 6.2. Throughout the study it has been identified that in three dimensions a wingtip vortex is present and that this has a large impact on the performance of the wing. The focus of the different configurations was to control this wingtip vortex to improve the aerodynamic performance.

Table 6.2 non-dimensional morphing chord start location at root and tip.

Configuration Number	Root start location (x_{s_root}/c)	Tip start location (x_{s_tip}/c)
Configuration 1	0.9	0.10
Configuration 2	0.9	0.18
Configuration 3	0.8	0.16
Configuration 4	0.8	N/A
Configuration 5	0.9	N/A

From looking at Figure 6.16 and Figure 6.17, it was identified that each configuration was a compromise between maximum lift and maximum efficiency. It was identified in (section 5.3) that starting the morphing start location at the latest position along the chord produced the maximum lift on a two-dimensional aerofoil. This was due to the Kutta condition fixing the trailing edge pressure causing the pressure to increase upstream of the trailing edge, the pressure at any point on the lower surface is directly related to the distance from that point on the lower surface to the ground as seen in Figure 4.7. Morphing at a later start location caused the pressure to increase more rapidly on the lower surface resulting in an overall higher pressure on the lower surface. This was also seen in three dimensions on the optimised wing, where starting the morphing location later along both the root and tip chord produced the highest amount of lift (Figure 6.16). Configuration 2 produced the highest amount of lift whereas configuration 4 produced the lowest lift.

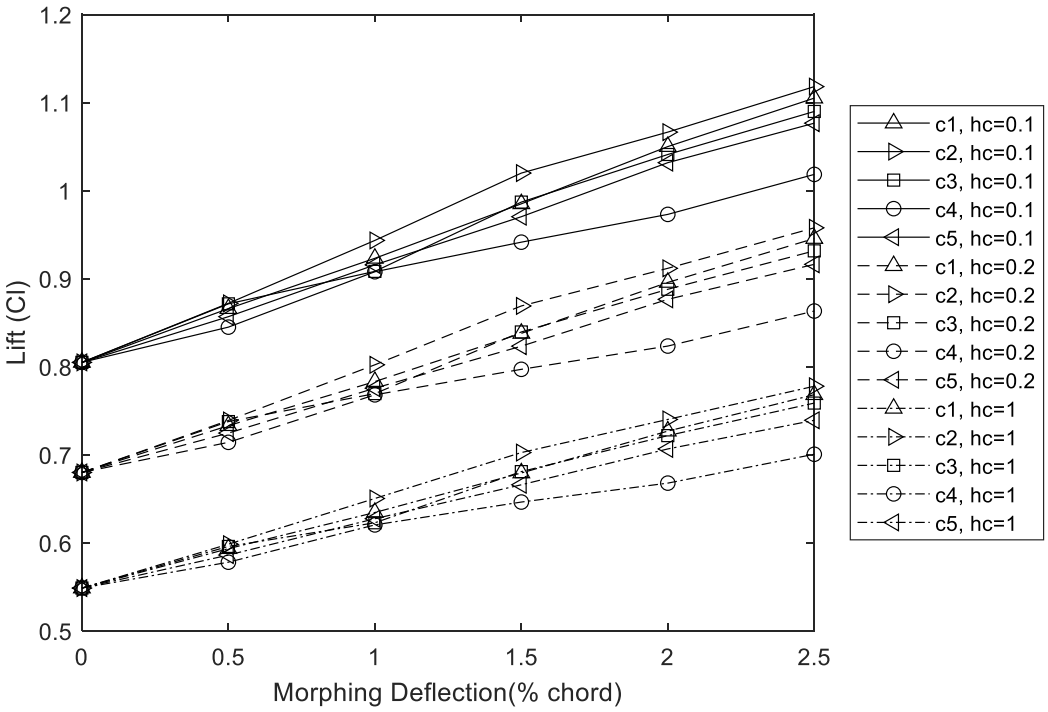

Figure 6.16: Lift of optimised wing morphed statically at 10% and 20% ground clearance and freestream for 5 morphing configurations.

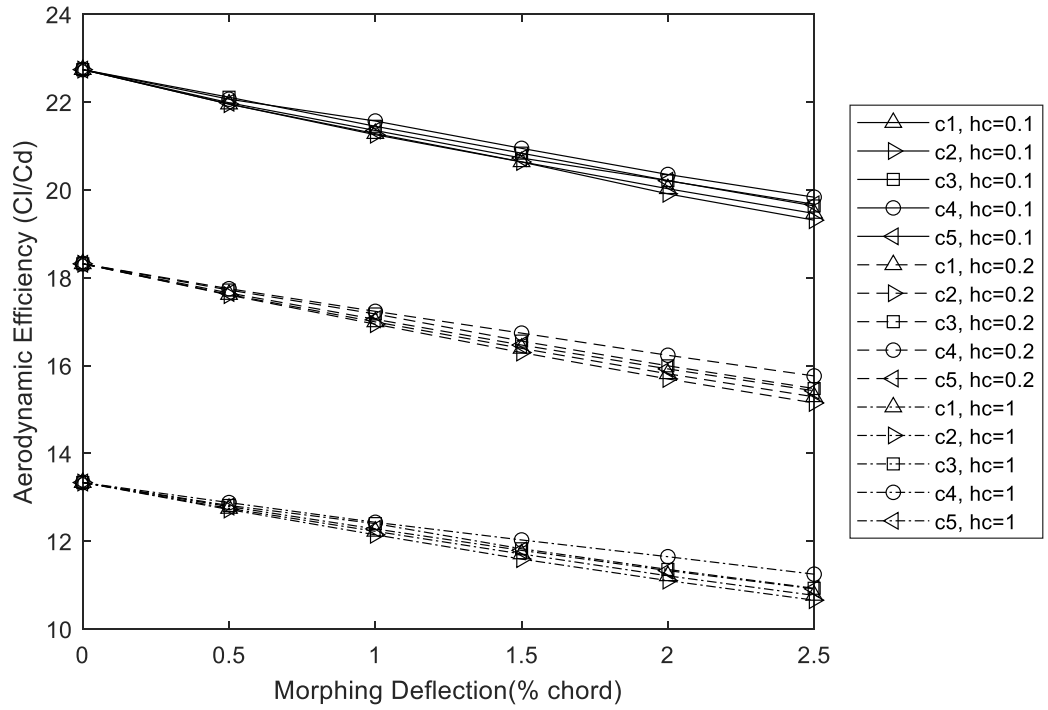

Figure 6.17: Aerodynamic efficiency of optimised wing morphed statically at 10% and 20% ground clearance and freestream for 5 morphing configurations.

Both configurations 1 and 2 produced similar levels of lift however starting the morphing of the wingtip at an earlier location for configuration 1 may improve manufacturability, especially, for small UAV wings. In freestream, the later morphing still produced the highest level of lift due to the greater downward turning of the flow increasing the circulation of the wing.

Observing the drag (Figure 6.18) it was seen for all trailing edge displacements that the drag decreased as the ground clearance was reduced as seen throughout this study due to reduced induced drag when in ground effect. The reduction in drag for the non-morphed wing was 15% and the reduction in drag for the fully morphed wing was 20% when bringing the wing from freestream to ground effect. The main reason the fully morphed showed larger reductions in drag was due to the morphed wing initially having a higher downwash in freestream. Similar amounts of downwash for the non-morphed and fully morphed when in ground effect was observed. Therefore, at maximum trailing edge deflection, there was a greater amount of downwash reduction which caused the largest difference in drag reduction. For all configurations tested, the drag increased at a greater rate than the lift as the wing was morphed which resulted in the aerodynamic efficiency decreasing as the wing was morphed (Figure 6.17).

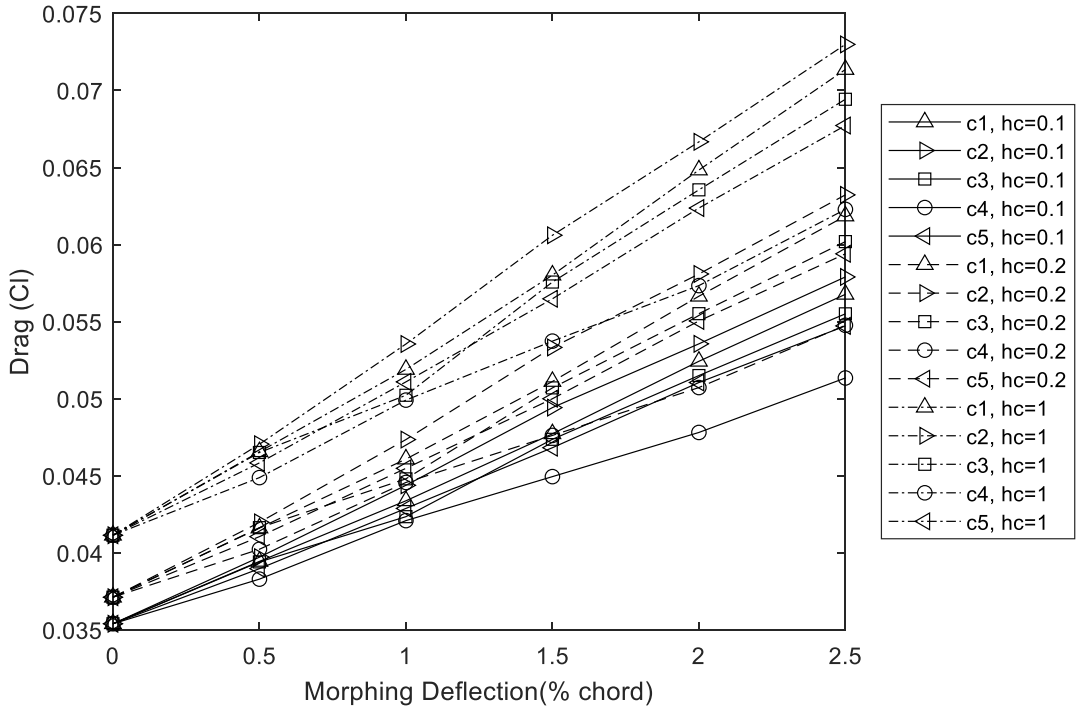

Figure 6.18: Drag of optimised wing morphed statically at 10% and 20% ground clearance and freestream for 5 morphing configurations.

Comparing the effect of ground clearance on the lift, it was seen in (Figure 6.16) that in ground effect all configurations had a higher lift than freestream, looking at the pressure on the lower surface (Figure 6.19) showed that baseline wing with no-morphing had an increase in pressure on the lower surface from ground effect. Increasing the morphing in freestream caused the lift of the wing to increase due to increased circulation of the wing from the increased camber. Bringing the morphed wing into ground effect from freestream showed even higher gains in pressure on the lower surface, this was due to the morphed wing trailing edge was closer to the ground than the non-morphed which increased the ground effect enhancement. The morphed wing in ground effect, therefore, showed increased lift from both the increased camber and ground effect

enhancement. It was also seen in Figure 6.19 that the stagnation point at the leading edge moved downstream on the lower surface a greater amount when the wing was morphed from 0% to 2.5% trailing edge deflection in freestream compared to ground effect.

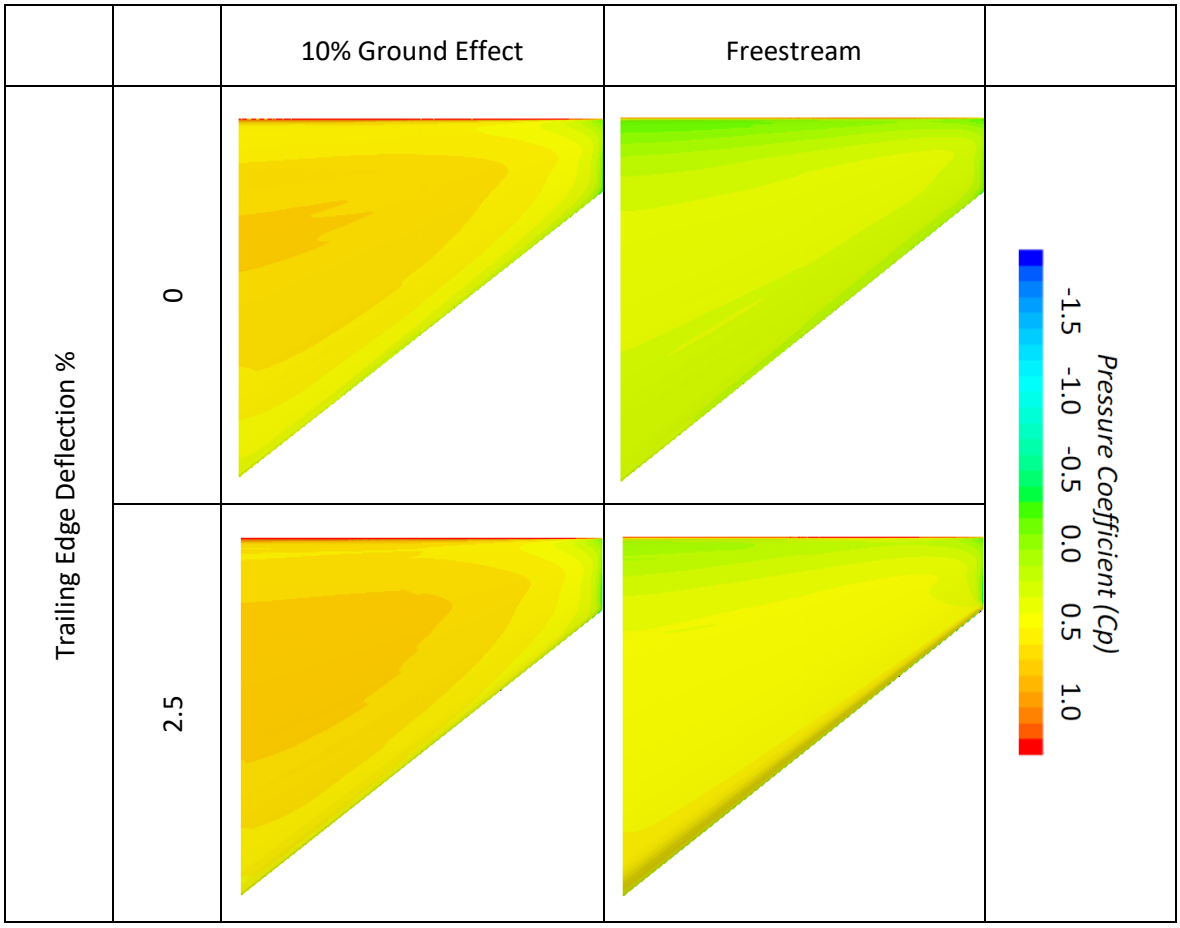

Figure 6.19: Configuration 2 static deflection in 10% ground effect and freestream.

Analysing the pressure across the span shows (Figure 6.19) a large variation in pressure in the spanwise direction. At the wingtip, the pressure was identical for all configurations and trailing edge deflections from the wingtip vortex. This was due to the pressure at this location being defined by the core pressure of the wingtip vortex. The larger pressure at the wing root seen at higher deflections caused a larger spanwise driven flow, which due to the forward wing tip position did not feed the wingtip vortex like the rectangular wing but caused the flow to leave the trailing edge.

Figure 6.20 shows the lower surface pressure comparing configurations 2 and 4 in 10% ground effect. For configuration 4, the trailing edge at the wingtip was a greater distance away from the ground compared to configuration 2 which resulted in a greater lift for configuration 2. This was seen in (Figure 6.20) when comparing the lower surface pressures of configurations 2 and 4 (highest and lowest lift) in 10% ground effect. The images in (Figure 6.20) are orientated so that the leading edge was to the top and the mid-span root is on the left. At zero deflection, both wings are identical in geometry and therefore the lower surface pressure was identical. For small

deflections of 0.5% in 10% ground effect, configuration 2 showed to have a 1.8% higher lift than configuration 4 which was seen in Figure 6.20 due to a greater amount of high pressure on the lower surface. As the deflection increased to 2.5% trailing edge deflection, the difference in lift increased to 9% between configurations 2 and 4. From Figure 6.20 it is seen the magnitude of pressure is much higher for configuration 2 and the high pressure is spread out over a much larger proportion of the lower surface.

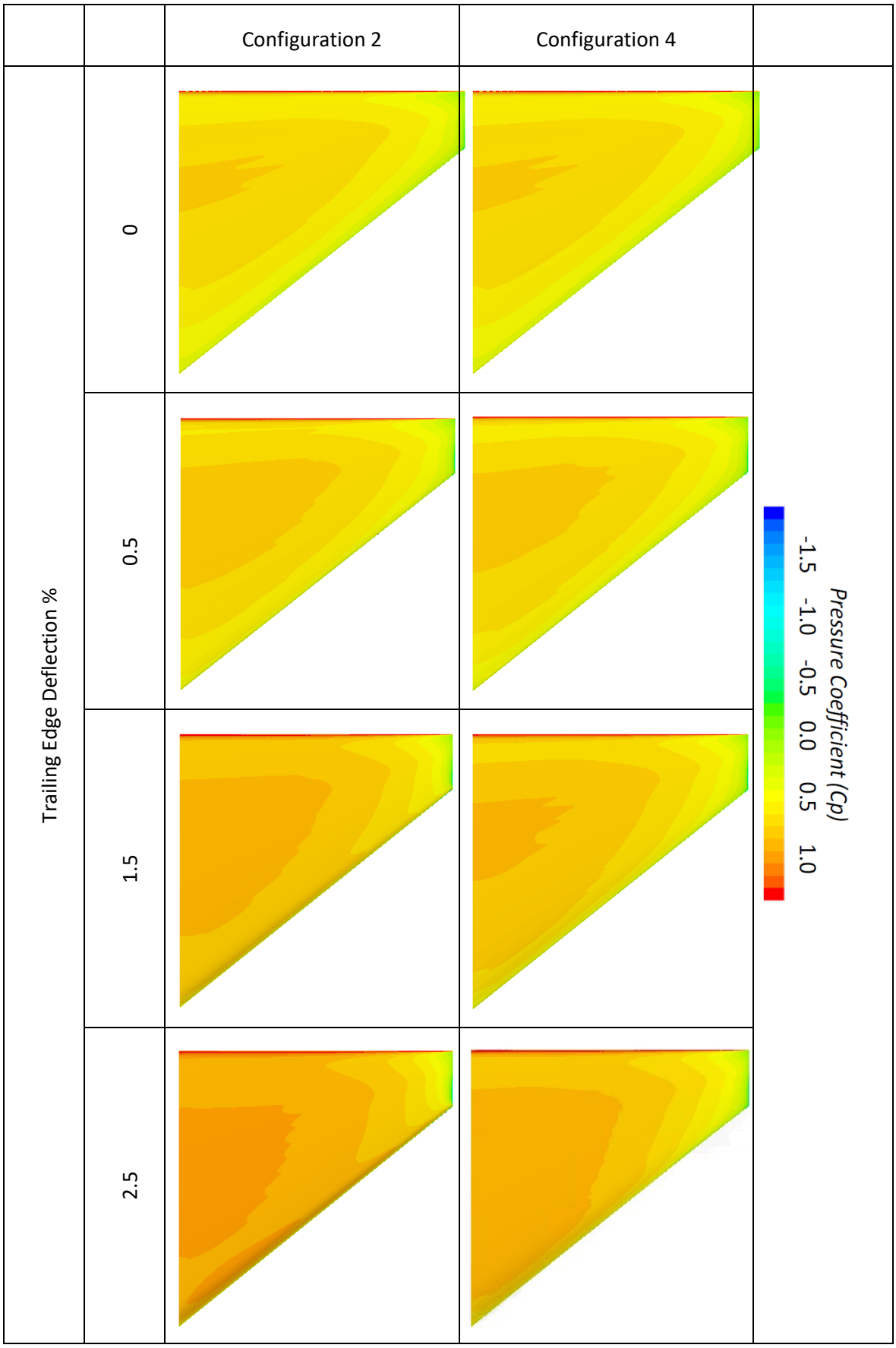

Figure 6.20: Configuration 2 and 4 static deflections in 10% ground effect.

Analysing (Figure 6.21) the vorticity at 20% chord downstream of the trailing edge clearly showed the main wingtip vortex. Interestingly the wingtip vortex had a stronger core for the 80% start

location at the root and zero at the tip (configuration 4) compared to the 90% at the root and 18% at the tip start locations (configuration 2). This was due to the higher pressure trying to cause a stronger vortex, but the proximity of the ground does not allow the vortex to fully form. The higher pressure beneath the wing for configuration 2 also caused the wing tip vortex to be pushed outboard.

For both configurations, the secondary counter-rotating vortex was seen to roll up from the ground. The higher pressure beneath the wing for configuration 2 caused a thicker boundary layer on the ground. Interestingly for configuration 4, it was seen there was a third area of vorticity inboard of the wingtip vortex. This was due to earlier separation at the wingtip on the upper surface which the wingtip vortex dragged this separated flow around the main wingtip vortex shown in Figure 6.22. This may seem to go against what was said in section 4.4 where it was discussed that a wingtip vortex reduces separation at the wingtip but configuration 4 has unequal morphing along the span with zero morphing at the wingtip.

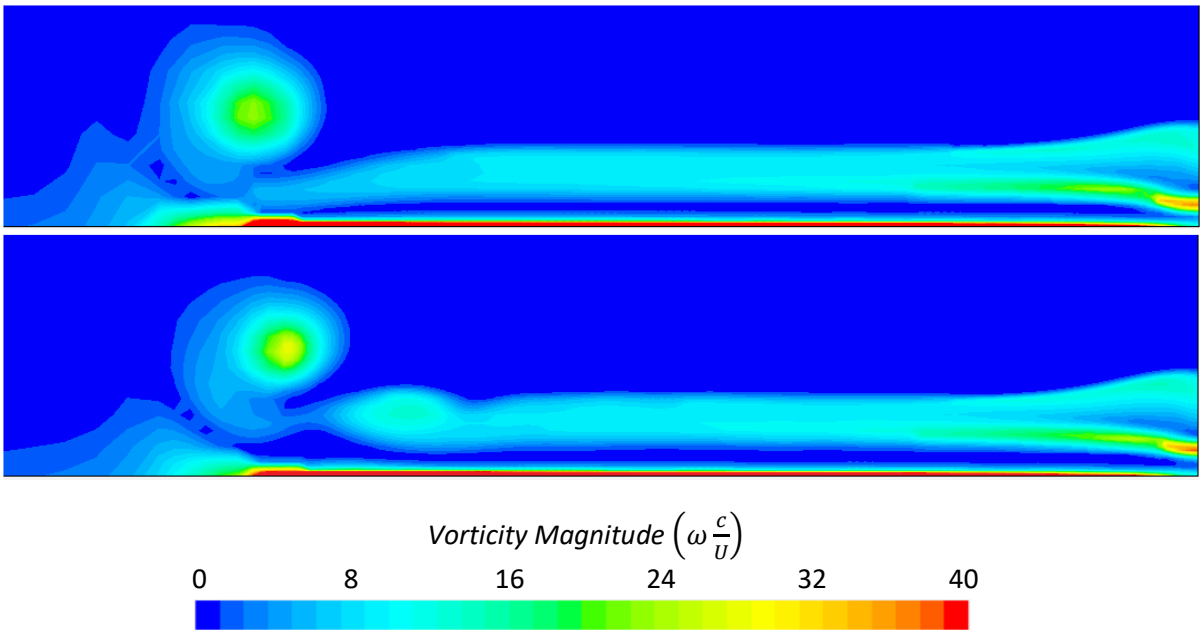

Figure 6.21: Vorticity magnitude at 20% chord downstream of optimised NACA6409 in 10% ground effect for configuration 2 (top) and configuration 4 (lower).

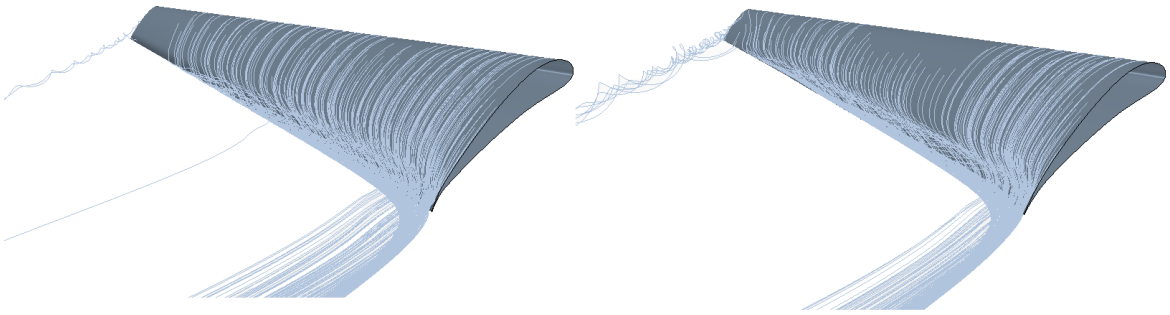

Figure 6.22: Streamlines of configuration 2 (left) and configuration 4 (right) in 10% ground effect.

Comparing the morphed optimised wing to the morphed rectangular wing (Figure 6.23) has seen that the same principles apply to both wings. Morphing both wings in ground effect increased the lift of the wing due to increased circulation of the wing and enhanced ground effect. Also, both showed a greater reduction in drag when bringing the morphed wing from freestream to ground effect compared to bringing the non-morphed baseline wing from freestream to ground effect. Both wings showed the lift increased due to an increase in pressure on the lower surface, which drove the spanwise flow that feed the wingtip vortex. The main difference between the rectangular and optimised was the forward wing tip position of the wing caused the streamlines to flow along the trailing edge towards the root of the wing. The rectangular wing however saw the flow leaving the trailing edge to feed the wingtip vortex, which increased the induced drag of the wingtip vortex.

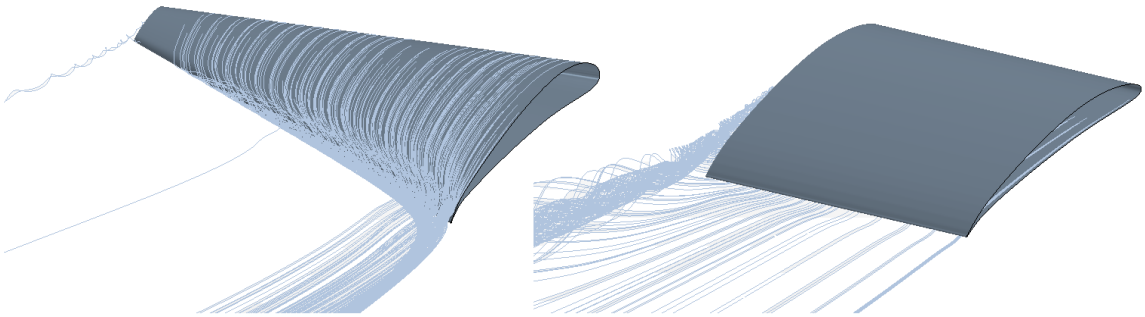

Figure 6.23: Streamlines of configuration 2 (left) and rectangular wing at 4 degrees AoA (right) in 10% ground effect.

6.4 FishBAC Wingtip Morphing

6.4.1 Static Wingtip Deflection Discussion

Throughout this study and literature FishBAC morphing was applied in the chordwise direction, this section investigates applying the FishBAC morphing to the spanwise direction building on the knowledge gained by Wei & Zhigang (2012) for tiltable wingtips. The wing used in this section was shown in the schematic shown in methodology in Figure 3.28.

Two tests were carried out, first, the ground clearance of the wing was kept constant at 10% with the wingtip being deflected. Second, take-off was simulated by changing the ground clearance of the wing whilst fixing the wingtip at 2% clearance from the ground and comparisons made to a non-morphing wingtip varying ground clearance. Two start locations of z/c =0.4 and 0.8 in the span direction were tested and compared.

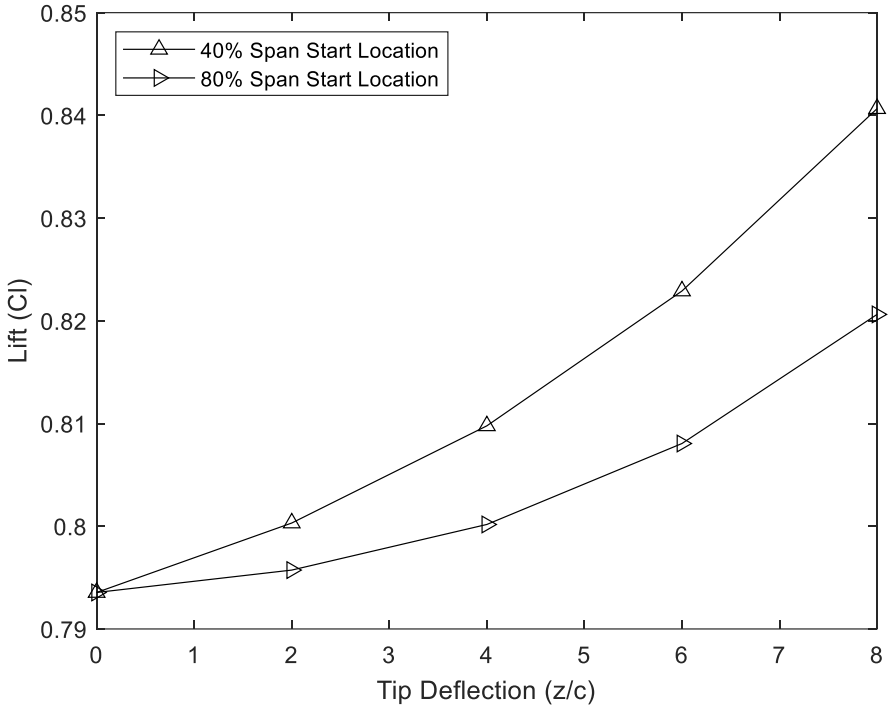

Figure 6.24: Wingtip deflection lift in 10% ground clearance.

Analysing the lift (Figure 6.24), fixed ground clearance has shown that the lift increased as the wingtip was deflected. Comparing the lower surface (Figure 6.25) of the zero and 8% morphed wingtip showed the lift gain caused by an increase in pressure on the lower surface. This can be seen where the higher pressure extends a greater distance along the span, and a higher pressure magnitude for the 40% start location.

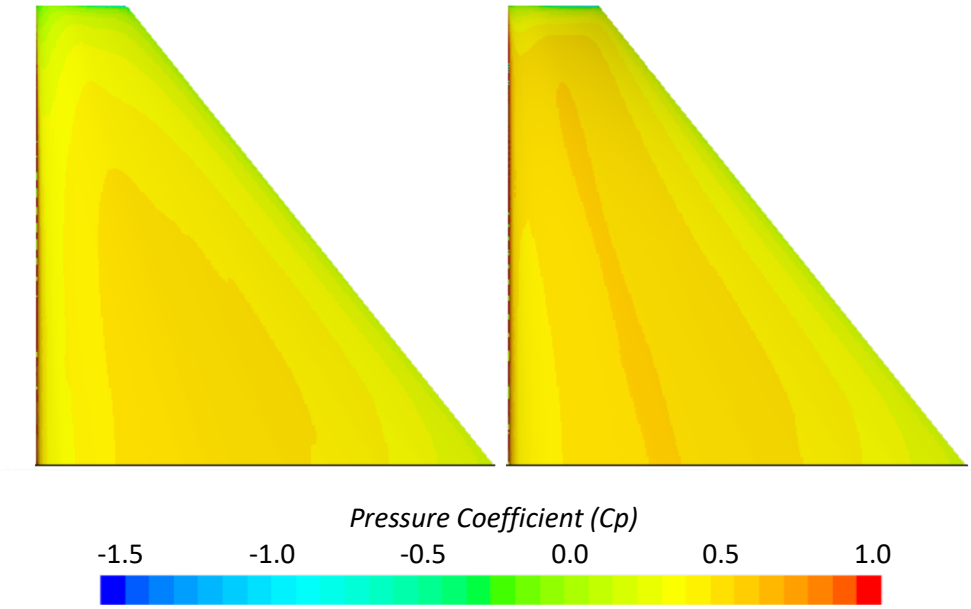

Figure 6.25: Lower surface pressure coefficient in 10% ground effect with zero morphing (left) and morphing starting at 40% along the span and deflected 8% (right).

The gain in overall pressure was found to be caused by the wingtip vortex interaction with the ground and reduced leakage beneath the wing. Analysing the pressure coefficient (Figure 6.26 upper) for a non-morphed wing on a plane 20% downstream of the trailing edge shows the high pressure at the root of the aerofoil which drives a spanwise flow feeding the wingtip vortex as discussed in section 4.4. The high pressure reduced along the span as the air flowed around the wingtip towards the lower pressure region on the upper surface. Morphing the wingtip decreased the clearance between the wingtip and ground and reduced the leakage of flow around the wingtip. This reduced the pressure drop in the spanwise direction on the lower surface, which resulted in an overall higher pressure on the lower surface shown in (Figure 6.26 lower) increasing the overall lift.

The wingtip vortex was visible (Figure 6.26) by the low-pressure core, when the wingtip deflection increased, the velocity of flow exiting the wingtip increased due to the conservation of mass. This increase in velocity around the wingtip caused the lower pressure core for the deflected wingtip.

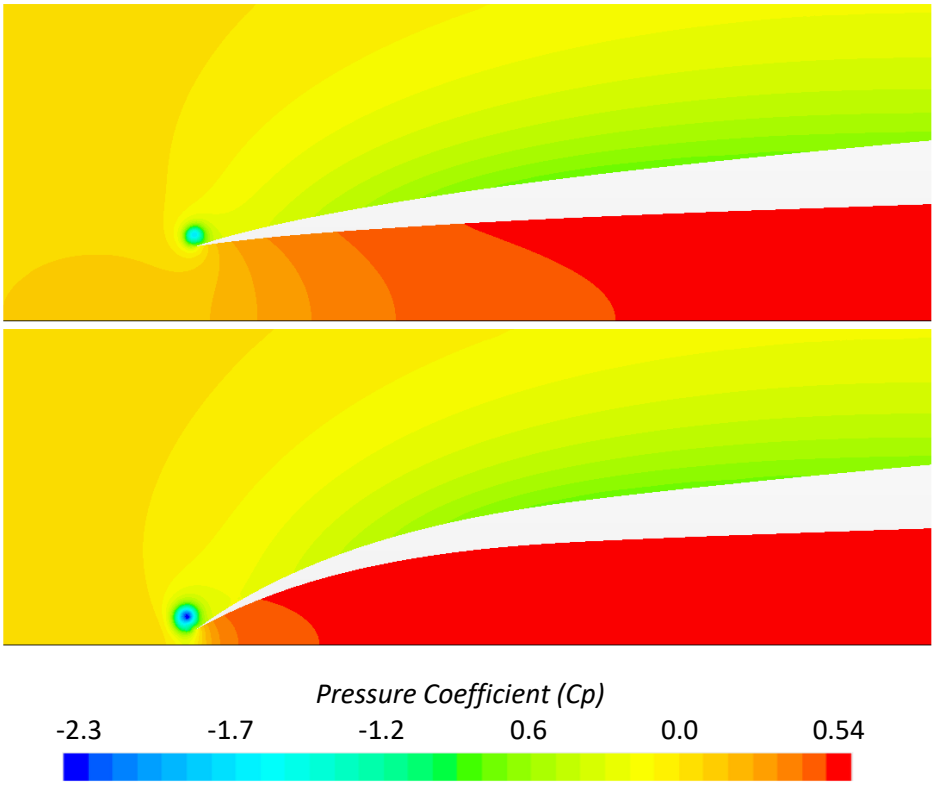

Figure 6.26: Pressure coefficient of wing in 10% ground effect at a location 20% from the leading edge for zero morphing (upper) and 8% deflection starting at 40% span from root (lower).

Comparing the vorticity of the zero and T/c = 8% morphed wings on multiple planes behind the wings showed distinctive differences in the wingtip vortices and showed how the vortex developed downstream (Figure 6.27). First, it was seen that the vorticity intensity of the wingtip vortex increased as the wingtip deflection T/c was increased in ground effect for both the 40% and 80% start locations. It was seen that the wingtip vortex was pulled downwards with the wingtip as the wingtip was morphed also seen by Wei & Zhigang (2012) who investigated tiltable wingtips. The wingtip vortex remained located on the upper surface of the wing throughout the morphing.

For the plane located at 10% downstream from the trailing edge, it was seen that the wingtip vortex began to roll up earlier and was a larger diameter for the morphed wingtip compared to the zero morphed wing. As the wingtip vortex travelled downstream, the vortex moved outboard seen for the zero morphing, 40% and 80% morphing start locations where the vorticity reduced, and the diameter of the wingtip vortex increased downstream.

For the morphed wing of 40% and 80% start location, it was seen with the high wingtip deflection in Figure 6.27 that a distinct boundary layer formed on the ground. At a location of 20% downstream of the trailing, it was seen this boundary layer separated and formed a secondary

counter-rotating vortex. As the main vortex grew in diameter downstream, the secondary vortex was pushed outboard. Due to the high proximity of the wingtip for the zero morphing, a boundary layer only formed on the zero morphing at a location of 100% chord downstream of the trailing edge due to the increased diameter of the wingtip vortex.

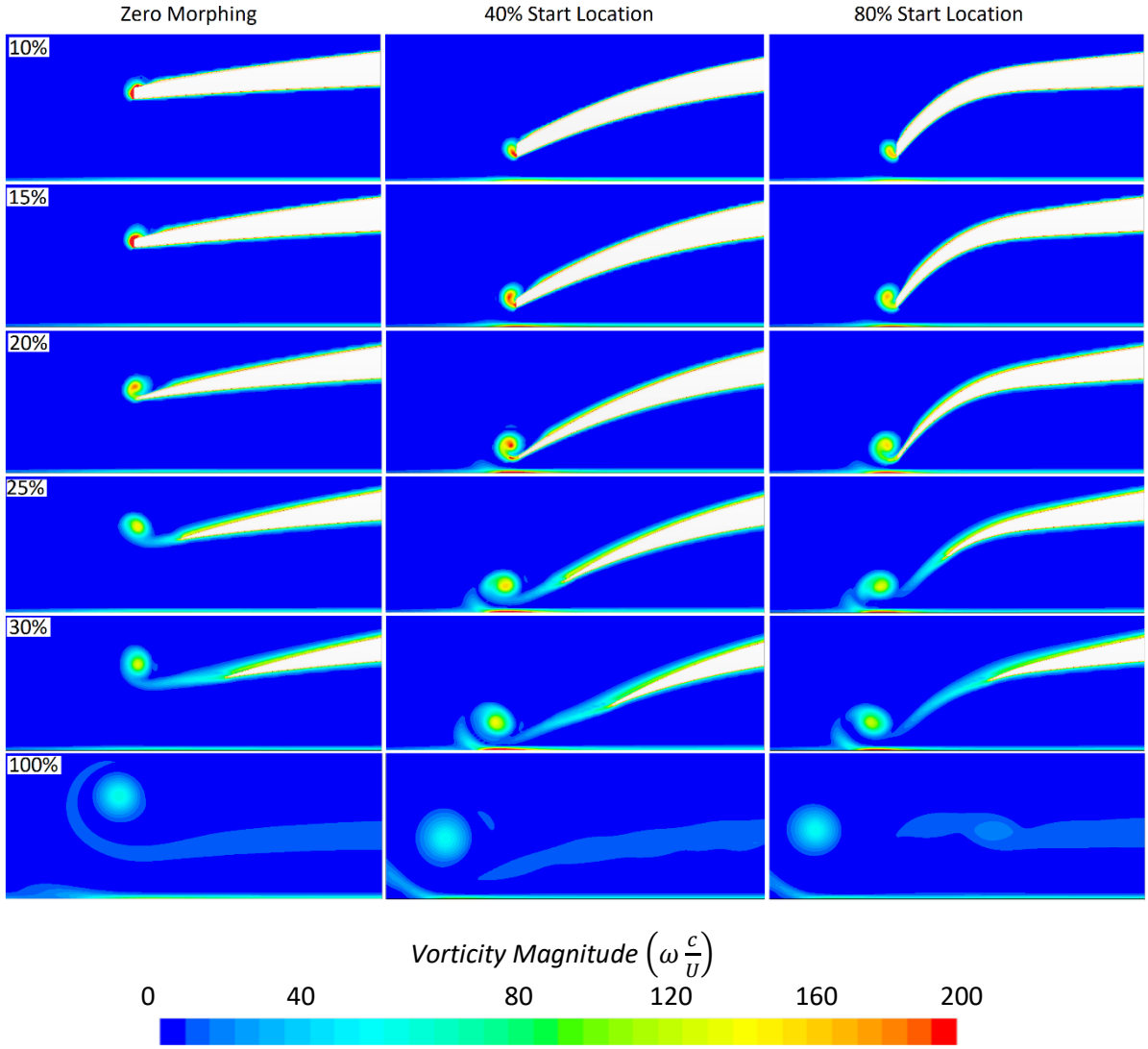

Figure 6.27: Vorticity plots showing the front view of wing on planes located from 10% to 100% chord length from the leading edge with zero morphing (left), 8% tip deflection for 40% span start location (middle) and 80% span start location (right) in 10% GE.

So far it has been seen that deflecting the wingtip increased the pressure beneath the wing but analysing the lift in Figure 6.24, it was seen the lift was higher for the 40% span start location. This was due to higher pressure on the lower surface of the 40% start location along the span shown in Figure 6.28. The reason the pressure was higher for the 40% start location was due to the distance between the lower surface and ground was smaller for the 40% start location shown in (Figure 6.29) from the earlier start location. This increases the ground effect enhancement from the wing as the trailing edge becomes closer to the ground on the morphed proportion of the wing. This

increased the pressure upstream of the trailing edge as seen in the two-dimensional study (section 4.3) when reducing the ground clearance. Overall, the lift for the wingtip morphed wings was seen to increase due to better sealing of the lower surface and enhanced ground effect.

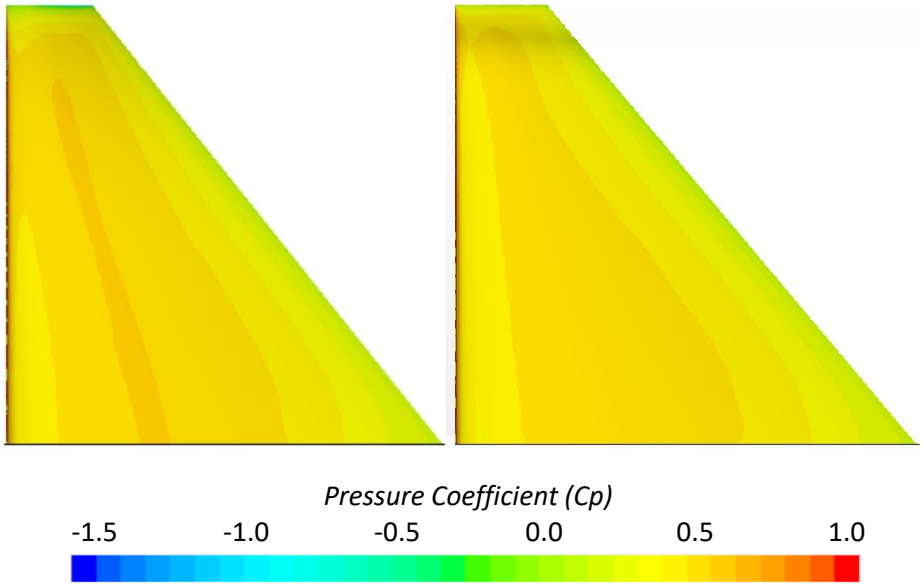

Figure 6.28: Low surface pressure coefficient for 40% start location (left) and 80% start location (right) in 10% ground effect.

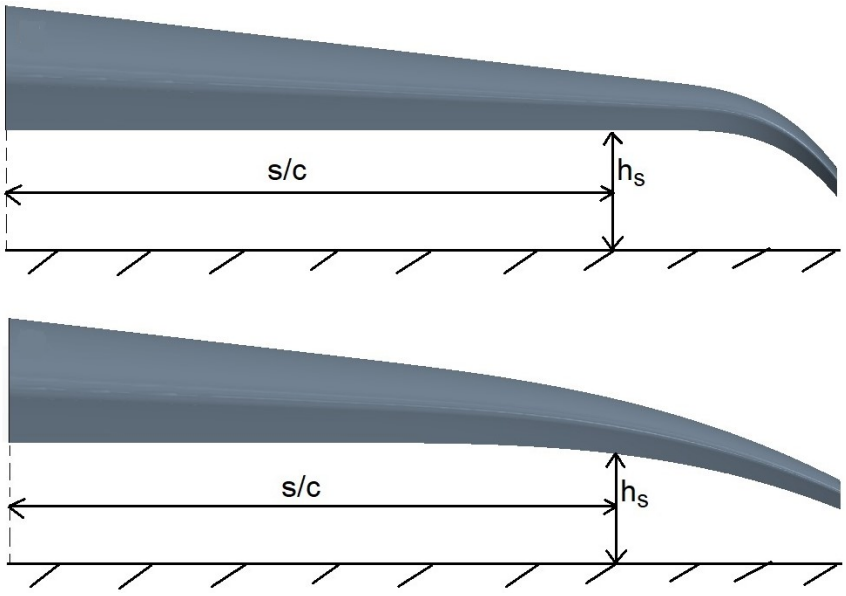

Figure 6.29: Front view of 80% (top) and 40% (lower) start location-morphed wing.

This can be visualised by looking at the pressure on a plane at 20% chord downstream of the leading edge in Figure 6.30. Increasing the start location reduced the location where the pressure began to drop in the spanwise direction. It was seen at the tip the pressure was identical for the 8% morphed wings for both the 80% and 40% start locations. This showed there was a greater rate of deceleration of flow in the spanwise direction for the 40% span start location seen by the

change of pressure at the wingtip (Figure 6.30). Comparing the wingtip vortex for the 40% and 80% (Figure 6.27 middle and right) start location showed the vorticity was much higher for the 40% wingtip. The boundary layer separation on the ground was shown to be independent of the start location of morphing along the span shown by the boundary layer and secondary wingtip vortex being identical for the 40 and 80%.

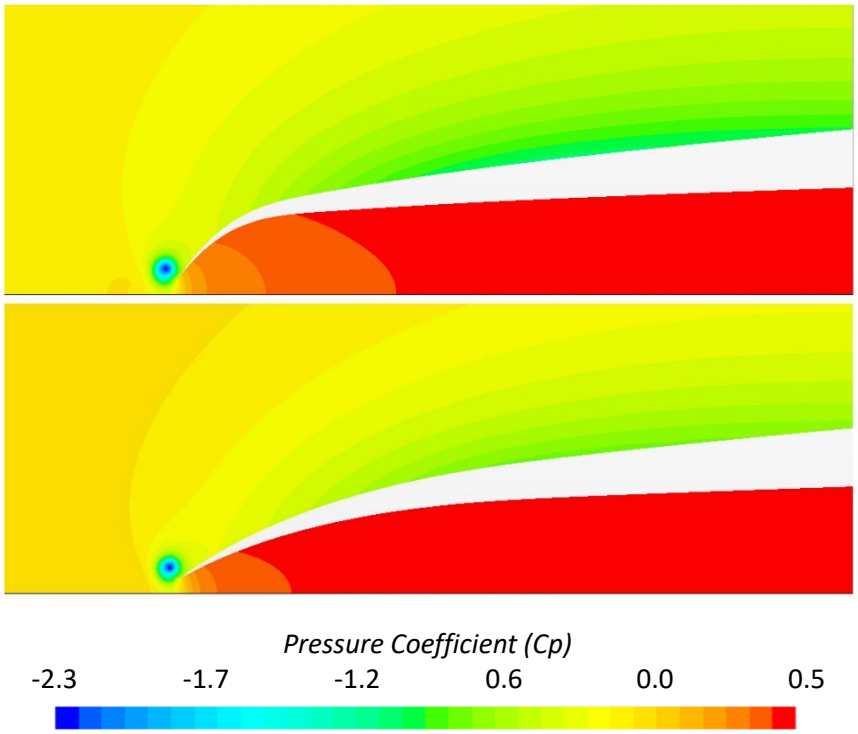

Figure 6.30: Pressure coefficient of wing in 10% ground effect at a location 20% from the leading edge for 80% (upper) and 40% (lower) span start location span from the root with 8% deflection.

Applying the morphing in the spanwise direction in this section showed to be opposite to applying the FishBAC morphing in the chordwise direction in Chapter 5. Applying the morphing in the chordwise direction showed that a later start location caused higher lift, this was due to the Kutta condition fixing the trailing edge pressure causing the effects of morphing to be seen upstream of the trailing edge. The Kutta condition does not apply for wingtips therefore an earlier start location enhanced ground effect.

Figure 6.31 showed the drag for the 40% and 80% start locations, it was seen the 40% start location in the span direction had the lowest drag. This was due to a greater proportion of the wing being closer to the ground which reduced the induced drag of the wing from the proximity of the ground. This resulted in a higher aerodynamic efficiency seen in Figure 6.32. It is also seen that the closer the wingtip was to the ground caused the highest aerodynamic efficiency.

Therefore, there is a compromise of high aerodynamic efficiency and substantial ground clearance at the tip to allow the WIG craft to roll.

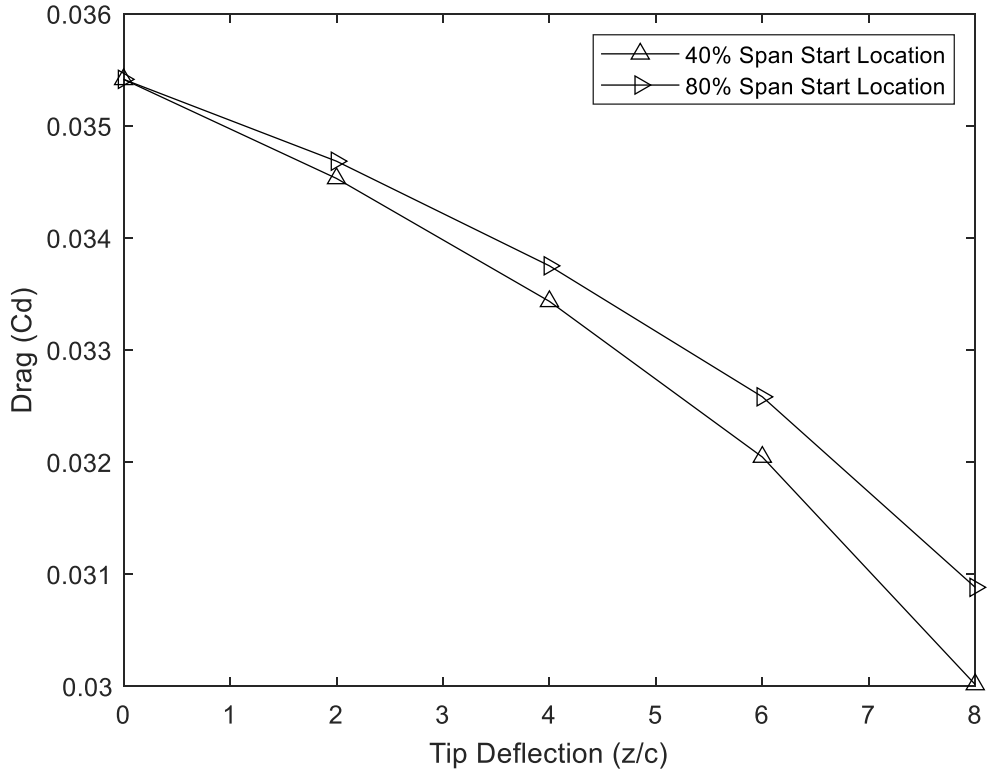

Figure 6.31: Wingtip deflection drag in 10% ground clearance.

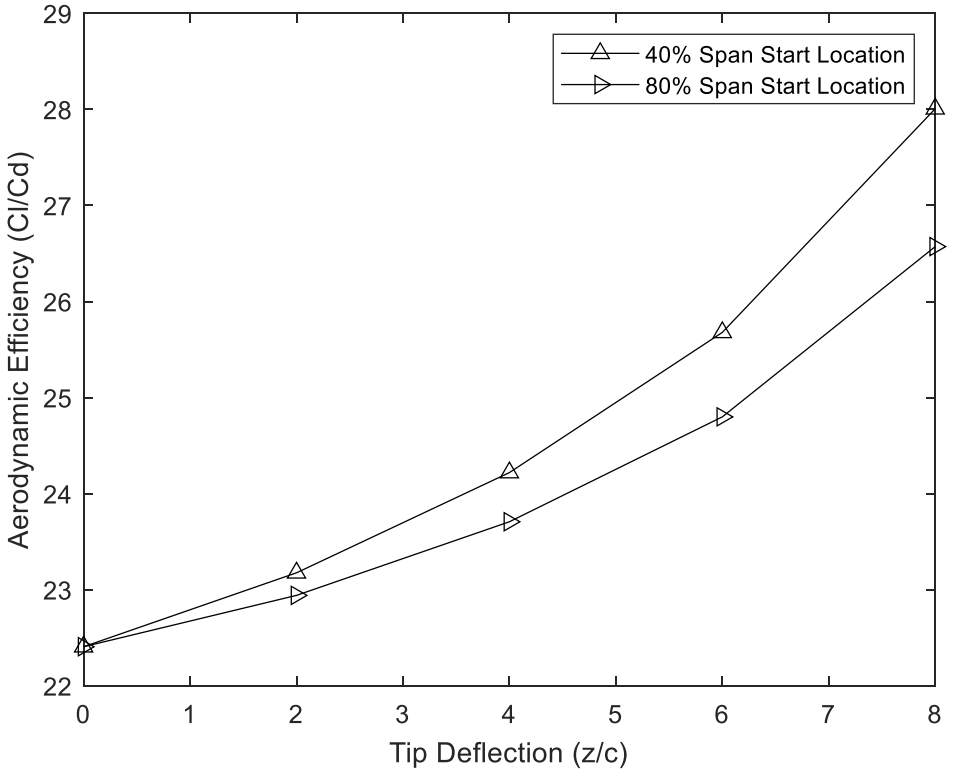

Figure 6.32: Wingtip deflection aerodynamic efficiency in 10% ground clearance.

6.4.2 Constant Wingtip Clearance with FishBAC Morphing

An aircraft will vary its altitude during flight for example during take-off until reaching cruising altitude or a WIG craft to climb to avoid an obstacle in the sea. It was previously seen in section 6.4.1 that the highest efficiency wings were for the smallest ground clearance, tests are carried out in this section for a constant wingtip clearance and whilst the root height varies as the WIG craft altitude varies during flight.

Although it was found that the 40% start location in the span direction had greater performance in 10% ground effect when the wingtip was morphed, this section still considers both 40% and 80% span start locations to see the performance of both these locations at different ground clearances. Throughout the study in section 6.4.2 a constant wingtip clearance of 2% root chord was maintained, therefore in Figure 6.33, Figure 6.34 and Figure 6.35 a ground clearance of h/c = 2% had zero morphing and increasing to h/c = 10% had a morphed deflection of T/c = 8%.

It was seen increasing the ground clearance reduced the lift reduced Figure 6.33 as the ground effect enhancement reduced for both the morphed wingtip and non-morphed configurations. For the z/c = 40% the lift was higher than z/c = 80% due to the greater proportion of the wing being closer to the ground which caused greater ground effect enhancement for the z/c = 4% wing. At h/c = 10% ground clearance the lift was 3.3% higher for z/c = 80% and 6.6% higher for z/c = 40% compared to the non-morphed. At h/c = 15% ground clearance it was seen there was a gain of 4% lift and a gain of 7% compared to the non-morphed. Identical gains in lift were seen at h/c = 30% as the ground clearance h/c = 0.15. This shows for extreme ground effect of h/c = 2% and h/c = 5% that there is little benefit in terms of lift gains from morphing the wingtips.

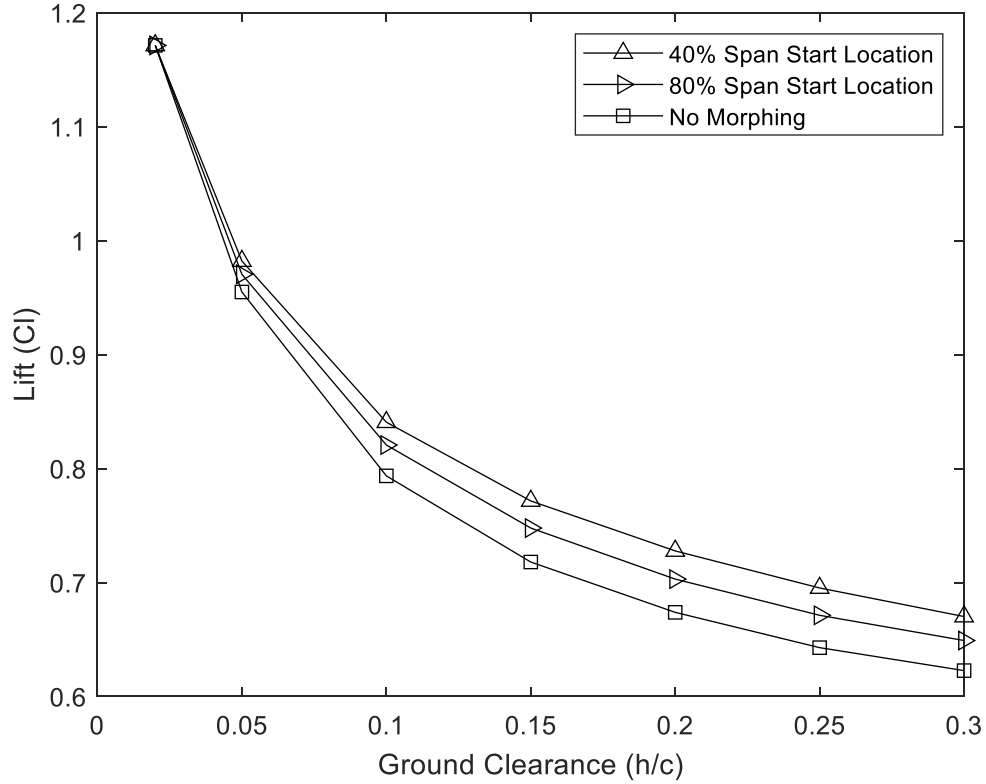

Figure 6.33: Constant clearance between tip and ground varying wing root clearance lift.

For the non-morphed optimised wing, the drag increased as the ground clearance increased as seen in section 4.5. For both z/c = 40% and z/c = 0.80% this was not seen, increasing the ground clearance for both wings caused a reduction in drag shown in Figure 6.34. The induced drag of the wingtip vortex did not increase as the wingtip was still in ground effect for all ground clearances tested yet the blockage beneath the wing reduced as the air could pass more freely beneath the wing. The reason the z/c = 40% span location had a slightly lower drag than the z/c = 80% was due to the greater proportion of the trailing edge was closer to the ground for the z/c = 40% therefore there was less downwash for the z/c = 40% wing. A local minimum drag was seen at h/c = 15% then the drag began to increase as the amount of downwash increased as the wing was moved away from the ground.

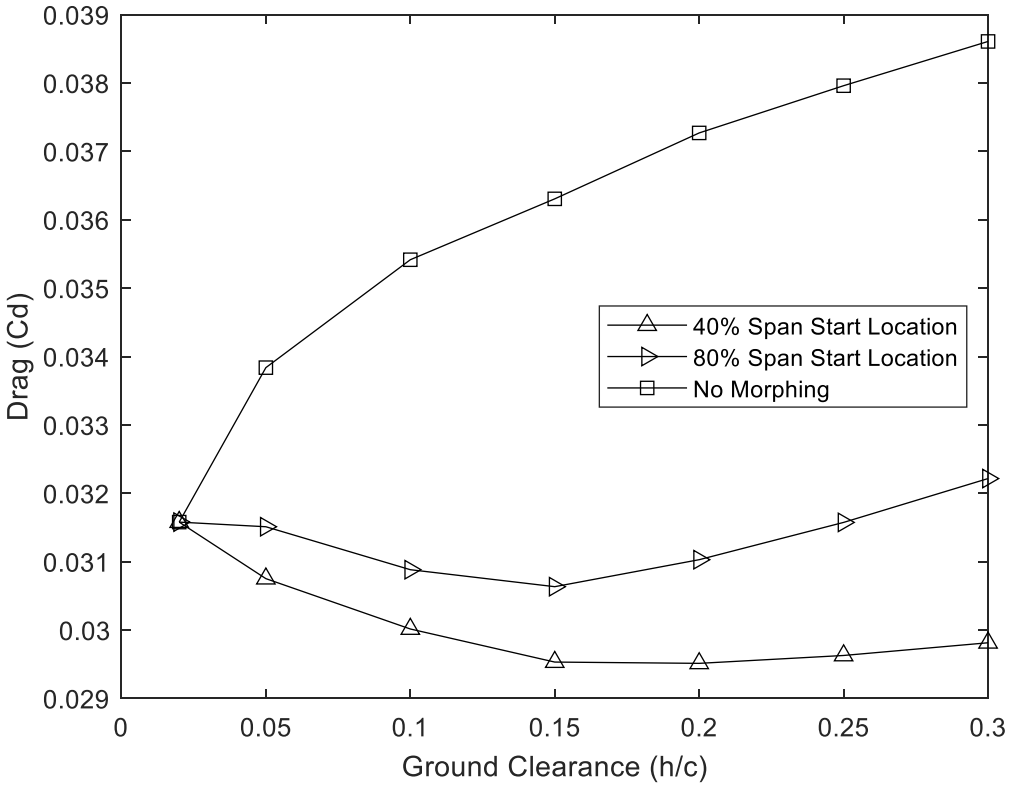

Figure 6.34: Constant clearance between tip and ground varying wing root clearance drag.

The drag showed a reduction of 15% for z/c = 40% and 12% reduction for z/c = 80% for h/c = 10% ground clearance. Increasing the ground clearance to h/c = 15% caused a reduction in drag of 15% for z/c = 80% and a reduction of 17% drag and for a ground clearance of h/c = 30% the drag reduced by 17% for z/c = 80% and reduced by 23% for z/c = 40%. This showed within the range of ground clearances tested that the drag reduced, and the highest reductions were for higher ground effects compared to the non-morphed wing. Opposite to the lift where there were minimal gains in lift for h/c = 2% and h/c = 5%, the drag showed large reductions compared to the non-morphed aerofoil. Overall, it was seen that the aerodynamic efficiency was higher for the 40% start location and the lowest for the non-morphing as the ground clearance was increased shown in Figure 6.35.

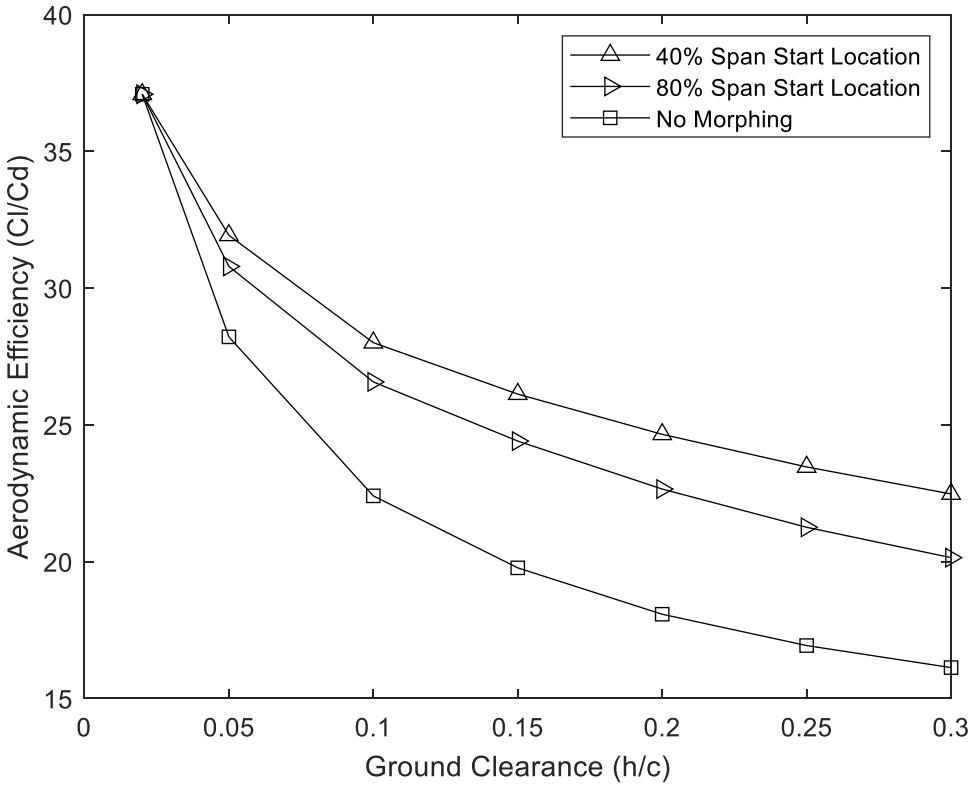

Figure 6.35: Constant clearance between tip and ground varying wing root clearance aerodynamic efficiency.

The vorticity of the morphed wingtips of z/c = 40%, z/c = 80% and non-morphed wings were analysed (Figure 6.36) for a range of ground clearances on a plane 0.2c downstream of the trailing edge. In extreme ground effect of h/c = 2%, the vorticity plots (Figure 6.36) showed a wingtip vortex with a secondary counter-rotating vortex rolling up as mentioned in section 4.4. For the zero-morphing baseline wing, as the ground clearance increased the distance between the wingtip vortex core and ground increased which eliminated the secondary counter-rotating vortex. For the morphed wingtip, it was seen that the wingtip vortex remained at the wingtip just above the ground which resulted in the secondary counter-rotating vortex remaining throughout the ground clearance. This was in agreement with Wei & Zhigang (2012) who saw this for tiltable wingtips in ground effect. The strength however of the secondary counter-rotating vortex reduced as the ground clearance increased for the morphed wingtip due to a reduction of pressure on the lower surface reducing the spanwise flow on the lower surface.

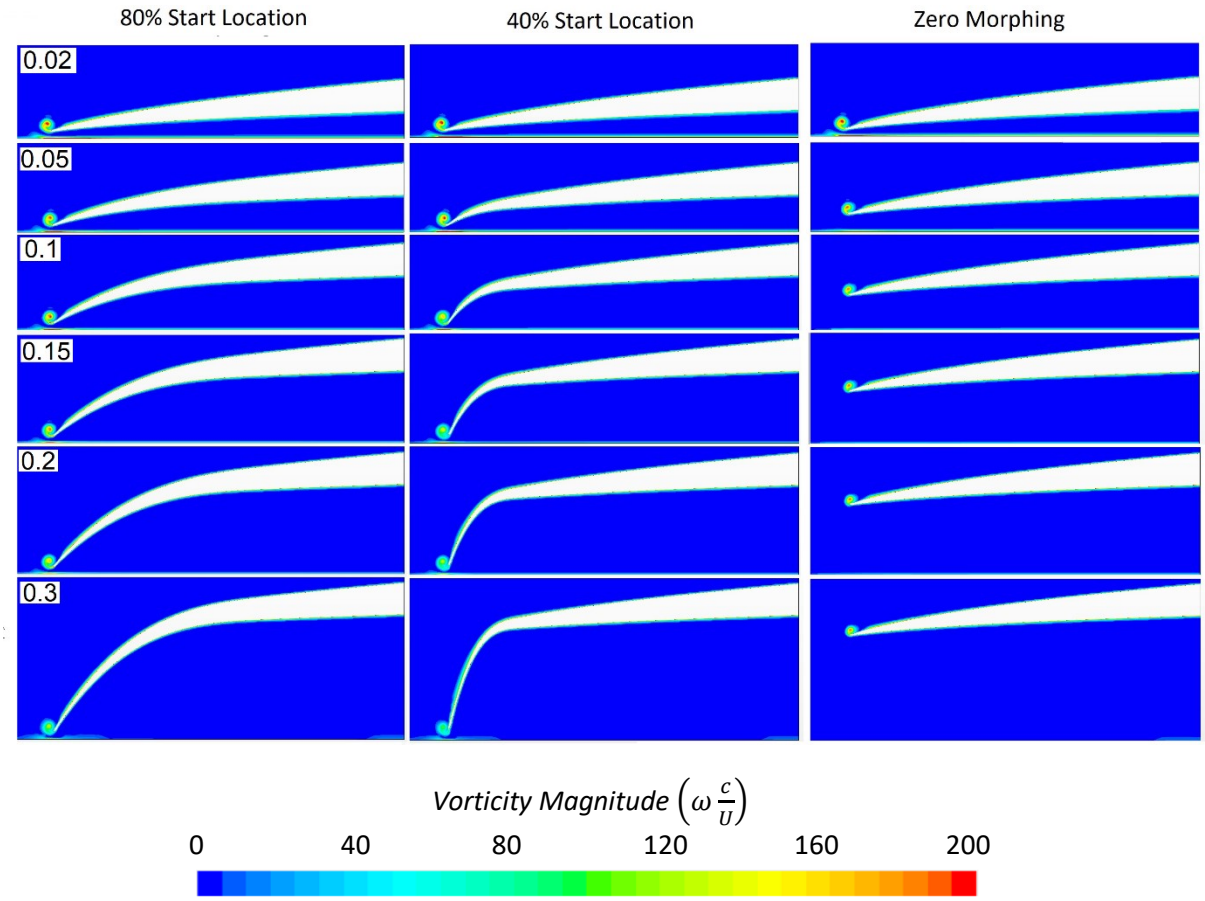

Figure 6.36: Pressure coefficient on a plane at location 20% from leading edge behind aerofoil keeping wingtip clearance fixed (left and middle) whilst varying root ground clearance (h/c) compared to wing without morphing (right) varying ground clearance.

6.5 Span Extending Morphing

Wing in ground effect vehicles tend to have low aspect ratio wings as a low span is required to prevent the wingtips from touching the ground when roll inputs are put into the aircraft which flying above water can cause the craft to crash. The literature review identified the span could be increased in freestream for endurance using symmetrical morphing and the span varied asymmetrical eliminating control surfaces.

Span morphing in this study was carried out for different ground clearances on both the rectangular wing and optimised wing using steady-state RANS. The results show for all span lengths that the optimised wing had higher lift (Figure 6.37), lower drag (Figure 6.38) and higher aerodynamic efficiency (Figure 6.39).

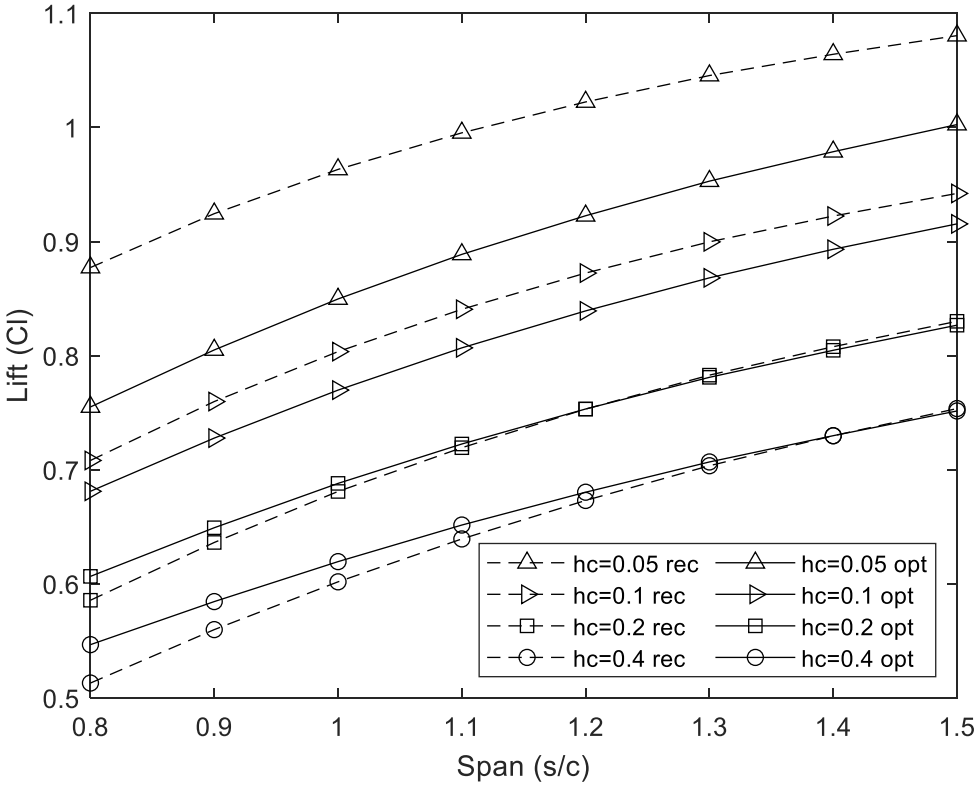

Figure 6.37: Span morphing lift rectangular and optimised NACA6409 wing.

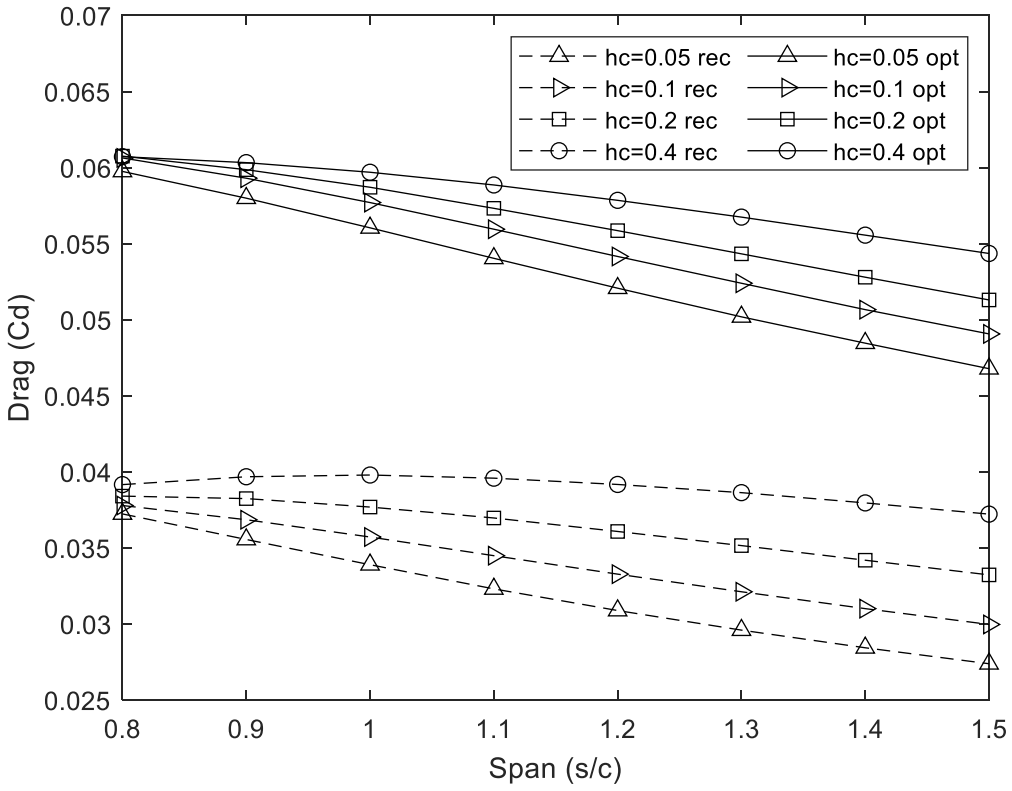

Figure 6.38: Span morphing total drag rectangular and optimised NACA6409 wing.

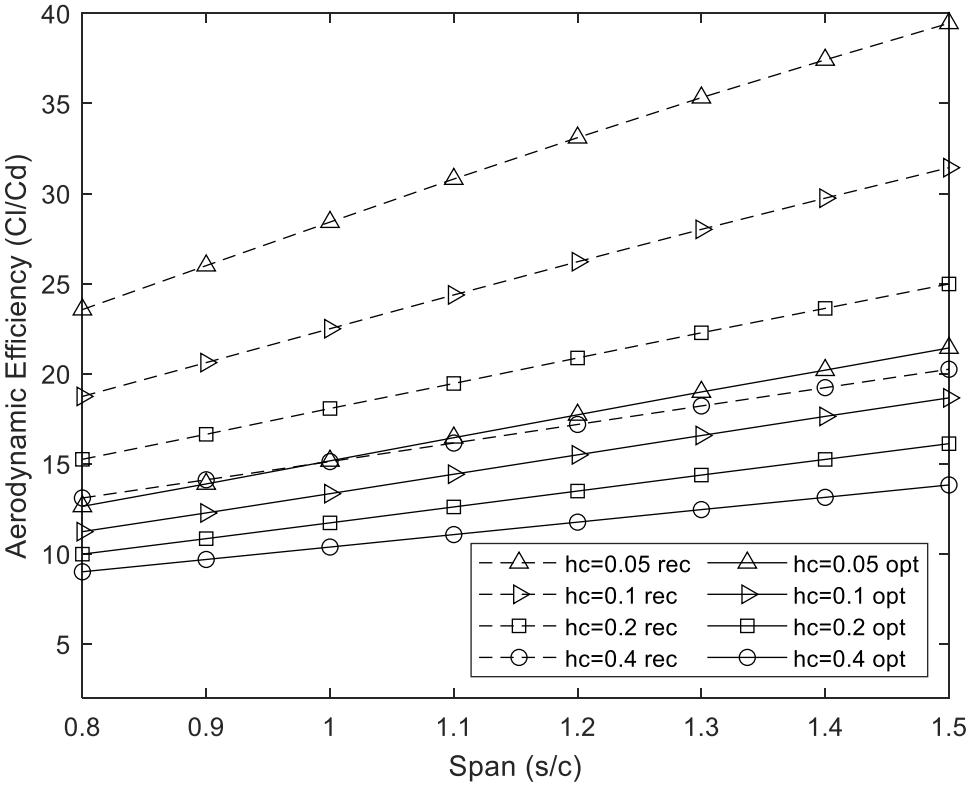

Figure 6.39: Span morphing aerodynamic efficiency rectangular and optimised NACA6409 wing.

Both the rectangular and optimised wings showed the lift increased as the span increased for all ground clearances seen in Figure 6.37 which was in agreement with (Y. Yu et al., 2009) who tested span morphing in freestream. The aerodynamic efficiency in Figure 6.39 also increased as the span of the wing increased which was also in agreement with (Beaverstock et al., 2015; Y. Yu et al., 2009).

For the drag, both the skin friction and pressure drag must be considered when varying the span of the wing due to the changing planform area of the wing which when summed, gives the total drag of the wing. Both the skin friction and pressure drag are proportional to the surface area of the wing which morphing the wing by extending the span varies the wing surface area. Analysing the skin friction and pressure drag for the optimised wing (Figure 6.40) showed that the pressure drag is far more dominant than the skin friction drag. For 40% ground clearance the pressure drag initially increased as the span increased from 80% to 100% then decreased as the span increased. For ground clearances smaller than h/c = 40% it was seen the pressure drag immediately reduced as the span increased. The amount the pressure drag reduction was far greater for smaller ground clearances. For the optimised wing, the pressure drag was reduced by 6% for h/c = 40% when the span was increased from 80% to 150% span. At a ground clearance of h/c = 10% the pressure drag was reduced by 25% and at a ground clearance of h/c = 5%, the pressure drag was reduced by 33%. This was in agreement with (Ajaj et al., 2012) however the skin friction increased whereas the results in Figure 6.40 showed the skin friction drag decreased. The key difference in this study

was that ultra-low aspect ratio wings in ground effect were investigated. As mentioned in section 4.4 the high pressure at the root of the wing drove a spanwise flow towards the wingtip.

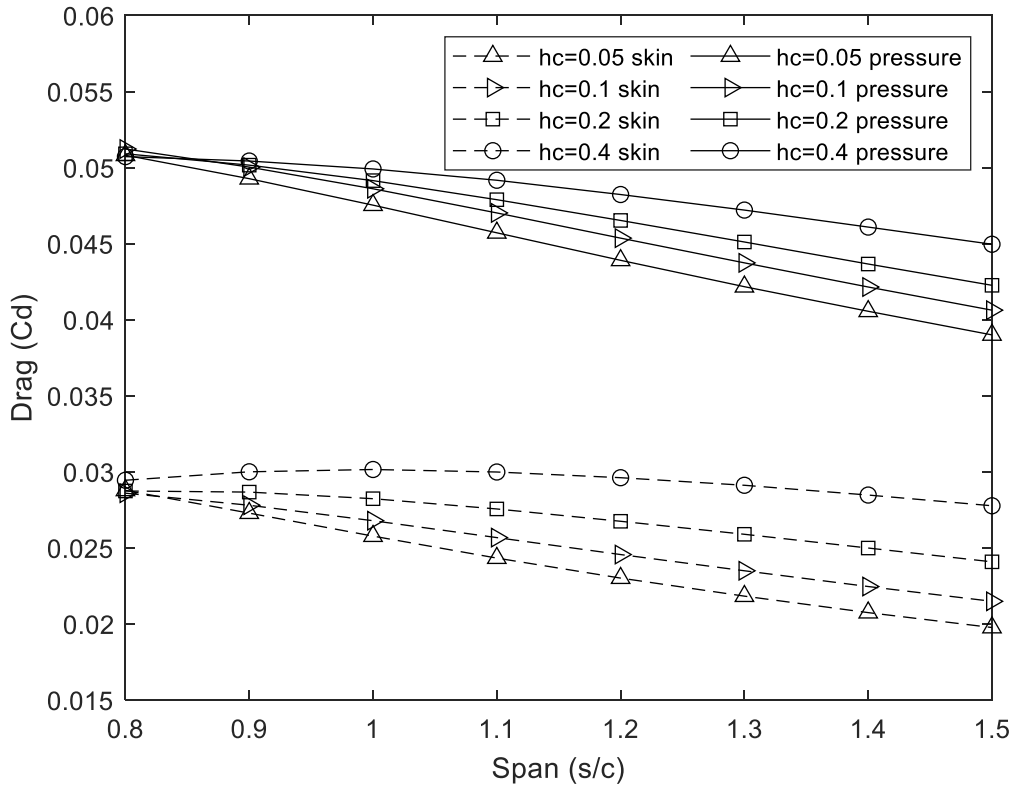

Figure 6.40: Span morphing skin friction and pressure drag for optimised NACA6409 wing.

This can be seen in Figure 6.41 when looking at the distance from the edge of the high-pressure zone to the wingtip. For the 80% start location the pressure varies across the entire span compared to the 150% span where the pressure only varies near the wingtip. This means for the larger span wings that there is less of a spanwise flow, therefore, there is less friction drag and therefore the drag is reduced. For the high aspect ratio wing seen in (Ajaj et al., 2012) the spanwise flow remains a similar length therefore the lift increased as the span increased in the study in freestream (Ajaj et al., 2012).

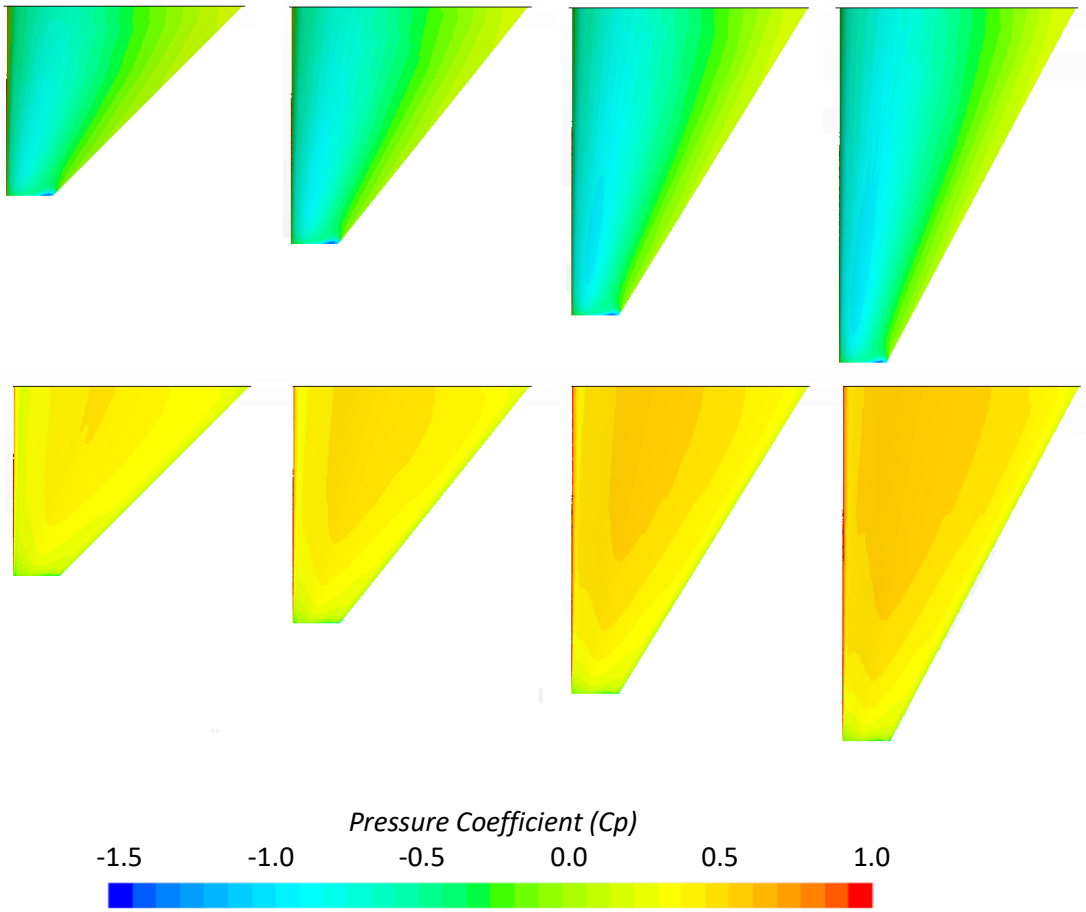

Figure 6.41: NACA6409 at 4 degrees AoA in 10% GE upper surface (top) and lower surface (lower) at 80% span (left), 100%, 130% and 150% span (right) pressure coefficient.

Analysing the surface pressure coefficient (Figure 6.41) shows the upper surface had little impact from the span morphing, as the span increased the area of suction increased which increased the overall lift. On the lower surface, however, the pressure coefficient is significantly affected by the span. It was identified in section 4.4 that the wingtip induces a spanwise flow which affected the pressure coefficient on the lower surface. Increasing the span resulted in a smaller proportion of the wing lower surface being affected by the wingtip vortex. The lower surface pressure shows the 130% and 150% span had a higher-pressure coefficient at the mid-span compared to the 80% and 100% span. In the rectangular wing study, the higher pressure beneath the wing feeds the wingtip vortex. For the optimised however, it was seen in section 4.5 that due to the forward seep that most of the streamlines left the trailing edge rather than feeding the wing tip vortex. This was the same for the span where an increased span meant the flow left the trailing edge rather than feeding the wingtip vortex.

For the optimised wing with a tip chord of 20% of the root chord, the vorticity was analysed on a plane (Figure 6.42) at a 30% distance of the root chord from the leading edge. It was observed increasing the span has minimal impact on the wingtip vortex. Both the diameter and vorticity of the wingtip vortex remained constant when varying the span. Increasing the span only moved the

wingtip vortex outboard as the wingtip moved outboard. This showed higher aspect ratio wings are less influenced by the wingtip vortex and have less induced drag from the wingtip vortex.

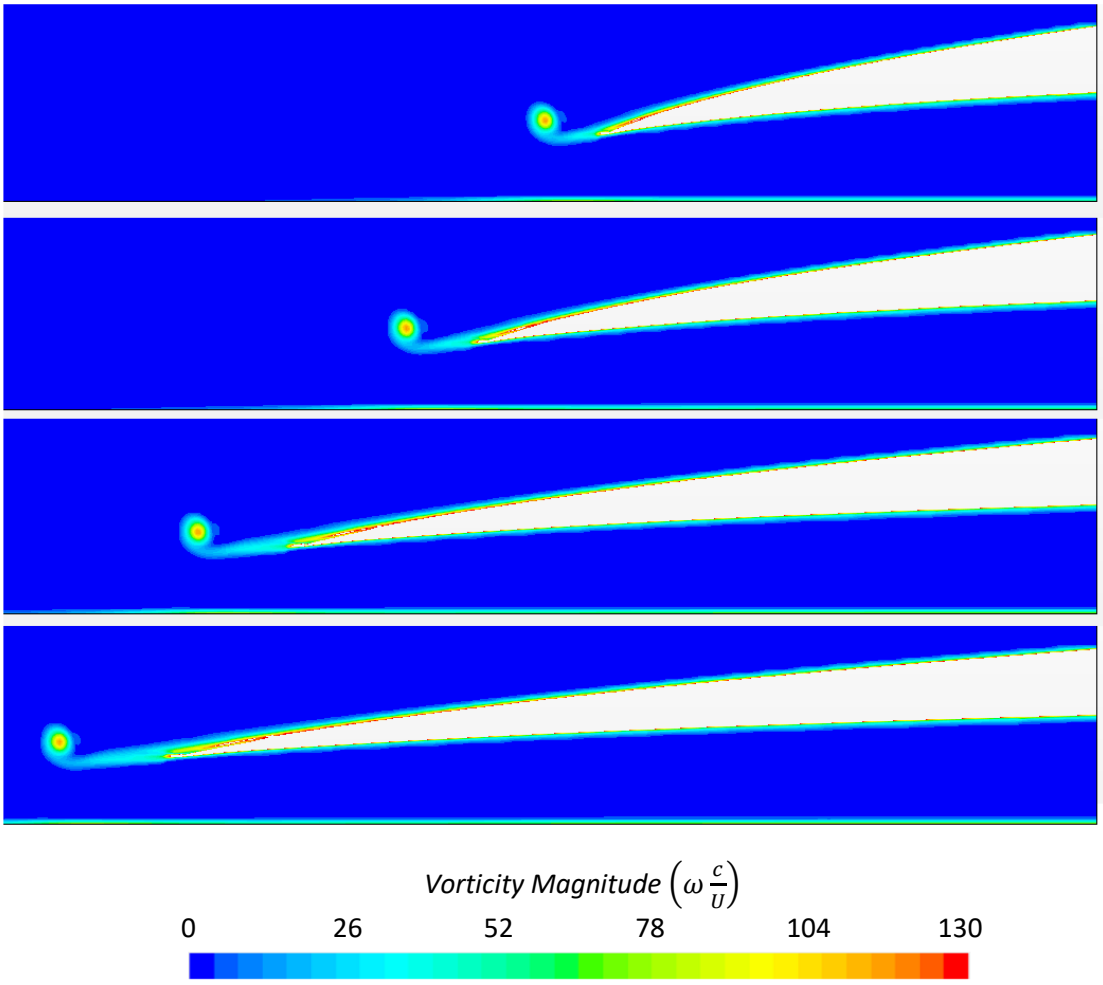

Figure 6.42: NACA6409 at 4 degrees AoA in 10% ground effect at 80% (top), 100%, 130% and 150% (lower) span showing vorticity at 30% of the root chord from leading edge.

6.6 Summary

First, in this section, the size of the morphed section in the span direction was analysed by varying the inboard and outboard span start location with the FishBAC morphing applied in the camber direction at a start location of x_s = 80%. It was found that full-span morphing allowed smaller deflection than partial-span morphing to achieve the same levels of lift. For full a morphed trailing edge at a deflection of 2.5% it was seen a smaller morphed section along the span was more aerodynamically efficient. Partial span morphing saw extra vortices appear on the transition section between the non-morphed and morphed part of the wing.

Next, a full-span morphing was applied to the optimised wing from section 4.5 where different start locations at the root and tip were investigated. It was seen that a later start location of both

the root and tip in the chord direction produced the highest lift but an earlier start location at the root without morphing the tip showed the highest aerodynamic efficiency.

Throughout the study the FishBAC morphing was only applied in the chord direction, extending on literature where tiltable wingtips were investigated the FishBAC morphing was applied in the spanwise direction. It was seen morphing the wingtips dramatically improve the lift and reduced the drag compared to the non-morphed wing at the same ground clearance. Also, an earlier morphing start location resulted in a higher lift as the trailing edge was brought closer to the ground which also reduced the downwash which reduced induced drag.

Lastly, in this chapter span morphing was investigated to increase the span. Typically, WIG craft have a low aspect ratio due to low span length as a large span limits the roll of the craft before a wingtip touches the ground which flying above water could cause the craft to crash. It was seen that large spans increased the aerodynamic efficiency, therefore UAV crafts using morphing wings could have a high span for cruising and a low span to allow manoeuvrability.

Chapter 7 Morphing Effect on Aircraft Performance

7.1 Introduction

In this study, CFD investigations were carried out on aerofoils in ground effect and morphing was applied to the NACA6409 to improve the performance of the aerofoil in ground effect. Morphing was also applied in three dimensions to increase the span and apply the FishBAC morphing in the span direction to investigate morphing wingtips. So far in this study, gains in aerodynamic performance from applying the various morphing types have been quantified in terms of aerodynamic efficiency. This chapter shows these gains applied to a wing in ground effect UAV in terms of flight time (endurance) and flight distance (range).

7.2 UAV Overview

To be able to quantify the endurance and range gains, an aircraft first need to be selected and due to aircraft regulations, the work was applied to UAV craft. The UAV used in this study was shown in Figure 6.1 which is a wing in ground effect craft with a 1.7m span, length of 1.3m, root chord of 0.8m and total a weight of 8.02kg. The construction of the craft was mostly carbon fibre except for control surfaces which were 3d printed, electronics, fasteners, and wing ribs. The use of carbon fibre reduced the total weight and increased the strength of the craft. A unique feature was the wings and tail which compromised of wood ribs and a carbon fibre structural skin. The skin eliminated the need for spars and reduced the weight of the craft.

Figure 7.1: Wing in Ground Effect UAV.

The aircraft used an electric ducted fan unit for propulsion which was located within the fuselage with the exhaust at the rear of the craft and the inlet for the fan on top of the craft seen by the large inlet scoop. The EDF unit is powered by two 6s lithium polymer battery packs wired in parallel supplying 22.2v and 8000mAh. Two separate lithium polymer power packs were used to power the receiver and servos on the craft for dual redundancy along with a Spektrum AR9110 which also uses dual redundancy. Three separate satellite receivers were placed in different locations on the craft to ensure at least one receiver is aligned with the transmitter antenna. Due to the rapid changes in lift due to ground effect causing the craft to be sensitive for the pilot to fly, a stabilisation unit was incorporated into the electronics to assist with roll and pitch.

7.3 CFD set-up and Mesh Independence

CFD analysis was carried out on the UAV to determine the lift and drag of the craft with each wing configuration which can then be used in the range and flight time equations. The UAV required a separate mesh independence study and CFD set-up. CFD of the UAV was carried out using steady-state RANS with the k-omega SST model. The aircraft was symmetrical; therefore, half the model was simulated. The inlet of the domain was set to velocity inlet, the outlet set to pressure outlet and the domain walls set to slip. The ground was set as wall condition and a tangential velocity vector was applied to the floor to simulate a moving ground set to the freestream velocity. The size of the domain was 5 lengths upstream, 15 lengths downstream, 4 lengths above and 5.4 lengths wide. The ground plane distance was set according to the ground clearance. The freestream velocity was set to match the Reynolds number of 320,000 used throughout this study.

The UAV was powered by an EDF fan which was modelled using a pressure outlet on the duct inlet on top of the craft and a velocity inlet on the duct outlet with the velocity set according to mass conservation. The CFD set-up had the air intake as a pressure outlet and the fan outlet set as a velocity inlet. To determine the boundary conditions for the inlet and outlet an experiment was carried out using the UAV shown by the schematic (Figure 7.2). The fan outlet pressure was measured using a Pitot tube and the forward force was measured using a load sensor. Two rollers were used to reduce the friction between the UAV and the ground.

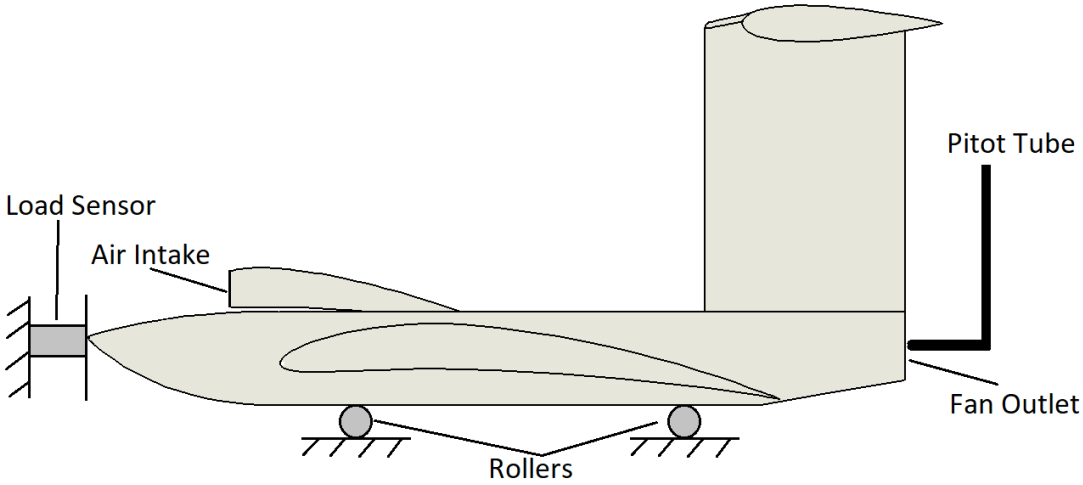

Figure 7.2: Schematic of UAV measurement test.

The pressure was then converted into velocity using Bernoulli's equation and shown against the calculated freestream and intake velocity in Figure 7.3 along with the measured thrust as the throttle position was varied. The exhaust velocity on the velocity outlet boundary could be set according to the freestream velocity used in this study to achieve a Reynolds number of 320,000. By applying conservation of mass through the duct system, the intake velocity was plotted in Figure 7.3.

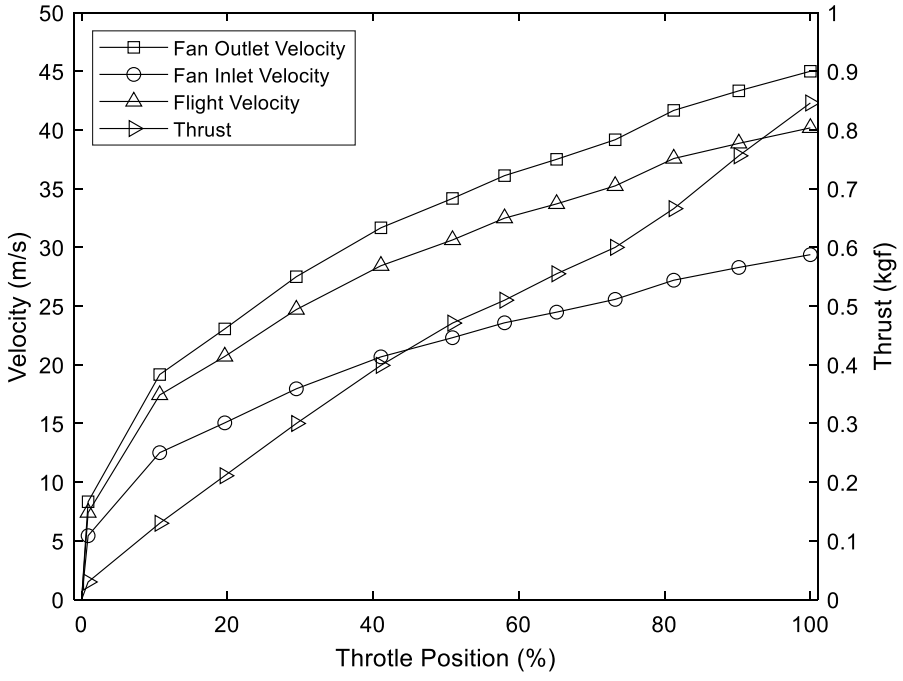

Figure 7.3: UAV flight and fan air velocity and thrust against throttle position.

A mesh independence study was carried out for the UAV to ensure the solution was independent of the mesh size. The mesh at the wall of the UAV was sized to keep a y^+ of approximately 1 as recommended in the CFD user manual for the k-omega SST model (*User Manual Star CCM+ 14.04.013*, 2019). Refinement was applied around the UAV to restrict the growth of cells around

the UAV in the near field. The cells were allowed to grow to the far field domain walls to reduce the cell count, the final mesh was shown in Figure 7.4.

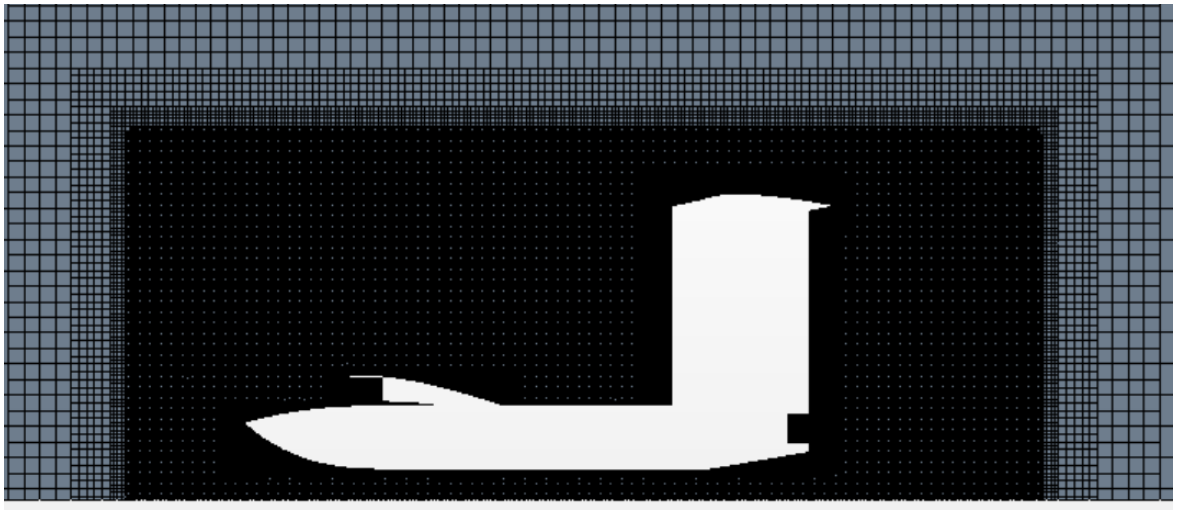

Figure 7.4: UAV slice of 3D mesh on the symmetry plane.

The mesh independence study of the UAV was carried out using the method explained in section 4.2.1. Three meshes were listed in Table 7.1 for the fine, medium, and coarse mesh for the entire UAV. For the size of the mesh and the corresponding lift and drag coefficients, it was found the zero-grid spacing for the lift was Cl = 0.688 and Cd = 0.663.

Table 7.1: RANS mesh cell count with corresponding lift and drag values in two dimensions.

Mesh Refinement	Cell Count	Cl	Cd
Fine	124880340	0.688	0.667
Medium	31521470	0.692	0.676
Coarse	11999212	0.721	0.704

Using the grid convergence index the zero-grid spacing was checked to ensure the zero-grid spacing was an asymptote. The values were approximately 1 therefore the zero-grid spacing was confirmed. The zero-grid spacing lift and drag values were then used to check the error for each of the mesh refinements shown in section 4.2.1. The fine mesh was selected and carried forward for the UAV study as the medium mesh showed a large error for the drag.

Table 7.2: RANS mesh size error in two dimensions.

Mesh Refinement	Cl error%	Cd error %
Fine	0.06	0.65
Medium	0.55	2.02
Coarse	4.64	6.44

7.4 Aircraft and Wing Data

Several wing configurations were tested and compared against a baseline rectangular wing to improve the aerodynamic performance. The total lift and drag of the wing configurations and UAV combined are shown in Table 7.3. Summarising the wing configurations in Table 7.3, a rectangular wing in freestream and ground effect were initially listed which were a NACA6409 profile with an aspect ratio of 2. The optimised wing was the wing identified in section 4.5 that a tip chord of 20% of the root chord and an angle of attack of 4-degree at the root and 6-degree at the tip. Increasing the span of the optimised wing was investigated in section 6.5 and was found the that 150% produced the highest aerodynamic efficiency. In section 6.4 the morphing was applied in the spanwise direction where the deflection of the wingtip sealed the high pressure beneath the wing increasing lift and reducing induced drag. Periodic morphing at a Strouhal number of 3.58 starting the morphing at 25% from the leading edge and displacing the trailing edge by 1% was seen to have the highest aerodynamic efficiency at 4 degrees angle of attack in two dimensions. This was then extended and was applied to the wing in three dimensions for the rectangular, optimised and optimised 150% span using lifting line theory. All the wings in ground effect were carried out at a ground clearance of 10% of the chord. Figure 7.5 shows the baseline rectangular wing and the optimised wing on the UAV.

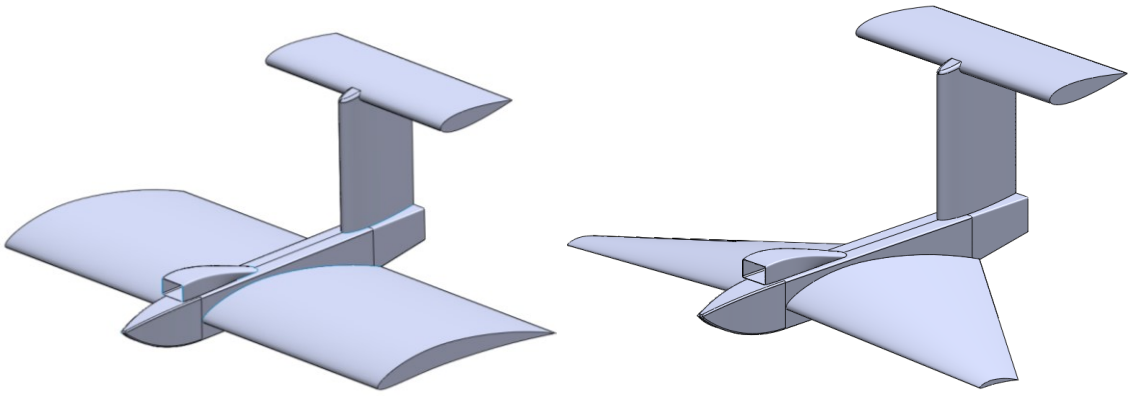

Figure 7.5: UAV with rectangular (left) and optimised (right) wings.

Table 7.3: Aircraft total lift and drag for wing configurations tested in this study.

Wing CAD model	Wing	Cl	Cd	Cl/Cd
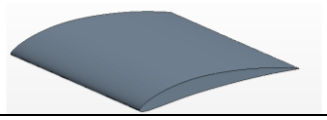	Freestream	0.532	0.0582	13.57
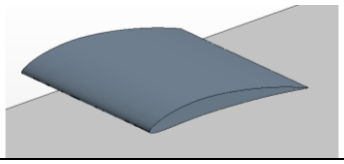	Rectangular Baseline	0.726	0.0548	14.57
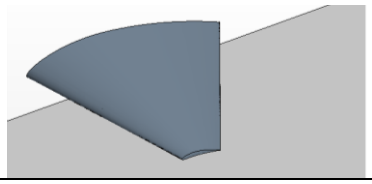	Optimised	0.826	0.0418	22.7
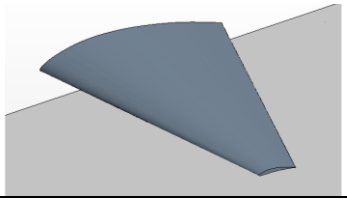	Optimised with 150% span increase	0.963	0.0364	31.43
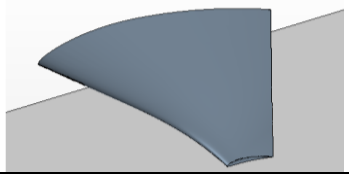	FishBAC applied in span direction	0.862	0.0364	32.43
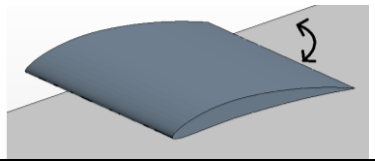	Periodic Morphing	0.817	0.0543	15.04
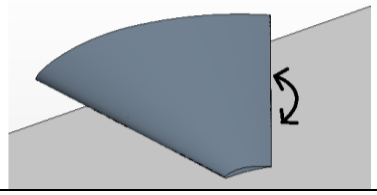	Periodic Morphing Optimised Wing	0.927	0.0365	25.38
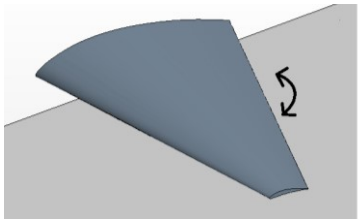	Periodic Optimised 150% Span	1.085	0.0294	36.96

Real aircraft wings are of finite length and WIG craft wings typically have very low aspect ratios so three-dimensional effects are extremely important. Although the periodic morphing was carried out in two dimensions in section 5.5, this was a good initial analysis due to the vast number of

variables including morphing start position, frequency, trailing edge deflection, angle of attack and ground clearance due to lower computational costs compared to three dimensions. Due to high computational costs and time constraints, the periodic morphing data was data extrapolated to three dimensions using lifting line theory.

The effect of finite span can be seen in Figure 7.6, the three-dimensional wing had a reduction in lift. The main reason for this was due to the wingtip vortices providing a downward pressure on the upper surface which reduced the total suction on the upper surface. As the wingtip vortices are located at the wingtips, the greatest effect on the pressure distribution was at the wingtip. This caused a non-uniform lift distribution along the span with the total lift produced less than a 2d aerofoil profile.

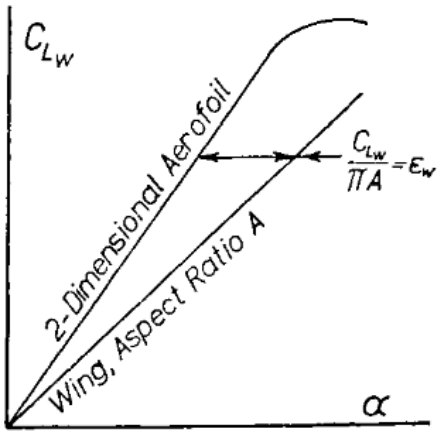

Figure 7.6: Lift infinite and finite span vs angle of attack (Irving, 1966).

Prandtl's lifting line theory is a simple solution for predicting the lift of an upswept three-dimensional wing with assumptions of inviscid and incompressible flow described in section 3.3. However, the estimation for the lift using Prandtl's lifting line theory was not valid due to the low aspect ratio wing (Kundu et al., 2016) used in this study. Prandtl's lifting line theory was adapted by Helmbold (1942) and an approximation was derived (Eq 7.1) for low aspect ratio wings where a_o is lift in two dimensions and Λ is the sweep angle of the wing.

$$a = \frac{a_o \cos \Lambda}{\sqrt{1 + \left(\frac{a_o \cos \Lambda}{\pi AR}\right)^2} + \frac{a_o \cos \Lambda}{\pi AR}} \tag{7.1}$$

$$\frac{dCl}{d\alpha} = a \tag{7.2}$$

Equation 7.2 shows the gradient of the lifting line seen in Figure 7.6 and the equation Eq. (7.1) previously mentioned represents the gradient of the lifting line. Integrating Eq. (7.2) resulted in an

integration constant, setting the angle of attack to zero resulted in the constant equalling the lift in two dimensions at zero degrees angle of attack. Substituting Eq. (7.1) into the integrated Eq. (7.2) yields Eq. (7.3). The value a_o represents the gradient from the 2d lift curve and along with the lift of the two-dimensional aerofoil at zero degrees AoA, the value of lift can be estimated in three dimensions. The estimated value using lifting line theory for three dimensions was compared to the non-morphing CFD carried out in this study, and a small correction factor of 0.68 was used to adjust the gradient of the lifting line to match the CFD. The data was added to Table 7.3 using Eq. (7.3) for both the straight and tapered wings in three dimensions using periodic morphing.

$$Cl = \left[\frac{a_o \cos \Lambda}{\sqrt{1 + \left(\frac{a_o \cos \Lambda}{\pi AR}\right)^2} + \frac{a_o \cos \Lambda}{\pi AR}}\right] \alpha + Cl_{2D,\alpha=0} \tag{7.3}$$

The total drag of the wing is a sum of the induced drag and section profile drag shown in Eq. (7.4). The Oswald efficiency is represented by *e* which is a span efficiency accounting for the non-elliptical lift distribution of general shaped wing (J. D. Anderson, 2008). This generally is difficult to determine but analytical relations do exist (Samoylovitch & Strelets, 2000) however as simulations have been carried out in three dimensions the efficiency can be determined. The value of *e* was found to be 0.134 for a straight wing with an aspect ratio of 2 and a value of 0.102 for a tapered wing with an aspect ratio of 3.33 and a tip chord of 20%. With the estimated lift value determined in this section for the straight and optimised wings and with the Oswald efficiency determined, Eq. (7.4) was used to estimate the total drag for the straight and optimised periodic morphing wings from the two-dimensional data.

$$C_D = C_{D\_profile} + C_{D\_induced} = C_{D\_profile} + \frac{C_L^2}{eAR} \tag{7.4}$$

7.5 Effect on UAV range and Endurance

The range is a measure of how far an aircraft can travel and the endurance is the flight time. Traditionally this is calculated using the take-off and landing weight of an aircraft for liquid fuel aircraft for both piston and jet aircraft (J. D. Anderson, 1999; McCormick, 1995; Traub, 2011) however the UAV used in this study was electric powered and therefore has a constant weight during flight. The performance of an electric aircraft was presented by Traub (2011) for the endurance in hours Eq. (7.5) and the range in Eq. (7.6) which considers the propulsion system and the battery behaviour and effective capacity depending on the current draw. The values for the battery and UAV values are presented in Appendix A.6 which are used in Eq. (7.5).

$$E = \left[\frac{\eta V C_{batt}}{\frac{1}{2}U^3 S C_D + \frac{2W^2 K}{\rho U b}}\right]^{n_{batt}} \quad 7.5$$

$$R = EU \quad 7.6$$

Using the equation for the endurance (7.5) and range (7.6), the range and endurance of the UAV with each wing configuration were plotted in Figure 7.7 and Figure 7.8 for different flight speeds for the WIG craft.

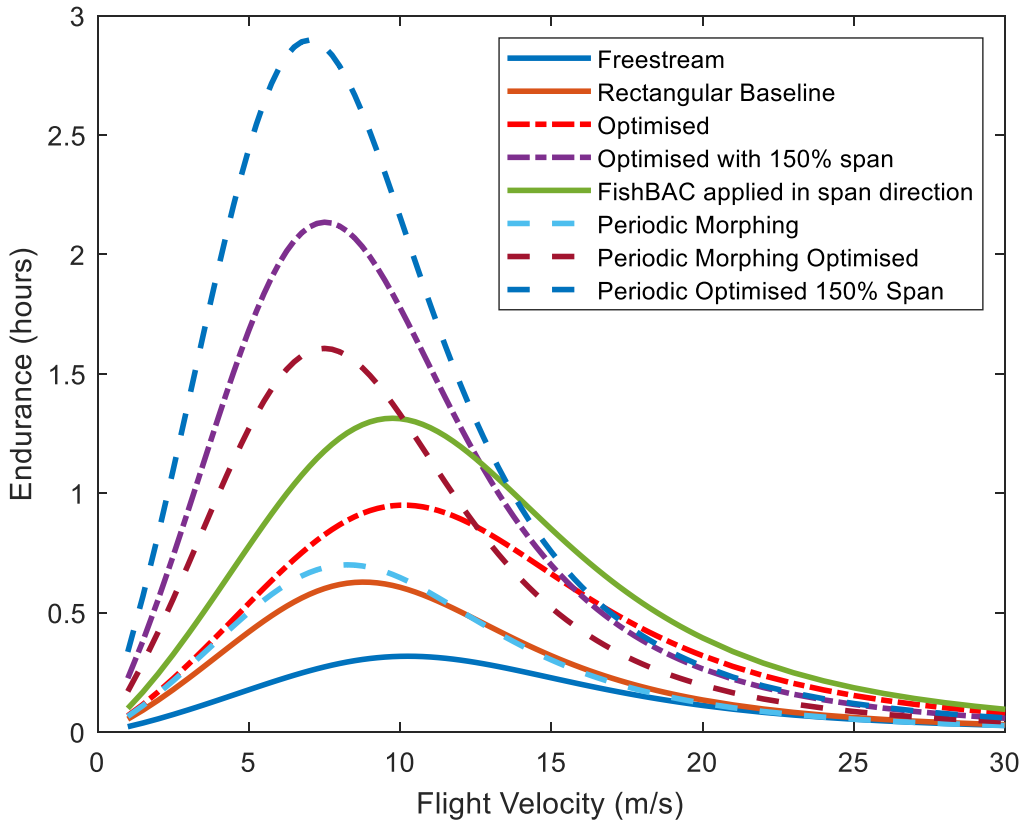

Figure 7.7: Endurance of wing configurations on UAV.

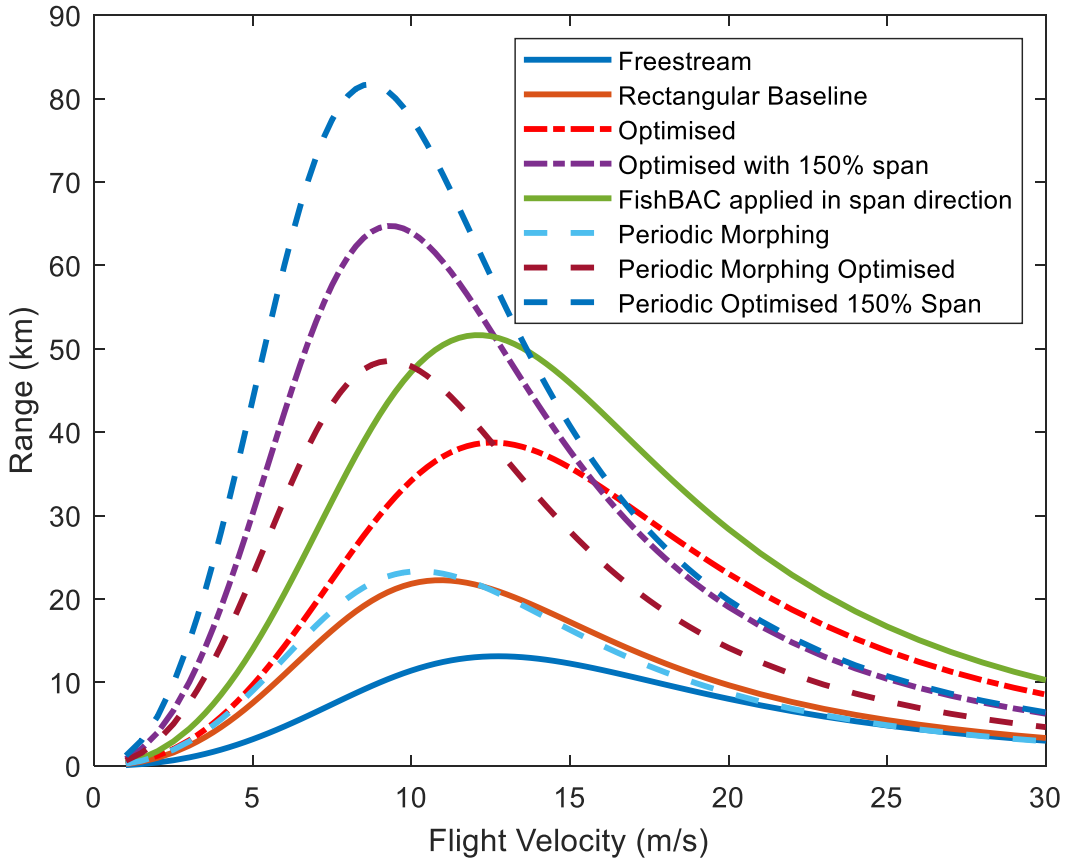

Figure 7.8: Range of wing configurations on UAV.

The baseline rectangular wing in freestream was seen to have a peak endurance of 0.31 hours (Figure 7.7) at a flight velocity of 11m/s and a range (Figure 7.8) of 13.12km at a velocity of 13m/s. Bringing the wing into ground effect with a clearance of 10% chord has seen that the endurance increased to 0.63 hours at 9m/s and range increased to 22.25 at 11m/s. This was an increase in endurance of 103.2% and range of 69.5% from bringing the wing from freestream to ground effect which shows the huge potential and benefits of flying in ground effect. It was seen the peak endurance and range occurred at a lower flight velocity as the wing was brought into ground effect.

In section 4.5 , an optimisation study was carried out where it was found a forward wing tip position with a 20% tip chord had higher performance than a rectangular wing. In ground effect, the optimised wing showed a peak endurance of 0.95 hours at 10m/s and a range of 38.65km at 13m/s which was an improvement of 50.8% endurance time and an increase in range of 73.7% compared to the rectangular wing in ground effect.

WIG craft typically have low aspect ratio wings to allow the craft to roll without a wingtip touching the ground which in water can be especially dangerous causing the craft to crash, however, larger spans increase the aerodynamic efficiency. By applying span morphing the WIG craft can have a low span for manoeuvring and a large span for cursing. A span increase of 150% caused the peak

endurance of 2.12 hours at 7m/s and a range of 63.97km at 10m/s which corresponded to an increase in the endurance of 123.2% and a range of 65.6% compared to the rectangular wing in ground effect. At 150% span, the optimum flight speed was reduced by 2m/s for the endurance and 4m/s for the range.

Applying periodic morphing for the rectangular wing showed an endurance of 0.7 hours at 8m/s and a range of 23.29km at 10m/s, this was an increase of 11% endurance and 4.7% range increase. When considering the energy to periodically morph the wing, as well as the gain in the complexity of the system, the gains seen for the rectangular wing, do not show significant performance improvement compared to the baseline rectangular wing in ground effect. However, applying the periodic morphing to the optimised wing showed much larger gains in range and endurance. The optimised wing with periodic morphing had a peak endurance of 1.59 hours at 8m/s and a range of 48.4km at 9m/s which was an increase of 252.3% endurance time and 217.5% increase in range compared to the baseline rectangular wing in ground effect. The 150% span with periodic morphing showed an endurance of 2.9 hours at 9m/s and a range of 81.46km at 9m/s which was an increase of 460.3% endurance and 362% in range compared to the baseline wing. Comparing the optimised wing to the optimised wing with periodic morphing showed a gain in the endurance of 0.64 hours (a gain of 67%) and a gain in the range of 9.75km (a gain of 20%) showing the potential for periodic morphing wings in ground effect.

Finally applying FishBAC morphing in the spanwise direction showed an endurance of 1.31 hours at 10m/s and a range of 51.64km at 12m/s which was an increase of 132.1% endurance and 107.9% increase in range compared to the baseline rectangular wing ground effect.

Reductions in flight velocity for optimum range and endurance were seen for the rectangular wing in ground effect compared to freestream. This was also seen for the optimised 150% span in ground effect compared to the optimised wing in ground effect. Improving the endurance and range further by applying periodic morphing showed no further reductions in flight speed where the peak endurance and range occurred.

It was seen for all the wings that a peak endurance (Figure 7.7) and peak range (Figure 7.8) occur however the peaks of maximum endurance and maximum range do not coincide with each other. This means the mission of the craft needs to be either selected for maximum range or maximum endurance. Figure 7.7 and Figure 7.8 also show that higher-performing wings are more sensitive to flight velocity. For the rectangular wing in freestream which has a peak endurance of 0.31 hours at 11m/s and peak range of 13.12km at 13m/s, if the flight velocity was varied either side of these two corresponding optimum velocities, the endurance and range would vary a minimal amount. However, for the highest performing wing (periodic morphing 150% span) there is a much larger variation in endurance and range as the flight velocity is varied. For the rectangular

wing, decreasing the flight velocity by 2m/s showed a decrease in endurance of 0.03 hours and a decrease in range by 0.67km compared to the periodic morphing 150% span wing the endurance reduced by 0.16 hours and range reduced by 11.56km. Increasing the flight velocity by 2m/s for the rectangular wing decreased the endurance by 0.02 hours and range by 0.52km compared to the optimised 150% periodic morphing where the endurance was reduced by 0.36 hours and the range reduced by 4.47km. This shows either side of the optimum velocity, the range and endurance reduced a greater amount for higher-performing wings. Also reducing the velocity from the corresponding optimum velocity saw a much greater reduction in endurance and range compared to increasing flight velocity from the optimum velocity.

It was assumed that the WIG craft flew at a constant flight velocity for comparison of the wings however in reality there will be a high current draw initially as the craft takes off during acceleration and as the velocity changes during flight. The current draw (Eq. 7.7) at different flight velocities is given by the power required to maintain the flight velocity divided by voltage and power system efficiency.

$$i = \frac{P_{req}}{V\eta} = \frac{\left(0.5\rho U^3 b C_{D0} + \frac{2W^2K}{\rho U b}\right)}{V\eta} \tag{7.7}$$

For the peak endurance and range, the corresponding current draw was shown in Table 7.4. The range and endurance were lowest in freestream which corresponded to the highest current draw. Bringing the UAV into ground effect reduced the current draw by approximately 5amps. The lowest current draw was seen for the periodic morphing at a 150% span of 2.31 Amps when flying at the peak endurance velocity and 2.24 Amps for the peak range.

Table 7.4: Current draw at peak endurance and range.

Wing	Current at Max endurance (Amps)	Current at Max range (Amps)
Freestream	12.30	11.10
Rectangular Baseline	7.07	6.57
Optimised	5.39	5.08
Optimised with 150% span	2.85	2.79
FishBAC applied in span direction	4.19	4.05
Periodic Morphing	6.66	5.96
Periodic Morphing Optimised	5.58	4.64
Periodic Optimised 150% Span	2.31	2.24

Applying the periodic morphing to the rectangular and 150% span wing decreased the current draw. Applying periodic morphing to the optimised wing showed a reduction in flight velocity at which the peak endurance and range occurred. For the optimised wing the velocity for peak endurance reduced from 10m/s for non-morphing to 8m/s for morphing and. For the range this reduced from 11m/s for non-morphing to 10m/s for morphing. It was seen that the current is

dependent on velocity Eq. (7.7) and because of the cubic term, reducing the flight velocity caused an overall increase in power required to sustain the flight velocity.

Initially, it was seen there was a high current draw at 1m/s, especially in freestream where the current draw was substantially higher than ground effect. The current draw reduced for all cases as the flight speed increased with the 150% span and periodic 150% span showing the lowest current draw. At approximately 17m/s the three wings (FishBAC applied in span, optimised, and optimised with periodic morphing) which show similar current values, become the lowest current drawing. Figure 7.9 shows the battery current draw for the UAV wings across the velocity range.

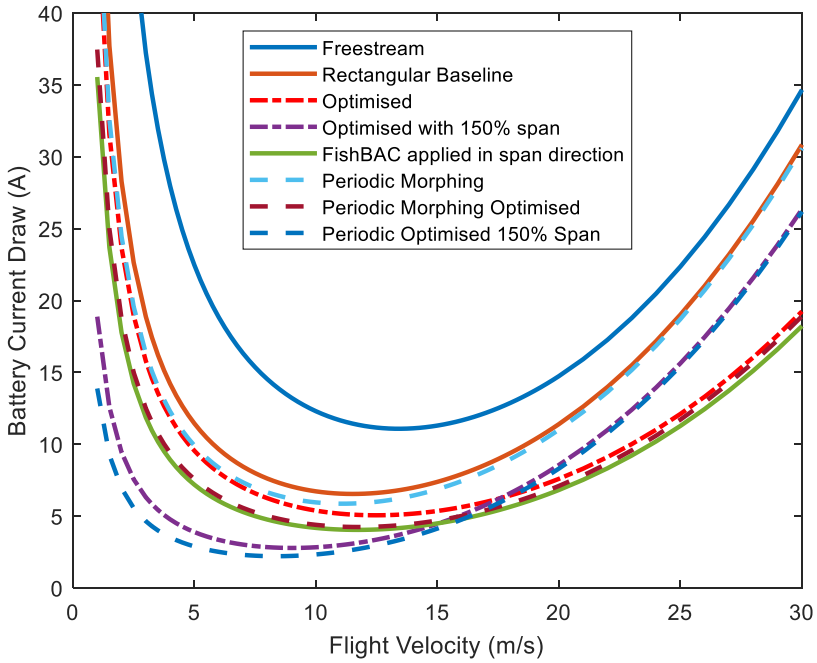

Figure 7.9: UAV battery current draw.

7.6 Summary

In this chapter, the gains in aerodynamic efficiency of the different wing configurations seen throughout this study have been applied to a UAV and the gains in performance have been quantified in terms of endurance and range. The UAV selected had a 1.7m wingspan and a mass of 8.02kg made from carbon fibre. The craft used an electric ducted fan propulsion system which used literature formulation for endurance and range, the flight time and distance the aircraft travelled were compared for each wing configuration.

Overall, it was seen that applying periodic morphing to the optimised wing in ground effect had increased the endurance by 252.3% and range by 217.5% compared to a rectangular non-morphing wing in ground effect. For cruising further improvements can be made by increasing the

span to 150% which caused an improvement in endurance by 460.3% and range by 362% compared to the rectangular wing ground effect.

Chapter 8 Conclusion

8.1 Overview

In this study, it was identified in the literature review that wings in ground effect and morphing wings had been individually studied heavily. This study aimed to combine these two areas of research to investigate morphing wings in ground effect to improve the aerodynamic efficiency of a wing in ground effect. The research intended to reduce fuel consumption of wing in ground effect craft through morphing techniques; however, due to manned aircraft regulations, this was demonstrated on a UAV. This section highlights this study's key findings and makes recommendations for future work in this area of research.

8.2 Key findings

First, in this study, an aerofoil selection process was carried out to see which aerofoil profiles work best in ground effect. In two dimensions, thin and high-camber concave aerofoils have high aerodynamic efficiency due to having the highest lift values. The high-camber concave aerofoils produced high lift due to the higher distance between the ground and the aerofoil lower surface compared to the distance between the trailing and ground. In three dimensions, the high-camber aerofoils produced the highest lift, showing the highest levels of high pressure beneath the wing. This high pressure beneath the wing for the high-camber aerofoils fed the wingtip vortex a greater amount which caused the highest levels of drag compared to low-camber aerofoils. Therefore, a compromise between high lift and high aerodynamic efficiency must be made during aerofoil selection, as well as considering the thickness of the aerofoil for structural considerations. In this study, the NACA6409 aerofoil was chosen from over 30 aerofoils as this aerofoil showed good compromise between lift and efficiency as well as being of substantial thickness for structural loads and storage or morphing systems.

FishBAC morphing was applied to a two-dimensional NACA6409 using steady RANS simulations. The Kutta condition fixed the trailing edge pressure, which caused the pressure to increase upstream of the trailing edge on the lower surface as the trailing edge deflection was increased, enhancing ground effect.

Throughout the study, it was seen that small angles of attack are used due to the earlier stall of wings in the ground effect. For angles of attack up to 4 degrees, it was seen small trailing edge deflections between 0.5% and 1% of the chord can increase the aerodynamic efficiency when applying the FishBAC morphing. For wings in ground effect, stall occurred earlier compared to

freestream; applying morphing to the aerofoil caused an even lower stall angle of the wing in ground effect. Therefore, morphing wings in ground effect should be run at low angles of attack to prevent stall. Comparing the morphing start location in the chord direction showed varying the start location only varied the pressure between the trailing edge and the morphing start location. Therefore, a later morphing start location would cause a greater pressure rise between the trailing edge and the start location. This caused a greater amount of lift for a later start location due to the greater amount of higher pressure on the lower surface. Replacing traditional control surfaces with camber morphing has shown camber morphing to require smaller deflections for the same lift gain, reducing drag and overall gains in aerodynamic efficiency.

Periodic morphing was applied in two dimensions using the FishBAC morphing in a sinusoidal motion. It was found for a Strouhal number of 3.58 and morphing deflection of 1% chord that the aerodynamic efficiency increased by 81%, lift increased by 15% and drag reduced by 37%. A key finding here was that the periodic morphing aerofoil caused Von Karman wake shedding, which interacted with the ground plane and produced thrust. This was different to literature as it was seen in freestream that reversed Von Karman produced thrust whilst Von-Karman shedding increased drag. However, in this study, an extra phenomenon was seen. The interaction between the Von-Karman shedding and the ground motion outweighed the increased drag mechanism of the interaction of the counter-rotating vortices.

An optimisation study was carried out for the three-dimensional wing, where it was found the greatest factor in performance was the wingtip vortex. At the wing root, a lower angle of attack had a lower pressure compared to higher root angles of attack. Therefore, there was a lower spanwise flow on the lower surface feeding the wingtip vortex, which increased the aerodynamic efficiency. A tip chord of 20% of the root increased the aspect ratio, which was of advantage in ground effect as WIG craft typically have low aspect ratios. The small tip chord with forward wing tip position reduced the spanwise flow even further, which reduced the amount of flow feeding the wingtip vortex, which reduced drag and increased the aerodynamic efficiency.

In three dimensions, the proportion of span that camber morphing was applied was varied by varying the start and end location along the span. A smooth transition was modelled between the non-morphed and morphed proportion along the span. It was seen applying the camber morphing along the full span length allows for lower trailing edge deflections compared to partial span morphing, which increases the aerodynamic efficiency. Applying the full span length morphing to the optimised wing, the morphing start location in the chord direction for both the root and tip was varied. It was seen that a later start location at both the tip and root had the highest lift, which was also seen for the camber morphing in two dimensions.

The FishBAC morphing was also applied along in the span direction for the optimised wing to morph the wingtips. Two tests were carried out; the first was constant root height varying the wingtip deflection, and the second was keeping a constant wingtip clearance and varying to root ground clearance. The first test found increasing the wingtip deflection in ground effect was found to seal the high pressure beneath the wing, which resulted in higher lift and lower drag. This was more effective the closer the wingtip was to the ground. Starting the morphing earlier in the span direction meant a greater proportion of the wing was closer to the ground compared to a later start location along the span. This was seen to be the opposite for applying the FishBAC morphing in the chord direction, where a later span start location caused higher gains in lift. This was due to the wingtip pressure not being fixed by the Kutta condition, unlike the trailing edge. Therefore, starting the morphing earlier in the span direction caused a greater proportion of the wing to be closer to the ground, which enhanced ground effect. The second test fixed the wingtip clearance at a constant height; FishBAC morphing was applied along the span, varying the root ground clearance to simulate the WIG craft taking off. It was seen the morphed wingtip with constant clearance between the wingtip and ground had a large gain in aerodynamic efficiency across all root ground clearances compared to a non-morphing wingtip.

Span morphing to increase wing aspect ratio was also investigated between 80% to 150% of the original span. It was found a wingspan of 150% had the highest lift and aerodynamic efficiency and lowest drag compared to smaller spans. Increasing the span of the wing using morphing allowed the range and endurance to be increased of the WIG craft in ground effect. Span morphing also allows the wing to be retracted to allow the craft to roll in ground effect without a wingtip touching the ground, which could cause the craft to crash.

Lastly, it was seen throughout this study that the wing performance was quantified in terms of aerodynamic efficiency. To better quantify these gains in performance, the range and endurance of these wings were analysed on a UAV wing in ground effect craft. Bringing a rectangular wing from freestream with a range of 13.12km and endurance of 0.32 hours to ground effect increased the range to 22.25km and the endurance to 0.65 hours, showing the benefits of flying in ground effect. Replacing the rectangular wing with the optimised wing showed the endurance to increase to 0.95 hours and range to 38.65km. Compared to the rectangular wing in ground effect this was an increase of 50.8% in endurance and 73.7% in range for the optimised wing in ground effect. Further gains can be made by applying morphing where periodic morphing applied to the optimised wing increased the endurance to 1.59 hours and range to 48.4km. Applying the periodic morphing to the 150% span increased the endurance to 2.9 hours and range to 81.46km.

8.3 Future Work

In this project, an area of research was identified where there was a gap in the literature which this research project aimed to fill however there are several areas for future research.

- An aerofoil selection study was first carried out; however, this could be further investigated. Rather than using pre-defined aerofoil, shape optimisation could be applied to the aerofoil for different flight conditions and recommendations made for aerofoil shape morphing. Artificial Intelligence and machine learning could also be used to expand the aerofoil selection process to 100s of aerofoils by simulating a select few profiles.
- It was demonstrated in section 5.5 that periodic morphing increased aerodynamic efficiency in two dimensions; however, this was only extended to three dimensions using the lifting line theory due to time and cost constraints. Therefore, further CFD should be carried out in three dimensions with periodic morphing to gain an understanding of the three-dimensional flow characteristics.
- There were an extensive number of variables throughout the study, especially for the periodic morphing, which included angle of attack, ground clearance, Reynolds number, morphing start location, morphing frequency and trailing edge displacement. This was carried out for one aerofoil, so swapping out aerofoil geometry would significantly increase the number of simulations. Running the periodic morphing in three dimensions would also significantly increase the number of variables which also increases the number of simulations. With the advancement of AI and machine learning, simulations could be run, and machine learning used to find a large number of solutions.
- It was seen periodic morphing can reduce separation on the upper surface and increase lift; the periodic morphing was only carried out at 4 degrees angle of attack as it was identified that low angles of attack perform best in ground effect. Future work could look at applying periodic morphing at higher angles of attack in ground effect due to delay stall, which could further increase the aerodynamic efficiency. Also, an increased range of Strouhal numbers and trailing edge deflections could be tested, and the propulsive performance further investigated of periodic morphing aerofoils.
- Periodic morphing was used to delay the stall of the NACA6409 aerofoil using the highest-performing trailing edge deflection and trailing edge displacement found at an angle of attack of 4 degrees. Therefore, varying the trailing edge deflection and morphing frequency can be varied across the range of angles of attack to further improve performance and possibly delay stall. Adding an angle of attack variable would significantly increase the number of variables, so Artificial Intelligence (AI) and machine learning could be used to investigate delaying stall.

- It was assumed in this study that the ground plane was flat and ridged, and although this gives a good understanding of aerodynamics and simplifies the study, in real-world situations, this is very unlikely. Therefore, future work of testing the morphing wings in ground effect can be carried out over defined wavey ground in CFD or experimentally with a UAV in real-world flight testing or water tanks.
- Validation was carried out by using data from other studies; therefore, wind tunnel validation can be carried out to ensure the same flow conditions, set-up and control of uncertainties and errors of the experiment. In section 5.2.1, the validation had to be carried out against other CFD data due to a lack of experimental data; therefore, a wind tunnel study can be carried out to fill the gap in experimental data.
- The stability of wings in ground effect has been known to be a downside of WIG craft since the 1950s seen in the literature review. Due to time constraints, the stability of morphing wings in ground effect was not investigated in this study. Future work would involve an extensive study on the stability of wings in ground effect. This can be carried out experimentally on a UAV where sensors can measure acceleration when pitching the aircraft. Also, stability gyros can be used to maintain stable and level flight as the aerodynamic forces change due to uneven ground and as the aircraft ground clearance varies.
- It was seen in this study that the aircraft range and endurance could be extended using different morphing methods, including increasing span, morphing wingtips and periodic morphing. Flight tests of the UAV can be carried out to confirm these gains in performance as well as identify losses such as servo energy consumption to perform the periodic morphing.

Appendix A

A.1 2D Aerofoil Tabulated Data

NACA0012

AoA	h/c	Cd	Cl	Cm	Cl/Cd	y+
0	0.005	0.02	0.447416	-0.08	19.1	4.6
2	0.005	0.02	-0.04284	0.14	-1.9	0.8
4	0.005	0.02	0.408887	-0.02	26.7	0.9
6	0.005	0.01	0.859433	-0.21	58.6	1.0
8	0.005	0.02	1.13149	-0.33	64.0	1.1
10	0.005	0.04	1.29261	-0.40	32.7	1.1
12	0.005	0.20	1.6896	-0.52	8.5	1.0
14	0.005	0.26	1.75262	-0.54	6.8	1.0
16	0.005	0.46	2.17763	-0.72	4.7	0.9
18	0.005	0.66	2.2692	-0.94	3.4	0.8
0	0.01	0.03	-0.45941	0.19	-18.3	0.7
2	0.01	0.02	0.003874	0.07	0.2	0.7
4	0.01	0.01	0.464129	-0.09	33.7	0.9
6	0.01	0.01	0.793343	-0.20	55.3	1.0
8	0.01	0.02	1.02545	-0.28	60.4	1.1
10	0.01	0.02	1.18208	-0.34	50.3	1.2
12	0.01	0.18	1.5786	-0.45	8.7	1.0
14	0.01	0.25	1.69368	-0.50	6.9	1.0
16	0.01	0.42	2.06699	-0.62	5.0	1.0
18	0.01	0.65	2.3146	-0.91	3.6	0.9
0	0.02	0.02	-0.22233	0.09	-13.9	0.7
2	0.02	0.01	0.160773	-0.02	11.8	0.7
4	0.02	0.01	0.473394	-0.11	35.5	0.8
6	0.02	0.01	0.727717	-0.19	50.7	0.9
8	0.02	0.02	0.930994	-0.25	55.7	1.0
10	0.02	0.02	1.08712	-0.30	51.0	1.2
12	0.02	0.11	1.25364	-0.31	10.9	1.0
14	0.02	0.24	1.63471	-0.45	6.9	1.0
16	0.02	0.28	1.61427	-0.46	5.7	1.0
18	0.02	0.56	2.20022	-0.74	3.9	0.9
0	0.04	0.01	-0.05379	0.02	-4.0	0.7
2	0.04	0.01	0.215217	-0.05	16.6	0.7
4	0.04	0.01	0.455187	-0.11	34.1	0.8
6	0.04	0.01	0.673451	-0.17	46.3	0.9
8	0.04	0.02	0.858855	-0.22	51.0	1.0
10	0.04	0.02	1.0184	-0.27	49.2	1.1
12	0.04	0.03	1.13015	-0.30	37.5	1.2
14	0.04	0.21	1.51309	-0.38	7.2	1.0
16	0.04	0.31	1.73398	-0.47	5.6	1.0
18	0.04	0.50	2.07628	-0.62	4.2	1.0
0	0.1	0.01	-0.00261	0.00	-0.2	0.7
2	0.1	0.01	0.218503	-0.05	16.9	0.7
4	0.1	0.01	0.430629	-0.11	31.7	0.8
6	0.1	0.01	0.630325	-0.16	42.1	0.9
8	0.1	0.02	0.816559	-0.20	47.3	1.0
10	0.1	0.02	0.982011	-0.25	46.6	1.1
12	0.1	0.03	1.10867	-0.28	38.6	1.2
14	0.1	0.19	1.40206	-0.33	7.6	1.0
16	0.1	0.31	1.73791	-0.44	5.7	1.1
18	0.1	0.49	2.10048	-0.58	4.3	1.0

NACA4412

AoA	h/c	Cd	Cl	Cm	Cl/Cd	y+
0	0.005	0.02	-0.07083	-0.06	-3.8	0.6
2	0.005	0.01	0.741416	-0.14	61.2	0.6
4	0.005	0.01	1.08605	-0.18	82.7	0.8
6	0.005	0.02	1.28222	-0.19	81.6	0.9
8	0.005	0.02	1.42126	-0.19	71.9	1.1
10	0.005	0.03	1.53636	-0.29	55.8	1.2
12	0.005	0.04	1.6022	-0.27	43.3	1.3
14	0.005	0.07	1.69854	-0.25	23.5	1.3
16	0.005	0.23	2.04257	-0.25	8.9	1.1
18	0.005	0.20	1.76537	-0.24	8.7	1.2
0	0.01	0.01	0.235615	-0.40	17.0	0.7
2	0.01	0.01	0.682696	-0.35	54.7	0.6
4	0.01	0.01	0.96172	-0.31	72.0	0.8
6	0.01	0.02	1.15574	-0.29	74.4	0.9
8	0.01	0.02	1.30253	-0.28	68.3	1.0
10	0.01	0.02	1.41354	-0.47	56.7	1.2
12	0.01	0.04	1.55752	-0.41	35.3	1.3
14	0.01	0.06	1.56393	-0.36	24.1	1.3
16	0.01	0.17	1.8266	-0.34	10.7	1.1
18	0.01	0.35	2.20308	-0.33	6.2	1.0
0	0.02	0.01	0.351597	-0.51	26.9	0.6
2	0.02	0.01	0.641141	-0.44	49.7	0.6
4	0.02	0.01	0.869333	-0.40	63.0	0.7
6	0.02	0.02	1.051	-0.37	66.9	0.9
8	0.02	0.02	1.19866	-0.36	63.9	1.0
10	0.02	0.02	1.31351	-0.55	54.9	1.1
12	0.02	0.03	1.39992	-0.48	40.6	1.2
14	0.02	0.05	1.40896	-0.43	30.7	1.3
16	0.02	0.16	1.75737	-0.40	11.2	1.4
18	0.02	0.22	1.77243	-0.39	8.2	1.1
0	0.04	0.01	0.38622	-0.57	29.5	0.6
2	0.04	0.01	0.611524	-0.54	45.6	0.6
4	0.04	0.01	0.81031	-0.45	56.0	0.7
6	0.04	0.02	0.982669	-0.42	60.2	0.9
8	0.04	0.02	1.13197	-0.41	59.6	1.0
10	0.04	0.02	1.2509	-0.63	53.1	1.1
12	0.04	0.03	1.34589	-0.55	42.8	1.2
14	0.04	0.04	1.37038	-0.45	32.2	1.3
16	0.04	0.10	1.60792	-0.43	15.8	1.4
18	0.04	0.25	1.97858	-0.44	7.8	1.3
0	0.1	0.01	0.391118	-0.66	29.2	0.6
2	0.1	0.01	0.593791	-0.57	42.5	0.6
4	0.1	0.02	0.782321	-0.68	51.1	0.7
6	0.1	0.02	0.957474	-0.56	55.5	0.8
8	0.1	0.02	1.11486	-0.51	55.6	1.0
10	0.1	0.02	1.24818	-0.64	51.6	1.1
12	0.1	0.03	1.35153	-0.71	43.1	1.2
14	0.1	0.04	1.42429	-0.53	34.5	1.3
16	0.1	0.08	1.56849	-0.72	20.9	1.4
18	0.1	0.19	1.96342	-0.75	10.4	1.5

NACA6409

AoA	h/c	Cd	Cl	Cm	Cl/Cd	y+
0	0.005	0.01	0.696522	-0.36	60.1	0.8
2	0.005	0.01	1.08339	-0.33	93.8	0.7
4	0.005	0.01	1.27174	-0.31	93.1	0.9
6	0.005	0.02	1.40203	-0.29	82.7	1.1
8	0.005	0.02	1.50375	-0.29	65.7	1.2
10	0.005	0.05	1.57122	-0.46	33.2	1.3
12	0.005	0.13	1.82665	-0.41	13.7	1.2
14	0.005	0.18	1.98123	-0.37	11.3	1.1
16	0.005	0.25	2.09747	-0.35	8.4	1.1
18	0.005	0.46	2.37232	-0.34	5.1	1.0
0	0.01	0.01	0.669264	-0.51	58.3	0.8
2	0.01	0.01	0.960703	-0.45	81.2	0.7
4	0.01	0.01	1.15391	-0.41	85.1	0.8
6	0.01	0.02	1.29873	-0.38	79.1	1.0
8	0.01	0.02	1.41099	-0.38	66.4	1.2
10	0.01	0.04	1.51301	-0.55	38.0	1.3
12	0.01	0.11	1.64267	-0.49	15.0	1.3
14	0.01	0.17	1.91787	-0.45	11.4	1.2
16	0.01	0.24	2.08123	-0.42	8.8	1.1
18	0.01	0.45	2.36956	-0.42	5.3	1.1
0	0.02	0.01	0.629747	-0.57	52.6	0.8
2	0.02	0.01	0.866842	-0.52	69.8	0.7
4	0.02	0.01	1.05404	-0.47	75.9	0.8
6	0.02	0.02	1.20412	-0.45	73.7	1.0
8	0.02	0.02	1.32358	-0.45	64.8	1.2
10	0.02	0.03	1.41426	-0.60	47.5	1.3
12	0.02	0.07	1.46757	-0.56	19.7	1.4
14	0.02	0.14	1.76122	-0.50	12.5	1.2
16	0.02	0.22	2.05346	-0.47	9.2	1.2
18	0.02	0.36	2.29156	-0.48	6.4	1.2
0	0.04	0.01	0.603764	-0.67	47.8	0.8
2	0.04	0.01	0.810911	-0.60	61.2	0.7
4	0.04	0.01	0.991221	-0.53	67.4	0.8
6	0.04	0.02	1.1462	-0.48	67.9	1.0
8	0.04	0.02	1.27531	-0.48	62.8	1.2
10	0.04	0.03	1.37175	-0.68	51.6	1.3
12	0.04	0.04	1.42063	-0.65	32.5	1.4
14	0.04	0.11	1.55851	-0.58	14.5	1.3
16	0.04	0.19	1.91168	-0.50	10.0	1.2
18	0.04	0.32	2.24229	-0.51	7.1	1.2
0	0.1	0.01	0.595995	-0.69	45.1	0.8
2	0.1	0.01	0.793948	-0.67	56.6	0.7
4	0.1	0.02	0.977203	-0.65	62.7	0.8
6	0.1	0.02	1.14264	-0.59	64.0	1.0
8	0.1	0.02	1.28467	-0.55	59.9	1.1
10	0.1	0.03	1.39829	-0.83	51.7	1.3
12	0.1	0.04	1.46046	-0.82	38.5	1.4
14	0.1	0.10	1.57233	-0.73	15.4	1.4
16	0.1	0.18	1.84668	-0.69	10.5	1.3
18	0.1	0.33	2.3156	-0.70	7.1	1.3

NACA6412

AoA	h/c	Cd	Cl	Cm	Cl/Cd	y+
0	0.005	0.01	0.487555	-0.29	33.7	0.7
2	0.005	0.01	1.04055	-0.44	80.8	0.6
4	0.005	0.02	1.27391	-0.51	84.2	0.7
6	0.005	0.02	1.42277	-0.55	76.1	0.8
8	0.005	0.03	1.54495	-0.59	59.2	0.9
10	0.005	0.03	1.61816	-0.61	62.2	1.1
12	0.005	0.06	1.74161	-0.68	27.0	1.2
14	0.005	0.11	1.87832	-0.77	17.2	1.2
16	0.005	0.17	1.93677	-0.68	11.3	1.1
18	0.005	0.31	2.2578	-0.78	7.2	1.0
0	0.01	0.01	0.576921	-0.29	43.7	0.7
2	0.01	0.01	0.919661	-0.38	69.3	0.6
4	0.01	0.02	1.14015	-0.44	75.5	0.7
6	0.01	0.02	1.29811	-0.49	71.1	0.8
8	0.01	0.02	1.41968	-0.52	62.0	0.9
10	0.01	0.03	1.51383	-0.55	49.0	1.0
12	0.01	0.03	1.6073	-0.58	49.6	1.2
14	0.01	0.09	1.76428	-0.68	20.2	1.2
16	0.01	0.20	1.92063	-0.82	9.7	1.3
18	0.01	0.26	2.13925	-0.72	8.3	1.0
0	0.02	0.01	0.588242	-0.28	44.0	0.7
2	0.02	0.01	0.83776	-0.35	60.3	0.6
4	0.02	0.02	1.0355	-0.40	67.0	0.7
6	0.02	0.02	1.19087	-0.44	65.3	0.8
8	0.02	0.02	1.31615	-0.47	58.5	0.9
10	0.02	0.03	1.41166	-0.49	50.1	1.0
12	0.02	0.05	1.53009	-0.54	29.2	1.1
14	0.02	0.06	1.53454	-0.54	25.0	1.2
16	0.02	0.15	1.75038	-0.70	11.3	1.3
18	0.02	0.14	1.85175	-0.59	13.6	1.1
0	0.04	0.01	0.585144	-0.28	42.4	0.7
2	0.04	0.01	0.791033	-0.33	53.9	0.6
4	0.04	0.02	0.973585	-0.37	60.1	0.7
6	0.04	0.02	1.1267	-0.41	60.1	0.8
8	0.04	0.02	1.25449	-0.44	55.4	0.9
10	0.04	0.03	1.36172	-0.46	47.6	1.0
12	0.04	0.04	1.42944	-0.48	37.0	1.1
14	0.04	0.06	1.47835	-0.50	26.6	1.2
16	0.04	0.14	1.74334	-0.67	12.7	1.3
18	0.04	0.32	2.20785	-0.91	6.8	1.3
0	0.1	0.01	0.582014	-0.28	40.3	0.7
2	0.1	0.02	0.77593	-0.32	50.2	0.6
4	0.1	0.02	0.957935	-0.36	56.1	0.7
6	0.1	0.02	1.11794	-0.40	56.7	0.8
8	0.1	0.02	1.25666	-0.43	53.6	0.9
10	0.1	0.03	1.37852	-0.46	48.1	1.0
12	0.1	0.04	1.48153	-0.49	34.3	1.1
14	0.1	0.06	1.52196	-0.50	24.0	1.2
16	0.1	0.11	1.65783	-0.58	15.0	1.3
18	0.1	0.26	2.12706	-0.87	8.2	1.4

b707_19

AoA	h/c	Cd	Cl	Cm	Cl/Cd	y+
0	0.005	0.02	0.454086	-0.12	21.0	3.6
2	0.005	0.03	0.393079	-0.03	14.8	1.1
4	0.005	0.02	0.344822	-0.01	17.7	1.1
6	0.005	0.04	0.803881	-0.19	22.7	1.1
8	0.005	0.08	1.23295	-0.37	15.3	1.1
10	0.005	0.14	1.52871	-0.47	11.3	1.0
12	0.005	0.19	1.67716	-0.52	8.6	1.0
14	0.005	0.29	1.88888	-0.60	6.6	1.0
16	0.005	0.41	2.01744	-0.69	4.9	0.9
18	0.005	0.67	2.35948	-0.98	3.5	0.9
0	0.01	0.03	-0.38877	0.16	-13.3	0.9
2	0.01	0.02	-0.04378	0.07	-2.4	1.0
4	0.01	0.02	0.429832	-0.09	27.0	1.0
6	0.01	0.02	0.731531	-0.18	29.6	1.2
8	0.01	0.07	1.04615	-0.29	15.9	1.1
10	0.01	0.13	1.40364	-0.41	11.1	1.0
12	0.01	0.18	1.59926	-0.47	9.0	1.0
14	0.01	0.26	1.71161	-0.52	6.7	1.0
16	0.01	0.38	1.97883	-0.63	5.2	1.0
18	0.01	0.65	2.36645	-0.93	3.6	0.9
0	0.02	0.02	-0.2366	0.08	-14.0	0.9
2	0.02	0.01	0.146974	-0.03	10.1	1.0
4	0.02	0.01	0.454378	-0.12	30.4	1.0
6	0.02	0.02	0.684492	-0.18	35.7	1.2
8	0.02	0.05	0.897929	-0.24	17.0	1.2
10	0.02	0.11	1.2526	-0.35	11.3	1.1
12	0.02	0.16	1.48668	-0.41	9.1	1.1
14	0.02	0.26	1.70289	-0.49	6.7	1.0
16	0.02	0.37	1.9232	-0.59	5.1	1.0
18	0.02	0.55	2.17881	-0.77	4.0	0.9
0	0.04	0.01	-0.04945	0.01	-3.5	0.9
2	0.04	0.01	0.212854	-0.06	15.5	1.0
4	0.04	0.01	0.444794	-0.12	30.2	1.0
6	0.04	0.02	0.641185	-0.17	35.2	1.1
8	0.04	0.04	0.812873	-0.21	19.3	1.2
10	0.04	0.09	1.10909	-0.30	11.7	1.2
12	0.04	0.16	1.40024	-0.38	9.0	1.1
14	0.04	0.23	1.61699	-0.44	6.9	1.1
16	0.04	0.32	1.76357	-0.49	5.4	1.1
18	0.04	0.59	2.34868	-0.76	4.0	1.0
0	0.1	0.01	0.005454	-0.02	0.4	0.9
2	0.1	0.01	0.221469	-0.07	16.3	1.0
4	0.1	0.01	0.423743	-0.12	28.5	1.1
6	0.1	0.02	0.607145	-0.16	33.6	1.1
8	0.1	0.04	0.754264	-0.19	20.8	1.2
10	0.1	0.09	1.03405	-0.27	12.1	1.2
12	0.1	0.15	1.35805	-0.35	9.1	1.2
14	0.1	0.24	1.62792	-0.43	6.8	1.1
16	0.1	0.35	1.83073	-0.51	5.2	1.1
18	0.1	0.56	2.3019	-0.72	4.1	1.0

be50

AoA	h/c	Cd	Cl	Cm	Cl/Cd	y+
0	0.005	0.01	0.720243	-0.33	73.7	0.6
2	0.005	0.01	1.05134	-0.43	100.9	1.0
4	0.005	0.01	1.23511	-0.48	98.8	1.2
6	0.005	0.02	1.3615	-0.51	74.8	1.4
8	0.005	0.07	1.51683	-0.56	21.6	1.3
10	0.005	0.15	1.75406	-0.60	11.9	1.2
12	0.005	0.21	1.86974	-0.62	8.8	1.2
14	0.005	0.30	1.98278	-0.65	6.5	1.1
16	0.005	0.46	2.19491	-0.76	4.8	1.1
18	0.005	0.82	2.32416	-1.12	2.8	0.9
0	0.01	0.01	0.632725	-0.29	61.8	0.6
2	0.01	0.01	0.920357	-0.36	86.4	0.9
4	0.01	0.01	1.118	-0.42	91.0	1.2
6	0.01	0.02	1.26395	-0.46	78.7	1.4
8	0.01	0.04	1.35047	-0.48	37.5	1.5
10	0.01	0.13	1.65142	-0.55	12.8	1.2
12	0.01	0.21	1.85991	-0.59	8.8	1.2
14	0.01	0.28	1.93295	-0.61	7.0	1.1
16	0.01	0.47	2.23183	-0.74	4.8	1.1
18	0.01	0.75	2.50918	-1.01	3.4	1.0
0	0.02	0.01	0.567405	-0.25	52.4	0.7
2	0.02	0.01	0.813025	-0.32	72.3	0.9
4	0.02	0.01	1.01088	-0.37	80.6	1.2
6	0.02	0.02	1.17068	-0.41	76.8	1.4
8	0.02	0.02	1.2769	-0.43	53.4	1.5
10	0.02	0.10	1.46978	-0.48	15.1	1.3
12	0.02	0.19	1.79061	-0.56	9.2	1.2
14	0.02	0.27	1.92204	-0.58	7.2	1.2
16	0.02	0.39	2.11311	-0.66	5.4	1.2
18	0.02	0.77	2.57641	-1.05	3.3	1.0
0	0.04	0.01	0.527662	-0.23	46.2	0.7
2	0.04	0.01	0.745388	-0.29	62.2	0.8
4	0.04	0.01	0.938124	-0.34	70.8	1.1
6	0.04	0.02	1.10631	-0.38	71.2	1.4
8	0.04	0.02	1.23595	-0.41	58.6	1.5
10	0.04	0.07	1.36475	-0.44	20.6	1.5
12	0.04	0.16	1.65529	-0.50	10.1	1.3
14	0.04	0.26	1.88276	-0.56	7.4	1.3
16	0.04	0.36	2.04839	-0.61	5.7	1.2
18	0.04	0.70	2.59322	-0.93	3.7	1.1
0	0.1	0.01	0.508494	-0.23	42.4	0.7
2	0.1	0.01	0.716037	-0.28	56.1	0.8
4	0.1	0.01	0.909962	-0.32	64.2	1.1
6	0.1	0.02	1.09079	-0.37	66.4	1.4
8	0.1	0.02	1.24179	-0.40	58.2	1.6
10	0.1	0.05	1.3453	-0.43	29.4	1.6
12	0.1	0.15	1.60885	-0.48	10.6	1.4
14	0.1	0.27	1.98598	-0.57	7.2	1.3
16	0.1	0.37	2.15658	-0.62	5.9	1.3
18	0.1	0.74	2.80127	-0.97	3.8	1.2

boe106

AoA	h/c	Cd	Cl	Cm	Cl/Cd	y+
0	0.005	0.02	-0.17663	0.06	-8.5	0.6
2	0.005	0.01	0.494823	-0.14	36.4	0.6
4	0.005	0.01	0.941037	-0.31	70.5	0.8
6	0.005	0.02	1.18985	-0.40	76.6	0.9
8	0.005	0.02	1.35388	-0.46	69.2	1.1
10	0.005	0.03	1.47703	-0.51	55.6	1.2
12	0.005	0.04	1.60495	-0.57	38.1	1.3
14	0.005	0.08	1.65269	-0.61	21.0	1.4
16	0.005	0.26	2.02015	-0.82	7.9	1.3
18	0.005	0.37	2.20366	-0.72	5.9	1.0
0	0.01	0.02	0.045933	-0.03	3.0	0.6
2	0.01	0.01	0.527486	-0.17	40.1	0.6
4	0.01	0.01	0.850364	-0.28	62.9	0.7
6	0.01	0.02	1.07301	-0.35	69.5	0.9
8	0.01	0.02	1.23562	-0.40	65.3	1.0
10	0.01	0.03	1.3568	-0.44	54.3	1.2
12	0.01	0.04	1.43962	-0.47	39.9	1.3
14	0.01	0.07	1.52681	-0.53	21.2	1.4
16	0.01	0.16	1.8392	-0.73	11.3	1.5
18	0.01	0.30	2.06841	-0.64	7.0	1.1
0	0.02	0.01	0.220839	-0.10	16.1	0.6
2	0.02	0.01	0.530591	-0.18	40.3	0.6
4	0.02	0.01	0.778473	-0.26	56.2	0.7
6	0.02	0.02	0.976098	-0.31	62.7	0.8
8	0.02	0.02	1.13341	-0.36	61.0	1.0
10	0.02	0.02	1.25141	-0.39	52.3	1.1
12	0.02	0.03	1.34065	-0.42	41.0	1.2
14	0.02	0.05	1.37396	-0.44	25.9	1.3
16	0.02	0.15	1.69055	-0.65	11.4	1.5
18	0.02	0.20	1.86492	-0.64	9.3	1.2
0	0.04	0.01	0.28088	-0.12	21.1	0.6
2	0.04	0.01	0.515839	-0.18	38.4	0.6
4	0.04	0.01	0.724909	-0.24	50.4	0.7
6	0.04	0.02	0.908483	-0.29	56.6	0.8
8	0.04	0.02	1.06172	-0.33	56.3	1.0
10	0.04	0.02	1.18727	-0.36	51.1	1.1
12	0.04	0.03	1.28519	-0.39	41.5	1.2
14	0.04	0.05	1.35273	-0.42	28.4	1.3
16	0.04	0.11	1.59578	-0.56	14.4	1.5
18	0.04	0.28	2.04961	-0.82	7.4	1.6
0	0.1	0.01	0.291819	-0.13	21.9	0.6
2	0.1	0.01	0.498415	-0.18	36.0	0.6
4	0.1	0.01	0.694564	-0.23	46.4	0.7
6	0.1	0.02	0.875634	-0.27	52.2	0.8
8	0.1	0.02	1.03665	-0.31	53.0	1.0
10	0.1	0.02	1.17106	-0.35	49.5	1.1
12	0.1	0.03	1.29263	-0.38	42.0	1.2
14	0.1	0.04	1.35989	-0.40	33.9	1.3
16	0.1	0.08	1.49267	-0.47	19.7	1.5
18	0.1	0.20	1.79152	-0.67	8.9	1.6

c72

AoA	h/c	Cd	Cl	Cm	Cl/Cd	y+
0	0.005	0.01	0.763258	-0.3052	65.7	0.6
2	0.005	0.01	1.1094	-0.418	88.0	0.8
4	0.005	0.02	1.30317	-0.48099	86.1	1.0
6	0.005	0.02	1.43891	-0.52454	75.1	1.1
8	0.005	0.03	1.54566	-0.56105	59.6	1.2
10	0.005	0.04	1.61793	-0.58986	40.6	1.3
12	0.005	0.16	1.79648	-0.62748	11.5	1.1
14	0.005	0.26	2.08393	-0.67488	7.9	1.0
16	0.005	0.41	2.25493	-0.76118	5.5	1.0
18	0.005	0.86	2.33679	-1.08085	2.7	0.8
0

Appendix A

Clark W						
AoA	h/c	Cd	Cl	Cm	Cl/Cd	y+
0	0.005	0.02	-0.12111	-0.03	-6.5	0.7
2	0.005	0.01	0.67093	-0.24	55.7	0.6
4	0.005	0.01	1.03072	-0.36	80.7	0.8
6	0.005	0.02	1.23793	-0.44	81.8	0.9
8	0.005	0.02	1.38463	-0.49	73.2	1.1
10	0.005	0.03	1.49803	-0.53	58.7	1.2
12	0.005	0.04	1.59163	-0.57	43.5	1.3
14	0.005	0.16	1.82401	-0.61	11.1	1.0
16	0.005	0.26	2.05208	-0.66	7.8	1.0
18	0.005	0.42	2.24133	-0.76	5.4	0.9
0	0.01	0.01	0.168689	-0.10	12.1	0.7
2	0.01	0.01	0.620888	-0.23	50.4	0.6
4	0.01	0.01	0.912717	-0.32	70.4	0.8
6	0.01	0.01	1.11467	-0.38	74.4	0.9
8	0.01	0.02	1.2682	-0.43	69.3	1.0
10	0.01	0.02	1.38572	-0.46	57.9	1.1
12	0.01	0.03	1.4948	-0.51	43.5	1.2
14	0.01	0.09	1.65714	-0.61	18.0	1.3
16	0.01	0.24	1.97909	-0.62	8.3	1.0
18	0.01	0.38	2.20153	-0.71	5.8	1.0
0	0.02	0.01	0.285237	-0.14	21.9	0.7
2	0.02	0.01	0.581169	-0.22	45.9	0.6
4	0.02	0.01	0.818851	-0.28	61.0	0.8
6	0.02	0.02	1.0078	-0.34	66.4	0.9
8	0.02	0.02	1.16161	-0.38	64.3	1.0
10	0.02	0.02	1.28136	-0.41	56.1	1.1
12	0.02	0.03	1.36794	-0.43	44.5	1.2
14	0.02	0.04	1.36692	-0.42	35.0	1.3
16	0.02	0.14	1.64547	-0.49	11.5	1.1
18	0.02	0.33	2.09235	-0.63	6.4	1.0
0	0.04	0.01	0.320109	-0.15	24.8	0.7
2	0.04	0.01	0.549741	-0.21	42.0	0.6
4	0.04	0.01	0.75475	-0.26	53.6	0.7
6	0.04	0.02	0.933541	-0.31	59.1	0.9
8	0.04	0.02	1.09048	-0.35	59.7	1.0
10	0.04	0.02	1.21421	-0.38	54.0	1.1
12	0.04	0.03	1.31046	-0.40	43.8	1.2
14	0.04	0.04	1.35858	-0.41	33.2	1.3
16	0.04	0.10	1.58066	-0.55	15.3	1.4
18	0.04	0.23	1.85335	-0.50	8.0	1.1
0	0.1	0.01	0.325403	-0.15	24.8	0.7
2	0.1	0.01	0.529518	-0.20	38.9	0.6
4	0.1	0.01	0.72391	-0.25	49.2	0.7
6	0.1	0.02	0.903533	-0.29	54.8	0.9
8	0.1	0.02	1.06499	-0.33	55.1	1.0
10	0.1	0.02	1.20322	-0.36	52.0	1.1
12	0.1	0.03	1.31492	-0.39	44.2	1.2
14	0.1	0.04	1.38708	-0.41	35.8	1.3
16	0.1	0.07	1.50519	-0.47	21.3	1.4
18	0.1	0.16	1.7602	-0.45	10.8	1.2

Clark Y						
AoA	h/c	Cd	Cl	Cm	Cl/Cd	y+
0	0.005	0.02	-0.18539	0.00	-9.6	0.7
2	0.005	0.01	0.633925	-0.23	52.2	0.6
4	0.005	0.01	1.02082	-0.36	80.7	0.8
6	0.005	0.01	1.23612	-0.44	82.7	1.0
8	0.005	0.02	1.38333	-0.49	73.6	1.1
10	0.005	0.03	1.49356	-0.53	57.4	1.2
12	0.005	0.05	1.57065	-0.56	34.4	1.3
14	0.005	0.16	1.75739	-0.62	11.3	1.1
16	0.005	0.25	2.02876	-0.65	8.2	1.0
18	0.005	0.39	2.22504	-0.74	5.7	1.0
0	0.01	0.01	0.130443	-0.09	9.2	0.7
2	0.01	0.01	0.604701	-0.22	49.1	0.6
4	0.01	0.01	0.905432	-0.32	70.2	0.8
6	0.01	0.01	1.11307	-0.38	75.1	0.9
8	0.01	0.02	1.26661	-0.43	69.8	1.1
10	0.01	0.02	1.38451	-0.46	57.6	1.2
12	0.01	0.04	1.46979	-0.50	37.0	1.3
14	0.01	0.11	1.63423	-0.61	14.8	1.4
16	0.01	0.21	1.89102	-0.58	9.2	1.1
18	0.01	0.35	2.14175	-0.68	6.2	1.1
0	0.02	0.01	0.272752	-0.13	20.9	0.7
2	0.02	0.01	0.577141	-0.22	45.7	0.6
4	0.02	0.01	0.81764	-0.28	61.2	0.8
6	0.02	0.02	1.00998	-0.34	67.2	0.9
8	0.02	0.02	1.16266	-0.38	64.8	1.0
10	0.02	0.02	1.28389	-0.41	56.5	1.2
12	0.02	0.03	1.36435	-0.44	41.8	1.3
14	0.02	0.07	1.41867	-0.47	21.7	1.3
16	0.02	0.16	1.72426	-0.52	10.9	1.1
18	0.02	0.30	2.0361	-0.60	6.8	1.1
0	0.04	0.01	0.317625	-0.15	24.6	0.7
2	0.04	0.01	0.551553	-0.21	42.2	0.6
4	0.04	0.01	0.758647	-0.26	54.2	0.7
6	0.04	0.02	0.93956	-0.31	60.0	0.9
8	0.04	0.02	1.09432	-0.35	60.1	1.0
10	0.04	0.02	1.22124	-0.38	54.7	1.2
12	0.04	0.03	1.32496	-0.41	44.9	1.3
14	0.04	0.05	1.39222	-0.44	28.4	1.3
16	0.04	0.15	1.70703	-0.62	11.5	1.4
18	0.04	0.22	1.78362	-0.47	8.2	1.1
0	0.1	0.01	0.325183	-0.15	24.8	0.7
2	0.1	0.01	0.532687	-0.20	39.2	0.6
4	0.1	0.01	0.728672	-0.25	49.7	0.7
6	0.1	0.02	0.910245	-0.30	55.4	0.9
8	0.1	0.02	1.0726	-0.33	56.0	1.0
10	0.1	0.02	1.21224	-0.37	52.7	1.1
12	0.1	0.03	1.32732	-0.40	44.2	1.3
14	0.1	0.04	1.3961	-0.42	32.7	1.3
16	0.1	0.13	1.69239	-0.60	13.0	1.5
18	0.1	0.18	1.7987	-0.46	10.0	1.2

DHMTU 10_10.2_10_60_21.5						
AoA	h/c	Cd	Cl	Cm	Cl/Cd	y+
0	0.005	0.02	0.101295	-0.02	6.6	0.6
2	0.005	0.01	0.626574	-0.18	48.7	0.9
4	0.005	0.01	0.942599	-0.30	67.9	1.2
6	0.005	0.02	1.12246	-0.37	54.8	1.4
8	0.005	0.05	1.23013	-0.41	22.5	1.3
10	0.005	0.09	1.5456	-0.53	16.9	1.2
12	0.005	0.14	1.77299	-0.59	13.0	1.1
14	0.005	0.19	1.95777	-0.64	10.3	1.1
16	0.005	0.28	2.1109	-0.70	7.5	1.1
18	0.005	0.75	2.62268	-1.07	3.5	0.9
0	0.01	0.01	0.182514	-0.07	13.1	0.7
2	0.01	0.01	0.570692	-0.19	44.7	0.8
4	0.01	0.01	0.841443	-0.27	61.6	1.1
6	0.01	0.02	1.02343	-0.33	59.3	1.4
8	0.01	0.04	1.08555	-0.34	27.9	1.3
10	0.01	0.09	1.38794	-0.47	15.9	1.3
12	0.01	0.12	1.65688	-0.54	13.4	1.2
14	0.01	0.17	1.85581	-0.59	10.9	1.2
16	0.01	0.25	2.03493	-0.64	8.2	1.1
18	0.01	0.44	2.31718	-0.78	5.3	1.1
0	0.02	0.01	0.254086	-0.11	19.3	0.7
2	0.02	0.01	0.530209	-0.19	41.1	0.7
4	0.02	0.01	0.755028	-0.25	54.6	1.0
6	0.02	0.02	0.929452	-0.30	57.3	1.3
8	0.02	0.03	1.01388	-0.31	40.1	1.4
10	0.02	0.08	1.17236	-0.38	15.6	1.3
12	0.02	0.11	1.46811	-0.46	13.4	1.2
14	0.02	0.16	1.75572	-0.54	10.8	1.2
16	0.02	0.23	1.97881	-0.60	8.5	1.2
18	0.02	0.40	2.25381	-0.72	5.6	1.1
0	0.04	0.01	0.279165	-0.12	21.4	0.7
2	0.04	0.01	0.497672	-0.18	37.7	0.7
4	0.04	0.01	0.693011	-0.23	48.7	1.0
6	0.04	0.02	0.860977	-0.27	53.0	1.3
8	0.04	0.02	0.975622	-0.30	45.1	1.4
10	0.04	0.06	1.07857	-0.34	18.6	1.4
12	0.04	0.09	1.26803	-0.38	13.5	1.3
14	0.04	0.14	1.60112	-0.47	11.1	1.2
16	0.04	0.21	1.86921	-0.54	8.9	1.2
18	0.04	0.36	2.16949	-0.66	6.1	1.2
0	0.1	0.01	0.280915	-0.13	21.4	0.7
2	0.1	0.01	0.477345	-0.17	35.1	0.7
4	0.1	0.01	0.661164	-0.22	45.0	1.0
6	0.1	0.02	0.826942	-0.26	49.3	1.2
8	0.1	0.02	0.959413	-0.29	45.8	1.4
10	0.1	0.04	1.01756	-0.30	23.8	1.4
12	0.1	0.09	1.23086	-0.36	13.6	1.4
14	0.1	0.14	1.57385	-0.45	11.1	1.3
16	0.1	0.21	1.87312	-0.53	9.0	1.3
18	0.1	0.34	2.21612	-0.64	6.5	1.2

DHMTU 12_35.3_10.2_80.12						
AoA	h/c	Cd	Cl	Cm	Cl/Cd	y+
0	0.005	0.03	0.37681	-0.10	12.1	4.8
2	0.005	0.02	0.239953	-0.05	13.9	2.2
4	0.005	0.02	0.834657	-0.25	51.4	0.7
6	0.005	0.02	1.12013	-0.36	52.9	3.9
8	0.005	0.03	1.29883	-0.44	40.0	3.2
10	0.005	0.05	1.44194	-0.51	26.4	1.1
12	0.005	0.10	1.6275	-0.63	16.2	6.0
14	0.005	0.10	1.69635	-0.65	16.3	3.7
16	0.005	0.14	1.77907	-0.70	12.9	4.7
18	0.005	0.19	1.86022	-0.76	9.9	1.4
0	0.01	0.02	-0.22471	0.05	-10.8	1.6
2	0.01	0.02	0.379991	-0.11	24.2	2.1
4	0.01	0.02	0.772734	-0.24	47.6	0.7
6	0.01	0.02	1.0136	-0.32	49.2	4.0
8	0.01	0.03	1.17504	-0.38	38.9	4.4
10	0.01	0.05	1.30337	-0.44	26.6	4.1
12	0.01	0.09	1.55002	-0.59	16.6	1.2
14	0.01	0.13	1.73636	-0.69	13.2	5.4
16	0.01	0.15	1.75375	-0.70	11.4	5.6
18	0.01	0.15	1.52307	-0.54	9.9	5.3
0	0.02	0.02	0.074371	-0.04	4.6	3.1
2	0.02	0.02	0.438214	-0.14	28.8	1.2
4	0.02	0.02	0.718529	-0.23	43.8	2.1
6	0.02	0.02	0.925563	-0.29	46.0	3.7
8	0.02	0.03	1.08428	-0.34	38.0	0.9
10	0.02	0.04	1.23615	-0.41	28.2	3.8
12	0.02	0.08	1.43621	-0.52	18.0	5.0
14	0.02	0.12	1.69931	-0.66	13.9	3.6
16	0.02	0.11	1.47247	-0.52	13.4	5.1
18	0.02	0.18	1.7439	-0.68	9.7	1.4
0	0.04	0.02	0.184392	-0.08	12.1	0.7
2	0.04	0.02	0.448884	-0.15	29.4	0.6
4	0.04	0.02	0.682185	-0.22	40.9	2.5
6	0.04	0.02	0.874209	-0.27	43.6	3.4
8	0.04	0.03	1.04396	-0.33	39.0	0.9
10	0.04	0.04	1.20971	-0.39	30.0	1.0
12	0.04	0.07	1.43068	-0.50	20.7	1.2
14	0.04	0.13	1.71598	-0.66	13.4	5.1
16	0.04	0.14	1.66375	-0.63	11.6	1.3
18	0.04	0.20	1.79717	-0.71	9.1	6.7
0	0.1	0.01	0.214229	-0.09	14.3	1.4
2	0.1	0.02	0.440453	-0.15	28.3	0.6
4	0.1	0.02	0.651875	-0.21	37.9	1.6
6	0.1	0.02	0.837335	-0.26	40.6	3.2
8	0.1	0.03	0.996925	-0.30	36.5	2.8
10	0.1	0.04	1.14819	-0.36	29.6	1.0
12	0.1	0.06	1.35197	-0.45	21.0	5.6
14	0.1	0.11	1.66684	-0.61	14.9	5.3
16	0.1	0.11	1.72935	-0.63	15.4	1.4
18	0.1	0.14	1.62862	-0.01	11.8	3.2

e58						
AoA	h/c	Cd	Cl	Cm	Cl/Cd	y+
0	0.005	0.01	0.90043	-0.47	78.0	0.9
2	0.005	0.01	1.18165	-0.54	95.9	0.9
4	0.005	0.01	1.32933	-0.57	89.3	1.4
6	0.005	0.02	1.43114	-0.59	60.3	1.6
8	0.005	0.07	1.59276	-0.63	23.8	1.4
10	0.005	0.12	1.79372	-0.66	15.6	1.3
12	0.005	0.18	1.95134	-0.69	11.0	1.3
14	0.005	0.24	2.05435	-0.71	8.4	1.3
16	0.005	0.40	2.38126	-0.83	6.0	1.2
18	0.005	0.80	2.49611	-1.20	3.1	1.1
0	0.01	0.01	0.851793	-0.44	74.5	0.9
2	0.01	0.01	1.08023	-0.49	86.9	0.9
4	0.01	0.01	1.2387	-0.53	84.9	1.3
6	0.01	0.02	1.35211	-0.55	66.2	1.6
8	0.01	0.05	1.44422	-0.57	28.2	1.5
10	0.01	0.10	1.70664	-0.62	16.3	1.3
12	0.01	0.17	1.91866	-0.67	11.5	1.3
14	0.01	0.23	2.02576	-0.69	8.7	1.3
16	0.01	0.34	2.22621	-0.75	6.5	1.3
18	0.01	0.62	2.58037	-1.02	4.1	1.2
0	0.02	0.01	0.802999	-0.41	67.2	0.8
2	0.02	0.01	1.00173	-0.46	77.7	0.9
4	0.02	0.01	1.16057	-0.49	78.3	1.3
6	0.02	0.02	1.28203	-0.51	67.8	1.6
8	0.02	0.03	1.3379	-0.51	38.4	1.6
10	0.02	0.09	1.6162	-0.59	17.1	1.4
12	0.02	0.16	1.8744	-0.64	11.9	1.3
14	0.02	0.23	2.03484	-0.68	8.8	1.3
16	0.02	0.34	2.21043	-0.74	6.6	1.4
18	0.02	0.59	2.63131	-0.99	4.5	1.2
0	0.04	0.01	0.778633	-0.40	61.1	0.8
2	0.04	0.01	0.962616	-0.44	70.0	0.9
4	0.04	0.02	1.12115	-0.47	72.2	1.3
6	0.04	0.02	1.25241	-0.50	66.5	1.6
8	0.04	0.03	1.32679	-0.50	45.8	1.7
10	0.04	0.08	1.51675	-0.55	18.6	1.5
12	0.04	0.15	1.8482	-0.63	12.3	1.4
14	0.04	0.22	2.02769	-0.66	9.2	1.4
16	0.04	0.31	2.19467	-0.71	7.0	1.4
18	0.04	0.57	2.67383	-0.96	4.7	1.3
0	0.1	0.01	0.782714	-0.40	57.3	0.8
2	0.1	0.01	0.968079	-0.44	65.2	0.9
4	0.1	0.02	1.13636	-0.48	67.6	1.3
6	0.1	0.02	1.28269	-0.51	63.7	1.6
8	0.1	0.03	1.37105	-0.51	47.4	1.7
10	0.1	0.07	1.52046	-0.55	20.3	1.6
12	0.1	0.15	1.88735	-0.64	12.3	1.5
14	0.1	0.23	2.13423	-0.69	9.2	1.5
16	0.1	0.33	2.34054	-0.74	7.1	1.5
18	0.1	0.60	3.00023	-1.01	5.0	1.4

e376						
AoA	h/c	Cd	Cl	Cm	Cl/Cd	y+
0	0.005	0.02	0.56684	-0.25	32.6	5.8
2	0.005	0.01	1.13404	-0.47	103.1	6.3
4	0.005	0.01	1.32335	-0.52	107.1	6.5
6	0.005	0.02	1.43343	-0.55	93.4	6.6
8	0.005	0.03	1.51643	-0.58	58.8	7.0
10	0.005	0.10	1.68767	-0.65	16.7	7.2
12	0.005	0.16	1.86294	-0.64	12.0	6.9
14	0.005	0.23	2.00855	-0.65	8.8	6.7
16	0.005	0.36	2.11242	-0.69	5.8	6.2
18	0.005	0.69	2.4353	-0.94	3.5	6.3
0	0.01	0.05	0.53154	-0.26	10.9	5.9
2	0.01	0.01	1.00981	-0.41	83.4	5.9
4	0.01	0.01	1.23795	-0.47	103.4	6.1
6	0.01	0.01	1.36702	-0.51	94.6	6.2
8	0.01	0.02	1.46553	-0.53	72.8	6.4
10	0.01	0.07	1.57802	-0.61	24.0	6.9
12	0.01	0.14	1.77087	-0.61	12.8	6.7
14	0.01	0.21	1.98138	-0.64	9.4	6.4
16	0.01	0.30	2.07562	-0.65	6.9	6.2
18	0.01	0.57	2.38903	-0.81	4.2	5.7
0	0.02	0.02	0.455312	-0.20	20.5	5.6
2	0.02	0.01	0.896652	-0.36	65.4	5.7
4	0.02	0.01	1.14165	-0.43	94.5	5.9
6	0.02	0.01	1.29087	-0.46	91.3	5.9
8	0.02	0.02	1.41174	-0.50	78.6	6.1
10	0.02	0.03	1.48469	-0.52	49.9	6.4
12	0.02	0.11	1.60198	-0.55	14.8	6.8
14	0.02	0.19	1.89487	-0.60	10.2	6.0
16	0.02	0.27	2.0918	-0.64	7.7	5.9
18	0.02	0.55	2.39606	-0.79	4.4	5.6
0	0.04	0.03	0.493968	-0.22	18.7	5.7
2	0.04	0.02	0.859029	-0.34	45.5	5.4
4	0.04	0.01	1.06826	-0.39	82.9	5.7
6	0.04	0.01	1.23425	-0.43	83.7	5.7
8	0.04	0.02	1.37787	-0.47	77.2	5.9
10	0.04	0.02	1.48525	-0.50	61.6	6.1
12	0.04	0.09	1.65803	-0.60	18.9	6.6
14	0.04	0.14	1.73096	-0.53	12.4	6.1
16	0.04	0.24	2.05026	-0.60	8.5	5.8
18	0.04	0.42	2.32716	-0.70	5.5	5.6
0	0.1	0.02	0.456481	-0.20	18.9	5.8
2	0.1	0.02	0.782537	-0.31	46.2	5.9
4	0.1	0.01	1.04713	-0.38	74.9	5.6
6	0.1	0.02	1.2335	-0.43	78.5	5.7
8	0.1	0.02	1.40189	-0.47	74.0	5.8
10	0.1	0.02	1.54189	-0.51	64.1	6.0
12	0.1	0.05	1.6667	-0.56	34.3	6.5
14	0.1	0.13	1.7665	-0.54	13.8	6.4
16	0.1	0.24	2.07756	-0.60	8.6	5.8
18	0.1	0.42	2.45892	-0.72	5.9	5.7

e396						
AoA	h/c	Cd	Cl	Cm	Cl/Cd	y+
0	0.005	0.02	0.157358	-0.18	7.9	2.2
2	0.005	0.01	0.956711	-0.43	75.0	0.6
4	0.005	0.02	1.40517	-0.56	75.2	1.2
6	0.005	0.03	1.52492	-0.60	57.9	1.4
8	0.005	0.04	1.65748	-0.66	40.0	3.7
10	0.005	0.08	1.64547	-0.64	21.6	1.6
12	0.005	0.15	1.90425	-0.70	13.0	6.6
14	0.005	0.20	2.09372	-0.73	10.4	1.2
16	0.005	0.33	2.30467	-0.79	6.9	1.1
18	0.005	0.33	2.30467	-0.79	6.9	1.1
0	0.01	0.01	0.47262	-0.28	34.2	0.7
2	0.01	0.01	0.887813	-0.39	67.7	0.6
4	0.01	0.01	1.12704	-0.46	75.7	0.8
6	0.01	0.02	1.29199	-0.50	70.5	1.1
8	0.01	0.02	1.41095	-0.53	59.2	7.1
10	0.01	0.03	1.49961	-0.56	52.6	1.5
12	0.01	0.08	1.67673	-0.66	21.1	1.7
14	0.01	0.12	1.65824	-0.59	14.3	1.4
16	0.01	0.21	2.08471	-0.73	10.0	1.2
18	0.01	0.32	2.29454	-0.77	7.3	4.7
0	0.02	0.01	0.573839	-0.30	43.3	0.6
2	0.02	0.01	0.843628	-0.37	61.7	5.7
4	0.02	0.02	1.04435	-0.42	67.9	2.9
6	0.02	0.02	1.19877	-0.46	65.5	3.6
8	0.02	0.02	1.31711	-0.49	56.5	7.4
10	0.02	0.03	1.41132	-0.51	44.6	1.4
12	0.02	0.06	1.50364	-0.55	26.7	1.6
14	0.02	0.12	1.6576	-0.66	13.8	1.7
16	0.02	0.14	1.77589	-0.57	12.5	1.3
18	0.02	0.28	2.23449	-0.73	7.9	1.2
0	0.04	0.01	0.601834	-0.30	44.1	0.6
2	0.04	0.01	0.818217	-0.36	56.7	0.6
4	0.04	0.02	1.002	-0.40	62.4	3.8
6	0.04	0.02	1.15135	-0.44	61.4	1.0
8	0.04	0.02	1.27522	-0.46	55.3	7.1
10	0.04	0.03	1.36937	-0.49	42.4	6.1
12	0.04	0.05	1.43693	-0.51	29.3	1.6
14	0.04	0.07	1.49134	-0.54	20.8	1.8
16	0.04	0.11	1.68277	-0.53	15.8	1.4
18	0.04	0.23	2.04513	-0.63	8.9	5.1
0	0.1	0.01	0.610181	-0.30	42.9	0.6
2	0.1	0.02	0.812251	-0.35	53.0	0.6
4	0.1	0.02	0.994388	-0.40	57.9	0.8
6	0.1	0.02	1.15342	-0.43	57.8	1.0
8	0.1	0.02	1.29128	-0.47	53.7	1.3
10	0.1	0.03	1.39615	-0.49	44.9	3.2
12	0.1	0.04	1.45097	-0.50	37.0	1.6
14	0.1	0.06	1.5432	-0.54	24.9	1.7
16	0.1	0.13	1.76652	-0.60	13.2	1.5
18	0.1	0.20	1.97115	-0.61	9.7	1.4

Eiffel 385						
AoA	h/c	Cd	Cl	Cm	Cl/Cd	y+
0	0.005	0.01	0.936684	-0.37	74.1	0.6
2	0.005	0.01	1.21962	-0.46	84.9	0.8
4	0.005	0.02	1.38428	-0.51	78.4	0.9
6	0.01	0.02	1.50446	-0.55	66.1	1.0
8	0.005	0.03	1.60555	-0.58	47.5	1.1
10	0.005	0.05	1.72397	-0.65	34.0	1.2
12	0.005	0.12	1.98067	-0.82	16.0	1.3
14	0.005	0.19	2.0186	-0.85	10.4	1.3
16	0.005	0.29	2.22277	-0.92	7.8	1.2
18	0

FX77_121

AoA	h/c	Cd	Cl	Cm	Cl/Cd	y+
0	0.005	0.01	0.128172	-0.01	9.0	0.7
2	0.005	0.01	0.74411	-0.22	62.5	0.6
4	0.005	0.01	1.05783	-0.34	81.4	0.9
6	0.005	0.02	1.25451	-0.42	79.3	1.2
8	0.005	0.02	1.3919	-0.47	61.1	1.3
10	0.005	0.07	1.5655	-0.59	22.1	1.4
12	0.005	0.19	1.84118	-0.75	9.8	1.3
14	0.005	0.23	1.86698	-0.65	8.1	1.2
16	0.005	0.25	2.0163	-0.64	8.0	1.2
18	0.005	0.47	2.24321	-0.72	4.8	1.1
0	0.01	0.01	0.223272	-0.06	16.8	0.8
2	0.01	0.01	0.646444	-0.20	53.1	0.6
4	0.01	0.01	0.930361	-0.29	71.3	0.8
6	0.01	0.02	1.1337	-0.36	73.8	1.1
8	0.01	0.02	1.2785	-0.41	62.4	1.3
10	0.01	0.04	1.41943	-0.49	31.7	1.4
12	0.01	0.14	1.75032	-0.69	12.4	1.4
14	0.01	0.22	1.89856	-0.70	8.5	1.2
16	0.01	0.23	1.87053	-0.57	8.1	1.2
18	0.01	0.39	2.18452	-0.66	5.6	1.2
0	0.02	0.01	0.266783	-0.09	20.7	0.9
2	0.02	0.01	0.573043	-0.18	45.5	0.6
4	0.02	0.01	0.821027	-0.25	61.2	0.8
6	0.02	0.02	1.02033	-0.31	66.1	1.0
8	0.02	0.02	1.1793	-0.36	61.9	1.2
10	0.02	0.03	1.30824	-0.41	42.2	1.4
12	0.02	0.10	1.63156	-0.61	16.2	1.5
14	0.02	0.21	1.91079	-0.72	9.3	1.3
16	0.02	0.18	1.68934	-0.49	9.2	1.3
18	0.02	0.34	2.04507	-0.60	6.1	1.2
0	0.04	0.01	0.276197	-0.09	21.4	0.9
2	0.04	0.01	0.522404	-0.16	40.2	0.6
4	0.04	0.01	0.74302	-0.22	53.1	0.7
6	0.04	0.02	0.938047	-0.28	59.2	1.0
8	0.04	0.02	1.10267	-0.33	57.9	1.2
10	0.04	0.03	1.24109	-0.37	46.2	1.4
12	0.04	0.07	1.48117	-0.50	21.4	1.5
14	0.04	0.17	1.86023	-0.68	10.8	1.4
16	0.04	0.20	1.95273	-0.65	9.6	1.3
18	0.04	0.26	1.81965	-0.48	7.1	1.2
0	0.1	0.01	0.269871	-0.09	20.7	0.9
2	0.1	0.01	0.489346	-0.15	36.4	0.7
4	0.1	0.01	0.699805	-0.20	48.0	0.7
6	0.1	0.02	0.894838	-0.26	53.6	0.9
8	0.1	0.02	1.07151	-0.31	54.5	1.2
10	0.1	0.03	1.22209	-0.35	46.5	1.3
12	0.1	0.05	1.41396	-0.44	27.2	1.5
14	0.1	0.15	1.8399	-0.66	12.4	1.5
16	0.1	0.23	2.11857	-0.73	9.1	1.4
18	0.1	0.23	1.81742	-0.47	8.0	1.3

GOE395

AoA	h/c	Cd	Cl	Cm	Cl/Cd	y+
0	0.005	0.01	0.777243	-0.38	52.0	5.1
2	0.005	0.01	1.19784	-0.52	105.2	6.5
4	0.005	0.01	1.35689	-0.56	99.8	7.0
6	0.005	0.02	1.46761	-0.59	85.3	6.4
8	0.005	0.03	1.55526	-0.61	58.8	7.2
10	0.005	0.09	1.7049	-0.67	18.3	7.2
12	0.005	0.15	1.90685	-0.69	12.9	6.6
14	0.005	0.21	2.05328	-0.70	9.8	7.4
16	0.005	0.30	2.13201	-0.73	7.0	6.6
18	0.005	0.55	2.43673	-0.91	4.4	6.3
0	0.01	0.01	0.817111	-0.39	72.0	5.0
2	0.01	0.01	1.07848	-0.46	94.8	6.2
4	0.01	0.01	1.2536	-0.51	94.9	6.6
6	0.01	0.02	1.38031	-0.54	84.4	6.0
8	0.01	0.02	1.47698	-0.56	64.2	6.7
10	0.01	0.05	1.52076	-0.58	33.2	6.9
12	0.01	0.08	1.66072	-0.61	21.3	6.3
14	0.01	0.20	2.0284	-0.68	10.1	7.0
16	0.01	0.29	2.16659	-0.71	7.5	6.4
18	0.01	0.54	2.45165	-0.89	4.6	6.1
0	0.02	0.01	0.738894	-0.35	64.2	4.8
2	0.02	0.01	0.968047	-0.41	81.6	6.0
4	0.02	0.01	1.15138	-0.46	85.9	6.4
6	0.02	0.02	1.29247	-0.49	80.4	5.7
8	0.02	0.02	1.40373	-0.52	67.2	6.4
10	0.02	0.03	1.45504	-0.53	44.8	6.5
12	0.02	0.11	1.63806	-0.58	15.2	6.1
14	0.02	0.18	1.95094	-0.64	10.8	6.6
16	0.02	0.27	2.14585	-0.69	8.1	6.1
18	0.02	0.45	2.40567	-0.81	5.4	6.0
0	0.04	0.01	0.685025	-0.32	55.9	4.7
2	0.04	0.01	0.896642	-0.38	70.1	5.8
4	0.04	0.01	1.08313	-0.42	76.2	6.3
6	0.04	0.02	1.23758	-0.46	74.7	5.6
8	0.04	0.02	1.36585	-0.49	66.9	6.3
10	0.04	0.03	1.44436	-0.51	50.6	6.3
12	0.04	0.07	1.50939	-0.54	22.8	7.4
14	0.04	0.14	1.74432	-0.55	12.7	6.5
16	0.04	0.24	2.06305	-0.64	8.7	6.0
18	0.04	0.39	2.37341	-0.75	6.1	6.0
0	0.1	0.01	0.666373	-0.32	51.1	4.7
2	0.1	0.01	0.873492	-0.37	63.2	5.8
4	0.1	0.02	1.06918	-0.42	69.9	6.3
6	0.1	0.02	1.24146	-0.46	70.0	5.5
8	0.1	0.02	1.39008	-0.49	64.0	6.2
10	0.1	0.03	1.49343	-0.52	52.7	6.3
12	0.1	0.05	1.56019	-0.54	32.9	6.6
14	0.1	0.13	1.73145	-0.54	13.3	6.6
16	0.1	0.25	2.16025	-0.66	8.7	5.9
18	0.1	0.39	2.45454	-0.75	6.3	6.1

GOE802b

AoA	h/c	Cd	Cl	Cm	Cl/Cd	y+
0	0.005	0.02	0.697316	-0.33	46.4	0.7
2	0.005	0.01	1.13564	-0.47	94.2	0.6
4	0.005	0.01	1.32993	-0.53	94.0	0.7
6	0.005	0.02	1.46573	-0.57	84.2	0.9
8	0.005	0.02	1.57563	-0.60	70.1	1.0
10	0.005	0.03	1.66825	-0.64	54.2	1.1
12	0.005	0.05	1.73322	-0.67	35.1	1.2
14	0.005	0.14	1.92571	-0.82	13.5	1.3
16	0.005	0.30	2.21407	-0.93	7.5	1.1
18	0.005	0.41	2.33427	-0.80	5.8	1.0
0	0.01	0.02	0.658967	-0.31	42.5	0.7
2	0.01	0.01	0.999875	-0.40	80.0	0.6
4	0.01	0.01	1.2031	-0.46	85.5	0.7
6	0.01	0.02	1.3541	-0.50	80.2	0.9
8	0.01	0.02	1.47378	-0.54	68.8	1.0
10	0.01	0.03	1.57373	-0.57	52.7	1.1
12	0.01	0.04	1.60892	-0.58	40.8	1.2
14	0.01	0.11	1.78946	-0.71	16.5	1.3
16	0.01	0.23	2.11618	-0.90	9.1	1.4
18	0.01	0.27	2.10911	-0.69	7.7	1.1
0	0.02	0.02	0.623827	-0.29	39.0	0.7
2	0.02	0.01	0.892587	-0.36	66.7	0.6
4	0.02	0.01	1.09076	-0.41	75.3	0.7
6	0.02	0.02	1.24914	-0.45	74.1	0.8
8	0.02	0.02	1.37575	-0.49	66.1	1.0
10	0.02	0.03	1.47354	-0.51	54.2	1.1
12	0.02	0.04	1.53457	-0.53	38.7	1.2
14	0.02	0.08	1.61941	-0.59	21.3	1.3
16	0.02	0.22	2.03878	-0.86	9.1	1.4
18	0.02	0.24	2.07318	-0.78	8.6	1.2
0	0.04	0.02	0.598445	-0.27	36.0	0.7
2	0.04	0.01	0.826083	-0.33	57.2	0.7
4	0.04	0.02	1.01609	-0.38	65.9	0.7
6	0.04	0.02	1.18133	-0.42	68.1	0.8
8	0.04	0.02	1.31613	-0.45	63.2	1.0
10	0.04	0.03	1.4253	-0.48	54.5	1.1
12	0.04	0.04	1.49401	-0.50	42.6	1.2
14	0.04	0.06	1.61279	-0.56	27.7	1.3
16	0.04	0.16	1.92088	-0.76	12.3	1.4
18	0.04	0.30	2.30701	-0.93	7.7	1.5
0	0.1	0.02	0.586541	-0.27	33.6	0.8
2	0.1	0.02	0.798757	-0.32	51.5	0.7
4	0.1	0.02	0.991388	-0.37	60.3	0.7
6	0.1	0.02	1.16622	-0.41	62.4	0.8
8	0.1	0.02	1.31894	-0.45	60.0	1.0
10	0.1	0.03	1.44033	-0.48	52.9	1.1
12	0.1	0.04	1.5383	-0.50	43.0	1.2
14	0.1	0.05	1.63576	-0.54	33.3	1.3
16	0.1	0.12	1.83249	-0.67	15.4	1.4
18	0.1	0.33	2.39598	-0.98	7.4	1.5

GOE803

AoA	h/c	Cd	Cl	Cm	Cl/Cd	y+
0	0.005	0.02	0.71253	-0.34	39.3	5.1
2	0.005	0.01	1.22127	-0.53	106.6	5.6
4	0.005	0.01	1.38506	-0.57	104.4	6.6
6	0.005	0.02	1.50052	-0.60	94.0	6.6
8	0.005	0.02	1.59995	-0.63	78.9	7.1
10	0.005	0.03	1.68432	-0.65	60.9	6.8
12	0.005	0.04	1.76252	-0.69	40.0	6.9
14	0.005	0.18	1.95153	-0.70	10.8	7.4
16	0.005	0.26	2.05925	-0.70	7.9	6.2
18	0.005	0.50	2.37193	-0.84	4.8	6.0
0	0.01	0.02	0.671979	-0.32	34.2	5.0
2	0.01	0.01	1.10615	-0.47	96.4	5.3
4	0.01	0.01	1.28375	-0.52	99.0	6.2
6	0.01	0.02	1.41777	-0.55	91.9	6.0
8	0.01	0.02	1.52908	-0.58	79.0	6.6
10	0.01	0.03	1.61796	-0.60	62.1	6.4
12	0.01	0.04	1.70195	-0.64	39.6	6.5
14	0.01	0.08	1.78842	-0.70	21.9	7.9
16	0.01	0.25	2.07964	-0.68	8.4	6.1
18	0.01	0.42	2.3221	-0.77	5.6	6.0
0	0.02	0.02	0.634873	-0.30	29.8	4.9
2	0.02	0.01	0.99863	-0.42	82.6	5.0
4	0.02	0.01	1.1842	-0.47	89.7	5.9
6	0.02	0.02	1.33353	-0.50	86.4	5.7
8	0.02	0.02	1.4583	-0.54	77.0	6.3
10	0.02	0.02	1.55198	-0.56	63.0	6.1
12	0.02	0.04	1.62455	-0.58	44.8	6.1
14	0.02	0.06	1.69712	-0.63	26.4	7.3
16	0.02	0.20	2.01059	-0.77	9.9	6.3
18	0.02	0.34	2.23679	-0.71	6.6	5.9
0	0.04	0.02	0.650195	-0.31	31.4	4.8
2	0.04	0.01	0.930076	-0.39	70.9	4.9
4	0.04	0.01	1.11753	-0.44	78.2	5.8
6	0.04	0.02	1.2794	-0.48	78.5	5.6
8	0.04	0.02	1.42078	-0.51	73.8	6.2
10	0.04	0.02	1.52866	-0.54	64.0	5.9
12	0.04	0.03	1.60551	-0.56	48.6	6.0
14	0.04	0.05	1.68261	-0.59	33.3	6.8
16	0.04	0.12	1.92765	-0.74	16.0	6.6
18	0.04	0.20	1.98505	-0.57	9.9	6.3
0	0.1	0.02	0.649883	-0.31	31.2	4.7
2	0.1	0.01	0.909908	-0.38	63.8	4.8
4	0.1	0.02	1.1065	-0.43	71.6	5.8
6	0.1	0.02	1.28638	-0.47	73.4	5.5
8	0.1	0.02	1.44622	-0.51	68.5	6.2
10	0.1	0.03	1.58149	-0.55	62.6	5.9
12	0.1	0.03	1.67112	-0.57	50.4	5.9
14	0.1	0.05	1.74577	-0.59	37.8	6.7
16	0.1	0.10	1.93207	-0.71	19.8	6.4
18	0.1	0.23	2.19128	-0.76	9.7	6.7

Sikorsky GS1

AoA	h/c	Cd	Cl	Cm	Cl/Cd	y+
0	0.005	0.02	0.086768	-0.10896	3.5	0.7
2	0.005	0.01	0.620516	-0.27	46.3	0.6
4	0.005	0.01	1.07685	-0.41	80.2	0.7
6	0.005	0.02	1.29688	-0.48	80.6	0.8
8	0.005	0.02	1.43998	-0.52	70.3	0.9
10	0.005	0.03	1.55092	-0.56	56.1	1.0
12	0.005	0.04	1.63093	-0.59	40.4	1.1
14	0.005	0.08	1.61195	-0.58	21.4	1.2
16	0.005	0.18	1.93467	-0.80	10.8	1.2
18	0.005	0.25	2.04244	-0.89	8.1	1.2
0	0.01	0.02	0.104503	-0.12	6.4	0.7
2	0.01	0.01	0.649235	-0.27	49.4	0.6
4	0.01	0.01	0.965109	-0.36	70.1	0.7
6	0.01	0.02	1.17257	-0.42	73.2	0.8
8	0.01	0.02	1.32157	-0.46	66.2	0.9
10	0.01	0.03	1.43686	-0.50	54.3	1.0
12	0.01	0.05	1.53868	-0.54	33.9	1.1
14	0.01	0.07	1.55885	-0.55	22.9	1.2
16	0.01	0.16	1.85751	-0.75	11.9	1.2
18	0.01	0.25	2.05672	-0.88	8.3	1.3
0	0.02	0.01	0.332011	-0.18	24.1	0.6
2	0.02	0.01	0.646222	-0.26	48.3	0.6
4	0.02	0.01	0.886113	-0.33	62.0	0.7
6	0.02	0.02	1.07263	-0.38	65.4	0.8
8	0.02	0.02	1.22122	-0.41	61.9	0.9
10	0.02	0.03	1.33745	-0.45	52.6	0.9
12	0.02	0.04	1.41242	-0.47	38.9	1.1
14	0.02	0.06	1.45539	-0.49	25.5	1.1
16	0.02	0.13	1.69226	-0.64	13.2	1.2
18	0.02	0.26	2.06433	-0.88	7.9	1.3
0	0.04	0.01	0.397085	-0.20	29.3	0.6
2	0.04	0.01	0.632073	-0.26	45.4	0.6
4	0.04	0.02	0.837871	-0.31	55.8	0.7
6	0.04	0.02	1.0127	-0.35	59.4	0.8
8	0.04	0.02	1.16057	-0.39	58.2	0.9
10	0.04	0.03	1.27792	-0.42	50.9	0.9
12	0.04	0.03	1.36392	-0.44	40.0	1.1
14	0.04	0.05	1.44669	-0.47	28.8	1.1
16	0.04	0.10	1.65056	-0.60	15.8	1.2
18	0.04	0.23	2.01219	-0.83	8.8	1.3
0	0.1	0.01	0.412508	-0.20	29.8	0.6
2	0.1	0.01	0.620968	-0.25	42.7	0.6
4	0.1	0.02	0.816228	-0.30	51.5	0.7
6	0.1	0.02	0.990872	-0.34	54.9	1.3
8	0.1	0.02	1.14931	-0.38	54.5	0.9
10	0.1	0.03	1.27974	-0.41	50.2	0.9
12	0.1	0.03	1.38812	-0.44	40.8	1.1
14	0.1	0.05	1.46882	-0.47	30.6	1.2
16	0.1	0.08	1.60902	-0.55	20.1	1.2
18	0.1	0.22	2.03889	-0.81	9.5	1.3

HS1708

AoA	h/c	Cd	Cl	Cm	Cl/Cd	y+
0	0.005	0.01	0.730435	-0.37	64.8	0.8
2	0.005	0.01	1.12761	-0.48	98.6	0.7
4	0.005	0.01	1.31631	-0.54	96.0	1.0
6	0.005	0.02	1.44758	-0.57	84.2	1.3
8	0.005	0.02	1.55104	-0.60	67.4	1.5
10	0.005	0.09	1.69304	-0.65	18.9	1.4
12	0.005	0.17	1.93568	-0.69	11.6	1.4
14	0.005	0.23	2.03752	-0.70	9.0	1.4
16	0.005	0.34	2.1918	-0.76	6.4	1.4
18	0.005	0.64	2.51908	-1.02	3.9	1.3
0	0.01	0.01	0.668043	-0.32	59.5	0.8
2	0.01	0.01	0.972594	-0.41	83.7	0.7
4	0.01	0.01	1.17474	-0.46	87.7	0.9
6	0.01	0.02	1.32363	-0.50	80.9	1.2
8	0.01	0.02	1.43802	-0.53	67.5	1.4
10	0.01	0.03	1.51867	-0.55	53.0	1.6
12	0.01	0.14	1.82052	-0.63	12.7	1.4
14	0.01	0.22	2.03014	-0.67	9.0	1.4
16	0.01	0.31	2.11849	-0.71	6.8	1.4
18	0.01	0.59	2.4945	-0.95	4.2	1.3
0	0.02	0.01	0.609622	-0.29	51.8	0.8
2	0.02	0.01	0.857361	-0.36	70.1	0.7
4	0.02	0.01	1.05462	-0.41	77.3	0.9
6	0.02	0.02	1.21119	-0.45	74.9	1.1
8	0.02	0.02	1.33298	-0.48	65.5	1.3
10	0.02	0.03	1.42751	-0.50	51.3	1.5
12	0.02	0.05	1.45657	-0.51	30.2	1.6
14	0.02	0.20	1.92636	-0.62	9.7	1.4
16	0.02	0.29	2.11136	-0.67	7.4	1.5
18	0.02	0.51	2.46993	-0.85	4.8	1.4
0	0.04	0.01	0.573571	-0.27	46.2	0.8
2	0.04	0.01	0.78905	-0.33	60.6	0.7
4	0.04	0.01	0.978251	-0.37	68.0	0.8
6	0.04	0.02	1.13914	-0.41	68.3	1.1
8	0.04	0.02	1.27031	-0.44	62.7	1.3
10	0.04	0.03	1.37049	-0.46	52.1	1.5
12	0.04	0.04	1.4341	-0.48	39.6	1.6
14	0.04	0.14	1.66209	-0.51	11.6	1.5
16	0.04	0.26	2.03231	-0.62	7.8	1.5
18	0.04	0.43	2.37024	-0.75	5.5	1.5
0	0.1	0.01	0.558106	-0.27	42.8	0.9
2	0.1	0.01	0.762837	-0.32	55.3	0.7
4	0.1	0.02	0.95288	-0.36	62.1	0.8
6	0.1	0.02	1.12338	-0.40	63.0	1.1
8	0.1	0.02	1.27241	-0.44	60.0	1.3
10	0.1	0.03	1.39011	-0.46	52.5	1.5
12	0.1	0.04	1.46765	-0.48	39.4	1.7
14	0.1	0.11	1.58333	-0.49	13.9	1.5
16	0.1	0.26	2.06055	-0.61	7.8	1.5
18	0.1	0.43	2.47137	-0.75	5.7	1.6

isa961

AoA	h/c	Cd	Cl	Cm	Cl/Cd	y+
0	0.005	0.01	0.734156	-0.31	67.2	0.6
2	0.005	0.01	1.07442	-0.41	91.7	0.8
4	0.005	0.01	1.27152	-0.48	91.5	1.1
6	0.005	0.02	1.40889	-0.52	79.9	1.3
8	0.005	0.03	1.50945	-0.55	55.2	1.4
10	0.005	0.07	1.60974	-0.62	23.2	1.5
12	0.005	0.17	1.87129	-0.64	11.0	1.3
14	0.005	0.24	1.99462	-0.65	8.4	1.2
16	0.005	0.36	2.18367	-0.72	6.0	1.2
18	0.005	0.76	2.52822	-1.05	3.3	1.1
0	0.01	0.01	0.650812	-0.27	57.1	0.6
2	0.01	0.01	0.941167	-0.35	78.6	0.7
4	0.01	0.01	1.14558	-0.42	83.4	1.0
6	0.01	0.02	1.29701	-0.46	77.3	1.3
8	0.01	0.02	1.40739	-0.49	59.8	1.4
10	0.01	0.04	1.46818	-0.51	33.3	1.5
12	0.01	0.14	1.66161	-0.55	12.0	1.3
14	0.01	0.23	1.95629	-0.62	8.6	1.2
16	0.01	0.34	2.15778	-0.68	6.3	1.2
18	0.01	0.72	2.54366	-1.00	3.5	1.1
0	0.02	0.01	0.590309	-0.24	49.4	0.7
2	0.02	0.01	0.834552	-0.31	66.6	0.7
4	0.02	0.01	1.03362	-0.37	74.0	1.0
6	0.02	0.02	1.19135	-0.41	71.9	1.2
8	0.02	0.02	1.31411	-0.44	61.6	1.4
10	0.02	0.03	1.38497	-0.46	41.7	1.5
12	0.02	0.10	1.56865	-0.57	15.8	1.6
14	0.02	0.18	1.76183	-0.53	9.8	1.3
16	0.02	0.30	2.07497	-0.63	6.9	1.3
18	0.02	0.63	2.52705	-0.89	4.0	1.2
0	0.04	0.01	0.551427	-0.23	44.1	0.7
2	0.04	0.01	0.765898	-0.28	57.9	0.7
4	0.04	0.01	0.955589	-0.33	64.9	0.9
6	0.04	0.02	1.11836	-0.37	65.6	1.2
8	0.04	0.02	1.2533	-0.41	60.2	1.4
10	0.04	0.03	1.34354	-0.43	46.3	1.5
12	0.04	0.06	1.48077	-0.50	23.7	1.6
14	0.04	0.15	1.6734	-0.50	11.4	1.4
16	0.04	0.25	1.92836	-0.54	7.6	1.3
18	0.04	0.53	2.43685	-0.77	4.6	1.2
0	0.1	0.01	0.530673	-0.22	40.7	0.7
2	0.1	0.01	0.733029	-0.27	52.3	0.7
4	0.1	0.02	0.923957	-0.32	59.2	0.9
6	0.1	0.02	1.0969	-0.36	60.9	1.1
8	0.1	0.02	1.24755	-0.40	57.5	1.3
10	0.1	0.03	1.36563	-0.43	48.4	1.5
12	0.1	0.05	1.44279	-0.46	30.1	1.6
14	0.1	0.18	1.76436	-0.60	9.8	1.6
16	0.1	0.24	1.8877	-0.51	7.9	1.4
18	0.1	0.53	2.52142	-0.77	4.8	1.3

K3311

AoA	h/c	Cd	Cl	Cm	Cl/Cd	y+
0	0.005	0.02	-0.06209	-0.02	-3.7	0.6
2	0.005	0.01	0.714883	-0.27	63.8	0.7
4	0.005	0.01	1.06095	-0.39	87.9	1.0
6	0.005	0.01	1.25635	-0.45	85.3	1.2
8	0.005	0.02	1.38216	-0.49	64.0	1.3
10	0.005	0.08	1.53757	-0.56	18.9	1.2
12	0.005	0.15	1.7829	-0.60	12.0	1.1
14	0.005	0.22	1.9545	-0.63	9.0	1.1
16	0.005	0.31	2.07744	-0.67	6.6	1.1
18	0.005	0.61	2.38853	-0.90	3.9	1.0
0	0.01	0.01	0.200407	-0.11	15

Appendix A

KC135						
AoA	h/c	Cd	Cl	Cm	Cl/Cd	y+
0	0.005	0.033646	0.94037	-0.23241	27.9	4.8
2	0.005	0.019509	0.151769	0.068589	7.8	0.8
4	0.005	0.014138	0.648374	-0.14246	45.9	0.9
6	0.005	0.014964	1.01716	-0.30245	68.0	1.0
8	0.005	0.019496	1.22748	-0.38946	63.0	1.2
10	0.005	0.073719	1.37142	-0.44569	18.6	1.2
12	0.005	0.160581	1.73246	-0.55136	10.8	1.1
14	0.005	0.223267	1.8732	-0.58923	8.4	1.1
16	0.005	0.354304	2.03175	-0.6658	5.7	1.0
18	0.005	0.642676	2.34555	-0.91169	3.6	1.0
0	0.01	0.020166	-0.21557	0.126087	-10.7	0.6
2	0.01	0.014402	0.257002	-0.02949	17.8	0.7
4	0.01	0.013391	0.657981	-0.17408	49.1	0.9
6	0.01	0.014696	0.933358	-0.27337	63.5	1.0
8	0.01	0.01823	1.12178	-0.3391	61.5	1.2
10	0.01	0.029295	1.23216	-0.37726	42.1	1.3
12	0.01	0.135291	1.56166	-0.4677	11.5	1.1
14	0.01	0.220223	1.82077	-0.55329	8.3	1.1
16	0.01	0.319912	2.00054	-0.6109	6.3	1.1
18	0.01	0.586031	2.32207	-0.82781	4.0	1.0
0	0.02	0.014441	0.000112	0.013845	0.0	0.7
2	0.02	0.013092	0.349305	-0.09218	26.7	0.7
4	0.02	0.013298	0.632503	-0.17993	47.6	0.9
6	0.02	0.014712	0.857968	-0.24945	58.3	1.0
8	0.02	0.017615	1.03151	-0.30155	58.6	1.1
10	0.02	0.023994	1.15148	-0.33669	48.0	1.2
12	0.02	0.097244	1.29711	-0.366	13.3	1.2
14	0.02	0.117417	1.45436	-0.46289	12.4	1.3
16	0.02	0.286437	1.90426	-0.55207	6.6	1.1
18	0.02	0.493145	2.20627	-0.7107	4.5	1.0
0	0.04	0.013111	0.111745	-0.039	8.5	0.8
2	0.04	0.012891	0.366654	-0.10935	28.4	0.7
4	0.04	0.013543	0.595539	-0.17289	44.0	0.8
6	0.04	0.015018	0.796175	-0.22829	53.0	1.0
8	0.04	0.017587	0.96564	-0.2745	54.9	1.1
10	0.04	0.02259	1.09146	-0.30774	48.3	1.2
12	0.04	0.03819	1.16809	-0.33396	30.6	1.3
14	0.04	0.123782	1.3625	-0.35485	11.0	1.2
16	0.04	0.262868	1.82454	-0.50272	6.9	1.1
18	0.04	0.447192	2.15852	-0.64358	4.8	1.1
0	0.1	0.012808	0.138188	-0.05251	10.8	0.8
2	0.1	0.01304	0.355364	-0.10832	27.3	0.7
4	0.1	0.013896	0.564114	-0.16233	40.6	0.8
6	0.1	0.015578	0.756761	-0.2121	48.6	1.0
8	0.1	0.018208	0.930104	-0.25681	51.1	1.1
10	0.1	0.022703	1.07098	-0.29251	47.2	1.2
12	0.1	0.033145	1.16319	-0.31834	35.1	1.3
14	0.1	0.062444	1.15546	-0.29922	18.5	1.3
16	0.1	0.266394	1.83515	-0.48843	6.9	1.2
18	0.1	0.41994	2.16351	-0.60481	5.2	1.1

M25						
AoA	h/c	Cd	Cl	Cm	Cl/Cd	y+
0	0.005	0.01912	0.540065	-0.20052	28.2	0.8
2	0.005	0.012541	1.02337	-0.36661	81.6	0.8
4	0.005	0.014118	1.24456	-0.44716	88.2	1.1
6	0.005	0.024143	1.37344	-0.50026	56.9	1.3
8	0.005	0.059481	1.51672	-0.58666	25.5	1.3
10	0.005	0.129243	1.75546	-0.72722	13.6	1.3
12	0.005	0.180433	1.90669	-0.74341	10.6	1.3
14	0.005	0.194701	1.988	-0.6871	10.2	1.3
16	0.005	0.246512	2.12732	-0.69472	8.6	1.2
18	0.005	0.200332	1.81963	-0.64726	9.1	1.3
0	0.01	0.021643	0.467799	-0.17949	21.6	0.8
2	0.01	0.013414	0.891044	-0.31401	66.4	0.7
4	0.01	0.013612	1.12721	-0.39029	82.8	1.0
6	0.01	0.018755	1.27719	-0.44267	68.1	1.3
8	0.01	0.043801	1.39262	-0.50478	31.8	1.4
10	0.01	0.113772	1.64269	-0.65986	14.4	1.4
12	0.01	0.183792	1.83904	-0.73051	10.0	1.3
14	0.01	0.172505	1.81245	-0.59869	10.5	1.3
16	0.01	0.227282	2.02941	-0.6415	8.9	1.3
18	0.01	0.463729	2.34577	-0.76552	5.1	1.2
0	0.02	0.021853	0.395825	-0.1494	18.1	0.9
2	0.02	0.01494	0.765325	-0.26583	51.2	0.6
4	0.02	0.013683	1.00028	-0.33448	73.1	0.9
6	0.02	0.016595	1.17088	-0.38813	70.6	1.2
8	0.02	0.031079	1.30679	-0.4462	42.0	1.4
10	0.02	0.087693	1.53166	-0.58333	17.5	1.4
12	0.02	0.166487	1.85787	-0.73912	11.2	1.4
14	0.02	0.154673	1.73931	-0.5818	11.2	1.3
16	0.02	0.199795	1.85271	-0.55336	9.3	1.3
18	0.02	0.31482	2.14421	-0.64799	6.8	1.3
0	0.04	0.024855	0.363301	-0.13884	14.6	0.9
2	0.04	0.017169	0.671921	-0.2308	39.1	0.7
4	0.04	0.014411	0.901071	-0.2922	62.5	0.8
6	0.04	0.016724	1.08181	-0.34506	64.7	1.1
8	0.04	0.023624	1.2392	-0.39869	52.5	1.4
10	0.04	0.062214	1.44509	-0.51174	23.2	1.5
12	0.04	0.147328	1.76048	-0.68005	11.9	1.4
14	0.04	0.181326	1.89861	-0.69277	10.5	1.4
16	0.04	0.152542	1.7228	-0.49437	11.3	1.4
18	0.04	0.273121	2.00204	-0.57558	7.3	1.3
0	0.1	0.026235	0.347677	-0.13377	13.3	0.9
2	0.1	0.018774	0.626696	-0.2131	33.4	0.7
4	0.1	0.015328	0.853182	-0.26975	55.7	0.8
6	0.1	0.017182	1.04579	-0.32323	60.9	1.1
8	0.1	0.022046	1.21754	-0.3754	55.2	1.4
10	0.1	0.050174	1.42139	-0.47257	28.3	1.5
12	0.1	0.133377	1.78033	-0.66532	13.3	1.5
14	0.1	0.20414	2.05995	-0.76815	10.1	1.5
16	0.1	0.165627	1.85739	-0.56004	11.2	1.4
18	0.1	0.225735	1.88427	-0.5094	8.3	1.4

MH115						
AoA	h/c	Cd	Cl	Cm	Cl/Cd	y+
0	0.005	0.012908	0.565539	-0.3239	43.8	0.9
2	0.005	0.011909	1.0746	-0.46591	90.2	0.6
4	0.005	0.014017	1.29199	-0.52724	92.2	0.9
6	0.005	0.017237	1.43034	-0.56505	83.0	1.1
8	0.005	0.022072	1.53518	-0.59401	69.6	5.1
10	0.005	0.033092	1.63662	-0.63066	49.5	1.6
12	0.005	0.057114	1.71499	-0.66763	30.0	1.8
14	0.005	0.156334	1.87997	-0.69068	12.0	1.4
16	0.005	0.22028	2.09188	-0.7049	9.5	1.3
18	0.005	0.389933	2.32565	-0.79438	6.0	1.2
0	0.01	0.01213	0.638036	-0.32671	52.6	0.9
2	0.01	0.012278	0.968937	-0.41517	78.9	5.9
4	0.01	0.014001	1.17215	-0.46798	83.7	5.1
6	0.01	0.016895	1.32437	-0.50827	78.4	6.5
8	0.01	0.021434	1.44704	-0.54255	67.5	1.4
10	0.01	0.028203	1.53971	-0.5692	54.6	6.8
12	0.01	0.057018	1.68688	-0.64024	29.6	1.8
14	0.01	0.105518	1.69669	-0.67306	16.1	1.9
16	0.01	0.206788	2.0101	-0.66696	9.7	1.3
18	0.01	0.3588	2.301	-0.76131	6.4	1.2
0	0.02	0.012434	0.647177	-0.31718	52.0	3.1
2	0.02	0.012929	0.891922	-0.37941	69.0	3.2
4	0.02	0.014505	1.085994	-0.42882	74.9	5.3
6	0.02	0.016981	1.24185	-0.468	73.1	1.0
8	0.02	0.021019	1.35959	-0.49574	64.7	7.4
10	0.02	0.027623	1.45803	-0.5218	52.8	2.9
12	0.02	0.037261	1.52403	-0.53959	40.9	1.7
14	0.02	0.066702	1.57536	-0.57312	23.6	1.9
16	0.02	0.137373	1.78173	-0.58755	13.0	1.5
18	0.02	0.304384	2.21446	-0.69907	7.3	1.3
0	0.04	0.013017	0.644008	-0.31093	49.5	0.8
2	0.04	0.013723	0.853754	-0.36261	62.2	3.6
4	0.04	0.015347	1.03567	-0.40692	67.5	0.7
6	0.04	0.017513	1.18638	-0.44119	67.7	6.1
8	0.04	0.020912	1.31797	-0.47231	63.0	6.2
10	0.04	0.026736	1.42073	-0.4969	53.1	7.2
12	0.04	0.037089	1.48738	-0.51309	40.1	1.7
14	0.04	0.050386	1.51483	-0.52133	30.1	5.9
16	0.04	0.163538	1.85236	-0.73592	11.3	2.0
18	0.04	0.188792	1.89613	-0.54643	10.0	1.4
0	0.1	0.013717	0.637928	-0.30728	46.5	4.0
2	0.1	0.014699	0.840711	-0.35716	57.2	2.7
4	0.1	0.016403	1.02862	-0.40305	62.7	0.7
6	0.1	0.018725	1.19457	-0.44196	63.8	9.3
8	0.1	0.022399	1.33785	-0.47534	59.7	2.9
10	0.1	0.027734	1.4559	-0.50279	52.5	1.5
12	0.1	0.036978	1.54475	-0.52463	41.8	1.7
14	0.1	0.067284	1.61907	-0.55595	24.1	1.8
16	0.1	0.109731	1.76183	-0.64319	16.1	2.0
18	0.1	0.14796	1.9518	-0.56107	13.2	1.5

MUE139						
AoA	h/c	Cd	Cl	Cm	Cl/Cd	y+
0	0.005	0.020435	-0.05726	-0.06081	-2.8	0.8
2	0.005	0.012529	0.775512	-0.27161	61.9	3.2
4	0.005	0.01352	1.12627	-0.38657	83.3	3.5
6	0.005	0.01611	1.32453	-0.45409	82.2	4.4
8	0.005	0.02032	1.46505	-0.503	72.1	0.8
10	0.005	0.028432	1.57748	-0.54713	55.5	0.8
12	0.005	0.045981	1.67634	-0.59488	36.5	0.9
14	0.005	0.091096	1.82214	-0.69071	20.0	1.0
16	0.005	0.192515	2.0703	-0.85895	10.8	1.1
18	0.005	0.380146	2.3601	-1.00381	6.2	1.2
0	0.01	0.014595	0.250383	-0.12129	17.2	2.4
2	0.01	0.012974	0.70491	-0.24417	54.3	4.6
4	0.01	0.013803	0.999001	-0.33307	72.4	3.4
6	0.01	0.016004	1.20006	-0.39477	75.0	0.7
8	0.01	0.019765	1.34861	-0.44117	68.2	0.8
10	0.01	0.026941	1.46861	-0.48376	54.5	0.8
12	0.01	0.040997	1.56633	-0.52489	38.2	5.9
14	0.01	0.079984	1.72306	-0.62078	21.5	4.5
16	0.01	0.173793	2.00138	-0.80224	11.5	1.2
18	0.01	0.393465	2.39155	-1.01872	6.1	2.8
0	0.02	0.013754	0.357255	-0.14762	26.0	2.1
2	0.02	0.013464	0.65902	-0.2284	48.9	0.6
4	0.02	0.014322	0.898716	-0.29426	62.8	0.7
6	0.02	0.016334	1.09109	-0.34814	66.8	0.8
8	0.02	0.019608	1.24229	-0.3907	63.4	3.8
10	0.02	0.025522	1.3656	-0.42943	53.5	0.8
12	0.02	0.037862	1.4607	-0.46603	38.6	4.1
14	0.02	0.068035	1.63686	-0.56052	24.1	5.3
16	0.02	0.166269	1.94646	-0.76139	11.7	5.3
18	0.02	0.296687	2.29931	-0.94092	7.7	1.2
0	0.04	0.013768	0.386137	-0.15562	28.0	0.7
2	0.04	0.014016	0.622782	-0.2158	44.4	0.6
4	0.04	0.015101	0.83235	-0.26945	55.1	0.7
6	0.04	0.016971	1.01736	-0.31758	59.9	0.7
8	0.04	0.019964	1.17247	-0.35827	58.7	4.9
10	0.04	0.024649	1.3077	-0.39742	53.1	0.8
12	0.04	0.033334	1.43108	-0.44056	42.9	0.9
14	0.04	0.05913	1.58323	-0.51758	26.8	1.0
16	0.04	0.151426	1.88736	-0.7121	12.5	1.1
18	0.04	0.296822	2.30319	-0.93578	7.8	4.8
0	0.1	0.014043	0.385978	-0.15518	27.5	2.6
2	0.1	0.014632	0.597967	-0.20665	40.9	1.6
4	0.1	0.015957	0.799149	-0.25604	50.1	2.9
6	0.1	0.017862	0.986537	-0.30255	55.2	0.8
8	0.1	0.021015	1.1538	-0.34517	54.9	0.8
10	0.1	0.025482	1.29452	-0.38215	50.8	5.4
12	0.1	0.032667	1.43541	-0.42786	43.9	3.6
14	0.1	0.052994	1.57755	-0.49177	29.8	1.0
16	0.1	0.121671	1.8664	-0.65939	15.3	3.1
18	0.1	0.269402	2.3568	-0.92585	8.7	5.4

PMC19						
AoA	h/c	Cd	Cl	Cm	Cl/Cd	y+
0	0.005	0.02396	-0.18487	0.218622	-7.7	0.7
2	0.005	0.013757	0.268161	0.022601	19.5	0.9
4	0.005	0.011986	0.78573	-0.20843	65.6	1.1
6	0.005	0.016723	1.08018	-0.33574	64.6	1.3
8	0.005	0.065135	1.32446	-0.44187	20.3	1.2
10	0.005	0.158548	1.60805	-0.50966	10.1	1.2
12	0.005	0.225565	1.73276	-0.53648	7.7	1.2
14	0.005	0.348633	1.92491	-0.60392	5.5	1.1
16	0.005	0.482451	2.06748	-0.68361	4.3	1.1
18	0.005	0.598523	1.52533	-0.70527	2.5	0.9
0	0.01	0.015802	-0.20147	0.142019	-12.8	0.8
2	0.01	0.01206	0.331972	-0.04865	27.5	0.8
4	0.01	0.011834	0.706147	-0.18738	59.7	1.1
6	0.01	0.014338	0.968998	-0.28445	67.6	1.3
8	0.01	0.037446	1.15249	-0.35838	30.8	1.3
10	0.01	0.129303	1.44208	-0.43086	11.2	1.2
12	0.01	0.218823	1.67445	-0.491	7.7	1.2
14	0.01	0.297266	1.79178	-0.5288	6.0	1.2
16	0.01	0.454654	2.01087	-0.63643	4.4	1.1
18	0.01	0.779121	2.44388	-0.98171	3.1	1.1
0	0.02	0.012917	0.01515	0.038118	-1.2	0.9
2	0.02	0.011685	0.340759	-0.07397	29.2	0.7
4	0.02	0.011956	0.628927	-0.16616	52.6	1.0
6	0.02	0.013654	0.865442	-0.24254	63.4	1.2
8	0.02	0.022553	1.0476	-0.30281	46.5	1.4
10	0.02	0.094646	1.2596	-0.36426	13.3	1.2
12	0.02	0.196199	1.5662	-0.43722	8.0	1.2
14	0.02	0.273589	1.71946	-0.47906	6.3	1.2
16	0.02	0.389562	1.89595	-0.53555	4.9	1.2
18	0.02	0.678071	2.33537	-0.80322	3.4	1.2
0	0.04	0.012149	0.055827	-0.00021	4.6	0.9
2	0.04	0.011713	0.323457	-0.07658	27.6	0.7
4	0.04	0.012265	0.564708	-0.146	46.0	0.9
6	0.04	0.013834	0.782083	-0.20953	56.5	1.2
8	0.04	0.018447	0.970697	-0.2657	52.6	1.4
10	0.04	0.06144	1.16483	-0.33969	19.0	1.4
12	0.04	0.151563	1.36729	-0.35235	9.0	1.2
14	0.04	0.254806	1.63674	-0.42899	6.4	1.2
16	0.04	0.349048	1.81064	-0.4774	5.2	1.2
18	0.04	0.602423	2.19538	-0.69619	3.6	1.2
0	0.1	0.011943	0.070632	-0.00978	5.9	0.9
2	0.1	0.011906	0.299256	-0.07028	25.1	0.7
4	0.1	0.012619	0.51995	-0.12924	41.2	0.9
6	0.1	0.014201	0.730886	-0.18682	51.5	1.2
8	0.1	0.017963	0.924834	-0.24107	51.5	1.4
10	0.1	0.043403	1.10862	-0.30629	25.5	1.4
12	0.1	0.132279	1.29378	-0.31845	9.8	1.3
14	0.1	0.255477	1.64991	-0.41034	6.5	1.3
16	0.1	0.363676	1.86091	-0.47503	5.1	1.3
18	0.1	0.621486	2.28975	-0.68662	3.7	1.3

PrandtI_d						
AoA	h/c	Cd	Cl	Cm	Cl/Cd	y+
0	0.005	0.023601	-0.54035	0.143624	-22.9	3.7
2	0.005	0.013456	0.268813	-0.06007	20.0	0.6
4	0.005	0.012422	0.745322	-0.22287	60.0	2.0
6	0.005	0.013969	1.02157	-0.32415	73.1	3.5
8	0.005	0.018178	1.19695	-0.38839	65.8	3.5
10	0.005	0.029165	1.30403	-0.42874	44.7	4.5
12	0.005	0.068701	1.42321	-0.50659	20.7	1.3
14	0.005	0.138966	1.65944	-0.53453	11.9	1.2
16	0.005	0.214907	1.94276	-0.61194	9.0	3.3
18	0.005	0.341293	2.12945	-0.68063	6.2	1.1
0	0.01	0.016577	-0.2227	0.062439	-13.4	1.8
2	0.01	0.012951	0.309059	-0.08828	23.9	0.6
4	0.01	0.012604	0.672083	-0.20395	53.3	0.8
6	0.01	0.013957	0.925997	-0.28799	66.3	2.8
8	0.01	0.017269	1.10339	-0.34643	63.9	3.5
10	0.01	0.025747	1.21802	-0.38548	47.3	1.2
12	0.01	0.049474	1.30401	-0.43008	26.4	4.0
14	0.01	0.10487	1.41854	-0.43234	13.5	3.1
16	0.01	0.188186	1.81572	-0.5509	9.6	4.1
18	0.01	0.310127	2.07763	-0.63869	6.7	4.8
0	0.02	0.014078	-0.02197	-0.00398	-1.6	0.9
2	0.02	0.012765	0.326554	-0.10318	25.6	3.3
4	0.02	0.012918	0.607742	-0.18641	47.0	0.7
6	0.02	0.014229	0.835275	-0.25513	58.7	3.3
8	0.02	0.016836	1.0125	-0.30851	60.1	1.9
10	0.02	0.023139	1.13514	-0.34606	49.1	1.2
12	0.02	0.038549	1.21018	-0.37509	31.4	4.7
14	0.02	0.126377	1.48889	-0.54705	11.8	1.4
16	0.02	0.147454	1.59566	-0.45129	10.8	4.2
18	0.02	0.277791	1.98321	-0.57831	7.1	3.5
0	0.04	0.013228	0.063046	-0.03546	4.8	1.7
2	0.04	0.012808	0.323767	-0.10633	25.3	0.6
4	0.04	0.013283	0.560727	-0.17238	42.2	0.7
6	0.04	0.01459	0.768582	-0.23057	52.7	0.9
8	0.04	0.01699	0.943276	-0.27951	55.5	3.3
10	0.04	0.021659	1.08532	-0.32119	50.1	2.3
12	0.04	0.033559	1.18775	-0.35758	35.4	1.3
14	0.04	0.084811	1.38894	-0.476	16.4	5.1
16	0.04	0.102376	1.44399	-0.37823	14.1	4.3
18	0.04	0.215157	1.76291	-0.47006	8.2	1.2
0	0.1	0.012951	0.089551	-0.04616	6.9	0.9
2	0.1	0.012995	0.313342	-0.10422	24.1	0.7
4	0.1	0.013701	0.528711	-0.16097	38.6	0.7
6	0.1	0.015112	0.731393	-0.21515	48.4	2.3
8	0.1	0.017584	0.910556	-0.26314	51.8	2.6
10	0.1	0.021713	1.06006	-0.30383	48.8	2.1
12	0.1	0.03152	1.17161	-0.3391	37.2	1.3
14	0.1	0.064198	1.30987	-0.41256	20.4	1.4
16	0.1	0.122122	1.589	-0.46317	13.0	3.7
18	0.1	0.190975	1.70393	-0.43577	8.9	3.6

R3A						
AoA	h/c	Cd	Cl	Cm	Cl/Cd	y+
0	0.005	0.018356	-0.19598	0.091092	-10.7	0.7
2	0.005	0.012204	0.604223	-0.16679	49.5	0.7
4	0.005	0.012495	1.01531	-0.32338	81.3	0.7
6	0.005	0.014605	1.25099	-0.41366	85.7	0.8
8	0.005	0.018042	1.41264	-0.47397	78.3	0.9
10	0.005	0.024309	1.53693	-0.52249	63.2	1.0
12	0.005	0.041996	1.65019	-0.58069	39.3	1.1
14	0.005	0.099415	1.8455	-0.70856	18.6	1.2
16	0.005	0.180122	2.06825	-0.81395	11.5	1.3
18	0.005	0.426383	2.313	-0.83768	5.4	1.3
0	0.01	0.014387	0.068984	-0.01047	4.8	0.8
2	0.01	0.012322	0.568797	-0.16654	46.2	0.7
4	0.01	0.012786	0.89657	-0.27615	70.1	0.7
6	0.01	0.014578	1.12704	-0.35412	77.3	0.8
8	0.01	0.017559	1.29991	-0.41252	74.0	0.9
10	0.01	0.022979	1.43093	-0.45485	62.3	0.9
12	0.01	0.036409	1.5458	-0.51016	42.5	1.0
14	0.01	0.079349	1.74823	-0.63099	22.0	1.2
16	0.01	0.161227	2.01385	-0.77255	12.5	1.3
18	0.01	0.391946	2.30347	-0.85363	5.9	1.3
0	0.02	0.013155	0.201774	-0.06422	15.3	0.8
2	0.02	0.012589	0.53249	-0.16068	42.3	0.7
4	0.02	0.013223	0.799622	-0.24091	60.5	0.7
6	0.02	0.01482	1.0162	-0.30659	68.6	0.7
8	0.02	0.017467	1.1928	-0.3606	68.3	0.9
10	0.02	0.021702	1.33558	-0.40592	61.5	0.9
12	0.02	0.031291	1.45595	-0.4525	46.5	1.0
14	0.02	0.065402	1.63791	-0.5544	25.0	1.1
16	0.02	0.144852	1.94987	-0.72588	13.5	1.3
18	0.02	0.313943	2.24021	-0.83373	7.1	1.4
0	0.04	0.012878	0.243764	-0.08272	18.9	0.8
2	0.04	0.012944	0.498806	-0.15187	38.5	0.7
4	0.04	0.01385	0.728766	-0.21531	52.6	0.7
6	0.04	0.015489	0.933139	-0.27227	60.2	0.8
8	0.04	0.017919	1.11331	-0.32341	62.1	0.9
10	0.04	0.021637	1.26551	-0.36804	58.5	0.9
12	0.04	0.028917	1.39575	-0.41272	48.3	1.0
14	0.04	0.056188	1.56451	-0.50013	27.8	1.1
16	0.04	0.126251	1.88513	-0.67556	14.9	1.2
18	0.04	0.257839	2.19287	-0.80698	8.5	1.4
0	0.1	0.012943	0.247666	-0.08562	19.1	0.8
2	0.1	0.01336	0.471459	-0.14266	35.3	0.7
4	0.1	0.014445	0.687188	-0.19868	47.6	0.7
6	0.1	0.016196	0.890479	-0.25225	55.0	0.8
8	0.1	0.019066	1.0754	-0.30201	56.4	0.8
10	0.1	0.022711	1.24406

A.2 3D Optimisation Study

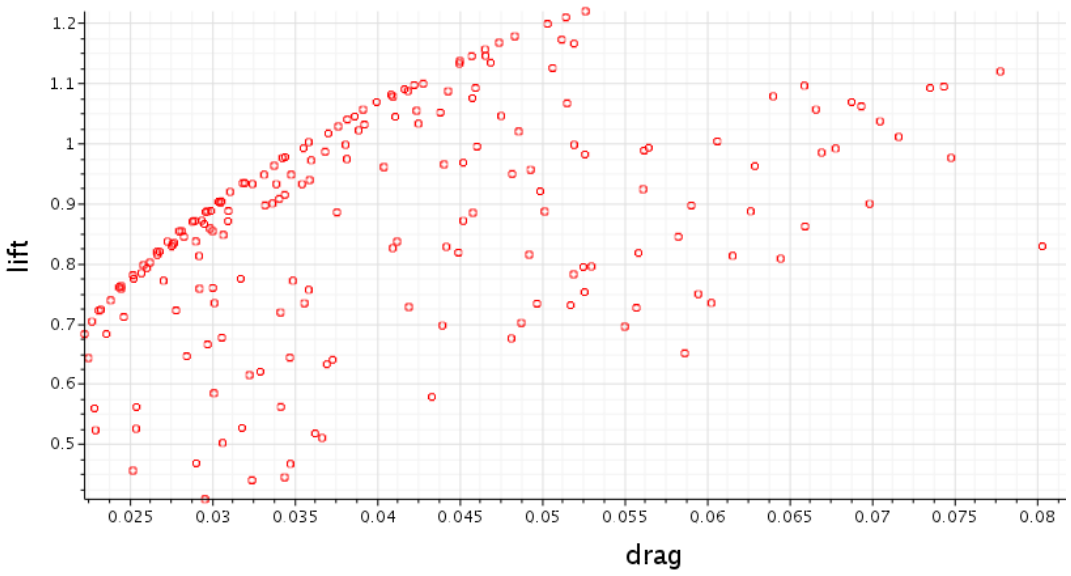

3D wing tip position, twist, and chord optimisation at h/c = 0.05 ground clearance.

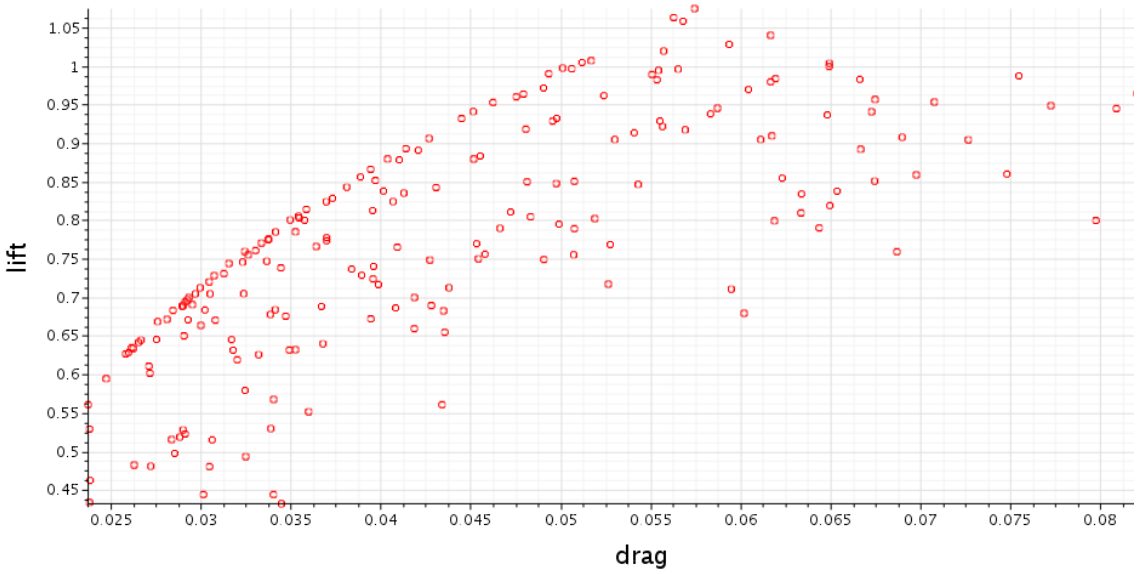

3D wing tip position, twist, and chord optimisation at h/c = 0.1 ground clearance.

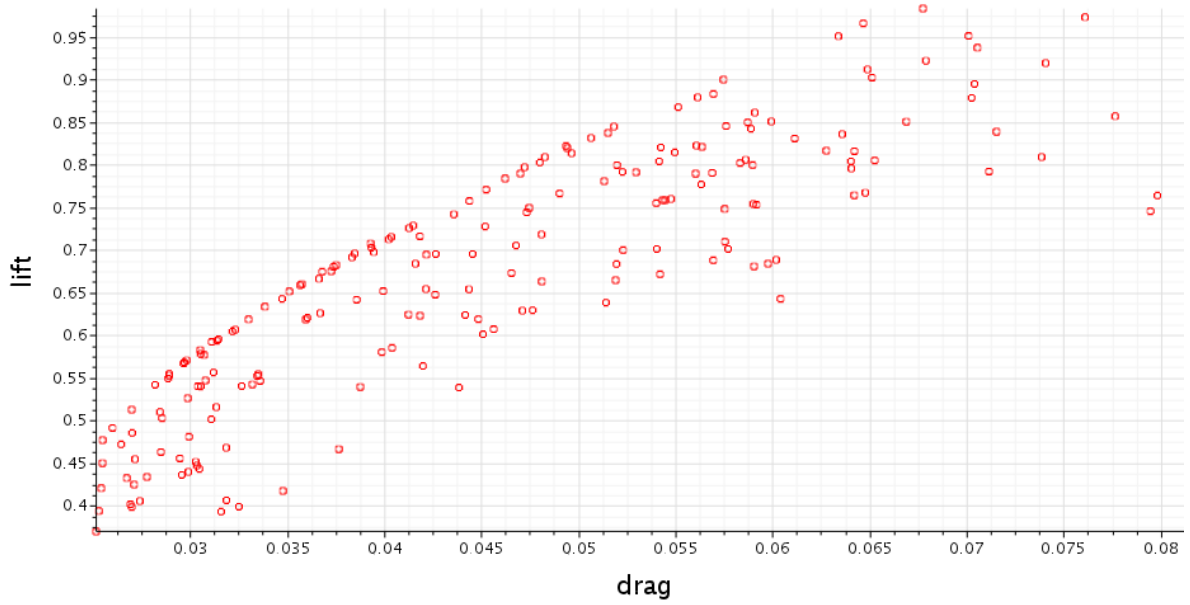

3D wing tip position, twist, and chord optimisation at h/c = 0.2 ground clearance.

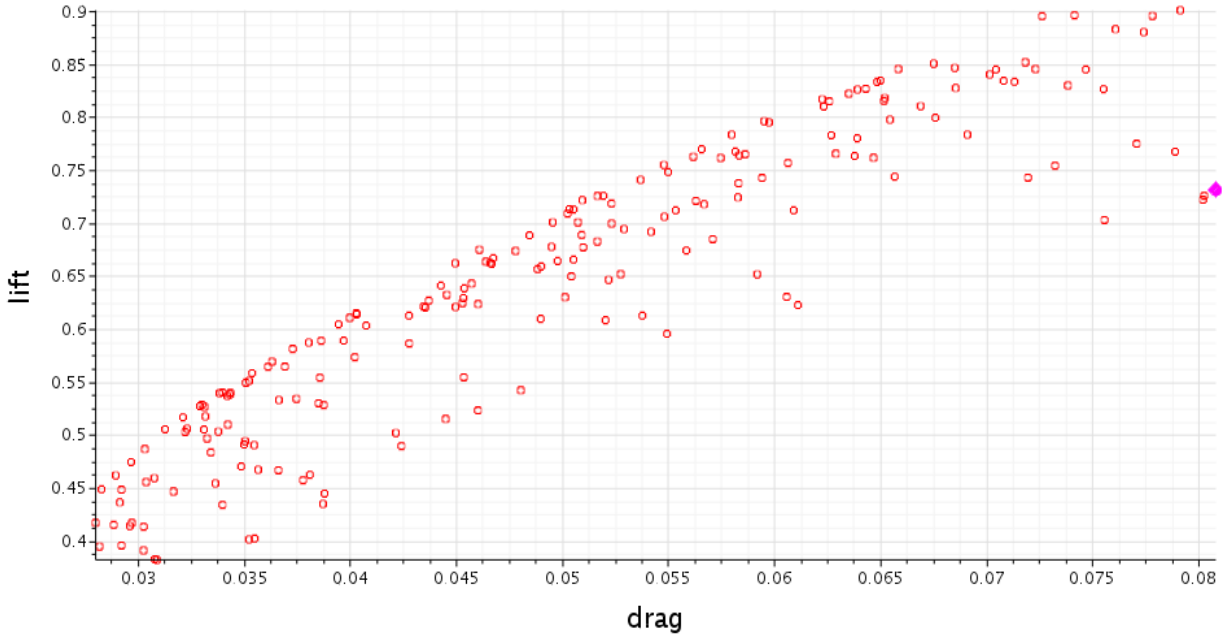

3D wing tip position, twist, and chord optimisation at h/c = 0.4 ground clearance.

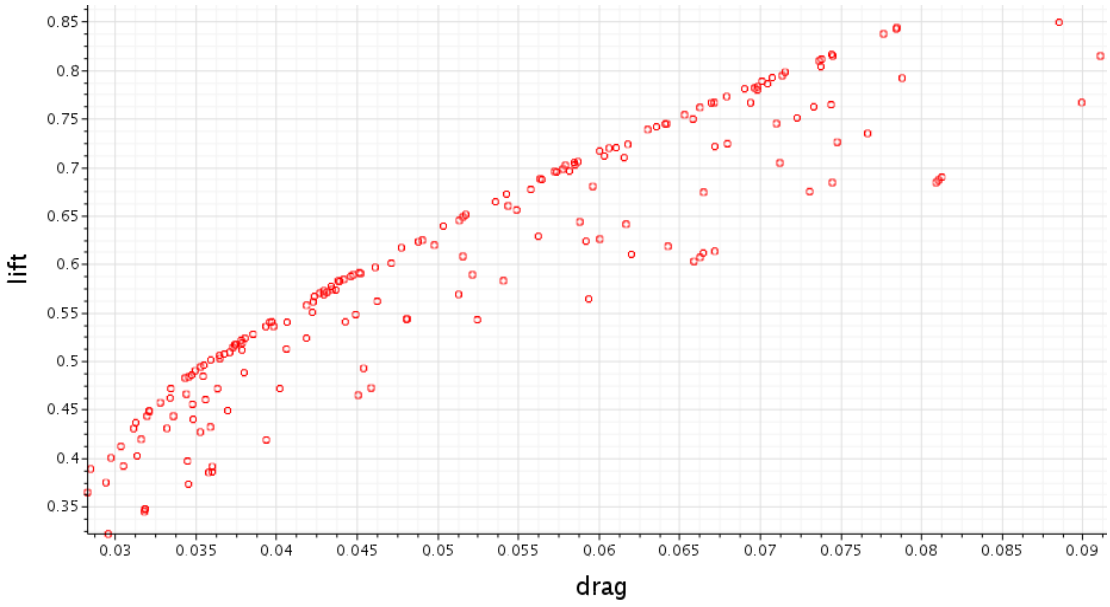

Figure 8.1: 3D wing tip position, twist, and chord optimisation at h/c = 1 ground clearance.

A.3 Morphed and Flap Aerofoil Comparison

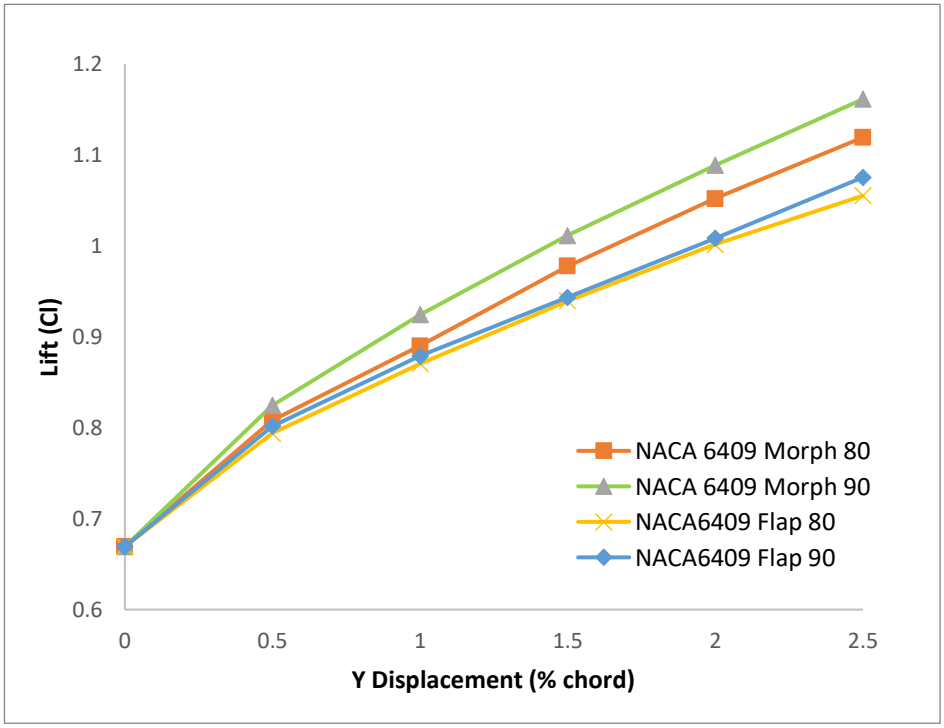

Appendix A

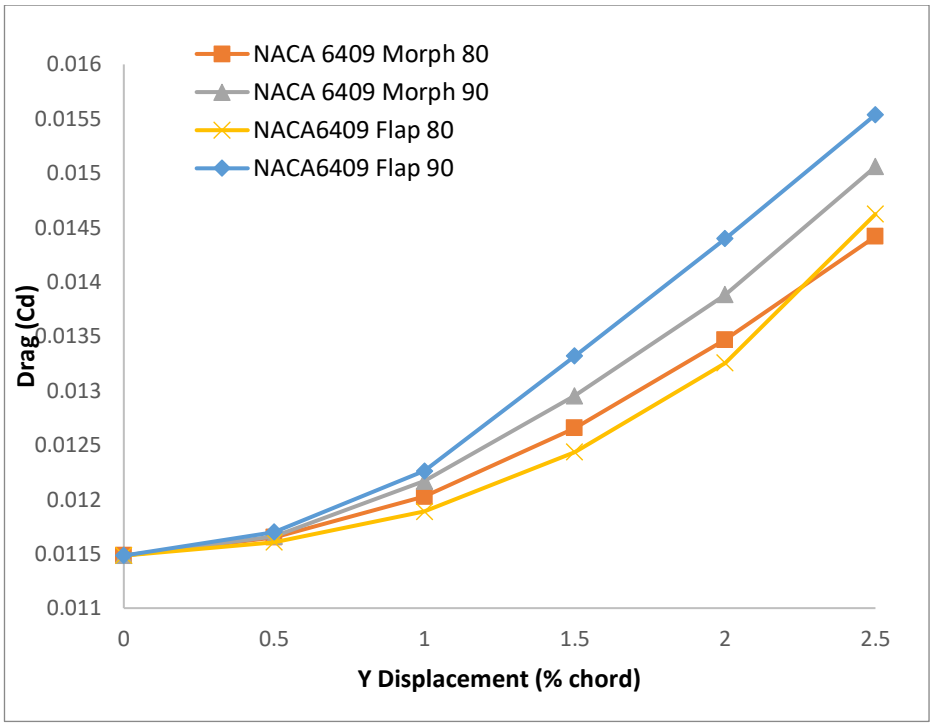
NACA 6409 Morph 80
NACA 6409 Morph 90
NACA6409 Flap 80
NACA6409 Flap 90
Drag (Cd)
0.016
0.0155
0.015
0.0145
0.014
0.0135
0.013
0.0125
0.012
0.0115
0.011
0
0.5
1
1.5
2
2.5
Y Displacement (% chord)

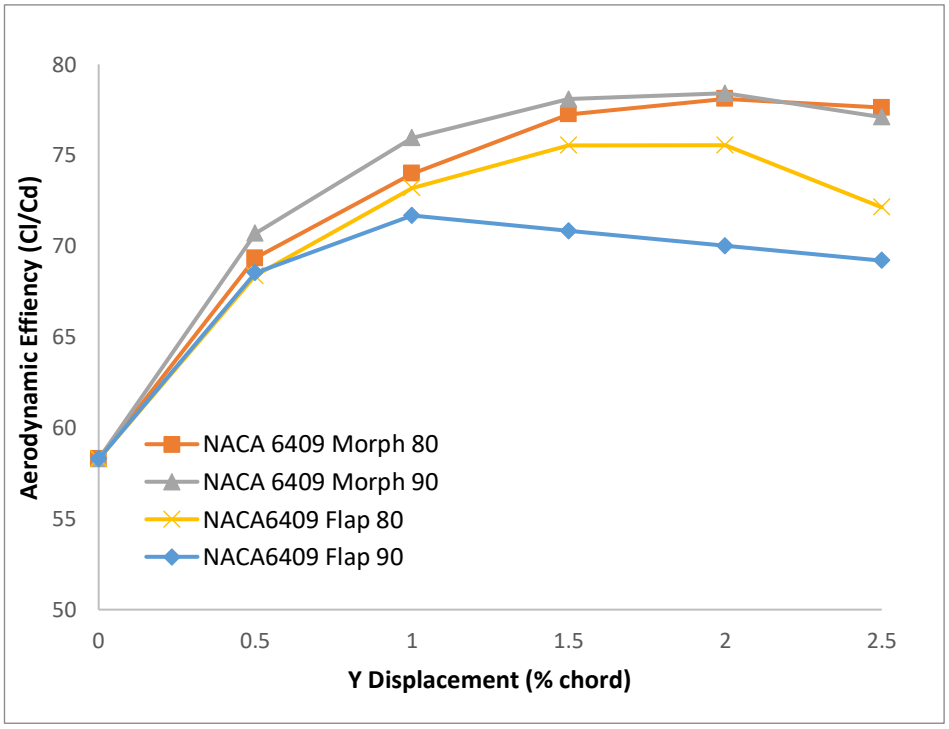
Aerodynamic Effiency (Cl/Cd)
80
75
70
65
60
55
50
NACA 6409 Morph 80
NACA 6409 Morph 90
NACA6409 Flap 80
NACA6409 Flap 90
0
0.5
1
1.5
2
2.5
Y Displacement (% chord)

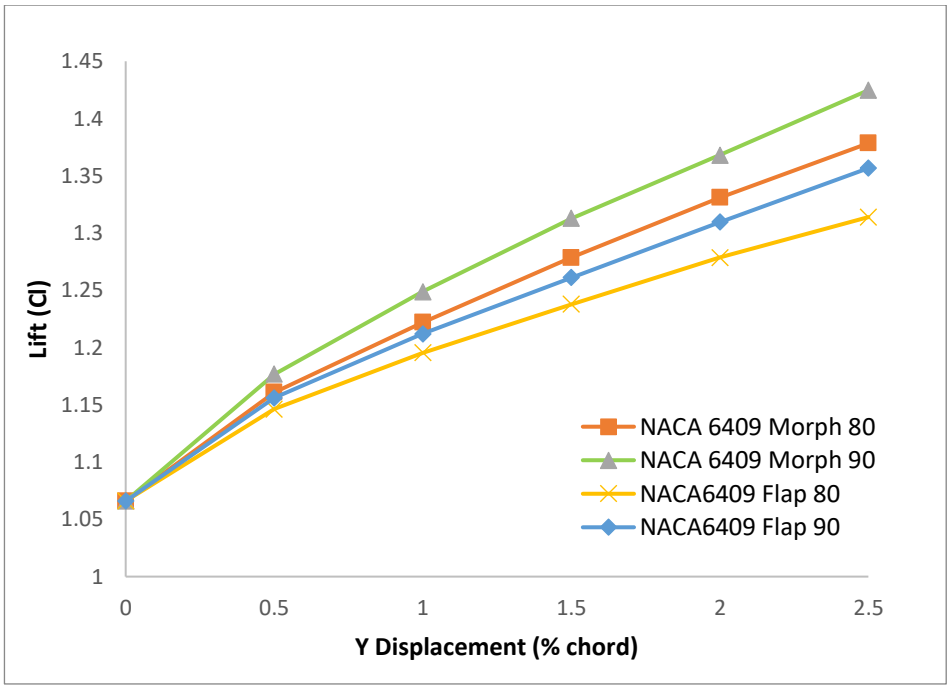
1.45
1.4
1.35
1.3
1.25
1.2
1.15
1.1
1.05
1
Lift (Cl)
0
0.5
1
1.5
2
2.5
Y Displacement (% chord)
NACA 6409 Morph 80
NACA 6409 Morph 90
NACA6409 Flap 80
NACA6409 Flap 90

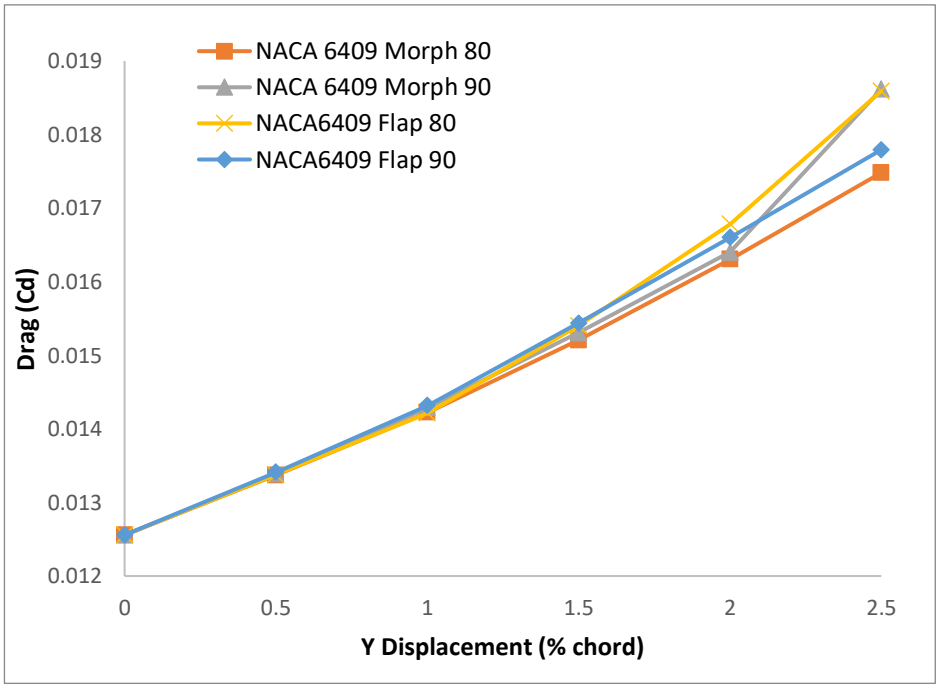
0.019
0.018
0.017
0.016
0.015
0.014
0.013
0.012
Drag (Cd)
0
0.5
1
1.5
2
2.5
Y Displacement (% chord)
NACA 6409 Morph 80
NACA 6409 Morph 90
NACA6409 Flap 80
NACA6409 Flap 90

Appendix A

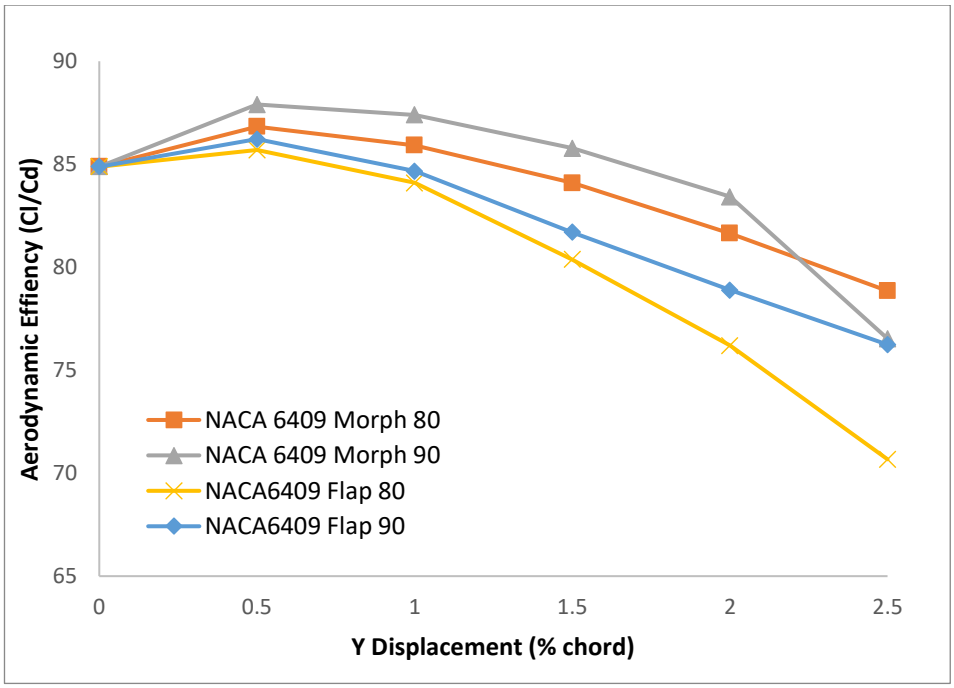
90
85
80
75
70
65
Aerodynamic Effiency (Cl/Cd)
0
0.5
1
1.5
2
2.5
Y Displacement (% chord)
NACA 6409 Morph 80
NACA 6409 Morph 90
NACA6409 Flap 80
NACA6409 Flap 90

A.4 16-degree AoA Freestream TKE.

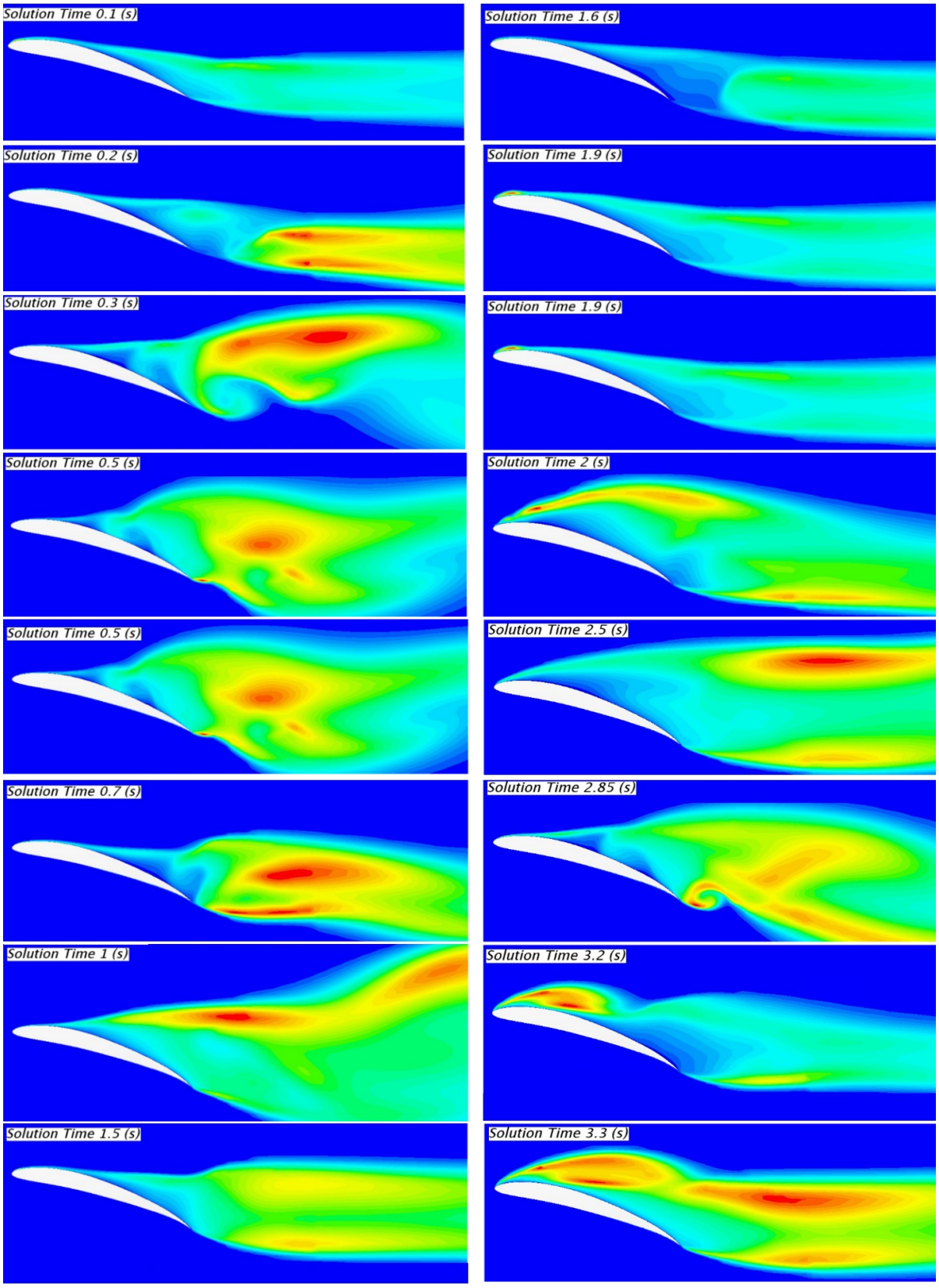

A.5 Rectangular Wing Morphed Span Length.

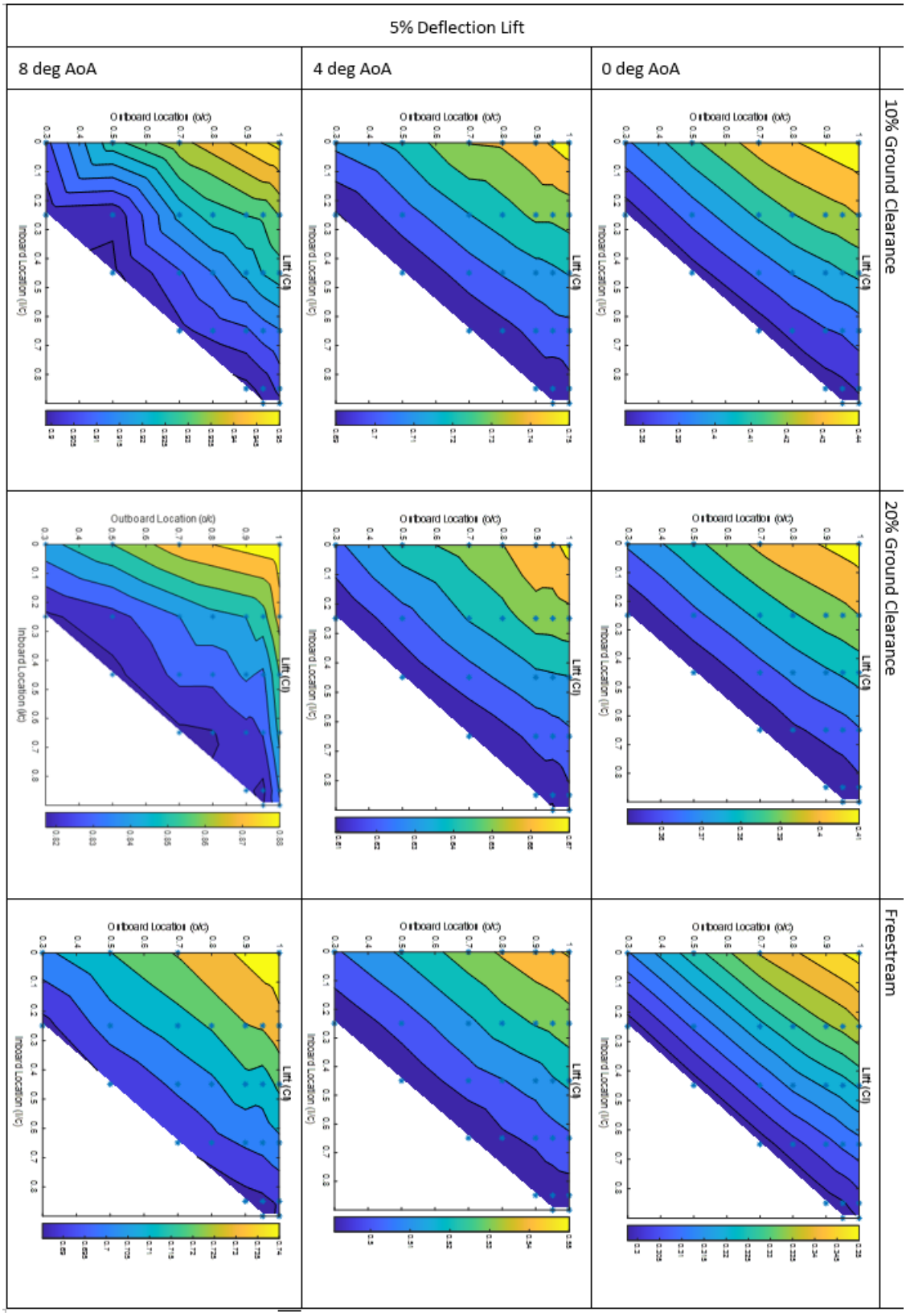

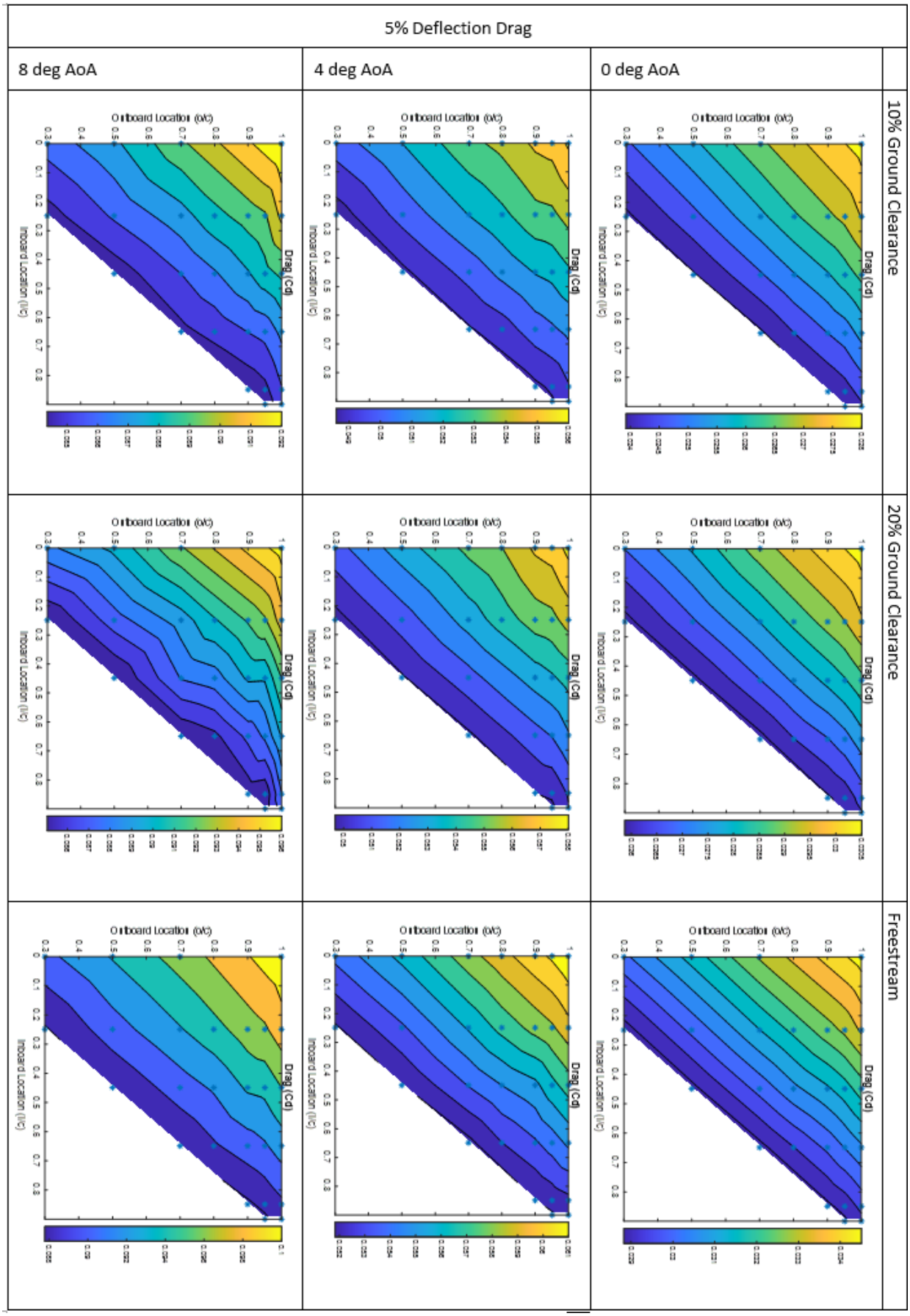
5% Deflection Drag
8 deg AoA
4 deg AoA
0 deg AoA
10% Ground Clearance
20% Ground Clearance
Freestream
Outboard Location (y/c)
Inboard Location (y/c)
Drag (Cd)

Appendix A

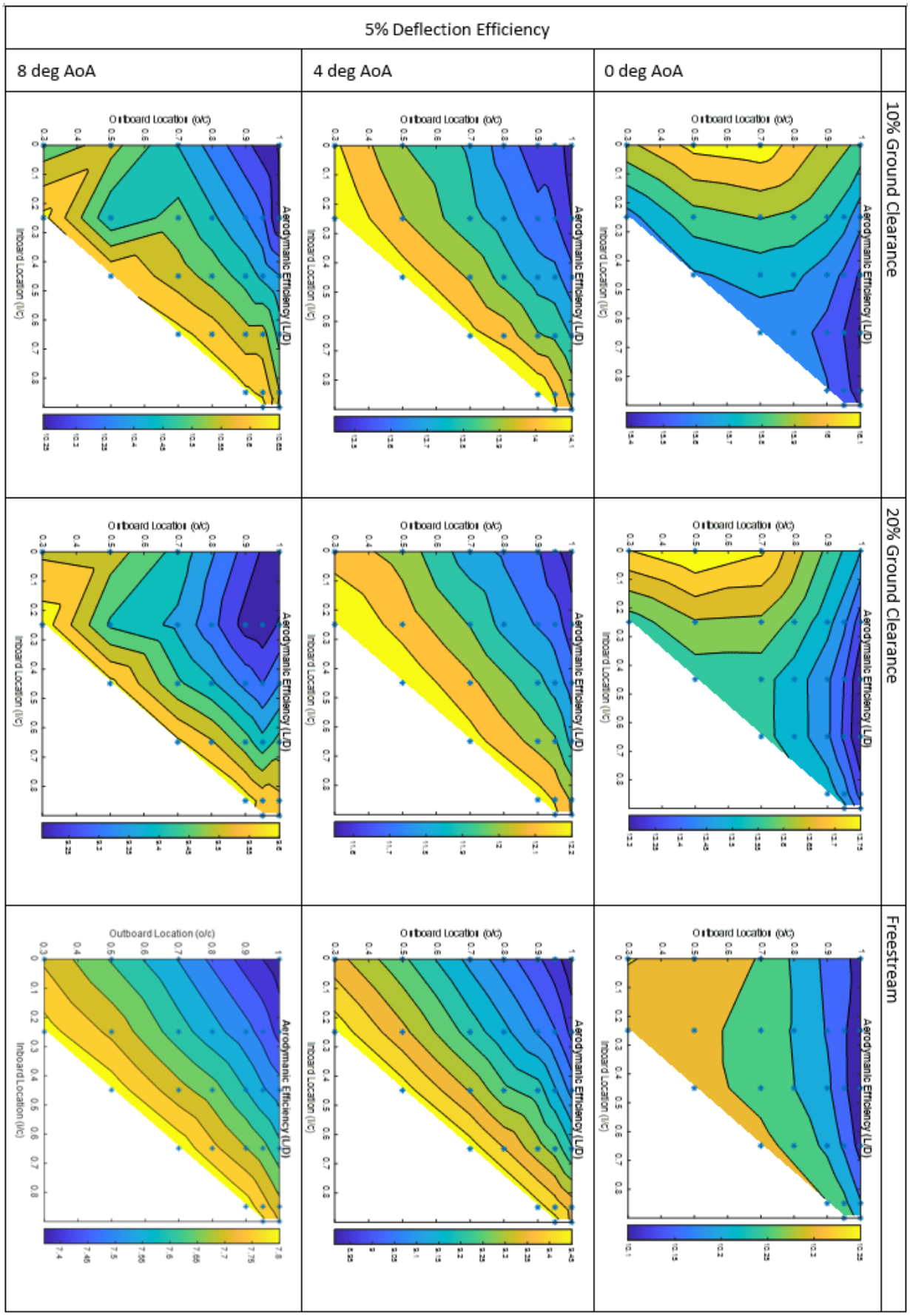
5% Deflection Efficiency
8 deg AoA
4 deg AoA
0 deg AoA
10% Ground Clearance
20% Ground Clearance
Freestream
Outboard Location (o/c)
Inboard Location (i/c)
Aerodynamic Efficiency (L/D)

10% Deflection Lift		
8 deg AoA	4 deg AoA	0 deg AoA
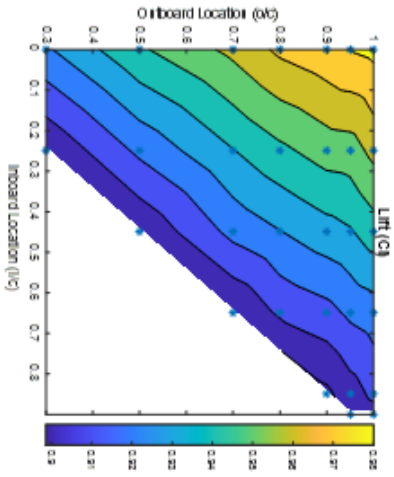	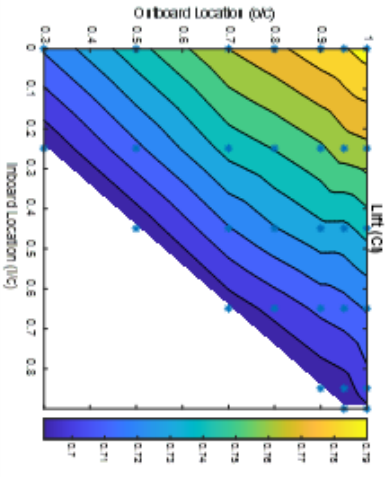	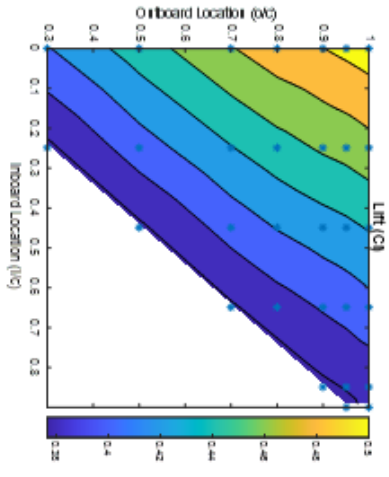
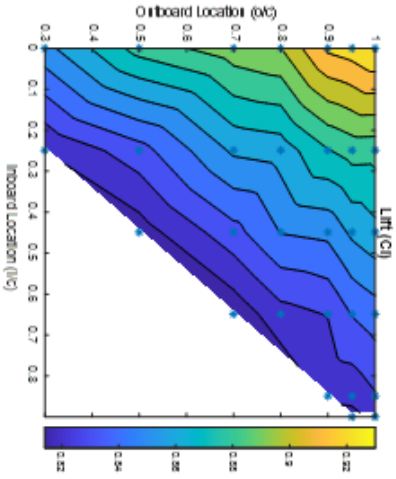	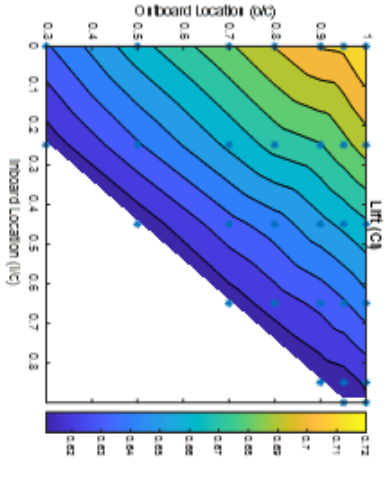	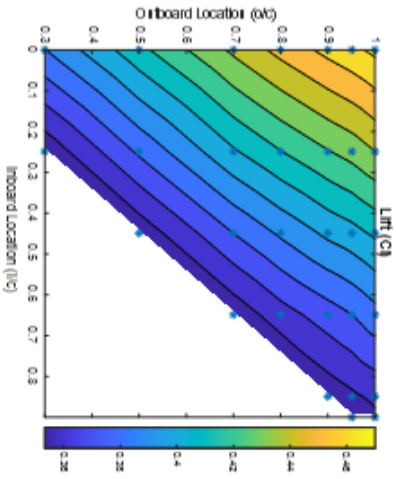
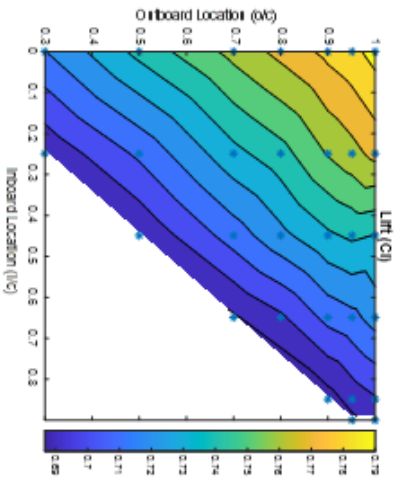	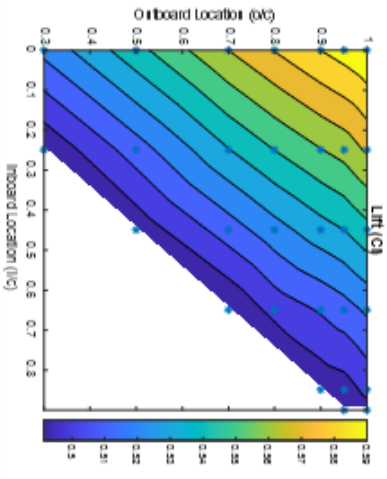	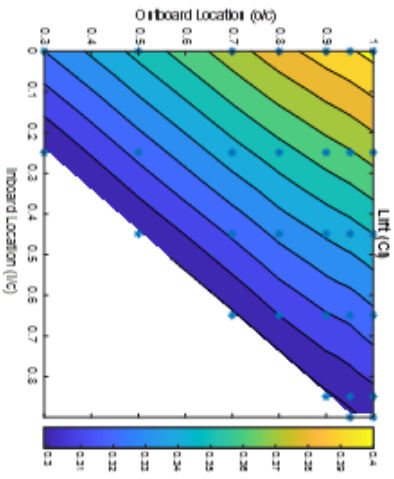

10% Ground Clearance
20% Ground Clearance
Freestream

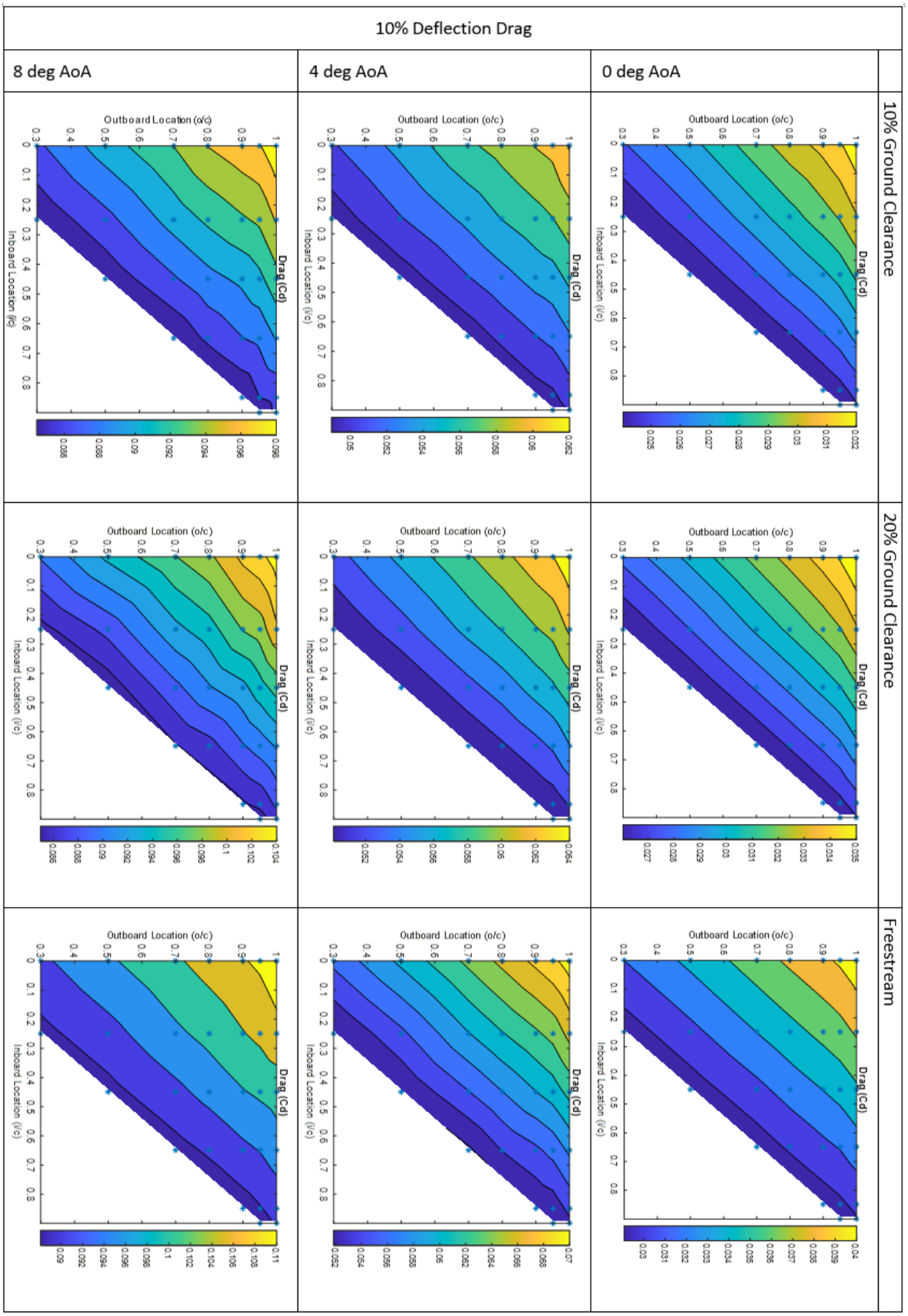
10% Deflection Drag
8 deg AoA
4 deg AoA
0 deg AoA
10% Ground Clearance
20% Ground Clearance
Freestream
Outboard Location (o/c)
Inboard Location (i/c)
Drag (Cd)

10% Deflection Efficiency		
0 deg AoA	4 deg AoA	8 deg AoA
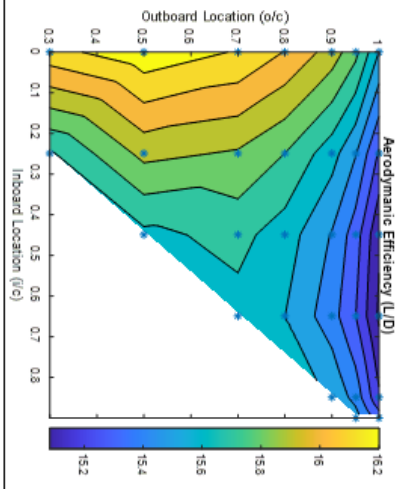	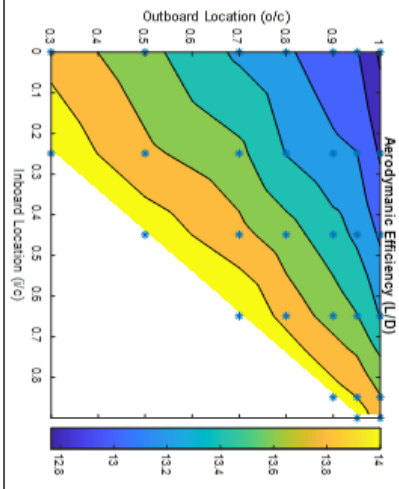	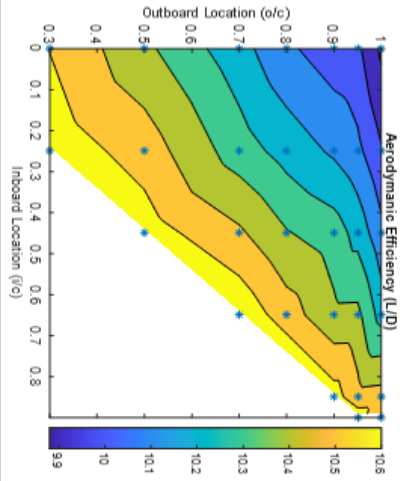
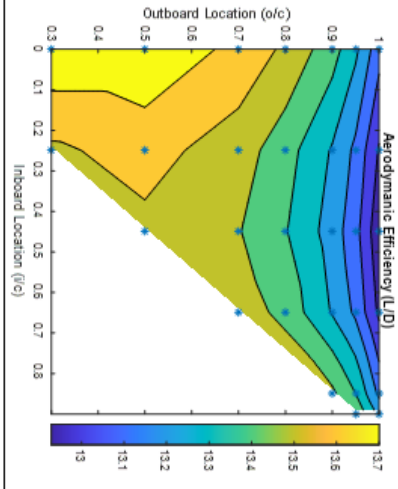	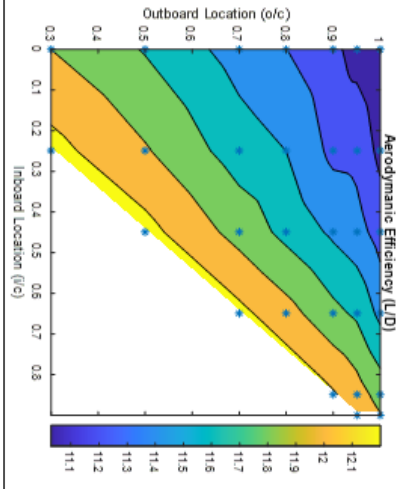	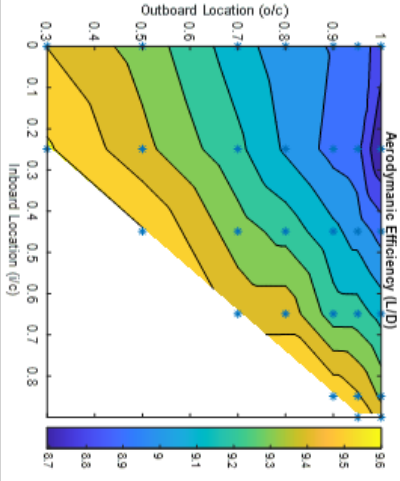
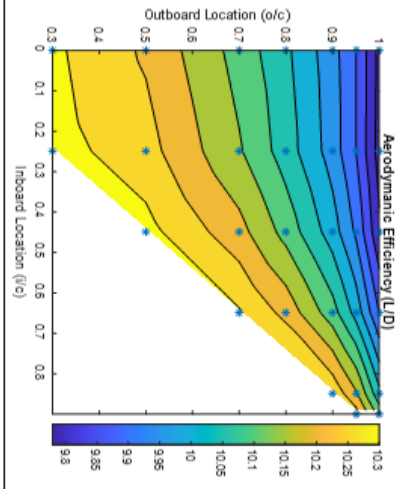	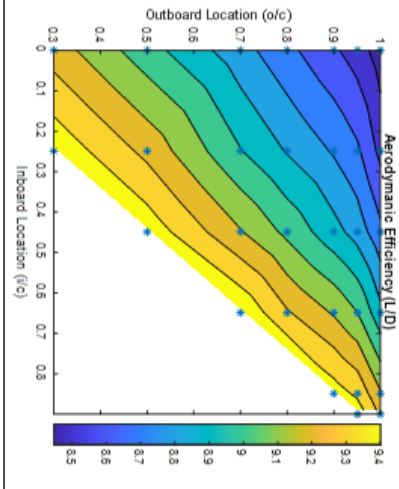	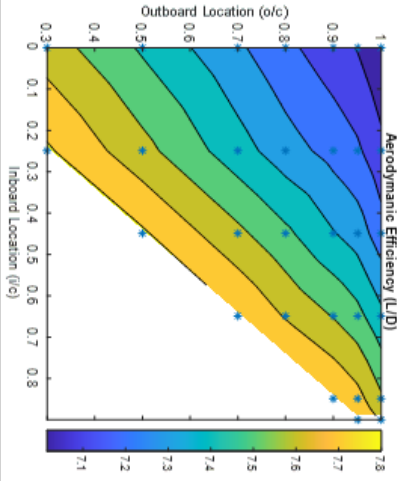

10% Ground Clearance

20% Ground Clearance

Freestream

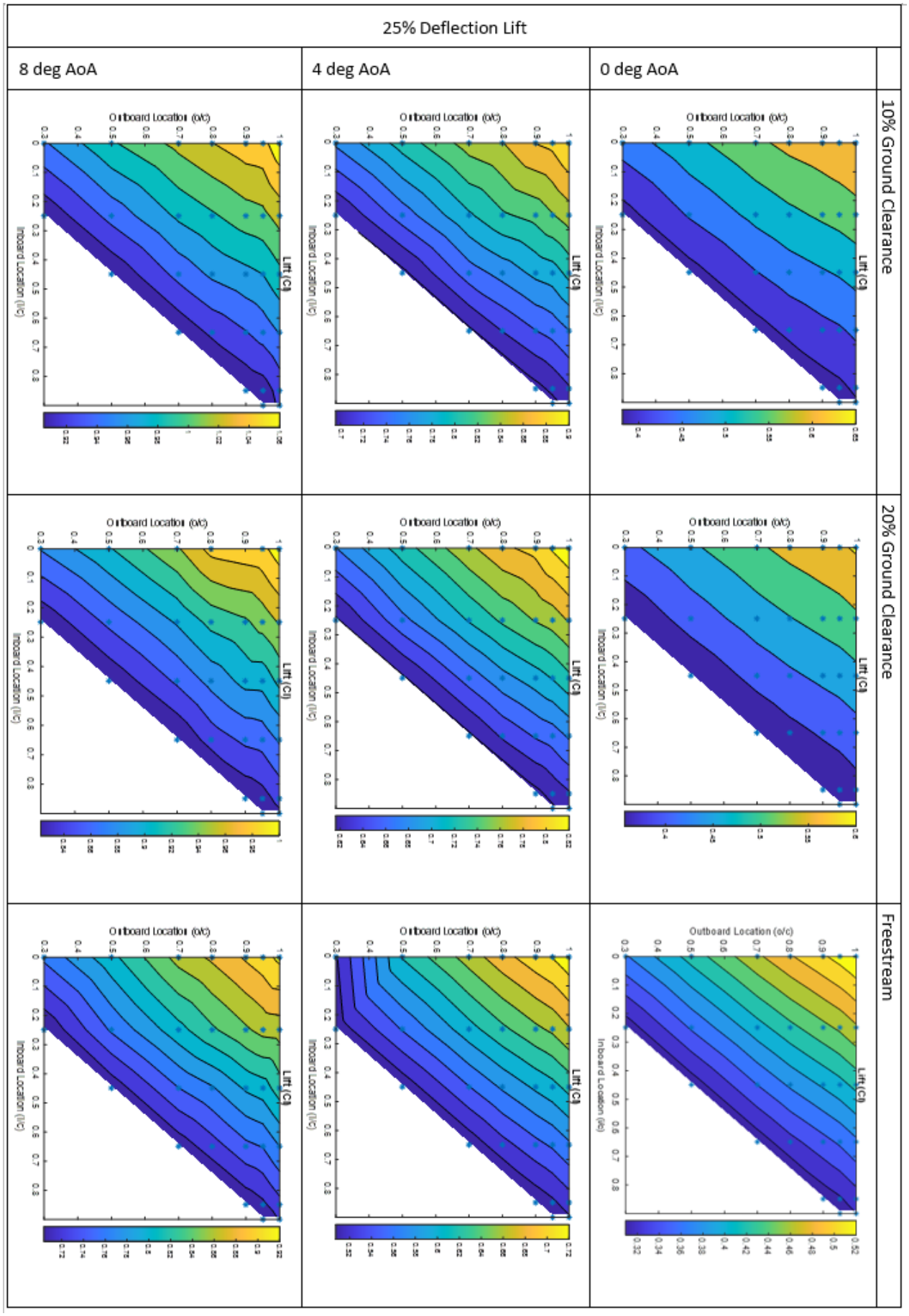
25% Deflection Lift
8 deg AoA
4 deg AoA
0 deg AoA
10% Ground Clearance
20% Ground Clearance
Freestream
Outboard Location (o/c)
Inboard Location (i/c)
Lift (Cl)

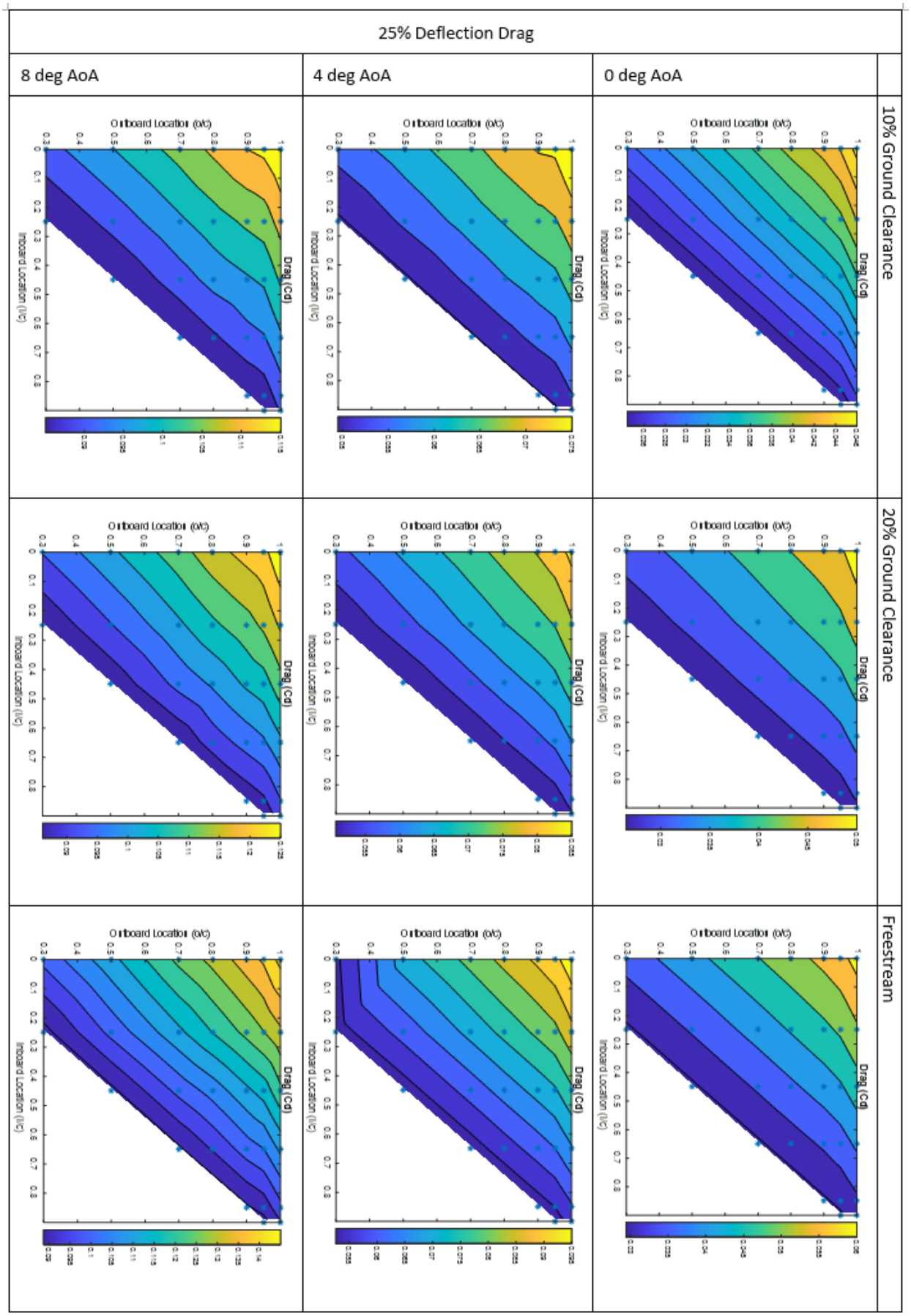
25% Deflection Drag
8 deg AoA
4 deg AoA
0 deg AoA
10% Ground Clearance
20% Ground Clearance
Freestream
Outboard Location (y/c)
Inboard Location (l/c)
Drag (Cd)

Appendix A

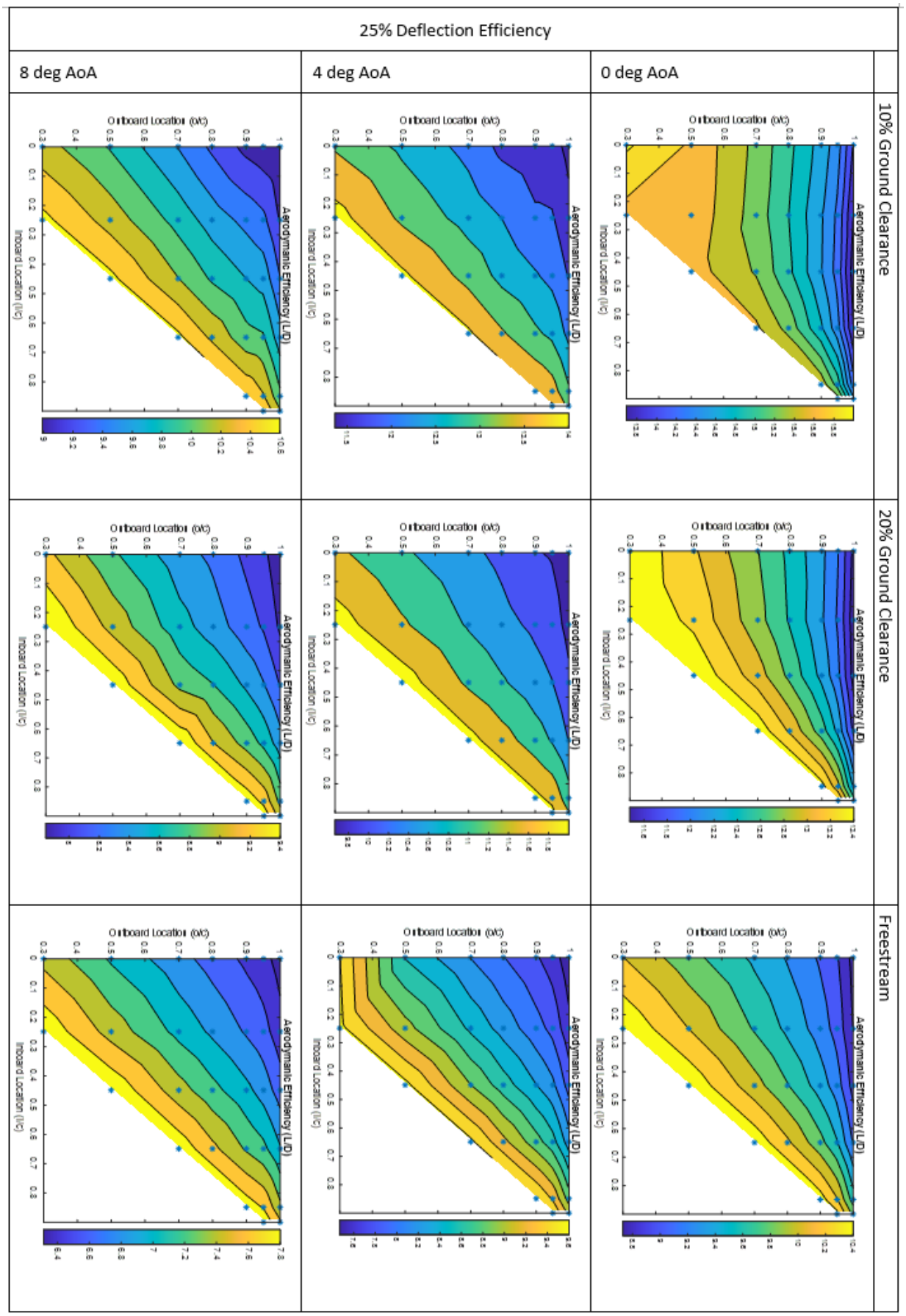
25% Deflection Efficiency
8 deg AoA
4 deg AoA
0 deg AoA
10% Ground Clearance
20% Ground Clearance
Freestream
Outboard Location (b/2)
Inboard Location (b/c)
Aerodynamic Efficiency (L/D)

A.6 UAV Battery and Power System Data

Battery temp and age parameter	n_{batt}	1.3
Combined total efficiency of power system	η	0.5
Battery Voltage	V	22.2v
Battery Capacity	C_{batt}	6-amp hours

Bibliography

Abdessemed, C. (2020). *Dynamic Mesh Framework for Morphing Wings CFD - User Defined Function* (Issue May).

Abdessemed, C., Bouferrouk, A., & Yao, Y. (2021). Aerodynamic and Aeroacoustic Analysis of a Harmonically Morphing Airfoil Using Dynamic Meshing. *Acoustics*, *3*(1), 177–199. https://doi.org/10.3390/acoustics3010013

Abdessemed, C., Bouferrouk, A., & Yao, Y. (2022). Effects of an Unsteady Morphing Wing with Seamless Side-Edge Transition on Aerodynamic Performance. *Energies*, *15*(3). https://doi.org/10.3390/en15031093

Abdessemed, C., Yao, Y., Bouferrouk, A., & Narayan, P. (2019). Flow Response to Rapid Morphing Flap Deflection. *54th 3AF International Conference on Applied Aerodynamics*, *March*, 1–10. https://uwe-repository.worktribe.com/output/850073

Abishek, R., Gulati, B., & Sinha, J. (2016). *Computational Analysis for Drag Reduction Using FishBAC Morphing Concept Fish Bone Active Camber Concept (FishBAC)* (Issue January).

Abramowski, T. (2007). Numerical investigation of airfoil in ground proximity. *Journal of Theoretical and Applied Mechanics*, *45*(January 2007), 425–436.

Ahmed, M. R., & Sharma, S. D. (2005). An investigation on the aerodynamics of a symmetrical airfoil in ground effect. *Experimental Thermal and Fluid Science*, *29*(6), 633–647. https://doi.org/10.1016/j.expthermflusci.2004.09.001

Ai, Q., Kamliya Jawahar, H., & Azarpeyvand, M. (2016). *Experimental investigation of aerodynamic performance of airfoils fitted with morphing trailing edges*. https://doi.org/10.2514/6.2016-1563

Ajaj, R. M., Friswell, M. I., Saavedra Flores, E. I., Little, O., & Isikveren, A. T. (2012). Span morphing: A conceptual design study. *Collection of Technical Papers - AIAA/ASME/ASCE/AHS/ASC Structures, Structural Dynamics and Materials Conference*, *January 2015*. https://doi.org/10.2514/6.2012-1510

Albring, T. A., Sagebaum, M., & Gauger, N. R. (2015). Development of a Consistent Discrete Adjoint Solver in an Evolving Aerodynamic Design Framework. In *16th AIAA/ISSMO Multidisciplinary Analysis and Optimization Conference*. American Institute of Aeronautics and Astronautics. https://doi.org/doi:10.2514/6.2015-3240

Bibliography

Alfonsi, G. (2009). Reynolds-averaged Navier-Stokes equations for turbulence modeling. *Applied Mechanics Reviews*, *62*(4), 1–20. https://doi.org/10.1115/1.3124648

Alulema, V. H., Valencia, E. A., Pillajo, D., Jacome, M., Lopez, J., & Ayala, B. (2020). Degree of Deformation and Power Consumption of Compliant and Rigid-linked Mechanisms for Variable-Camber Morphing Wing UAVs. In *AIAA Propulsion and Energy 2020 Forum*. American Institute of Aeronautics and Astronautics. https://doi.org/doi:10.2514/6.2020-3958

Andersen, A., Bohr, T., Schnipper, T., & Walther, J. H. (2017). Wake structure and thrust generation of a flapping foil in two-dimensional flow. *Journal of Fluid Mechanics*, *812*, R4. https://doi.org/10.1017/jfm.2016.808

Anderson, J. (2007). *Fundamentals of Aerodynamics* (4th Editio). McGraw Hill.

Anderson, J. D. (1999). *Aircraft perfmance and design* (Tata McGra, Vol. 358, Issue 207). McGraw Hill. https://soaneemrana.org/onewebmedia/AIRCRAFT PERFORMANCE AND DESIGN1.pdf

Anderson, J. D. (2008). *Introduction to Flight* (Sixth). McGraw Hill.

ANSYS. (2009). *Spalart-Allmaras Model Section 4.3*. ANSYS User Guide. https://www.afs.enea.it/project/neptunius/docs/fluent/html/th/node49.htm

Bae, J. S., Seigler, T. M., & Inman, D. J. (2005). Aerodynamic and static aeroelastic characteristics of a variable-span morphing wing. *Journal of Aircraft*, *42*(2), 528–534. https://doi.org/10.2514/1.4397

Baik, Y. S., Rausch, J., Bernal, L., Shyy, W., & Ol, M. (2010). Experimental Study of Governing Parameters in Pitching and Plunging Airfoil at Low Reynolds Number. In *48th AIAA Aerospace Sciences Meeting Including the New Horizons Forum and Aerospace Exposition*. American Institute of Aeronautics and Astronautics. https://doi.org/doi:10.2514/6.2010-388

Bashir, M., Lee, C. F., & Rajendran, P. (2017). Shape memory materials and their applications in aircraft morphing: An introspective study. *ARPN Journal of Engineering and Applied Sciences*, *12*(19), 5434–5446.

Bear, J. (1972). *Dynamics of Fluids in Porous Media*. American Elsevier.

Beaverstock, C. S., Woods, B. K. S., Fincham, J. H. S. M., & Friswell, M. I. (2015). Performance comparison between optimised camber and span for a morphing wing. *Aerospace*, *2*(3), 524–554. https://doi.org/10.3390/aerospace2030524

Benek, J., Buning, P., & Steger, J. (1985). A 3-D chimera grid embedding technique. In *7th*

Computational Physics Conference. American Institute of Aeronautics and Astronautics. https://doi.org/doi:10.2514/6.1985-1523

Bhadeshia, H. K. D. H. (2017). Twins & Martensite. In *Part IB Materials Science & Metallurgy* (pp. 53–58).

Biancolini, P. M. E., & Groth, C. (2014). *An Efficient Approach to Simulating Ice Accretion on 2D and 3D Airfoils*. 1–6.

Bishay, P. L., Burg, E., Akinwunmi, A., Phan, R., & Sepulveda, K. (2019). Development of a new span-morphing wing core design. *Designs*, *3*(1), 1–11. https://doi.org/10.3390/designs3010012

Blondeau, J., Richeson, J., & Pines, D. (2003). Design of a Morphing Aspect Ratio Wing Using an Inflatable Telescoping Spar. In *44th AIAA/ASME/ASCE/AHS/ASC Structures, Structural Dynamics, and Materials Conference*. American Institute of Aeronautics and Astronautics. https://doi.org/doi:10.2514/6.2003-1718

Bofeng, X., Junheng, F., Qing, L., Chang, X., Zhenzhou, Z., & Yue, Y. (2018). Aerodynamic performance analysis of a trailing-edge flap for wind turbines. *Journal of Physics: Conference Series*, *1037*(2), 0–8. https://doi.org/10.1088/1742-6596/1037/2/022020

Boudis, A., Bayeul-Lainé, A. C., Benzaoui, A., Oualli, H., Guerri, O., & Coutier-Delgosha, O. (2019). Numerical Investigation of the Effects of Nonsinusoidal Motion Trajectory on the Propulsion Mechanisms of a Flapping Airfoil. *Journal of Fluids Engineering, Transactions of the ASME*, *141*(4). https://doi.org/10.1115/1.4042175

Bowman, J., Sanders, B., & Weisshaar, T. (2002). Evaluating the Impact of Morphing Technologies on Aircraft Performance. In *43rd AIAA/ASME/ASCE/AHS/ASC Structures, Structural Dynamics, and Materials Conference*. American Institute of Aeronautics and Astronautics. https://doi.org/doi:10.2514/6.2002-1631

Bulletin, I. (2010). *VLM Tool for IDS Integration C ă t ă lin NAE INCAS – National Institute for Aerospace Research*. *2*(1), 37–48. https://doi.org/10.13111/2066-8201.20

Cella, U. (2012). *Aeroelastic Analysis of Aircraft Wind-Tunnel Model Coupling*. *49*(2). https://doi.org/10.2514/1.C031293

Cerra, D. F., & Katz, J. (2008). Design of a high-lift, thick airfoil for unmanned aerial vehicle applications. *Journal of Aircraft*, *45*(5), 1789–1793. https://doi.org/10.2514/1.36924

Chang, P. K. (1970). Characteristics of Separated Flows. *Separation of Flow*, 272–335.

https://doi.org/10.1016/b978-0-08-013441-3.50011-3

Chase, N., Rademacher, M., Goodman, E., Averill, R., & Sidhu, R. (2009). *A Benchmark Study of Multi-Objective Optimization Methods (BMK-3021)*. *November 2014*, 1–24.

Chati, Y. S., & Balakrishnan, H. (2018). Modeling of Aircraft Takeoff Weight Using Gaussian Processes. *Journal of Air Transportation*, *26*(2), 70–79. https://doi.org/10.2514/1.D0099

Chaturvedi, I., Jandyal, A., Wazir, I., Raina, A., & Ul Haq, M. I. (2022). Biomimetics and 3D printing - Opportunities for design applications. *Sensors International*, *3*(July), 100191. https://doi.org/10.1016/j.sintl.2022.100191

Chinnassamy, P., & Chen, Y. (2005). Application of Computational Fluid Dynamics on Smart Wing Design. In *43rd AIAA Aerospace Sciences Meeting and Exhibit*. American Institute of Aeronautics and Astronautics. https://doi.org/doi:10.2514/6.2005-637

Cho, M. (2021). Aerodynamics and the role of the earth's electric field in the spiders' ballooning flight. *Journal of Comparative Physiology A*, *207*. https://doi.org/10.1007/s00359-021-01474-6

Chow, J. S., Zilliac, G. G., & Bradshaw, P. (1997). Mean and Turbulence Measurements in the Near Field of a Wingtip Vortex. *AIAA Journal*, *35*(10), 1561–1567. https://doi.org/10.2514/2.1

Ciffone, D. L., & Pedley, B. (1979). Measured wake-vortex characteristics of aircraft in ground effect. *Journal of Aircraft*, *16*(2), 102–109. https://doi.org/10.2514/3.58491

Coleman, H., & Members, C. (2009). *ASME V&V 20-2009 Standard for Verification and Validation in Computational Fluid Dynamics and Heat Transfer (V&V20 Committee Chair and principal author)*. ASME.

D.Narasimhamurthy, V. (2004). *Unsteady-RANS Simulation of Turbulent Trailing-Edge Flow*. CHALMERS UNIVERSITY OF TECHNOLOGY.

Daynes, S., & Weaver, P. M. (2012). A morphing trailing edge device for a wind turbine. *Journal of Intelligent Material Systems and Structures*, *23*(6), 691–701. https://doi.org/10.1177/1045389X12438622

De Breuker, R., Abdalla, M., Gürdal, Z., & Lindner, D. (2007). Energy-based aeroelastic analysis of a morphing wing. *Modeling, Signal Processing, and Control for Smart Structures 2007*, *6523*(June 2015), 652308. https://doi.org/10.1117/12.716731

Detrick, M., Kwak, S.-K., & Yoon, H.-S. (2006). Morphing flight control surface for advanced flight performance. *Smart Structures and Materials 2006: Smart Structures and Integrated*

Systems, *6173*(April 2006), 61730A. https://doi.org/10.1117/12.658793

Dhileep, K., Kumar, D., Ghosh, S., Ali, S. F., & Arockiarajan, A. (2020). Numerical study of camber morphing in naca0012 airfoil. *Aiaa Aviation 2020 Forum*, *1 PartF*(June). https://doi.org/10.2514/6.2020-2781

Dong, L., Choi, K. S., Mao, X., & Wang, Y. (2022). Development and interaction of vortices over a very low aspect-ratio wing under pitch-up motion. *Journal of Fluid Mechanics*, *943*, 1–25. https://doi.org/10.1017/jfm.2022.451

Dougherty, F. C., Benek, J. A., & Steger, J. L. (1985). *On Applications of Chimera Grid Schemes to Store Separation*. 14. http://purl.access.gpo.gov/GPO/LPS92533

Elzey, D. M., Sofia, A. Y. N., & Wadley, H. N. G. (2005). A shape memory-based multifunctional structural actuator panel. *International Journal of Solids and Structures*, *42*(7), 1943–1955. https://doi.org/10.1016/j.ijsolstr.2004.05.034

Feszty, D., & Jakubík, T. (1998). 11 . Errors and Uncertainty in Cfd. *NGM_JF006_1: Computational Fluid Dynamics*, 1–16.

Fincham, J. H. S., & Friswell, M. I. (2015). Aerodynamic optimisation of a camber morphing aerofoil. *Aerospace Science and Technology*, *43*, 245–255. https://doi.org/10.1016/j.ast.2015.02.023

Fink, M. P., & Lastinger, J. L. (1986). AERODYNAMIC CHARACTERISTICS OF LOW - ASPECT -RATIO WINGS IN CLOSE PROXIMITY TO THE GROUND. *Biologia Centrali-Americaa*, *2*, v–413.

Flaig, J. (2019). *A different kettle of fish: is Airfish 8 plane-boat hybrid a marine travel game-changer?* https://www.imeche.org/news/news-article/a-different-kettle-of-fish-is-airfish-8-plane-boat-hybrid-a-marine-travel-game-changer

Florian, M. (1993). Zonal Two Equation k-w, Turbulence Models for Aerodynamic Flows. *AIAA*.

Frommer, J., & Crossley, W. (2005). Enabling Continuous Optimization for Sizing Morphing Aircraft Concepts. In *43rd AIAA Aerospace Sciences Meeting and Exhibit*. American Institute of Aeronautics and Astronautics. https://doi.org/doi:10.2514/6.2005-816

Gern, F. H., Inman, D. J., & Kapania, R. K. (2002). Structural and Aeroelastic Modeling of General Planform Wings with Morphing Airfoils. *AIAA Journal*, *40*(4), 628–637. https://doi.org/10.2514/2.1719

Greenblatt, D., & Wygnanski, I. J. (2000). Control of flow separation by periodic excitation. *Progress in Aerospace Sciences*, *36*(7), 487–545. https://doi.org/10.1016/S0376-

0421(00)00008-7

Grigorie, T. L., Botez, R. M., & Popov, A. V. (2015). How the Airfoil Shape of a Morphing Wing Is Actuated and Controlled in a Smart Way. *Journal of Aerospace Engineering*, *28*(1), 04014043. https://doi.org/10.1061/(asce)as.1943-5525.0000372

Grigorie, T. L., Popov, A. V., Botez, R. M., Mébarki, Y., & Mamou, M. (2009). Modeling and testing of a morphing wing in open loop architecture. *Proceedings of the IASTED International Conference on Identification, Control, and Applications, ICA 2009*, *August*, 22–30.

Groves-Raines, M. M., Araujo-Estrada, S. A., Mohamed, A., Watkins, S., & Windsor, S. P. (2022). Wind tunnel testing of an avian-inspired morphing wing with distributed pressure sensing. *2022 International Conference on Unmanned Aircraft Systems, ICUAS 2022*, 290–299. https://doi.org/10.1109/ICUAS54217.2022.9836045

Hahn, D., Scholz, P., & Radespiel, R. (2012). Vortex generation in a low speed wind tunnel and vortex interactions with a high-lift airfoil. *30th AIAA Applied Aerodynamics Conference 2012*, *June*, 1487–1504. https://doi.org/10.2514/6.2012-3024

Halloran, M., & O'Meara, S. (1999). *Wing in Ground Effect Review*. 5.

Harvey, J. . K., & Perry, F. J. (1971). *Flowfield Produced by Trailing Vortices in the Vicinity of the Ground*. *August*, 1659–1660.

Healy, F., Cheung, R., Neofet, T., Lowenberg, M., Rezgui, D., Cooper, J., Castrichini, A., & Wilson, T. (2022). Folding Wingtips for Improved Roll Performance. *Journal of Aircraft*, *59*(1), 15–28. https://doi.org/10.2514/1.C036372

Helmbold, H. B. (1942). Der unverwundene ellipsenflugel als tragende flanche. *Der Deutch Luftfahrtforsch*, 1942.

Hiemcke, C. (1994). *Design of a wing section in ground effect : application to high speed ground transportation*.

Houzeaux, G., Eguzkitza, B., Aubry, R., Owen, H., & Vázquez, M. (2014). A Chimera method for the incompressible Navier-Stokes equations. *International Journal for Numerical Methods in Fluids*, *75*(3), 155–183. https://doi.org/10.1002/fld.3886

Hu, H., Clemons, L., & Igarashi, H. (2011). An experimental study of the unsteady vortex structures in the wake of a root-fixed flapping wing. *Experiments in Fluids*, *51*(2), 347–359. https://doi.org/10.1007/s00348-011-1052-z

Hui, Z., Zhang, Y., & Chen, G. (2019). Aerodynamic performance investigation on a morphing

unmanned aerial vehicle with bio-inspired discrete wing structures. *Aerospace Science and Technology*, *95*, 105419. https://doi.org/10.1016/j.ast.2019.105419

Irving, F. G. (1966). Preliminary Considerations and Definitions. *An Introduction to the Longitudinal Static Stability of Low-Speed Aircraft*, 6–25. https://doi.org/10.1016/b978-1-4832-0019-4.50006-5

Jacob, J., & Smith, S. (2009). Design Limitations of Deployable Wings for Small Low Altitude UAVs. In *47th AIAA Aerospace Sciences Meeting including The New Horizons Forum and Aerospace Exposition*. American Institute of Aeronautics and Astronautics. https://doi.org/doi:10.2514/6.2009-745

Jamei, S., Maimun, A., & Azwadi, N. (2018). Ground boundary layers effect on aerodynamic coefficients of a compound wing with respect to design parameters. *Ocean Engineering*, *164*(April 2017), 228–237. https://doi.org/10.1016/j.oceaneng.2018.06.061

Jamei, S., Maimun, A., Mansor, S., Azwadi, N., & Priyanto, A. (2012). *Numerical Investigation on Aerodynamic Characteristics of a Compound Wing-in-Ground Effect*. *March 2015*. https://doi.org/10.2514/1.C031627

Jameson, A., Austin, F., Rossi, M., Van Nostrand, W. C., & Knowles, G. (1994). Static shape control for adaptive wings. *AIAA Journal*, *32*(9), 1895–1901. https://pdfs.semanticscholar.org/db22/16d1bd93692bd5bc7743e8f84b8c41caec45.pdf

Jasa, J. P., Hwang, J. T., & Martins, J. R. R. A. (2018). Design and Trajectory Optimization of a Morphing Wing Aircraft. In *2018 AIAA/ASCE/AHS/ASC Structures, Structural Dynamics, and Materials Conference*. American Institute of Aeronautics and Astronautics. https://doi.org/doi:10.2514/6.2018-1382

Je, J. B. (1995). Development and Application of WIG in Russia. *MARIC*, *No.1*.

Jeong, J., & Bae, J. S. (2022). Wind tunnel & Flight Test of VCCS Morphing UAV. *2022 International Conference on Unmanned Aircraft Systems, ICUAS 2022*, 1424–1431. https://doi.org/10.1109/ICUAS54217.2022.9836192

Jodin, G., Motta, V., Scheller, J., Duhayon, E., Döll, C., Rouchon, J. F., & Braza, M. (2017). Dynamics of a hybrid morphing wing with active open loop vibrating trailing edge by time-resolved PIV and force measures. *Journal of Fluids and Structures*, *74*, 263–290. https://doi.org/10.1016/j.jfluidstructs.2017.06.015

Jones, G., Santer, M., Debiasi, M., & Papadakis, G. (2018). Control of flow separation around an airfoil at low Reynolds numbers using periodic surface morphing. *Journal of Fluids and*

Structures, *76*, 536–557. https://doi.org/10.1016/j.jfluidstructs.2017.11.008

Jones, G., Santer, M., & Papadakis, G. (2018). Control of low Reynolds number flow around an airfoil using periodic surface morphing: A numerical study. *Journal of Fluids and Structures*, *76*, 95–115. https://doi.org/10.1016/j.jfluidstructs.2017.09.009

Jung, J. H., Kim, M. J., Yoon, H. S., Hung, P. A., Chun, H. H., & Park, D. W. (2012). Endplate effect on aerodynamic characteristics of threedimensional wings in close free surface proximity. *International Journal of Naval Architecture and Ocean Engineering*, *4*(4), 477–487. https://doi.org/10.2478/ijnaoe-2013-0112

Jung, K. H., Chunn, H. H., Kim, H. J., Chun, H. H., & Kim, H. J. (2008). Experimental investigation of wing-in-ground effect with a NACA6409 section. *Journal of Marine Science and Technology*, *13*(4), 317–327. https://doi.org/10.1007/s00773-008-0015-4

Kan, Z., Li, D., Xiang, J., & Cheng, C. (2020). Delaying stall of morphing wing by periodic trailing-edge deflection. *Chinese Journal of Aeronautics*, *33*(2), 493–500. https://doi.org/10.1016/j.cja.2019.09.028

Kang, W., Xu, M., Yao, W., & Zhang, J. (2020). Lock-in mechanism of flow over a low-Reynolds-number airfoil with morphing surface. *Aerospace Science and Technology*, *97*, 105647. https://doi.org/10.1016/j.ast.2019.105647

Kang, W., Zhang, J. zhong, Lei, P. fei, & Xu, M. (2014). Computation of unsteady viscous flow around a locally flexible airfoil at low Reynolds number. *Journal of Fluids and Structures*, *46*, 42–58. https://doi.org/10.1016/j.jfluidstructs.2013.12.010

Kao, K. H., & Liou, M. S. (1997). Application of Chimera/unstructured hybrid grids for conjugate heat transfer. *AIAA Journal*, *35*(9), 1472–1478. https://doi.org/10.2514/2.270

Katam, V., LeBeau, R., & Jacob, J. (2005). Simulation of Separation Control on a Morphing Wing with Conformal Camber. In *35th AIAA Fluid Dynamics Conference and Exhibit*. American Institute of Aeronautics and Astronautics. https://doi.org/doi:10.2514/6.2005-4880

Katz, Y., Nishri, B., & Wygnanski, I. (1989). The delay of turbulent boundary layer separation by oscillatory active control. *Physics of Fluids A*, *1*(2), 179–181. https://doi.org/10.1063/1.857555

Kilian, L., Shahid, F., Zhao, J. S., & Nayeri, C. N. (2022). Bioinspired morphing wings: Mechanical design and wind tunnel experiments. *Bioinspiration and Biomimetics*, *17*(4). https://doi.org/10.1088/1748-3190/ac72e1

Ko, S. H., Bae, J. S., & Rho, J. H. (2014). Development of a morphing flap using shape memory alloy actuators: The aerodynamic characteristics of a morphing flap. *Smart Materials and Structures*, *23*(7). https://doi.org/10.1088/0964-1726/23/7/074015

Koh, J. S. (2018). Design of shape memory alloy coil spring actuator for improving performance in cyclic actuation. *Materials*, *11*(11). https://doi.org/10.3390/ma11112324

Koochesfahani, M. M. (1987). Vortical patterns in the wake of an oscillating airfoil. *AIAA Journal*, *27*, 1200–1205.

Koochesfahani, M. M. (1989). Vortical patterns in the wake of an oscillating airfoil. *AIAA Journal*, *27*(9), 1200–1205. https://doi.org/10.2514/3.10246

Kumar, A., Das, T., & Samad, A. (2022). Effect of blade skew, endplate and casing grooveon the aerodynamic performance of Wells turbinefor OWC: a review. *Nature*, *388*, 539–547.

Kundu, P. K., Cohen, I. M., & Dowling, D. R. (2016). Fluid Mechanics (Sixth Edition). In *Fluid Mechanics (Sixth Edition)* (Sixth Edit). Academic Press. https://doi.org/https://doi.org/10.1016/B978-0-12-405935-1.01001-7

La, S., Joe, W. Y., Akbar, M., & Alsaidi, B. (2018). Surveys on Skin Design for Morphing Wing Aircraft: Status and Challenges. *2018 AIAA Aerospace Sciences Meeting*. https://doi.org/doi:10.2514/6.2018-0315

Lamorte, N., & Friedmann, P. (2012). Hypersonic Aeroelastic Stability Boundary Computations Using Radial Basis Functions for Mesh Deformation. In *18th AIAA/3AF International Space Planes and Hypersonic Systems and Technologies Conference*. American Institute of Aeronautics and Astronautics. https://doi.org/doi:10.2514/6.2012-5943

Lamorte, N., & Friedmann, P. P. (2013). Aerothermoelastic and Aeroelastic Studies of Hypersonic Vehicles using CFD. In *54th AIAA/ASME/ASCE/AHS/ASC Structures, Structural Dynamics, and Materials Conference*. American Institute of Aeronautics and Astronautics. https://doi.org/doi:10.2514/6.2013-1591

Leary, M., Schiavone, F., & Subic, A. (2010). Lagging for control of shape memory alloy actuator response time. *Materials and Design*, *31*(4), 2124–2128. https://doi.org/10.1016/j.matdes.2009.10.010

Lee, J., Han, C. S., & Bae, C. H. (2010). Influence of wing configurations on aerodynamic characteristics of wings in ground effect. *Journal of Aircraft*, *47*(3), 1030–1040. https://doi.org/10.2514/1.46703

Bibliography

Lee, T., & Gerontakos, P. (2004). Investigation of flow over an oscillating airfoil. In *Journal of Fluid Mechanics* (Vol. 512, pp. 313–341). https://doi.org/10.1017/S0022112004009851

Levy, Y. (2001). Numerical simulation of dynamically deforming aircraft configurations using overset grids. *Journal of Aircraft*, *38*(2), 349–354. https://doi.org/10.2514/2.2768

Li, D., Zhao, S., Da Ronch, A., Xiang, J., Drofelnik, J., Li, Y., Zhang, L., Wu, Y., Kintscher, M., Monner, H. P., Rudenko, A., Guo, S., Yin, W., Kirn, J., Storm, S., & Breuker, R. De. (2018). A review of modelling and analysis of morphing wings. *Progress in Aerospace Sciences*, *100*(September 2017), 46–62. https://doi.org/10.1016/j.paerosci.2018.06.002

Lim, J. W., McAlister, K. W., & Johnson, W. (2009). Hover performance correlation for Full-Scale and model-scale coaxial rotors. *Journal of the American Helicopter Society*, *54*(3), 0320051–03200514. https://doi.org/10.4050/JAHS.54.032005

Lissaman, P. B. S. (1983). Low-reynolds-number airfoils. *Annual Reviews Fluid Mechanics*, 223–239.

Liu, L., Friedmann, P. P., Bagnoud, F. X., & Padthe, A. K. (2008). An approximate unsteady aerodynamic model for flapped airfoils including improved drag predictions. *34th European Rotorcraft Forum 2008, ERF34*, *2*(July 2018), 1037–1081.

Lu, A., Tremblay-Dionne, V., & Lee, T. (2019). Experimental Study of Aerodynamics and Wingtip Vortex of a Rectangular Wing in Flat Ground Effect. *Journal of Fluids Engineering, Transactions of the ASME*, *141*(11), 1–11. https://doi.org/10.1115/1.4043593

Lund, T. S. (2003). mathematics with The Use of Explicit Filters Large Eddy Simulation. *International Journal of Computers & Mathematics with Applications*, *46*, 603–616. https://doi.org/10.1016/S0898-1221(03)00246-3

Lyu, Z., & Martins, J. (2015). *Aerodynamic Shape Optimization of an Adaptive Morphing Trailing-Edge Wing*. *52*(6). https://doi.org/10.2514/1.C033116

Macaraeg, M. (1998). Fundamental investigations of airframe noise. In *4th AIAA/CEAS Aeroacoustics Conference*. American Institute of Aeronautics and Astronautics. https://doi.org/doi:10.2514/6.1998-2224

Madan, A., Gupta, V. K., & Jain, A. K. (2022). Semi-Active Control of Building Frames subjected to Earthquakes using Smart Tendons composed of Shape Memory Alloys. *Proceedings of the 7th International Conference on Civil, Structural and Transportation Engineering (ICCSTE'22)*, *162*, 1–9. https://doi.org/10.11159/iccste22.162

Marco, P., Biancolini, E., & Groth, C. (2013). *Use of RBF Morph mesh morphing for the estimation of airfoil performances in presence of ice profiles*. 1–7.

Maries, A., Abedul Haque, M., Yilmaz, S. L., Nik, M. B., & Marai, G. E. (2012). Interactive exploration of stress tensors used in computational turbulent combustion. *Mathematics and Visualization*, *0*(202519), 137–156. https://doi.org/10.1007/978-3-642-27343-8_7

Martins, J. R. R. . (2016). Fuel Burn Reduction Through Wing Morphing. *Encyclopedia of Aerospace Engineering*, *May 2016*, 1–7. https://doi.org/10.1002/9780470686652.eae1007

McCormick, B. W. (1995). *Aerodynamics, aeronautics, and flight mechanics* (Second). Wiley.

Meskell, C., & Pellegrino, A. (2019). Vortex shedding lock-in due to pitching oscillation of a wind turbine blade section at high angles of attack. *International Journal of Aerospace Engineering*, *2019*(Viv). https://doi.org/10.1155/2019/6919505

Meyer, P., Traub, H., & Hühne, C. (2022). Actuated adaptive wingtips on transport aircraft: Requirements and preliminary design using pressure-actuated cellular structures. *Aerospace Science and Technology*, *128*, 107735. https://doi.org/10.1016/j.ast.2022.107735

Molland, A. F., & Turnock, S. R. (2007). *Marine Rudders and Control Surfaces (Principles, Data, Design and Applications)*. Butterworth-Heinemann. https://doi.org/https://doi.org/10.1016/B978-0-7506-6944-3.X5000-8

Molland, A. F., Turnock, S. R., & Hudson, D. A. (2017, August 16). *Physical Components of Hull Resistance*. Ship Resistance and Propulsion; Cambridge University Press. https://doi.org/10.1017/9781316494196.005

Monner, H. P., Breitbach, E., Bein, T., & Hanselka, H. (2000). Design aspects of the adaptive wing - the elastic trailing edge and the local spoiler bump. *Aeronautical Journal*, *104*(1032), 89–95.

Moosavian, A., Xi, F., & Hashemi, S. M. (2013). Design and motion control of fully variable morphing wings. *Journal of Aircraft*, *50*(4), 1189–1201. https://doi.org/10.2514/1.C032127

Muhammad Umer, H., Maqsood, A., Riaz, R., & Salamat, S. (2020). Stability Characteristics of Wing Span and Sweep Morphing for Small Unmanned Air Vehicle: A Mathematical Analysis. *Mathematical Problems in Engineering*, *2020*. https://doi.org/10.1155/2020/4838632

Nazif, H. R., & Basirat Tabrizi, H. (2014). Applying a non-equilibrium wall function in k-ε turbulent modelling of hydrodynamic circulating flow. *Applied Mathematical Modelling*, *38*(2), 588–598. https://doi.org/10.1016/j.apm.2013.06.038

Nebylov, A. V. (2010). Principles and systems of heavy WIG-craft flight control. In *IFAC*

Proceedings Volumes (Vol. 43, Issue 15). IFAC. https://doi.org/10.3182/20100906-5-JP-2022.00019

Nirooei, M. (2018). Aerodynamic and static stability characteristics of airfoils in extreme ground effect. *Proceedings of the Institution of Mechanical Engineers, Part G: Journal of Aerospace Engineering*, *232*(6), 1134–1148. https://doi.org/10.1177/0954410017708212

Ockfen, A. E., & Matveev, K. I. (2009). Aerodynamic characteristics of NACA 4412 airfoil section with flap in extreme ground effect. *International Journal of Naval Architecture and Ocean Engineering*, *1*(1), 1–12. https://doi.org/10.2478/ijnaoe-2013-0001

Park, K., Hong, C. H., Kim, K. S., & Lee, J. (2008). Effect of endplate shape on performance and stability of wings-in ground (WIG) craft. *World Academy of Science, Engineering and Technology*, *2*(11), 296–302.

Park, K., & Lee, J. (2008). Influence of endplate on aerodynamic characteristics of low-aspect-ratio wing in ground effect. *Journal of Mechanical Science and Technology*, *22*(12), 2578–2589. https://doi.org/10.1007/s12206-008-0805-y

Pecora, R. (2021). Morphing wing flaps for large civil aircraft: Evolution of a smart technology across the Clean Sky program. *Chinese Journal of Aeronautics*, *34*(7), 13–28. https://doi.org/10.1016/j.cja.2020.08.004

Pecora, R., Amoroso, F., & Lecce, L. (2012). Effectiveness of Wing Twist Morphing in Roll Control. *Journal of Aircraft*, *49*(6), 1666–1674. https://doi.org/10.2514/1.c000328

Pecora, R., Amoroso, F., & Magnifico, M. (2016). Toward the bi-modal camber morphing of large aircraft wing flaps: the CleanSky experience. *Industrial and Commercial Applications of Smart Structures Technologies 2016*, *9801*(May), 980106. https://doi.org/10.1117/12.2218415

Popov, A. V., Grigorie, L. T., Botez, R., Mamou, M., & Mébarki, Y. (2010). Closed-loop control validation of a morphing wing using wind tunnel tests. *Journal of Aircraft*, *47*(4), 1309–1317. https://doi.org/10.2514/1.47281

Profir, M. M. (2012). *Automated moving mesh techniques and re-meshing strategies in CFD applications using morphing and rigid Technical Report*. *c*.

Qu, Q., Jia, X., Wang, W., Liu, P., & Agarwal, R. K. (2014). Numerical study of the aerodynamics of a NACA 4412 airfoil in dynamic ground effect. *Aerospace Science and Technology*, *38*, 56–63. https://doi.org/10.1016/j.ast.2014.07.016

Qu, Q., Wang, W., Liu, P., & Agarwal, R. K. (2015). Airfoil aerodynamics in ground effect for wide

range of angles of attack. *AIAA Journal*, *53*(4), 1048–1061. https://doi.org/10.2514/1.J053366

Quinn, D. B., Moored, K. W., Dewey, P. A., & Smits, A. J. (2014). Unsteady propulsion near a solid boundary. *Journal of Fluid Mechanics*, *742*, 152–170. https://doi.org/10.1017/jfm.2013.659

Ramaprian, B. R., & Zheng, Y. (1997). Measurements in rollup region of the tip vortex from a rectangular wing. *AIAA Journal*, *35*(12), 1837–1843. https://doi.org/10.2514/2.59

Reisenthel, P. H., Nagib, H. M., & Koga, D. J. (1985). Control of Separated Flows Using Forced Unsteadiness. *Shear Flow Control Conference*. https://doi.org/10.2514/6.1985-556

Renken, J. (1985). Mission-adaptive wing camber control systems for transport aircraft. In *3rd Applied Aerodynamics Conference*. American Institute of Aeronautics and Astronautics. https://doi.org/doi:10.2514/6.1985-5006

Rodi, W. (1990). Experience with two-layer models combining the k-epsilon model with a one-equation model near the wall. In *29th Aerospace Sciences Meeting: Vol. 1*. https://doi.org/10.2514/6.1991-216

Rozhdestvensky, K. V. (2006). Wing-in-ground effect vehicles. *Progress in Aerospace Sciences*, *42*(3), 211–283. https://doi.org/10.1016/j.paerosci.2006.10.001

Russell, R. A., & Gorbet, R. B. (1995). Improving the response of SMA actuators. *Proceedings of 1995 IEEE International Conference on Robotics and Automation*, *3*, 2299–2304 vol.3. https://doi.org/10.1109/ROBOT.1995.525604

Samoylovitch, O., & Strelets, D. (2000). Determination of the Oswald effciency factor at the aeroplane design preliminary stage. *Elsevier*.

Scott, M. A., Montgomery, R. C., & Weston, R. P. (1998). Subsonic maneuvering effectiveness of high-performance aircraft that employ quasi-static shape change devices. *Smart Structures and Materials 1998: Industrial and Commercial Applications of Smart Structures Technologies*, *3326*(June 1998), 223. https://doi.org/10.1117/12.310637

Secanell, M., Suleman, A., & Gamboa, P. (2006). Design of a morphing airfoil using aerodynamic shape optimization. *AIAA Journal*, *44*(7), 1550–1562. https://doi.org/10.2514/1.18109

Selig, M. S., Donovan, J. F., & Fraser, D. B. (1989). *Airfoils at low speeds*. H.A. Stokely.

Shimoga, G., Kim, T., & Kim, S. (2021). *An Intermetallic NiTi-Based Shape Memory Coil Spring for Actuator Technologies*.

Bibliography

Shur, M., Spalart, P. R., Strelets, M., & Travin, A. (1999). Detached-eddy simulation of an airfoil at high angle of attack. In *Engineering Turbulence Modelling and Experiments 4* (pp. 669–678). https://doi.org/10.1016/b978-008043328-8/50064-3

Sinitsin, D. N. (1993). "Basic Summary on the Establishments of Domestic Ekranoplane and Some Problems on the Establishments of Future Passenger/Cargo Transport Ekranoplane", Proceedings of First International Conference on Ekranoplane. *Proceedings of First International Conference on Ekranoplane*.

Smith, A. M. O. (1975). High-lift aerodynamics. *Journal of Aircraft*, *12*(6), 501–530. https://doi.org/10.2514/3.59830

Sofla, A. Y. N., Elzey, D. M., & Wadley, H. N. G. (2009). Shape morphing hinged truss structures. *Smart Materials and Structures*, *18*(6). https://doi.org/10.1088/0964-1726/18/6/065012

Sofla, A. Y. N., Meguid, S. A., Tan, K. T., & Yeo, W. K. (2010). Shape morphing of aircraft wing: Status and challenges. *Materials and Design*, *31*(3), 1284–1292. https://doi.org/10.1016/j.matdes.2009.09.011

Sommerwerk, K., Michels, B., Lindhorst, K., Haupt, M. C., & Horst, P. (2016). Application of efficient surrogate modeling to aeroelastic analyses of an aircraft wing. *Aerospace Science and Technology*, *55*, 314–323. https://doi.org/10.1016/j.ast.2016.06.011

Soni, P., Anand Bharadwaj, S., & Ghosh, S. (2020). Optimization of the thrust to lift ratio using camber morphing in flapping airfoil. *AIAA Scitech 2020 Forum*, *1 PartF*(January). https://doi.org/10.2514/6.2020-1763

Spalart, P., & Allmaras, S. (1992). A One-Equation Turbulence Model for Aerodynamic Flows. In *AIAA* (Vol. 439). https://doi.org/10.2514/6.1992-439

Spalart, P. R. (2009). *Detached-Eddy Simulation* (pp. 181–201). The Annual Review of Fluid Mechanics.

Steger, J. L., & Benek, J. A. (1987). On the use of composite grid schemes in computational aerodynamics. *Computer Methods in Applied Mechanics and Engineering*, *64*(1–3), 301–320. https://doi.org/10.1016/0045-7825(87)90045-4

Svorcan, J., Wang, J. M., & Griffin, K. P. (2022). Current state and future trends in boundary layer control on lifting surfaces. *Advances in Mechanical Engineering*, *14*(7), 1–23. https://doi.org/10.1177/16878132221112161

SZODRUCH, J. (1985). The influence of camber variation on the aerodynamics of civil transport

aircraft. In *23rd Aerospace Sciences Meeting*. American Institute of Aeronautics and Astronautics. https://doi.org/doi:10.2514/6.1985-353

Szodruch, J., & Hilbig, R. (1988). *VARIABLE WING CAMBER FOR TRANSPORT AIRCRAFT*. *25*, 297–328.

Tadesse, Y., Thayer, N., & Priya, S. (2010). Tailoring the response time of shape memory alloy wires through active cooling and pre-stress. *Journal of Intelligent Material Systems and Structures*, *21*(1), 19–40. https://doi.org/10.1177/1045389X09352814

Tanida, Y. (2001). Ground Effect in Flight (Birds, Fishes and High-Speed Vehicle. *JSME International Journal Series B*, *44*(4), 481–486. https://doi.org/10.1299/jsmeb.44.481

Theodore, L. B., P. Incropera, F., P. DeWitt, D., & S. Lavine, A. (2011). *Fundamentals of Heat and Mass Transfer* (Seventh). John Wiley & Sons.

Traub, L. W. (2011). Range and endurance estimates for battery-powered aircraft. *Journal of Aircraft*, *48*(2), 703–707. https://doi.org/10.2514/1.C031027

Tremblay Dionne, V., & Lee, T. (2018). Ground effect on the aerodynamics of a naca 0015 airfoil with a plain trailing-edge flap. *Fluid Mechanics Research International Journal*, *2*(1). https://doi.org/10.15406/fmrij.2018.02.00015

Triantafyllou, M. S., Triantafyllou, G. S., & Gopalkrishnan, R. (1991). Wake mechanics for thrust generation in oscillating foils. *Physics of Fluids A*, *3*(12), 2835–2837. https://doi.org/10.1063/1.858173

Tsan-Hsing, S., William, L., Aamir, S., Zhigang, Y., & Jiang, Z. (1995). *A NEW ke EDDY VISCOSITY MODEL FOR HIGH REYNOLDS NUMBER TURBULENT FLOWS*. *24*(3), 227–238.

Tu, J., & Liu, C. (2008). *Computational Fluid Dynamics: A Practical Approach* (First). Elsevier Ltd. https://doi.org/https://doi.org/10.1016/B978-0-7506-8563-4.X5001-0

User Manual Star CCM+ 14.04.013: Vol. 14.04.013 (p. Transient Term). (2019).

Vale, J., Lau, F., & Suleman, A. (2013). Energy Efficiency Studies of A Morphing Unmanned Aircraft. *Journal of Aeronautics & Aerospace Engineering*, *02*(05). https://doi.org/10.4172/2168-9792.1000122

Versteeg, V., & Malalasekera, W. (1995). *An Introduction to Computational Fluid Dynamics, The Finite Volume Method*.

Vogt, J. W., & Barber, T. J. (2012). Ground effect phenomena about lift and downforce generating

cambered aerofoils. *International Journal of Numerical Methods for Heat and Fluid Flow*, *22*(2), 153–174. https://doi.org/10.1108/09615531211199809

Wang, C., Khodaparast, H., Friswell, M., Shaw, A., Xia, Y., & Walters, P. (2018). Development of a morphing wingtip based on compliant structures. *Journal of Intelligent Material Systems and Structures*, *29*, 1045389X1878307. https://doi.org/10.1177/1045389X18783076

Wang, J. J., Li, Y. C., & Choi, K. S. (2008). Gurney flap-Lift enhancement, mechanisms and applications. *Progress in Aerospace Sciences*, *44*(1), 22–47. https://doi.org/10.1016/j.paerosci.2007.10.001

Wang, Z., Du, L., Zhao, J., Thompson, M. C., & Sun, X. (2020). Flow-induced vibrations of a pitching and plunging airfoil. *Journal of Fluid Mechanics*, *885*. https://doi.org/10.1017/jfm.2019.996

Wei, Y., & Zhigang, Y. (2012). Aerodynamic investigation on tiltable endplate for WIG craft. *Aircraft Engineering and Aerospace Technology*, *84*(1), 4–12. https://doi.org/10.1108/00022661211194933

Weibel, R. E., & Hansman, R. J. (2005). Safety Considerations for Operation of Unmanned Aerial Vehicles in the National Airspace System. *Transportation*, *37*(March), 26–30.

Wilcox, D. C. (2006). *Turbulence Modeling for CFD* (Third). http://www.dcwindustries.com

Wilson, D. G., Berg, D. E., Barone, M. F., Berg, J. C., Resor, B. R., & Lobitz, D. W. (2009). Active aerodynamic blade control design for load reduction on large wind turbines. *European Wind Energy Conference and Exhibition 2009, EWEC 2009*, *1*(January 2009), 643–678.

Winslow, J., Otsuka, H., Govindarajan, B., & Chopra, I. (2018). Basic understanding of airfoil characteristics at low Reynolds numbers (104–105). *Journal of Aircraft*, *55*(3), 1050–1061. https://doi.org/10.2514/1.C034415

Woods, B. K. S., Bilgen, O., & Friswell, M. I. (2008). *Wind Tunnel Testing of the Fish Bone Active Camber Morphing Concept*. 1–14.

Woods, B. K. S., Fincham, J. H. S., & Friswell, M. I. (2014). *Aerodynamic Modelling of the Fish Bone Active Camber Morphing Concept*. *April 2016*.

Woods, B. K. S., Parsons, L., Coles, A. B., Fincham, J. H. S., & Friswell, M. I. (2016). Morphing elastically lofted transition for active camber control surfaces. *Aerospace Science and Technology*, *55*, 439–448. https://doi.org/10.1016/j.ast.2016.06.017

Wu, R., Liang, F., & Lin, W. (2012). Computational analysis on aerodynamics of the airfoil in ground effect. *Proceedings - 2012 International Conference on Computer Science and*

Electronics Engineering, ICCSEE 2012, *3*, 371–374. https://doi.org/10.1109/ICCSEE.2012.188

Wygnanski, I. J. (1993). *Method and Apparatus for Delaying the seperation of Flow Fram A Solid Surface*.

Xin, H. U. A., Rui, G. U., Jing-fu, J. I. N., Yi-rong, L. I. U., Qian, C., & Ying, Z. (2010). Numerical simulation and aerodynamic performance comparison between seagull aerofoil and NACA 4412 aerofoil under low Reynolds. *Advances in Natural Science*, *3*(2), 244–250.

Yang, Z.-G., Yang, W., & Jia, Q. (2010). Ground Viscous Effect on Stall of Wing in Ground Effect. *Engineering Applications of Computational Fluid Mechanics*, *4*(4), 521–531. https://doi.org/10.1080/19942060.2010.11015338

Yang, Z. Y. (2015). Large-eddy simulation: Past, present and the future. *Chinese Journal of Aeronautics*, *28*(1), 11–24. https://doi.org/10.1016/j.cja.2014.12.007

Young, J., & Lai, J. C. S. (2004). Oscillation frequency and amplitude effects on the wake of a plunging airfoil. *AIAA Journal*, *42*(10), 2042–2052. https://doi.org/10.2514/1.5070

Yu, K., Yin, W., Sun, S., Liu, Y., & Leng, J. (2009). Design and analysis of morphing wing based on SMP composite. *Industrial and Commercial Applications of Smart Structures Technologies 2009*, *7290*(May), 72900S. https://doi.org/10.1117/12.815712

Yu, Y., Li, X., Zhang, W., & Leng, J. (2007). Investigation on adaptive wing structure based on shape memory polymer composite hinge. *International Conference on Smart Materials and Nanotechnology in Engineering*, *6423*(May), 64231D. https://doi.org/10.1117/12.779394

Yu, Y., Liu, Y., & Leng, J. (2009). Design and aerodynamic characteristics of a span morphing wing. *Industrial and Commercial Applications of Smart Structures Technologies 2009*, *7290*(March 2009), 72900U. https://doi.org/10.1117/12.815675

Yun, L., Bliault, A., & Doo, J. (2010). *WIG craft and ekranoplan: Ground effect craft technology*. Springer. https://doi.org/10.1007/978-1-4419-0042-5

Zainal Abidin, Z., Tarisai Mativenga, P., & Harrison, G. (2020). Chilled Air System and Size Effect in Micro-milling of Nickel−Titanium Shape Memory Alloys. *International Journal of Precision Engineering and Manufacturing - Green Technology*, *7*(2), 283–297. https://doi.org/10.1007/s40684-019-00040-5

Zaini, H., & Ismail, N. I. (2016). A Review of Morphing Wing. *Mechanical Engineering Colloquium (MEC)*, *August*.

Zerihan, J. D. C. (2001). *An investigation into wings in ground effect*. *April*, Master's Thesis.

Bibliography

Zhang, X., Toet, W., & Zerihan, J. (2006). *Ground Effect Aerodynamics of Race Cars*. *59*(January). https://doi.org/10.1115/1.2110263